Computational Methods in Earthquake Engineering

Computational Methods in Applied Sciences

Volume 21

Series Editor

E. Oñate
International Center for Numerical Methods in Engineering (CIMNE)
Technical University of Catalunya (UPC)
Edificio C-1, Campus Norte UPC
Gran Capitán, s/n
08034 Barcelona, Spain
onate@cimne.upc.edu
www.cimne.com

For other titles published in this series, go to
www.springer.com/series/6899

Manolis Papadrakakis • Michalis Fragiadakis
Nikos D. Lagaros
Editors

Computational Methods in Earthquake Engineering

Springer

Editors
Manolis Papadrakakis
National Technical Univ. Athens
Inst. Structural Analysis &
Seismic Research
Iroon Polytechniou Str. 9
157 80 Athens
Greece
mpapadra@central.ntua.gr

Nikos D. Lagaros
National Technical Univ. Athens
Inst. Structural Analysis &
Seismic Research
Iroon Polytechniou Str. 9
157 80 Athens
Greece
nlagaros@central.ntua.gr

Michalis Fragiadakis
National Technical Univ. Athens
Inst. Structural Analysis &
Seismic Research
Iroon Polytechniou Str. 9
157 80 Athens
Greece
mfrag@mail.ntua.gr

ISSN 1871-3033
ISBN 978-94-007-0052-9 e-ISBN 978-94-007-0053-6
DOI 10.1007/978-94-007-0053-6
Springer Dordrecht Heidelberg London New York

© Springer Science+Business Media B.V. 2011
No part of this work may be reproduced, stored in a retrieval system, or transmitted in any form or by any means, electronic, mechanical, photocopying, microfilming, recording or otherwise, without written permission from the Publisher, with the exception of any material supplied specifically for the purpose of being entered and executed on a computer system, for exclusive use by the purchaser of the work.

Cover design: SPi Publisher Services

Printed on acid-free paper

Springer is part of Springer Science+Business Media (www.springer.com)

Preface

The book provides an insight on advanced methods and concepts for design and analysis of structures against earthquake loading. It consists of 25 chapters covering a wide range of timely issues in Earthquake Engineering. The goal of this Volume is to establish a common ground of understanding between the communities of Earth Sciences and Computational Mechanics towards mitigating future seismic losses. Due to the great social and economic consequences of earthquakes, the topic is of great scientific interest and is expected to be of valuable help to the large number of scientists and practicing engineers currently working in the field. The chapters of this Volume are extended versions of selected papers presented at the COMPDYN 2009 conference, held in the island of Rhodes, Greece, under the auspices of the European Community on Computational Methods in Applied Sciences (ECOMASS).

In the introductory chapter of Lignos et al. the topic of collapse assessment of structures is discussed. The chapter presents the analytical modeling of component behaviour and structure response from the early inelastic to lateral displacements at which a structure becomes dynamically unstable. A component model that captures the important deterioration modes, typically observed in steel members, is calibrated using data from tests of scale-models of a moment-resisting connection. This connection is used for the two-scale model of a modern four-story steel moment frame and the assessment of its collapse capacity through analysis.

The work of Adam and Jäger deals with the seismic induced global collapse of multi-story frame structures with non-deteriorating material properties, which are vulnerable to the P–Δ effect. The initial assessment of the structural vulnerability to P–Δ effects is based on pushover analyses. More information about the collapse capacity is obtained with the Incremental Dynamic Analyses using a set of recorded ground motions. In a simplified approach equivalent single-degree-of-freedom systems and collapse spectra are utilized to predict the seismic collapse capacity of the structures.

Sextos et al. focus on selection procedures for real records based on the Eurocode 8 (EC8) provisions. Different input sets comprising seven pairs of records (horizontal components only) from Europe, Middle-East and the US were formed in compliance with EC8 guidelines. The chapter deals with the study of the RC bridges of the Egnatia highway system and also with a multi-storey RC building that was damaged during the 2003 Lefkada (Greece) earthquake. More specifically,

the bridge was studied using alternative models and accounting for the dynamic interaction of the deck-abutment-backfill-embankment system as well as of the superstructure-foundation-subsoil system. The building was studied in both the elastic and inelastic range taking into consideration material nonlinearity as well as the surrounding soil. The results permit quantification of the intra-set scatter of the seismic response for both types of structures, thus highlighting the current limitations of the EC8 guidelines. Specific recommendations are provided in order to eliminate the dispersion observed in the elastic and the inelastic response though appropriate modifications of the EC8 selection parameters.

Assimaki et al. study how the selection of the site response model affects the ground motion predictions of seismological models, and how the synthetic motion site response variability propagates to the structural performance estimation. For this purpose, the ground motion synthetics are computed for six earthquake scenarios of a strike-slip fault rupture, and the ground surface response is estimated for 24 typical soil profiles in Southern California. Next, a series of bilinear single-degree-of-freedom oscillators is subjected to the ground motions computed using the alternative soil models and the consequent variability in the structural response is evaluated. The results show high bias and uncertainty in the prediction of the inelastic displacement ratio, when predicted using the linear site response model for periods close to the fundamental period of the soil profile.

The chapter of Kappos et al. addresses the issue of pushover analysis of bridges sensitive to torsion, using as case-study a bridge whose fundamental mode is purely torsional. Parametric analyses were performed involving consideration of foundation compliance, and various scenarios of accidental eccentricity that would trigger the torsional mode. An alternative pushover curve in terms of abutment shear versus deck maximum displacement (that occurs at the abutment) was found to be a meaningful measure of the overall inelastic response of the bridge. It is concluded that for bridges with a fundamental torsional mode, the assessment of their seismic response relies on a number of justified important decisions that have to be made regarding: the selection and the reliable application of the analysis method, the estimation of foundation and abutment stiffnesses, and the appropriate numerical simulation of the pertinent failure mechanism of the elastomeric bearings.

Pardalopoulos and Pantazopoulou investigate the spatial characteristics of a structure's deformed shape at maximum response in order to establish deformation demands in the context of displacement-based seismic assessment or redesign of existing constructions. It is shown that the vibration shape may serve as a diagnostic tool of global structural inadequacies as it identifies the tendency for interstorey drift localization and twisting due to mass or stiffness eccentricity. This chapter investigates the spatial displaced shape envelope and its relationship to the three-dimensional distribution of peak drift demand in reinforced concrete buildings with and without irregularities in plan and in height. A methodology for the seismic assessment of rotationally sensitive structures is established and tested through correlation with numerical results obtained from detailed time history simulations.

The chapter of Cotsovos and Kotsovos summarises the fundamental properties of concrete behaviour which underlie the formulation of an engineering finite element

model that is capable to realistically predict the behaviour of (plain or reinforced) concrete structural forms for a wide range of problems from static to impact loading, bypassing the problem of re-calibration. The already published evidence that support the proposed formulation is complemented by four typical case-studies. For each case-study, the numerical predictions are computed against experimental data revealing good agreement.

The chapter of Wijesundara et al. investigates the local seismic performances of fully restrained gusset plate connections through detailed finite element models of a single storey single-bay frame that is located at the ground floor of the four storey frame. The chapter presents a design procedure, proposing an alternative clearance rule for the accommodation of brace rotation. Local performances of FE models are compared in terms of strain concentrations at the beams, the columns and the gusset plates.

Vielma et al. propose a new seismic damage index and the corresponding damage thresholds. The seismic behavior of a set of regular reinforced concrete buildings designed according to the EC-2/EC-8 prescriptions for a high seismic hazard level are studied using the proposed damage index. Fragility curves and damage probability matrices corresponding to the performance point are then calculated. The obtained results show that the collapse damage state is not reached in the buildings designed according the prescriptions of EC-2/EC-8 and that the damage does not exceed the irreparable damage limit-state for the buildings studied.

The application of discrete element models based on rigid block formulations to the analysis of masonry walls under horizontal out-of-plane loading is discussed in the chapter of Lemos et al. The problems raised by the representation of an irregular fabric as a simplified block pattern are addressed. Two procedures for creating irregular block systems are presented. One using Voronoi polygons and another based on a bed and cross joint structure with random deviations. A test problem provides a comparison of various regular and random block patterns, showing their influence on the failure loads.

Papaloizou and Komodromos discus the computational methods appropriate for simulating the dynamic behaviour and the seismic response of ancient monuments, such as classical columns and colonnades. Understanding the behaviour and response of historic structures during strong earthquakes is useful for the assessment of conservation and rehabilitation proposals for such structures. Their seismic behaviour involves complicated rocking and sliding phenomena that very rarely appear in modern structures. The discrete element method (DEM) is utilized to investigate the response of ancient multi-drum columns and colonnades during harmonic and earthquake excitations by simulating the individual rock blocks as distinct rigid bodies.

The study on the seismic behaviour of the walls of the Cella of Parthenon when subjected to seismic loading is presented in the chapter of Psycharis et al.. Given that commonly used numerical codes for masonry structures or drum-columns are unable to handle the discontinuous behaviour of ancient monuments, the authors adopt the discrete element method (DEM). The numerical models represent in detail the actual construction of the monument and are subjected to the three components

of four seismic events recorded in Greece. Time domain analyses were performed in 3D, considering the non-linear behaviour at the joints. Conclusions are drawn based on the maximum displacements induced to the structure during the ground excitation and the residual deformation at the end of the seismic motion.

The chapter of Dolsek studies the effect of both aleatory and epistemic (modelling) uncertainties on reinforced concrete structures. The Incremental Dynamic Analysis (IDA) method, which can be used to calculate the record-to-record variability, is extended with a set of structural models by utilizing the Latin Hypercube Sampling (LHS) to account for the modelling uncertainties. The results showed that the modelling uncertainties can reduce the spectral acceleration capacity and significantly increase its dispersion.

The chapter of Taflanidis discusses the problem of the efficient design of additional dampers, to operate in tandem with the isolation system. One of the main challenges of such applications has been the explicit consideration of the nonlinear behavior of the isolators or the dampers in the design process. Another challenge has been the efficient control of the dynamic response under near-field ground motions. In this chapter, a framework that addresses both these challenges is discussed. The design objective is defined as the maximization of the structural reliability. A simulation-based approach is implemented to evaluate the stochastic performance and an efficient framework is proposed for performing the associated design optimization and for selecting values of the controllable damper parameters that optimize the system reliability.

Mitsopoulou et al. study a robust control system for smart beams. First the structural uncertainties of basic physical parameters are considered in the model of a composite beam with piezoelectric sensors and actuators subjected to wind-type loading. The control mechanism is introduced and designed to keep the beam in equilibrium in the event of external wind disturbances and in the presence of mode inaccuracies using the available measurement and control under limits.

Panagiotopoulos et al. examine through simple examples the performance and the characteristics of a methodology previously proposed by the authors on a variationally-consistent way for the incorporation of time-dependent boundary conditions in problems of elastodynamics. More specifically, an integral formulation of the elastodynamic problem serves as basis for enforcing the corresponding constraints, which are imposed via the consistent form of the penalty method, e.g. a form that complies with the norm and inner product of the functional space where the weak formulation is mathematically posed. It is shown that well-known and broadly implemented modelling techniques in the finite element method such as “large mass” and “large spring” techniques arise as limiting cases of this penalty formulation.

Sapountzakis and Dourakopoulos study the nonlinear dynamic analysis of beams of arbitrary doubly symmetric cross section using the boundary element method. The beam is able to undergo moderate large displacements under general boundary conditions, taking into account the effects of shear deformation and rotary inertia. The beam is subjected to the combined action of arbitrarily distributed or

concentrated transverse loading and bending moments in both directions as well as to axial loading. To account for shear deformations, the concept of shear deformation coefficients is used. Five boundary value problems are formulated and solved using the Analog Equation Method. Application of the boundary element technique yields a nonlinear coupled system of equations of motion. The evaluation of the shear deformation coefficients is accomplished from the aforementioned stress functions using only boundary integration.

The chapter of Papachristidis et al. presents the fiber method for the inelastic analysis of frame structures when subjected to high shear. Initially the fiber approach is presented within its standard, purely bending, formulation and it is then expanded to the case of high shear deformations. The element formulation follows the assumptions of the Timoshenko beam theory, while two alternative formulations, a coupled and a decoupled are presented. The numerical examples confirm the accuracy and the computational efficiency of the element formulation under monotonic, cyclic and dynamic/seismic loading.

A simplified procedure to estimate base sliding of concrete gravity dams induced by an earthquake is proposed in the chapter of Basili and Nuti. A simple mechanical model is developed in order to take into account the sources that primarily influence the seismic response of such structures. The dam is modelled as an elastic-linear single-degree-of-freedom-system. Different parameters are considered in the analysis such as the dam height, foundation rock parameters, water level, seismic intensity. As a result, a simplified methodology is developed to evaluate base residual displacement, given the dam geometry, the response spectrum of the seismic input, and the soil characteristics. The procedure permits to assess the seismic safety of the dam with respect to base sliding, as well as the water level reduction that is necessary to render the dam safe.

Papazafeiropoulos et al. provided a literature review and results from numerical simulations on the dynamic interaction of concrete dams with retained water and underlying soil. Initially, analytical closed-form solutions that have been widely used for the calculation of dam distress are outlined. Subsequently, the numerical methods based on the finite element method, which is unavoidably used for complicated geometries of the reservoir and/or the dam, are reviewed. Numerical results are presented illustrating the impact of various key parameters on the distress and the response of concrete dams considering the dam-foundation interaction.

Motivated by the earthquake response of industrial pressure vessels, Karamanos et al. investigate the externally-induced sloshing in spherical liquid containers. Considering modal analysis and an appropriate decomposition of the container-fluid motion, the sloshing frequencies and the corresponding sloshing (or convective) masses are calculated, leading to a simple and efficient method for predicting the dynamic behavior of spherical liquid containers. It is also shown that considering only the first sloshing mass is adequate to represent the dynamic behavior of the spherical liquid container within a good level of accuracy.

Jha et al. introduce a bilevel model for developing an optimal Maintenance Repair and Rehabilitation (MR&R) plan for large-scale highway infrastructure elements, such as pavements and bridges, following a seismic event. The maintenance

and upkeep of all infrastructure components is crucial for mobility, driver safety and guidance, and the overall efficient functioning of a highway system. Typically, a field inspection of such elements is carried out at fixed time intervals to determine their condition, which is then used to develop optimal MR&R plan over a given planning horizon.

Frangopol and Akiyama present a seismic analysis methodology for corroded reinforced concrete (RC) bridges. The proposed method is applied to lifetime seismic reliability analysis of corroded RC bridge piers, and the relationship between steel corrosion and seismic reliability is presented. It is shown that the analytical results are in good agreement with the experimental results regardless of the amount of steel corrosion. Moreover, after the occurrence of crack corrosion, the seismic reliability of the pier is significantly reduced.

Life cycle cost assessment of structural systems refers to an evaluation procedure where all costs arising from owing, operating, maintaining and ultimately disposing are considered. Life cycle cost assessment is considered as a significant assessment tool in the field of the seismic behaviour of structures. Therefore, in the chapter by Mitropoulou et al. two test cases are examined and useful conclusions are drawn regarding the behaviour factor q of EC8 and the incident angle that a ground motion is applied on a multi-storey RC building.

Bal et al. examine vulnerability assessment procedures that include code-based detailed analysis methods together with preliminary assessment techniques in order to identify the safety levels of buildings. Their chapter examines the effect of four essential structural parameters on the seismic behaviour of existing RC structures. Parametric studies are carried out on real buildings extracted from the Turkish building stock, one of which was totally collapsed in 1999 Kocaeli earthquake. Comparisons are made in terms of shear strength, energy dissipation capability and ductility. The mean values of the drop in the performance are computed and factors are suggested to be utilized in preliminary assessment techniques, such as the recently proposed P25 method that is shortly summarized in the chapter.

The aforementioned collection of chapters provides an overview of the present thinking and state-of-the-art developments on the computational techniques in the framework of structural dynamics and earthquake engineering. The book is targeted primarily to researchers, postgraduate students and engineers working in the field. It is hoped that this collection of chapters in a single book will be a useful tool for both researchers and practicing engineers.

The book editors would like to express their deep gratitude to all authors for the time and effort they devoted to this volume. Furthermore, we would like to thank the personnel of Springer Publishers for their kind cooperation and support for the publication of this book.

Athens
June 2010

Manolis Papadrakakis
Michalis Fragiadakis
Nikos D. Lagaros

Contents

Collapse Assessment of Steel Moment Resisting Frames Under Earthquake Shaking 1
Dimitrios G. Lignos, Helmut Krawinkler, and Andrew S. Whittaker

Seismic Induced Global Collapse of Non-deteriorating Frame Structures 21
Christoph Adam and Clemens Jäger

On the Evaluation of EC8-Based Record Selection Procedures for the Dynamic Analysis of Buildings and Bridges 41
Anastasios G. Sextos, Evangelos I. Katsanos, Androula Georgiou, Periklis Faraonis, and George D. Manolis

Site Effects in Ground Motion Synthetics for Structural Performance Predictions 67
Dominic Assimaki, Wei Li, and Michalis Fragiadakis

Problems in Pushover Analysis of Bridges Sensitive to Torsion 99
Andreas J. Kappos, Eleftheria D. Goutzika, Sotiria P. Stefanidou, and Anastasios G. Sextos

Spatial Displacement Patterns of R.C. Buildings Under Seismic Loads 123
Stylianos J. Pardalopoulos and Stavroula J. Pantazopoulou

Constitutive Modelling of Concrete Behaviour: Need for Reappraisal 147
Demetrios M. Cotsovos and Michael D. Kotsovos

Numerical Simulation of Gusset Plate Connection with Rhs Shape Brace Under Cyclic Loading 177
K.K. Wijesundara, D. Bolognini, and R. Nascimbene

Seismic Response of RC Framed Buildings Designed According to Eurocodes 201
Juan Carlos Vielma, Alex Barbat, and Sergio Oller

Assessment of the Seismic Capacity of Stone Masonry Walls with Block Models 221
José V. Lemos, A. Campos Costa, and E.M. Bretas

Seismic Behaviour of Ancient Multidrum Structures 237
Loizos Papaloizou and Petros Komodromos

Seismic Behaviour of the Walls of the Parthenon A Numerical Study 265
Ioannis N. Psycharis, Anastasios E. Drougas, and Maria-Eleni Dasiou

Estimation of Seismic Response Parameters Through Extended Incremental Dynamic Analysis 285
Matjaz Dolsek

Robust Stochastic Design of Viscous Dampers for Base Isolation Applications 305
Alexandros A. Taflanidis

Uncertainty Modeling and Robust Control for Smart Structures 331
A. Moutsopoulou, G.E. Stavroulakis, and A. Pouliezos

Critical Assessment of Penalty-Type Methods for Imposition of Time-Dependent Boundary Conditions in FEM Formulations for Elastodynamics 357
Christos G. Panagiotopoulos, Elias A. Paraskevopoulos, and George D. Manolis

Nonlinear Dynamic Analysis of Timoshenko Beams 377
E.J. Sapountzakis and J.A. Dourakopoulos

Inelastic Analysis of Frames Under Combined Bending, Shear and Torsion 401
Aristidis Papachristidis, Michalis Fragiadakis, and Manolis Papadrakakis

Seismic Simulation and Base Sliding of Concrete Gravity Dams 427
M. Basili and C. Nuti

Dynamic Interaction of Concrete Dam-Reservoir-Foundation: Analytical and Numerical Solutions 455
George Papazafeiropoulos, Yiannis Tsompanakis, and Prodromos N. Psarropoulos

Numerical Analysis of Externally-Induced Sloshing in Spherical Liquid Containers 489
Spyros A. Karamanos, Lazaros A. Patkas, and Dimitris Papaprokopiou

A Bilevel Optimization Model for Large Scale Highway Infrastructure Maintenance Inspection and Scheduling Following a Seismic Event 515
Manoj K. Jha, Konstantinos Kepaptsoglou, Matthew Karlaftis, and Gautham Anand Kumar Karri

Lifetime Seismic Reliability Analysis of Corroded Reinforced Concrete Bridge Piers 527
Dan M. Frangopol and Mitsuyoshi Akiyama

Advances in Life Cycle Cost Analysis of Structures 539
Chara Ch. Mitropoulou, Nikos D. Lagaros, and Manolis Papadrakakis

Use of Analytical Tools for Calibration of Parameters in P25 Preliminary Assessment Method 559
İhsan E. Bal, F. Gülten Gülay, and Semih S. Tezcan

Index 583

Collapse Assessment of Steel Moment Resisting Frames Under Earthquake Shaking

Dimitrios G. Lignos, Helmut Krawinkler, and Andrew S. Whittaker

Abstract Although design codes and standards of practice are written assuming that the probability of building collapse is low under extreme earthquake shaking, the likelihood of collapse in such shaking is almost never checked. This chapter discusses analytical modeling of component behavior and structure response from the onset of inelastic behavior to lateral displacements at which a structure becomes dynamically unstable. A component model that captures the important deterioration modes observed in steel components is calibrated using data from tests of scale-models of a moment-resisting connection. This connection is used in the construction of two scale models of a modern four-story steel moment frame. The scale models are tested through collapse on an earthquake simulator at the NEES facility at the University at Buffalo. The results of these simulator tests show that it is possible to predict the sidesway collapse of steel moment resisting frames under earthquake shaking using relatively simple analytical models provided that deterioration characteristics of components are accurately described in the models.

Keywords Collapse assessment · Deterioration · Cumulative damage effects · Shaking table collapse tests · Performance-based earthquake engineering · Steel structures

D.G. Lignos (✉)
McGill University, Department of Civil Engineering and Applied Mechanics,
Montreal, Quebec, H3A 2K6, Canada
e-mail: dimitrios.lignos@mcgill.ca

H. Krawinkler
Stanford University, Department of Civil and Environmental Engineering Stanford,
CA 94305-4020, USA
e-mail: krawinkler@stanford.edu

A.S. Whittaker
University at Buffalo, State University of New York at Buffalo (SUNY),
Department of Civil and Environmental Engineering, NY, 14260, USA
e-mail: awhittak@buffalo.edu

M. Papadrakakis et al. (eds.), *Computational Methods in Earthquake Engineering*,
Computational Methods in Applied Sciences 21, DOI 10.1007/978-94-007-0053-6_1,
© Springer Science+Business Media B.V. 2011

1 Introduction

The assessment of collapse of deteriorating structural systems requires the use of advanced analytical models that are able to reproduce the important deterioration modes of structural components subjected to monotonic and/or cyclic loading. However, until recently there were no physical test data available to validate and improve these models for reliable analytical predictions of structural response near collapse. Prior tests on steel frames, including those conducted at the University of California in the mid 1980s, did not focus on component deterioration and did not seek to collapse the frames [1, 2].

Herein, we associate collapse with sidesway instability, which is the consequence of successive reductions of the load carrying capacity of structural components to the extent that second-order ($P - \Delta$) effects, accelerated by component deterioration, overcome the gravity-load resistance of the structural frame.

This chapter focuses on recent advancements on modeling the deterioration of steel components for reliable collapse prediction of steel frame structures. These advancements take advantage of recent earthquake-simulator tests through collapse of two scale models of a modern four-story steel moment resisting frame and of cyclic and monotonic tests of components of the scale models conducted prior to and after the completion of the earthquake-simulator tests.

2 Component Deterioration Modeling

The hysteretic behavior of a structural component is dependent upon several structural parameters that affect its deformation and energy dissipation characteristics. This observation has been confirmed by numerous experimental studies that have lead to the development of a number of deterioration models for steel and reinforced concrete (RC) components.

In the early 1970s, several models [3–6] were developed that were able to simulate changes to the stiffness and strength of structural components in each loading cycle based on the maximum deformation that occurred in previous cycles. These models were applicable primarily to reinforced concrete (RC) components. Foliente [7] summarizes the main modifications of the widely known Bouc-Wen model [8, 9] (smooth models) proposed by others [10–12] to incorporate component deterioration. Song and Pincheira [13] developed a model that incorporated strength and post-capping strength deterioration, but not cyclic strength deterioration. Based on Iwan [14] and Mostaghel [15], Sivaselvan and Reinhorn [16] developed a versatile smoothed hysteretic model that could account for stiffness and strength degradation and pinching. This model has been used widely for numerical collapse simulation of large-scale structural systems [e.g., [17–19]. Ibarra et al. [20] developed a phenomenological deterioration model that can simulate up to four component deterioration modes depending on the hysteretic response of

the component (bilinear, peak-oriented, pinched). In this model, the rate of cyclic deterioration is controlled by a rule developed by Rahnama and Krawinkler [21], which is based on the hysteretic energy dissipated when the component is subjected to cyclic loading. The Ibarra model has been used in a number of studies of building collapse [22–25].

Lignos and Krawinkler [26] modified the deterioration model of Ibarra et al. [20] to address asymmetric component hysteretic behavior including different rates of cyclic deterioration in the two loading directions, residual strength and incorporation of an ultimate deformation θ_u at which the strength of a component drops to zero. This model is used in the remainder of this chapter. The phenomenological Ibarra-Krawinkler (IK) model is imposed on a backbone curve that defines a reference envelope for the behavior of a structural component and establishes strength and deformation bounds (see Fig. 1), and a set of rules that define the basic characteristics of the hysteretic behavior between the backbone curve. The main assumption for cyclic deterioration is that every component has a reference hysteretic energy dissipation capacity Et, regardless of the loading history applied to it. Lignos and Krawinkler [26] expressed the reference hysteretic energy dissipation capacity E_t as a multiple of $(M_y\theta_p)$,

$$E_t = \lambda\theta_p M_y \text{ or } E_t = \Lambda M_y \tag{1}$$

where, $\Lambda = \lambda\theta p$ is the reference cumulative deformation capacity, and θ_p and M_y are the pre-capping plastic rotation and effective yield strength of the component, respectively.

The basic deterioration rule by Rahnama and Krawinkler [21] has been modified for the case of asymmetric hysteretic response to consider different rates of cyclic

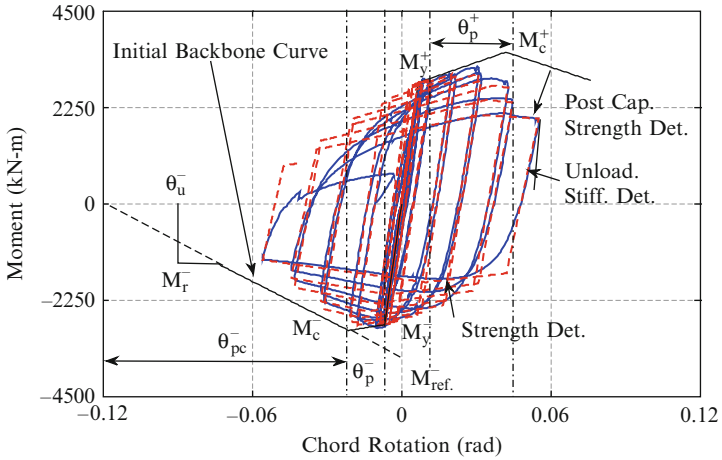


Fig. 1 Modified Ibarra – Krawinkler (IK) deterioration model; Backbone curve, basic modes of cyclic deterioration (Data from Ricles et al. [31])

deterioration in the positive and negative loading directions based on the following equation,

$$\beta_{s,c,k,i}^{+/-} = \left(\frac{E_i}{E_t - \sum_{j=1}^{i-1} E_j} \right)^{c} D^{+/-} \tag{2}$$

where $\beta_{s,c,k,i}^{+/-}$ is the parameter defining the deterioration in excursion i, denoted as $\beta_{s,i}^{+/-}$ for basic strength deterioration, $\beta_{c,i}^{+/-}$ for post-capping strength deterioration, and $\beta_{k,i}^{+/-}$ for unloading stiffness deterioration; E_i is the hysteretic energy dissipated in excursion i, and $D^{+/-}$ is a parameter with a value between 0 and 1 that defines the decrease in the rate of cyclic deterioration in the positive or negative loading direction. If the rate of cyclic deterioration is the same in both loading directions then $D^{+/-} = 1$ and the cyclic deterioration rule is essentially the same as that included in the original IK model [20]. The deteriorated yield moment M_i, post-capping moment $M_{ref,i}$ (see Fig. 1) and deteriorated unloading stiffness K_i per excursion i are given by the following equations,

$$M_i = (1 - \beta_{s,i}^{+/-}) M_{i-1} \tag{3}$$

$$M_{ref,i} = \left(1 - \beta_{c,i}^{+/-}\right) M_{ref,i-1} \tag{4}$$

$$K_i = (1 - \beta_{k,i}^{+/-}) K_{i-1} \tag{5}$$

Figure 1 shows the utility of the modified IK model by enabling a comparison of predicted and measured responses of the cyclic response of a steel beam equipped with a composite slab. The modifications to the deterioration rules of Ibarra et al. [20] were based on a database developed by Lignos and Krawinkler [26–28] for deterioration properties of steel components. The modified IK deterioration model has been implemented in a single degree of freedom (SDOF) nonlinear dynamic analysis program (SNAP) and two multi degree of freedom (MDOF) dynamic analysis platforms (DRAIN–2DX [29] and OpenSees [30]).

3 Prototype and Model Steel Frame for Experimental and Analytical Collapse Studies

To validate analytical modeling capabilities for collapse prediction of frame structures subjected to earthquakes, a coordinated analytical and experimental program was conducted using a modern, code-compliant [32, 33], two-bay, four-story steel moment resisting frame as a testbed. The structural system is a special moment resisting frame (SMRF) with reduced beam sections (RBS) designed per FEMA-350 [34]. Information on the design of the prototype building is presented

in [26]. Two 1:8 scale model frames, whose properties represent those of the prototype structure, were tested on the earthquake simulator of the Network for Earthquake Engineering Simulation (NEES) facility at the State University of New York at Buffalo (SUNY-UB) in the summer of 2007.

3.1 Scale Model Frames for Earthquake Simulator Collapse Tests

The prototype two-bay, four-story steel moment resisting frame that served as the testbed for the project was scaled to enable testing on the NEES simulator at SUNY-UB. Two nominally identical model frames were fabricated. The scale of the model frames was dictated by the capacity of the earthquake simulator. At a 1:8 model scale, the total weight of half of the structure was approximately 170 kN (40 kips) based on the similitude rules described by Moncarz and Krawinkler [35]. Figure 2 shows the scale model of the SMRF (denoted as the model frame) and a mass simulator used to simulate masses tributary to the frame. Both sub-structures were joined with axially rigid links at each floor level to transfer the $P - \Delta$ effect from the mass simulator to the test frame. Each link was equipped with a hinge at each end and a load cell to measure story forces. Information on the design of the model and its construction and erection are presented in [26].

The model frame consisted of elastic aluminum beam and column elements and elastic joints that are connected by plastic hinge (lumped plasticity) elements.

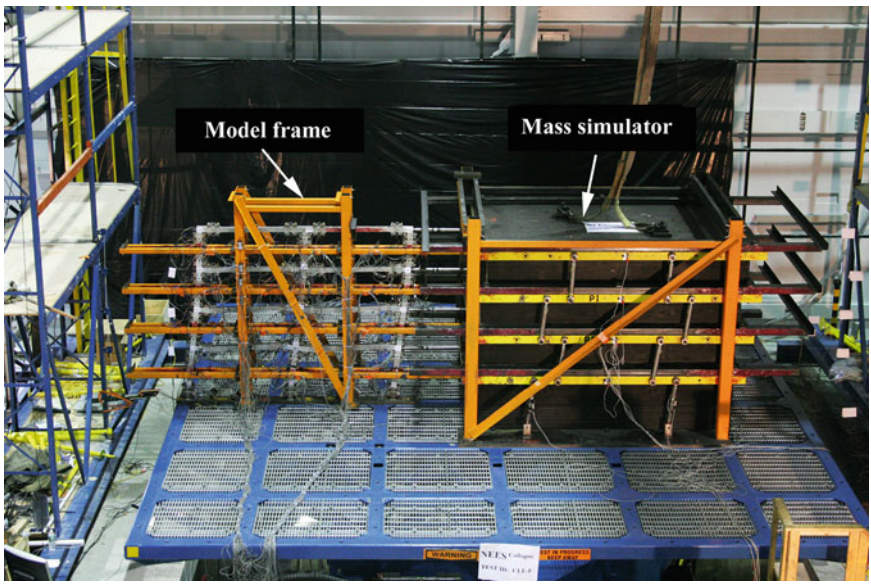


Fig. 2 Four-story scale model and mass simulator on the SUNY-UB NEES earthquake simulator

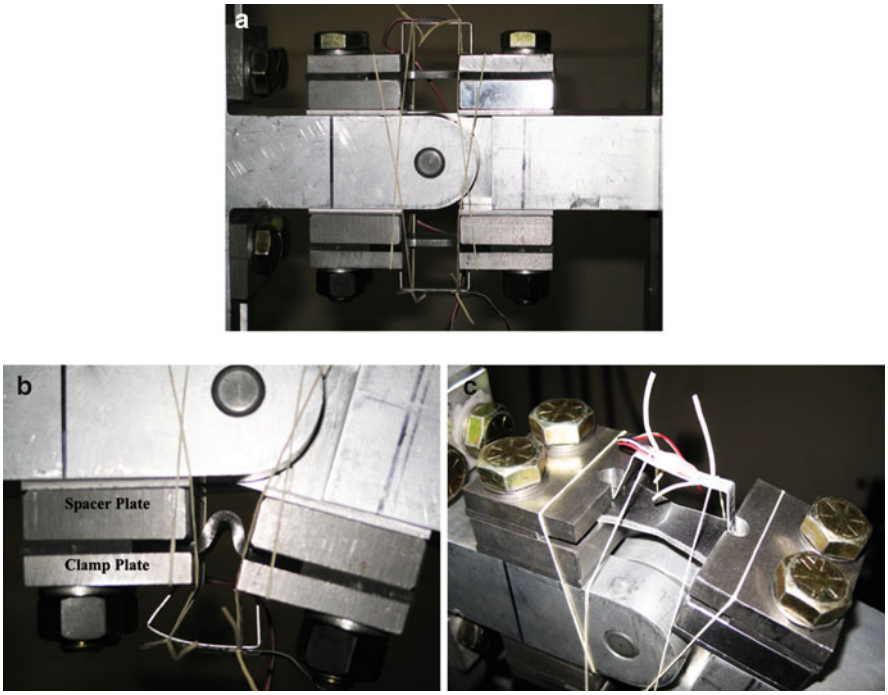


Fig. 3 Typical plastic hinge element of model frame (**a**) plastic hinge element, (**b**) bottom flange plate after buckling, (**c**) top flange plate after fracture

The mechanical properties of the elastic elements were selected to correctly scale element stiffness. The plastic hinge elements (see Fig. 3a) consisted of (a) two steel flange plates detailed to capture plastic hinging at the end of the beams and columns at the model scale, and (b) a spherical hinge to transfer shearing force. Spacer and clamp plates were used to adjust the buckling length of the flange plates (see Fig. 3b), that is, to control the strength and cyclic deterioration of the hinge elements. Figure 3c shows the top flange plate of the plastic hinge element after fracture. The final geometry and flange plate dimensions were the product of an experimental program [26] that included tests of fifty components similar to the one shown in Fig. 3a.

3.2 Hysteretic Response and Component Deterioration

To identify the deterioration parameters of the plastic hinge elements, a series of monotonic and cyclic tests were conducted with single-and double-flange plate configurations at the John A. Blume earthquake engineering laboratory at

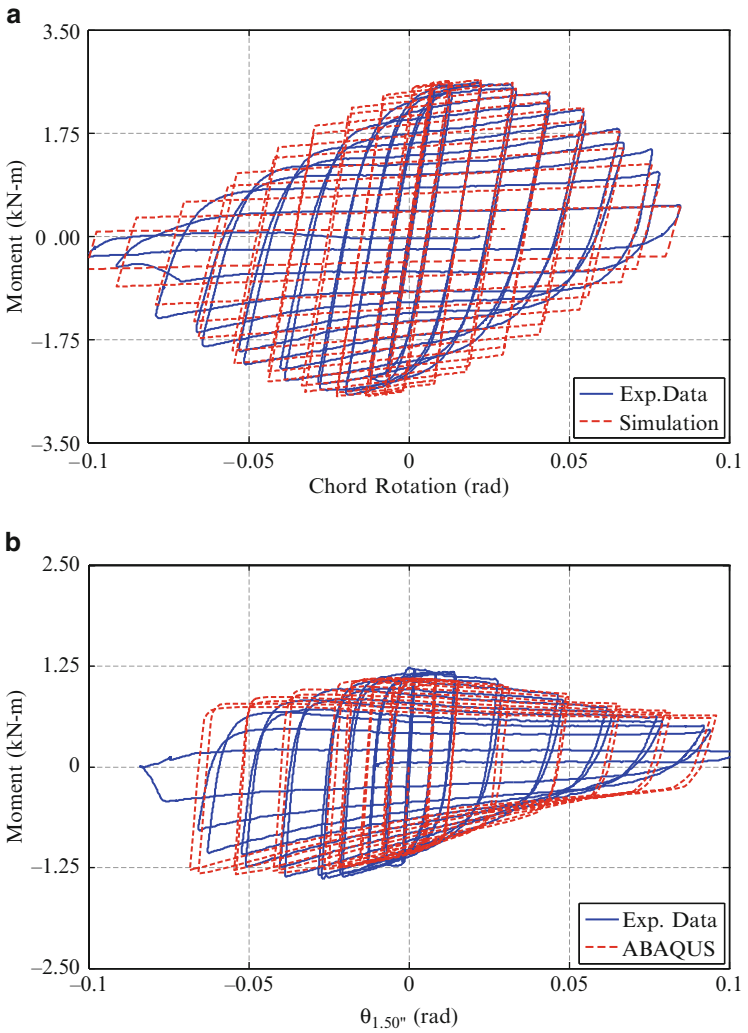


Fig. 4 Hysteretic behavior of various configurations together with calibration of analytical models; (**a**) plastic hinge element with two flange plates with calibrated IK deterioration model; (**b**) plastic hinge element with one flange plate with calibrated ABAQUS model including combined isotropic and kinematic hardening

Stanford University. A standard symmetrical loading protocol [32] was used for all component tests. The typical hysteretic response of a plastic hinge element with double flange plates is shown in Fig. 4a. From this figure it can be seen that the behavior of the specimen is pinched at deformations greater than 0.03 rad. Most of the pinching in the hysteretic response of the model connection is attributed to the absence of the web in the model plastic hinge element. In these elements, flange-plate buckling is not restrained by a web and during the subsequent load reversal;

Table 1 Component modeling parameters for pre–Buffalo collapse prediction

Location	K_e (kN − m/rad)	M_c/M_y	θ_p (rad)	θ_{pc} (rad)	Λ
C1S1B[a]	2,924	1.09	0.050	1.30	1.35
C1S1T[b]	2,331	1.10	0.050	1.30	1.35
F2B1R[c]	1,469	1.10	0.050	1.30	1.35
C1S3T[d]	1,265	1.10	0.050	1.30	1.35

[a]C1S1B: Column 1 in Story 1 at base, [b]C1S1T: Column 1 in Story 1 top location, [c]F2B1R: Floor 2 Beam 1 right location, [d]C1S3T: Column 1 in Story 3 at top

the flange straightens at a much reduced axial load before recovering its full tensile resistance, which causes the pinching behavior. The pinching is more evident in the moment-rotation diagram that is shown in Fig. 4b for a plastic hinge element with one flange plate subjected to negative bending.

The simulated (modified IK) hysteretic response of a plastic hinge element with two flanges is shown in Fig. 4a together with the experimental data. This model is unable to capture the pinching effect that is evident in all symmetric cyclic loading tests. However, the hysteretic behavior of the plastic hinge elements is captured fairly well since emphasis is placed on strength and stiffness deterioration. The hysteretic behavior of the plastic hinge element with one (or two) flange plates can be modeled accurately using a more refined continuous finite element model in ABAQUS [36] that includes combined isotropic and kinematic hardening (see Fig. 4b). The use of continuum models is computationally expensive for collapse simulations of a full moment frame. Table 1 summarizes the deterioration parameters of the modified IK model for the plastic hinge elements calibrated using data from the component tests conducted prior to the earthquake-simulator tests (pre-Buffalo collapse prediction). For a typical plastic hinge element, the ultimate rotation capacity is $\theta_u = 0.08$ rad based on a symmetric cyclic loading protocol and $\theta_u = 0.20$ rad based on monotonic loading.

4 Earthquake Simulator Testing Phases and Analytical Collapse Predictions

The earthquake-simulator collapse tests of the two scale models (denoted Frame 1 and 2) of the four-story steel moment resisting frame involved the incremental scaling of the ground motions such that they represented levels of shaking intensity of physical significance to the earthquake engineering profession. The test sequence for each of the two frames constitutes a *physical* Incremental Dynamic Analysis (IDA) [37]. The major difference between a physical IDA and a traditional (numerical simulation) IDA is that the latter analysis starts with an undamaged structure (zero initial conditions) whereas the former starts with the residual deformations of the prior simulation. We considered residual deformations in the numerical simulations performed as part of our validation studies.

For Frame 1, the Fault Normal (FN) component of the Canoga Park (CP) record of the 1994 Northridge earthquake (peer.berkeley.edu/scmat), scaled to 40%, 100% 150% and 190% of the intensity of the recorded motion, representing service level (SLE), design level (DLE), maximum considered (MCE), and collapse level earthquakes (CLE), respectively, was used for the physical simulations. The authors sought to investigate the effect of cumulative damage on collapse computations by using a long duration record (the FN component of the Llolleo record of the 1985 Chilean earthquake) for the MCE-level test of Frame 2 after using the CP ground motion for SLE and DLE-level tests. However the Llolleo record was not reproduced successfully in the earthquake-simulator test and the subsequent MCE-level test was performed using the CP record. During the CLE-level test (using the CP record), Frame 2 drifted in the opposite direction to that of Frame 1 but did not collapse. In the subsequent collapse-level test of Frame 2, denoted CLEF (intensity of 2.2 times the recorded Canoga Park motion), the frame drifted further in this direction and collapsed. Information on the response of both scale models is presented in [26]. The experimental data from these tests are available at the Network for Earthquake Engineering (NEES) repository.

4.1 Pre-Buffalo Collapse Predictions

The analytical predictions of the dynamic response of the two 4-story scale models (noted as pre-Buffalo predictions) prior to the earthquake-simulator experiments were used to develop the testing program described earlier. The highest intensity of shaking (CLE) was based on analytical collapse simulations using the modified IK model presented earlier after (1) calibrating the deterioration parameters of components using information from tests of components using a symmetric cyclic loading protocol (see Table 1); (2) using the theoretical input of the ground motion (not the achieved motion from the earthquake simulator) and (3) assuming 2% Rayleigh damping at the first and third mode periods of the model frame. Figure 5 shows the predicted and measured ground motion (GM) intensity scale factor versus roof drift (Δ/H) for each experiment of each frame. Based on the results presented in Fig. 5a, the response of Frame 1 is captured fairly well up to the MCE level of shaking. Based on the pre-test simulations, Frame 1 reaches 16% roof drift at 190% of the recorded Canoga Park record (CLE-level test). However, the experimental data show that Frame 1 experienced *only* 11% drift at this intensity of shaking. Frame 1 collapsed at 220% of the recorded Canoga Park record (denoted CLEF in Fig. 5a). Figure 5b summarizes numerical and physical simulation data for Frame 2. The analytical prediction indicates that Frame 2 should be close to collapse at the MCE level.

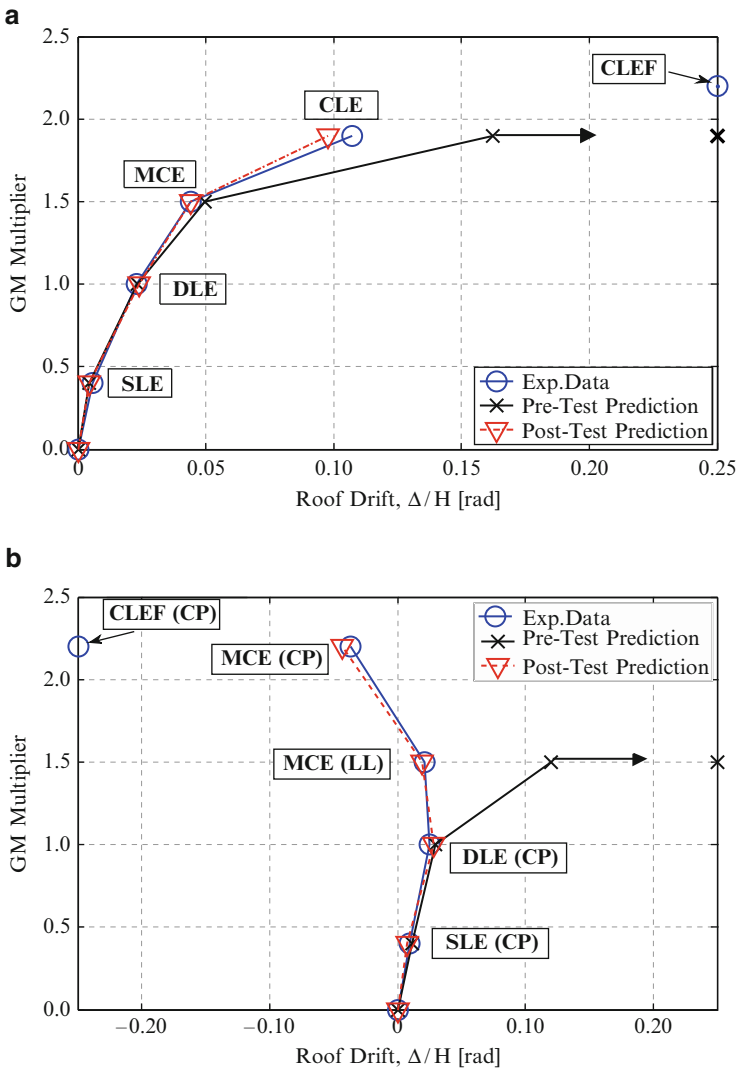


Fig. 5 IDAs of pre- and post-test analytical predictions together with experimental data for both 4-story scale models [26]. (**a**) Frame 1, (**b**) Frame 2

4.2 Post-Buffalo Collapse Predictions

To identify the reasons for the difference between the pre-Buffalo response predictions and the responses measured during the earthquake-simulator tests, the measured earthquake-simulator motions were used for the post-Buffalo numerical simulations. The effect of choice of values of the deterioration modeling parameters

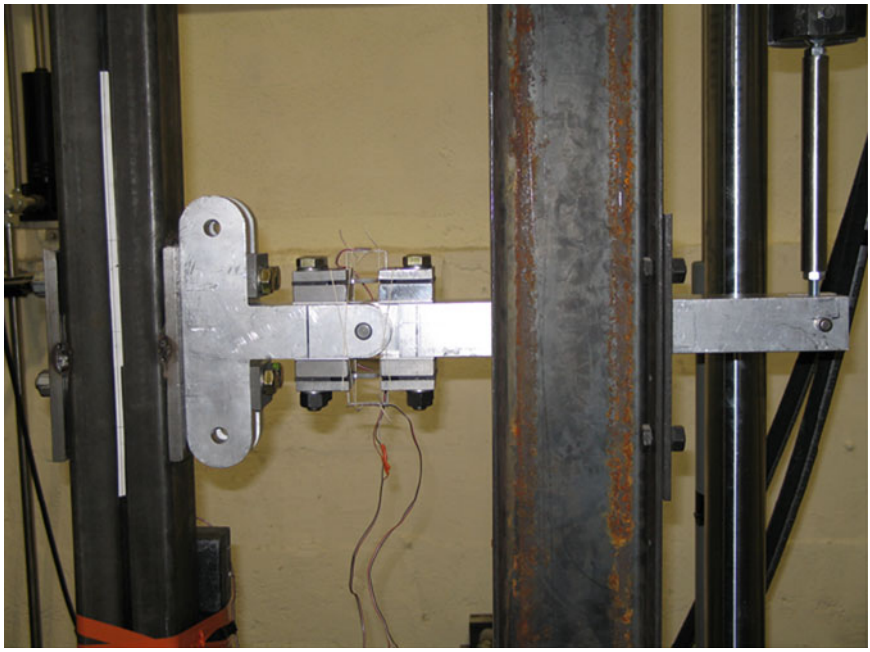


Fig. 6 Component subassembly for post-Buffalo test experimentation

on the results of numerical simulations was studied. A series of component tests were conducted for selected plastic hinge locations for which the recorded rotation histories were available from the earthquake-simulator tests. A plastic hinge subassembly (see Fig. 6) that was nominally identical to those installed in Frames 1 and 2 was used for the component tests. The rotation histories of these plastic hinge elements, denoted as $\theta_{1.5''}$, were deduced from clip gage extensometer measurements of the flange plate elongation during the earthquake-simulator tests.

To transform the rotation history into a tip displacement history for the component subassembly tests, the contributions of the components outside of the plastic hinge had to be estimated. An estimate of the moment history at the plastic hinge element was needed for these calculations, and a mathematical model of the hinge was developed using the modified IK model. The moment required to estimate the elastic contributions to the total actuator tip displacement was estimated using the predicted stiffness and deterioration parameters from the pre–Buffalo component tests (see Table 1) and the rotation history $\theta_{1.5''}$ measured from the earthquake simulator tests. The input rotation history of the plastic-hinge element was transformed into a tip displacement history for the component subassembly tests. Figure 7a and b show the experimentally deduced moment-rotation relationship for the exterior column base of Frames 1 and 2, respectively, together with the responses simulated using the modified IK model from SLE (elastic response) to CLEF (response near collapse). Table 2 summarizes the modeling parameters obtained from the post-Buffalo component tests.

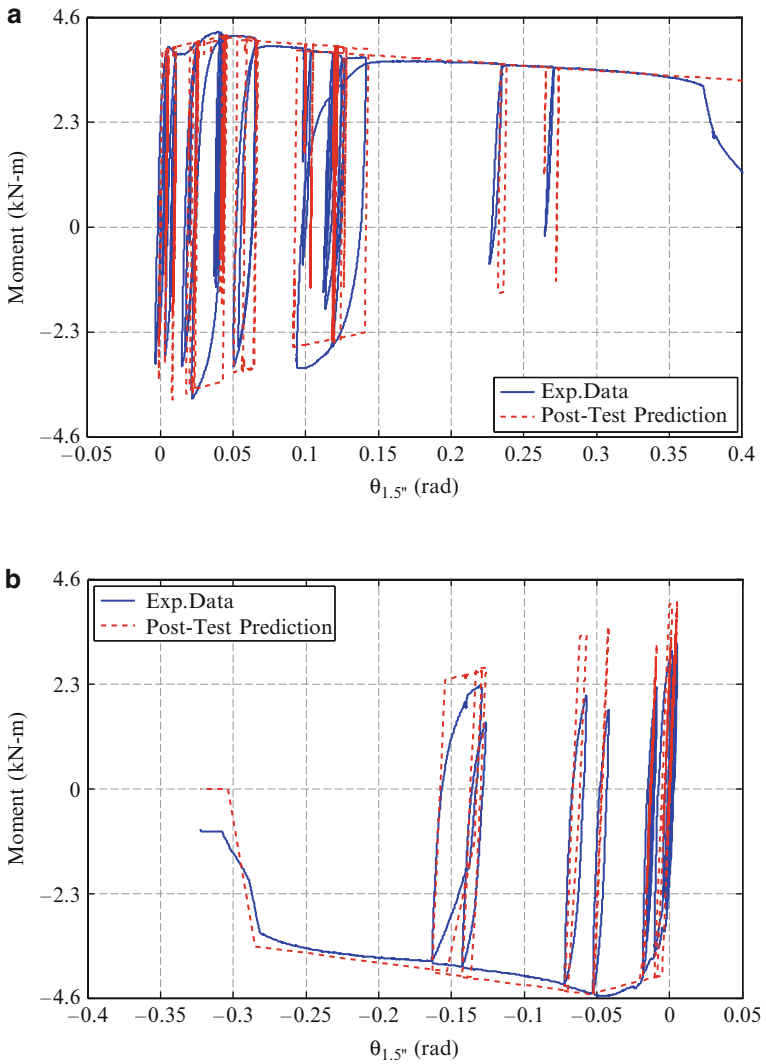


Fig. 7 Post-Buffalo component test using the earthquake simulator test rotation history from SLE to CLEF. (**a**) Exterior base column of Frame 1; (**b**) Exterior base column of Frame 2

Analysis of the results of the component tests discussed in this section permits an assessment of the effect of component deterioration at critical plastic hinge locations on building response. Figure 8 shows the moment equilibrium measured at one instant in time during the CLE- and CLEF-level ground motions. (For the CLEF-level shaking, the chosen instant in time is the incipient collapse level (ICL) and corresponds to a $\theta_{1.5''} = 0.37$ rad from Fig. 7a). The reductions in moment in the

Table 2 Component modeling parameters for post–Buffalo collapse prediction

Location	K_e (kN-m/rad)	M_c/M_y	θ_p (rad)	θ_{pc} (rad)	Λ
C1S1B	2,904	1.10	0.050	2.0	1.30
C1S1T	2,331	1.10	0.050	2.0	1.30
F2B1R	1,469	1.10	0.050	1.6	1.80
C1S3T	1,265	1.08	0.055	2.4	1.00

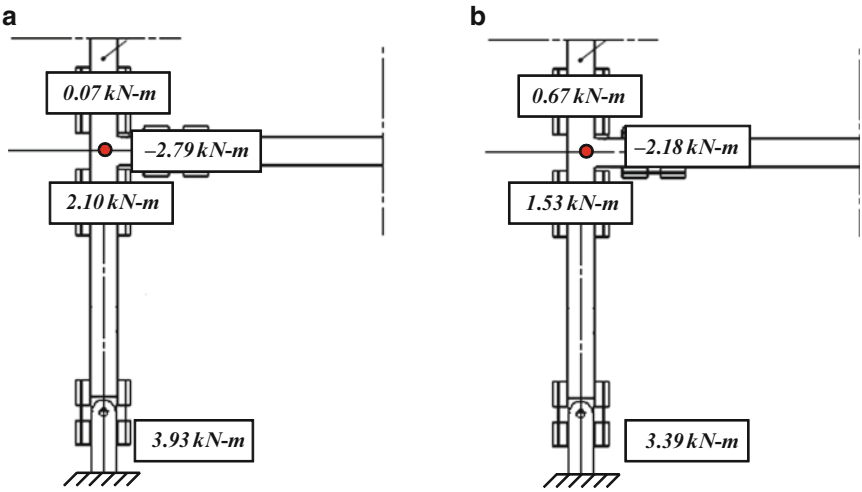


Fig. 8 Moment equilibrium of the exterior subassembly at an instant in time during CLE-level and CLEF-level shaking of Frame 1. (**a**) CLE, (**b**) ICL

plastic hinges at the column base and in the first floor beam from CLE to CLEF-level shaking are due to strength deterioration (see the reduction in moment in Fig. 7 at rotations greater than 0.05 rad).

4.3 Post-Buffalo Response Predictions to Collapse

The purpose of the post-Buffalo response predictions described in this section was to investigate whether the seismic behavior of the two model frames could be predicted better by modifying the analytical model based on information that became available from the earthquake-simulator tests and the post-Buffalo component tests described in the previous section.

The recorded earthquake simulator motions were used for the post-Buffalo response predictions of the building frame. The input and measured motions of the simulator for the DLE shaking of Frame 1 are shown in Fig. 9 at the prototype scale.

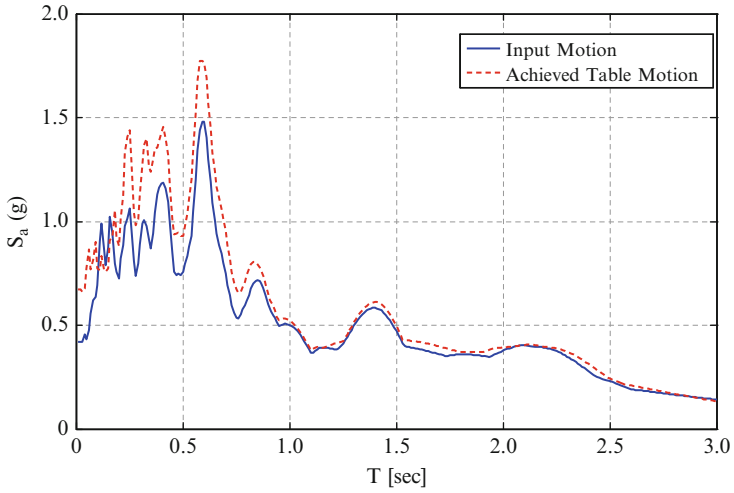


Fig. 9 Input versus measured Canoga Park motions for DLE shaking

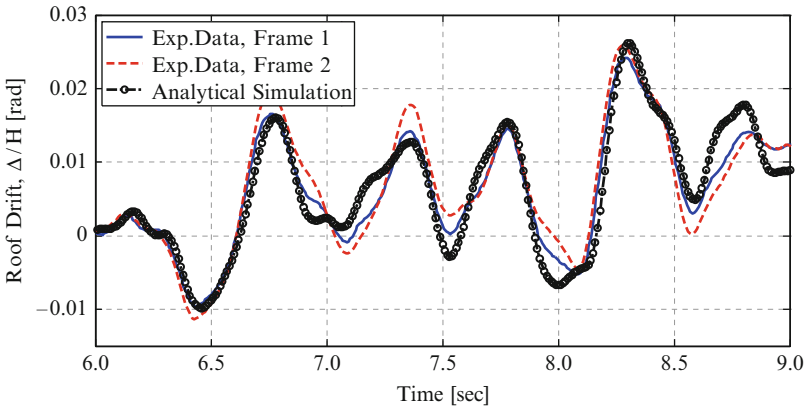


Fig. 10 Comparisons of roof drift histories between Frames 1 and 2 at DLE shaking; measured and simulated response

At the first mode period of the prototype building (=1.32 s), the match between the spectral ordinates is near perfect. The differences between the input and measured motions were small for all tests except for the Llolleo MCE motion for Frame 2 (see [26]).

During the earthquake-simulator tests, Frames 1 and 2 exhibited considerable friction damping that we attributed primarily to the spherical hinges of the mass simulator gravity links shown in Fig. 2. For the post-Buffalo response predictions, a friction element was inserted at each end of each gravity link of the mass simulator. At shaking levels greater than the DLE level, the effect of friction on the dynamic response of the two frames was small as seen in Fig. 10. This figure shows

the measured and simulated DLE roof-drift response for Frames 1 and 2. Friction damping has an impact on the response for shaking levels less than the DLE.

Except for the post-capping plastic rotation (θ_{pc}), the values of the deterioration parameters in Tables 1 and 2 are very similar. The differences in the cumulative plastic rotation capacity (Λ) for F2B1R and C1S3T are not important because Ibarra and Krawinkler [22] have shown that changes in the value of this parameter of the magnitude seen here do not have a significant effect on the collapse capacity of deteriorating structural systems. The calibrated values of θ_{pc} are greater in Table 2 (post-Buffalo test series) than Table 1 (pre-Buffalo test series). A smaller value of this parameter increases the $P - \Delta$ effect because the structure deflects more and collapse occurs earlier.

Figure 5 shows results (denoted as Post-Test Prediction) of the simulated IDAs computed using the deterioration parameters of Table 2 and initial conditions equal to the residual deformations in the previous numerical simulation. The predictions match the measurements very well. Note that very small time steps were required for the numerical simulations to be stable at large deformations of the frame.

Figures 11 and 12 show the roof drift histories obtained from the CLE-level and CLEF-level earthquake simulator tests and from the post-Buffalo numerical simulations for Frames 1 and 2, respectively. The results of the numerical and physical simulations match well for both cases.

4.4 Predicted Base Shear Histories to Collapse

The instrumentation scheme employed for the earthquake-simulator tests permitted an assessment of the $P - \Delta$ effects through collapse of the frames. Figure 13 shows the normalized inertial base shear history (V^a_{Base}) for CLEF-level shaking of

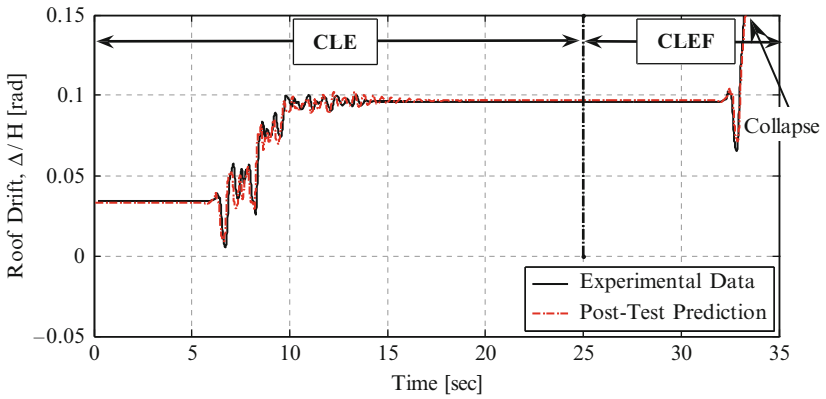


Fig. 11 Comparison of roof drift history for Frame 1 for CLE- and CLEF-level shaking between post-Buffalo numerical simulations and experimental data

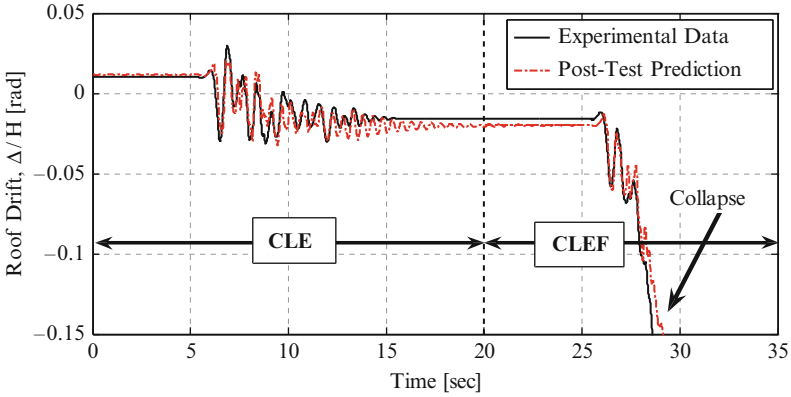


Fig. 12 Comparison of roof drift history for Frame 2 for CLE- and CLEF-level shaking between post-Buffalo numerical simulations and experimental data

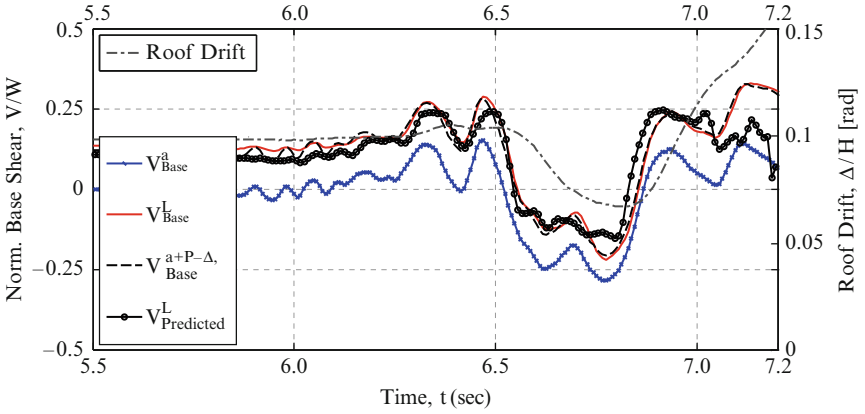


Fig. 13 Base shear history for Frame 1 at CLEF-level shaking

Frame 1. The inertial force history at each floor was computed as the product of the floor mass and absolute translational acceleration history. The inertial force base shear history was computed by summing the floor histories of inertial force. The normalized base shear history was computed as the base shear history divided by the total weight (W) of Frame 1 (=180 kN). The normalized effective base shear history (V^{L}_{Base}) computed as the sum of the axial forces in the links joining the frame to the mass simulator, divided by W, is also shown in the figure. The difference between the two base shear histories is due to $P-\Delta$ effects. The drift history at the roof of the frame is also shown in the figure (dashed line in legend, scale on right hand margin of the figure) to enable a qualitative assessment of the $P-\Delta$ effect. Also shown is the normalized effective base shear ($V^{a+P-\Delta}_{Base}$) computed as the sum

of V_{Base}^{a} and Pδ/h where P is the weight (=180 kN), δ is the first story drift and h is the height of the first story (=62.5 cm). There is an excellent match between the three normalized effective base shear histories.

5 Summary and Conclusions

This chapter summarizes recent developments in the simulation of collapse of moment resisting frames. The work involved numerical simulations and small- and large-scale physical testing of components and systems. Small-scale experiments were conducted to develop numerical robust models of steel moment-resisting connections that can capture deterioration of strength and stiffness. These models were used to simulate the seismic response of a code-compliant four-story steel moment-resisting frame through collapse and to develop an earthquake-simulator testing program. The earthquake-simulator testing of two scale models of the four-story frame provided the first set of physical test data on the response of framed structures to a wide range of earthquake-shaking intensity through collapse. The results of the earthquake-simulator testing program also enabled the authors to refine the numerical models developed prior to the earthquake-simulator testing program. Detailed information on the research project can be found in Lignos and Krawinkler [26]. The key findings from the research work described in this chapter are:

1. Robust hysteretic models capable of simulating deterioration in strength in plastic hinge regions are needed to predict collapse of steel frames structures.
2. Second-order ($P-\Delta$) effects can substantially influence the response of ductile, framed structures near the point of incipient collapse.
3. Hysteretic macro-models of structural components should be derived from testing using loading protocols consistent with the expected shaking (intensity, duration, etc) and the mechanical properties of the framing system in which the components are to be installed. A critical modeling parameter is the post-capping rotation capacity.

The authors acknowledge that the profession's understanding of building collapse, what triggers collapse, and how collapse propagates through a building structure is in its infancy. The work described in this chapter has improved the state-of-art. Much more research work is required to address the questions posed above, together with experimental data from real building systems that include composite floor slabs atop steel beams and three-dimensional effects.

Acknowledgments This study is based on work supported by the United States National Science Foundation (NSF) under Grant No. CMS-0421551 within the George E. Brown, Jr. Network for Earthquake Engineering Simulation Consortium Operations. The financial support of NSF is gratefully acknowledged. The authors also thank REU students Mathew Alborn, Melissa Norlund and Karhim Chiew for their invaluable assistance during the earthquake simulator collapse test series. The successful execution of the earthquake-simulator testing program would not have been possible without the guidance and skilled participation of the laboratory technical staff at the SUNY-Buffalo NEES facility. Any opinions, findings, and conclusions or recommendations expressed in this paper are those of the authors and do not necessarily reflect the views of NSF.

References

1. Uang CM, Bertero VV (1986) Earthquake simulation tests and associated studies of a 0.3-scale model of a six-story concentrically braced steel structure. Report No. UCB/EERC-86/10. Earthquake Engineering Research Center, University of California, Berkeley, CA
2. Whittaker AS, Uang CM, Bertero VV (1989) Experimental behavior of a dual steel system. J Struct Div ASCE 115(1):183–200
3. Hisada T, Nakagawa K, Izumi M (1962) Earthquake response of structures having various restoring force characteristics. Proceedings of Japan National Conference on Earthquake Engineering, pp 63–68
4. Clough RW, Johnston SB (1966) Effect of stiffness degradation on earthquake ductility requirements. Proceedings of Second Japan National Conference on Earthquake Engineering, pp 227–232
5. Mahin SA, Bertero VV (1972) Rate of loading effect on uncracked and repaired reinforced concrete members. Report EERC No. 73-6. Earthquake Engineering Research Center, University of California, Berkeley, CA.
6. Takeda T, Sozen M, Nielsen N (1970) Reinforced concrete response to simulated earthquakes. J Struct Div 96 (ST12):2557–2573
7. Foliente G (1995) Hysteresis modeling of wood joints and structural systems. J Struct Eng ASCE 121(6):1013–1022
8. Bouc R (1967) Forced vibration of mechanical system with hysteresis. Abstract Proceedings of the 4th conference on nonlinear oscillations. Prague, p. 315
9. Wen Y.-K (1980) Equivalent linearization for hysteretic systems under random excitation. J Appl Mech 47:150–154
10. Baber T, Noori MN (1986) Modeling general hysteresis behavior and random vibration application. J Vibrat Acous Stress Reliabil 108:411–420
11. Casciati F (1989) Stochastic dynamics of hysteretic media. J Struct Safety Amsterdam 6:259–269
12. Reinhorn AM, Madan A, Valles RE, Reichmann Y, Mander JB (1995) Modeling of masonry infill panels for structural analysis. Report. NCEER-95-0018. State University of New York, Buffalo, NY
13. Song J, Pincheira J (2000) Spectral displacement demands of stiffness and strength degrading systems. Earthq Spect 16(4):817–851
14. Iwan WD (1966) A distributed-element model for hysteresis and its steady-state dynamic response. J Appl Mech 33(42):893–900
15. Mostaghel N (1999) Analytical description of pinching, degrading hysteretic systems. J Eng Mech ASCE 125(2):216–224
16. Sivaselvan MV, Reinhorn AM (2000) Hysteretic models for deteriorating inelastic structures. J Eng Mech ASCE 126(6):633–640
17. Sivaselvan MV, Reinhorn AM (2006) Lagrangian approach to structural collapse simulation. J Eng Mech ASCE 132:795–805
18. Lavan O, Sivaselvan MV, Reinhorn AM, Dargush GF (2009) Progressive collapse analysis through strength degradation and fracture in the Mixed Lagrangian Formulation. Earthq Eng Struct Dynam 38(13):1483–1504
19. Sivaselvan MV, Lavan O, Dargush GF, Kurino H, Hyodo Y, Fukuda R, Sato K, Apostolakis G, Reinhorn AM (2009) Numerical collapse simulation of large-scale structural systems using an optimization-based algorithm. Earthq Eng Struct Dynam 38(5):655–677
20. Ibarra LF, Medina RA, Krawinkler H (2005) Hysteretic models that incorporate strength and stiffness deterioration. Earthq Eng Struct Dynam 34(12):1489–1511
21. Rahnama M, Krawinkler H (1993) Effect of soft soils and hysteresis models on seismic design spectra. Report No. TB 108. John A. Blume Earthquake Engineering Research Center, Department of Civil Engineering, Stanford University, Stanford, CA
22. Ibarra LF, Krawinkler H (2005) Global collapse of frame structures under seismic excitations. Report No. PEER 2005/06. Pacific Earthquake Engineering Research Center, University of California, Berkeley, CA

23. Zareian F, Krawinkler H (2009) Simplified performance based earthquake engineering. Rep. No. TB 169. The John A. Blume Earthquake Engineering Research Center, Stanford University, Stanford, CA
24. Federal Emergency Management Agency (FEMA) (2009). Quantification of building seismic performance factors. Report FEMA P695, Federal Emergency Management Agency, Washington, DC
25. Zareian F, Lignos DG, Krawinkler H (2010) Evaluation of seismic collapse performance of steel special moment resisting frames using FEMA P695 (ATC-63) methodology. Proceedings of Structures Congress ASCE, Orlando, FL, 12–14 May 2010
26. Lignos DG, Krawinkler H (2009) Sidesway collapse of deteriorating structural systems under seismic excitations. Report No. TB 172. John A. Blume Earthquake Engineering Research Center, Department of Civil and Environmental Engineering, Stanford University, Stanford, CA
27. Lignos DG, Krawinkler H (2007) A database in support of modeling of component deterioration for collapse prediction of steel frame structures. Proceedings of Structures Congress ASCE, Long Beach, CA
28. Lignos DG, Zareian F, Krawinkler H (2010) A steel database for deterioration modeling of steel beams with RBS under cyclic loading. Proceedings of Structures Congress ASCE, Orlando, FL, 12–14 May 2010
29. Prakash V, Powell GH, Campbell S (1993) DRAIN-2DX: Basic program description and user guide. Report No. UCB/SEMM-1993/17. University of California, Berkeley, CA
30. Open Sees (2009) Open system for earthquake engineering simulation, Version 2.2.1, Pacific Earthquake Engineering Research Center (PEER). http://opensees.berkeley.edu. University of California, Berkeley, CA
31. Ricles JM, Zhang X, Lu LW, Fisher J (2004) Development of seismic guidelines for deep-column steel moment connections. Report No. 04-13, Advanced Technology for Large Structural Systems
32. American Institute of Steel Construction (AISC) (2005) Seismic provisions for structural steel buildings, including supplement No. 1. American Institute of Steel Construction, Inc, Chicago, IL
33. International Code Council (ICC) (2003) International Building Code IBC 2003. International Code Council, Birmingham, AL
34. SAC Joint Venture (SAC) (2000) Recommended seismic design criteria for new steel moment frame buildings. Report No. FEMA 350, Federal Emergency Management Agency, Washington, DC
35. Moncarz PD, Krawinkler H (1981) Theory and application of experimental model analysis in earthquake engineering. Report No. TB. 50, John A. Blume Earthquake Engineering Center, Department of Civil Engineering, Stanford University, Stanford, CA
36. Hibbitt, Karisson and Sorensen (HKS) (2005) ABAQUS Version 6.5 for advanced mechanical simulation. Pawtucket, RI
37. Vamvatsikos D, Cornell CA (2002) Incremental dynamic analysis. Earthq Eng Struct Dynam 31(3):491–514

Seismic Induced Global Collapse of Non-deteriorating Frame Structures

Christoph Adam and Clemens Jäger

Abstract In a severe seismic event the destabilizing effect of gravity loads, i.e. the P-delta effect, may be the primary trigger for global collapse of quite flexible structures exhibiting large inelastic deformations. This article deals with seismic induced global collapse of multi-story frame structures with non-deteriorating material properties, which are vulnerable to the P-delta effect. In particular, the excitation intensity for P-delta induced structural collapse, which is referred to as collapse capacity, is evaluated. The initial assessment of the structural vulnerability to P-delta effects is based on pushover analyses. More detailed information about the collapse capacity renders Incremental Dynamic Analyses involving a set of recorded ground motions. In a simplified approach equivalent single-degree-of-freedom systems and collapse capacity spectra are utilized to predict the seismic collapse capacity of regular multi-story frame structures.

Keywords Collapse capacity spectra · Dynamic instability · P-delta

1 Introduction

In flexible structures gravity loads acting through lateral displacements amplify structural deformations and stress resultants. This impact of gravity loads on the structural response is usually referred to as P-delta effect. For a realistic building in its elastic range the P-delta effect is usually negligible. However, it may become of significance at large inelastic deformations when gravity loads lead to a negative slope in the post-yield range of the lateral load-displacement relationship. In such

C. Adam (✉)
University of Innsbruck, Department of Civil Engineering Sciences, 6020 Innsbruck, Austria
e-mail: christoph.adam@uibk.ac.at

C. Jäger
University of Innsbruck, Department of Civil Engineering Sciences, 6020 Innsbruck, Austria
e-mail: clemens.jaeger@uibk.ac.at

M. Papadrakakis et al. (eds.), *Computational Methods in Earthquake Engineering*,
Computational Methods in Applied Sciences 21, DOI 10.1007/978-94-007-0053-6_2,
© Springer Science+Business Media B.V. 2011

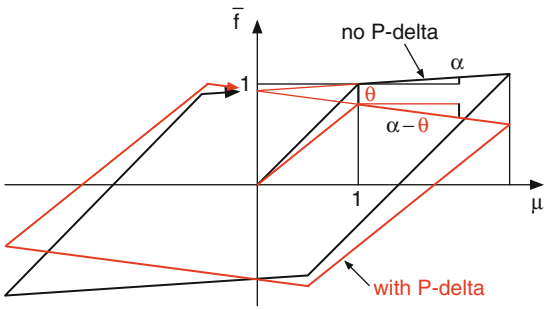


Fig. 1 Normalized bilinear cyclic behavior of a SDOF system with and without P-delta effect

a situation large gravity loads combined with seismically induced large inelastic deformations amplify the lateral displacements in a single direction. The seismic collapse capacity of the structure is exhausted at a rapid rate, and the system is no longer able to sustain its own gravity loads. Additionally, material deterioration accelerates P-delta induced seismic collapse.

A profound insight into the P-delta effect on the inelastic seismic response of structures is given e.g. by Bernal [1], Gupta and Krawinkler [2], Aydinoglu [3], Ibarra and Krawinkler [4], and Lignos and Krawinkler [5]. Asimakopoulos et al. [6] and Villaverde [7] provide an overview on studies dealing with collapse by dynamic instability in earthquake excited structures.

In an inelastic single-degree-of-freedom (SDOF) system the gravity load generates a shearing of its hysteretic force-displacement relationship. Characteristic displacements (such as the yield displacement) of this relationship remain unchanged, whereas the characteristic forces (such as the strength) are reduced. As a result, the slope of the curve is decreased in its elastic and post-elastic branch of deformation. The magnitude of this reduction can be expressed by means of the so-called stability coefficient [8]. As a showcase in Fig. 1 the P-delta effect on the hysteretic behavior of a SDOF system with non-deteriorating bilinear characteristics is visualized. In this example the post-yield stiffness is negative because the stability coefficient θ is larger than the hardening ratio α.

Fundamental studies of the effect of gravity on inelastic SDOF systems subjected to earthquakes have been presented in Bernal [8] and MacRae [9]. Kanvinde [10], and Vian and Bruneau [11] have conducted experimental studies on P-delta induced collapse of SDOF frame structures. Asimakopoulos et al. [6] propose a simple formula for a yield displacement amplification factor as a function of ductility and the stability coefficient. Miranda and Akkar [12] present an empirical equation to estimate the minimum lateral strength up to which P-delta induced collapse of SDOF systems is prevented. In Adam et al. [13–15] so-called collapse capacity spectra have been introduced for the assessment of the seismic collapse capacity of SDOF structures.

In multi-story frame structures gravity loads may impair substantially the complete structure or only a subset of stories [2]. The local P-delta effect may induce collapse of a local structural element, which does not necessarily affect the stability of the complete structure. An indicator of the severity of the local P-delta effect is

the story stability coefficient, Gupta and Krawinkler [2]. Alternatively, Aydinoglu [3] proposes the use of the geometric story stiffness instead of the story stability coefficient. However, a consistent relationship between the local P-delta effect and the global P-delta effect, which characterizes the overall impact of gravity loads on the structure, cannot be established due to dynamic interaction between adjacent stories in a multi-story frame structure [2].

In several papers, see e.g. Takizawa and Jennings [16], Bernal [17], Adam et al. [18], it is proposed to assess the global P-delta effect in frame structures by means of equivalent single-degree-of-freedom (ESDOF) systems. If the story drifts remain rather uniformly distributed over the height, regardless of the extent of inelastic deformation, a global assessment of the P-delta effect by means of ESDOF systems is not difficult. Thereby, it is assumed that P-delta is primarily governed by the fundamental mode. As recently shown [19] this assumption holds true also for tall buildings. However, if a partial mechanism develops, the global P-delta effect will be greatly affected by the change of the deflected shape, and it will be amplified in those stories in which the drift becomes large [1, 3]. In such a situation an adequate incorporation of P-delta effects in ESDOF systems is a challenging task.

In this paper a methodology is presented, which allows a fast quantification of the global P-delta effect in highly inelastic regular MDOF frame structures subjected to seismic excitation. Emphasis is given to the structural collapse capacity. Results and conclusions of this study are valid only for non-deteriorating cyclic behavior, i.e. strength and stiffness degradation is not considered.

2 Structural Vulnerability to Global P-Delta Effects

2.1 Assessment of the Vulnerability to Global P-Delta Effects

Initially, it must be assessed whether the considered structure is vulnerable to P-delta effects. Strong evidence delivers the results of a global pushover analysis [2]. During this nonlinear static analysis gravity loads are applied, and subsequently the structure is subjected to lateral forces. The magnitude of these forces with a predefined invariant load pattern is amplified incrementally in a displacement-controlled procedure. As a result the global pushover curve of the structure is obtained, where the base shear is plotted against a characteristic deformation parameter. In general the lateral displacement of the roof is selected as characteristic parameter. It is assumed that the shape of the global pushover curve reflects the global or the local mechanism involved when the structure approaches dynamic instability.

In Fig. 2 the effect of gravity loads on the global pushover curve of a multi-story frame structure is illustrated. Figure 2a shows the global pushover curve, where gravity loads are either disregarded or of marginal importance. The pushover curve of Fig. 2b corresponds to a very flexible multi-story frame structure with a strong impact of the P-delta effect leading to a reduction of the global lateral stiffness. In

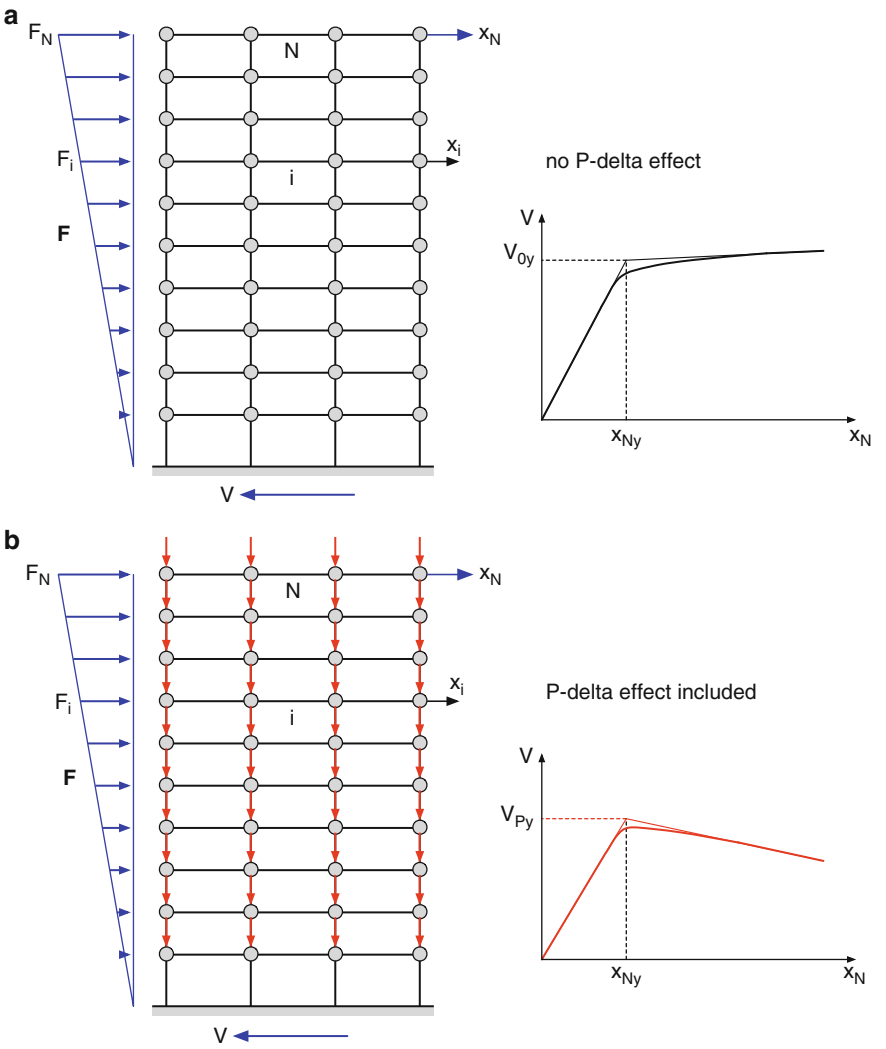


Fig. 2 Multi-story frame structure and corresponding global pushover curves. (**a**) Pushover analysis disregarding the P-delta effect. (**b**) Pushover analysis considering the P-delta effect

very flexible structures gravity loads even may generate a negative post-yield tangent stiffness as shown in Fig. 2b [20]. If severe seismic excitation drives such a structure in its inelastic branch of deformation a state of dynamic instability may be approached, and the global collapse capacity is attained at a rapid rate. From these considerations follows that a gravity load induced negative post-yield tangent stiffness in the global pushover curve requires an advanced investigation of P-delta effects [2]. It is emphasized that collapse induced by static instability must be investigated separately.

2.2 Example

Exemplarily, the structural vulnerability to P-delta effects of a generic single-bay 15-story frame structure according to Fig. 3a is assessed. All stories are of uniform height h, and they are composed of rigid beams, elastic flexible columns, and rotational springs at the ends of the beams. Nonlinear behavior at the component level is modeled by non-degrading bilinear hysteretic behavior of the rotational springs (compare with Fig. 3b) to represent the global cyclic response under seismic excitation. The strength of the springs is tuned such that yielding is initiated simultaneously at all spring locations in a static pushover analysis (without gravity loads) under an inverted triangular design load pattern. To each joint of the frame an identical point mass is assigned. The bending stiffness of the columns and the stiffness of the springs are tuned to render a straight line fundamental mode shape. Identical gravity loads are assigned to each story to simulate P-delta effects. This implies that axial column forces due to gravity increase linearly from the top to the bottom of the frame. The frame structure has a fundamental period of vibration of $T_1 = 3.0\,s$, which makes it rather flexible. The base shear coefficient, defined as

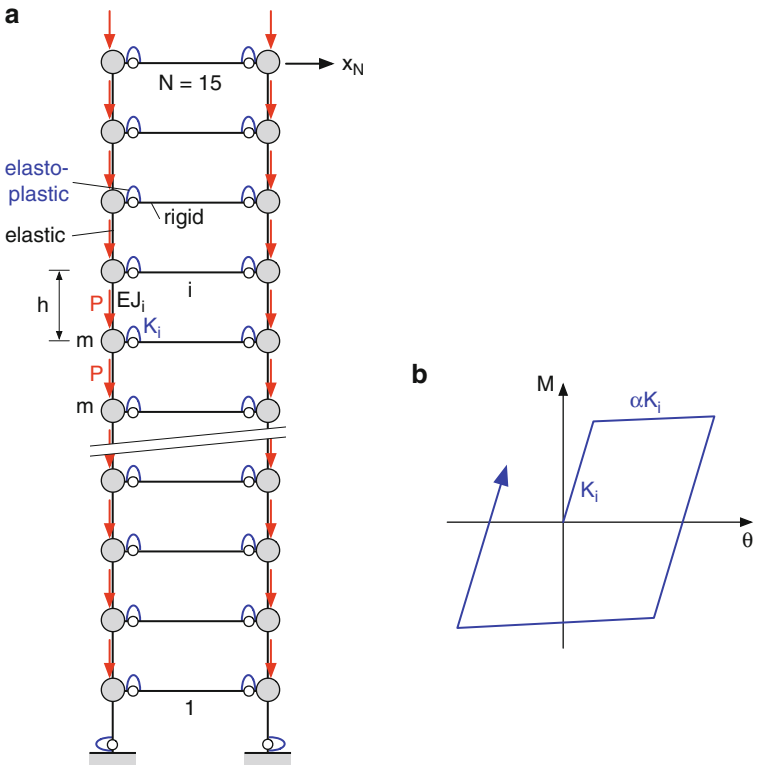


Fig. 3 (**a**) Generic 15-story frame structure. (**b**) Bilinear hysteretic loop of the rotational springs

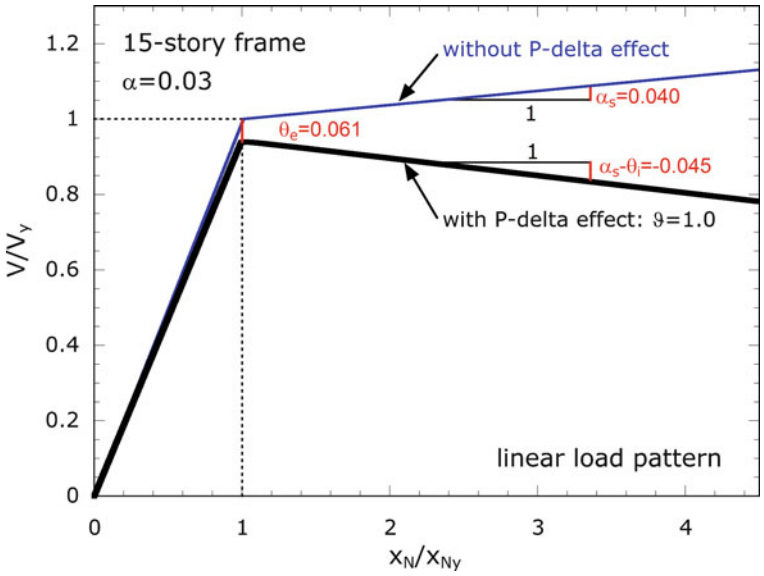


Fig. 4 Global pushover curves of a 15-story frame structure based on a linear load pattern considering and disregarding P-delta effects

ratio between yield base shear V_y and total weight $W(\gamma = V_y/W)$, is $\gamma = 0.1$. For additional dynamic studies structural damping is considered by means of mass proportional Rayleigh damping of 5% of the first mode.

Figure 4 shows normalized base shear against normalized roof drift relations of this structure as a result of static pushover analyses utilizing an inverted triangular load pattern both considering and omitting gravity loads, respectively. Axial gravity loads are based on a ratio of life load plus dead load to dead load of 1.0, i.e. coefficient $\vartheta = 1.0$. Both global pushover curves exhibit a sharp transition from elastic to inelastic branch of deformation. This behavior can be attributed to specific tuning of the yield strength as specified above. The graphs of this figure demonstrate the expected softening effect of the gravity loads. Both elastic and inelastic global stiffness decrease. For this particular structure the presence of gravity loads leads to a negative stiffness in the post-yield range of deformation. From this outcome it can be concluded that this frame structure may become vulnerable to collapse induced by global P-delta effects.

From the global pushover curve without P-delta a global hardening ratio α_S of 0.040 can be identified, which is larger than the individual hardening coefficients α of the rotational springs of 0.03.

As outlined by Medina and Krawinkler [20] there is no unique global stability coefficient for those structures, which cannot be modeled a priori as SDOF systems. The global force-displacement behavior represented by the global pushover curve exhibits in its bilinear approximation an elastic stability coefficient and an inelastic stability coefficient, compare with Fig. 4. Recall that a stability coefficient is a measure of the decrease of the structural stiffness caused by gravity loads.

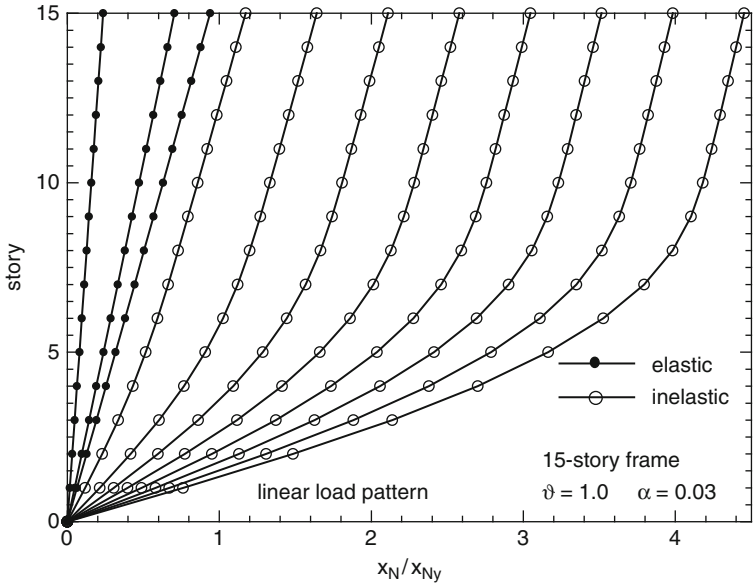


Fig. 5 Deflected shapes of a 15-story frame structure from a pushover analysis

For the actual example problem the following elastic stability coefficient θ_e and inelastic stability coefficient θ_i can be determined: $\theta_e = 0.061$, $\theta_i = 0.085$. The negative slope of the normalized post-yield stiffness is expressed by the difference $\alpha_S - \theta_i = -0.045$.

In Fig. 5 corresponding displacement profiles of the frame structure in presence of P-delta effects are depicted. As long as the structure is deformed elastically the deflected shapes are relatively close to a straight line. However, once the structure yields there is a concentration of the maximum story drifts in the lower stories. As the roof displacement increases, the bottom story drift values increase at a rapid rate [20]. This concentration of the displacement in the bottom stories is characteristic for regular frame structures vulnerable to the P-delta effect. Comparative calculations have shown that the displacement profiles are close to a straight line even in the inelastic range of deformation when gravity loads are disregarded.

3 Assessment of the Global Collapse Capacity

3.1 Incremental Dynamic Analysis

Incremental Dynamic Analysis (IDA) is an established tool in earthquake engineering to gain insight into the non-linear behavior of seismic excited structures [21]. Subsequently, the application of IDAs for predicting the global collapse capacity of multi-story frame structures, which are vulnerable to P-delta effects, is summarized.

For a given structure and a given acceleration time history of an earthquake record dynamic time history analyses are performed repeatedly, where in each subsequent run the intensity of the ground motion is incremented. As an outcome a characteristic intensity measure is plotted against the corresponding maximum characteristic structural response quantity for each analysis. The procedure is stopped, when the response grows to infinity, i.e. structural failure occurs. The corresponding intensity measure of the ground motion is referred to as collapse capacity of the building for this specific ground motion record. There is no unique definition of intensity of an earthquake record. Examples of the intensity measure are the peak ground acceleration (PGA) and the 5% damped spectral acceleration at the structure's fundamental period $S_a(T_1)$.

Since the result of an IDA study strongly depends on the selected record, IDAs are performed for an entire set of n ground motion records, and the outcomes are evaluated statistically. In particular, the median value of the individual collapse capacities CC_i, $i = 1, \ldots, n$, is considered as the representative collapse capacity CC for this structure and this set of ground motion records,

$$CC = med\,\langle CC_i, i = 1, \ldots, n\rangle \tag{1}$$

3.2 Example

In the following the global collapse capacity of the generic 15-story frame structure presented in Sect. 2.2 is determined. The collapse capacity is based on a set of 40 ordinary ground motion records (records without near-fault characteristics), which were recorded in California earthquakes of moment magnitude between 6.5 and 7, and closest distance to the fault rupture between 13 and 40 km on NEHRP site class D (FEMA 368, 2000). This set of seismic records, denoted as LMSR-N, has strong motion duration characteristics insensitive to magnitude and distance. A statistical evaluation of this bin of records and its characterization is given in [14].

In Fig. 6 IDA curves are shown for each record with light gray lines. For this example the normalized spectral acceleration at the structure's fundamental period,

$$\frac{S_a(T_1)}{g\gamma} \tag{2}$$

is utilized as relative intensity measure. This parameter is plotted against the normalized lateral roof displacement x_N,

$$\frac{x_N}{S_d(T_1)} \tag{3}$$

where S_d is the 5% damped spectral displacement at the fundamental period of vibration.

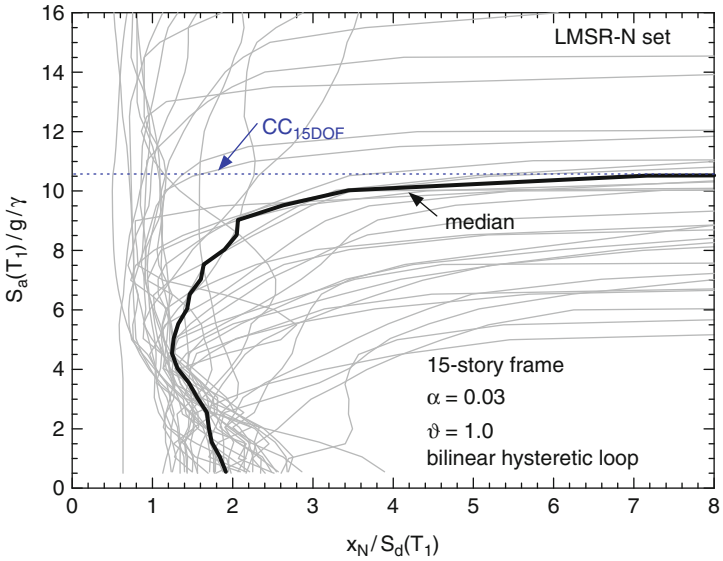


Fig. 6 IDA curves for 40 ground motion records. Median IDA curve. Median collapse capacity CC_{15DOF} of a generic 15-story frame with a fundamental period of vibration of 3.0 *s*

Subsequently, an arbitrary IDA curve is picked from the entire set and its behavior discussed exemplary. When the relative seismic intensity is small the structure is deformed elastically. With increasing intensity the normalized roof displacement becomes smaller because energy is dissipated through ductile structural deformations. However, at a certain level of intensity the IDA curves bends at a rapid rate towards collapse. When the IDA curve approaches a horizontal tangent, the collapse capacity of the structure for this particular accelerogram is exhausted. The entire set of IDA curves shows that the IDA study is ground motion record specific. To obtain a meaningful prediction of the global collapse capacity the median IDA curve is determined, which is shown in Fig. 6 by a fat black line. The median IDA curve approaches a horizontal straight dashed line. This line indicates the relative median collapse capacity CC_{15DOF} of this 15-degree-of-freedom (15DOF) structure subjected to the LMSR-N bin of records:

$$CC_{15DOF} = 10.5 \tag{4}$$

Figure 7 shows time histories of normalized interstory drifts of the frame structure in a state of dynamic instability induced by a single seismic event. The corresponding ground motion record "LP89agw" is included in the LMSR-N bin. It can be seen that after time $t = 15\,s$ the ratcheting effect dominates the dynamic response of the bottom stories, i.e. the deformation increases in a single direction. Because the displacements grow to infinity, collapse occurs at a rapid rate. The largest interstory drift develops in the first story. With rising story number the relative story

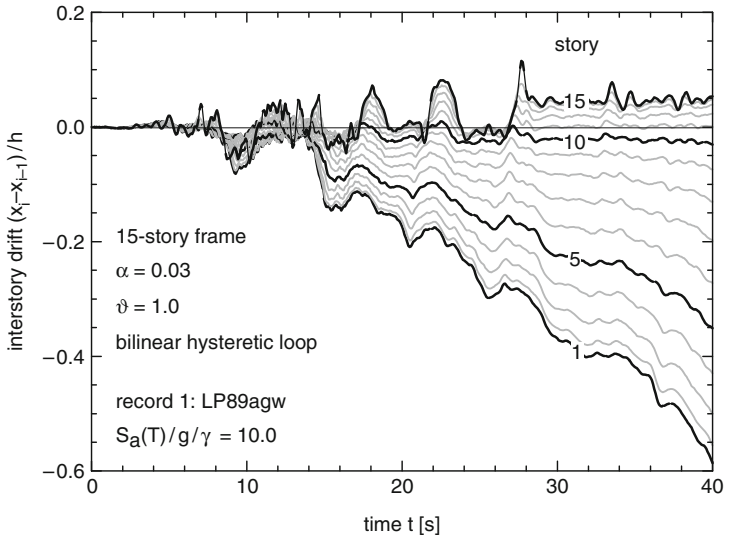


Fig. 7 Global collapse of the 15-story frame structure induced by an individual ground motion record: time history of normalized interstory drifts

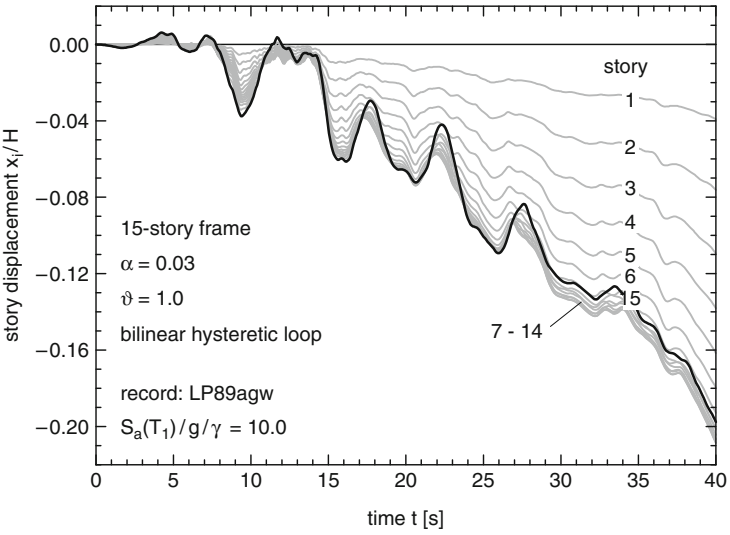


Fig. 8 Global collapse of the 15-story frame structure induced by an individual ground motion record: time history of normalized story displacements

displacements become smaller. In the upper stories a residual deformation remains in opposite direction. This behavior can be attributed to higher mode effects.

The corresponding story displacements are depicted in Fig. 8. They are normalized by the total height H of the structure. With increasing story number the

interstory drifts accumulate to larger story displacements. However, the largest story displacements do not occur at the roof ($i = 15$) thanks to higher mode effects as illustrated above.

4 Simplified Assessment of the Global Collapse Capacity

For large frame structures with many DOFs and a large set of ground motion records the IDA procedure is computational expensive. Thus, it is desirable to provide simplified methods for prediction of the global collapse capacity of structures sensitive to P-delta effects with sufficient accuracy.

Because in regular frame structures P-delta effects are mainly controlled by lateral displacements of the lower stories it is reasonable to assume that these effects can be captured by means of ESDOF systems even in tall buildings in which upper stories are subjected to significant higher mode effects [18]. Application of an ESDOF system requires that shape and structure of the corresponding large frame are regular. Thus, the following considerations are confined to regular planar multi-story frame structures as shown in Fig. 9a, which furthermore exhibit non-deteriorating inelastic material behavior under severe seismic excitation.

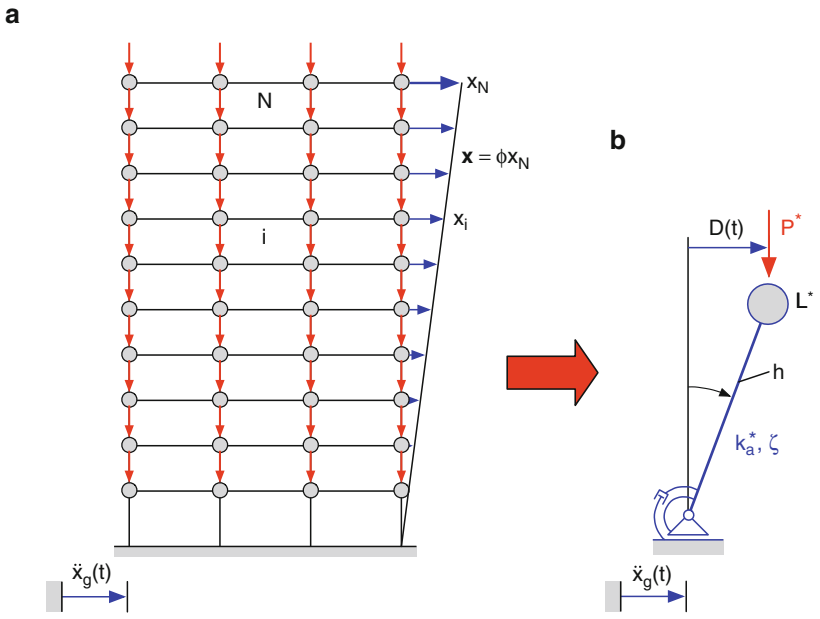


Fig. 9 (**a**) Multi-story frame structure, and (**b**) corresponding equivalent single-degree-of-freedom system

4.1 Equivalent Single-Degree-of-Freedom System

The employed ESDOF system is based on a time-independent shape vector $\boldsymbol{\phi}$, which describes the displacement vector $\mathbf{x}$ of the MDOF structure regardless of its magnitude,

$$\mathbf{x} = \boldsymbol{\phi}\, x_N,\ \phi_N = 1 \tag{5}$$

and on global pushover curves of corresponding pushover analyses applied to the original structure disregarding and considering vertical loads, respectively. The lateral pushover load $\mathbf{F}$ is assumed to be affine to the displacement vector $\mathbf{x}$,

$$\mathbf{F} = \boldsymbol{\phi}\, F_N \tag{6}$$

Examples of such global pushover curves are shown in Figs. 2 and 4. Details of the proposed ESDOF system can be found in Fajfar [22] and Adam et al. [18].

According to [18] and [22] displacement D of the ESDOF system (Fig. 9b) is related to the roof displacement x_N as follows,

$$D = \frac{m^*}{L^*} x_N,\ L^* = \boldsymbol{\phi}^{\mathrm{T}}\mathbf{M}\,\mathbf{e},\ m^* = \boldsymbol{\phi}^{\mathrm{T}}\mathbf{M}\,\boldsymbol{\phi} \tag{7}$$

$\mathbf{M}$ is the mass matrix of the original frame structure, and $\mathbf{e}$ denotes the influence vector, which represents the displacement of the stories resulting from a static unit base motion in direction of the ground motion $\ddot{x}_g$.

The backbone curve of the ESDOF spring force f_S^* is derived from the base shear V of the global pushover curve (without P-delta effect) according to [18, 22]

$$f_S^* = \frac{m^*}{L^*} V \tag{8}$$

In contrast to a real SDOF system no unique stability coefficient does exist for an ESDOF oscillator, since the backbone curve of the ESDOF system is based on the global pushover curve [1, 20]. As illustrated in Fig. 10 a bilinear approximation of

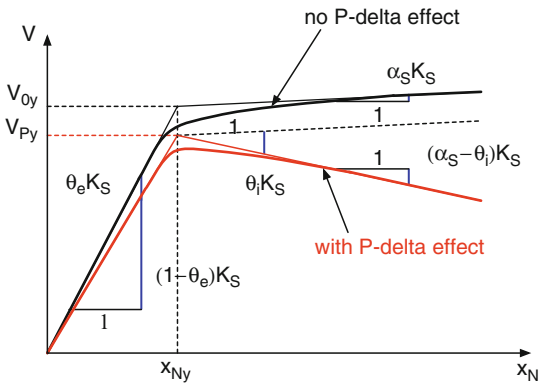


Fig. 10 Global pushover curves with and without P-delta effect and their bilinear approximations

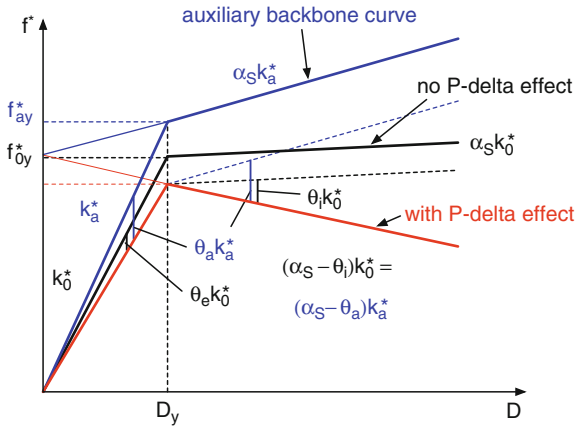


Fig. 11 Backbone curves with and without P-delta effect and auxiliary backbone curve

the backbone curve renders an elastic stability coefficient θ_e and an inelastic stability coefficient θ_i. Analyses have shown that θ_i is always larger than θ_e, $\theta_i > (>)\theta_e$ [20]. Thus, loading of the ESDOF system by means of an equivalent gravity load, which is based on the elastic stability coefficient θ_e, leads to a "shear deformation" of the hysteretic loop of the ESDOF system, where the post-tangent stiffness is overestimated. Consequently, the hazard of collapse would be underestimated. Ibarra and Krawinkler [4] propose to employ an auxiliary backbone curve, which features a uniform stability coefficient θ_a, compare with Fig. 11. In [4, 18] the parameters of the auxiliary backbone curve are derived as:

$$\theta_a = \frac{\theta_i - \theta_e \alpha_S}{\upsilon},\ k_a^* = \frac{\upsilon}{1-\alpha_S} k_0^*,\ f_{ay}^* = \frac{\upsilon}{1-\alpha_S} f_{0y}^*,\ \upsilon = 1 - \theta_e + \theta_i - \alpha_S \quad (9)$$

Subsequently, an appropriate hysteretic loop is assigned to the auxiliary backbone curve, which is sheared by θ_a when the ESDOF system is loaded by the equivalent gravity force P^* [14]:

$$P^* = \theta_a \, k_a^* \, h \quad (10)$$

This situation is illustrated in Fig. 12, where exemplarily a bilinear hysteretic curve is assigned to the auxiliary backbone curve. Now, the normalized equation of motion of the auxiliary ESDOF system can be expressed in full analogy to a real SDOF system as [14]

$$\frac{1}{\omega_a^{*2}} \ddot{\mu}^* + 2\zeta \frac{1}{\omega_a^*} \dot{\mu}^* + \left(\bar{f}_S^* - \theta_a \mu^* \right) = -\frac{\ddot{x}_g}{g\,\gamma^*} \quad (11)$$

with

$$\mu^* = \frac{D}{D_y},\ \bar{f}_S^* = \frac{f_{aS}^*}{f_{ay}^*},\ \omega_a^* = \sqrt{\frac{k_a^*}{L^*}} \quad (12)$$

In Eqs. 11 and 12 μ^* is the non-dimensional horizontal displacement of mass L^* of the ESDOF, and D_y characterizes the yield displacement. $\bar{f}_S^*$ denotes the

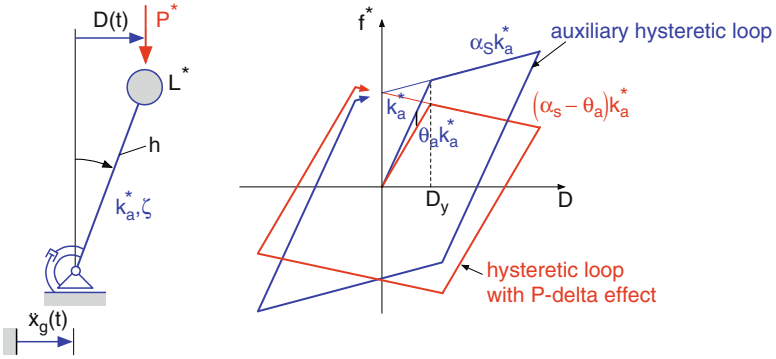


Fig. 12 Auxiliary equivalent single-degree-of-freedom system with bilinear hysteretic behavior

non-dimensional spring force, which is the ratio of the auxiliary spring force f_{aS}^* and its yield strength $f_{ay}^* \cdot \omega_a^*$ represents the circular natural frequency of the auxiliary ESDOF system, and k_a^* is the corresponding stiffness. The equivalent base shear coefficient γ^* of the ESDOF system is calculated from the base shear coefficient $\bar{\gamma}$ of the MDOF system according to [18]

$$\gamma^* = \frac{\bar{\gamma}}{\lambda_{MDOF}}, \; \bar{\gamma} = \frac{V_y}{Mg}, \; \lambda_{MDOF} = \frac{L^{*2}}{m^* M} \tag{13}$$

V_y is the base shear at the yield point, and M the (dynamic effective) total mass of the MDOF structure.

4.2 Collapse Capacity Spectra

Adam et al. [13–15] propose to utilize collapse capacity spectra for the assessment of the collapse capacity of SDOF systems, which are vulnerable to the P-delta effect. In [15] it is shown that the effect of gravity loads on SDOF systems with bilinear hysteretic behavior is mainly characterized by means of the following structural parameters:

- The elastic structural period of vibration T
- The slope of the post-tangential stiffness expressed by the difference $\theta - \alpha$ of the stability coefficient θ and the strength hardening coefficient α
- The viscous damping coefficient ζ (usually taken as 5%)

In [15] design collapse capacity spectra are presented as a function of these parameters. As an example in Figs. 13 and 14 collapse capacity spectra and the corresponding design collapse capacity spectra, respectively, are shown for SDOF systems with stable bilinear hysteretic behavior [15]. They are based on the LMSR-N set of 40 ground motions. Here, the collapse capacity CC is defined as the median of the 40 individual collapse capacities CC_i, $i = 1, \ldots, 40$,

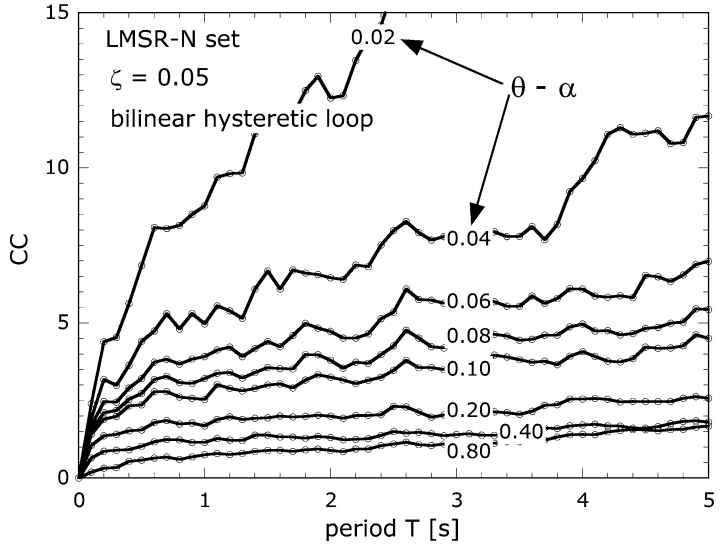


Fig. 13 Collapse capacity spectra of single-degree-of-freedom systems with bilinear hysteretic loop

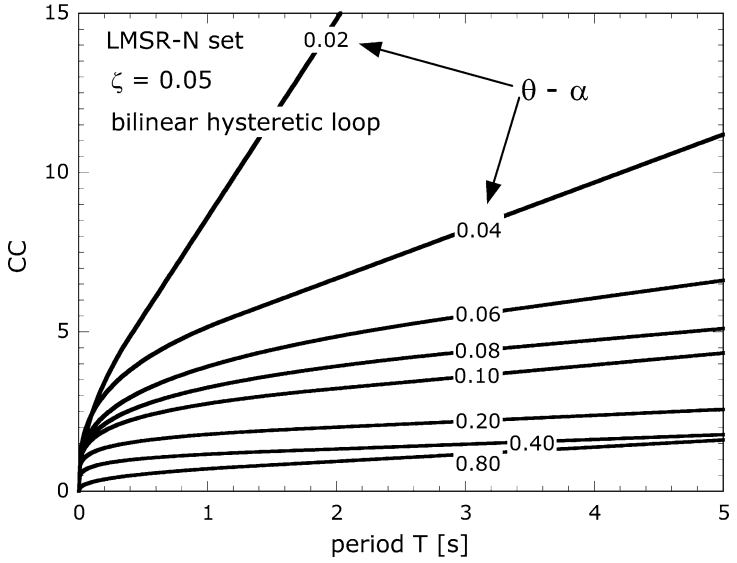


Fig. 14 Design collapse capacity spectra of single-degree-of-freedom systems with bilinear hysteretic loop

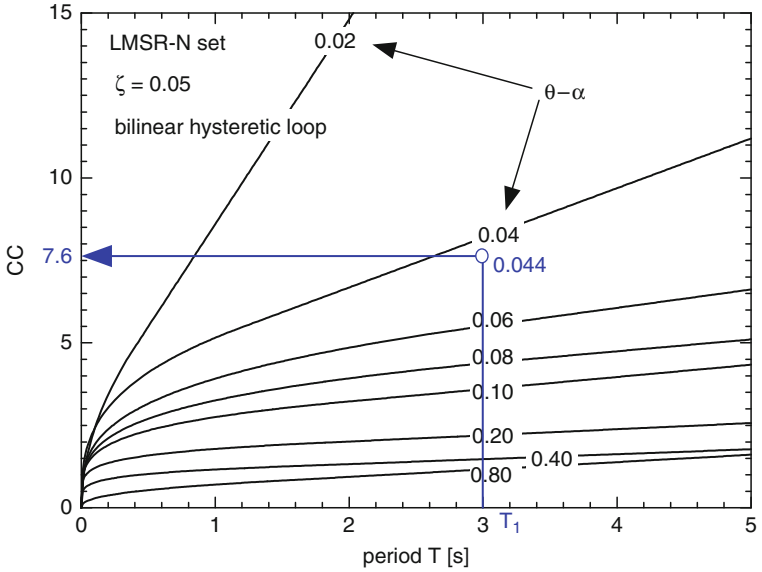


Fig. 15 Application of design collapse capacity spectra to an equivalent single-degree-of-freedom system

$$CC = med\,\langle CC_i, i = 1, \ldots, 40\rangle \tag{14}$$

which are for these spectra the 5% damped spectral acceleration at the period of vibration T, where structural collapse occurs [15],

$$CC_i = \frac{S_a(T)|_i}{g\gamma} \tag{15}$$

Application of design collapse capacity spectra is simple: an estimate of the elastic period of vibration T, stability coefficient θ and hardening ratio α of the actual SDOF structure need to be determined. Subsequently, from the chart the corresponding collapse capacity CC can be read as shown in Fig. 15.

4.3 Application of Design Collapse Capacity Spectra to Multi-Story Frame Structures

ESDOF systems allow the application of design collapse capacity spectra for assessing the collapse capacity of multi-story frame structures. Thereby, T and $\theta - \alpha$ of a SDOF system are replaced by the fundamental period T_1 of the actual MDOF system (without P-delta), and the difference of the auxiliary stability coefficient and hardening coefficient $\theta_a - \alpha_S$. α_S is the hardening coefficient taken from the global pushover curve without P-delta effect. From the design collapse capacity spectrum

a prediction of the related collapse capacity CC is obtained. The actual collapse capacity of the ESDOF system, i.e. the normalized median intensity of earthquake excitation at collapse, is subsequently determined from, compare with Eq. 13,

$$CC_{ESDOF} = \frac{CC}{\lambda_{MDOF}} \tag{16}$$

This outcome represents an approximation of the collapse capacity CC_{MDOF} of the actual MDOF building,

$$CC_{MDOF} \approx CC_{ESDOF} \tag{17}$$

4.4 Example

In an example problem the application of ESDOF systems and collapse spectra for the prediction of the global collapse capacity of multi-story frame structures is illustrated. For this purpose the generic 15-story frame structure of Sect. 2.2 is utilized. Recall that the fundamental period of this structure is $T_1 = 3.0\,s$, and the elastic stability coefficient, the inelastic stability coefficient and the hardening ratio, respectively, are: $\theta_e = 0.061$, $\theta_i = 0.085$, $\alpha_S = 0.040$. The auxiliary stability coefficient according to Eq. 9 is $\theta_a = 0.084$, and thus $\theta_a - \alpha_S = 0.044$. Coefficient λ_{MDOF}, Eq. 13, is derived as: $\lambda_{MDOF} = 0.774$.

Application of design collapse capacity spectra as illustrated in Fig. 15 renders the collapse capacity $CC = 7.6$. Division by the coefficient λ_{MDOF} results in the collapse capacity of the ESDOF system,

$$CC_{ESDOF} = 7.6\,\frac{1}{0.774} = 9.83 \tag{18}$$

Comparing this outcome with the result of the IDA procedure on the actual 15-story frame structure according to Eq. 4, $CC_{15DOF} = 10.5$, reveals that CC_{ESDOF} is for this example a reasonable approximation of the collapse capacity.

In addition, Fig. 16 shows the collapse capacity of the 15-story frame for different magnitudes of gravity loads, i.e. the ratio ϑ of life plus dead load to dead load is varied from 1.0 to 1.6. The latter value is considered only for curiosity. Median, 16% percentile and 84% percentile collapse capacity derived from IDAs are depicted by black lines. These outcomes are set in contrast to the median collapse capacity from a simplified assessment based on ESDOF systems and collapse capacity spectra represented by a dashed line. It can be seen that in the entire range the simplified prediction of the collapse capacity underestimates the "exact" collapse capacity. In other words, the simplified methodology renders for this example results on the conservative side. Note that the modification of the fundamental period T_1 by P-delta is not taken into account.

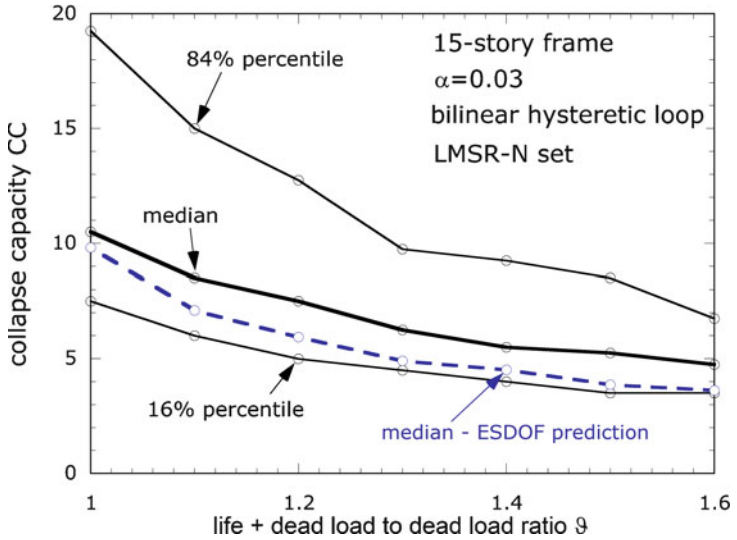


Fig. 16 Collapse capacity of a 15-story frame structure for different magnitudes of gravity loads. Comparison with simplified assessment (*dashed line*)

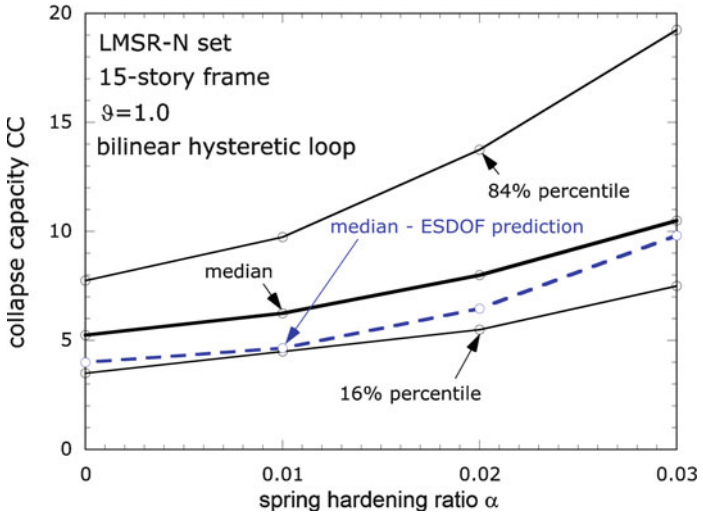


Fig. 17 Collapse capacity of a 15-story frame structure for different hardening ratios of the bilinear springs. Comparison with simplified assessment (*dashed line*)

The same holds true when the hardening ratio of the bilinear springs is varied from 0.0 to 0.03, compare with Fig. 17. Application of ESDOF systems combined with collapse spectra renders median collapse capacities smaller than the actual ones. As expected it can be observed that the collapse capacity rises with increasing post-yield stiffness.

5 Conclusions

The vulnerability of seismic excited flexible inelastic multi-story frame structures to dynamic instabilities has been evaluated. In particular a simplified methodology for assessment of the global collapse capacity has been proposed, which is based on equivalent single-degree-of-freedom systems and collapse capacity spectra. The result of an example problem presented in this study suggests that the application of equivalent single-degree-of-freedom systems and collapse capacity spectra is appropriate to estimate the seismic P-delta effect in highly inelastic regular multi-story frame structures provided that they exhibit non-deteriorating inelastic material behavior under severe seismic excitation.

References

1. Bernal D (1998) Instability of buildings during seismic response. Eng Struct 20:496–502
2. Gupta A, Krawinkler H (2000) Dynamic P-delta effect for flexible inelastic steel structures. J Struct Eng 126:145–154
3. Aydinoglu MN (2001) Inelastic seismic response analysis based on story pushover curves including P-delta effects. Report No. 2001/1, KOERI, Istanbul, Department of Earthquake Engineering, Bogazici University
4. Ibarra LF, Krawinkler H (2005) Global collapse of frame structures under seismic excitations. Report No. PEER 2005/06, Pacific Earthquake Engineering Research Center, University of California, Berkeley, CA
5. Lignos DG, Krawinkler H (2009) Sidesway collapse of deteriorating structural systems under seismic excitations. Report No. TB 172, John A. Blume Earthquake Engineering Research Center, Department of Civil and Environmental Engineering, Stanford University, Stanford, CA
6. Asimakopoulos AV, Karabalis DL, Beskos DE (2007) Inclusion of the P-Δ effect in displacement-based seismic design of steel moment resisting frames. Earthquake Eng Struct Dyn 36:2171–2188
7. Villaverde R (2007) Methods to assess the seismic collapse capacity of building structures: state of the art. J Struct Eng 133:57–66
8. Bernal D (1987) Amplification factors for inelastic dynamic P-Δ effects in earthquake analysis. Earthquake Eng Struct Dyn 15:635–651
9. MacRae GA (1994) P-Δ effects on single-degree-of-freedom structures in earthquakes. Earthquake Spectra 10:539–568
10. Kanvinde AM (2003) Methods to evaluate the dynamic stability of structures – shake table tests and nonlinear dynamic analyses. In: EERI Paper Competition 2003 Winner. Proceedings of the EERI Meeting, Portland
11. Vian D, Bruneau M (2003) Tests to structural collapse of single degree of freedom frames subjected to earthquake excitation. J Struct Eng 129:1676–1685
12. Miranda E, Akkar SD (2003) Dynamic instability of simple structural systems. J Struct Eng 129:1722–1726
13. Adam C, Spiess J-P (2007) Simplified evaluation of the global capacity of stability sensitive frame structures subjected to earthquake excitation (in German). In: Proceedings of the D-A-CH meeting 2007 of the Austrian association of earthquake engineering and structural dynamics, September 27–28, 2007, Vienna, CD-ROM paper, paper no. 30, 10 pp

14. Adam C (2008) Global collapse capacity of earthquake excited multi-degree-of-freedom frame structures vulnerable to P-delta effects. In: Yang YB (ed) Proceedings of the Taiwan – Austria joint workshop on computational mechanics of materials and structures, 15–17 November 2008, National Taiwan University, Taipei, Taiwan, pp 10–13
15. Adam C, Jäger C (submitted) Seismic collapse capacity of basic inelastic structures vulnerable to the P-delta effect
16. Takizawa H, Jennings PC (1980) Collapse of a model for ductile reinforced concrete frames under extreme earthquake motions. Earthquake Eng Struct Dyn 8:117–144
17. Bernal D (1992) Instability of buildings subjected to earthquakes. J Struct Eng 118:2239–2260
18. Adam C, Ibarra LF, Krawinkler H (2004) Evaluation of P-delta effects in non-deteriorating MDOF structures from equivalent SDOF systems. In: Proceedings of the 13th World Conference on Earthquake Engineering, 1–6 August 2004, Vancouver BC, Canada. DVD-ROM paper, 15 pp, Canadian Association for Earthquake Engineering
19. Adam C, Jäger C (2010) Assessment of the dynamic stability of tall buildings subjected to severe earthquake excitation. In: Proceedings of the International Conference for highrise towers and tall buildings 2010, 14–16 April 2010, Technische Universität München, Munich, Germany. CD-ROM paper, 8 pp
20. Medina RA, Krawinkler H (2003) Seismic demands for nondeteriorating frame structures and their dependence on ground motions. In: Report No. 144, John A. Blume Earthquake Engineering Research Center, Department of Civil and Environmental Engineering, Stanford University, Stanford, CA
21. Vamvatsikos D, Cornell CA (2002) Incremental dynamic analysis. Earthquake Eng Struct Dyn 31:491–514
22. Fajfar P (2002) Structural analysis in earthquake engineering – a breakthrough of simplified non-linear methods. In: Proceedings of the 12th European Conference on Earthquake Engineering, CD-ROM paper, Paper Ref. 843, 20 pp, Elsevier

On the Evaluation of EC8-Based Record Selection Procedures for the Dynamic Analysis of Buildings and Bridges

Anastasios G. Sextos, Evangelos I. Katsanos, Androula Georgiou, Periklis Faraonis, and George D. Manolis

Abstract This chapter focuses on an assessment of the selection procedure for real records based on Eurocode 8 provisions, through a study of the performance of R/C bridges of the Egnatia highway system and of a multi-storey R/C building damaged during the Lefkada earthquake of 2003 in Greece. More specifically, the bridge was studied by using six alternative models and accounting for the dynamic interaction of the deck-abutment-backfill-embankment system as well as of the superstructure-foundation-subsoil system, while the building was studied in both the elastic and inelastic range taking into consideration material nonlinearity as well as the surrounding soil. Furthermore, different input sets comprising seven pairs of records (horizontal components only) from Europe, Middle-East and the US were formed in compliance with EC8 guidelines. The results of these parametric analyses permit quantification of the intra-set scatter of the seismic response for both structures, thus highlighting the current limitations of the EC8 guidelines. The chapter concludes with specific recommendations that aim at eliminating the dispersion observed in the elastic and more so in the inelastic response though appropriate modifications of EC8-proposed selection parameters.

Keywords Recorded accelerograms · Ground motion selection process · Eurocode 8 · R/C building · Twin bridge · Finite element models · Elastic and inelastic response · Response scatter

A.G. Sextos (✉), E.I. Katsanos, A. Georgiou, and P. Faraonis
Division of Structural Engineering, Department of Civil Engineering,
Aristotle University of Thessaloniki, 54124 Greece
e-mail: asextos@civil.auth.gr; katsanos@civil.auth.gr; georgant@civil.auth.gr; pfaraoni@civil.auth.gr

G.D. Manolis
Laboratory of Statics and Dynamics of Structures, Department of Civil Engineering,
Aristotle University of Thessaloniki, 54124 Greece
e-mail: gdm@civil.auth.gr

M. Papadrakakis et al. (eds.), *Computational Methods in Earthquake Engineering*,
Computational Methods in Applied Sciences 21, DOI 10.1007/978-94-007-0053-6_3,
© Springer Science+Business Media B.V. 2011

1 Introduction

During the last decade, elastic and inelastic dynamic analyses in the time domain have been made feasible for complex structures with thousands of degrees of freedom, thanks to rapidly increasing computational power and the evolution of engineering software. As a result, time-domain analysis is prescribed in the majority of modern seismic codes. On the other hand, recent work has shown that among all sources of uncertainty stemming from the (structural and soil) material properties, the design assumptions and the earthquake-induced ground motion, the latter seems to be the most unpredictable [1] and has a significant impact on the variability observed in the structural response [2]. Ground motions appear random in space and time, due to the inherent complexity of the path that seismically induced waves follow as they travel from the fault-plane source through bedrock [3] and finally through the soil layers to reach the foundation level of a structure [4]. The local site effects also cause modifications to the seismic motion, both in terms of frequency and amplitude [4, 5].

Given the above uncertainties, and despite the relatively straightforward seismic code framework regarding transient dynamic analysis with primarily the use of a response target spectrum representing the seismic loading, it is still the designer's responsibility to find a 'reasonable' way for selecting one or more sets of 'appropriate' earthquake records, a task that is technically easy, but at the same time difficult since any discrepancies in the computed structural response must be kept reasonably low. This is a complex task that cannot be accomplished on a 'trial and error' basis without understanding the basic concepts behind selection and scaling of earthquake records for use in dynamic analysis, as is evident in the current literature output [6]. In other words, the current code framework for ground motion record selection is considered to be rather simplified compared to the potential impact of the selection process on the dynamic analysis, thus giving the false impression that structural analysis results are as robust as the refined finite element model used permit them to be.

Some state-of-the-art methods [7–10] have been proposed in order to optimize the selection and scaling process of real records, but it is unlikely that these methods can be used in common practice as of yet. On the other hand, seismic codes take advantage of the existing databases and strong-motion arrays currently available and propose the use of earthquake accelerograms that comply with general pre-defined criteria, while satisfying specific spectral matching requirements. Nevertheless, selecting and scaling an appropriate set of earthquake records that would lead to a stable mean of structural response is neither ensured nor even achievable. Equally troubling, the number of records required to ensure the above requirement cannot be easily assessed in advance [11].

The study presented herein investigates the feasibility of selecting real records sets on the basis of the current EC8 provisions, for the seismic assessment through dynamic analysis of an existing building in the island of Lefkada in western Greece and of one bridge in Egnatia highway in northern Greece. More specifically, the multi-storey building from Lefkada was studied not only because it was heavily

damaged by a severe seismic event (Ms = 6.4, on 14.08.2003), but also because both an earthquake record and an in-situ soil investigation of the vicinity are available.

By performing a plethora of linear and nonlinear dynamic analyses of these structures with the use of multiple sets of selected earthquake records, the aim of this chapter is to:

1. Assess the feasibility and effectiveness of the earthquake record selection process prescribed in Eurocode 8
2. Quantify the record-to-record variability of the structural response (elastic and inelastic) for different EC8-compliant selection alternatives
3. Investigate the implications and importance, in terms of structural response, of various individual earthquake record selection criteria such as the epicentral distance and the seismotectonic environment
4. Assess the relative importance of different earthquake record selection criteria
5. Study the selection procedure adopted in relation to various modeling approaches and assumptions and their combined impact to the calculated structural discrepancy and
6. Propose simple improvements that could potentially reduce scatter in the structural response when the selection is made according to Eurocode 8

2 Selection of Seismic Input for Dynamic Analysis According to Eurocode 8

2.1 Record Selection on the Basis of EC8, Part 1

Eurocode 8, Part 1 [12] prescribes that earthquake loading as required for conducting dynamic analyses of buildings, may be defined by either generated artificial or simulated acceleration time histories that are compatible to the target code spectra, or appropriately selected, recorded seismic motions depending on the type of structural assessment and data available at the building site. It is notable that the use of artificial records is described in more detail in EC8 compared to either real or simulated records for which it is outlined that: *the use of recorded accelerograms – or of accelerograms generated through a physical simulation of source and travel path mechanisms – is allowed, provided that the samples used are adequately qualified with regard to the seismogenetic features of the sources and to the soil conditions appropriate to the site, and their values are scaled to the value of* a_g *S for the zone under consideration* (Sect. 3.2.3.1.3.1).

The sets (or bins) of accelerograms that are selected by the designer, regardless whether they are real, simulated or artificial must satisfy the following criteria:

1. The mean of the zero period spectral response acceleration values (calculated from the individual time histories selected) has to be higher than the value of a_g S for the site in question.

2. The mean of the 5% damped elastic spectrum that is calculated from all time histories should be no less than 90% of the corresponding value of the 5% damped EC8 elastic response spectrum, in the range of periods between $0.2T_1$ and $2T_1$, where T_1 is the fundamental period of the structure in the direction where the accelerogram is applied (Sect. 3.2.3.1.2.4).
3. A minimum of three accelerograms has to be selected in each set. When three different accelerograms are used, the structural demand is determined from the most unfavorable value that occurs from the corresponding dynamic analyses. On the other hand, in case that at least seven different (real, artificial or simulated) records are used, the design value of the action effect Ed can be derived from the average of the response quantities that result from all the analyses (Sect. 4.3.3.4.3).

When a spatial model is required for the dynamic analysis, EC8 states that the seismic motion should consist of three simultaneously acting accelerograms representing the two horizontal and the vertical component of strong ground motion; however, the same record must not be used simultaneously along both horizontal directions. The vertical component of seismic motion should only be considered if the design vertical ground acceleration for type A ground, a_{vg}, is greater than $0.25g$ or in other special cases (Sect. 4.3.3) such as long structural members and base-isolation systems. As a result, in most cases, a set of excitation records is formed for the two horizontal components only.

2.2 Record Selection on the Basis of EC8, Part 2

It is interesting to notice that for the case of bridges, EC8-Part2 [13], provides more detailed guidelines compared to EC8-Part1 for the selection of earthquake input for linear as well as non-linear dynamic analysis. In particular, simulated records can only be utilized in case the required number of recorded ground motions cannot be reached. Nevertheless, despite the fact that EC8-Part2 shares the same spectral shapes and site classification with those in Part 1, additional criteria are provided regarding spectral matching (Sect. 3.2.3.3):

1. For each selected seismic event considering both horizontal components, the joint SRRS spectrum should be determined, by taking the square root of the sum of squares of the 5% damped spectra of each component.
2. Based on the above, a spectrum of the ensemble of earthquakes shall be formed by taking the average value of the SRSS spectra of the individual earthquakes of the previous step.
3. Given the fact that the ensemble spectrum for each event is inevitably higher than that of its individual components, a threshold of 1.3 times (compared to 0.9 prescribed in Part 1) the 5% damped design seismic spectrum is required. This is for the period range between $0.2T_1$ and $1.5T_1$, where T_1 is the fundamental period of the mode of the (ductile) bridge, or the effective period (T_{eff}) of the isolation system in the case of a base-isolated bridge.

4. Record scaling is permitted, but the scale factor required from the previous step shall be uniform for each pair of seismic motion components.

It is also notable that some more specific provisions are provided regarding moderate to long bridge spans that are sensitive to the spatial variation of seismic motion (Sect. 3.3 and Annex D) and bridges where the vertical component of seismic motion is important (Sects. 3.2.3 and 4.1.7) as well as cases where near source effects are deemed significant (Sect. 3.2.2.3 of EC8 [13]).

3 Case Studies for Evaluation of EC8-Based Earthquake Record Selection for Buildings and Bridges

3.1 Case Study 1: Nonlinear Dynamic Analysis of an Irregular R/C Building in Lefkada, Greece

3.1.1 Overview of the Lefkada Earthquake

The Lefkada earthquake of August 14, 2003 measured 6.4 of magnitude and was the most powerful seismic event since 1995 in that area, which is characterized by the highest seismicity in Greece. This fact is reflected in the Greek Seismic Code where the peak ground acceleration is set at $0.36g$. The epicenter was located 8.5 miles under sea, approximately 20 miles north-west of Lefkada Island. Four strong aftershocks of magnitudes 5.3–5.5 followed the main shock in of the next 24 h. The shock caused severe damages to reinforced concrete buildings, roads, quay walls, water and wastewater systems. Furthermore, extensive rock falls occurred all over the island, interrupting the road network and disrupting access at several locations.

The acceleration time histories shown in Fig. 1 were recorded by the permanent array of the Institute of Engineering Seismology and Earthquake Resistant Structures in Thessaloniki [14]. The intensity of the earthquake is clearly demonstrated since a maximum horizontal ground acceleration of $0.36g$ was recorded.

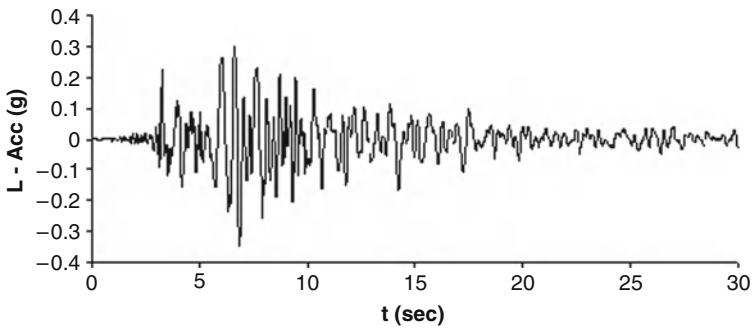


Fig. 1 Longitudinal component of recorded ground motion during the Lefkada earthquake (M_s = 6.4, 14.08.2003) [14]

3.1.2 Structural Configuration and Regional Soil Profile

The structure in the present chapter is a four-storey R/C building (including pilotis), located in the city of Lefkada that was heavily damaged during the seismic event. This building has been studied in the past [15], because all structural and foundation configuration plans, soil profile and earthquake records in its vicinity were reliably known. As a result, it offers the advantage that all simulations can be verified by matching the numerical prediction with the observed inelastic response of the building. The structure was constructed in 1979 according to the current seismic code. More specifically, the earthquake forces, described by a seismic factor $\varepsilon = 0.16g$, were applied uniformly with height as defined by the Greek Seismic Code of 1959, while member design was performed on the basis of the 1954 Reinforced Concrete Code. The building is irregular in plan as can be seen in Fig. 2, since the ground floor of 5.65 m in height was used as a super market and a 3.0 m high loft was constructed at the back of the store causing a discontinuous distribution of the stiffness in elevation. Concrete class is considered equivalent to the current C16/20, while St.III steel bars were used for longitudinal reinforcement and St.I for the transverse [16]. The soil conditions at the location of the structure as well as through-out the



Fig. 2 The multi-storey R/C building (case study 1)

overall bay area are characterized by very soft soil strata classified as category D to X according to EC8 [17]. In particular, based on in-situ geotechnical investigations, the superficial layer comprises debris to a depth of 3.5 m, followed by a layer of clay of medium to high density down to a depth of 4.6 m. From 4.6 to 10.3 m the soil is considered as loose, liquefiable, silty sand, followed by 1 m of silt with varying percentage of loose sand and a deep layer of medium plasticity marl. Given the above conditions, the structure was supported on a set of small and dense pile groups (61 piles of diameter equal to $d = 0.52$ m and length $L = 18.0$ m) connected with pile caps and tie beams (0.30×0.80 m).

The damage observed [15] during the 2003 earthquake was mainly concentrated at the perimeter of the building and at the ground level, where most columns suffered flexural failure, with the exception of the side short columns which exhibited shear failure.

3.1.3 Numerical Analysis Framework of R/C Building

For the structural assessment of the building under various sets (bins) of earthquake ground motions, a large number of nonlinear dynamic analyses were performed [18] using finite element software (Zeus-NL [19]). As can be seen in Fig. 3a, all structural elements, were modeled using the corresponding three-dimensional cubic frame elements provided by the Zeus-NL FE library. Slabs were considered as external loads acting on the beams, while rigid diaphragm action at each storey was achieved through appropriate strut connections. To obtain more accurate results from the analysis, and given the damage concentration at the columns of the ground floor, the corresponding elements were discretised into four sub-elements of unequal length (i.e., 15%, 35%, 35% and 15% of the overall member length). The lumped mass element (L_{mass}) was used to define the lumped masses at the joints for the dynamic analysis.

Complex concrete behavior under cyclic loading, residual strength, stiffness degradation and the interaction between flexural and axial behavior were taken into consideration by the inherent fiber (distributed plasticity) model of the program. Based on the steel and concrete material stress-strain relationships,

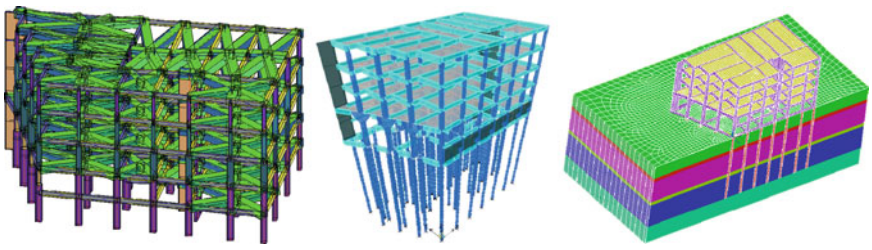


Fig. 3 Case study 1: **(a)** Model 'A'-reference model (ZEUS-NL, *left*), (**b**) Model 'C' (ETABS, *middle*) and (**c**) Model 'D' (Ansys, *right*) of the building

moment-curvature analysis was conducted to predict the ductility and member nonlinear behavior under varying loads. Along these lines, two material models were used in the ZEUS-NL model:

1. The bilinear elasto-plastic model with kinematic strain-hardening (stl1) was used to model the reinforcement and rigid connections and
2. The uniaxial constant confinement concrete model (conc2) that was used for the concrete

The three parameters required for the first model were as follows: Young's modulus ($E = 200{,}000\,N/mm^2$), yield strength ($\sigma_y = 220\,N/mm^2$) and a strain-hardening parameter ($\mu = 0.05$). For the second model, four parameters were defined: compressive strength ($f'_c = 16\,N/mm^2$), tensile strength ($f_t = 1.9\,N/mm^2$), maximum strain ($\varepsilon_{co} = 2$) corresponding to f'_c, and a confinement factor ($k = 1.20$) based on the model of Mander et al. [20]. Time history analyses were conducted using the Newmark algorithm with parameters $\beta = 0.25$ and $\gamma = 0.5$.

3.1.4 Soil-Structure Interaction Aspects and Validation of the Reference Finite Element Model

Given soft soil conditions at the location and being aware of the high computational cost associated with a nonlinear time history analysis of the overall soil-structure system, alternative finite element models of increasing soil modeling refinement were developed. The aim was to decide whether it was indeed necessary to account for soil compliance in the reference finite element model whose inelastic response was assessed for various sets of accelerograms selected according to EC8 procedures outlined in Sect. 2.1.

Thus, apart from 'Model A', namely the 3-D, fixed-base, frame model developed using Zeus-NL that was described previously, three additional finite elements models were developed:

- 'Model B': a fixed-base, spatial frame model using the finite element program ETABS [21], identical to the first one with the exception of shear wall modeling using 2D shell elements and the representation of short columns formed by the presence of masonry infill was created solely for validation purposes.
- 'Model C': an extension of the latter model, where the pile foundation is modeled using length-dependent horizontal Winkler-type springs [22] in the two horizontal directions, accounting for both stiffness reduction and damping increase at the layers exhibiting liquefaction [15] (see Fig. 3b).
- 'Model D': a refined 3-D model developed with the use of the finite element program ANSYS [23], considering the exact soil stratification after appropriate modification of their geotechnical properties resulting from a separate site response analysis, again considering soil liquefaction at particular layers (see Fig. 3c, [24]).

Table 1 summarizes the first six periods, derived by modal analysis for each one of the aforementioned models. The results indicate absolute agreement between the

Table 1 Dynamic characteristics of the four alternative finite element models developed in order to identify the importance of soil compliance

Mode	Period (s) 'Model A' (Zeus-NL, fixed-base)	'Model B' (ETABS, fixed-base)	'Model C' (ETABS, piles with springs)	'Model D' (ANSYS, 3DSoil-piles)
1st	0.539	0.527	0.584	0.693
2nd	0.439	0.433	0.505	0.624
3rd	0.401	0.395	0.455	0.573
4th	0.173	0.180	0.196	0.233
5th	0.134	0.141	0.164	0.197
6th	0.126	0.128	0.158	0.183

fixed-base models ('A' and 'B'), thus establishing a first level of confidence with respect to the simulation of the elastic response of the building. From the first two models, it is clearly observed that the fundamental mode of the structure is primarily torsional due to the lack of adequate shear walls, irregularity in plan and the divergence between the centers of stiffness and mass.

Comparing the fixed-base models with the flexible-base ones, it is concluded that soil compliance leads to a fundamental period elongation of the order of 10–25% for the case of spring-supported piles and 3-D soil modeling, respectively. A first comment is that the 3-D representation of the subsoil volume diverges from the Winkler-type solution, a fact attributed to the inherent difficulty in obtaining compatibility between the modulus of elasticity of the soil and the spring parameters considered in the case of laterally supported piles [25]. Next, since the 3-D soil-structure system is most refined, the effect of soil compliance is non-negligible compared to the fixed-base case, at least in terms of the dynamic characteristics. This is also anticipated given the soft soil profile and the reduction of soil stiffness due to liquefaction (also introduced in the finite element model based on information from liquefaction-dependent site response analysis).

The presence of soil does not affect the sequence of vibration modes of the fixed-base system (i.e., the torsional vibration mode remains fundamental and dominant, while the order of the higher modes also remains unaffected). Moreover, 'Model D' has significantly higher computational cost compared to 'Model A', without providing any further refinement with regard to modeling of the reinforced concrete behavior under cyclic loading (i.e., use of the built-in concrete material and element Solid65 would require 3-D modeling of the building, while its numerical stability in transient analysis is rather questionable).

For all practical purposes, 'Model A' is preferred as the reference model and offers an additional advantage in that the dynamic characteristics of the building are explicitly affected by concrete section yielding only and not by the flexibility of the soil. Thus, potential scatter in structural demand that may result from the earthquake records selection process can be isolated from the coupling effect of soil-structure interaction and can be studied more efficiently.

3.1.5 Quantification of Damage

The performance of buildings under earthquakes and the ensuing damage cannot be assessed solely on the basis of structural demand. For this reason, numerous local damage indices have been proposed in the literature, essentially relating demand with member capacity. These damage indices are generally subdivided into three groups: non-cumulative, cumulative, and combined [26], depending on the response parameters that are used, such as maximum deformation, hysteric behavior, fatigue, deformation and energy absorption. Each index has its advantages in terms of robustness and computational simplicity. Due to significant torsional sensitivity of the case study building, conventional damage indices were deemed insufficient to reflect 3-D structural behavior and bi-directional damage. In order to provide a more reliable and robust damage measure for this particular case, the following demand-to-capacity ratio (DCR), proposed by Jeong and Elnashai [26], was calculated for all columns at ground level:

$$DCR = \sqrt{\left(\frac{\Delta_x}{\Delta_{u,x}}\right)^2 + \left(\frac{\Delta_y}{\Delta_{u,y}}\right)^2} \quad (1)$$

In the above, Δ_x and Δ_y are the interstory drift in the x and y directions, respectively, while subscript u denotes ultimate condition of interstory drift which is computed individually for each column and equals the drift where the column curvature reaches its ultimate value under an average value of axial force. Details regarding the analytical and computational [27] means to derive the above DCR index can be found in [18].

3.2 *Case Study 2: Linear Dynamic Analysis of Twin R/C Bridges in Kavala, Northern Greece*

3.2.1 Overview of the Twin Bridges

The second Kavala Bypass Ravine Bridge in Fig. 4 is a newly built bridge located on Sect.13.7 of the Egnatia highway [28], a 670 km road tracing the ancient Roman way crossing northern Greece from its western to eastern ends. Its overall length is 170 m and comprises two statically independent branches, with four identical simply supported spans of 42.50 m. Each span is built using four precast post-tensioned I-beams of 2.80 m height supporting a continuous deck (without joints) of 26 cm thickness and 13 m width. The I-beams are supported on laminated elastomeric bearings, located at the two abutments and the three intermediate piers (M1, M2 and M3). The latter have a 4.0 × 4.0 m hollow cross-section, 40 cm wall thickness and heights equal to 30 m (M1 and M3) and 50 m (M2). The foundation system of the piers consists of large caissons founded on relatively stiff soil (class 'A' according to both the Greek Seismic Code [29] and EC8 soil classifications). The four deck spans are interconnected through a 2.0 m long and 20 cm thick continuity slab



Fig. 4 The second Kavala bypass ravine bridge of the Egnatia highway (case study 2)

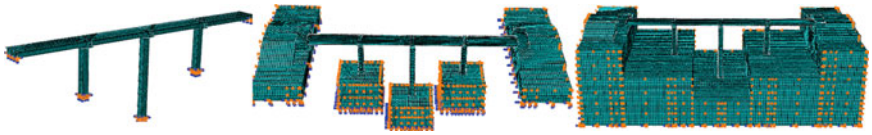


Fig. 5 Case study 2: FEM model '3D-Fixed' (*left*), model '3D-3DSoil' (*middle*) and model '3DTwin-3DSoil' (*right*) of the twin bridges

over the piers. The bridge site belongs to Seismic Zone I [29], characterized by a peak ground acceleration of 0.16 g. Finally, this particular bridge is continuously monitored by Egnatia S.A., the agency responsible for its daily operation.

3.2.2 Numerical Analysis Framework of Twin R/C Bridges

In order to assess the relative importance of the modeling assumptions, a series of finite element models was developed with increasing levels of complexity [30]. The numerical simulations were carried out using ABAQUS 6.8 [31], starting from a reference fixed-base frame superstructure ('1D-Fixed'), then a spring supported frame bridge ('1D-Springs') for which the foundation dynamic impedance matrix was derived according to analytical expressions given in Gazetas [32] and finally a 3D fixed-base superstructure ('3D-Fixed') where bearings, I-beams and stoppers were all modeled with maximum detail in 3D (Fig. 5a). Having established a good level of confidence between 1D and 3D finite element models through various verification-type analyses involving the exact geometry of the abutment-backfill-embankment system and the middle piers-caisson-soil substructure system, second-level ('3D-3DSoil') employing 73,170 elements was implemented (Fig. 5b). Furthermore, a monolithic abutment-deck connection was also investigated, creating an alternative model ('3DInt-3DSoil') as an upper bound for the abutment contribution to the resistance for the imposed seismic forces. Finally, the most

refined model developed ('3DTwin-3DSoil') comprised, 243580 C3D8R-type elements and involved both branches of the twin bridge, their abutments and caissons as well as a large soil volume underneath (Fig. 5c). Due to the size of these models and the associated computational cost, all analyses were linear elastic using cracked section properties (i.e., two third of the gross stiffness according to the Greek seismic code [29]) for the piers and appropriately reduced soil stiffness based on the observed strains. A uniform Rayleigh damping of 6% was adopted for the system and absorbing lateral boundaries were also added in order to eliminate wave reflections.

4 Selection of Earthquake Record Sets for Nonlinear and Linear Analysis of the Structures Under Investigation

4.1 General Aspects

Currently, numerous sources are available for obtaining earthquake strong motion records. A review of available (both on-line and off-line) strong-motion databases may be found in Ref. [33]. For an evaluation of the EC8 earthquake record selection procedure through linear and nonlinear dynamic analyses of the two case studies, records were retrieved from the European Strong-Motion Database (ESD) [34, 35] (*http://www.isesd.cv.ic.ac.uk*) and the Pacific Earthquake Engineering Research Center database (NGA-PEER) [36] (*http://peer.berkeley.edu/nga/*).

An effort was made by grouping records in sets (bins) to account for the whole grid of EC8 provisions, namely to establish spectral matching with the code spectrum and to match the specific geological conditions of the structures under study. These last conditions are (a) seismotectonic environment typical of the shallow depth earthquakes that occur in the south-eastern Mediterranean Sea basin, (b) appropriate peak ground acceleration values reflecting the zones of the Greek seismic code where the structure are situated and (c) similar soil conditions. However, a relaxing of some of the above criteria was inevitable, since strict and simultaneous application of all guidelines limited, in some cases significantly, the available number of the eligible records.

4.2 Sets of Selected Records and Mean Spectra for Nonlinear Analysis of the Lefkada Irregular Building (Case Study 1)

Four different sets of accelerograms (denoted as A1, B1, C1 and D1) were formed, plus an alternative fifth set (denoted as E1) comprising accelerograms recorded from California. Each set consists of seven pairs of the horizontal components of strong motions recorded from various seismic events. These records were initially searched for matching the soft soil conditions at the building site as well as the high

peak ground accelerations of 0.36 g (seismic zone III, Greek seismic code [29]). Moreover, the preliminary selection procedure considered all seismotectonic conditions appropriate to the site. However, it was found that the above criteria could not be satisfied simultaneously by the first four sets, since only few records come from the Balkans or Italy (which has similar seismotectonic conditions) on soft soil formations characterized also by peak ground acceleration exceeding 0.2 g. As a result, it was decided that no further specifications could be imposed regarding particular source parameters (e.g., rupture mechanism), path characteristics or strong-motion duration, the latter being a controversial criterion given its almost 40 different definitions [37]. The aforementioned selection criteria were further relaxed and accelerograms from all over Europe and the Middle East were considered eligible, and the restriction of matching the exact soil profile was also relaxed.

Next, the accelerograms used to form the five different record sets were selected to match the EC8 quantitative criteria (a) to (c) described in detail in Sect. 2.1. It is recalled that criteria (a) and (b) impose spectral matching between the average response spectrum of the individual records and the code spectrum. However, for the irregular and torsionally sensitive building of case 1 for which simultaneous bi-directional excitation was deemed necessary, it was decided that some of the more detailed matching requirements prescribed in EC8-Part2 [13] should be used. Therefore, the SRSS response spectra of each pair of horizontal components of the selected records were computed and the mean spectra of the seven SRSS-combined spectra were calculated. These spectra were finally compared with the 1.3 times the values of the reference 5% damped elastic code spectrum in the period range between $0.2T_1$ and $2T_1$, where $T_1 = 0.539$ s is the fundamental period of the case study building.

Despite relaxing the preliminary selection criteria, the high level of target peak ground acceleration (equal to 0.36 g) as well as the wide range where spectral matching was required (i.e. $0.108\,\text{s} < T_1 < 1.08\,\text{s}$) still reduced significantly the earthquake records that satisfy the above criteria, a fact that has been pointed out by other researchers for areas of high seismicity [38]. As a result, the selection criteria were further relaxed and the target peak ground acceleration was set to 0.24 g, as if the structure was located in seismic zone II (instead of III) according to the Greek Seismic Code [29]. Apparently this lack of earthquake record availability for areas characterized by high seismicity is an issue that questions the applicability of the EC8-based record selection process and requires further investigation. Alternatively, use of properly scaled records to lower (as compared to the target value) initial peak ground acceleration values seems to be the only feasible solution currently.

Based on the previous discussion, set A1 consists of 14 accelerograms, recorded mainly on soft soils from South Europe and the Middle East and generally characterized by high values of PGA. This selection seems to be closer to the above criteria and possibly reflects the first choice of a designer for this building. In addition, sets B1, C1 and D1 include seven pairs of horizontal components of strong motions selected on the basis of their epicentral distance R, a selection parameter that is not explicitly imposed by EC8 but is commonly adopted in many relevant studies. In particular, the records selected in sets B1, C1 and D1 are characterized by

distances R $\geq$ 35 km, 15 $\leq$ R $\leq$ 35 km and R $\leq$ 15 km, respectively. This distinction was necessary to investigate the effect of distance (and of the seismic scenario that could possibly be adopted) on the inelastic response of the building. Searching through the PEER-NGA database, an alternative set E1 was formed using seven pairs of horizontal components, recorded on the near-field (R $\leq$ 15 km) and on soft soils in California. The reason for developing such a set is to investigate the potential implications of selecting records from a different seismotectonic environment, although recent studies (e.g., [39]) have shown no systematic differences between ground motions in western North America versus those in Europe and the Middle East. Tables 2–6 summarize the selected records and Figs. 6–10 illustrate the SRSS spectra of the seven pairs of accelerograms and their corresponding mean spectra for all sets, as compared to the EC8 spectrum.

As can be seen in Figs. 6–10, the mean spectra of all sets do satisfy EC8 provisions about spectral matching, as they exceed 1.3 times the target spectrum at all periods in the range 0.108 s $<$ T_1 $<$ 1.08 s. It is interesting to note that in case the target PGA criterion was required as a match (i.e., seismic zone III and $a_g = 0.36\,g$), none of the above mean spectra would meet this requirement. With the exception of the scaled records of set A1 (in order to match the target spectrum the records were scaled down uniformly by a common factor equal to 0.69), no further scaling is performed in order to avoid possible bias in the structural response [40]. Furthermore, closer inspection of the figures shows that it was necessary to include a seismic record of sizeable spectral accelerations, primarily to meet the spectral matching requirement at longer periods (close to $2T_1$).

The result of this decision to use at least one pair of horizontal components that could possibly result in strong inelastic response in the building, questions

Table 2 Selected records for set A1

Event (Country)	Date	Magnitude	Soil	File code
Gazli (Uzbekistan)	17.05.1976	7.04	Very soft	000074
Montenegro (Montenegro)	15.04.1979	7.04	Stiff	000196
Tabas (Iran)	16.09.1978	7.33	Stiff	000187
Erzincan (Turkey)	13.03.1992	6.75	Stiff	000535
Kocaeli (Turkey)	17.08.1999	7.80	Unknown	001226
Duzce (Turkey)	12.11.1999	7.30	Unknown	001560
Ionian (Greece)	11.04.1973	5.73	Soft	000042

Table 3 Selected records for set B1

Event (Country)	Date	Magnitude	Soil	File code
Friuli (Italy)	06.05.1976	6.50	Soft	000047
Campano Lucano (Italy)	23.11.1980	6.87	Soft	000289
Manjil (Iran)	20.06.1990	7.32	Soft	000475
Tabas (Iran)	16.09.1978	7.33	Stiff	000187
Kocaeli (Turkey)	17.08.1999	7.80	Unknown	001226
Duzce (Turkey)	12.11.1999	7.30	Unknown	001560
Spitak (Armenia)	07.12.1988	6.76	Soft	000439

Table 4 Selected records for set C1

Event (Country)	Date	Magnitude	Soil	File code
Gazli (Uzbekistan)	17.05.1976	7.04	Very soft	000074
Ionian (Greece)	11.04.1973	5.73	Soft	000042
Alkyon (Greece)	24.02.1981	6.69	Soft	000333
Campano Lucano (Italy)	23.11.1980	6.87	Rock	000290
Kocaeli (Turkey)	17.08.1999	7.80	Unknown	001257
Friuli (Italy)	06.05.1976	6.50	Rock	000055
Montenegro (Montenegro)	15.04.1979	7.04	Stiff	000196

Table 5 Selected records for set D1

Event (Country)	Date	Magnitude	Soil	File code
Umbro-Marchigiano (Italy)	26.09.1997	5.50	Stiff	000591
Dinar (Turkey)	10.011995	6.07	Soft	000879
Kocaeli (Turkey)	17.08.1999	7.80	Unknown	001231
Kalamata (Greece)	13.09.1986	5.75	Stiff	000414
Duzce (Turkey)	12.11.1999	7.30	Unknown	001703
Erzincan (Turkey)	13.03.1992	6.75	Stiff	000535
Ionian (Greece)	11.04.1973	5.73	Soft	000042

Table 6 Selected records for set E1

Event (Country)	Date	Magnitude	Soil
Coyote Lake (California, USA)	06.08.1979	5.74	Soft
Imperial Valley (California, USA)	15.10.1979	6.53	Soft
Loma Prieta (California, USA)	18.10.1989	6.93	Soft
Superstition Hills (California, USA)	24.11.1987	6.54	Soft
Westmorland (California, USA)	26.04.1981	5.90	Soft
Northridge (California, USA)	17.01.1994	6.69	Soft
Morgan Hill (California, USA)	24.04.1984	6.19	Soft

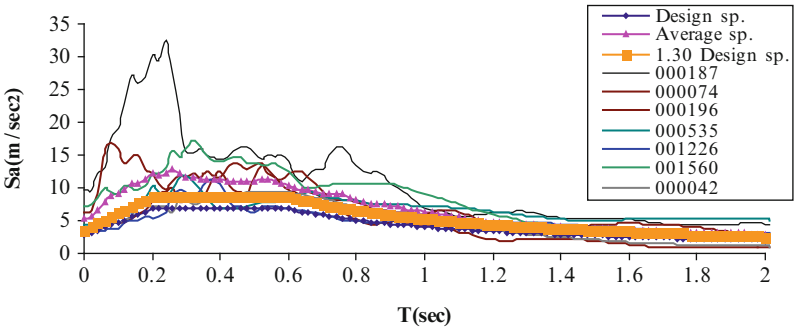


Fig. 6 Site class C–Zone II. Response, average and design spectra for set A1

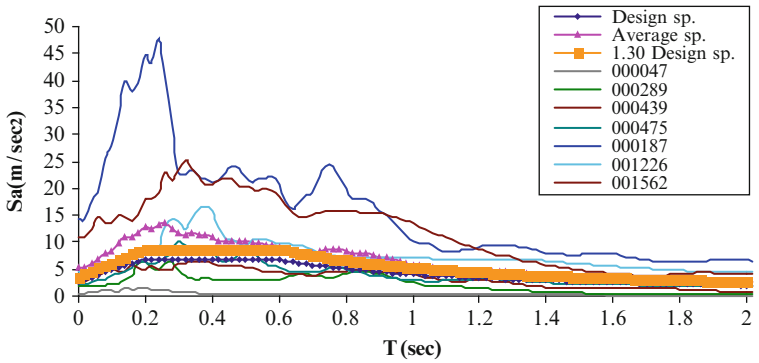


Fig. 7 Site class C–Zone II. Response, average and design spectra for set B1

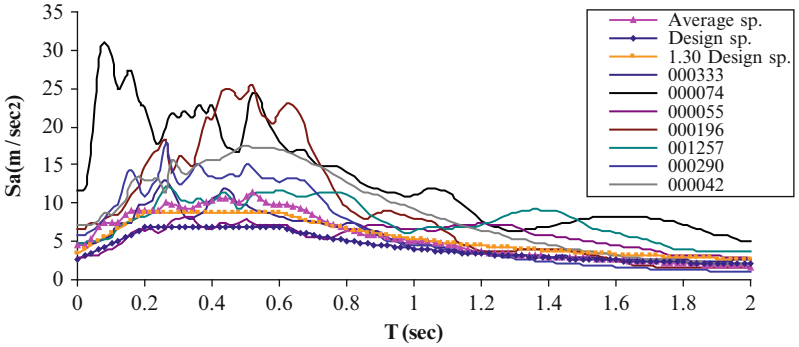


Fig. 8 Site class C–Zone II. Response, average and design spectra for set C1

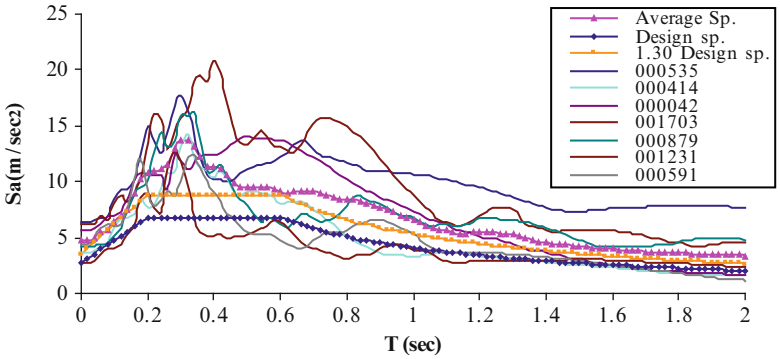


Fig. 9 Site class C–Zone II. Response, average and design spectra for set D1

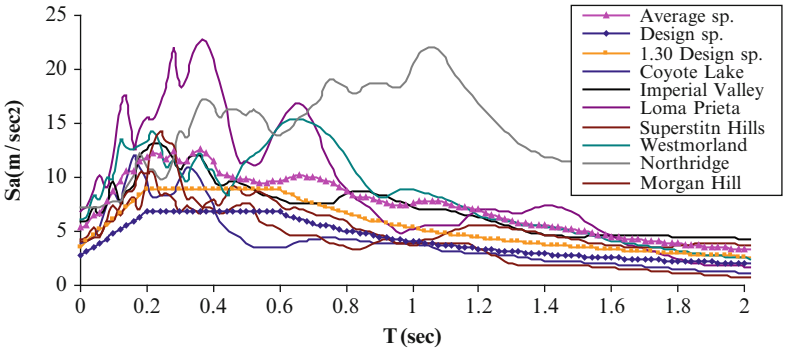


Fig. 10 Site class C–Zone II. Response, average and design spectra for set E1

the overall rational of 'averaging' action effects in the structure obtained partially from elastic and partially from inelastic response under the seven pairs of records of a given set. It is therefore seen as necessary to further examine the required range of spectral matching, especially for longer periods and the threshold value of $2T_1$, bearing in mind that the fundamental period T_1 of the structure is not expected to double (at least for structures designed for low to moderate ductility level), unless the latter is subjected to very high seismic forces and suffers excessive structural damage. It has to be noted that the presence of soft soil and foundation compliance should not be confused with period elongation during seismic excitation, since the flexibility of the soil-structure system influences the initial fundamental period of the structure, prior to and independently of any earthquake loading.

4.3 Sets of Selected Records and Mean Spectra for Linear Analysis of the Kavala Twin Bridges (Case Study 2)

Linear analyses using six alternative finite elements models of the twin R/C bridges were implemented in order to evaluate the EC8-based earthquake record selection procedure. For this reason, two different sets of seven pairs of horizontal components of strong motions (denoted hereafter as A2, B2) were formed with the use of natural records, retrieved from the European Strong-Motion Database (ESD) [34, 35]. The criteria imposed by EC8 and the general discussion about the critical issues of records selection, as discussed in the previous section, are also valid here. Within this framework, the records were searched for stiff soil conditions of the building site (according to both EC8 and Greek seismic code soil classifications), as well as for a low value of peak ground acceleration of 0.16 g (Greek code seismic zone I). Moreover, this selection process considered the seismotectonic conditions appropriate to the site. As a result, accelerograms recorded from the South–eastern Europe as well as the Middle East were selected for the sets. It is interesting that record selection for linear analysis of the twin R/C bridges does not share the same

difficulties as in the previous case of the R/C building. This is because the high target PGA and the very soft soil conditions, which gave an insufficient number of eligible records and finally resulted in an almost compulsory relaxation of the whole selection procedure, are in contrast with the low target peak acceleration and the stiff soils of the current case study. The total 14 horizontal component pairs of strong motion (see Tables 7 and 8) were selected in such a way that fulfilled the criteria imposed by EC8-Part2 [13] about the bi-directional excitation of bridges. As it can be seen in Figs. 11 and 12, the mean spectra derived by the averaging of the SRSS spectra for each set, comply with the 1.3 times the values of the code spectrum in the period

Table 7 Selected records for set A2

Event (Country)	Date	Magnitude	Soil	File code
Friuli (Italy)	15.09.1976	5.98	Alluvium	000138
Biga (Turkey)	05.07.1983	6.02	Stiff	000352
Campano Lucano (Italy)	23.11.1980	6.87	Stiff	000288
Lazio Abruzo (Italy)	07.05.1984	5.79	Stiff	000366
Manjil (Iran)	20.06.1990	7.32	Alluvium	000476
Montenegro (Montenegro)	15.04.1979	7.04	Stiff	000196
Umbro-Marchgiano (Italy)	26.09.1997	5.9	Stiff	000602

Table 8 Selected records for set B2

Event (Country)	Date	Magnitude	Soil	File code
Montenegro (Montenegro)	24.05.1979	6.34	Stiff	000228
Umbro-Marchgiano (Italy)	14.10.1997	5.6	Stiff	000640
Caldiran (Turkey)	24.11.1976	7.34	Stiff	000153
Friuli (Italy)	11.09.1976	5.52	Stiff	000123
Heraklio (Greece)	01.03.1984	3.9	Stiff	000355
Ionian (Greece)	23.03.1984	6.16	Stiff	002015
Kars (Turkey)	30.10.1983	6.74	Stiff	000354

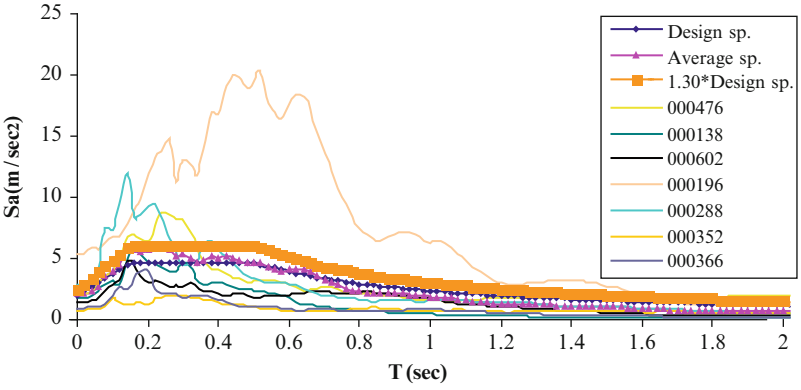


Fig. 11 Site class B–Zone I. Response, average and design spectra for set A2 records

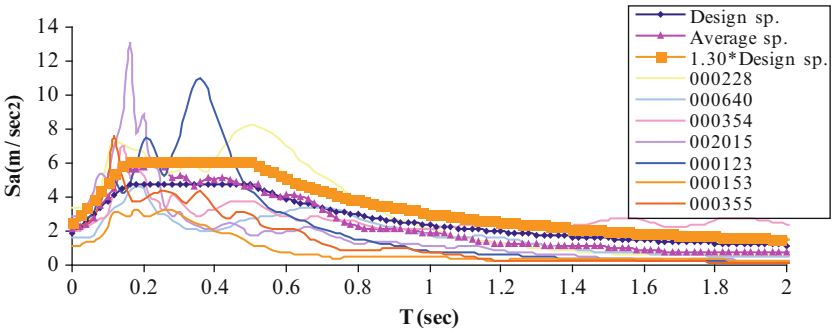


Fig. 12 Site class B–Zone I. Response, average and design spectra for set B2 records

range between $0.2T_1$ and $1.5T_1$, where $T_1 = 1.319$ s is the fundamental period of the reference bridge model ('1D-Fixed'). Although it was easier to obtain eligible records in this case than in the previous one, the use of at least one pair of strong horizontal components and the scaling of records (uniform scaling factor was equal to 2.36 for the records of set A2 and 2.77 for set B2, respectively) were necessary to establish the required spectral matching. Furthermore, the records were applied at the support level of the fixed-based structures, or were appropriately deconvoluted to bedrock for the case of finite element models where the soil volume was modeled to reflect the local soil conditions in yield different amplification between abutments and piers. The vertical component of seismic actions (Sects. 3.2.2.4 and 4.1.7 of EC8 [13]), near source effects (Sect. 7.4.1.3 of EC8 [13]) as well as the explicit (i.e., ground motion variability attributed to local site effects) asynchronous excitation (Sects. 3.3 and Annex D of EC8 [13]) were not considered. The latter decision was based on the observations in previous studies for the particular bridges [41–43] where because of the short overall length of the structure, the importance of wave incoherency and of passage effects was minor compared to the effect of local soil conditions.

5 Dynamic Analysis Results

5.1 Response of the Lefkada Irregular Building (Case Study 1)

Bi-directional non-linear dynamic analyses of the R/C building under study were performed for the selected earthquake records, using the finite element program Zeus-NL. Damage was assessed through the demand-to-capacity ratio given in Eq. 3.1. These DCR values were calculated for some key columns at the ground floor of the building and for all record sets (see Sect. 4.2). It is recalled that damage initiates when interstory drift is greater than the interstory drift which corresponds to yield conditions in either x or y direction. A first observation is that intra-set

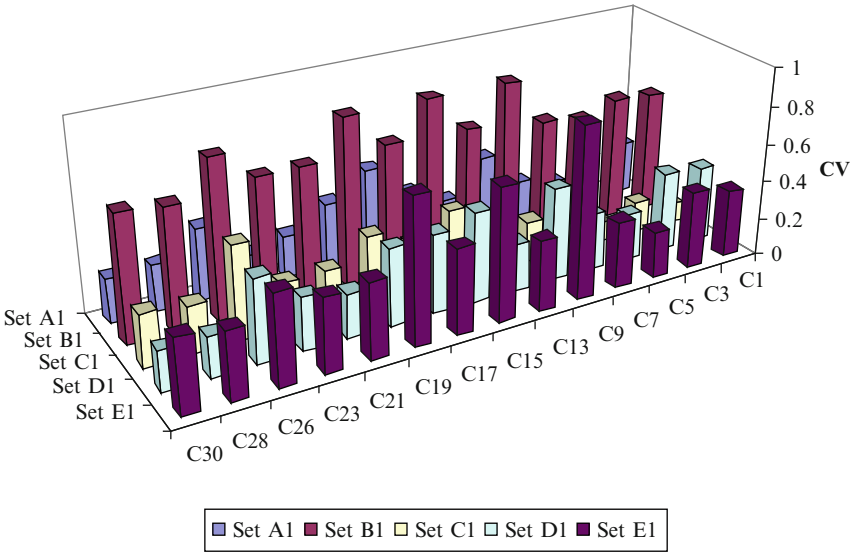


Fig. 13 Coefficient of variation of DCR values of characteristic columns at ground level, computed for excitations with records from all sets (intra-set scatter)

scatter, which is quantified by the coefficient of variation (CV) of the DCR values for a given column under the seven pairs of horizontal strong motion of a given set, calculated for all sets A1 to E1, is non-negligible (see Fig. 13). This scatter is more pronounced in set B1 (far-field motions from European earthquake events) where for all ground floor columns the coefficient of variation of the DCR exceeds 0.59. In contrast, selection based on commonly adopted criteria, such as the set A1 records, results in lower but still noticeable intra-set scatter (maximum CV among all columns is 0.48). This scatter is attributed to the adverse effect of the very strict criterion imposed by EC8 for obtaining matching at long periods up to $2T_1$ and the obligatory selection of strong motion records. It is also noted that the 'dominating' property of severe strong motions is more apparent in the response scatter, since a particular record has high spectral values in the resonance period range.

All the above information negates the main purpose of earthquake record selection, which is to form a set of ground motions that would lead to the same inelastic structural response. It is seen that this is not met using the EC8 selection procedure, at least not for the case of irregular buildings founded on soft soils and located in areas of high seismicity. Furthermore, had the designer decided to form a set consisting of only three pairs of earthquake records and then obtained the maximum structural response (a correct decision according to EC8), then the significantly stronger earthquake records required to establish spectral matching along such a wide period range would not only affect the intra-set scatter but basically dominate the maximum structural response, resulting in unrealistically high member forces and displacements.

5.2 *Response of the Kavala Twin Bridges (Case Study 2)*

For the six alternative finite element models presented in Sect. 3.2.2, 14 transient and bi-directional dynamic analyses were performed using the corresponding pairs of earthquake records from two sets (A2 and B2). Only the complex '3DTwin-3DSoil' model was subjected to a single pair of records, due to excessive computational cost. Figure 14 plots the values of the coefficient of variation, calculated for the pier top displacement demand, of all three piers (M1, M2 and M3) and for each specific direction. These values represent the intra-set scatter of the response results. In general, CV values derived from the first set of accelerograms (A2) were significantly higher than values from the second set (B2), because set A2 consists of a pair of strong horizontal motions (see Fig. 11) that dominates and results in large discrepancy. This observation is in agreement with the findings from case study 1 (see Sect. 5.1). It is also noted that intra-set scatter is once more apparent for the response in the longitudinal direction instead of the transverse one. This is probably caused by neglecting abutment-embankment stiffness in the transverse direction, in contrast to the longitudinal one. As a result, the selection of records constitutes a major factor for the response scatter derived from dynamic analyses. Finally, modeling issues combined with the use of damage measures also influences to a minor degree the discrepancy in the response. A de-coupling of the selection procedure from the above factors is deemed necessary in order to investigate more this phenomenon more thoroughly.

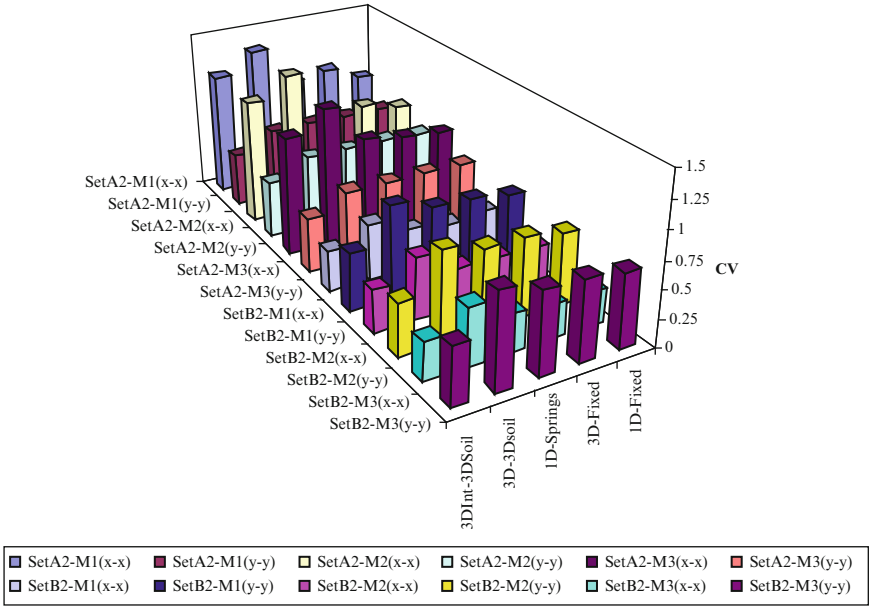


Fig. 14 Coefficient of variation of displacements (both directions) of the three piers computed from all models excited with records from the two sets (intra-set scatter)

6 Concluding Remarks

This chapter aims to quantify the effect that EC8-based earthquake record selection strategy has on structural response through nonlinear analysis of an existing, multi-storey irregular building damaged during the Lefkada, Greece earthquake of 2003 as well as of linear analysis of an R/C bridge in the Egnatia highway system in Northern Greece. The main conclusions are as follows:

- The number of records that can be retrieved from current strong-motion databases to fulfill the selection requirements imposed by EC8 (general criteria and spectral matching requirements) in case of structures founded on soft soils and located in areas of high seismicity is very limited and more detailed guidelines should be provided to aid the designer.
- Even for moderate or low levels of seismicity (i.e., PGA $= 0.24\,g$ or $0.16\,g$) the intra-set scatter of the structural response (elastic or inelastic) of either an irregular building or a bridge cannot be neglected. We conclude that the main objective of selecting and scaling real accelerograms to form a set of ground motions which not only satisfy the expected seismic scenario but also induce the same inelastic response (in terms of mean or some target percentile response) that would be recovered if the structure was analyzed with a large set of 'suitable' ground motions, cannot be met [11].
- It can be surmised that discrepancy in the structural response cannot be attributed to the selection process proposed by EC8 as a whole, but rather to the wide period range for which spectral matching is imposed (i.e., $0.2T_1 < T_1 < 2T_1$ for buildings and $0.2T_1 < T_1 < 1.5T_1$ for bridges). The particular requirement results in selection of at least one record (or one pair of horizontal components of strong motions for bi-directional excitation) with high spectral accelerations at long periods to 'correct' the mean spectrum of the selected earthquake records with respect to the target one, which in turn produces unrealistic structural response. As result, use of a dominating, 'correction-type' earthquake record questions the overall rational of 'averaging' the action effects of a structure obtained partially from elastic and partially from inelastic response analysis for the seven records of a given set.
- Based on the above observations, the range for spectral matching of the target spectrum and the mean spectrum derived by the seven SRRS spectra should be limited to $0.2T_1 < T_1 < 1.3T_1$; this should also be the proposed matching range for bridge analysis. Ideally, the upper bound of this range could be a function of seismic zone, since period elongation is directly related to structural yielding and to the level of seismic forces. The upper bound of the period interval may also be related to behavior factor q that expresses the necessary level of inelastic response for which the structure has been designed. It is believed that structures designed for low to moderate ductility (i.e., not corresponding to ductility class 'high' in Eurocode 8) do not require spectral matching at long periods that are no longer related to the expected structural response. Similarly, the lower bound of the period range for which spectral matching is desired could be considered as a

function of higher mode contributions. This would not necessarily equal $0.2T_1$, but approach the lower period T_L of the highest mode of vibration of the structure for which the activated mass is about 90% of the total mass.

The above conclusions cannot be generalized since they have been drawn from a limited set of linear and nonlinear dynamic analyses of two particular case studies. Further studies should be conducted taking into account different seismic zones, seismic scenarios, soil conditions as well as other types of structures and ways of modeling in order to confirm the conclusions reported here. However, uncertainty related to the selection of earthquake ground motion constitutes one of the most important analysis parameters, thus emphasizing the necessity for more advanced seismic code provisions for selection of ground motions appropriate in transient dynamic analysis.

Acknowledgements The authors wish to thank Dr P. Panetsos of EGNATIA S.A. in Thessaloniki, Greece, for his valuable assistance regarding our study of the Kavala Bridge. Thanks are also due to Prof. A. Kappos, scientific responsible of the research project entitled 'Seismic Protection of Bridges' funded by the Greek Secretariat for Research and Technology, within the framework of which some of the preliminary analyses regarding the Kavala bridge were conducted. Finally, the authors wish to thank Dr N. Theodoulidis of the Institute of Engineering Seismology and Earthquake Engineering in Thessaloniki, Greece, for his contribution on various seismological aspects of the earthquake record selection process.

References

1. Kappos AJ (2002) Earthquake loading. In: Kappos AJ (ed) Dynamic loading and design of structures. Spon Press, London
2. Padgett J, Desroches R (2007) Sensitivity of seismic response and fragility to parameter uncertainty. J Struct Eng 133(12):1710–1718
3. Papageorgiou AS, Aki K (1983) A specific barrier model for the quantitative description of inhomogeneous faulting and the prediction of strong ground motion: I. Description of the model. Bull Seism Soc Am 73:693–722
4. Manolis GD (2002) Stochastic soil dynamics. Soil Dyn Earthquake Eng 22:3–15
5. Lekidis V, Karakostas Chr, Dimitriu P, Margaris B, Kalogeras I, Theodulidis N (1999) The Aigio (Greece) seismic sequence of June 1995: seismological, strong motion data and effects of the earthquakes on structures. J Earthquake Eng 3(3):349–380
6. Katsanos EI, Sextos AG, Manolis GD (2009) Selection of earthquake ground motion records: a state-of-the-art review from a structural engineering perspective. Soil Dyn Earthquake Eng. doi:10.1016/j.soildyn. 2009.10.005
7. Shome N, Cornell CA, Bazzurro P, Carballo JE (1998) Earthquakes, records and nonlinear responses. Earthquake Spectra 14(3):469–500
8. Baker J, Cornell CA (2006) Spectral shape, epsilon and record selection. Earthquake Eng Struct Dyn 32:1077–1095
9. Luco N, Cornell CA (2007) Structure-specific scalar intensity measures for near-source and ordinary earthquake motions. Earthquake Spectra 23(2):357–395
10. Tothong P, Luco N (2007) Probabilistic seismic demand analysis using advanced ground motion intensity measures. Earthquake Eng Struct Dyn 36:1837–1860
11. Hancock J, Bommer JJ, Stafford PJ (2008) Numbers of scaled and matched accelerograms required for inelastic dynamic analyses. Earthquake Eng Struct Dyn 37:1585–1607

12. CEN (2003) Comité Européen de Normalisation TC250/SC8, Eurocode 8: Design provisions of structures for earthquake resistance. Part 1: General rules, seismic actions and rules for buildings. prEN1998-1, Brussels
13. CEN (2005) Comité Européen de Normalisation, Eurocode 8: Design provisions of structures for earthquake resistance. Part 2: Bridges. prEN1998-2, Brussels
14. Margaris B, Papaioannou C, Theodoulidis N, Savvaidis A, Anastasiadis A, Klimis N et al. (2003) Preliminary observations on the August 14, 2003 Lefkada island (western Greece) earthquake. EERI special earthquake report (Joint report by Institute of Engineering Seismology and Earthquake Engineering, National Technical University of Athens & University of Athens, Athens)
15. Sextos AG, Pitilakis K, Kirtas E, Fotaki V (2005) A refined computational framework for the assessment of the inelastic response of an irregular building that was damaged during the Lefkada earthquake. In: Proceedings of the 4th European workshop on the seismic behaviour of irregular and complex structures, Thessaloniki, Greece
16. Papathanasiou A, Papatheodorou I (2007) Rehabilitation of a building damaged in Lefkada during the 14.08.2003 earthquake In: Proceedings of the 16th Hellenic concrete conference, Alexandroupolis, Greece (in Greek)
17. Giarlelis C, Lekka D, Mylonakis G, Anagnostopoulos S, Karabalis D (2006) Performance of a 3-storey RC structure on soft soil in the M6.4 Lefkada, 2003, Greece, earthquake. In: Proceedings of the 1st European conference on earthquake engineering and seismology, Geneva, Switzerland
18. Georgiou A (2008) Selection of time-histories for nonlinear analysis assessment of asymmetric structures. MSc Thesis, Department of Civil Engineering, Aristotle University, Thessaloniki, Greece (in Greek with English summary)
19. Elnashai AS, Papanikolaou V, Lee DH, ZEUS-NL (2002) User manual, Mid-America Earthquake Center (MAE) report
20. Mander JB, Priestley MJN, Park R (1988) Theoretical stress-strain model for confined concrete. J Struct Eng 114(8):1804–1826
21. Computers and Structures Inc (2003) ETABS: integrated building design software v.8. User's Manual, Berkeley, CA
22. Makris N, Gazetas G (1992) Dynamic soil-pile interaction. Part II. Lateral and seismic response. Earthquake Eng Struct Dyn 21(2):145–162
23. ANSYS Inc User's Manual v.10.0, Canonsburg, PA
24. Meletlidis K (2008) Study of dynamic seismic response of a multi-storey RC building, damaged by Lefkada earthquake. Undergraduate Thesis, Department of Civil Engineering, Aristotle University, Thessaloniki, Greece (in Greek)
25. Kappos A, Sextos A (2001) Effect of foundation type and compliance on seismic response of RC bridges. J Bridge Eng 6(2):120–130
26. Jeong SH, Elnashai AS (2005) Analytical assessment of an irregular RC frame for full-scale 3D pseudo-dynamic testing. Part I: Analytical model verification. J Earthquake Eng 9(1): 95–128
27. Kappos AJ (1993) RCCOLA-90: A microcomputer program for the analysis of the inelastic response of reinforced concrete sections. Department of Civil Engineering, Aristotle University of Thessaloniki, Greece
28. Ntotsios E, Karakostas C, Lekidis V, Panetsos P, Nikolaou I, Papadimitriou C, Salonikos T (2008). Structural identification of Egnatia odos bridges based on ambient and earthquake induced vibrations. Bull Earthquake Eng 7(2):485–501
29. EPPO (2000) Hellenic Antiseismic Code (EAK 2000). Ministry of Public Works, Athens
30. Faraonis P (2009) Seismic response of an existing R/C bridge considering embankment – abutment – superstructure interaction. MSc Thesis, Department of Civil Engineering, Aristotle University of Thessaloniki, Greece (in Greek with English summary)
31. Abacus (2009) Abacus Standard User's manual version 6.8. Hibbitt, Karlsson and Sorensen, 1080 Main Street Pawtucket, RI
32. Gazetas G (1991) Formulae and charts for impedance functions of surface and embedded foundations. J Geotech Eng 117(9):1363–1381

33. Bommer JJ, Acevedo A (2004) The use of real earthquake accelerograms as input to dynamic analysis. J Earthquake Eng 8(1):43–91
34. Ambraseys NN, Smit P, Berardi R, Rinaldis D, Cotton F, Berge C (2000) Dissemination of European Strong-Motion Data (CD-ROM collection). European Commission, DGXII, Science, Research and Development, Bruxelles
35. Ambraseys NN, Douglas J, Rinaldis D, Berge-Thierry C, Suhadolc P, Costa G, Sigbjornsson R, Smit P (2004) Dissemination of European strong-motion data, vol. 2 (CD-ROM collection). Engineering and Physical Sciences Research Council, United Kingdom
36. Chiou B, Darragh R, Gregor N, Silva W (2008) NGA project strong-motion database. Earthquake Spectra 24(1):23–44
37. Hancock J, Bommer JJ (2007) Using spectral matched records to explore the influence of strong-motion duration on inelastic structural response. Soil Dyn Earthquake Eng 27:291–299
38. Iervolino I, Maddaloni G, Cosenza E (2008) Eurocode 8 compliant real record sets for seismic analysis of structures. J Earthquake Eng 12:54–90
39. Stafford JP, Strasser OF, Bommer JJ (2008) An evaluation of the applicability of the NGA models to ground-motion prediction in the Euro-Mediterranean region. Bull Earthquake Eng 6:149–177
40. Luco N, Bazzurro P (2008) Does amplitude scaling of ground motion records result in biased nonlinear structural drift responses. Earthquake Eng Struct Dyn 36:1813–1835
41. Sextos A, Pitilakis K, Kappos A (2003a) A global approach for dealing with spatial variability, site effects and soil-structure-interaction for non-linear bridges. Part 1: methodology and analytical tools. Earthquake Eng Struct Dyn 32(4):607–627
42. Sextos A, Kappos A, Pitilakis K (2003b) Inelastic dynamic analysis of RC bridges accounting for spatial variability of ground motion, site effects and soil-structure interaction phenomena. Part 2: parametric analysis. Earthquake Eng Struct Dyn 32(4):629–652
43. Sextos A, Kappos A (2008) Seismic response of bridges under asynchronous excitation and comparison with EC8 design rules. Bull Earthquake Eng 7:519–545

Site Effects in Ground Motion Synthetics for Structural Performance Predictions

Dominic Assimaki, Wei Li, and Michalis Fragiadakis

Abstract We study how the selection of site response model affects the ground motion predictions of seismological models, and in turn how the synthetic motion site response variability propagates to the structural performance estimation. For this purpose, we compute ground motion synthetics for six earthquake scenarios of a strike-slip fault rupture, and estimate the ground surface response for 24 typical soil profiles in Southern California. We use viscoelastic, equivalent linear and nonlinear analyses for the site response simulations, and evaluate the ground surface motion variability that results from the soil model selection. Next, we subject a series of bilinear single degree of freedom oscillators to the ground motions computed using the alternative soil models, and evaluate the consequent variability in the structural response. Results show high bias and uncertainty of the inelastic structural displacement ratio predicted using the linear site response model for periods close to the fundamental period of the soil profile. The amount of bias and the period range where the structural performance uncertainty manifests are shown to be a function of both input motion and site parameters. We finally derive empirical correlations between the site parameters and the variability introduced in structural analyses based on our synthetic ground motion simulations.

Keywords Nonlinear · Ground motion · Site response · Bilinear · Drift · Variability

1 Introduction

With the emerging trends of performance-based design engineering, nonlinear structural response analyses are increasingly involved in the aseismic design of structures and the development of design criteria. Since design level ground motion recordings

D. Assimaki (✉) and W. Li
School of Civil and Environmental Engineering, Georgia Institute of Technology, USA
e-mail: dominic@gatech.edu; liwei19742001@gmail.com

M. Fragiadakis
Department of Civil and Environmental Engineering, University of Cyprus, P.O. Box 20537, 1678 Nicosia, Cyprus
e-mail: mfrag@mail.ntua.gr

M. Papadrakakis et al. (eds.), *Computational Methods in Earthquake Engineering*, Computational Methods in Applied Sciences 21, DOI 10.1007/978-94-007-0053-6_4,
© Springer Science+Business Media B.V. 2011

are scarce, engineers often rely on the use of artificial time-histories, modified from real earthquake recordings to be compatible with regional hazard-consistent design spectra (Design Spectrum Compatible Acceleration Time History, DSCTH). Indeed, the so-called Uniform Hazard Spectrum (UHS) evaluated from Probabilistic Seismic Hazard Analyses (PSHA) of regional ground motion data is nowadays the most frequently employed target spectrum in seismic structural analysis. Nonetheless, as pointed out by Katsanos et al. [38], there exist many studies (e.g. [8, 55, 60]) that question the validity of using the UHS as a single event target spectrum, arguing that it is in fact an envelope of spectra corresponding to different seismic sources. Therefore, use of UHS may result in design motions unrealistically corresponding to multiple earthquakes from multiple sources occurring simultaneously.

Alternatively, synthetic ground motions computed via stochastic or physics-based fault rupture simulations may be used in nonlinear structural performance estimations. Indeed, the recent advancements in the numerical representation of dynamic source rupture predictions as well as the development of 3D crustal velocity and fault system models for seismically active regions have led to broadband ground motion simulations of realistic seismic waveforms over the engineering application frequency range ($<$10 Hz). To investigate the accuracy of structural response predictions obtained via synthetic ground motions, Bazzurro et al. [6] used seven source simulation techniques to compute the structural response of inelastic Single Degree of Freedom (SDOF) oscillators, and statistically compared the results to the structural response predicted when using real accelerograms. They showed that synthetic ground motions produce structural responses that are less variable and less severe than those caused by real records in the short period range, the range of wavelengths comparable to the thickness of near-surface soil layers that were not simulated by Bazzurro et al. [6].

Indeed, the response of soils to strong earthquake loading has been shown to significantly affect the amplitude, frequency content and duration of seismic motions (e.g. [7, 13, 16, 21, 24, 29, 33, 36, 65, 66, 71]), and the consequent effects of site response on the performance of structures have been investigated in the past. More specifically, Whitman and Protonotarios [70] studied the inelastic response of structures with different fundamental periods to site-modified ground motions. They found that the inelastic response spectra for site-modified motions did not show pronounced peaks at the fundamental period of the soil profile, and that the inelastic response had not affected significantly the details of the frequency content for given peak ground acceleration and velocity. They also suggested that one should be conservative in selecting design forces for stiff structures resting upon soft ground. O'Connor and Ellingwood [56] compared the statistics of demand parameters obtained from ground motions generated using three alternative site-dependent stochastic models, i.e. the Modified Kanai-Tajimi model [37, 57, 67], Boore's spectral model [11] and the Auto-regresssive Moving Average (ARMA) model [25]. They concluded that no stochastic model alone was sufficient to fully characterize the ground motion and reproduce the structural inelastic response, and that each model parameter affected differently the various response quantities. Miranda [51] evaluated the strength reduction factor (R) demands of SDOF

systems for ground motions recorded on firm and soft sites. He observed that strength reduction factors of systems on soft soil sites with periods of vibration near the predominant period of the ground motion are typically much larger than the displacement ductility ratio. As a result, the response of those systems was shown to deviate from the equal displacement rule. This observation was confirmed by subsequent studies by the author [52,61], where it was shown that the inelastic deformation ratios of SDOF systems from motions recorded on soft sites are much lower that those obtained using motions recorded on firm sites, provided that the fundamental period of the SDOF oscillator is close the fundamental period of the soft site.

The above studies confirm that the response of soil layers does affect the inelastic response of structures, and intuitively, if the ground motion is strong enough to cause inelastic structural deformation, it should most probably also trigger nonlinear effects particularly at soft sites. The extent, however, to which soil nonlinearity affects the inelastic structural response, has not been quantitatively established, primarily due to lack of a statistically significant number of strong ground motion records on soft sites and the coarse discretization between soil and rock adopted in the above studies. For example, the average PGA of ground motions collected by Ruiz-García and Miranda [61] is on the order of 0.03 g, which is not strong enough to cause nonlinear effects even for soft sites. As a result, limited guidance exists both in engineering practice and in the seismological literature regarding the models that should be employed for the prediction of the response in synthetic ground motion simulations intended for inelastic structural response analyses.

In this study, we try to quantify the effects of soil response on the inelastic structural performance prediction by combining downhole strong motion observations and broadband ground motion synthetics for characteristic soft site conditions in Southern California. More specifically, we investigate the variability in structural demand caused by the soil model adopted for the site response predictions in the ground motion simulations. By resorting to the synthetic motions, we are able to subject the soil profiles to design level ground motions of different magnitude and distance combinations, and study the demand on buildings subjected to ground motions as a function of the site response characteristics. Overarching goal of this study is the development of quantitative guidelines for the efficient integration of nonlinear site response models into large-scale end-to-end physics-based ground motion simulations intended for structural performance predictions.

The soil sites used in this study are the calibration sites compiled by Stewart and co-workers as part of the PEER 2G02 project Calibration Sites for Validation of Nonlinear Geotechnical Models (http://cee.ea.ucla.edu/faculty/CalibrationSites/Webpage/main.htm). Detailed velocity profiles down to a hundred meters depth were available for the majority of sites, along with the dynamic soil parameters expressed as modulus reduction and material damping curves. To investigate the role of the site response model in the evaluation structural response, we implemented four kinds of site response models that are discussed in a section that follows. The effect of using different soil models for the structural performance assessment will be quantified as the bias and uncertainty in the inelastic deformation ratios of bilinear SDOF systems.

2 Site Conditions and Synthetic Ground Motions

Table 1 lists the sites used in this study and the corresponding NEHRP site classification based on the weighted average shear wave velocity of the top 30 m of the profile (V_{s30}). With the exception of the Port Island site, all other sites are located in Southern California. In terms of site conditions, we investigate the response of 8 NEHRP class C sites, 11 class D sites and 5 class E sites with V_{s30} ranging from 142 to 692 m/s. The shear wave velocity profiles of the sites are shown in Fig. 1.

The crustal model used for the simulation of broadband ground motion synthetics was extracted from the SCEC CVM IV (http://www.data.scec.org/3Dvelocity/), and strong ground motion synthetics were computed for multiple rupture scenarios of a strike-slip fault rupture over a wide range of epicentral distances. More specifically, acceleration time-histories were evaluated using a dynamic rupture source model [46] for medium and large magnitude events ($M_w = 3.5, 4.0, 5.0, 6.0, 6.5$ and 7.5) on a $100 \times 120\,km^2$ surface station grid (Fig. 2a) with spacing of 5 km. Note that the low frequency synthetics (<1 Hz) were computed for a deterministic 3D crustal

Table 1 Site conditions for selected stations used in the study

Location	Station name	Symbol	NEHRP site class	V_{s30} (m/s)
Corralitos	Eureka Canyon Road	CLS	C	462.8
El Centro	El Centro Array #7	E07	D	213.4
El Centro	Meloland Overcrossing	MEL	E	192.7
Emeryville	Pacific Park Plaza	EME	E	187.8
Gilroy	Gilroy Array #2	G02	D	300.0
Halls Valley	Halls Valley	HAL	D	265.6
Los Angeles	Rinaldi Receiving Stn.	RIN	D	328.2
Los Angeles	Epiphany	EPI	D	281.8
Los Angeles	Obregon Park	OBR	C	457.4
Los Angeles	Sepulveda VA	SEP	C	370.0
Newhall	Fire Station	NEW	D	276.5
Oakland	Outer Harbor Wharf	OOH	D	245.1
Pacoima	Pacoima Kagel Canyon	PKC	C	509.0
Redwood City	Apeel #2	A02	E	141.9
San Francisco	International Airport	SFO	E	213.9
Santa Clara	IBM Almaden, Santa Teresa Hill	STH	C	621.0
Santa Cruz	UCSC Lick Observatory	LOB	C	691.7
Simi Valley	Knolls School	KNO	C	555.1
Sylmar	Olive View Hospital	SYL	D	442.7
Sylmar	Jensen Generator Bldg.	JGB	C	526.2
El Centro	Meloland – Vertical Array	ELC	E	192.7
Eureka	Somoa Bridge – Vertical Array	EUR	D	187.1
Kobe	Port Island – Vertical Array	KPI	D	201.3
Los Angeles	La Cienega – Vertical Array	LAC	D	258.3

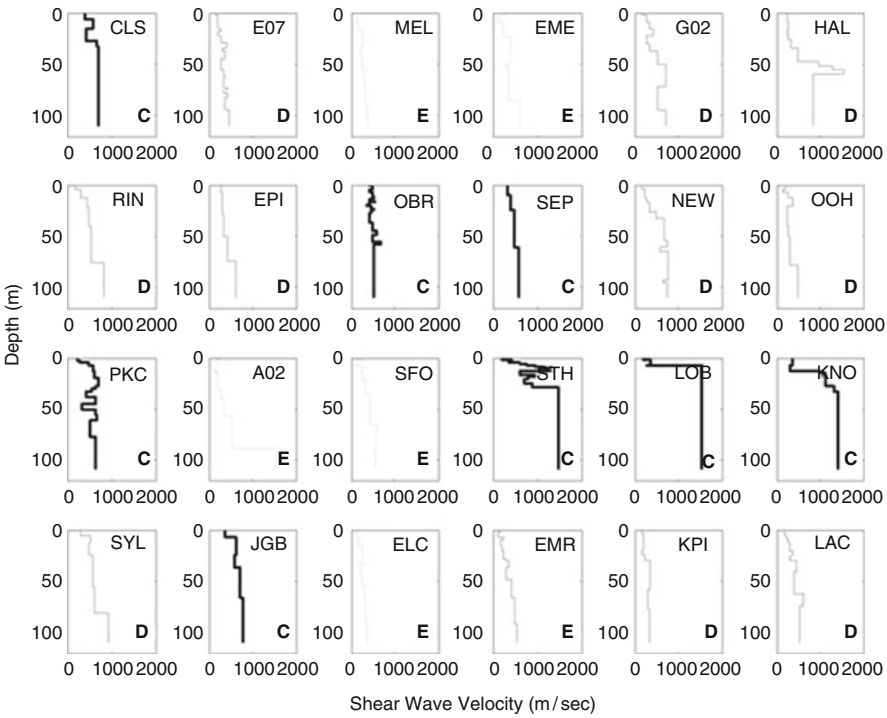


Fig. 1 Shear wave velocity profiles at all the sites collected (The annotation in each figure denote the symbol of corresponding station; class C sites depicted by *solid lines*, class D sites by *light lines* and class E sites by *dotted lines*)

velocity structure using a finite-difference method, while broadband components ($1 < f < 10$ Hz) were computed for a 1D heterogeneous velocity model using a frequency-wave-number method. For more details on the ground motion synthetics and the dynamic soil properties at the downhole array sites, the reader is referred to Assimaki et al. [2] and Li et al. [43].

3 Strong Motion Site Response Analyses

The engineering community has long believed that sediment nonlinearity is significant, a perspective that has been widely confirmed based on laboratory studies [23, 27, 28, 63, 64] where observed stress–strain loops implied a reduced effective shear modulus and an increased material energy absorption (damping) at higher levels of strain (Fig. 3). This relationship has been shown to describe the in-situ soil response to earthquake loading as well, and site response calculations need to accommodate these strain dependencies through nonlinear constitutive relations. Currently, two approaches are conventionally used to model cyclic soil response,

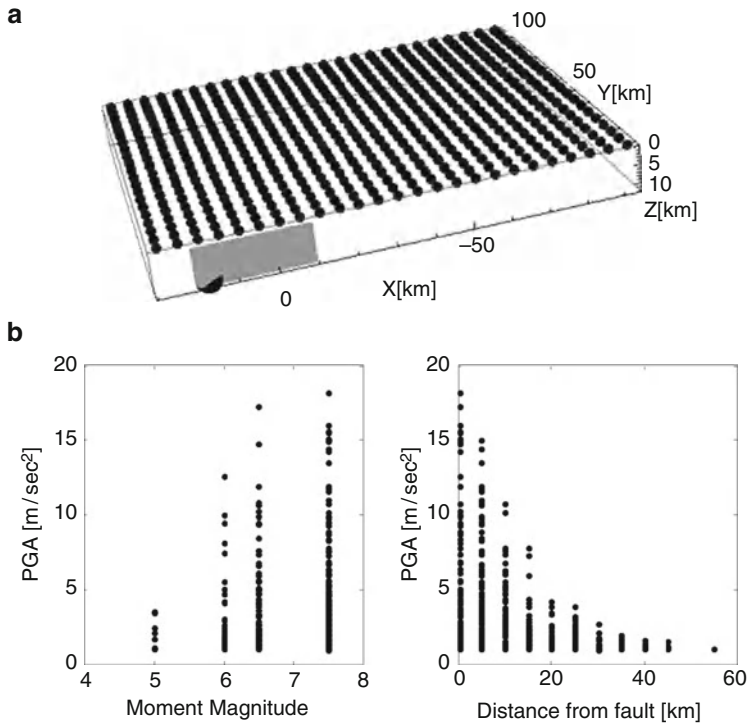


Fig. 2 (**a**) Station layout over a 100 × 120 km^2 grid where broadband ground-motion time histories were evaluated for a series of strike-slip rupture scenarios by means of the hybrid low-frequency/high-frequency approach with correlated source parameters [46]; (**b**) magnitude, distance and PGA distributions of the synthetic rock outcrop motions used in the ground response and corresponding structure response analysis

equivalent-linear and nonlinear models. The models are briefly described in the following sections, and successively implemented for the prediction of nonlinear site response analyses.

3.1 Equivalent Linear Models

The equivalent-linear approach, introduced by Seed and Idriss [63], approximates a second order nonlinear equation by a linear operator by defining a characteristic strain, which is assumed to be constant for the duration of the excitation. Moduli and damping curves (Fig. 3) are then used to define new parameters for each layer. The linear response calculation is repeated, new characteristic strains evaluated, and iterations are performed until convergence. This stepwise analysis procedure has been formalized into a computer code termed SHAKE [62], which currently is the most widely used analysis package for 1D site-specific response calculations.

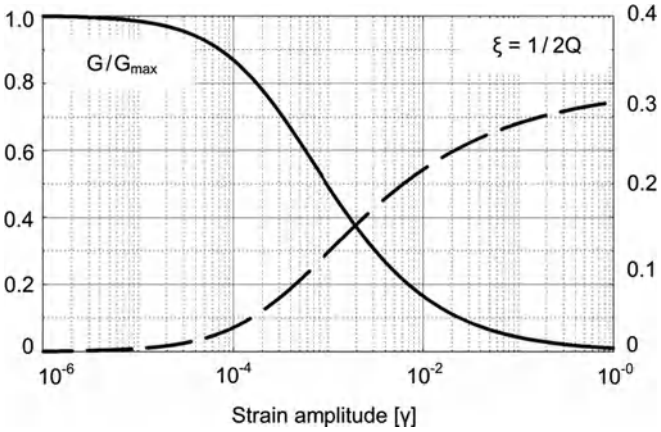


Fig. 3 Typical modulus degradation (G/G_{max}) and damping (ξ) vs. cyclic shear strain amplitude (γ), characteristic of nonlinear soil response

The advantages of the equivalent-linear approach are that the mathematical simplicity of linear analysis is preserved and the determination of nonlinear parameters is avoided.

Despite the effectiveness of the approach for the analysis of relatively stiff sites subjected to intermediate levels of strain ($<10^{-3}$), however, the equivalent linear method has been shown to overestimate the peak ground acceleration for large events, and artificially suppress the high frequency components when applied for the analysis of deep sites. An alternative methodology that accounts for the frequency-dependence of strain amplitudes and associated dynamic soil properties has been proposed by Assimaki and Kausel [1], and has been shown to yield more satisfactory results for deep sedimentary deposits; the applicability of the alternative formulation, however, is still limited to the medium strain levels [30].

The linear stress–strain material behavior and total stress approach associated with equivalent linear models, entirely prohibits their use for problems that involve large levels of strain (e.g. near-fault motions), deep and/or soft and very soft sedimentary sites. Both the original formulation of the equivalent linear method and the frequency-dependent modified algorithm are being implemented in the ensuing for ground surface response analyses to the ensemble of ground motion time-histories, and the divergence of their predicted response from the incremental nonlinear analyses is reported to illustrate their range of applicability for the site conditions under investigation.

3.2 Nonlinear Models: Monotonic and Hysteretic Behavior

In the nonlinear formulations of transient soil behavior, the wave equation is directly integrated in the time-domain and the material properties are adjusted to

the instantaneous levels of strain and loading path according to the mathematical description of nonlinear stress–strain model and hysteretic (loading and unloading) soil response. As a result, nonlinear constitutive models can simulate soil behavioral features unavailable in the equivalent linear formulation such as updated stress–strain relationships and/or cyclic modulus degradation, which are critical for the prediction of large strain problems at soft sedimentary sites.

In this study, we evaluated the nonlinear simulations by means of the central difference method as described in Bardet and Tobita [3]. Figure 4 illustrates schematically the geometry and boundary conditions of the response simulations conducted for a horizontally stratified system of homogeneous layers laterally extending to infinity and subjected to vertically propagating horizontally polarized shear waves.

We used the modified Kondnor and Zelasko (MKZ) hyperbolic model ([49, 50]) to idealize the monotonic loading (backbone curve) of the soil layers:

$$\tau = \frac{G_{\max}\gamma}{1 + \beta\left(\frac{\gamma}{\gamma_r}\right)^s} \tag{1}$$

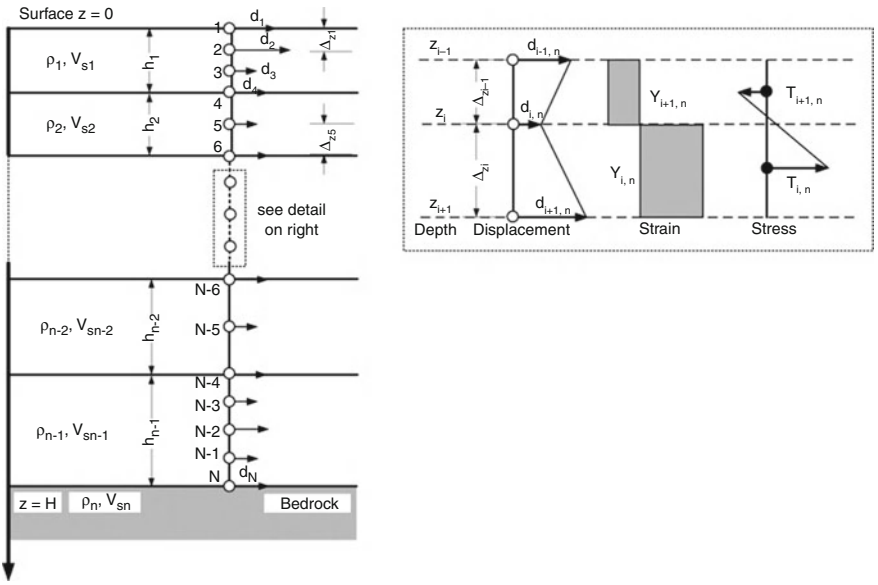


Fig. 4 Schematic representation of spatial discretization for a one-dimensional soil deposit system, and detail illustrating the definition of displacement, strain and stress in the finite difference formulation. The displacement d and stress τ are evaluated at N grid nodes, which define sublayers within layers. The displacement of node i at time step t_n is denoted $d(z_i, t_n) = d_{i,n}$, where z_i is the depth of node i. Similarly, the stress and strain at node i at time step t_n are denoted $\tau_{i,n}$ and $\gamma_{i,n}$ (modified from Bardet [4])

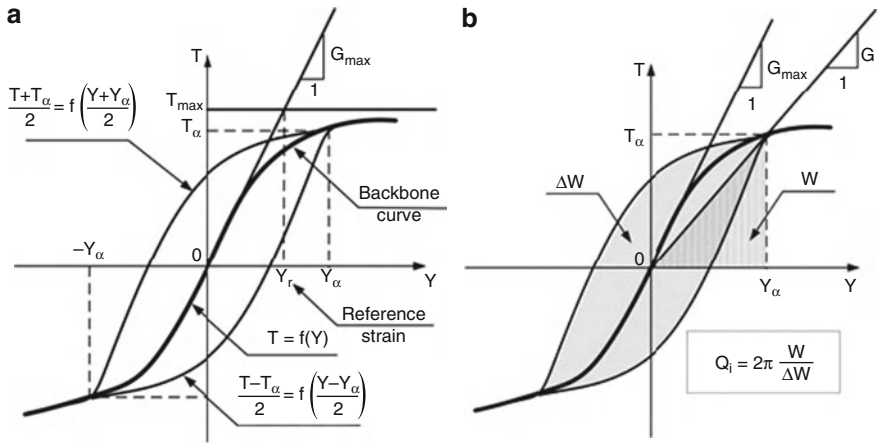


Fig. 5 (**a**) Schematic representation of original Masing unloading-reloading criteria and definition of reference strain and stress reversal point of the hysteresis loop; (**b**) Schematic representation of secant shear modulus (G), elastic stored strain energy (W) and dissipation energy (ΔW), and definition of hysteretic intrinsic attenuation Q_i

where G_{max} is the low-strain (linear) shear modulus, γ_r, γ_r and s are three independent parameters that can be evaluated by fitting the modulus reduction curve, and γ_r and γ_r denote the shear stress and the shear strain, respectively.

For the representation of the hysteretic soil behavior in transient loading, we employed the extended Masing rules; this scheme comprises the two original Masing criteria [48] schematically illustrated in Fig. 5 namely:

(i) The shear modulus on each loading reversal is equal to the maximum tangent modulus of the initial loading (backbone) curve, and
(ii) The unloading and reloading branches of the hysteresis loop are translated and scaled replicas of the backbone (initial loading) curve by a factor constant throughout the loading time-history and equal to 2.0

as well as two additional criteria to describe the unloading and reloading branches of the hysteresis loop, namely:

(iii) The unloading and reloading curves follow the backbone curve if the previous maximum amplitude of the shear strain is exceeded, and
(iv) If the current reloading or unloading curve intersects the curve described by a previous reloading or unloading, the stress–strain relationship follows that previous curve

The set of rules (i)–(iv) is consistent with a series of mechanical models described by Iwan [35], according to which the shear strain may be easily decomposed into elastic and plastic components as required by the formulation of incremental elasto-plasticity. The Iwan model implemented in this study for the incremental solution

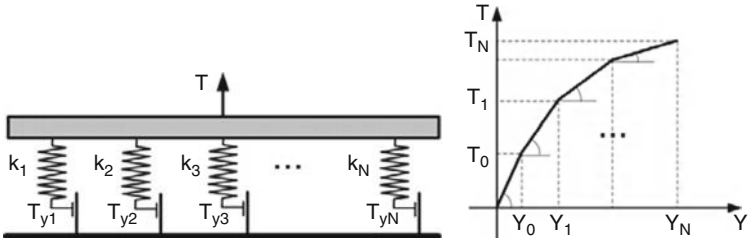


Fig. 6 Iwan [35] model of elastoplastic springs in parallel simulating the nonlinear stress–strain soil behavior, and corresponding approximation of continuous backbone curve by a series of linear segments

of the wave equation in nonlinear media consists of a group of N elastic-perfectly plastic elements in parallel, each comprising a linear elastic spring and a rigid slip element connected as shown in Fig. 6.

The number of elastoplastic elements and corresponding stiffness and Coulomb resistance values were in each case selected to fit the target material model behavior ($\tau = f(\gamma)$). Based on this mathematical representation originally proposed by Iwan [35] and Mroz [54], the multi-linear shear stress–strain behavior for N elastoplastic springs subjected to a strain amplitude γ is:

$$\tau = \sum_{i=1}^{N} \frac{k_i}{N} \cdot \gamma + \sum_{i=n+1}^{N} \frac{\tau_{yi}}{N} \tag{2}$$

where k_{i} is the shear stiffness of the ith element, τ_{yi} is the critical slipping (Coulomb) stress of the ith element, n is the number of elastoplastic elements that remain elastic upon the application of a strain increment, and τ is the estimated level of shear stress at a given level of strain amplitude γ. The first and second terms of the right-hand side of Eq. (2) indicate the elastic and plastic components respectively, of the total stress τ. Note that the form of the stress–strain relationship for subsequent unloading at any reversal point may be evaluated by means of the response of the three following groups of slip elements: (i) elements that did not yield upon previous loading remain elastic; (ii) elements under the state of yielding that have stopped slipping after reversal; and (iii) elements that have yielded during loading and now yield in the opposite direction.

As can be readily seen, the Iwan model provides a very convenient tool for the simulation of soil behavior that is consistent with the extended Masing rules and was thus selected for the purpose of this work. More specifically, 500 elasto-plastic elements were used to ensure the accuracy of the simulated soil response to high frequency transient loading.

The memory-variable representation of frequency-independent Q was implemented in the simulations of nonlinear site response. This technique can be implemented to accurately model frequency dependent or independent Q over

a wide range of frequencies using a linear combination of multiple relaxation mechanisms; it was originally described by Day and Minster [22] and successively implemented by Emmerich and Korn [26] and Carcione et al. [15]. We implemented this method in the nonlinear site response time-domain simulations using the rheology formulation of a generalized Maxwell body, modified by Liu and Archuleta [45] as follows:

$$\tau(t) = G\left[\gamma(t) - \sum_{k=1}^{N} \varsigma_k\right] \tag{3}$$

where ζ_k are memory variables that correspond to the solution of the following first order set of differential equations, with τ_k being the relaxation times and wk being the weight coefficients:

$$\tau_k \frac{d\varsigma_k(t)}{dt} + \varsigma_k(t) = w_k\, \gamma(t) \tag{4}$$

The accuracy of low strain damping modeling depends on the accuracy of estimation of τ_k and w_k. The nonlinear simulations in this chapter were evaluated by means of the empirical interpolating algorithm proposed by Ma and Liu [47]. The suggested values for τ_k and w_k are shown in Table 2. The weight coefficients w_k for a target value of damping ratio are calculated using the interpolation formula:

$$w_k^{\xi} = \chi(\chi\alpha_k + \beta_k) \tag{5}$$

where the values of α_k and β_k are also listed in Table 2. Finally, the factor depends only on the target value of and is estimated by the following expression:

$$\chi = \left[3.071 + 1.433\left(\frac{1}{2\xi}\right)^{-1.158} \ln\left(\frac{1}{10\xi}\right)\right] \Big/ \left[1 + \frac{0.2075}{\xi}\right] \tag{6}$$

An example of implementation of the above equation within the context of a time-domain direct integration of the wave equation is shown in Fig. 6 for a target value of

Table 2 Relaxation coefficients for modeling frequency-independent small strain damping (Q_{min}) in this study (Liu and Archuleta [45])

K	W_k	α_k	β_k
1	1.72333×10^{-3}	1.66958×10^{-2}	8.98758×10^{-2}
2	1.80701×10^{-3}	3.81644×10^{-2}	6.84635×10^{-2}
3	5.38887×10^{-3}	9.84666×10^{-3}	9.67052×10^{-2}
4	1.99322×10^{-2}	-1.36803×10^{-2}	1.20172×10^{-1}
5	8.49833×10^{-2}	-2.85125×10^{-2}	1.30728×10^{-1}
6	4.09335×10^{-1}	-5.37309×10^{-2}	1.38746×10^{-1}
7	2.05951	-6.65035×10^{-2}	1.40705×10^{-1}
8	13.2629	-1.33696×10^{-1}	2.14647×10^{-1}

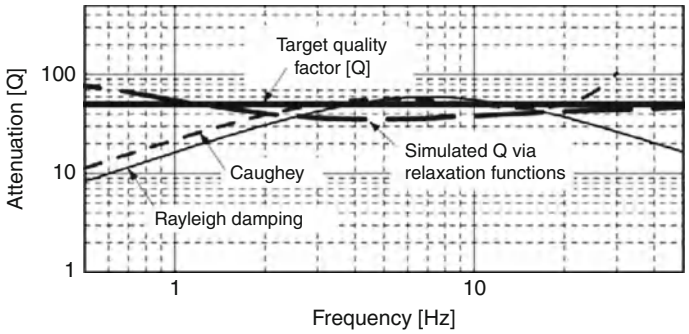


Fig. 7 Typical example of target low-strain damping (intrinsic attenuation) simulation by means of the Rayleigh damping formulation, the Caughey damping, and the memory-variable technique [45] implemented in this study

low-strain material damping (or Q = 50), and the effectiveness of this formulation may be readily seen by comparison to the Rayleigh damping [17] and higher-order Caughey damping (e.g. [32]) formulations (Fig. 7).

3.3 Calibration of Nonlinear Soil Parameters

For each one of the nonlinear models, the input parameters were selected to optimally fit the available experimental data of soil modulus reduction and damping vs. shear strain amplitude. For this purpose, a genetic algorithm was implemented, with objective function targeted to simultaneously minimize the square error between the measured and theoretically predicted modulus reduction and damping data as follows:

$$\sum_{i=1}^{N}\{w_i[O_G(\gamma_i)-G(P,\gamma_i)]\}^2+\sum_{j=1}^{N}\{w_j[O_\xi(\gamma_j)-\xi(P,\gamma_j)]\}^2 \qquad (7)$$

where w_i and w_j are the weight coefficients of the global search, $O_G(\gamma_i)$ and $O_\xi(\gamma_j)$ are the ith and jth experimental points for the modulus reduction and damping curves at γ_i and γ_j strain amplitudes correspondingly, and $G(P,\gamma_i)$ and $\xi(P,\gamma_j)$ are the corresponding predicted values as a function of the model parameters P. In particular for the representation of small-strain intrinsic attenuation, the experimentally measured value was subtracted from the damping curve prior to the stochastic search since the evaluation of anelastic intrinsic attenuation is only a function of the modulus reduction function. Successively, for each model investigated, the small-strain damping was implemented in the finite difference formulation by means of the memory variable technique described above, a formulation yielding a frequency-independent intrinsic attenuation across the frequency and strain spectra of interest.

4 Site Response Modeling Variability

The effects of nonlinear model selection in ground motion simulations have been recently investigated by various researchers, and published studies have primarily focused on the New Madrid seismic zone (NMSZ), a region of high seismic hazard and low seismicity where the response of sedimentary deposits has been shown to be critical in the prediction of future earthquake scenario. Among others, Park and Hashash [58, 59] developed an integrated probabilistic seismic hazard analysis procedure that incorporated nonlinear site effects (PSHA-NL), where site effects were directly accounted for by propagating the motions using nonlinear and equivalent linear site response analyses. Cramer et al. [20] generated a suite of seismic hazard maps for Memphis, Shelby County, Tennessee that account for the site response of sediments in the Mississippi Embayment (ME), where the strong motion sediment response was simulated by the equivalent linear computer code SHAKE91 [34], as well as by implementing the nonlinear site response codes DEEPSOIL [31, 32] and TREMORKA ([9], written communication; [39]). They showed that SHAKE91 overly damps the high-frequency components of motion, and that DEEPSOIL has a lower high-frequency response than TREMORKA. They reported that uncertainty in site amplification primarily arised from uncertainties in the site-specific dynamic soil properties and the choice of nonlinear code used to calculate site response. Although uncertainties have not been quantified, preliminary work showed that the median site response predicted by different algorithms may differ by 50% for the same set of input parameters.

Successively, Cramer [19] combined the methodology by Cramer et al. [20] with the reference profile approach of Toro and Silva [68] to better estimate seismic hazard in the ME. Improvements over previous approaches included using the 2002 national seismic-hazard model, fully probabilistic hazard calculations, calibration of site amplification with improved nonlinear soil-response estimates, and estimates of uncertainty. In addition to the aforementioned computer codes, the nonlinear finite difference code NOAH [9, 10] was examined for implementation in the site-amplification distribution calculation procedure. In this study, Cramer [19] quantified the added uncertainty in site amplification estimates due to the choice of soil-response program, and results suggested a range of 20–50% for PSHA ground-motion hazard estimates. He added that if this uncertainty were to be incorporated into a site-amplification logic tree, site-amplification distribution variability would be increased and site-specific PSHA values would likely increase, in particular, at low probabilities of exceedance (<0.001).

In the following sections, we estimate the variability in site response predictions introduced by the alternative soil models, and also compared the site-specific results to the NGA empirical amplification factors by Boore and Atkinson [12] for each of the 24 profiles investigated and the ensemble of synthetic ground motions. Attenuation relations account for site effects at soil profiles by scaling the frequency response of the BC-boundary reference site ($V_{s30} = 760\,m/s$) outcrop motion as a function of the ground motion intensity level and the site conditions; here, the Peak Ground Acceleration (PGA) was used as ground motion intensity measure,

while the NEHRP V_{s30} classification (14) was used to describe the site conditions. Next, the amplification factors are estimated and the empirical model is employed to approximate the ground surface response as follows:

$$FAS_{GS}(\omega) = EAF_{BA}(\omega) \cdot FAS_{RO}(\omega) \tag{8}$$

where FAS denotes the Fourier amplitude spectrum, GS and RO refer each to the Ground Surface and Rock Outcrop motions, and EAF_{BA} is the amplification factor expressed as:

$$EAF_{BA}(\omega) = Sa_{Vs30}(\omega)/Sa_{BC}(\omega) \tag{9}$$

where $Sa_{\mathrm{Vs}}30$ and Sa_{BC} are respectively the spectral acceleration ordinates evaluated for the soil site and the reference site.

The divergence of site-specific ground motion predictions from the empirically estimated site response, as well as the deviation between the site-specific analyses for different soil models was next evaluated as a function of the site and ground motion characteristics.

For the site specific viscoelastic, equivalent linear and nonlinear analyses, ground motion synthetics computed on rock-outcrop were deconvolved to estimate the incident seismic motion at 100 m depth, where nonlinear effects are not likely to manifest during strong motions for the soil conditions studied here. Successively, the estimated incident motions were propagated through the 24 soil profiles to the surface by means of the three site response models investigated. Weak ground motions (rock-outcrop PGA $< 1\ \mathrm{m/s^2}$), which are unlikely to cause yielding of medium soft to soft profiles and the overlying structures, were excluded from the ground and structural response analyses. Overall, 510 out of 6,300 synthetic ground motions were selected for our simulations; Fig. 2b depicts the magnitude (M), PGA and distance (R)-to-fault distribution of these motions.

Next, the deviation between nonlinear and linear elastic ground surface predictions for all profiles and all synthetic motions was evaluated. Assimaki et al. [2] used this measure to describe the extent of soil nonlinearity manifesting during strong ground motion. Note that the nonlinear model used here was benchmarked by Assimaki et al. [2] by comparison with downhole array recordings; thus, the deviation of linear site response from the 'true' nonlinear predictions is expected to increase as the intensity of nonlinear effects in the soil increases.

Denoting the spectral acceleration at period T_i of the linear site response prediction as SA_i^{LIE} and the spectral acceleration at period T_i of the nonlinear prediction as SA_i^{MKZ}, the divergence between the responses is evaluated as:

$$e_{SA} = \mu(e_{SA}) = \mu\left(\log\left(\frac{SA_i^{LIE}}{SA_i^{MKZ}}\right)\right) \tag{10}$$

where the operator μ corresponds to the non-weighted average, and the subscript i refers to period T_i. The averaged error is here evaluated for periods between 0.2 and 2.0 s, a range that covers the dominant period of most common structures.

Assimaki et al. [2] expressed the error between linear and nonlinear predictions (e_{SA}) as a function of the ground motion intensity, frequency content and soil profile characteristics. For soil profiles with soft layers likely to respond nonlinearly during a strong event, the amplitude and frequency content of input motion describe whether the seismic waves will "see" the soft layers and whether they "carry" sufficient energy to impose large strains and cause nonlinearity. The rock outcrop PGA (PGA_{RO}) was used to describe the ground motion intensity, and a dimensionless index referred to as frequency index (I_F) to quantify the similarity between the transfer function of the profile and the Fourier amplitude spectrum of the incident motion. Large I_F means large amplification potential of the input motion as it propagates through the soil profile, and if the amplified motion is characterized by a high $\mathrm{PGA_{RO}}$, it will most likely trigger nonlinear soil effects. Assimaki et al. [2] expressed the frequency index I_F as

$$I_F = \frac{2\sum_{i=1}^{N} ATF_i FAS_i}{\sum_{i=1}^{N} ATE_i ATF_i + \sum_{i=1}^{N} FAS_i FAS_i} \tag{11}$$

where ATF_i and FAS_i are the amplitude of the elastic transfer function of the profile and the Fourier amplitude spectrum of incident motion at the ith frequency point, normalized by their respective peak value, and N is the total number of frequency points in the range of interest, namely 0 Hz to twice the fundamental frequency of the site.

Figure 8 shows the variation of the e_{SA} as a function of I_F and PGA_{RO} for three sites. As can be readily seen, the deviation between linear and nonlinear predictions, e_{SA}, increases with increasing ground motion intensity (i.e. PGA_{RO}) and increasing frequency index (I_F), and attains maximum values at the up-right corner of the contour plot. The $\mathrm{PGA_{RO}} - I_F$ regions of large e_{SA} values correspond to combinations of sites and incident ground motions with large sensitivity of the site response predictions on the selection of the soil model. In these cases, Assimaki et al. [2] recommended that nonlinear analyses should be employed to ensure credibility of the site response analyses.

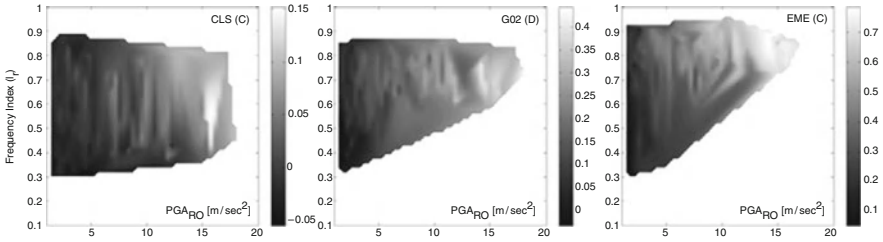


Fig. 8 Contour maps of the prediction error ($\mathrm{e_{SA}}$) as a function of the peak ground acceleration ($\mathrm{PGA_{RO}}$) at rock-outcrop and frequency index ($\mathrm{I_F}$) for selected sites

Figure 8 also shows that the quantitative dependency of e_{SA} on PGA_{RO} and I_F is site-specific. Li and Assimaki [42] identified the following empirical relation between e_{SA}, ground motion and soil profile parameters to describe the variability in absolute e_{SA} values as a function of the site characteristics:

$$e_{SA} = \alpha \frac{760}{V_{S30}} PGA_{RO} + \beta Amp I_F + \varepsilon \tag{12}$$

where α and β are regression coefficients, *Amp* is the site amplification at the fundamental period of the soil site, and ∈ is the normally distributed residual of the regression. This equation can be used as a proxy to describe the extent of nonlinear soil effects expected during a given event at a given site, and the associated uncertainties as a function of the soil profile and the ground motion characteristics. Regression coefficients α and β were also estimated by Assimaki et al. [2] for a limited number of sites, which along with an error threshold $e_{SA} \leq e_{SA}^{\max}$, can be used to quantitatively determine whether nonlinear simulations are required for site response predictions at a given site during a given event.

While details of the study above are beyond the scope of the present work, the same concept of soil and ground motion dependency will be used in the following sections to illustrate how the soil model implemented for the prediction of site response affects the estimation of inelastic structural performance measures.

5 Uncertainty and Bias in Structural Response Predictions

We next investigate how the modeling variability in site response analyses propagates to the prediction of inelastic structural response for a series of nonlinear SDOF oscillators. More specifically, we estimate the bias and uncertainty in structural response introduced by the soil model, using the nonlinear site response analyses as reference. The inelastic deformation ratio (C) is used as an Engineering Demand Parameter (EDP) to measure the displacement demand, while its variability resulting from the selection of the soil model is mapped as a function of the site- an ground-motion characteristics described above, namely as a function of $\mathrm{PGA_{RO}}$ and I_{F}.

5.1 Inelastic Deformation Ratio

The inelastic deformation ratio (C) is defined as the ratio of the peak deformation (u_{m}) of an inelastic oscillator to its corresponding linear (u_0) response (see Fig. 9). This ratio varies considerably as a function of period and approaches unity only in the displacement-sensitive spectral region of the oscillator response, which is the basis of the so-called equal deformation rule ($u_{\mathrm{m}}/u_0 = 1$) [69].

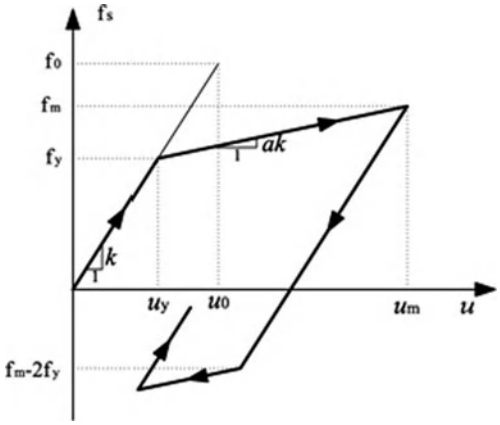


Fig. 9 Bilinear force-deformation relationship of inelastic SDOF system and corresponding notation for elastic and post-yield characteristics

When expressed as a function of the elastic vibration period T_n and the ductility factor μ, the inelastic deformation ratio (C) may be used to determine the inelastic deformation demand of a structure with given global ductility capacity; on the other hand, when expressed as a function of the elastic vibration period and the yield-strength reduction factor R_y (Eq. 13), it can be used to estimate the inelastic deformation of an existing structure with known lateral strength. Compared to the alternative indirect method of $R_y - \mu - T_n$ relations, this direct method can give relatively unbiased estimation of the peak deformation of an inelastic SDOF system [18, 53].

A bilinear force-displacement response $f_s(u, \operatorname{sgn} \dot{u})$ schematically shown in Fig. 9 was selected to simulate the idealized inelastic structural response of a series of SDOF oscillators. As shown in Fig. 9, the elastic stiffness of the model is k and the post-yield stiffness is αk, where α is defined as the post-yield stiffness ratio. The yield strength of the oscillator is f_y and the yield deformation u_y. Within the linear elastic range namely $u = [0 \sim u_y]$ the system has a natural vibration T_n period and damping ratio ξ. The yield strength reduction factor of the structure (R_y) is defined as

$$R_y = \frac{f_0}{f_y} = \frac{u_0}{u_y} \tag{13}$$

where f_0 and u_0 are the minimum yield strength and yield deformation required for the structure to remain elastic during the ground motion, or the peak response values for the corresponding linear system. The peak force in the inelastic system is f_m (Fig. 9). The peak deformation of the bilinear system is denoted by u_m and the corresponding ductility ratio μ is defined as

$$\mu = \frac{u_m}{u_y} \tag{14}$$

Finally, it can be shown that the inelastic deformation ratio (C) can be evaluated as

$$C = \frac{u_m}{u_0} = \frac{\mu}{R_y} \tag{15}$$

When the equal displacement rule applies, $C = 1$, or $\mu = R_{\mathrm{y}}$. To ensure a uniform intermediate inelastic level in the nonlinear oscillators, we focused primarily on the constant yield strength reduction factor ($R_{\mathrm{y}} = 4$) approach and we also investigated the constant ductility ratio ($\mu = 4$) approach instead of keeping constant the yield strength (f_{y}) of the oscillator. Therefore, in order to have the same R_{y} factor for all our analyses, we simply tune the oscillators f_{y} according to the record's first mode spectral acceleration. The reason is that the highly variable intensity (PGA $=$ $0.1 \sim 2.0$ g) of the ground motions will cause also high inelastic demands on the oscillator of constant yield strength, i.e. constant yield acceleration for structure with unit mass was fixed, which will totally overshadow the signature of site effects in the structural response.

5.2 Bias and Uncertainty in Inelastic Deformation Prediction

We next evaluate the variability in inelastic deformation ratio (C) predictions for each of the different site response methods for structures with different fundamental period and yield strength, f_{y}. The results are differentiated using subscripts corresponding to abbreviations of the site response methods. Specifically, the C values corresponding to the empirical amplification model are denoted as $\mathrm{C_{EAF}}$; similarly, the C values corresponding to the linear visco-elastic models are denoted as $\mathrm{C_{LIE}}$; the C values of the equivalent linear models are denoted as C_{EQL}; and the C values of the modified Kondner and Zelasko (MKZ) model as C_{MKZ}.

In this section, for brevity only some representative results from three sites with NEHRP class C (site CLS), D (site G02), and E (site EME) are shown to illustrate our key observations. The statistical correlation analysis between bias in the prediction of the displacement demand, C and the site parameters using the results from all the sites will be shown at the end of the section.

Figure 10 shows $\mathrm{C_{EAF}}$, $\mathrm{C_{LIE}}$, $\mathrm{C_{EQL}}$ and $\mathrm{C_{MKZ}}$ for $R_{\mathrm{y}} = 4$ as functions of the fundamental period ($\mathrm{T_n}$) of the inelastic SDOF for the selected sites. The C values are averaged within five different $\mathrm{PGA_{RO}}$ bins shown in the legend to illustrate the PGA dependency. It can be readily seen that the $\mathrm{C_{LIE}}$ curves show no PGA dependency, i.e. the $\mathrm{C_{LIE}}$ curves from different $\mathrm{PGA_{RO}}$ groups almost coincide one another. The reason is that the site amplification of LIE model is independent of the intensity of the incident motion, and therefore it only uniformly alters the frequency content of the incident motion. Although the intensities of the ground responses are highly variable, their frequency contents are same, which results in intensity-independent $\mathrm{C_{LIE}}$ values for the constant $\mathrm{R_y}$ structure model.

$\mathrm{C_{EAF}}$ curves show a slight PGA dependency and the overall shapes are similar to those of the C_{LIE} curves. The site amplification of EAF model is derived based on the mean spectral acceleration (SA) ordinates predicted by the NGA relations.

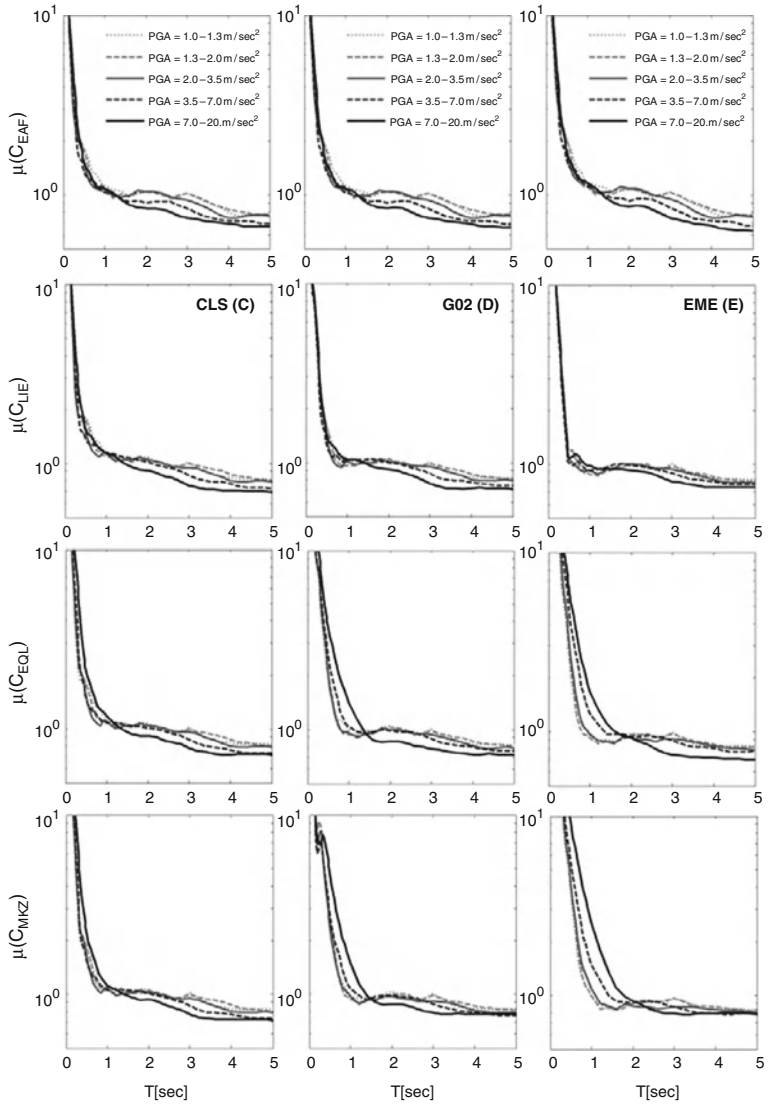


Fig. 10 Mean inelastic deformation ratio (C) of bilinear SDF structures with constant strength reduction factors ($R_y = 4$) (averaged within the PGA bins shown in the legend) evaluated using ground motions from different site response models as a function of the natural elastic vibration period of the bilinear SDOF (The site response models are differentiated by the subscript of C. Empirical Amplification Factor model EAF; Linear Viscoelastic model LIE; Equivalent Linear model EQL; and Modified Kondner-Zelasko model MKZ)

The mean SA predictions can only reflect a blended average site response effect, which will result in a relatively uniform or smooth site amplification. Therefore, the performance of the EAF model is similar to that of the LIE model.

By contrast to C_{LIE} and C_{EAF}, C_{EQL} and C_{MKZ} show obvious PGA dependency, i.e. the C_{EQL} and C_{MKZ} curves from different PGA_{RO} groups deviate from one another, with C_{EQL} or C_{MKZ} associated with higher PGA_{RO} showing higher C values. Since the same constant yield strength reduction factor ($R_y = 4$) SDOF models are used to calculate the C_{EQL} and C_{MKZ} values, the only source of the PGA_{RO} dependency is the difference in the frequency content of the ground motions due to adoption of different site response models. Both the amplitude and frequency content of the input motion will be substantially modified as a result of the nonlinear site response when the intensity of the input motion is high enough, and this modification in the amplitude and the frequency content can be realistically approximated by the EQL and MKZ models. Usually the higher the intensity of the incident motion, the larger the change in the frequency content of the ground response relative to the linear elastic response, which results in the deviation in the prediction of the inelastic deformation ratio C.

In order to have a quantitative description of the effect of nonlinear site response on the C prediction, the bias and uncertainty in predictions of C will be represented as the ratio of the mean C predictions from different models, which denoted by $Q_{\mu C}$, over the ratio between coefficient of variation (COV) of C predictions from different models, denoted as $Q_{\sigma C}$. Considering that the MKZ model is the most realistic of the four, we always take the quantities (i.e. mean and COV) associated with this model as denominator when taking the ratio. For instance, the ratio between mean C predictions from LIE model and MKZ model can be expressed as $Q_{\mu C} = \mu_{CLIE}/\mu_{CMKZ}$; and the ratio between the COV of C predictions from LIE model and MKZ model can expressed as $Q_{\sigma C} = \sigma_{CLIE}/\sigma_{CMKZ}$. Therefore, the deviation of $Q_{\mu C}$ or $Q_{\sigma C}$ from unity indicates deviation of the C prediction due to the adoption of different site response methodologies and thus propagation of the sensitivity of the ground response assessment to the prediction of the structural inelastic performance.

Figure 11 shows the $Q_{\mu C}$ for $R_y = 4$ at selected sites as a function of the elastic vibration period of the SDOF system, normalized by the fundamental period of the site. The mean C values here are averaged within the ranges of PGA_{RO} indicated by the legend. As mentioned before, a constant R_y was here selected to illustrate results of our study, namely depict the propagation of ground motion modeling variability to the inelastic structural response prediction while keeping the inelastic structural characteristics invariable.

It can be seen from Fig. 11 that the LIE and EAF models give biased C predictions relative to the MKZ model for all three sites, and the bias reaches the peak value around the abscissa of unity (note that the lower the value of $Q_{\mu C}$ the higher bias), i.e. when the elastic vibration period of the SDOF system is close the to natural period of the site. Furthermore, the bandwidth of the bias is proportional to the natural period of the site, i.e. is a function of the site stiffness. As expected, the performance of EAF model is very similar to the LIE model since both of them give the same bias value and bias range. The bias in C prediction caused by EQL model is much lower than that of EAF and LIE model and as expected, the stiffer the site, the better the performance of EQL model. This is because the strain level at a stiffer site is smaller for seismic excitations of the same intensity, and the smaller the strain level, the smaller the deviation between the EQL and MKZ model predictions.

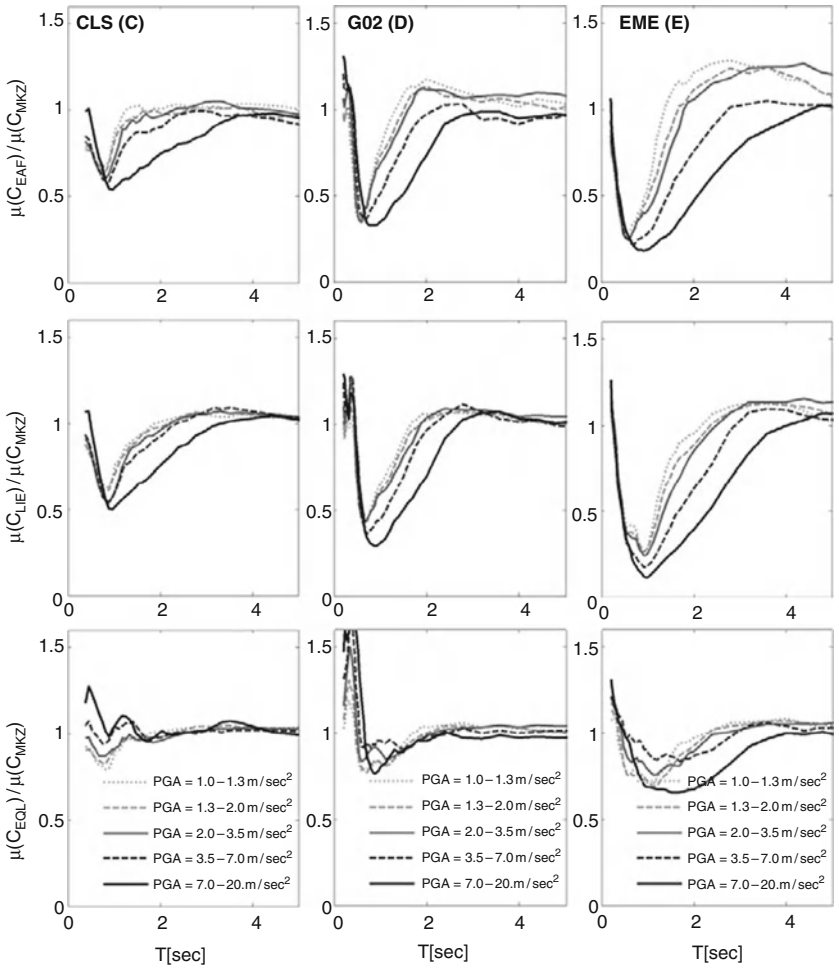


Fig. 11 The ratio between mean inelastic deformation ratios of bilinear SDF structures ($R_y = 4$) (counted within the PGA bins shown in the legend) evaluated using ground motions from different site response models (differentiated by the subscript of C) as a function of the elastic natural vibration period of the bilinear SDF system normalized by the fundamental period of the site

The PGA_{RO} and site dependency of the bias can be clearly seen in Fig. 11. As can be inferred from previous observations, the higher PGA_{RO}, the higher bias in the C prediction by the LIE and EAF models. Similarly, the softer the site, the higher the bias introduced in the C predictions by the LIE and EAF models. Since the PGA_{RO} values and the relative stiffness of the sites are directly associated with the extend of nonlinearity in the ground response, the high PGA_{RO} and site dependency of $Q_{\mu C}$ lead to the conjecture that the bias in the C prediction is due to the inability of LIE and EAF models to capture the nonlinear effect in the ground response. For simplicity, we take only $Q_{\mu C} = \mu_{CLIE}/\mu_{CMKZ}$ as the quantitative measure of the bias in the prediction of the mean C demand.

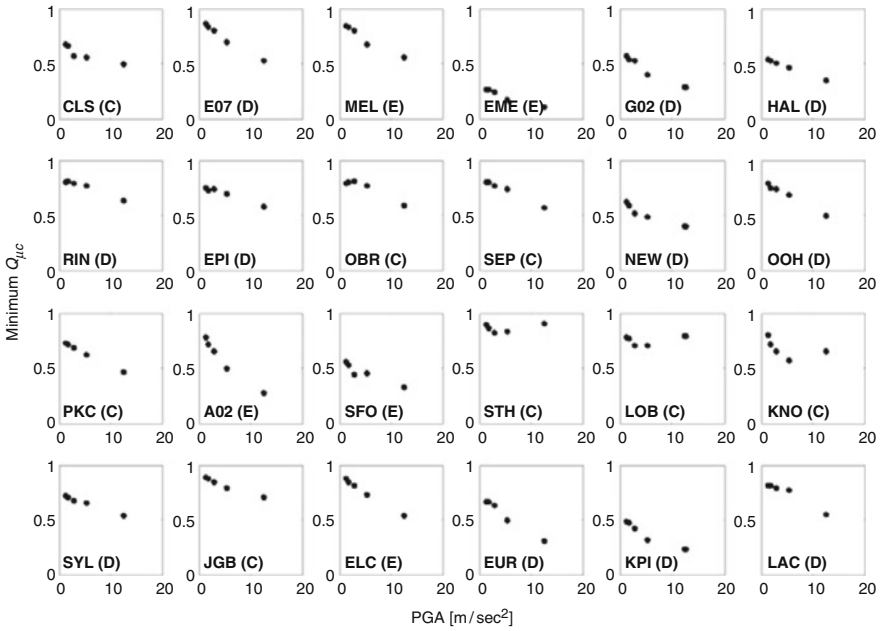


Fig. 12 The correlation between Q value (evaluated at the period of highest bias) and PGA for each site ($R_y = 4$)

For each site, the $Q_{\mu C}$ value in each PGA bin at the period of highest bias is plotted as function of PGA_{RO} in Fig. 12. Clearly, different sites show different degree of PGA dependency. If the degree of dependency is measured using the linear regression slopes to the data of each $Q_{\mu C}$ vs. PGA plot, and we name the absolute values of the slopes proportion coefficients, it can be shown that there is some correlation between these proportion coefficients and the V_{s30} values of the sites, which illustrated in Fig. 13. It can be readily seen that the softer the site (i.e. lower V_{s30} value), the higher the PGA dependency of $Q_{\mu C}$ value. This observation also implies that the nonlinear site effects are most likely the origin of bias in the mean C estimation because softer sites are more susceptible to nonlinear deformations.

It should be noted here that although the trend in site dependency and PGA dependency of $Q_{\mu C}$ is very clear when the C values are grouped (averaged) in PGA bins, the original Q_C values without averaging of C are highly scattered. Figure 14 shows the minimum Q_C value for all the motions at selected sites. As can been observed in Fig. 14, the Q_C may reach very low value even at very low PGA.

Analogous to Fig. 11, the C values from different site response can be averaged within frequency index (I_F) bins before taking the ratio, to show the I_F dependency of inelastic response bias. Figure 15 shows the $Q_{\mu C}$ and $Q_{\sigma C}$ for $R_y = 4$ at selected sites as a function of the elastic vibration period of the SDOF normalized by the fundamental period of the site; the mean C values here are averaged within the ranges of I_F indicated by the legend. The trend of bias indicated by $Q_{\mu C}$ and $Q_{\sigma C}$ is very similar to what shown in Fig. 11, except that the I_F dependency of $Q_{\mu C}$ and

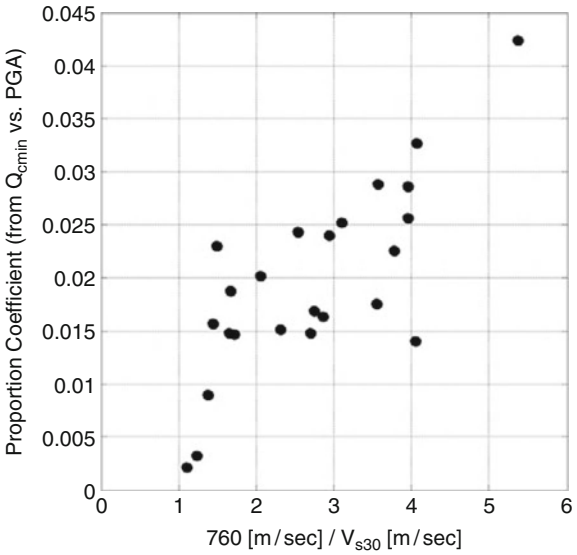


Fig. 13 Correlation between the proportion coefficient (slope of Minimum $Q_{\mu C}$ vs. PGA) in Fig. 12 and V_{s30} ($R_y = 4$)

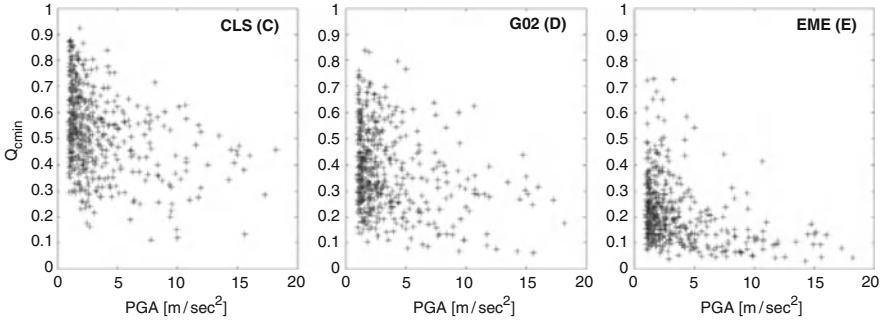


Fig. 14 Minimum Q value versus PGA for selected sites ($R_y = 4$). Scattering in data is much more pronounced than averaging Q within PGA bins as in Fig. 12

$Q_{\sigma C}$ is not as prominent as the PGA dependency. This observation is consistent with the fact that PGA dependency estimated for the site response prediction error by the alternative methods in the Sect. 4 is stronger than the I_F dependency.

Similar to Fig. 12, the $Q_{\mu C}$ value in each I_F bin at the period of highest bias can be plotted as function of I_F for all the sites as shown in Fig. 16. It can be readily seen that some sites do show strong dependency of $Q_{\mu C}$ on I_F, while others do not. If the minimum Q value of each site in Fig. 16 is taken as a representative bias degree of the site, which is denoted as Q_{Cmin}, it seems these Q_{Cmin} values have some correlation with the amplification amplitude at the fundamental frequency of the

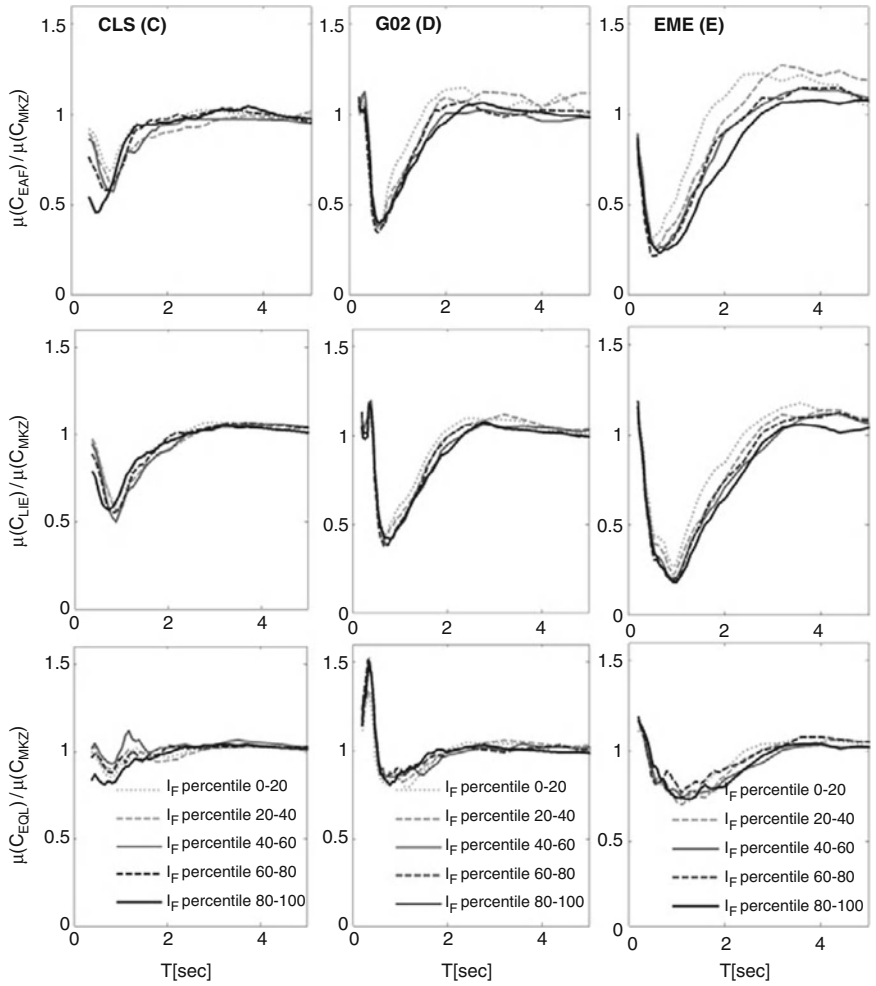


Fig. 15 The ratio between mean inelastic deformation ratios of bilinear SDF structures with constant strength reduction factors ($R_y = 4$) (averaged within the I_F bins shown in the legend) evaluated using ground motions from different site response models (differentiated by the subscript of C) as a function of the elastic natural vibration period of the bilinear SDF system normalized by the fundamental period of the site

site, which shown in Fig. 17. Again, it can be shown in Fig. 18 that the individual minimum Q values without C averaging are actually very scattered and that very low Q may appear even in the low PGA range.

It should be noted again that since constant R_y models are used to calculate the inelastic structure response, the bias in C prediction is purely caused by the differences in the frequency content of the ground motions for different site response models. Such differences in the frequency content maybe significant and cause large discrepancy the C prediction, even though the differences in amplitudes are very small as in the low PGA scenarios.

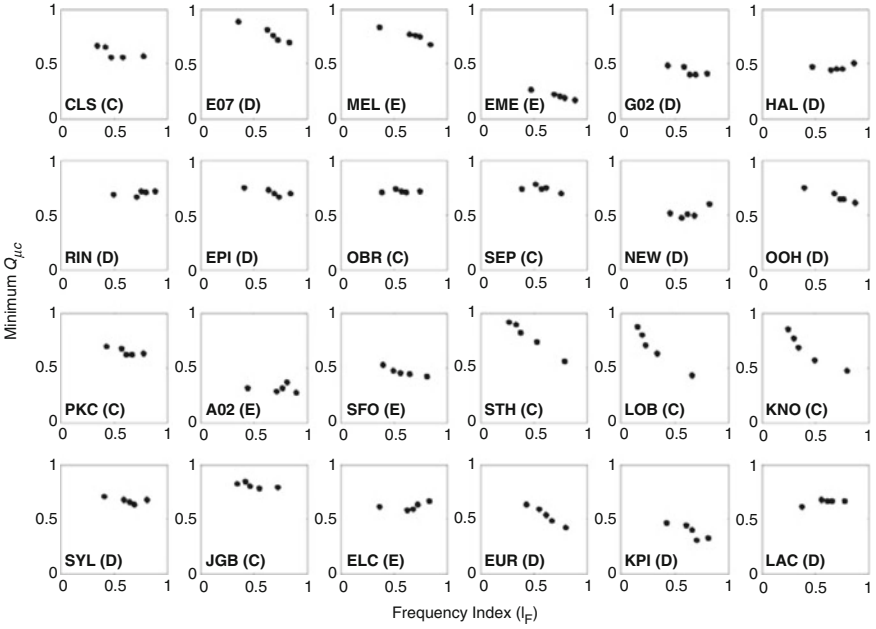


Fig. 16 Correlation between minimum Q value (evaluated at the period of highest bias) and frequency index (I_F) for each site (Ry = 4)

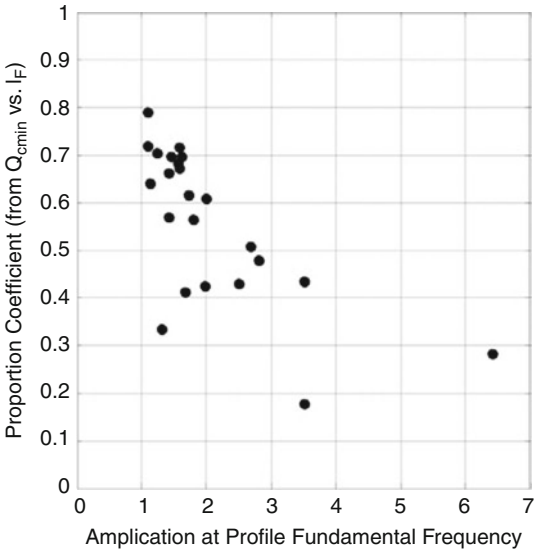


Fig. 17 The correlation between the slope of minimum Q in Fig. 16 and the amplification at the fundamental frequency of the soil profile, evaluated from the linear elastic site response (R_y = 4)

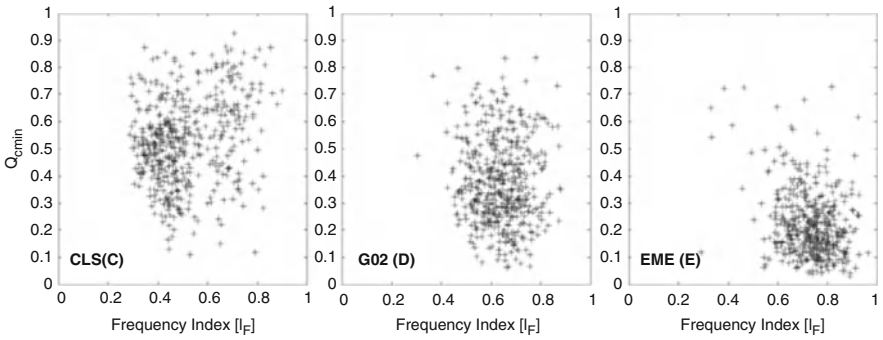


Fig. 18 Minimum Q value versus I_F for selected sites (Ry = 4). Scattering in data is much more pronounced than averaging Q within I_F bins as in Fig. 15

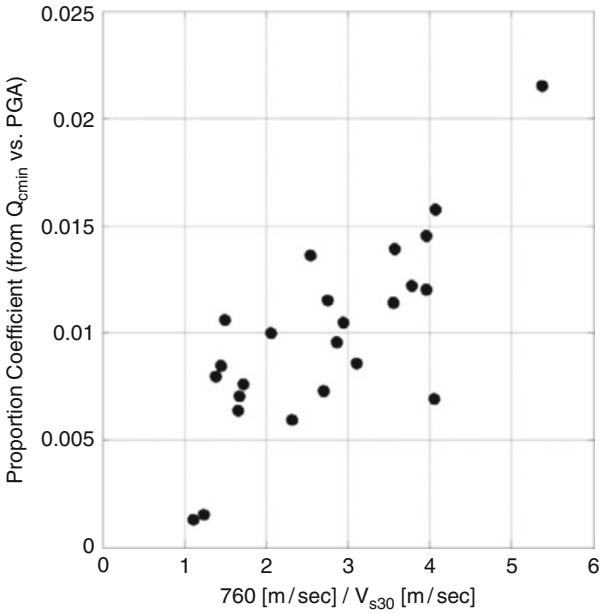


Fig. 19 Correlation between the proportion coefficient (slope of Minimum Q vs. PGA) and V_{s30} for constant ductility demand ($\mu = 4$)

Analogous to Figs. 13 and 17, we present the correlation between and bias in C prediction for the constant ductility ratio case ($\mu = 4$) in Figs. 19 and 20. The general trends are almost same as what shown in Figs. 13 and 17. The difference is that the bias in the constant ductility case is consistently less than in the case of constant strength reduction case. The reason is that the inelasticity levels in the

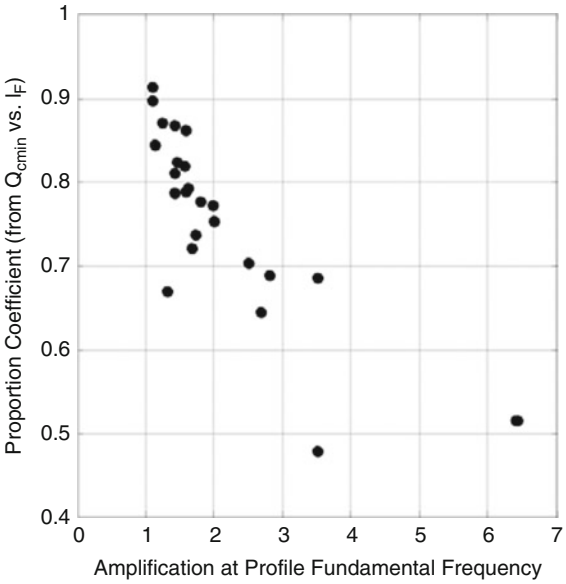


Fig. 20 The correlation between the slope of minimum Q in Fig. 16 and the amplification at the fundamental frequency of the soil profile for constant ductility demand ($\mu = 4$)

bilinear SDOF structures in the constant $\mu = 4$ case are always lower than those in the constant $R_y = 4$ case and thus less inelastic deformations happen in the constant $\mu = 4$ case.

Finally, it should be noted that the bias trends in Figs. 11 and 15 are consistent with results published by Bazzurro et al. [6], which were based on the comparison between the inelastic structural response obtained using synthetic and recorded ground motions. This consistency also implies that bias in the latter study may be caused by insufficient consideration of the nonlinear site effect in the synthetic ground motion predictions.

6 Conclusions

We investigated the uncertainty in nonlinear structural response predictions that results from site response models implemented in synthetic ground motion simulations. We studied typical profiles in Southern California, and first estimated the divergence between linear and validated nonlinear site response predictions in an intensity-frequency ($PGA_{RO} - I_F$) domain. We observed a consistent pattern of prediction error in ground response, with high intensity-high frequency index regions reflecting large deviation between elastic and nonlinear predictions, independent of the soil profile characteristics. We next established quantitative relations

between this prediction error and site-motion parameters, which enable –given a profile and an incident ground motion- the estimation of mean and variance of expected site response prediction error relative to nonlinear time domain solutions.

Next, the propagation of site response modeling uncertainty to the assessment of inelastic SDOF structural response revealed consistent bias and uncertainty by the linear site response model in the prediction of inelastic deformation. The results indicate that, for most of the sites with exception of the very stiff ones, the predicted inelastic deformation ratios using ground motions from visco-elastic site response models are consistently lower than those using ground motions from incremental nonlinear site response models around particular period range. The results also show that the former are less variable than the latter. These observations imply that the design based on inelastic SDOF analysis using the synthetic motions without considering nonlinear site effects may be on the unsafe part as a result of underestimation of the mean and uncertainty of deformation demand.

It was found that the mean bias in the inelastic deformation ratio (C) prediction has good correlation with some characteristics of input ground motions and site parameters. In general, the bias in C predictions increase with increasing ground motion intensity (PGA), decreasing V_{s30}, and increasing first mode amplification. Overall, the bias is reduced as more elaborate site response models are implemented.

This ground motion (PGA and I_F) and site (V_{s30} and first mode amplification) dependency of the mean bias in C predictions implies that the source of bias is most likely the inability of simplified models (linear viscoelastic, empirical amplification factors) to capture nonlinear site effects and the corresponding altering of ground motion frequency content. This conjecture is also favorable to the establishment of a guideline for efficient integration of nonlinear site response models into end-to-end ground motion simulations.

Acknowledgments This research was supported by the Southern California Earthquake Center. SCEC is funded by NSF Cooperative Agreement EAR-0106924 and USGS Cooperative Agreement 02HQAG0008. The SCEC contribution number for this chapter is 1344.

References

1. Assimaki D, Kausel E (2002) An equivalent linear algorithm with frequency- and pressure-dependent moduli and damping for the seismic analysis of deep sites. Soil Dyn Earthq Eng 22:959–965
2. Assimaki D, Li W, Steidl J, Schmedes J (2008) Quantifying nonlinearity susceptibility via site response modeling uncertainty at three sites in the Los Angeles basin. Bull Seismol Soc Am 98(5):2364–2390
3. Bardet JP, Tobita T (2001a) Nonlinear earthquake site response analysis. User's manual. Report, Civil Engineering Department, University of Southern California, Los Angeles, California, USA
4. Bardet JP, Tobita T (2001b) NERA: A computer program for nonlinear earthquake site response analyses of layered soil deposits. Technical report, University of Southern California
5. Bardet JP, Ichii K, Lin CH (2000) EERA A computer program for equivalent-linear earthquake site response analyses of layered soil deposits. Technical report, University of Southern California http://gees.usc.edu/GEES/Software/EERA2000/EERAManual.pdf

6. Bazzurro P, Sjoberg B, Luco N (2004) Post-elastic response of structures to synthetic ground motions. Technical report, AIR Worldwide Co, San Francisco
7. Berrill J (1977) Site effects during the San Fernando, California, earthquake. In Proceedings of the Sixth World Conference on Earthquake Engineering, India pp 432–438
8. Bommer J, Scott S, Sarma S (2000) Hazard-consistent earthquake scenarios. Soil Dyn Earthq Eng 19:219–231
9. Bonilla LF (2001) NOAH: user's manual. Institute for Crustal Studies, University of California, Santa Barbara, 38 pp
10. Bonilla LF, Archeleta RJ, Lavellee D (2004) Hysteretic and dilatant behavior of cohesionless soils and their effects on nonlinear site response: field data observations and modeling. Bull Seism Soc Am 95:2373–2395
11. Boore DM (1983) Stochastic simulation of high-frequency ground motions based on seismological models of the radiated spectra. Bull Seism Soc Am 73:1865–1894
12. Boore DM, AtkinsonGM (2008) Ground-motion prediction equations for the average horizontal component of PGA, PGV, and 5%-damped PSA at spectral periods between 0.01 s and 10.0 s. Earthq Spectra 24(1):99–138, PEER NGA
13. Borcherdt RD, Gibbs JF (1976) Effects of local geological conditions in the San Francisco bay region on ground motions and the intensities of the 1906 earthquake. Bull Seism Soc Am 66(2):467–500
14. Building Seismic Safety Council (BSSC) (2003) NEHRP recommended provisions for seismic regulations for new buildings and other structures (FEMA 450). Technical report, prepared by the Building Seismic Safety Council for the Federal Emergency Management Agency, Washington, DC
15. Carcione JM, Kosloff D, Kosloff R (1988) Wave propagation in a linear viscoacoustic medium. Geophys J Roy Astr Soc 93:393–407
16. Chin B-H, Aki K (1991) Simultaneous study of the source, path, and site effects on strong ground motion during the 1989 Loma Prieta earthquake: a preliminary result on pervasive nonlinear site effects. Bull Seism Soc Am 81(5):1859–1884
17. Chopra A (2000) Dynamics of Structures: Theory and Applications to Earthquake Engineering (2nd Edition) Prentice Hall, 844 pages, ISBN-10: 0130869732
18. Chopra AK, Chintanapakdee C (2004) Inelastic deformation ratios for design and evaluation of structures: single-degree-of-freedom bilinear systems. J Struct Eng 130(9):1309–1319
19. Cramer C (2006) Quantifying the uncertainty in site amplification modeling and its effects on site-specific seismic-hazard estimation in the upper Mississippi embayment and adjacent areas. Bull Seism Soc Am 96(6):2008–2020
20. Cramer CH, Gomberg JS, Schweig ES, Waldron BA, Tucker K (2004). Memphis, Shelby County, Tennessee, seismic hazard maps, US Geological Survey. Open-File Report 04–1294, 41 pp
21. Darragh RB, Shakal AF (1991) The site response of two rock and soil station pairs to strong and weak ground motion. Bull Seism Soc Am 81(5):1885–1899
22. Day SM, Minster JR (1984) Numerical simulation of attenuated wavefields using a Pade approximant method. Geophys J Roy Astr Soc 78:105–118
23. Drnevich VP, Hall JR Jr, Richart FE Jr (1966) Large amplitude vibration effects on the shear modulus of sand. University of Michigan Report to Waterways Experiment Station, Corps of Engineers, U.S. Army, Contract DA-22-079-eng-340
24. Duke C, Mal A (1978) Site and source effects on earthquake ground motion. Technical report, University of California, Los Angeles
25. Ellis GW, Cakmak AS (1987) Modeling earthquake ground motions in seismically active regions using parametric time series methods. Technical report, NCEER-87-0014, National Center for Earthquake Engineering Research
26. Emmerich H, Korn M (1987) Incorporation of attenuation into time-domain computations of seismic wave fields. Geophysics 52:1252–1264
27. Hardin BO, Drnevich VP (1972a) Shear modulus and damping in soil: measurement and parameter effects. J Soil Mech Found Div ASCE 98:603–624

28. Hardin BO, Drnevich VP (1972b) Shear modulus and damping in soil: design equations and curves. J Soil Mech Found Div ASCE 98:667–692
29. Hartzell S (1992) Site response estimation from earthquake data. Bull Seism Soc Am 82(6):2308–2327
30. Hartzell SH, Bonilla LF, Williams RA (2004) Prediction of nonlinear soil effects. Bull Seism Soc Am 94(5):1609–1629
31. Hashash YMA, Park D (2001) Non-linear one-dimensional seismic ground motion propagation in the Mississippi embayment. Eng Geol 62:185–206
32. Hashash YMA, Park D (2002) Viscous damping formulation and high frequency motion propogation in non-linear site response analysis. Soil Dyn Earthq Eng 22:611–624
33. Idriss I, Seed H (1968) Seismic response of horizontal soil layers. J Soil Mech Found Div ASCE 94(4):1003–1031
34. Idriss IM, Sun JI (1992) User's manual for SHAKE91. Center for Geotechnical Modeling, Department of Civil and Environmental Engineering, University of California, Davis, CA
35. Iwan WD (1967) On a class of models for the yielding behavior of continuous and composite systems. J Appl Mech 34(3):612–617
36. Joyner WB, Warrick ER, Adolph I, Oliver A (1976) Analysis of seismograms from a downhole array in sediments near San Francisco Bay. Bull Seism Soc Am 66(3):937–958
37. Kanai I (1961) An empirical formula for the spectrum of strong earthquake motions. Bull Earthq Res Inst 39:85–95
38. Katsanos EI, Sextos AG, Manolis GD (2010) Selection of earthquake ground motion records: A state-of-the-art review from a structural engineering perspective. Soil Dyn Earthq Eng 30(4):157–169
39. Kausel E, Assimaki D (2002) Seismic simulation of inelastic soils via frequency-dependent moduli and damping. J Eng Mech 128:34–47
40. Konder RL, Zelasko JS (1963) A hyperbolic stress-strain formulation for sands. In: Proceedings of 2nd Pan American conference on soil mechanics and foundation engineering, Brazil, pp 289–324
41. Kramer SL (1996) Geotechnical earthquake engineering. Prentice-Hall, Upper Saddle River, NJ, 653 pages, Prentice Hall (January 7, 1996), ISBN-10: 0133749436
42. Li W, Assimaki D (2010) Site and ground motion dependent parametric uncertainty of nonlinear site response analyses in earthquake simulations. Bull Seism Soc Am 100(3)
43. Li W, Assimaki D, Fragiadakis M (2009) Nonlinear site response modeling variability in "rupture-to-rafters" ground motion simulations. In: Proceedings 2nd international conference on computational methods in structural dynamics and earthquake engineering (COMPDYN 2009), Rhodes, Greece, 22–24 June 2009
44. Liu P-C, Archuleta RJ (2002) The effect of a low-velocity surface layer on simulated ground motion. Seism Res Lett 73:267
45. Liu P-C, Archuleta RJ (2006) Efficient modeling of Q for 3D numerical simulation of wave propagation. Bull Seism Soc Am 96(4A):1352–1358
46. Liu P-C, Archuleta RJ, Hartzell SH (2006) Prediction of broadband ground-motion time histories: hybrid low/high-frequency method with correlated random source parameters. Bull Seism Soc Am 96:2118–2130
47. Ma S, Liu P-C (2006) Modeling of the perfectly matched layer absorbing boundaries and intrinsic attenuation in explicit finite-element methods. Bull Seism Soc Am 96(5):1779–1794
48. Masing G (1926) Eigenspannungen und Verfertigung beim Messing. Proceedings 2nd international congress on applied mechanics, Zurich
49. Matasovic N, Vucetic M (1993a) Cyclic characterization of liquefiable sands. J Geotech Eng 119(11):1805–1822
50. Matasovic J, Vucetic M (1993b) Analysis of seismic records obtained on November 24, 1987 at the Wildlife Liquefaction Array. Research Report, Civil Engineering Department, University of California, Los Angeles, 94 pp
51. Miranda E (1993) Site-dependent strength-reduction factors. J Struct Eng 119(12):3503–3519
52. Miranda E (2000) Inelastic displacement ratios for structures on firm sites. J Struct Eng 126(10):1150–1159

53. Miranda E (2001) Estimation of inelastic deformation demands of SODF systems. J Struct Eng 127(9):1005–1012
54. Mroz Z, Shrivastava HP, Dubey RN (1976) A non-linear hardening model and its application to cyclic loading. Acta Mechanica 25:51–61
55. Naeim F, Lew M (1995) On the use of design spectrum compatible time histories. Earthq Spectra 11:111–127
56. O'Connor IM, Ellingwood BR (1992) Site-dependent models of earthquake ground motion. Earthquake Eng Struct Dyn 21:573–589
57. Paparizos IG (1986) Some observations on the random response of hysterestic systems. Technical report, Report No. EERL86-02, The California Institute of Technology
58. Park D, Hashash YMA (2004) Soil damping formulation in nonlinear time domain site response analysis. J Earthq Eng 8(2):249–274
59. Park D, Hashash YMA (2005) Evaluation of seismic site factors in the Mississippi embayment. II. Probabilistic seismic hazard analysis with nonlinear site effects. Soil Dyn Earthq Eng 25:145–156
60. Reiter I (1990) Earthquake hazard analysis – issues and insights. Columbia University Press, New York
61. Ruiz-Garcia J, Miranda E (2004) Inelastic displacement ratios for design of structures on soft soils sites. J Struct Eng 130(12):2051–2061
62. Schnabel PB, Lysmer J, Seed HB (1972) SHAKE: A computer program for earthquake response analyses of horizontally layered sites. Technical report, Earthquake Engineering Research Center, Report No. EERC 72–12, University of California, Berkeley
63. Seed HB, Idriss IM (1970) Soil moduli and damping factors for dynamic response analyses. Earthquake Engineering Research Center, University of California at Berkeley, UCB/EERC-70/10
64. Seed HB, Wong RT, Idriss IM, Tokimatsu K (1984) Moduli and damping factors for dynamic analyses of cohesionless soils. University of California at Berkeley, UCB/EERC-84
65. Silva WJ, Stark CL (1992) Source, path, and site ground motion model for the 1989 M 6.9 Loma Prieta earthquake. Technical report, California Division of Mines and Geology, Final report
66. Su F, Aki K, Teng T, Koyanagi S, Mayeda M (1992) The relation between site-amplification factor and surficial geology in central California. Bull Seism Soc Am 82:580–602
67. Tajimi K (1960) A statistical method of determining the maximum response of a building structure during an earthquake. In: Proceedings of 2nd world conference on earthquake engineering, Tokyo and Kyoto, Japan
68. Toro GR, Silva WJ (2001) Scenario earthquakes for Saint Louis, MO, and Memphis, TN, and seismic hazard maps for the central United States region including the effect of site conditions, Risk Engineering, Inc., Boulder, Colorado, USGS Grant: Final Technical Report
69. Veletsos AN, Newmark NM, Chepalati C (1965) Deformation spectra for elastic and elastoplastic systems subjected to ground shock and earthquake motion. In: Proceedings of 3rd world conference on earthquake engineering, vol II. Wellington, New Zealand, pp 663–682
70. Whitman RV, Protonotarios JN (1977) Inelastic response to site-modified ground motions. J Geotech Eng Div 103:1037–1053
71. Wiggins J (1964) Effects of site conditions on earthquake intensity. J Struct Div ASCE 90(2):279–313

Problems in Pushover Analysis of Bridges Sensitive to Torsion

Andreas J. Kappos, Eleftheria D. Goutzika, Sotiria P. Stefanidou, and Anastasios G. Sextos

Abstract The study addresses the issue of pushover analysis of bridges sensitive to torsion, using as a case-study a straight, overpass bridge with two equal spans, whose fundamental mode is purely torsional. The deck is supported on a single pier consisting of two columns of cylindrical cross-section, monolithically connected to the deck, while it rests on its two abutments through elastomeric bearings. The seismic performance of the bridge was assessed in the longitudinal and transverse directions using non-linear static (pushover) and time-history analysis. An additional pushover analysis was carried out using the fundamental (torsional) mode loading. Parametric analyses were performed involving consideration of foundation compliance, and various scenarios of accidental eccentricity that would trigger the torsional mode. The pushover curves derived in the longitudinal and transverse directions highlight the satisfactory performance of the bridge, even for motions twice as strong as the design earthquake. On the other hand, one of the key points of this study is that, if one focuses on the fundamental torsional mode, the corresponding load pattern is anti-symmetric and the resulting base shear inevitably equal to zero, hence a 'standard' pushover curve cannot be drawn. Along these lines, an alternative pushover curve in terms of abutment shear vs. deck maximum displacement (that occurs at the abutment) was found to be a meaningful measure of the overall inelastic response of the bridge. Another interesting aspect is that assessment based on the torsional fundamental mode leads to failure of the elastomeric bearings, although the related displacements are not relevant since they are about an order of magnitude higher than the design displacement. Overall, it can be concluded that for bridges with a fundamental torsional mode, assessment of their seismic response relies on a number of justified important decisions that have to be made regarding the

A.J. Kappos (✉), E.D. Goutzika, and S.P. Stefanidou
Laboratory of Concrete and Masonry Structures, Department of Civil Engineering, Aristotle University of Thessaloniki, 54124 Greece
e-mail: ajkap@civil.auth.gr; elia2@civil.auth.gr; ssotiria@civil.auth.gr

A.G. Sextos
Division of Structural Engineering, Department of Civil Engineering, Aristotle University of Thessaloniki, 54124 Greece
e-mail: asextos@civil.auth.gr

M. Papadrakakis et al. (eds.), *Computational Methods in Earthquake Engineering*, Computational Methods in Applied Sciences 21, DOI 10.1007/978-94-007-0053-6_5,
© Springer Science+Business Media B.V. 2011

selection and reliable application of the analysis method adopted, the estimation of the foundation and abutment stiffnesses, and the appropriate numerical simulation of the pertinent failure mechanism of the elastomeric bearings used.

Keywords Bridges · Non-linear static (Pushover) analysis · Non-linear time-history analysis · Bearings · Torsional effects · Reinforced concrete

1 Introduction

It is now well-established that elastic analysis of structures subjected to seismic actions, typically in the form of response spectrum analysis, cannot always predict the hierarchy of the failure mechanisms, while it is not able to quantify the energy absorption and force redistribution that result from the gradual plastic hinge development within the structure. For this reason, the development of analytical methods that would permit the quantification of the degree of global and local ductility has increasingly attracted the attention of both researchers and designers [13]. Along these lines, nonlinear static (pushover) analysis has become a popular tool for the seismic assessment of buildings [1] and bridges [2, 3], despite the fact that its main advantage of lower computational cost, compared to nonlinear dynamic time-history analysis, is counter-balanced by its inherent restriction to structures wherein the fundamental mode dominates the response [3, 4].

To this end, the aforementioned non-linearity expected in bridges during strong ground motions, cannot be attributed solely to yielding of reinforced concrete sections, although these are the elements that are often purposely designed to exhibit inelastic behaviour. This is due to the fact that elastomeric bearings are also designed to resist seismic displacements, also for motions stronger than the design earthquake, while foundation and abutment soil behaves inelastically even at low levels of shear strain. The situation becomes even more complex in the case of bridges with a fundamental torsional mode since the typically adopted loading patterns and monitoring points are not adequate to describe in a realistic way the development of inelastic mechanisms throughout the structure. The objective of this paper is, therefore, to address pushover analysis of torsion-sensitive bridges, focussing on a real bridge with a torsional fundamental mode that has been designed to resist seismic forces through both capacity-designed elements and elastomeric bearings. The seismic performance and the torsional response of the bridge are examined using alternative analysis types and modelling approaches regarding the bearings and the supporting soil in order to investigate the range of applicability of the standard pushover analysis to such structures. A brief description of the structure assessed is presented first, followed by the analysis method and a critical evaluation of the results.

2 Overview of the Bridge Studied

The bridge selected as a case-study is a straight overpass (overcrossing) with two equal spans (instead of the commonly used three-span configuration) and total length equal to 31.5 m (Fig. 1). The deck consists of a 7.7 m wide reinforced concrete slab and is supported on a pier consisting of two columns of cylindrical cross-section of 1 m diameter and 5 m height, resting on a surface foundation with a stiff upper part of size 1.5 × 5 × 3 m as shown in Fig. 2. The deck is monolithically connected to the twin-column pier, while it rests on its two abutments through elastomeric bearings. Displacement of the deck in both the longitudinal and transverse directions is free at the abutments, due to the absence of deck restraint in either direction. It is noted, however, that the effect of a transverse restraint at the abutment is also investigated as part of the parametric analysis scheme. The seat-type abutments rest on surface foundations (footings).

The bridge was designed according to the provisions of the Greek Seismic Code (EAK-2000) [5] and the code (Circular E39/99) for seismic design of bridges [6], for seismic actions prescribed for zone I, i.e. a peak ground acceleration $a_g = 0.16\,g$. The behaviour (force-reduction) factor of the structure was estimated separately for its longitudinal and transverse directions (as prescribed by the Code, due to the different shear ratio of the pier in each direction) and was taken equal to 2.1 and 2.5, respectively, the design concept being that ductile behaviour was expected, with formation of plastic hinges in the pier columns (that were properly detailed for ductility).

The concrete class used was C20/25 (characteristic compressive cylinder strength $f_{ck} = 20\,MPa$) while S500 steel (characteristic yield strength $f_{yk} = 500\,MPa$) reinforcement was used throughout the structure. No prestressing reinforcement was used in the deck due to the relatively short spans.

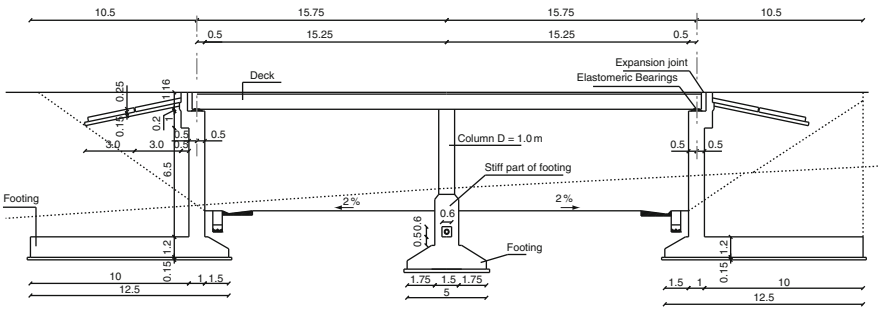


Fig. 1 General view of the overpass

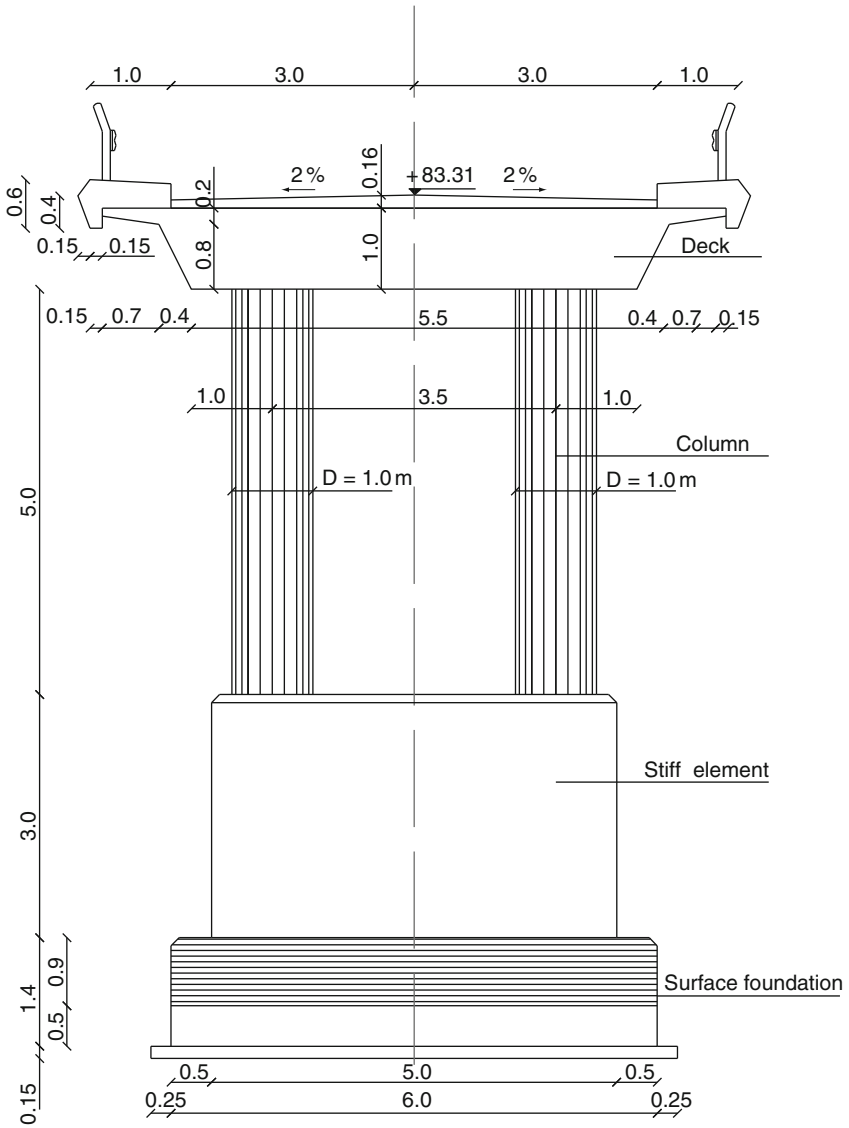


Fig. 2 Overview of the foundation-pier-superstructure system cross-section

3 Finite Element Modelling and Analysis of the Structure

3.1 Modelling Aspects

The bridge was modelled using the FEM software package SAP2000 [7]. Three alternative models were developed, wherein the deck was modelled as: (a) a 3D

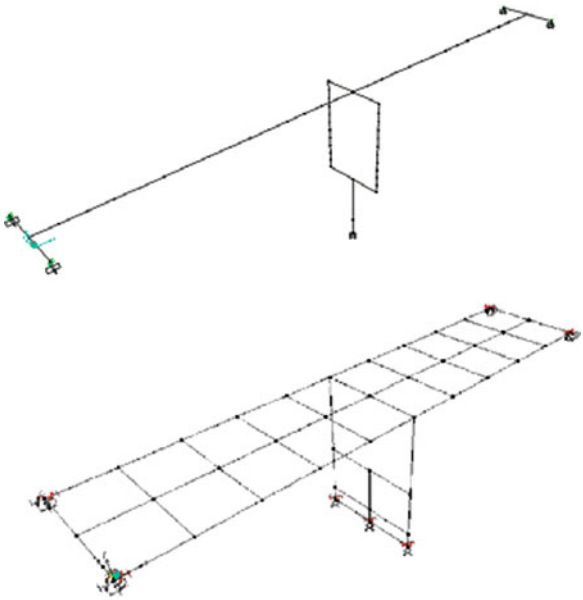


Fig. 3 Stick model (*top*) and grillage model (*bottom*) of the bridge under study

beam (stick model) (b) a grillage of 3D beams with appropriately defined stiffness, and (c) using shell elements. Models (b) and (c) were mainly intended for verifying the simpler stick model that was subsequently used for the seismic analysis and assessment of the bridge; the specific aim was to investigate the reliability of the assumption of using a (simple) 3D beam section for the particular deck. The grillage consisting of equivalent transverse and longitudinal beams for the deck, i.e. Model b (Fig. 3) was also useful for comparing the results of the present analysis with those of the original study of the bridge (carried out by a Greek engineering design firm). In both models, the monolithic connection of the deck to the pier, and of the pier to the stiff base was achieved using rigid elements. The detailed model using shell elements for the deck and the stiff base (Fig. 4) is deemed to be able to achieve a more realistic internal force transfer between the deck, the pier and the foundation.

The stiffness of the pier members was reduced as per the E39/99 guidelines (similar to those of EC8-2 [8]). More specifically, for the members that are designed to remain (essentially) elastic during the seismic event (i.e. the deck), the uncracked stiffness was used, whereas for the pier, wherein development of plastic hinging is anticipated under the design earthquake, the secant stiffness at yield, found equal to $EI_{eff} = 0.36EI_g$, was adopted, based on the maximum expected axial load. In order to investigate the effect of the interaction between the bridge and the supporting ground, different support conditions were investigated: (a) by assuming full fixity at the base of the pier and the abutments (Model 1); (b) by implementing linear springs, whose static (i.e. based on the envisaged type of analysis) stiffness

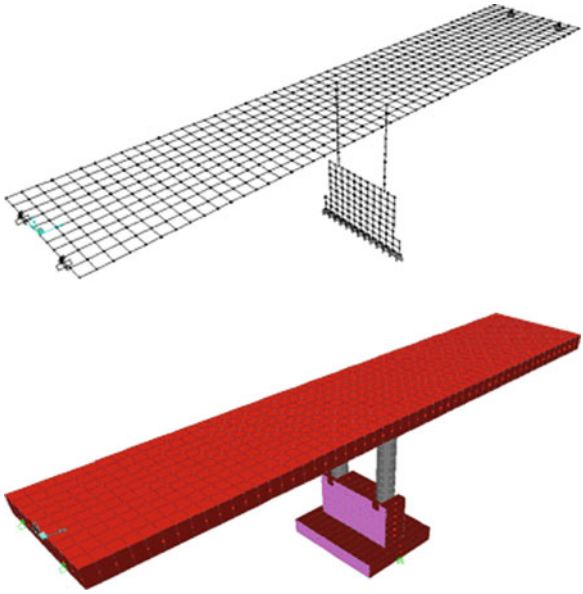


Fig. 4 Finite element model of the bridge using shell elements for the deck and the base

was evaluated using appropriate expressions for shallow foundations from the literature [9] (Model 2); (c) by introducing transverse restraint between the deck and the abutments as a means to investigate the effect of lateral restraint (Model 3), and (d) by directly connecting the pier and the footing without the stiff vertical element (Model 4). It is also noted that the soil springs used in Models 2–4 were derived for two distinct cases of soft and stiff soil. In models 3 and 4, the elastomeric bearings between the deck and the abutment were explicitly modelled using springs, the shear, axial and bending stiffness of which were estimated according to established practice [10]. In all cases, the shear modulus of soil was also reduced according to the design excitation level and the provisions of Eurocode 8 [8].

3.2 Modal and Response Spectrum Analysis of the Bridge

The dynamic characteristics estimated from the analyses of the stick and the shell element models, are found to be in acceptable agreement as seen in Table 1, where the natural periods and the relative participation factors are presented. The minor discrepancies observed can be attributed to the different modelling approach since the shell element model consists of more degrees of freedom compared to the stick model, thus leading to a natural period in the transverse direction ($T = 0.61$s) that is 8.2% higher. In any case, the differences are generally minor and in view of this, the stick model with 3D-beam elements for the deck is deemed quite reliable in terms

Table 1 Natural periods and modal participation factors of the stick and the shell model, assuming full fixity at the base of the pier

	Stick model		Shell element model	
Mode	Period T (s)	Modal participation factor	Period T (s)	Modal participation factor
First (torsional)	1.04	23.2%	1.12	23.9%
Second (longitudinal)	0.60	91.7%	0.61	91.7%
Third (transverse)	0.56	92.2%	0.61	92.3%

Table 2 Natural periods and modal participation factors of stick models 1 and 2

	Model 1		Model 2	
Mode	Period T (s)	Modal participation factor	Period T (s)	Modal participation factor
First (torsional)	1.04	23.2%	1.06	23.2%
Second (longitudinal)	0.60	91.7%	0.83	95.1%
Third (transverse)	0.56	92.2%	0.83	94.6%

Table 3 Natural periods and modal participation factors ('mpf') of stick models 2, 3 and 4 accounting for alternative analysis assumptions and design decisions for the boundary conditions of the bridge

	Model 2		Model 3		Model 4	
Mode	Period T (s)	mpf	Period T (s)	mpf	Period T (s)	mpf
Torsional	1.06	23.2%	0.05	20.1%	1.14	24.3%
Longitudinal	0.83	95.1%	0.83	95.1%	1.09	98.5%
Transverse	0.83	94.6%	0.14	83.6%	1.13	98.6%

of the (elastic) dynamic characteristics of the structure and the associated seismic force distribution. On the contrary, this is not the case for the grillage model, since its natural periods are substantially different; the periods computed were found equal to $T_{rz} = 1.47\,s$, $T_x = 1.04\,s$ and $T_y = 0.46\,s$ for the torsional and translational modes of vibration respectively, in contrast to $T_{rz} = 1.04\,s$, $T_x = 0.60\,s$ and $T_y = 0.56\,s$ that were found for the reference stick model.

When the static effect of soil-structure interaction is taken into consideration by introducing appropriate springs at the foundation-soil interface, the flexibility of the structure is increased (Table 2), as anticipated, and the natural periods of Model 2 are longer. It is noticed that the torsional mode ($T_{rz} = 1.04\,s$) was not affected by the boundary conditions of the pier, as it is dependent solely on the sensitivity to torsion of the deck. When transverse restraints are introduced at the abutments, while retaining the consideration of the soil compliance below the pier (Model 3), the longitudinal mode was not affected ($T_x = 0.83\,s$) compared to Model 2; on the contrary, both the transverse and the torsional natural periods were substantially reduced (by 83% and 96% respectively, i.e. the torsional mode was essentially suppressed) due to the lateral restraint of the deck ends, a fact that highlights the importance of lateral

Table 4 Seismic displacements of the deck in the longitudinal and transverse direction

Direction	Model 1	Model 2	Model 3	Model 4
Longitudinal (u_x, mm)	35.6	56.3	56.3	80.0
Transverse (u_y, mm)	32.2	56.3	2.5	83.5

restraints with regard to the overall seismic performance of a bridge. In the case of Model 4, consideration of a longer (8 m) pier supported directly on the foundation, a rather more common design approach, was found to lead to periods longer by 7% for the torsional mode, 24% for the longitudinal mode and 27% for the transverse mode. It has to be noted, that in this case, the order of modes is also reversed as the transverse mode of the bridge is affected to a greater extent, hence the structure becomes more flexible in the transverse direction than along the longitudinal one, a fact clearly attributed to the influence of the stiff base on lateral vibration.

To study the seismic response of the bridge, a Response Spectrum analysis was also performed using the design spectrum of the Greek Seismic Code (this is the type of analysis actually required by the Code). In Table 4, the seismic displacements of the deck are presented for the four alternative models. It is observed that, as anticipated, deck displacements increase from Model 1 to the (more flexible) Model 4. It is also noticeable that, especially in the case of Model 3, the deck mass centre was displaced by only 2.5 mm due to the transverse restraint at the abutments. In Models 1, 2 and 4 the seismic displacements correspond to the lateral edge of the deck since the presence of bearing-type deck-to-abutment connections and the subsequent torsional sensitivity of the bridge lead to higher transverse displacements at the end supports compared to the deck centre. Due to both the lack of lateral restraints and the presence of taller columns, Model 4 was found to lead to higher displacements, a fact that hints to the reason why the stiff base between the pier and the foundation footing was introduced in the actual design of the bridge.

4 Assessment of the Bridge Performance

Having examined and compared the three alternative models involving different finite element discretizations of the deck, the bridge was assessed using non-linear static (pushover) analysis of the preferred (mainly for reasons of simplicity) stick model, as discussed in the following.

4.1 Inelastic Modelling and Analysis Aspects

Pushover analysis was carried out with the aid of the FE program SAP2000 [7]. The inelastic behaviour of the critical cross-sections of the pier was evaluated using the fibre analysis program RCCOLA-90 [11]. The resulting interaction surfaces

(N-M_x-M_y) and moment-rotation (M-θ) curves were then imported into the critical locations of the finite element model using the built-in plastic hinges of SAP. The assessment was performed for all the alternative models (1–4), wherein the parameters related to foundation compliance and bearing supports were described previously. Moreover, additional parametric analyses were performed for Model 2 in order to examine various scenarios of accidental eccentricity that was expected to trigger the torsional mode.

Another interesting point, related specifically to the seismic assessment of the bridge through non-linear static analysis procedures, is the selection of an appropriate monitoring point (with respect to which pushover curves for the structure would be drawn). In bridges, unlike the case of buildings, the shape of the pushover curve inherently depends on the location of the monitoring point. The displacement of this monitoring point is used not only as a parameter of the pushover curve, but also to establish the seismic demand on the structure. For the overcrossing studied here, the location of the mass centre of the structure (the recommended monitoring point in EC8-2 [8]) was used only for assessment along the longitudinal direction; on the contrary, it was the abutment that was adopted as the monitoring point for the structure in the case of transverse excitation, since *this* was found to be the point of maximum displacement in this direction. This selection of monitoring point is the appropriate choice for bridges with decks unrestrained in the transverse direction, as also found in other recent studies [2, 4].

The elastic spectrum of the Greek Code was used to define the target displacements along the two principal axes. Due to the fact that the prevailing modes in the two directions had relatively long periods ($T_{x,o}$ and $T_{y,o} > 0.5$ s), the equal displacement approximation was valid in this case and the estimation of target displacements was simplified.

4.2 Foundation Compliance

Pushover curves for the bridge in the longitudinal and transverse directions are illustrated in Figs. 5 and 6. It is observed that in the case of flexible support conditions the initial stiffness of the system is reduced, as anticipated. For the same reason, the yield and ultimate displacements are increased, while the sequence of plastic hinge formation differs from the fixed-base model due to the different internal force redistribution. The target displacement of the structure, for the design earthquake, is increased up to 35% (in the case of soft soil conditions). The available ductility of the system was found lower in the case of soft soil conditions ($q_\mu = 3.8$ in the longitudinal direction and $q_\mu = 3.75$ in the transverse leading to combined behavior factors, which also include overstrength effects, $q_{avail} = 7.5$ and $q_{avail.} = 8.8$ respectively) compared to the assumption of stiff soil which leads to $q_\mu = 6.7$ and $q_\mu = 6.9$ in the longitudinal and transverse direction and an approximately uniform value of $q_{avail} = 12.3$ for both directions. In all the above cases, the high available ductility manifests a desirable response of the bridge under earthquake loading.

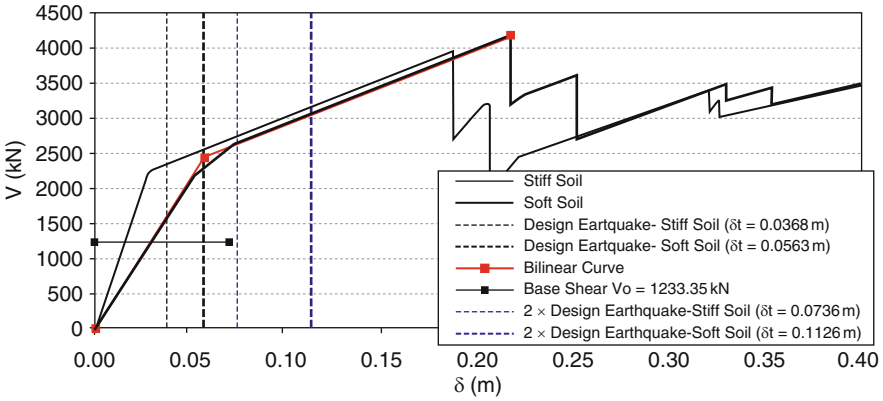


Fig. 5 Pushover curve and seismic assessment of the bridge (longitudinal direction)

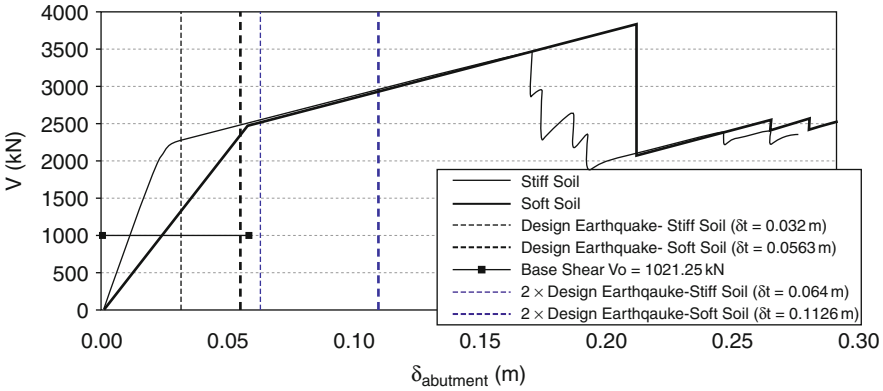


Fig. 6 Pushover curve and seismic assessment of the bridge (transverse direction)

The ductility demand for the design earthquake, corresponding to the case where the deck displacement equals the target displacement (calculated from the design spectrum), was also estimated. It was found equal to 1.7 and 1.0, for the case of stiff and soft soil conditions, respectively; this is a clear indication of the well-known overstrength of structures designed to modern codes (the ratio V_y/V_o of yield force to design base shear, see Figs. 5 and 6). The different ductilities resulting from different assumptions regarding the foundation soil stiffness (when foundation compliance is accounted for in the analysis) show that, depending on this assumption, the bridge is predicted either to enter (slightly) into the inelastic range under the design earthquake loading, or to remain essentially elastic. It is worth pointing out that even for twice the design earthquake intensity, the plastic rotation demand at the

pier critical locations, is well below the available supply ($\theta_{p,avail.} = 0.031$ rad). As a consequence, the performance of the bridge in the longitudinal direction is deemed as very satisfactory. The same can be observed for excitation along the transverse direction, as can be inferred from the data in Fig. 6.

4.3 Modelling of Bearings

An interesting observation from the pushover curves presented in Figs. 5 and 6 is their rather unusual shape subsequent to pier failure; in particular, the strength of the system is found to increase thereafter. This apparently unrealistic situation can be simply attributed to the fact that as the bearings were essentially modelled with linear springs, failure of the pier leads to significant redistribution of internal forces, especially given the assumed linearly increasing strength and the lack of a failure mechanism for the bearings. As a result, the bearings tend to carry a higher percentage of the applied base shear that is approximately equal to 70% compared to the 30% that they carried prior to pier failure.

Clearly, such a continuous increase in strength is not realistic, nor does it lead to a conservative assessment of the bridge; of course, in a design context, one would not consider assessing the bridge for damage states beyond the failure of the pier (substantial drop in strength, as shown in Figs. 5 and 6). Notwithstanding the feasibility of assessing such heavy damage states (which are, nevertheless relevant in vulnerability and risk analysis), an effort was made to numerically simulate the non-linear force-displacement relationship of the elastomeric bearings, using information available in the literature and in the E39/99 guidelines. In the $\tau - \gamma$ models of Fig. 7, it is seen that as the shear strain γ of the bearing increases from 1.0 to 2.0, its stiffness is increased, while for strains $\gamma > 2$ a plastic condition is assumed up to the level of maximum strain $\gamma_{bu} = 5$ (horizontal displacement $t_{el.} \cdot \gamma_{bu} = 0.52$ m in the specific case) that corresponds to complete failure of the bearing.

Based on the above, revised pushover curves for the transverse direction were drawn, shown in Fig. 8 (bold lines). It is seen that the overall resistance of the structure is more rational and the residual strength of the structure remains, as one would normally expect, constant, subsequent to pier failure. Moreover, pier failure is observed at a displacement of 0.22 m, a value that is equal to less than half the value (0.52 m) that the bearings can sustain without failure. This observation implies that simply including elastomeric bearings in the analytical model (with some effective stiffness) might not be sufficient if a 'full-range' assessment of seismic performance is sought; in this case, the non-linear response and failure mechanism of the bearings should be properly considered.

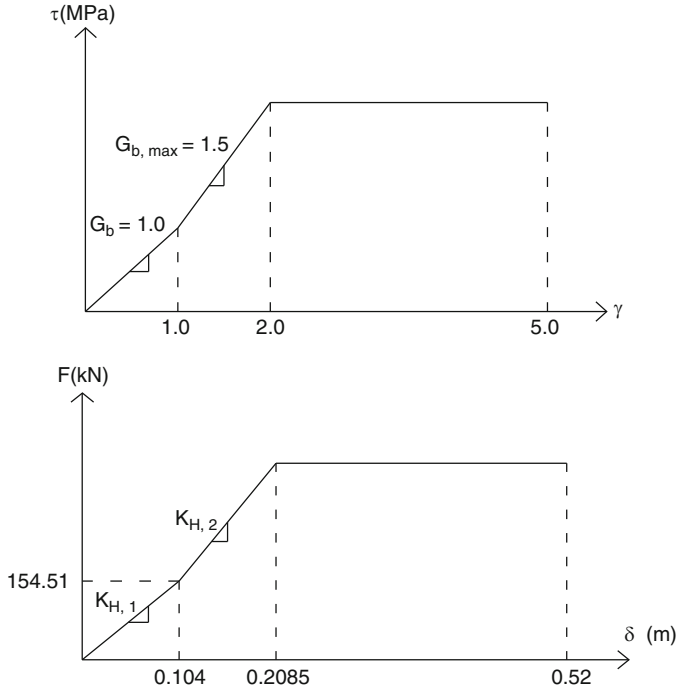


Fig. 7 Nonlinear shear stress-strain constitutive law (*left*) and force-displacement relationship (*right*) for elastomeric bearings

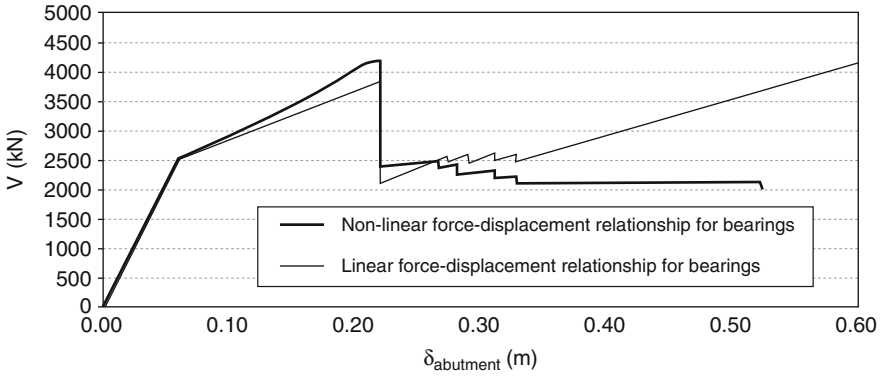


Fig. 8 Pushover curve of the bridge in the transverse direction for the case of linear and nonlinear force-displacement relationship used for the elastomeric bearings

4.4 Pushover Analysis for Torsional Loading Pattern

Another interesting issue is related to the loading pattern to be adopted for assessing the torsional mode contribution. It is noted that the modal load pattern of the

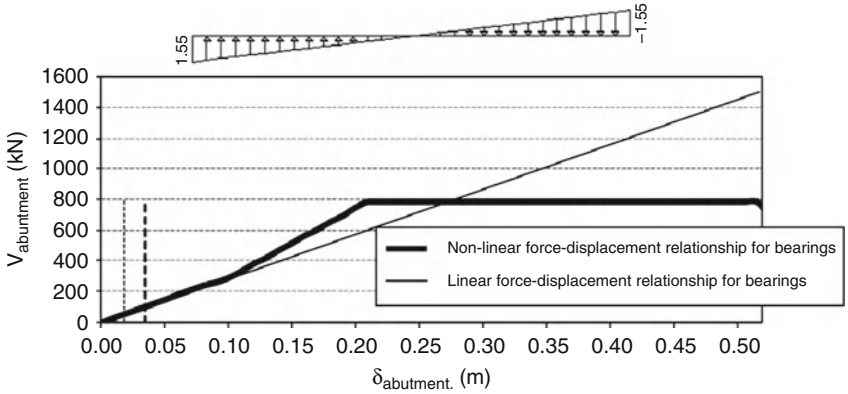


Fig. 9 Abutment shear vs. deck maximum displacement according to the fundamental torsional mode

torsional mode is anti-symmetric (Fig. 9) and the resulting base shear is zero, hence it is simply not feasible to draw a standard pushover curve in terms of base shear versus monitoring point displacement. For such cases, use of an alternative pushover curve is proposed here (Fig. 9), which is drawn in terms of abutment (rather than base) horizontal shear versus deck maximum displacement at the location of the abutment. It is noted that the target displacement estimated from the torsional load distribution (equal to $\delta_t = 0.0174$ m) is substantially lower than those predicted for the translational modes, since the two-column pier connected to the rigid base behaves as a stiff frame, thus providing the bridge with a high torsional resistance, while due to the symmetry of the bridge there are no stiffness eccentricities. In the case of nonlinear modelling of the elastomeric bearings, failure of the bearings indeed precedes pier failure; nevertheless the displacement required to cause pier failure is an order of magnitude higher than the design displacement. On the other hand, the lack of deck restraint in the transverse direction leads to large displacements at the abutments (> 0.52 m) that cannot be sustained by the bearings.

An additional parametric analysis was performed with the assumption that the bridge deck is roller-supported at the abutments (e.g. use of pot bearings). In this case, the deck was considered as completely unrestrained in the longitudinal as well as the transverse direction, but the vertical displacement and the rotation were assumed restrained. Figure 10 illustrates the pushover curve of the bridge in the transverse direction where a reduction of approximately 30% of the overall strength of the bridge is observed.

4.5 Influence of Pier Configuration

Having assessed the bridge for various soil conditions and different deck-to-abutment support assumptions, the bridge was subsequently assessed, by assuming

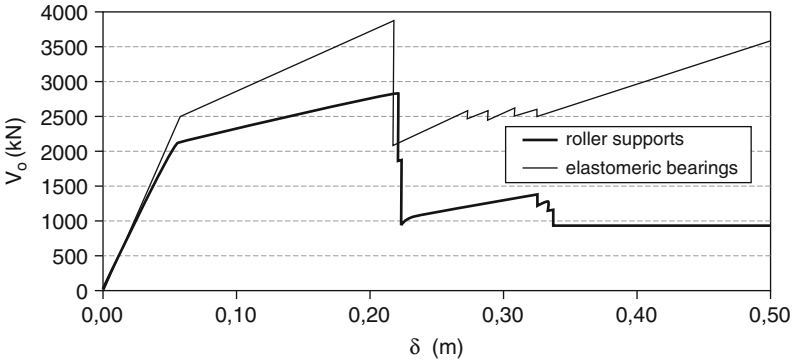


Fig. 10 Pushover curve of the bridge (transverse direction) assuming roller supports and elastomeric bearings at the abutments

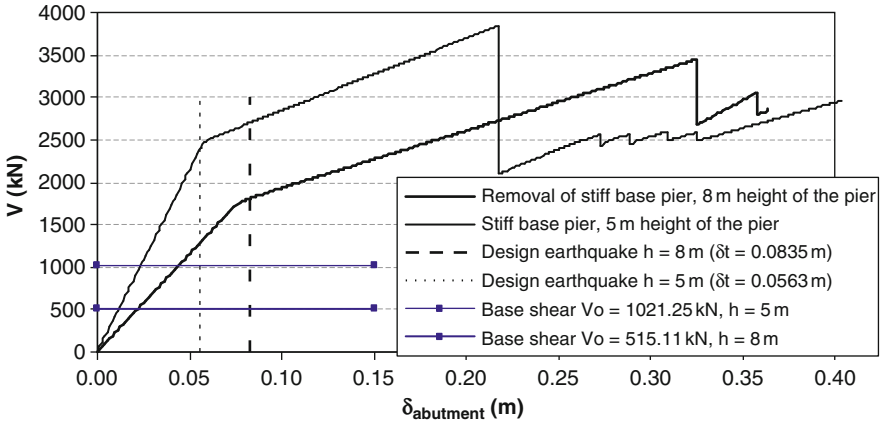


Fig. 11 Pushover curve of the bridge (transverse direction) with and without the stiff base for the pier

that the stiff base through which the pier rests on its footing does not exist and the pier height is equal to 8 m instead of 5 m. As already mentioned, this fourth Model is identical to Model 2 (i.e. soil compliance is also accounted for) with the exception of the pier height. As seen in the pushover curve of the system in the transverse direction that is illustrated in Fig. 11, the resistance of the system (base shear at first yield) was reduced by 30% (from 2,500 to 1,800 kN) while the system stiffness was also decreased by about 50% compared to the reference Model 2. The reduction of the maximum shear force was less significant (of the order of 10%) but maximum displacement was approximately 30% higher for the case of the 8 m pier. On the other hand, the behaviour factor of the system was found equal to $q_{avail.} = 14.4$ for the transverse direction, a rather high value that can be attributed to the relatively low design base shear ($V_o = 515.11$ kN) that in turn leads to a

higher overstrength factor ($q_s = V_y/V_o$). The ductility of the system analysed is high, but is accompanied by larger displacements which apparently were one of the reasons why the designer opted for providing the stiff base used for connecting the pier with the foundation (Fig. 4); as noted earlier, this also increased the resistance to torsion of the bridge.

4.6 Torsional Sensitivity

As already described in Section 3.2, the dynamic characteristics of the bridge are of particular interest since not only the fundamental mode is torsional ($T_{rz} = 1.04$ s), but its participation factor is only 23%, whereas the two translational modes are clearly dominant, with participation factors that exceed 95%. Therefore, in order to investigate the effect of this torsional sensitivity to the response of the bridge in the transverse direction, two scenarios of (additional) accidental eccentricity were also considered. Firstly, the bridge was directly subjected to a torsional moment $M_t = \pm F \cdot e$ (where accidental eccentricity e was taken equal to 3% of the overall bridge length) and a lateral force F following the distribution of the third mode (involving transverse displacements). Due to the application of the above torsional moment at the mass centre of the bridge, the deck exhibits an asymmetric deformation, hence the lateral displacements of the deck at the location of the abutments are different. As a second 'scenario', the accidental eccentricity was implicitly introduced by assuming a reduced shear modulus of one set of elastomeric bearings due to possible decay and/or accidental dislocation (which are not uncommon in practice). In both scenarios, the seismic displacements at the abutments consist of a translational (u_o) and a torsional (u_θ) component, as depicted in Fig. 12.

Table 5 presents the transverse seismic displacements of the deck for the above two cases of accidental eccentricity. Reference Model 2 represents the case of the purely translational deformation of the deck due to the symmetric load pattern. Clearly, the accidental eccentricity, in both scenarios, increases the torsional component (u_θ); however, the translational component still dominates the overall response even in the case of roller supports.

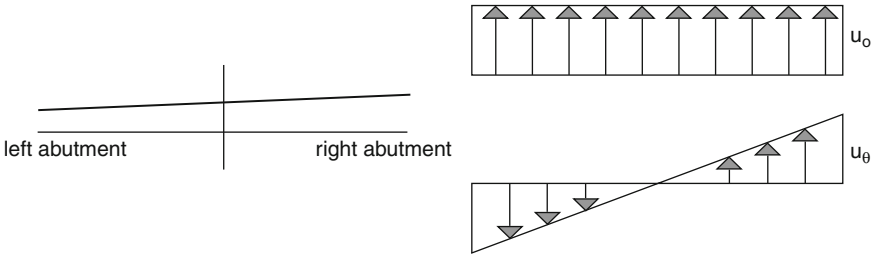


Fig. 12 Deck deformation in the transverse direction and the corresponding displacement decomposition into a translational (u_o) and a torsional (u_θ) component

Table 5 Target displacement due to transverse excitation for the alternative models

	Reference Model 2	Eccentricity due to F-M_t	Eccentricity due to $^1/_2$ GA_{eff} at one bearing	Roller supports	Eccentricity due to F-M_t and roller supports
u_o (mm)	56.3	59.3	57.9	59.3	7.12
u_θ (mm)	0.72	17.9	5.80	0.77	0.90

Table 6 Target displacements due to torsional excitation for the alternative models

	Reference Model 2	Eccentricity $^1/_2$ GA_{eff} of one elastom. bearing	Roller supports
u_o (mm)	17.5	19.4	26.5

Finally, the target displacement of the deck due to the fundamental torsional mode is presented in Table 6. It is pointed out that a purely torsional excitation is not feasible; however, the seismic displacement due to a torsional load pattern was evaluated for research purposes (to get a deeper insight into the bridge's dynamic response). It is observed that the maximum displacement occurs, as anticipated, in the model where roller supports were introduced between the deck and the abutments. This can be attributed to the fact that the sliding support of the deck at the location of the abutments significantly reduces the torsional resistance of the bridge. The reference Model 2, on the other hand, is associated with the smaller target displacement due to the relatively higher restraint provided by the elastomeric bearings. Not surprisingly, the assumption of reduced bearing stiffness leads to an intermediate level of target displacements with respect to the other two cases. It is notable, though, that in all three cases, the seismic displacement that is attributed to the torsional mode is substantially lower compared to the target displacement along the longitudinal and transverse direction primarily to the stiff frame action of the pier which provides significant torsional stiffness.

5 Assessment of the Bridge Performance Using Time-History Analysis

Due to the torsional sensitivity of the particular bridge and the aforementioned assumptions required in order to evaluate its inelastic seismic response using pushover analysis, it was deemed necessary to duplicate the parametric analysis scheme by applying a set of (more rigorous) nonlinear time history analyses (NL-THA). This verification concerns displacements, nonlinear deformations (i.e., plastic rotations), base shear vs. deck displacement relationships and the failure mechanism hierarchy (i.e., succession of the formation of plastic hinges). Finally, the torsional sensitivity of the bridge was comparatively assessed.

Along these lines, a series of NL-THA's was performed using three artificial records compatible with the Greek Seismic Code (EAK2000) elastic spectrum (for moderate soil B and $a_g = 0.16\,g$), generated using the computer code ASING [14]. The Hilbert-Hughes-Taylor direct integration method was used for the NL-THA (with a value of $a = -0.3$, time step $\Delta t = 0.01$ and a total of 2,000 steps corresponding to 20 s of earthquake input). The Rayleigh damping model was used, and parameters α and β were defined assuming constant damping 5% for the first two modes. It is noted that plastic hinging in piers had to be modelled slightly differently in the case of NL-THA compared to the pushover analysis, due to inherent limitations of the software used. In particular, non-linear rotational spring elements were used in NL-THA, while the built-in beam hinge feature of SAP2000 was implemented in the models set up for pushover analysis. The nonlinear behaviour of the spring elements is considered uniaxial. The mass and the rotational inertia were computed for the rotational spring elements, while the moment-rotation relationship (M-θ) used was taken the same as the one used for pushover analysis, as derived from fibre analysis performed for each particular pier section, by means of the computer program RCCOLA [11]. The hysteretic model used for the analysis was the Takeda multilinear plastic model.

All the models presented in Sect. 3.1 were also assessed using NL-THA. Additionally two parametric analyses were performed concerning Model 2, assuming non-linear behaviour of the elastomeric bearings (Model 2-1) and roller-support of the bridge deck at the abutments (Model 2-2). In order to evaluate the results of pushover analyses, two NL-THA's were performed for each model concerning each direction (longitudinal and transverse) separately. The seismic performance of the bridge was assessed for two intensity levels corresponding to the intensity of the design earthquake (life safety performance level) and twice the design earthquake (collapse prevention performance level).

5.1 Verification of Displacements

As a first level of verification, the maximum displacement of the monitoring point resulting from NL-THA was compared with the target displacement calculated in the framework of pushover analysis, separately for the longitudinal (x-x) and the transverse (y-y) direction and for two different intensity levels (design earthquake and twice the design earthquake). Since three artificial records were used for the NL-THA for each direction and intensity level, the maximum response value obtained was the one to be compared with the target displacement (Figs. 13 and 14).

It is noted that the deck centre was taken as the monitoring point for the assessment of the bridge in the longitudinal direction, while the end of the deck was used for the assessment in the transverse direction (see also the section "Pushover Analysis for Torsional Loading Pattern"). As shown in Figs. 13 and 14, a good agreement is observed between the two different inelastic analysis methods independently of the bridge model examined, the directions examined and the earthquake intensity

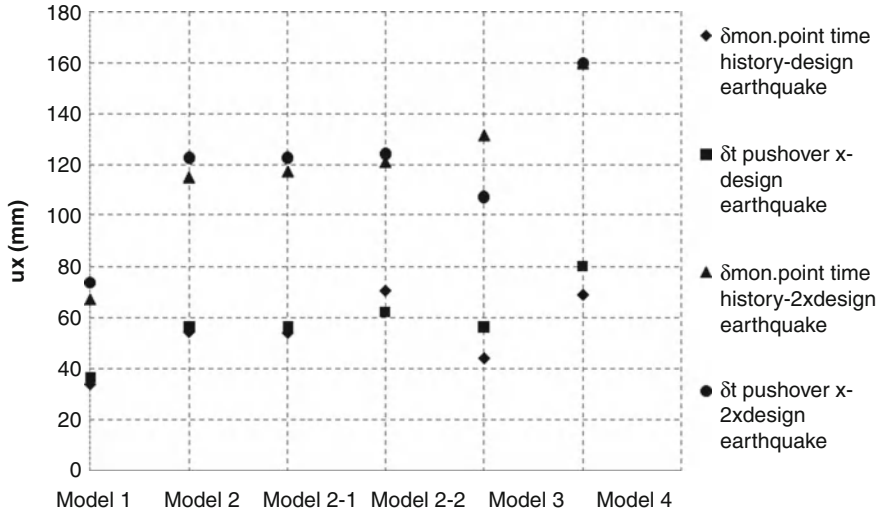


Fig. 13 Comparison of the maximum displacement of the monitoring point in x-direction to the target displacement calculated for pushover-x analysis

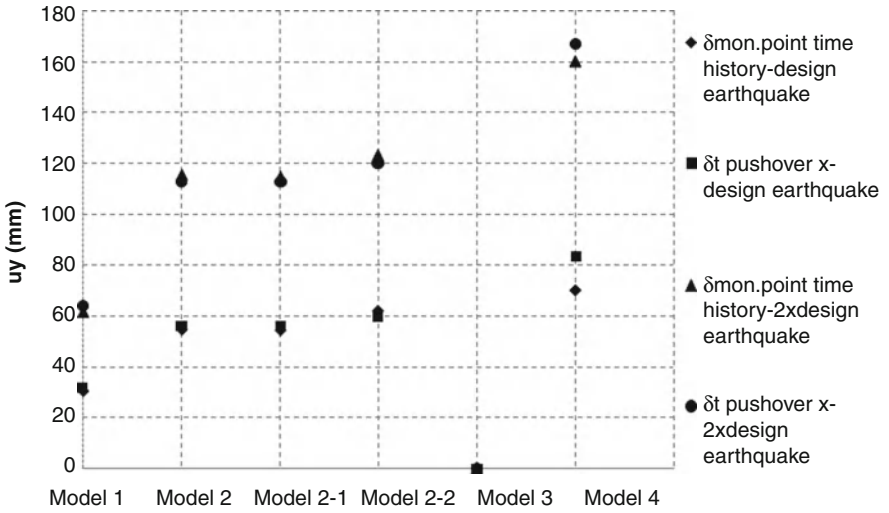


Fig. 14 Comparison of the maximum displacement of the monitoring point in y-direction to the target displacement calculated for pushover-y analysis

level. In particular, the difference is lower than 5% in all cases with the exception of Model 3 for twice the design earthquake where it reaches 20%. The displacement patterns obtained from NL-THA were also reasonably close to those from pushover analysis.

5.2 *Verification of Nonlinear Deformations and Failure Mechanism*

Having obtained a reasonable agreement between the two nonlinear methods (i.e. static and dynamic) on the basis of maximum displacements, the comparison was extended to the prediction of the level of damage in terms of plastic deformations of the bridge piers. Shown in Figs. 14–16, are the maximum plastic rotations θ_p of models 1 and 2, concerning both directions and intensity levels. It is seen that the plastic hinge rotation demand is greater at the base of the piers for Model 1, and at the top of the pier for Model 2 (with foundation compliance), which is consistent with the hierarchy of failure derived from pushover analysis.

With regard toplastic hinge rotation demand, it is first noted that in all cases shown in Tables 7–9 peak demands are lower than the available capacity ($\theta_p = 0.031$ rad) not only for the design, but also for twice the design, earthquake. Hence, the conclusion drawn from pushover analysis, that the bridge does enter the inelastic range but is far from collapse even for twice the design earthquake, is confirmed by the NL-THA's performed for all Models (1–4, including the additional Models 2-1 and 2-2).

Regarding the values of plastic hinge rotation demand (θ_p) found in each case, a reasonable agreement was observed between the estimates of pushover and NL-THA; recall that in addition to other differences in the two types of analysis, plastic hinges were also modelled differently. The agreement is much better in the case of twice the design earthquake, since in this case the structure enters well into the inelastic range, whereas for the design earthquake very small θ_p-values

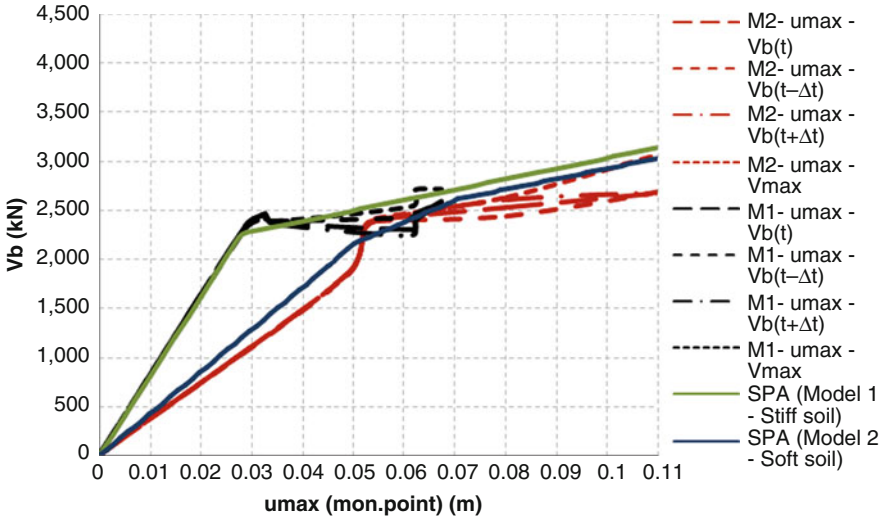


Fig. 15 Pushover curves in x-direction derived for Models 1 and 2, and the corresponding dynamic pushover curves

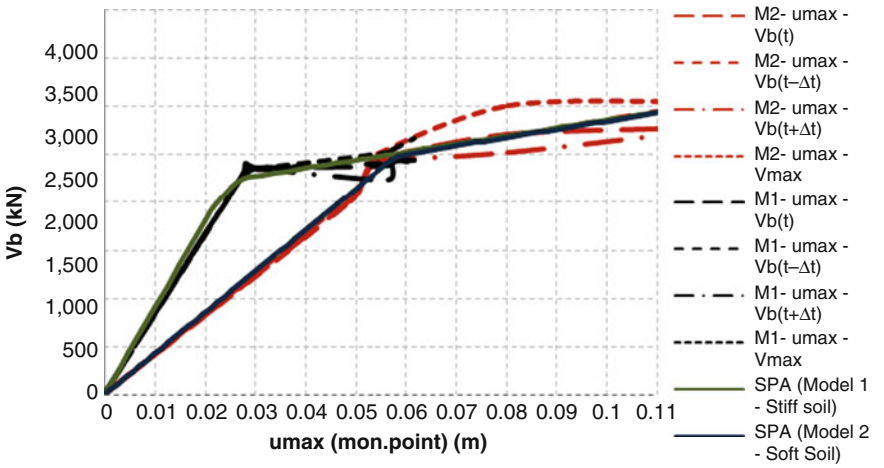


Fig. 16 Pushover curves in y-direction derived for Models 1 and 2, and the corresponding dynamic pushover curves

Table 7 Plastic hinge rotations θ_p for Model 1, in x- and y-direction, for design earthquake intensity level

Longitudinal direction (x–x)				
	Base1	Base2	Top1	Top2
Time history	0.00070	0.00143	0.00070	0.00095
Pushover	0.00190	0.00190	0.00147	0.00147
Transverse direction (y–y)				
	Base1	Base2	Top1	Top2
Time history	0.00131	0.00132	0.00086	0.00085
Pushover	0.00113	0.00207	0.00067	0.00171

Table 8 Plastic hinge rotations θ_p for Model 1, in x- and y-direction, for twice the design earthquake intensity level

Longitudinal direction (x–x)				
	Base1	Base2	Top1	Top2
Time history	0.00806	0.00806	0.00774	0.00774
Pushover	0.00883	0.00883	0.00835	0.00835
%	8.76%	8.76%	7.30%	7.30%
Transverse direction (y–y)				
Time history	0.00842	0.00842	0.00798	0.00798
Pushover	0.00738	0.00833	0.00688	0.00795
%	14.02%	1.12%	16.03%	0.35%

Table 9 Plastic hinge rotations θ_p for Model 2, in x- and y-direction, for twice the design earthquake intensity level

Longitudinal direction (x–x)				
	Base1	Base2	Top1	Top2
Time history	0.00948	0.00948	0.01377	0.01377
Pushover	0.00713	0.00713	0.01145	0.01145
%	32.91%	32.91%	20.27%	20.27%
Transverse direction (y–y)				
Time history	0.01123	0.01122	0.01133	0.01134
Pushover	0.01029	0.01010	0.01040	0.01020
%	9.13%	11.13%	8.95%	11.13%

are recorded and the apparently substantial discrepancies shown in Table 7 for the longitudinal direction are not really meaningful, since the total rotations are similar in both analyses (due to the good match of displacements) and the plastic part of the rotation is very small (around 0.001). For the higher intensity level, differences were less than about 15% in the (fixed base) Model 1, and about 30% in Model 2 (with foundation springs).

5.3 Base-Shear-Displacement Relationship

It was also deemed necessary to compare the results of the *standard* pushover analysis (SPA) with the *dynamic pushover* curves [12], derived from NL-THA. In line with previous studies like [12], three different combinations of base shear and maximum displacement of the monitoring point were used in order to derive the dynamic pushover curves:

- Maximum displacement u_{max} at the control point vs. simultaneous base shear of the bridge $V_b(t)$ hereafter denoted as $u_{max} - V_b(t)$.
- Maximum displacement u_{max} at the control point vs. the base shear that takes place at the previous step of the maximum displacement at the control point $V_{b(t-\Delta t)}$, hereafter denoted as $u_{max} - V_b(t - \Delta t)$; or the base shear that takes place after the step of the maximum displacement at the control point $V_{b(t+\Delta t)}$, denoted as $u_{max} - V_{b(t+\Delta t)}$.
- Maximum displacement u_{max} at the control point vs. maximum base shear of the bridge V_{bmax}, hereafter denoted as $u_{max} - V_{bmax}$. It has to be noted that the corresponding response quantities do not take place at the same time during the excitation of the bridge.

For the dynamic pushover curve, the base shear as well as the displacement of the control point, were extracted from the database of the NL-THA results for each intensity level. It is clear from Figs. 15–18 that the pushover curve derived from standard pushover analysis is in reasonable agreement with the *dynamic* ones as

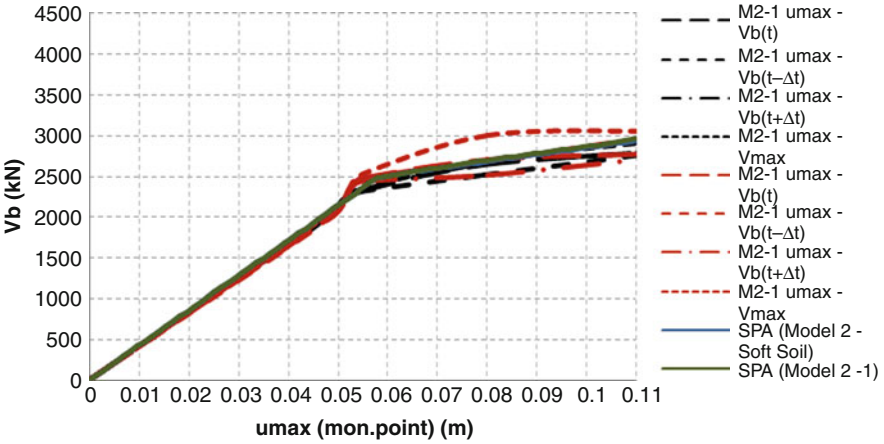


Fig. 17 Pushover curves of y-direction derived for Models 2 and 2-1, and the corresponding dynamic pushover curves

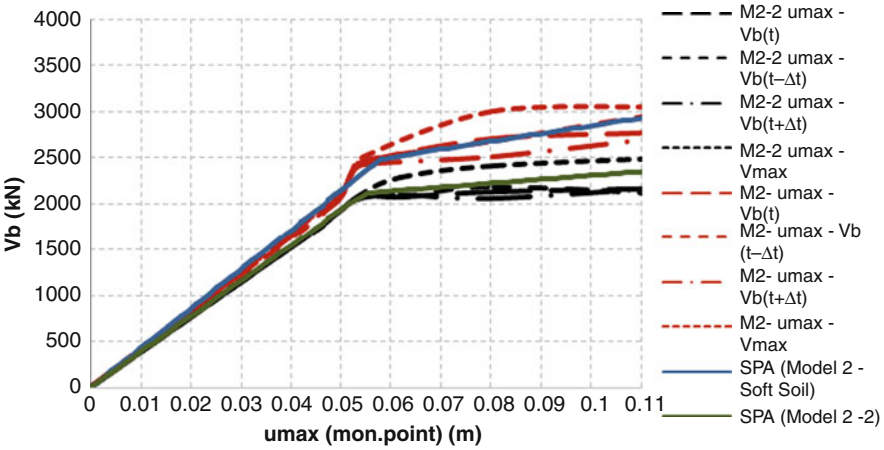


Fig. 18 Pushover curves of y-direction derived for Models 2 and 2-2, and the corresponding dynamic pushover curves

derived from the more rigorous NL-THA. The greater differences observed concern the $u_{max} - V_{bmax}$ relationship, and can be attributed to the fact that the response quantities examined do not take place simultaneously during earthquake excitation. It is also recalled that the control point for the assessment of the seismic performance of the particular bridge in the transverse direction is the end point of the deck.

5.4 Torsional Sensitivity

A final level of verification of the pushover analysis results is related to the evaluation of the torsional sensitivity of the bridge studied. It is again confirmed by NL-THA that the torsional component (u_θ) of the response of the monitoring point is significantly lower than the translational one, a fact that can be primarily attributed to the high torsional resistance provided by the stiff pier and the use of elastomeric bearings at the deck-abutment interface. As a result, the structure cannot be considered as torsionally sensitive.

6 Conclusions

This study focused on pushover analysis of bridges with a significant torsional mode, using as an example a straight overcrossing with two equal spans, whose fundamental mode is purely torsional. Through an extensive parametric analysis scheme it was demonstrated that the performance of the bridge is satisfactory even for loading that corresponds to twice the level of the design earthquake. From an analysis point of view, it was shown that the reliability of the seismic assessment performed is related to a number of important assumptions regarding: (a) the consideration of the torsional nature of the fundamental mode; (b) the selection of an appropriate monitoring point for drawing the pushover curve in the transverse direction (the end, rather than the mass centre, of the deck was adopted herein), as well as of a proper measure of the applied loading when anti-symmetric loading patterns are used, in a modal pushover context (the horizontal shear at the abutment was used here); (c) the accurate estimation of foundation compliance and the subsequent computation of the static stiffness to be used for the pier foundations; (d) the decision made for the boundary conditions at the location where the deck rests on the abutment, and (e) the appropriate numerical simulation of the non-linear force-displacement relationship and the pertinent failure mechanism of the elastomeric bearings used. All the above decisions were found to play a significant role in the final assessment of the bridge and as such, they have to be dully justified in each case, and sensitivity analyses should be performed wherever necessary (and feasible, if the study is carried out within a design office environment).

Another important observation made was that seismic displacements derived from the torsional excitation of the bridge demonstrate that the bridge is not particularly sensitive to torsion, despite the fact that the fundamental mode *is* torsional. As a result, proper assessment of this bridge should be primarily based on the longitudinal and transverse loading distributions, as it was shown that, even under torsional loading patterns, pier failure precedes bearing failure (at the abutments). Regarding the torsional sensitivity of the bridge which was highlighted by the modal analysis results, it was concluded that torsional deformation is not critical, mainly due to the high torsional resistance provided by the stiff pier and the use of elastomeric bearings (in lieu of pot bearings that are commonly used at this location) at the

deck-abutment interface. It is deemed that further investigation could contribute towards the development of a more generalised non-linear static analysis procedure for short bridges with a first torsional mode.

All the above results were verified using NL-THA, a fact that justifies the aforementioned assumptions made in the framework of pushover analysis for dealing with the peculiarities of the structure examined.

References

1. Krawinkler H, Seneviratna G (2004) Pros and cons of a pushover analysis of seismic performance evaluation. Eng Struct 20(4–6):452–464
2. Isakovic T, Fischinger M (2006) Higher modes in simplified inelastic seismic analysis of single column bent viaducts. Earth Eng Struct Dyn 35(1):95–114
3. Paraskeva TS, Kappos AJ, Sextos AG (2006) Extension of modal pushover to seismic assessment of bridges. Earth Eng Struct Dyn 35(11):1269–1293
4. Paraskeva TS, Kappos AJ (2010) Further development of a multimodal pushover analysis procedure for seismic assessment of bridges. Earth Eng Struct Dyn 39 (2):211–222
5. Ministry of Public Works of Greece. Greek Seismic Code – EAK 2000 (amended June 2003), Athens, 2000 (in Greek)
6. Ministry of Environment, Regional Planning, and Public Works, Circular 39/99: Guidelines for the Seismic Design of Bridges (1999) Athens (in Greek)
7. Computers and Structures Inc. SAP2000 Nonlinear Version 10 (2005) User's reference manual, Berkeley, CA
8. CEN (Comité Européen de Normalisation) Eurocode 8 (2005) Design provisions of structures for earthquake resistance – Part 2: Bridges (EN1998-2), CEN Brussels
9. Mylonakis G, Nikolaou S, Gazetas G (2006) Footings under seismic loading: analysis and design issues with emphasis on bridge foundations. Soil Dyn Earth Eng 26(9):824–853
10. Naeim F, Kelly J M (1999) Design of seismic isolated structures, from theory to practice. Wiley, New York
11. Kappos AJ (1993) RCCOLA-90: a microcomputer program for the analysis of the inelastic response of reinforced concrete sections, Department of Civil Engineering, Aristotle University of Thessaloniki, Greece
12. Kappos AJ, Paraskeva TS (2008) Nonlinear static analysis of bridges accounting for higher mode effects. Nonlinear Static Methods for Design/Assessment of 3D Structures, Lisbon, Portugal
13. Priestley MJN, Seible F, Calvi GM (1996) Seismic design and retrofit of bridges. Wiley, New York
14. Sextos A, Pitilakis K, Kappos A (2003) Inelastic dynamic analysis of RC bridges accounting for spatial variability of ground motion, site effects and soil-structure interaction phenomena. Part 1: methodology and analytical tools. Earth Eng Struct Dyn 32(4):607–627

Spatial Displacement Patterns of R.C. Buildings Under Seismic Loads

Stylianos J. Pardalopoulos and Stavroula J. Pantazopoulou

Abstract The spatial characteristics of a structure's deformed shape at the state of maximum response is a valuable tool for establishing deformation demands in the context of displacement-based seismic assessment or redesign of existing construction. The vibration shape may serve as a diagnostic tool of global structural inadequacies as it identifies the tendency for interstorey drift localization and twisting due to mass or stiffness eccentricity, but may also be used likewise to guide the strategy for redesign. This chapter investigates the spatial displaced shape envelope and its relationship to the three-dimensional distribution of peak drift demand in reinforced concrete buildings with and without irregularities in plan and in height. Elastic and inelastic dynamic analyses have been carried out, with parameters of investigation being the structural configuration and the earthquake characteristics. Results illustrate that the envelope of the seismic displacements of the structure may be approximated by a linear combination of the translational fundamental shapes in the two principal directions in plan and a pure twisting mode as calculated at the centre of mass by vibration-analysis in the respective directions while each time restraining any type of orthogonal motion. Using these concepts a methodology for seismic assessment of rotationally sensitive structures is established and tested through correlation with numerical results obtained from detailed time history simulations.

Keywords Deformed shape · Seismic assessment · Interstorey drift · Irregular buildings · Reinforced concrete buildings · Mode shape · Torsion · Rotation · Retrofit

1 Introduction

The significance of the fundamental response shape as a diagnostic tool for seismic assessment of existing structures has been illustrated in recent studies in the field of seismic assessment [8]. Note that the fundamental shape is a compound

S.J. Pardalopoulos (✉) and S.J. Pantazopoulou
Department of Civil Engineering, Demokritus University of Thrace, Xanthi, Greece
e-mail: spardalo@civil.duth.gr

M. Papadrakakis et al. (eds.), *Computational Methods in Earthquake Engineering*, Computational Methods in Applied Sciences 21, DOI 10.1007/978-94-007-0053-6_6,
© Springer Science+Business Media B.V. 2011

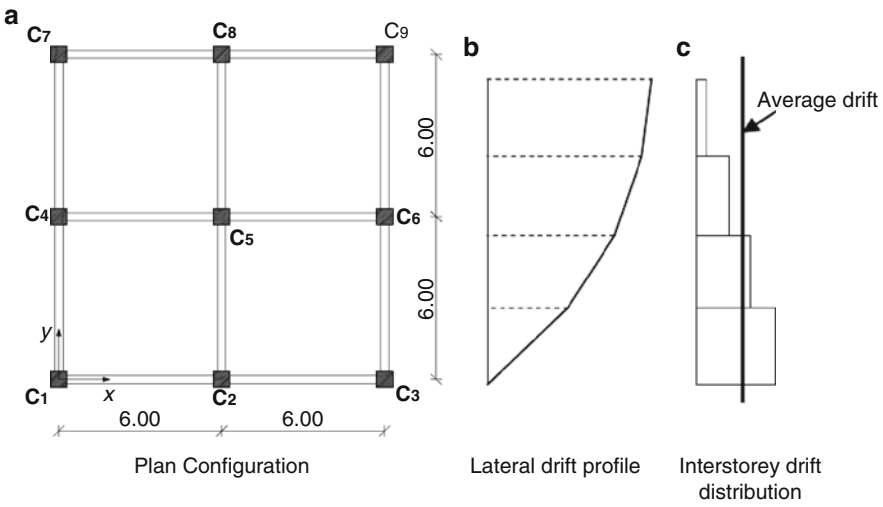


Fig. 1 Lateral displacement profile and distribution of interstorey drift of a R.C. building. Damage is expected to localize in regions where interstorey drift exceeds the average drift (**a**) Plan Configuration (**b**) Lateral drift profile (**c**) Interstorey drift distribution

property much more meaningful than the period itself, as it conveys information about the tendency for localization of deformation demand. Thus, it may be used to identify likely points of concentration of anticipated damage through the distribution of relative drift, while at the same time identifying lack of stiffness and the relative significance of possible mass or stiffness discontinuities, as shown in Fig. 1. A central step in spectra-based assessment and re-design of an existing structure is the derivation of the properties of a generalized single degree of freedom system (SDOF) responding in the fundamental mode of the actual structure. If the fraction of participating mass in the mode considered also exceeds 80% of the total, which is usually the case for shear-type frame-buildings, then the SDOF idealization in the fundamental mode produces a close approximation of the response maxima.

In the following discussion, the type of building considered may have mass/stiffness irregularities in plan or heightwise, but it is nevertheless assumed to behave with rigid (inextensible) diaphragms, so that the motion of each floor may be represented by three degrees of freedom, associated with the centre of mass. Of those, two are translations, here assumed to be oriented along two orthogonal axes in plan (in order to achieve a diagonal mass matrix). The third degree of freedom is twisting rotation about a vertical axis. Twisting is excited by a corresponding action, such as a rotational component in the ground motion, or by translational motions in the presence of mass or stiffness plan irregularities. In the latter case, the buildings' translational modes also contain contributions from twisting. Thus, the spatial distribution of each translational mode of a rotationally sensitive building departs from the ideal translational mode shape (of an identical building where twisting were restrained) in the corresponding direction by an amount $\pm\beta_i \cdot \theta$, where β_i represents

participation of the fundamental twisting mode shape, θ, in the ith translational mode of the building. This component is referred to hereon as *in-floor variability* due to torsion. Therefore, to extend the use of the fundamental mode shapes as a diagnostic tool for demand localization in three dimensional structures with a strong spatial component of response, it is necessary to determine the modification due to rotation, imparted on the fundamental shape coordinates (these are established in the context of this chapter at the Mass Centre). The above concept may be extended further to redesign of substandard structures after assessment, through systematic *correction* of the deflected shape so as to achieve a near-uniform distribution of deformation or interstorey drift demand. This requires, apart from the necessary enhancement of storey stiffness at the point of localization [7, 8], to also minimize the in-storey variability of the spatial response shape, quantified by the rotational contributions to the fundamental shape (i.e., the component in the spatial mode shape that is responsible for the term $\pm\beta_i \cdot \theta$).

Practically, at the stage of redesign, it is necessary to have control on the terms of the equation used to evaluate the fundamental mode. Eigenvalue solvers are readily available for this purpose and can easily produce the spatial modes given the mass and stiffness distribution in the system. However, what is needed, at least during preliminary design where the retrofit strategy is being determined, is a reverse process where the required stiffness (assuming no mass alterations) need be estimated, so as to yield the selected *corrected* spatial shape of response [8]. Developing a process of approximation of the reverse relationship between modal shape and stiffness is pursued in the present study. The proposed methodology is calibrated against numerical simulation results.

2 Comparison Between the Fundamental Mode Shape and the Peak Response Displacement Profile of R.C. Structures

To establish the relevance of the fundamental mode shape for the needs of design and seismic assessment of reinforced concrete structures, this property is compared with the deformed shape assumed by the structure at the state of maximum response of the building during strong ground motion. Determining a structure's seismic performance is a complex issue, affected by parameters that concern both the structural configuration and the seismic input. For the needs of the present study, a series of reinforced concrete building models have been subjected to elastic and inelastic dynamic analyses for a suite of recorded strong ground motions so as to generate a testbed of numerical results necessary to evaluate the validity of the above premise.

The geometry of building models which have been utilized in the present study was based on a prototype six-storey reinforced concrete building, that was designed according to EC8 [4] *Type 1* spectrum for moderate ductility demand and a peak ground acceleration of 0.16 g. The reference building has a constant, rectangular plan configuration with two 6.00 m bays in each principal direction (Fig. 1a).

All floors have a constant height of 3.00 m. Gravity design loads included, apart from self weight, a uniformly distributed load of 1.00 kN/m^2 and a linear load of 4.20 kN/m on beams to account for infill walls. A uniformly distributed live load of 2.00 kN/m^2 was also considered. Column sections were assumed 0.60 m^2; beam sections were 0.60 m high, 0.30 m wide. The monolithic slab was 0.18 m thick and was assumed axially rigid for the purposes of the analysis. Column longitudinal reinforcement comprised four 18 mm diameter bars, placed at the section corners and sixteen equally spaced 16 mm diameter bars on the four faces (total bar area equal to 1.17% of the column section). Top and bottom beam longitudinal reinforcement comprised three 14 mm diameter bars throughout the member's length; additional bars were placed where required to sustain higher bending moments. Uniaxial concrete compressive strength, f_c, was taken equal to 30 MPa, whereas the reinforcement yield stress, f_y, was assumed equal to 500 MPa.

Several models were derived by modifications of the geometry of the above described reference building. These models were subjected to a series of elastic and inelastic dynamic analyses. Buildings considered are classified in three major groups depending on the plan configuration in the upper floors. Thus, models classified in group *A* have a typical reference plan configuration in all floors (Fig. 1a), whereas those classified in group *B* have a 50% setback above the midheight. Models classified in group *C* feature a floor plan reduction by 50% in all floors directly above the third of the building's height, and a 75% setback in all floors above two thirds of the building's height (one × one bay plan in the upper floors). Models included in the present study comprise all possible variations of the above three groups ranging from two to six floor buildings, as illustrated in Table 1. Three-dimensional drawings of group *A*, *B* and *C* buildings are illustrated on a six-storey model in Fig. 2.

Parametric dynamic analyses of the three groups of models were carried out using the OpenSees 2.1.0 finite element analysis platform (http://peer.berkeley.edu/OpenSees). In all cases, columns were modeled as linear elements with rigid links in the joint regions, whereas beams were modeled as T-shaped cross – section linear elements (the effective width was taken equal to $b_w + 2 \cdot d$, i.e. 1.4 m). The elastic modulus was taken equal to $2 \cdot f_c/\varepsilon_{cy}$; concrete compressive strain at strength attainment was taken as $\varepsilon_{cy} = 0.0022$. For the elastic analyses, gross section properties were assumed for the columns ($EI_{eff} = EI_{gr}$). Longitudinal fiber discretization was used in order to conduct nonlinear flexural calculations for the critical sections in inelastic analyses. Steel properties were represented by a uniaxial bilinear stress-strain relationship with kinematic hardening (*Steel01* Material in the program suite)

Table 1 Building models considered in the dynamic analyses

Number of floors	Plan Configuration		
	Group A	Group B	Group C
2	√	√	
3	√		√
4	√	√	
5	√		
6	√	√	√

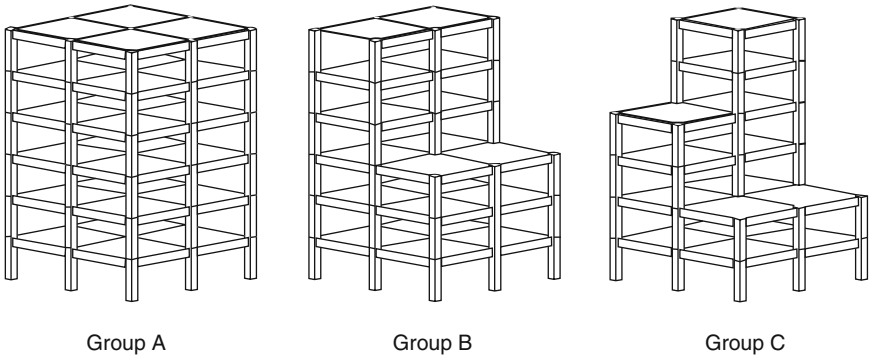


Fig. 2 Six-storey sample of group *A*, *B* and *C* buildings

with initial elastic steel modulus equal to 200 GPa and a strain-hardening ratio of 0.005. Inelastic concrete behavior was modeled using the uniaxial Kent-Scott-Park concrete stress-strain envelope with degrading unloading/reloading hysteresis loops (Karsan-Jirsa type), with no tensile strength (*Concrete01* Material) having an initial tangent modulus of $2 \cdot f_{cy}/\varepsilon_{cy}$ ($f_{cy} = 30$ MPa, $\varepsilon_{cy} = 0.0022$) and an ultimate strength and deformation capacity of $f_{cu} = 22.7$ MPa, and $\varepsilon_{cu} = 0.0035$. Ten points of integration were used along the typical column height in each step of the dynamic analysis. In both elastic and inelastic analyses, elastic beam stiffness EI_{eff}, was taken equal to 40% of the corresponding gross section property, EI_{gr}; sensitivity evaluation of modeling procedures with reference to various models illustrated that consideration of beam inelasticity in the model had a negligible effect on the magnitude of the three highest periods of each structure. In all the analyses cases, mass properties were lumped at the Centre of Mass of each individual structural member, whereas damping was taken equal to 5% (*Rayleigh* damping).

To account for the effect of the ground motion parameters a suite of ten earthquake records was used in conducting elastic and inelastic analyses. Damages seen during resent earthquakes with a rupture zone located near urban areas (Northridge 1994, Kobe 1995, Athens 1999, Kocaeli 1999) highlight the significance of the frequency content, besides the familiar parameters such as peak ground acceleration (*PGA)*, moment magnitude, M_w, and duration of the earthquake. Near-fault ground motions (i.e. motions recorded within 20 km from the rupture fault, with the dynamic consequences of forward-directivity) are characterized by few, long-period pulses, with large amplitudes in the velocity time-history that in some cases can control the performance of structures [1, 2]. From among the ten earthquake datasets considered in the analyses, five were recorded in the near-fault zone (i.e. within 20 km from the rapture fault) and possess forward directivity characteristics, whereas the other five datasets were recorded at sites with a distance from the rupture fault ranging from 22 to 57 km. Criteria for the selection of the earthquake records were: (a) an earthquake moment magnitude $M_w > 6.0$ on the Richter scale, (b) that the peak ground acceleration in one at least of the two orthogonal horizontal

acceleration components of the ground motion record should exceed 0.50 g in near-fault records or 0.35 g in far-fault ones and (c) the recording instrument should be located at ground level, in free-field sites or in one-storey structures, so that the records would be free of amplification parameters due to structural vibration. An effort was made to include records from most of the geological site conditions that a structure could be build on, as well as to consider most of the rupture mechanisms (as outlined in Tables 2–4). Recorded datasets were selected from the PEER Strong Motion Database (http://peer.berkeley.edu/smcat) and the COSMOS virtual data center (www.cosmos-eq.org).

Based on the largest ground acceleration value between the two orthogonal components of each earthquake record, the ten datasets were scaled to four different levels of PGA, namely 0.16, 0.24, 0.36 and 0.50 g, that were subsequently used in the elastic and inelastic analyses cases. The 5% damped earthquake spectra of the records scaled to 1.00 PGA are plotted in Fig. 3a and b for the components applied in the longitudinal (x) and the transverse (y) directions of the structural models respectively.

Displacement profiles which were obtained from the dynamic time history analyses were normalized with respect to the displacement at the top of the corresponding structural model and are subsequently compared with the corresponding fundamental mode in the direction of the applied seismic action. In the large number

Table 2 Ground motions considered in the study

Earthquake	Date	Region	Moment magnitude	Mechanism
Imperial Valley	15-10-1979	California	6.5	Strike-slip
Whittier Narrows	01-10-1987	California	6.1	Reverse-oblique
Loma Prieta	18-10-1989	California	6.9	Reverse-oblique
Cape Mendocino	25-04-1992	California	7.0	Reverse
Northridge	17-01-1994	California	6.7	Reverse
Kobe	16-01-1995	Japan	6.9	Strike-slip
Chi-Chi	20-09-1999	Taiwan	7.6	Reverse-oblique
Duzce	12-11-1999	Turkey	6.5	Strike-slip

Table 3 Records used in time-history analyses of model structures

Earthquake	Station	Closest to fault distance (km)	Record type
Imperial Valley	6605 Delta	22.03	Far fault
Whittier Narrows	CSMIP 24436	43.00	Far fault
Loma Prieta	CDMG 58223	58.65	Far fault
Cape Mendocino	CSMIP 89005	15.5	Near fault
Northridge	DWP 75	5.19	Near fault
Northridge	CDMG 24400	37.36	Far fault
Kobe	CUE Takatori	1.47	Near fault
Chi-Chi	TCU 052	0.66	Near fault
Chi-Chi	TCU 095	45.18	Far fault
Duzce	ERD Bolu	12.04	Near fault

Table 4 Peak ground acceleration, velocity and displacement of the earthquake horizontal components

		Longitudinal component			Transversal component		
Record type	Station	PGA (g)	PGV (cm/sec)	PGD (cm)	PGA (g)	PGV (cm/sec)	PGD (cm)
Near-fault	Cape Mendocino	1.497	126.12	36.07	1.039	40.52	14.80
	Northridge	0.828	117.51	34.22	0.493	74.58	28.69
	Kobe	0.611	127.13	35.77	0.616	120.67	32.72
	Chi-Chi	0.419	118.45	246.15	0.348	158.96	184.42
	Duzce	0.728	56.42	23.07	0.822	62.07	13.55
Far-fault	Imperial Valley	0.238	26.0	12.06	0.351	33.0	19.02
	Whittier Narrows	0.449	20.14	1.29	0.644	22.87	1.68
	Loma Prieta	0.239	25.47	4.20	0.329	27.86	6.03
	Northridge	0.563	24.55	2.79	0.355	16.72	1.44
	Chi-Chi	0.712	49.13	24.45	0.379	62.00	51.75

of cases both for the elastic and the inelastic analyses, good correlation was obtained, the fundamental translational mode representing the average of the spread of possible values. Figures 4 and 5 summarize the translational components of the first mode and the associated normalized displacement profiles obtained from elastic and inelastic dynamic analyses respectively for the six-storey sample of group *A* buildings, subjected to the suite of applied motions scaled to 0.36g. Both figures refer to the translational displacements of the *C*5 central column; the first mode in the case of inelastic analyses is estimated after application of the G + 0.30 Q combination of gravity loads. Similarly, Figs. 6 and 7 illustrate the correlation between the translational components of the first mode and the corresponding normalized displacement profile at the state of maximum seismic response along the axis of column *C*5 in the six-storey group *B* building, when elastic and inelastic responses are considered. Dispersion of the results is greater in the inelastic as compared to the elastic response analyses. However, this comparison concerns the first mode calculated before the earthquake, where the structure possesses only minor stiffness reduction caused by the application of G + 0.30 G combination gravity loads. Analyses results indicate that the building's first mode calculated after each earthquake, when inelastic structural response is considered, correlates better with the peak seismic displacement profile caused by the associated earthquake.

3 Approximation to the Fundamental Translational Mode Shapes of Rotationally-Sensitive Structures

The preceding analyses point to the conclusion that the translational shape assumed by a structure undergoing seismic excitation is governed at peak points in the time history by a significant participation of the fundamental mode of vibration to the extent that the interstorey drift distribution pattern implicit in the fundamental mode

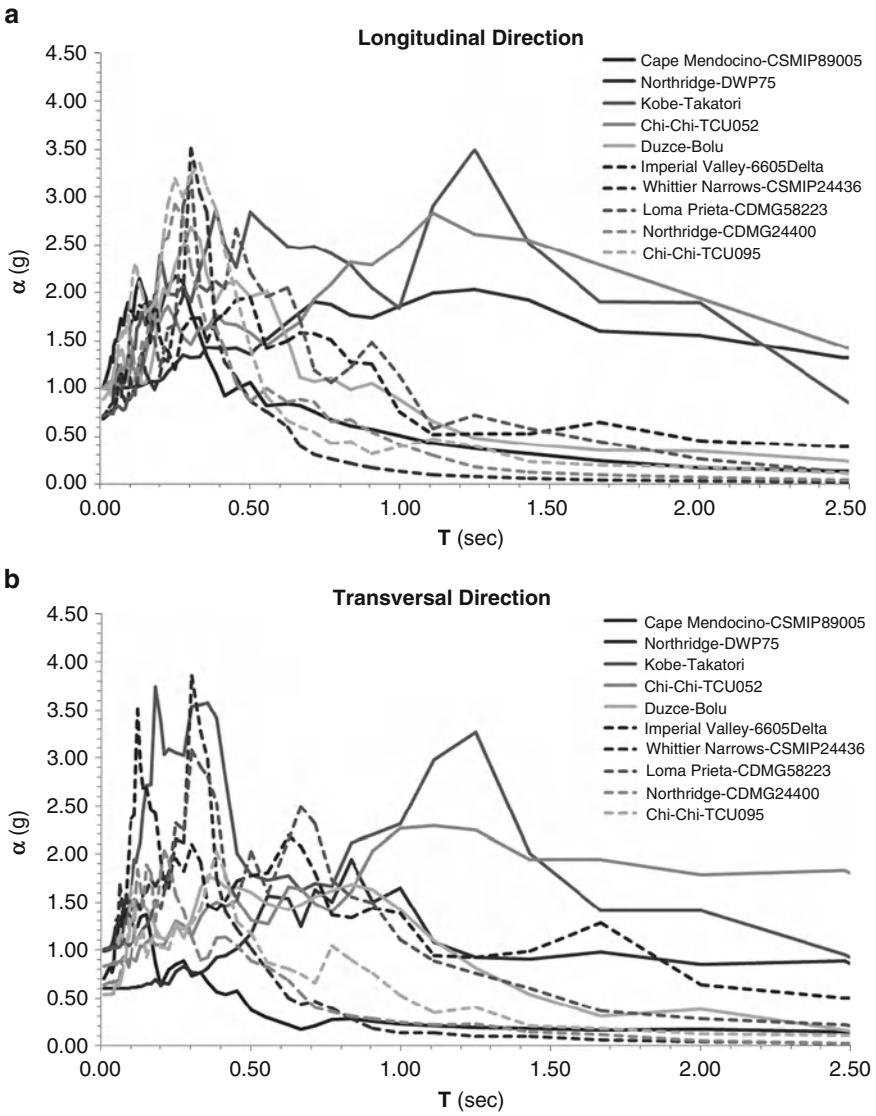


Fig. 3 Response spectra of the earthquake records used in the analyses, scaled to 1.00 gPGA. (**a**) records used in the E-W direction of the structural model, (**b**) records used in the N–S direction

shape of a structure may be used to assess a-priori the likelihood of damage localization in a structure. Thus, by examining the fundamental shape of vibration, it may expected that serious or severe inelastic response may be anticipated in locations throughout the structure where interstorey drift exceeds significantly the average drift value (i.e. peak displacement/building height, Fig. 1c); this diagnosis then may

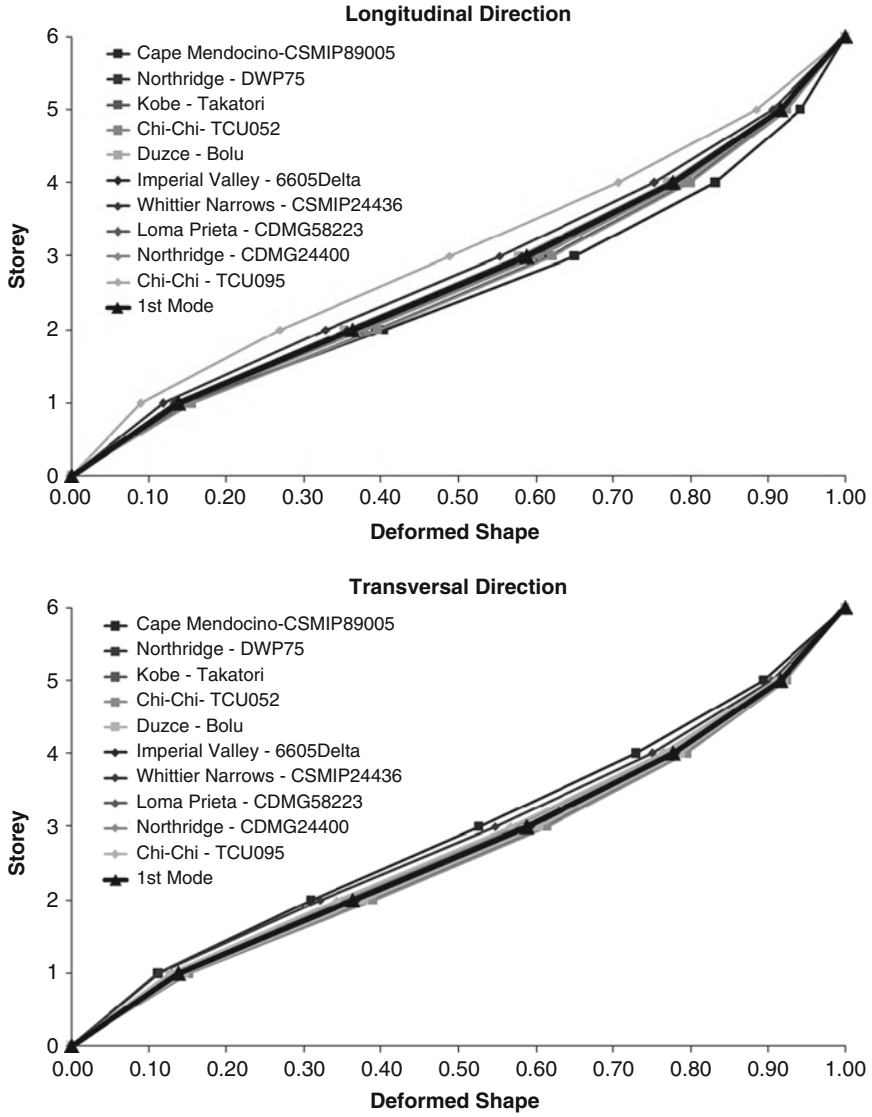


Fig. 4 Normalized lateral displacement profiles at maximum seismic response of the central column (C5); six-storey building, group *A*, elastic analyses

be used to also dictate the primary objective of a retrofit strategy, namely modification of the respective building properties aiming to achieve a minimal deviation between local interstorey drift and average lateral drift. From the practical point of view, implementation of this idea relies on the ability to readily assess the implications on the fundamental shape, effected by interventions on stiffness (or strength) of individual floors. In this regard, standard eigenvector analysis can only be used

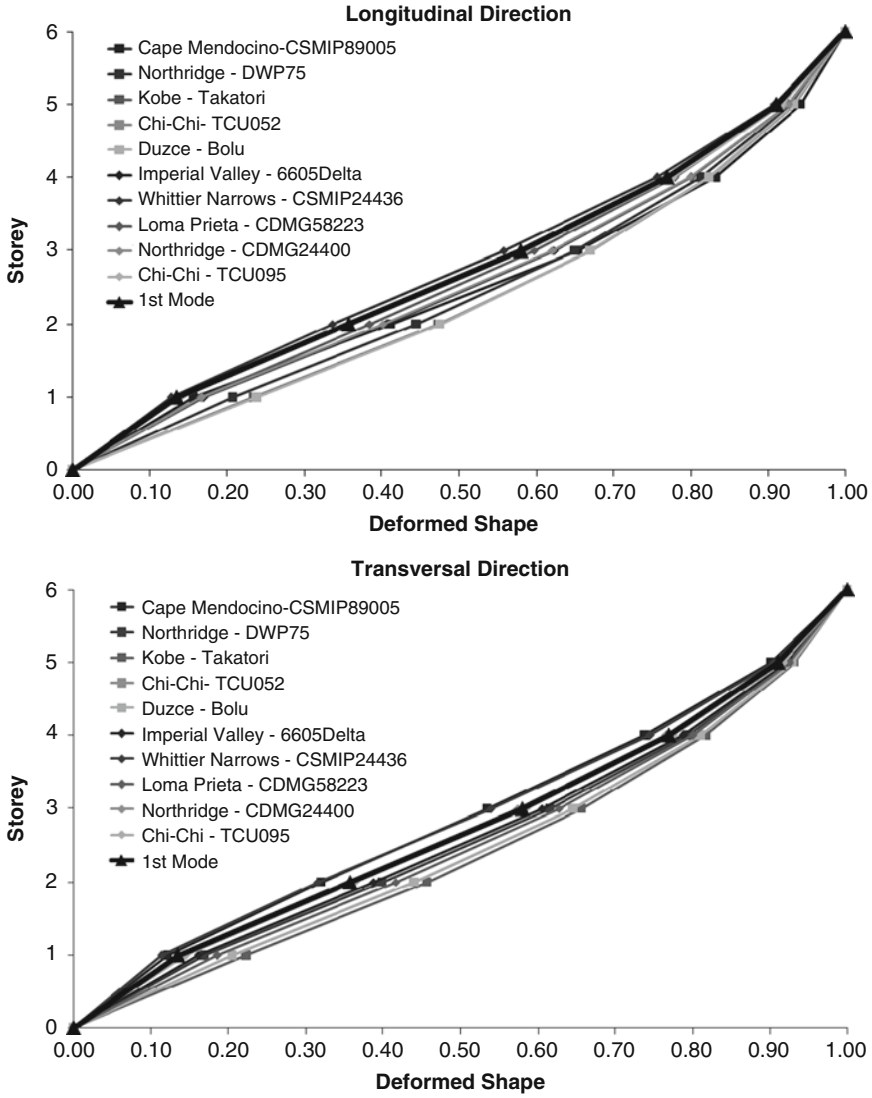


Fig. 5 Normalized lateral displacement profiles at maximum seismic response of the central column (C5); six-storey building, group *A*, inelastic analyses

to verify the implications of an upgrading scheme that includes selective stiffness modification, but cannot be used to guide the redesign process. The reason is that in such an approach several iterations would be necessary until convergence could be achieved to such stiffness values as would be necessary in order to produce a desirable pattern of interstorey drift distribution.

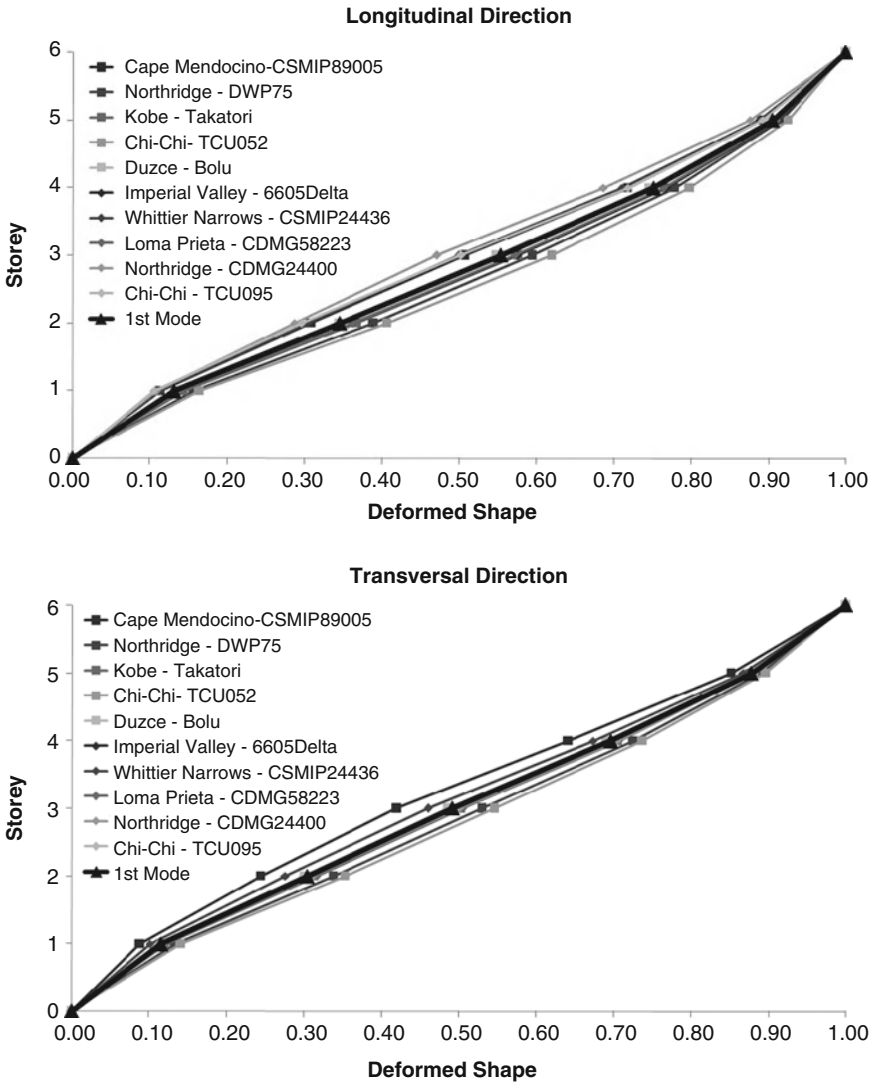


Fig. 6 Normalized lateral displacement profiles at maximum seismic response of the central column (C5); six-storey building, group *B*, elastic analyses

In this section, this objective is addressed by the development of simple tools by which to readily relate the value and location of the necessary stiffness additions required to control the pattern of interstorey drift distribution. This pattern is referred to hereon as target response shape for the structure, which, in three dimensional structures may be composed by translational as well as rotational components of response.

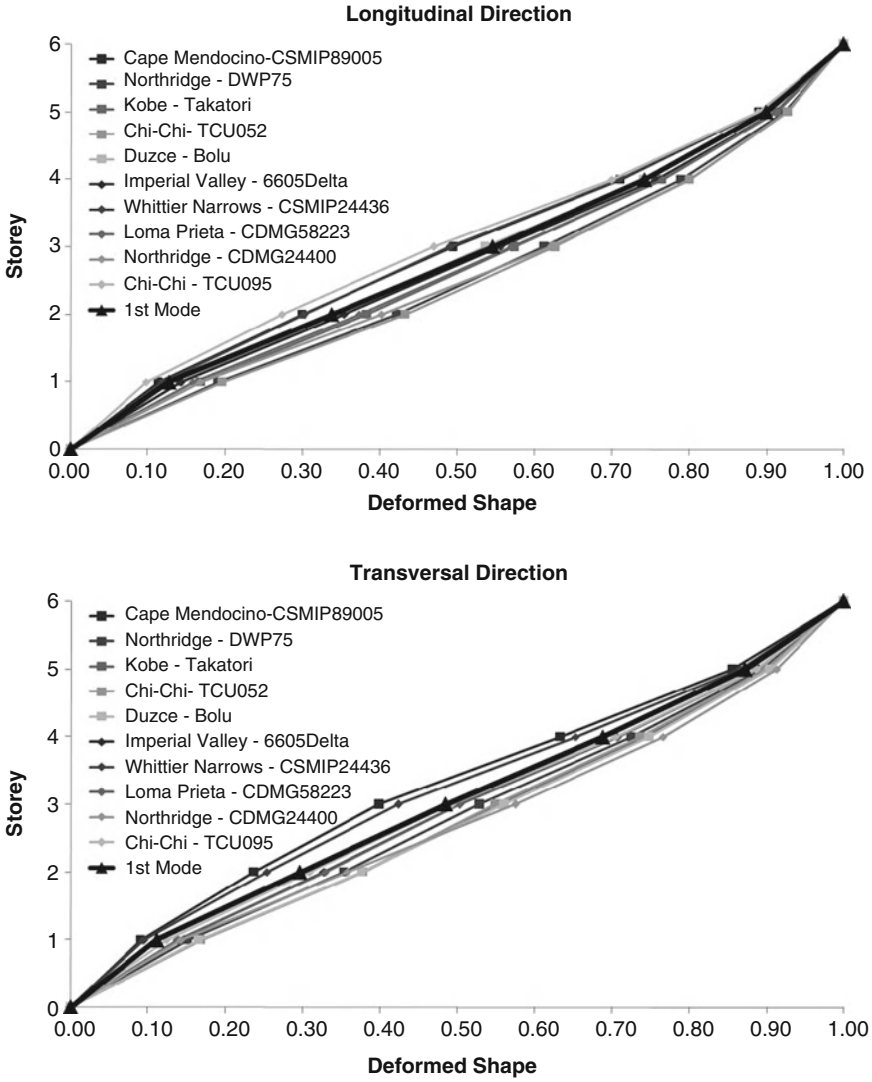


Fig. 7 Normalized lateral displacement profiles at maximum seismic response of the central column (C5); six-storey building, group *B*, inelastic analyses

3.1 Methodology

To address the need of a straightforward method for approximating the three dimensional fundamental mode shape of a multi-storey system, consider a building with a constant floor plan as shown in Fig. 8, and degrees of freedom associated with the motion of the center of mass. For a building with such strong plan irregularity it

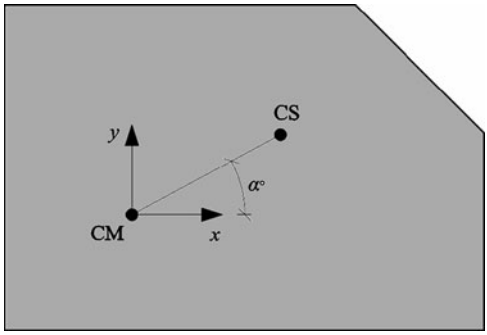


Fig. 8 Typical plan of torsionally coupled system

is expected that each basic translational mode (in either x or y direction) contains, apart from the primary translational motion, a strong torsional contribution and a weak component in the orthogonal translational direction. In a simplified sense, it may be said that if an inextensible floor system (diaphragm), which intrinsically possesses three independent orthogonal degrees of freedom (dof) at the Centre of Mass may be idealized as rigid, then the translations of the various points in plan become coupled with the rotation due to compatibility.

For a unit translation in the y direction of the floor system illustrated in Fig. 8, the required forces developing at the Centre of Mass are $\mathrm{K_{yy}} = 1 \cdot \mathrm{K_y}$; $\mathrm{K_{xy}} = 0$; $\mathrm{K_{\theta y}} = \mathrm{K_y} \cdot (\mathrm{e} \cdot \cos\alpha)$, where α is the angle contained between the x axis and the line connecting the Centers of Stiffness (CS) and Mass (CM), whereas e is the distance between these two points. Similarly, a unit translation in the x direction requires forces $\mathrm{K_{xx}} = 1 \cdot \mathrm{K_x}$; $\mathrm{K_{xy}} = 0$; $\mathrm{K_{\theta x}} = -\mathrm{K_x} \cdot (\mathrm{e} \cdot \sin\alpha)$. Finally, for a unit rotation about the storey Centre of Mass, the required forces are $\mathrm{K_{\theta\theta}} = 1 \cdot \mathrm{K_\theta}$; $\mathrm{K_{y\theta}} = \mathrm{K_y} \cdot (\mathrm{e} \cdot \cos\alpha)$; $\mathrm{K_{x\theta}} = -\mathrm{K_x} \cdot (\mathrm{e} \cdot \sin\alpha)$. Within a given floor, stiffness coefficients K_x, K_y and K_θ comprise the lateral stiffness contributions of the individual floor elements, $k_{x,i}$ and $k_{y,i}$, as follows (the second subscript denotes the ith element):

$$k_x = \sum_{i=1}^{N} k_{x,i}; \quad k_y = \sum_{i=1}^{N} k_{y,i}$$
$$k_\theta = \sum_{i=1}^{N} k_{x,i} \cdot (y_i - e \cdot \sin a)^2 + \sum_{i=1}^{N} k_{y,i} \, (x_i - e \cdot \cos a)^2 \tag{1}$$

whereas the floor eccentricity is estimated from Eq. (2):

$$e \cdot \cos a = \sum_{i=1}^{N} k_{y,i} \cdot x_i \Big/ \sum_{i=1}^{N} k_{y,i}; \quad e \cdot \sin a = \sum_{i=1}^{N} k_{x,i} \cdot y_i \Big/ \sum_{i=1}^{N} k_{x,i} \tag{2}$$

The associated eigenvalue problem is given by Eq. (3), whereby the coordinates in the degrees of freedom in y and θ are obtained by setting the corresponding

coordinate in dof x, Ψ_{xq}, equal to 1:

$$\omega_q^2 \cdot \begin{bmatrix} m & 0 & 0 \\ 0 & m & 0 \\ 0 & 0 & J_m \end{bmatrix} \cdot \begin{Bmatrix} \Psi_{xq} \\ \Psi_{yq} \\ \Psi_{\theta q} \end{Bmatrix}$$

$$= \begin{bmatrix} K_x & 0 & -K_x \cdot e \cdot \sin a \\ 0 & K_y & K_y \cdot e \cdot \cos a \\ -K_x \cdot e \cdot \sin a & K_y \cdot e \cdot \cos a & K_\theta \end{bmatrix} \cdot \begin{Bmatrix} \Psi_{xq} \\ \Psi_{yq} \\ \Psi_{\theta q} \end{Bmatrix} \tag{3}$$

where q assumes one of the values x, y, θ. Note that the degree of coupling in the stiffness matrix between the x and θ directions, or between the y and θ directions is a function of eccentricity, whereas coupling between x and y is very weak and indirect since the corresponding off-diagonal terms, $K_{xy} = K_{yx} = 0$. Thus, a floor system with an eccentricity between its centers of Stiffness and Mass and dofs located at the mass center may be assumed to have a coupled mode of vibration in each primary direction of action that is approximated by a pure translational component (corresponding to the motion of the respective Centre of Mass) and a superimposed rotational component, its magnitude being a function of stiffness eccentricity and rotational mass. Note here that if the system were entirely uncoupled (i.e., coincident centers of stiffness and mass), then the system would have three uncoupled vibration modes, with natural frequencies $\omega_{x,o}$, $\omega_{y,o}$, $\omega_{\theta,o}$ equal to $(K_x/m)^{1/2}$, $(K_y/m)^{1/2}$ and $(K_\theta/J_m)^{1/2}$ respectively. Here, these values and the corresponding mode shapes of the associated uncoupled system, $\Phi_{x,o}, \Phi_{y,o}, \Phi_{\theta,o}$ are used as a first order approximation to the actual frequencies and mode shapes of the actual system, i.e., $\omega_x, \omega_y, \omega_\theta$ and Ψ_x, Ψ_y, and Ψ_θ.

Consider the translational inertia of the floor system under an excitation in the x direction. Then the forces acting at the center of stiffness are equal to:

$$F_x = m \cdot S_a; \quad M_\theta = F_x \cdot e \cdot \sin\alpha \tag{4}$$

The associated displacements of the Centre of Mass, Δ_x and Θ respectively, are:

$$\Delta_x = \frac{F_x}{K_x} = \frac{m}{K_x} \cdot S_\alpha = \omega_{x,0}^2 \cdot S_a$$

$$\Theta = \frac{M_\theta}{K_\theta} = \frac{F_x \cdot e \cdot \sin a}{K_\theta} = \frac{\Delta_x \cdot K_x}{K_\theta} \cdot e \cdot \sin\alpha = \frac{K_x \cdot e \cdot \sin\alpha}{K_\theta} \cdot \Delta_x \tag{5a}$$

Similarly, for a seismic excitation, S_α, in y direction, the displacements at the Centre of Mass are:

$$\Delta_y = \frac{F_y}{K_y} = \frac{m}{K_y} \cdot S_\alpha = \omega_{y,0}^2 \cdot S_a$$

$$\Theta = \frac{M_\theta}{K_\theta} = \frac{-F_y \cdot e \cdot \cos a}{K_\theta} = \frac{-\Delta_y \cdot K_y}{K_\theta} \cdot e \cdot \cos\alpha = \frac{-K_y \cdot e \cdot \cos\alpha}{K_\theta} \cdot \Delta_y \tag{5b}$$

From Eq. (5a) and (5b) it is evident that the developing displacements of the coupled floor system depend on the characteristics of an associated torsionally decoupled system, that possesses the same translational mass, m, and stiffness K_x, K_y as the coupled system. Furthermore, the rotational term is mainly a function of the system's rotational stiffness resisting twist and of the eccentricity between the centers of Mass and Stiffness. In the general case, any point P in the floor plan that is subjected to a seismic excitation of an arbitrary direction, at a distance y_P from the Centre of Mass, will displace by the amount $\Delta_x - \beta_x \cdot \Delta_x \cdot (y_P - e \cdot sin\alpha) = \Delta_x \cdot (1 - \beta_x \cdot (y_P - e \cdot sin\alpha))$ in the x direction and by the amount $\Delta_y + \beta_y \cdot \Delta_y \cdot (y_P - e \cdot cos\alpha) = \Delta_y \cdot (1 + \beta_y \cdot (y_P - e \cdot cos\alpha))$ in the y direction, where coefficients β_x and β_y represent the participation of twist in the x and y translational modes of the coupled system respectively.

The above concept is now extended to a multi-storey system, utilizing the generalized system properties. These enable idealization of the actual response by that of an equivalent SDOF; generalized properties are work equivalent mass and stiffness properties of the actual multi-dof system vibrating in its fundamental mode. For a multi-storey system with a constant floor plan (i.e. a constant eccentricity in all floors), a vibration in the fundamental mode in the x axis produces at the Centre of Mass of the top floor a displacement along the x axis, $\Delta_{x,top}$, and a rotation, Θ_{top}. Considering the implicit relationship between the translational displacements at the Centre of Mass of the coupled system with those of the corresponding uncoupled system, the following approximation to the profile of translational displacements of any point P in the top floor is obtained:

$$\begin{aligned}\Delta_{x,P} &= \Delta_{x,top} \cdot \Psi_x \cong \Delta_{x,top} \cdot \Phi_x \\ &= \Delta_{x,top} \cdot \Phi_{x,o} - \Theta_{top} \cdot (y_P - e \cdot \sin\alpha) \cdot \Phi_{\theta,o} \\ &= \Delta_{x,top} \cdot \left[\Phi_{x,o} - \frac{K_x^* \cdot e \cdot \sin\alpha}{K_\theta^*} \cdot (y_P - e \cdot \sin\alpha) \cdot \Phi_{\theta,o} \right] \end{aligned} \tag{6}$$

where, $K^*{}_x$ and $K^*{}_\theta$, are the generalized stiffness values for the x-translational and the rotational lowest modes of the multi-storey system. Therefore, the true spatial fundamental mode of vibration, Ψ_x, is approximated by the sum of contributions of the torsionally uncoupled system, $\Phi_{x,o}$ and $\Phi_{\theta,o}$ along the x and θ axes of motion according with:

$$\Psi_x = \Phi_{x,o} - \beta_x^* \cdot \Phi_{\theta,o} \cdot (y_P - e \cdot \sin\alpha); \quad \beta_x^* = \frac{K_x^*}{K_\theta^*} \cdot e \cdot \sin\alpha \tag{7}$$

Similar equations may be developed for the multi-storey system which is vibrating in its lowest translational mode in the y-direction, Ψ_y, as:

$$\Psi_y = \Phi_{y,o} + \beta_y^* \cdot \Phi_{\theta,o} \cdot (x_P - e \cdot \cos\alpha); \quad \beta_y^* = \frac{K_y^*}{K_\theta^*} \cdot e \cdot \cos\alpha \tag{8}$$

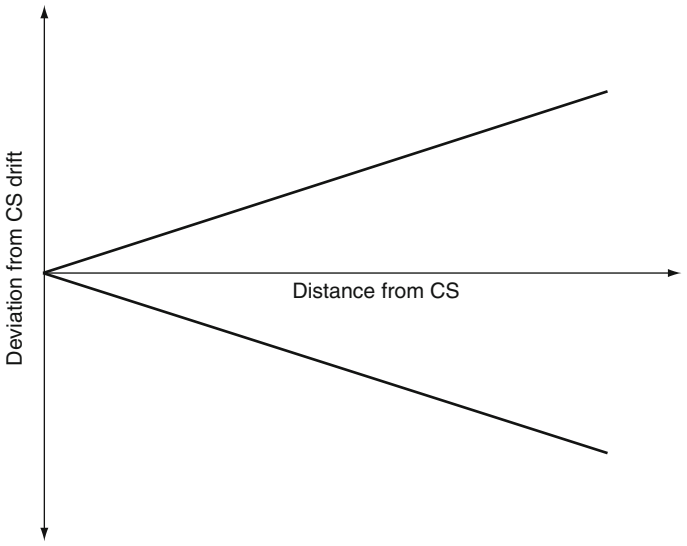


Fig. 9 Interstorey drift deviation between CS and storey columns due to their distance from CS

Coefficients β^*_x and β^*_y represent the participation of twist in the x-translational and the y-translational principal modes of the coupled multi-storey system respectively, as a function of the stiffness properties and the eccentricity between the Centre of Stiffness and the Centre of Mass and the fundamental modes of the associated uncoupled system. This term is responsible for the deviation from the average value of interstorey drift, from column to column within a single storey; thus, according to Eq. (8) and depending on the distance of the column under consideration from the center of stiffness, the interstorey drift increases or decreases linearly from the average storey value which is prescribed by the translational properties of the structure as per Fig. 9.

3.2 Proposed Method for Calculating the Maximum Translational Seismic Response of R.C. Buildings

Based on the preceding analysis, a procedure for approximating the distribution of interstorey drift of rotationally sensitive multi-storey buildings through the displacement profile implicit in the fundamental translational mode of vibration is proposed for the needs of assessment and preliminary formulation of a retrofit strategy. The methodology applies to structures with well established rigid-diaphragm action in each floor, regardless of plan configuration. For convenience, in applying the proposed methodology, the center of mass of each floor of the building is established as a point of reference for determination of the building's deformed shape,

whereby two orthogonal translational and one rotational dofs are associated with each floor. Calculation of the fundamental translational mode of a frame building is a relatively straightforward, standard procedure that can be performed either by hand-calculation, or through the use of a finite element analysis software. Recall however that the intended use in a rehabilitation framework is to explicitly control the shape of the fundamental mode through selective intervention; it is therefore convenient to separate the influence of the rotational from the translational dofs in the resulting profiles, so as to enable targeted interventions that aim (a) to correct the variation in the displacement profile within a single floor (minimizing the in-floor variability) and (b) improving the heightwise interstorey drift pattern. A convenient interpretation of Eqs. (7) and (8) that enables targeted interventions of the type described here is that the fundamental translational mode of a torsionally sensitive structure, Ψ_x, may be approximated by a first order term, $\Phi_{x,o}$, which represents the fundamental mode if the twisting influence is neglected, and a correction term, $\beta^*{}_x \cdot \Phi_{\theta,o}$, which separately accounts for this influence. The uncoupled fundamental translational modes may be calculated from a standard Stodola-type approach, which may be easily formulated so as to prescribe the targeted mode shape in a rehabilitation strategy [8].

Thus, in the absence of translational-rotational coupling, in each primary direction of action, free vibration in the fundamental mode is expressed by the equation:

$$\omega_{q,\mathrm{o}}^2 \cdot \underline{D}_{q,\mathrm{o}} \cdot \underline{\Phi}_{q,\mathrm{o}} = \underline{\Phi}_{q,\mathrm{o}}; \quad q = x, \quad y, \quad \text{or} \quad \theta \tag{9}$$

where, $\underline{D}_{q,\mathrm{o}} = \underline{F}_{q,\mathrm{o}} \cdot \underline{M}_{q,\mathrm{o}}$ is the uncoupled structure's dynamic matrix, $\underline{F}_{q,\mathrm{o}}$ is the flexibility matrix and $\underline{M}_{q,\mathrm{o}}$ the mass matrix of the associated uncoupled system in the direction of interest, identified by the value of q. For a multi-storey building with a constant plan configuration heightwise, examined only in one direction of interest at the time, the diagonal terms of $\underline{F}_{q,\mathrm{o}}$ are easily obtained given the storey stiffness, K_x, K_y, or K_θ calculated at the Centre of Mass. For example, for the uncoupled motion in the x-direction the associated eigenvalue problem has the form:

$$\omega^2 \cdot \underbrace{\begin{bmatrix} \frac{1}{K_{1,x}} & \frac{1}{K_{1,x}} & \cdots & \frac{1}{K_{1,x}} \\ & \frac{1}{K_{1,x}} + \frac{1}{K_{2,x}} & \cdots & \frac{1}{K_{1,x}} + \frac{1}{K_{2,x}} \\ & & \ddots & \vdots \\ \text{symm} & & & \frac{1}{K_{1,x}} + \frac{1}{K_{2,x}} + \cdots + \frac{1}{K_{N,x}} \end{bmatrix}}_{F_{x,0}} \cdot \underbrace{\begin{bmatrix} m_1 & & & \\ & m_2 & & \\ & & \ddots & \\ & & & m_N \end{bmatrix}}_{m_x} \cdot \begin{bmatrix} \Phi_{x,1} \\ \Phi_{x,2} \\ \vdots \\ 1 \end{bmatrix} = \begin{bmatrix} \Phi_{x,1} \\ \Phi_{x,2} \\ \vdots \\ 1 \end{bmatrix} \tag{10}$$

where $K_{1,x}, K_{2,x}, \ldots K_{N,x}$ are the translational stiffnesses in the x-direction of the first floor, second floor, etc. up to the Nth floor, $\Phi_{x,1}, \Phi_{x,2} \ldots$ are the corresponding

coordinates of the fundamental decoupled mode in the x-direction (normalized with respect the value at the top), $m_1, m_2..m_N$ are the translational masses of the corresponding floors and ω is the natural frequency of the system. The above equation may be used in two alternative ways: first to establish a simple iterative process by which to evaluate the corresponding mode (this is a Stodola-type iteration, where values are assumed for the modal vector in the left hand side, whereas the improved estimate is the result of the multiplication, i.e. the vector in the right-hand side). A second way is to evaluate the required stiffness terms in order for the mode to assume a prescribed shape consistent with a desirable pattern of interstorey drift [8]. In this second option, a simple system of equations is created, whereby the modal coordinates are introduced in both the left and right-hand sides as known values, whereas the necessary relationship between stiffness terms ($K_{1,x}, K_{2,x}, \ldots K_{N,x}$) required to produce this drift pattern in the structure is easily resolved from the above. Similar equations may be established for the two orthogonal directions of motion of the uncoupled system (i.e. the y-direction and the twisting z-axis).

Because the flexibility matrix is multiplied with the diagonal mass matrix, the off-diagonal terms of $\underline{F}_{q,o}$ do not need to be determined in the first approximation. This enables the establishment of simple equations between the deformed shape, $\underline{\Phi}_{q,o}$ and the dynamic matrix, $\underline{D}_{q,o}$, of the structure. Once the uncoupled vibration shapes of the building are determined, the coupled translational shapes in the x and y direction, Ψ_x and Ψ_y respectively, may be approximated by Eqs. (7) and (8), where the generalized stiffness values are equal to:

$$K_x^* = \sum_{i=1}^{N} K_{x,i} \cdot \Delta\Phi_{x,o-i}^2, \quad K_y^* = \sum_{i=1}^{N} K_{y,i} \cdot \Delta\Phi_{y,o-i}^2,$$
$$K_\theta^* = \sum_{i=1}^{N} K_{\theta,i} \cdot \Delta\Phi_{\theta,o-i}^2 \tag{11}$$

In the case of multistory buildings with setbacks, to maintain the simplicity of calculation secured by a diagonal mass matrix, $\underline{M}_{q,o}$, the dynamic dofs should be associated with the center of mass of each floor; thus, the points of reference in such an idealization would not be collinear (i.e. they generally do not lie on a single vertical axis). Any other option for the selection of points of reference would generally yield full matrices both for the stiffness/flexibility as well as for the mass. In this case a computer-assisted procedure may be utilized for the purposes of assessment, although in re-design a direct handle on the relationship between external intervention and resulting effect on the targeted deflected shape would be more useful. The uncoupled translational fundamental modes of the building, $\Phi_{q,o}$, ($q = x$ or y) can be calculated by restraining the translational degrees of freedom of all diaphragm joints of the torsionally coupled system in directions orthogonal to q (for example, for $q = x$, translation in y would be restrained). The uncoupled rotational fundamental mode, $\Phi_{\theta,o}$, would be calculated by restraining the dofs of the reference points in the building's diaphragms from motion, in either x or y directions and

considering modal analysis. The coupled translational shapes of the building, Ψ_x and Ψ_y, are then calculated by Eqs. (7) and (8), where e_i is the eccentricity between the Center of Mass and the Centre of Stiffness of each floor diaphragm. The final translational building shapes, Φ_x and Φ_y are obtained by normalizing the coupled translational shapes, Ψ_x and Ψ_y.

3.3 Example Analysis

Consider the three-storey building illustrated in Fig. 10, with a plan configuration similar to that of *Group C* buildings utilized before in dynamic analyses. Storey height of the building equals to 3.00 m (clear column height = 2.40 m), with total building height being 9.00 m. For convenience, columns are assumed to be axially inextensible, whereas beams and joints are rigid. Column coordinates, with respect to the coordinate system illustrated in Fig. 1a and sectional dimensions are presented in Table 5. Column translational stiffness is calculated as: $k_q = 12 \cdot E \cdot I_q / h_{st}$, where q equals to x or y; $h_{st} = 2.40$ m; $E = 29$ GPa. Column torsional stiffness is not considered. Location of Centre of Mass and mass properties of each floor, as considered in the example, are presented in Table 6. Location of Centre of Stiffness and the stiffness properties of each storey, calculated according to Eqs. (1) and (2), are presented in Table 7.

To illustrate the adequacy of the proposed methodology for approximating the fundamental mode shape of rotationally-sensitive structures, the normalized modal

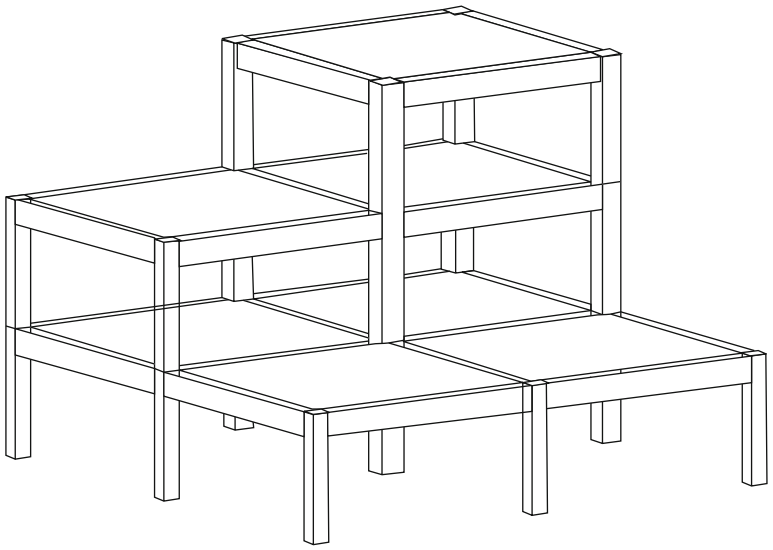


Fig. 10 Building used in the methodology application example

Table 5 Column geometrical and stiffness properties

	Column Coordinates		Sectional dimensions		Column stiffness		
Column	x(m)	y (m)	b_x (m)	b_y (m)	k_x (kN/m)	k_y (kN/m)	k_θ (kNm/rad)
C_1	0.00	0.00	0.40	0.40	53,704	53,704	0
C_2	6.00	0.00	0.40	0.40	53,704	53,704	0
C_3	12.00	0.00	0.40	0.40	53,704	53,704	0
C_4	0.00	6.00	0.40	0.40	53,704	53,704	0
C_5	6.00	6.00	0.60	0.60	271,875	271,875	0
C_6	12.00	6.00	0.50	0.50	131,113	131,113	0
C_7	0.00	12.00	0.40	0.40	53,704	53,704	0
C_8	6.00	12.00	0.50	0.50	131,113	131,113	0
C_9	12.00	12.00	0.50	0.50	131,113	131,113	0

Table 6 Location of centre of mass and inertial properties of each storey

	CM properties			
Storey	X_{CM}(m)	Y_{CM} (m)	m (t)	J_m (tm)
3	9.000	9.000	20.15	471.18
2	6.000	9.000	40.29	942.36
1	6.000	6.000	80.59	1,884.71

Table 7 Location and stiffness properties at each storey's Centre of Stiffness

	CS properties				
Storey	X_{CS} (m)	Y_{CS} (m)	K_x (kN/m)	K_y (kN/m)	K_θ (kNm/rad)
3	8.365	8.365	665,213	665,213	10,453,5938
2	7.202	8.453	772,620	772,620	114,202,604
1	6.995	6.995	933,731	933,731	123,869,271

Table 8 Uncoupled normalized displacement shape of Column $C5$, from modal analyses

	Finite element analysis results		
Storey	$\Phi_{x,o}$	$\Phi_{y,o}$	$\Phi_{\theta,o}$
3	1.000	1.000	1.000
2	0.850	0.850	0.772
1	0.502	0.502	0.386

displacement envelope of the central column, $C5$, was determined and compared with the corresponding spatial mode shape obtained from 3-D finite element modal analysis. Table 8 presents the uncoupled drift shapes of column C5, as calculated from modal analyses:

Considering the uncoupled drift shapes of $C5$ and the building stiffness properties calculated along the $C5$ reference axis, the systems generalized stiffness properties are calculated from Eq. (10), as per:

$$K_x^* = K_y^* = 933731 \cdot 0.502^2 + 772620 \cdot 0.348^2 + 665213 \cdot 0.150^2 = 344,033\,\text{kN/m}$$

$$K_\theta^* = 99727308 \cdot 0.386^2 + 74541384 \cdot 0.385^2 + 59332992 \cdot 0.228^2 = 26267128\,\text{kNm/rad}$$

Table 9 Twist coefficients and determined first mode coupled drift shapes in x and y direction of $C5$ column

	Direction x			Direction y		
Storey	β_x	Ψ_x	Φ_x	β_y	Ψ_y	Φ_y
3	0.028	0.934	1.000	0.028	1.066	1.000
2	0.029	0.795	0.852	0.014	0.864	0.810
1	0.012	0.498	0.533	0.012	0.507	0.475

Table 10 First mode coupled drift shapes in x and y direction of C5 column, obtained from finite element modal analysis

Storey	Φ_x	Φ_y
3	1.000	1.000
2	0.886	0.823
1	0.560	0.479

The coupled translational components of the first mode along the vertical axis of $C5$ column are determined from Eqs. (7) and (8), by calculating in each floor the drift coefficients, β_x and β_y and adding the translational displacement due to twist in each of the two uncoupled translational displacement patterns. Note that in the case of buildings with a variable plan heightwise, the eccentricity factors in Eqs. (7) and (8) refer to the individual floor distance between the center of stiffness and the point of reference where the dof are defined in the analysis (here the nodes on C5). Table 9 summarizes the above procedure, whereas Table 10 presents the corresponding coupled translational drift components associated with the first mode as obtained by a finite element modal analysis of the three-dimensional building. Examination of these results, as well as the corresponding drift shapes of Fig. 11, confirms the adequacy of the proposed method.

4 Conclusions

In this chapter, the relationship between the fundamental mode shape and the displacement profile at maximum seismic response of torsionally sensitive R.C. structures was explored. For this purpose, a series of buildings with different structural systems and plan configurations were subjected to several elastic and inelastic analyses to a dataset of ten strong recorded earthquakes, from which five possessed near-fault characteristics and the resulting deformed shapes at the state of maximum seismic response were compared with those of the associated fundamental modes. From the results, it was clear that the shape of the principal translational- twisting mode of the tested structures matches well the displacement response distribution obtained after analyzing the structure to the earthquake records.

This result was deemed an important basis for the establishment of retrofit strategies, whereby at the preliminary stage, response may be improved by targeting for a fundamental mode shape that would produce a desirable pattern of interstorey drift

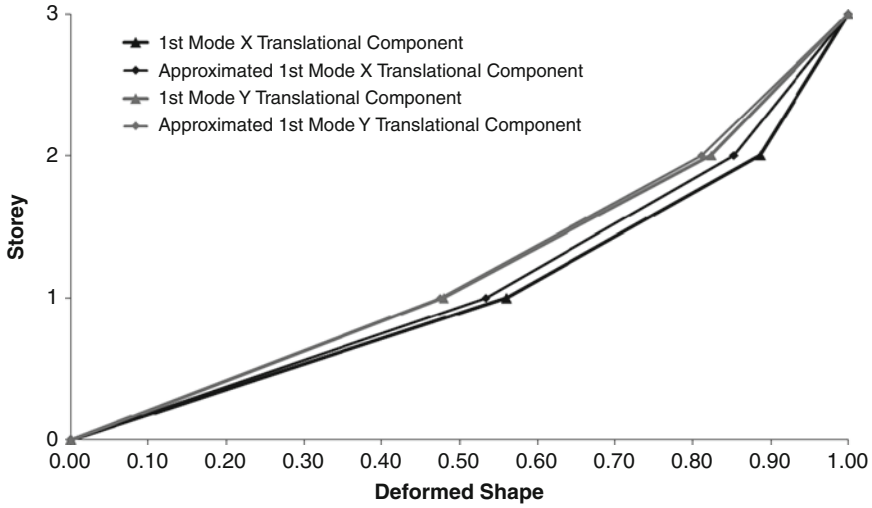


Fig. 11 First Mode translational drift shapes of C5 column, obtained from finite element modal analysis and application of the proposed methodology

and therefore damage. This concept had been developed for planar frames in the past. To extend this concept in three-dimensional structures with torsional component in their lateral response, a method to approximate the fundamental translational mode shape has been developed, by separating the contributions to translation and twisting from the corresponding basic modes of an associated decoupled system. This enables direct control over those stiffness terms responsible for the distribution of interstorey drift heightwise, from those responsible for the variation of interstorey drift between vertical members of a single floor (in-floor variability of drift which is owing to the twisting component). Thus it was possible to establish a reverse relationship between target mode shape and translational and rotational stiffness distribution in the present study, which forms the basic element of rehabilitation strategies of seismically deficient structures. The procedure is easily followed in the case of practical applications, regardless of the structure's geometric configuration. Also presented was a numerical example of the proposed methodology, whereby the adequacy of the procedure was demonstrated.

References

1. Alavi B, Krawinkler H (2004) Behavior of moment-resisting frame structures subjected to near-fault ground motions. Earthq Eng Struct Dynam 33:687–706
2. Bray JD, Rodriguez-Marek A (2004) Characterization of forward-directivity ground motions in the near-fault region, Soil Dynam Earthq Eng 24:815–828
3. COSMOS virtual data center, Consortium of organizations for strong motion observation systems. http://www.cosmos-eq.org

4. Eurocode 8 (2004) Design of structures for earthquake resistance. European Committee for Standardization, Brussels
5. OpenSees, Open System For Earthquake Simulation. Pacific Earthquake Engineering Research Center. http://peer.berkeley.edu/OpenSees
6. PEER SM Database, Pacific Earthquake Engineering Research Center Strong Motion Database. http://peer.berkeley.edu/smcat
7. Thermou GE, Pantazopoulou SJ, Elnashai AS (2007) Design methodology for seismic upgrading of substandard RC structures. J Earthq Eng 11(4):582–606
8. Thermou G, Elnashai A, Pantazopoulou SJ (2009), Retrofit Yield Spectra for the Seismic Upgrading of Existing R.C. Buildings, Session Keynote paper, CD ROM Proceedings, COMPDYN 2009, Rhodes, 22–24 June

Constitutive Modelling of Concrete Behaviour: Need for Reappraisal

Demetrios M. Cotsovos and Michael D. Kotsovos

Abstract The present article summarises the fundamental properties of concrete behaviour which underlie the formulation of an engineering finite element model capable of realistically predicting the behaviour of (plain or reinforced) concrete structural forms in a wide range of problems ranging from static to impact loading without the need of any kind of re-calibration. The already published evidence supporting the proposed formulation is complemented by four additional typical case studies presented herein; for each case, a comparative study is carried out between numerical predictions and experimental data which reveal good agreement. Such evidence validates the material characteristics upon which the FE model's formulation is based and provides an alternative explanation regarding the behaviour of structural concrete and how it should be modelled which contradicts the presently (widely) accepted assumptions adopted in the majority of FE models used to predict the behaviour of concrete.

Keywords Brittle behaviour · Concrete · Constitutive law · Short-term static and dynamic loading · Nonlinear finite element analysis · Structural concrete

1 Introduction

Most finite-element (FE) packages (e.g. ABAQUS, ADINA, LS-DYNA, etc.) that may be used for the analysis of concrete structures under a wide range of loading conditions, extreme loading conditions such as those encountered in impact and explosion situations inclusive, rely on the use of constitutive models which place emphasis on the description of post-peak concrete characteristics such as,

D.M. Cotsovos (✉)
Concept Engineering Consultants, 8 Warple Mews, Warple Way, London W3 0RF, UK
e-mail: dkotsovos76@yahoo.co.uk

M.D. Kotsovos
Laboratory of Concrete Structures, National Technical University of Athens, Greece
e-mail: mkotsov@central.ntua.gr

M. Papadrakakis et al. (eds.), *Computational Methods in Earthquake Engineering*, Computational Methods in Applied Sciences 21, DOI 10.1007/978-94-007-0053-6_7,
© Springer Science+Business Media B.V. 2011

for example, strain softening, tension stiffening, shear-retention ability, etc, coupled with stress- and/or strain-rate sensitivity when blast or impulsive types of loading are considered. The derivation of such constitutive models has been based on a variety of theories, including plasticity [1, 2], viscoplasticity [3–7], continuum damage mechanics [8–11] or a combination of these theories [12, 13].

However, the application of FE packages in practical structural analysis has shown that such constitutive relationships are case-study dependent, since the solutions obtained are realistic only for particular problems such as, for example, reinforced-concrete (RC) walls [1, 12, 14–16] and RC frames [17, 18] under earthquake loading, plain-concrete prisms or cylinders [2, 5, 6, 9, 19–21], RC beams [12], RC slabs [3] and RC plates [22] under impact loading, etc; in order to extend, therefore, the applicability of the packages to a different set of problems modifications, sometimes significant, of the constitutive relationships are required. The cause of the above apparent lack of generality is considered to mainly relate, on the one hand, to the misinterpretation of the observed material behaviour and, on the other, to the use of experimental data of questionable validity for the calibration of the constitutive relationships.

To this end, the aim of the present article is twofold: (a) to provide an indication of the concepts which are widely used for modelling concrete behaviour and (b) to summarise the main findings of already published work which has shown, not only that these concepts are incompatible with valid experimental data on concrete behaviour, but, also, that the analytical description of such data can lead to the development of a general and objective FE analysis package capable of yielding realistic predictions of the response of a wide range of plain and RC structural forms under static monotonic loading [23]. This package has recently been extended to static cyclic and dynamic (ranging from earthquake to impact) loading regimes [24] and formed the basis of ongoing research work on the behaviour of various structural RC members under such loading conditions; four typical case studies are extracted from this work and presented herein as further evidence of the validity of the material model which underlies the development of the FE package.

2 Concepts Underlying the Modelling of Structural Concrete

An indication of the concepts which underlie most methods currently used for the analysis (and the design) of concrete structures may be obtained by reference to the truss model shown in Fig. 1; this is the simplest form of truss widely used to represent the physical state of a simply supported beam-like RC element under transverse loading. In fact, such an element is considered to start behaving as a truss once inclined cracking occurs, with the compressive zone and the flexural reinforcement forming the longitudinal struts and ties, respectively, the stirrups forming the transverse ties, whereas the cracked concrete of the element web is assumed to allow the formation of inclined struts.

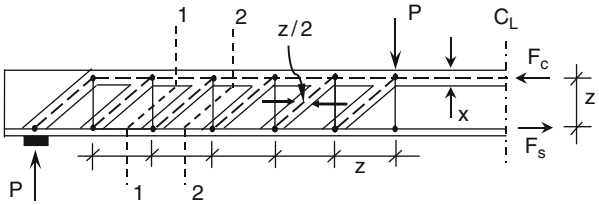


Fig. 1 Truss model of a beam-like RC element

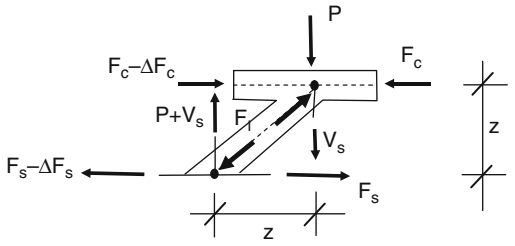


Fig. 2 Portion of truss in Fig. 1 between cuts 1-1 and 2-2

Adopting a truss model implies that the inclined struts and the transverse ties form the path along which the applied load is transferred from its point of application (at the truss-member joints at the upper face of the beam-like RC element) to the supports. The load transfer is effected as indicated in Fig. 2 which shows, in isolation, the portion of the truss between two successive cuts (1-1 and 2-2 in Fig. 1) on either side of an inclined strut: the resultant ΔF_c of F_c and $F_c - \Delta F_c$ (i.e. the forces developing within the horizontal strut due to bending of the beam-like RC element) combines with the external load P acting at the upper end of the inclined strut and the force V_s transferred to this end by the vertical tie, and, through the inclined strut, the resulting force F_I is transferred to the lower end of the strut, where its vertical component $(P + V_s)$ is transferred to the vertical tie at this end, while its horizontal component balances the action of the resultant ΔF_s of F_s and $F_s - \Delta F_s$ (i.e. the forces developing within the horizontal tie due to bending of the beam-like RC element). Through the vertical tie at the lower end of the inclined strut, $P + V_s$ is transferred to the upper end of the inclined strut adjacent to the one considered in the figure, and, in this manner, the load transfer continues until the applied load reaches the support.

A fundamental prerequisite for adopting a truss model for the description of the physical state of a beam-like RC element is for cracked concrete in the element web to allow the formation of inclined struts capable of contributing to the load transfer described above. Such a prerequisite implies strain softening material characteristics, since the behaviour of cracked concrete under any state of stress is described by the post-peak branch of stress–strain curves such as those shown in Fig. 3 [23]. Moreover, the formation of inclined struts implies load transfer across the faces of cracks, since it is inevitable for the directions of inclined struts and cracks to

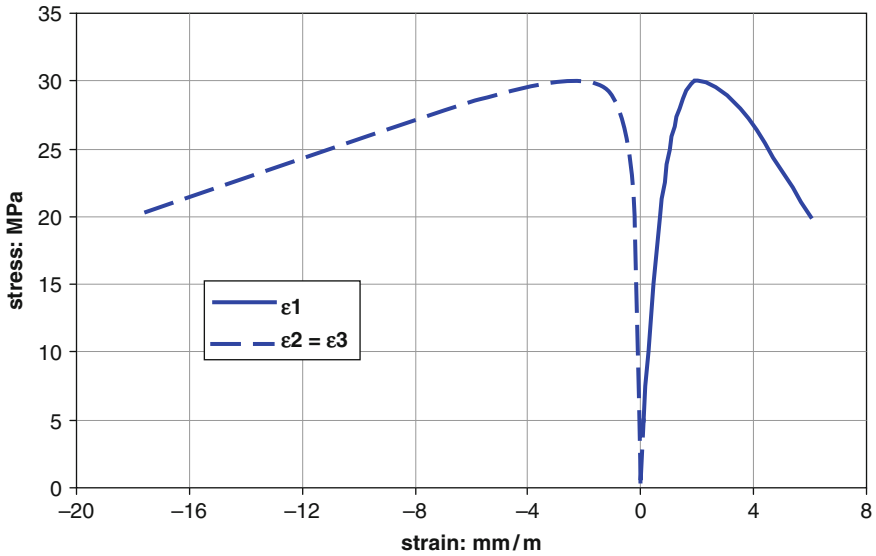


Fig. 3 Stress–strain curves established from tests on concrete cylinders in uniaxial compression applied through rigid steel platens without any means to reduce frictional restraint at the platen-specimen interface (ε_1 is the strain in the direction of the acting compression; ε_2, ε_3 are the strains at right angles to each other and to ε_1)

intersect as a result of the close spacing of the cracks forming within the web at the ultimate limit state of the element. Such a load transfer, however, further implies a shearing movement of the crack faces which is resisted by frictional forces developing on the crack faces.

Modelling the physical state of a beam-like RC element as a truss represents a typical case of modelling which reflects the deep-rooted belief that cracked concrete makes a significant contribution to the load-carrying capacity of a structural RC element. The means commonly adopted in order to impart a numerical scheme the capability of describing the above contribution take the form of a strain softening material law combined with a numerical model of the cracking processes which allows concrete to maintain part of its ability to resist a shearing movement after cracking. Such laws and models, however, are usually dependent on parameters which are evaluated through the use of experimental data and it is, in the authors. . . opinion, the choice and/or interpretation of the data used for this purpose the cause for the apparent lack of generality and objectivity that characterises most FE packages developed to date for the analysis of concrete structures. Generality and objectivity can only be achieved through the use of material models which are compatible with valid experimental information; in fact, the work presented herein is considered as a step into this direction.

3 Fundamental Concrete Properties

Brittle Post-peak Behaviour The experimental data on concrete behaviour used for the development of constitutive laws are obtained from tests on specimens such as, for example, cylinders, prisms, cubes, etc. Such specimens are subjected to various load combinations, usually applied (at least in one of the three principal directions) through rigid steel platens; the results obtained are expressed in the form of stress–strain curves which comprise a strain hardening branch followed (after the formation of cracks) by a strain softening one (see Fig. 3), the latter (as discussed in the preceding section) widely considered to be a fundamental material property. And yet, it has been known since the early 1980s [25, 26], and confirmed at the late 1990s [27], that only strain hardening may describe material behaviour under a definable state of stress; strain softening merely reflects the interaction between specimen and testing device, which, for the case of a predominantly compressive state of stress, is effected through the development of indefinable frictional stresses at the end faces of the specimen.

In fact, it has been shown that the rate of reduction of the residual concrete strength with increasing strain increases rapidly as the means to reduce the above frictional stresses becomes more effective (see Fig. 4) [25]; this rapid reduction of the residual strength indicates that were the frictional stresses completely eliminated, concrete would be characterised by a complete and immediate loss of load-carrying capacity as soon as the peak load level is attained. Such behaviour

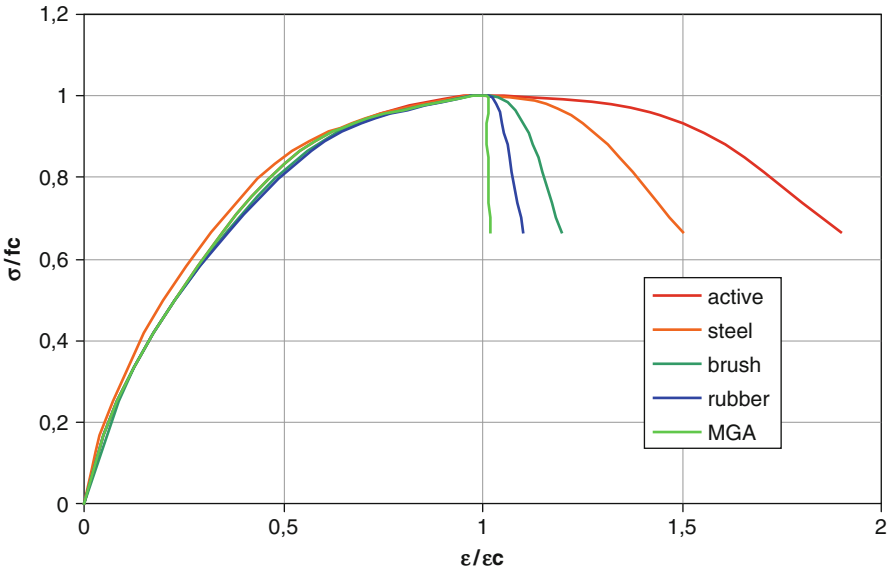


Fig. 4 Effect of means used to reduce friction at the platen-specimen interface on the axial stress–axial strain curve of concrete cylinders in uniaxial compression applied through rigid steel platens

sharply contrasts the assumption that a beam-like RC element can be modelled as a truss (as discussed in the preceding section), since the brittle nature of concrete does not allow the formation of inclined cracks within the cracked web of the RC element.

"Poisson's ratio" Effect The development of most constitutive relations of concrete behaviour published to date has been directly or indirectly based on the assumption of a constant value of the Poisson's ratio ($\boldsymbol{\nu}$) or that this important parameter takes values near failure that are considerably less than the true ones. However, such an assumption is in conflict with experimental data which show that $\boldsymbol{\nu}$ is essentially constant up to a value of the applied load equal to between approximately 30% and 50% of the peak load level; and that, beyond this load level, $\boldsymbol{\nu}$ increases at an increasing rate and attains a value that becomes significantly larger than 0.5 when the peak load level is reached (see Fig. 5) [28]. Such behaviour clearly indicates that concrete ceases to be a continuum beyond a load level close to, but not beyond, the peak load, a fact consistent with the material's brittle nature. And yet, all constitutive models adopted to date for the description of the strain softening behaviour of an essentially discontinuous material such as concrete are based on continuum mechanics theories.

The Significance of Small Transverse Stresses The dependence of $\boldsymbol{\nu}$ on the level of the state of stress results in values of the transverse expansion of concrete exhibiting a large variation within a structural RC element. For example, for the case of a beam-like RC element, the transverse expansion of the compressive zone at cross sections including deep primary flexural cracks is significantly larger than its counterpart at cross sections between two consecutive cross sections at locations of such cracks (see Fig. 6). The variation of the values of transverse expansion inevitably leads to the development of transverse stresses for deformation compatibility purposes. Although the size of these stresses is admittedly small, their effect on both the

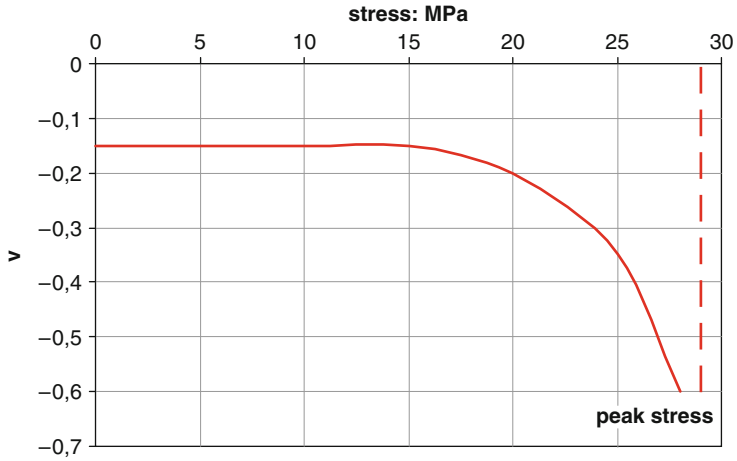


Fig. 5 Variation of the Poisson's ratio ($\boldsymbol{\nu}$) with increasing stress

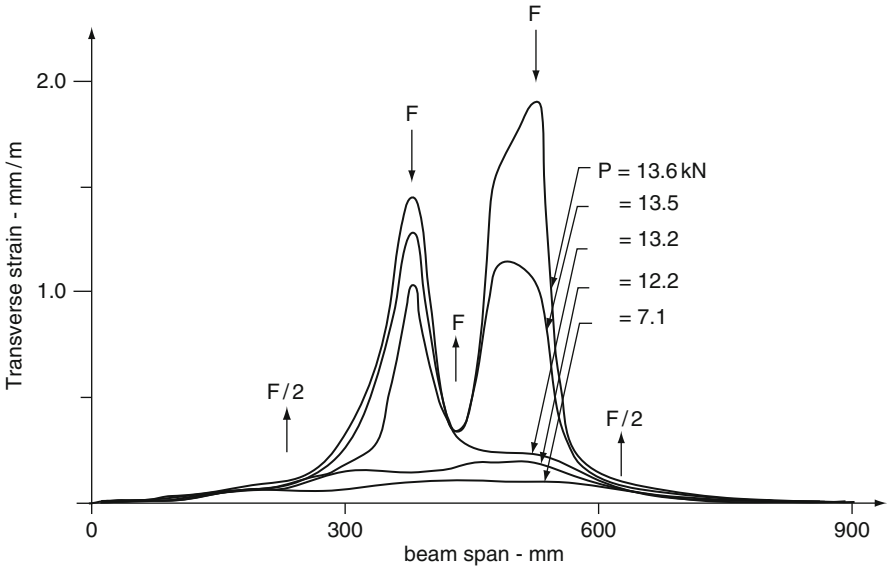
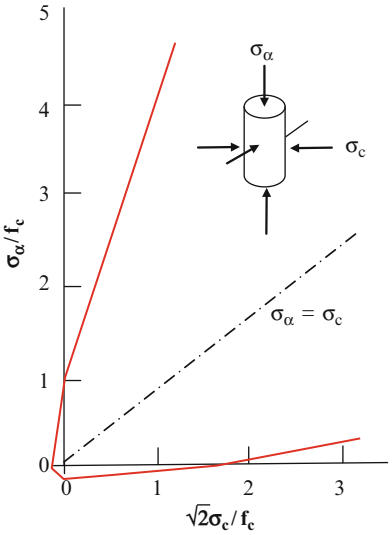


Fig. 6 Transverse expansion of compressive zone, with large strains corresponding to cross sections including primary flexural cracks (F: internal stress resultants developing for transverse deformation compatibility purposes; P: applied load)

Fig. 7 Effect of transverse stresses on concrete strength in axial direction



strength and the deformation of concrete is significant: small transverse stresses of the order of 10% f_c (where f_c is the uniaxial cylinder compressive strength), when compressive, can nearly double the strength of concrete in the orthogonal direction, and, when tensile, they may reduce it to zero (see Fig. 7). Hence, the presence of

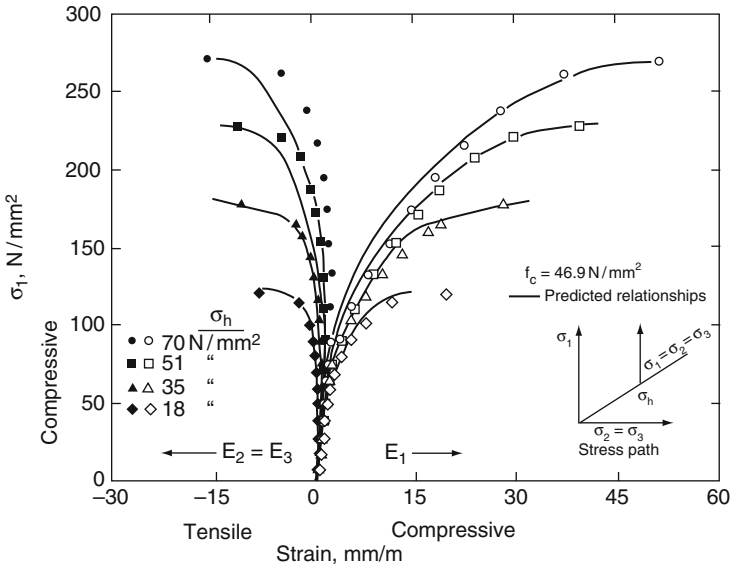


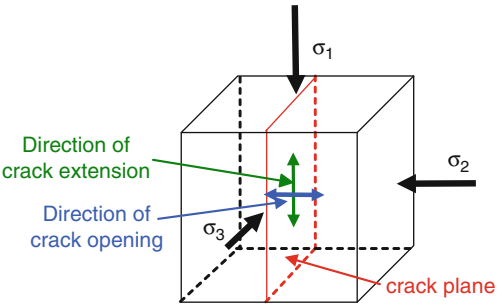
Fig. 8 Effect of transverse stresses on concrete deformation

small transverse stresses cannot be ignored. In fact, the large strains measured at the extreme compressive fibre of a beam-like RC element in flexure is due to the development of the above small transverse compressive stresses (see Fig. 8) rather than due to strain softening characteristics as widely considered [23].

Cracking Cracking occurs in localised regions of a structural RC element when the material strength is attained. The crack faces coincide with the plane of the maximum and intermediate principal stresses (assuming compression as positive) and opens in the orthogonal direction (i.e. in the direction of the minimum principal compressive stress or maximum principal tensile stress), whereas its extension occurs in the direction of the maximum principal stress (see Fig. 9) [23]. Such a cracking mechanism precludes any shearing movement of the crack faces and, therefore, contrasts widely assumed mechanisms of shear resistance such as, for example, those of aggregate interlock and dowel action, which can only be mobilised through the "shearing" movement of a crack's faces. As for the case of brittle material behaviour, such a cracking mechanism sharply contrasts the assumption that a beam-like RC element can be modelled as a truss (as discussed in the preceding section), since the lack of a shearing movement precludes the development of frictional forces at the crack faces and, as a result, the formation of inclined struts within the cracked web of the RC element is not possible.

Stress Path Independency The behaviour of concrete under increasing load may be expressed in the form of the relationships between normal and shear octahedral stresses (σ_o and τ_o) and strains (γ_o and ε_o) shown in Fig. 10. The figure shows that, while only ε_o varies with σ_o under hydrostatic stress, under deviatoric stress both γ_o and ε_o vary with τ_o [23]. More importantly, however, it has been shown experimentally that, under short-term loading conditions, the relationships are essentially

Fig. 9 Cracking mechanism



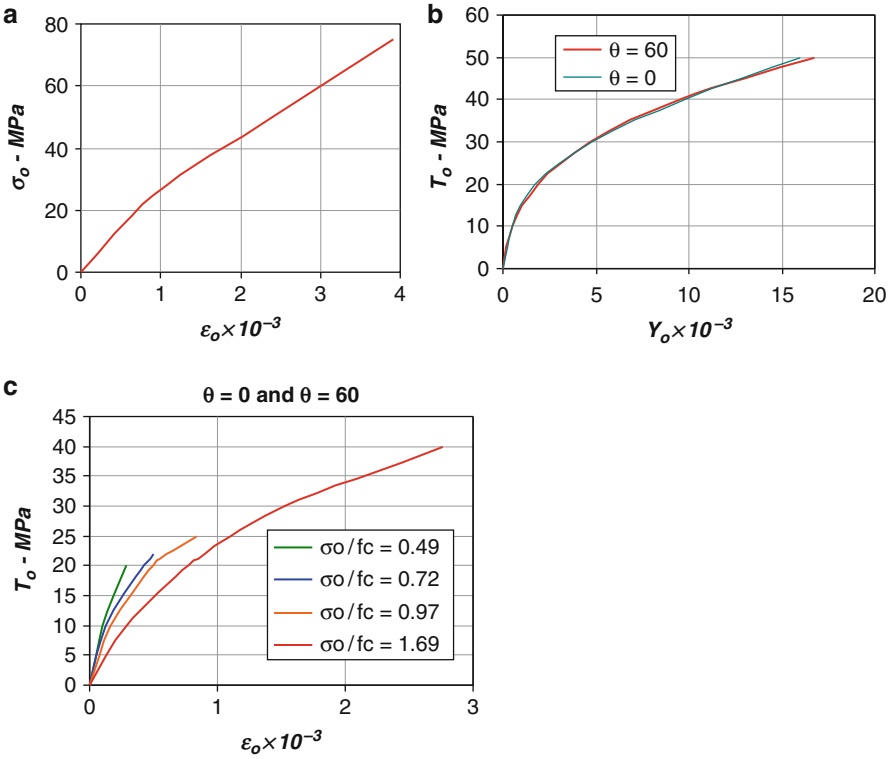


Fig. 10 Effect of stress path on the relationships between (**a**) σ_o and ε_o; (**b**) τ_o and γ_o; and (**c**) τ_o and ε_o

independent of the stress path adopted for the tests [23]. In fact, Fig. 10 indicates that the curves established experimentally by following two stress paths with $\theta = 60°$ ($\sigma_1 \geq \sigma_2 = \sigma_3$) and $\theta = 0°$ ($\sigma_1 = \sigma_2 \geq \sigma_3$) are essentially identical. A similar conclusion has also been drawn from the experimental data on concrete strength shown Fig. 11 which shows that the difference between the strength envelopes established for stress paths 1 and 2 disappears within the scatter of the experimental data [23].

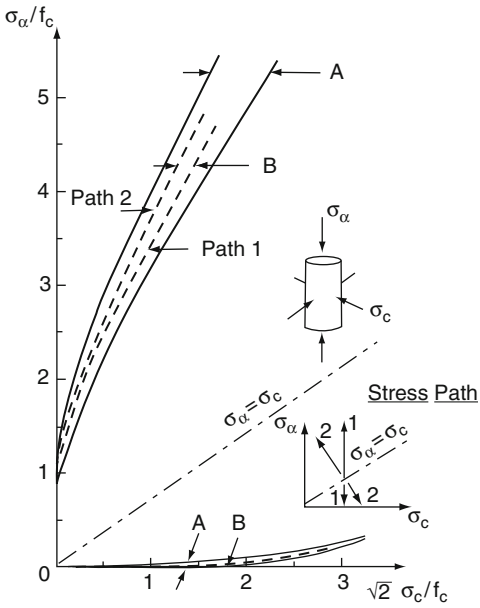


Fig. 11 Effect of stress path on strength envelope

Loading-Rate Independency The vast majority of existing constitutive models used for describing the behaviour of concrete under high rates of loading are based on the assumption that there is a link between the mechanical properties of concrete and the rate at which the loading is imposed ("loading-rate sensitivity"). However, it has recently been suggested that loading-rate sensitivity is based on an uncritical interpretation of the available experimental data, the latter describing structural, rather than material, response [24]. In the present work, the mechanical properties of concrete are considered to be independent of the loading rate, with the effect of the latter on the specimen behaviour being primarily attributed to the inertia effect of the specimen mass: this simple (and, arguably, obvious – though, at present, unorthodox) postulate was the subject of a numerical investigation which proved it capable of reproducing the experimental data available from past tests [24]. Moreover, this numerical investigation confirmed the importance and significance of the role that inertia plays in the specimen's response when subjected to high rates of loading.

4 Use of Concrete Properties in Finite-Element Analysis

4.1 Constitutive Law of Concrete Behaviour

A constitutive law of concrete behaviour (fully defined by a single material parameter - the uniaxial cylinder compressive strength f_c) with the characteristics described above is presented in detail in Ref. [23], and, therefore, it is only briefly discussed in the following.

Stress–Strain Behaviour Its analytical formulation has been based on an analysis of triaxial experimental stress–strain data expressed in the form octahedral normal and shear stresses (σ_o, τ_o) and strains (ε_o, γ_o). The variations of the secant and tangent values of the bulk modulus, $K_S = \sigma_o/\varepsilon_o$ and $K_T = d\sigma_o/d\varepsilon_o$, respectively, with σ_o may easily be established from $\sigma_o - \varepsilon_o$ curves (such as those shown in Fig. 10b) and expressed in the form graphically represented in Fig. 12a. Similarly, the variations of the secant and tangent values of the shear modulus, $G_S = \tau_o/\gamma_o$ and $G_T = d\tau_o/d\gamma\varepsilon_o$, respectively, with τ_o may easily be established from $\tau_o - \gamma_o$ curves (such as those shown in Fig. 10a) and expressed in the form graphically represented in Fig. 12b. In Fig. 12a and b, both modulae are normalised with respect to their tangent values (K_e and G_e) at the origin of the stress–strain curves, the latter values being essentially the elastic values, which have been shown to adequately describe material behaviour during unloading [23]. Moreover, the variation of ε_o with τ_o for a given σ_o (see Fig. 10c) – expressing the coupling between the hydrostatic and deviatoric components of stress and strain – is transformed into the variation of an *internal hydrostatic stress* σ_{int} with τ_o for a given σ_o, which is shown in Fig. 12c [23]. Stress σ_{int}, which represents the reduction caused by cracking to the internal tensile stresses, only develops during loading, as unloading does not cause any cracking and hence $\sigma_{int} = 0$.

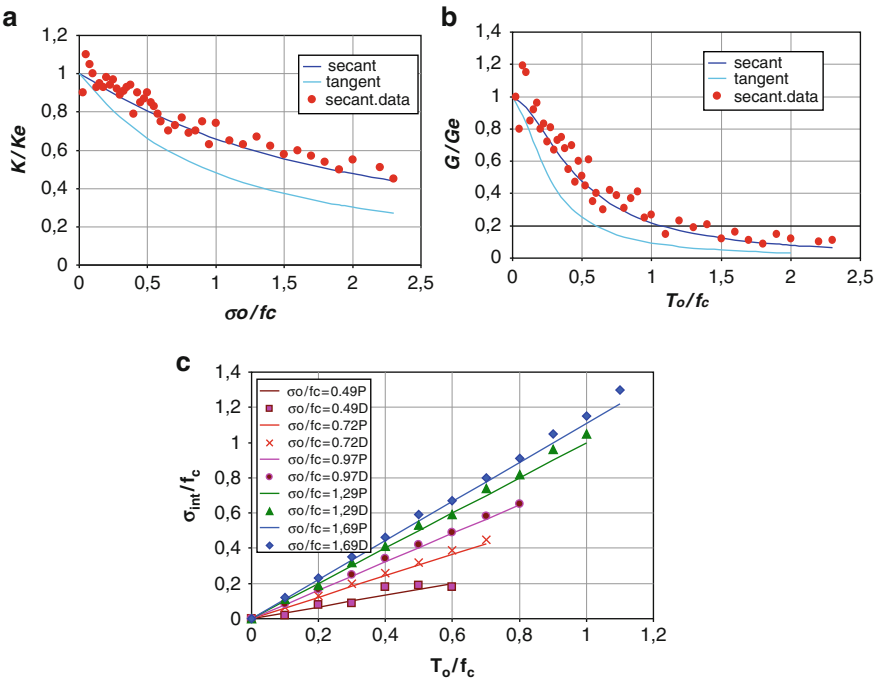


Fig. 12 Variations of: (**a**) secant (K_S) and tangent (K_T) values of the bulk modulus with σ_o; (**b**) secant (G_S) and tangent (G_T) values of the shear modulus with τ_o; and (**c**) internal stress state σ_{int} with σ_o and τ_o

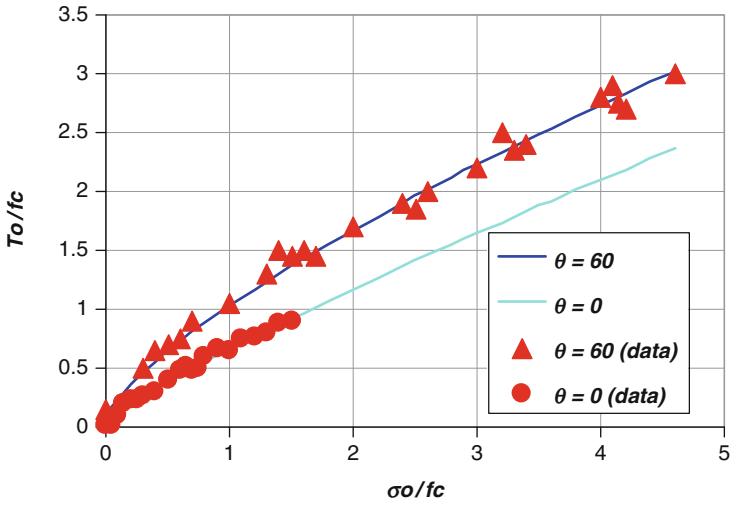


Fig. 13 Strength surface meridians corresponding to $\theta_o = 0°$ and $\theta_o = 60°$

Having expressed $K_S(K_T)$ and $G_S(G_T)$ as functions of σ_o and τ_o, respectively, and σ_{int} as a function of σ_o and τ_o, the strains corresponding to a given state of stress are easily obtained from Hooke's law by adding σ_{int} to σ_o [23].

Failure criterion: As for the case of the deformational properties, the analytical description of the failure criterion (strength surface) has also been based on a regression analysis of valid experimental data expressed in the form indicated in Fig. 13. Such data were used for the analytical description of the strength surface meridians corresponding to $\theta = 0°$ and $\theta = 60°$ and graphical representations of the resulting expressions are also shown in Fig. 13 [23]. For meridians corresponding to a value of the rotational variable θ between 0° and 60° the interpolation function derived by Willam and Warnke [29] may be used.

Cracking (Localised Failure) When the stress state at a given part of the structure corresponds to a point in stress space that lies outside the strength surface defined above, the material suffers localised failure which takes the form of a crack. In accordance with the cracking mechanism discussed in Sect. 3, failure is followed by immediate and complete loss of both load-carrying capacity perpendicularly to the crack plane and shear stiffness in the direction of crack extension: however, while the former is set to zero, the latter is reduced to a small percentage (1%) of its previous value, rather than set to zero, in order to minimize the risk of numerical instabilities. Crack formation is modelled by using the smeared-crack approach, with the cracks forming at Gauss points where the evaluation of the stresses takes place. Because of this, although each crack that forms corresponds to an actual crack in the structure, its effect spreads throughout the area that is associated with that Gauss point.

As the external load continues to increase, the stresses and strains acting at the location of a crack may lead to the formation of the new crack, and thus the problem

is reduced from a two-dimensional to a one-dimensional one, with the remaining stresses being the nominal stresses acting in the direction of the intersection of the two cracks. Finally, it is possible for a third crack to form, and, in this case, the corresponding Gauss point is considered to no longer be able to undertake any load, since it has practically suffered a total loss of stiffness (apart from shear stiffness which, for the reasons discussed above, has been given a very small value).

4.2 Constitutive Law for Steel Bars

The constitutive model used to describe the behaviour of steel reinforcement uses the simple form indicated in Fig. 14, where the stress–strain curve describes the behaviour of a steel bar under uniaxial compression or tension. It is divided into three linear sections. In each one of these sections, the material properties remain

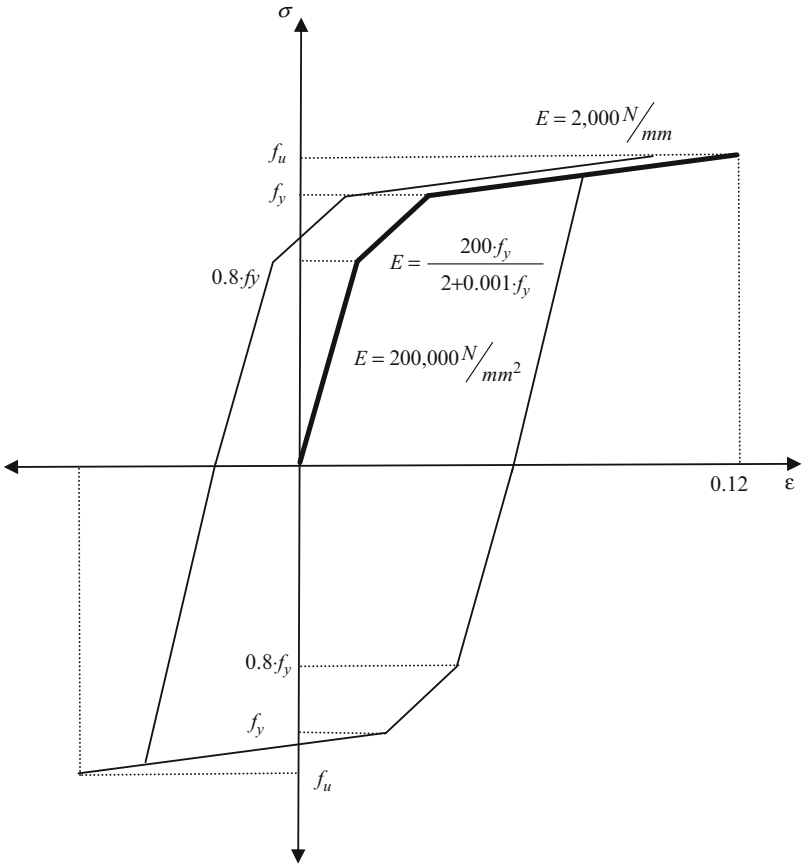


Fig. 14 Graphical representation of constitutive model for steel reinforcement

constant. The first and second sections of the stress–strain diagram are defined by the yield stress. The third section starts from the point where the stress is equal to the yield stress f_y and has a very small inclination, usually 1% of the slope of the first elastic section. As a result, small increases in stress cause large increases in strain. The steel-reinforcement fails when the strain attains its ultimate value ε_u. Figure 14 also depicts how load reversals can be accommodated by the stress–strain relations adopted for the reinforcement bars.

4.3 Concrete-Steel Interaction

It is considered that the concrete-steel interaction is adequately described by the assumption of perfect bond. The key argument for adopting this assumption is that the tensile strength of concrete is significantly lower than the value of the shear stress that causes bond failure on the basis of experimental evidence cited in Ref. [23], and, hence, the formation of a crack due to tensile failure of concrete will occur before the maximum shear stress predicted by any of the bond-slip laws adopted to date is attained.

5 Implementation in FE Analysis

The implementation in structural analysis of the constitutive laws of concrete, steel and their interaction with the above characteristics was achieved through the development of a finite-element (FE) package that is briefly described herein as its full details may be found elsewhere [23, 24, 30, 31]. This package, used in the past to predict the nonlinear behaviour of a wide range of RC structural forms under static monotonic loading [23], has now been extended to dynamic problems [24]. Its development has been based on a strategy which has been focused into minimising – if not eliminating – the likelihood of numerical instabilities associated with the brittle nature of concrete and has the following characteristic features:

- *Decision on loading or unloading*: The criterion for loading or unloading is checked at each integration point only once within each load step, at the start of the first iteration.
- *Separation of the processes of crack formation and crack closure*: Either the criterion for crack formation or that for crack closure is checked within a particular iteration.
- *Single crack formation or closure*: Only one crack (or at least a prescribed number cracks) is allowed to form or close within an iteration.

In spite of the restrictive nature of the above features, any inaccuracies that may result from their implementation in structural analysis is considered to be offset by the dramatic reduction in the likelihood of numerical instabilities. Moreover,

the third of the above features may be thought to have a physical meaning in that it allows for the effect of an existing crack (or crack pattern) on the subsequent cracking process.

The solution of dynamic problems is based on an implicit scheme, usually associated with problems with a longer duration, such as the earthquake problems, and the unconditionally stable average acceleration method [32]. The nonlinear dynamic problem (outlined in a simplified form in Fig. 15) is viewed as a sequence of equivalent static problems. At the beginning of each iteration and based on the values of displacement, velocity and acceleration obtained from the previous iteration, the effective stiffness and load matrices are calculated (from Eqs. (3) and (4)

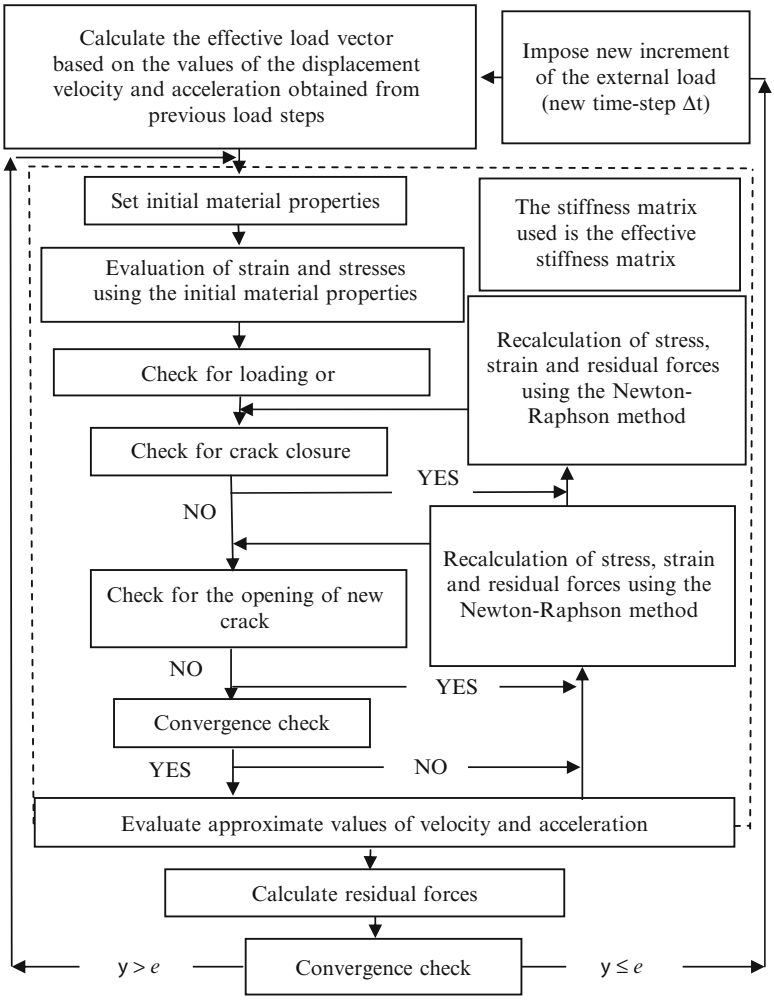


Fig. 15 Nonlinear iterative procedure

in Sect. 5.1) and an equivalent static problem is formulated. The solution process adopted for the equivalent static problem (described within the space enclosed by the dotted line in Fig. 15) is an iterative procedure on its own and its formulation is based on the Newton Raphson technique – suitably modified (as described in Sect. 5.2) so as to allow for the implementation of the proposed strategy – also used when dealing with static problems.

During the solution process of the equivalent static problem every Gauss point is checked, at first, in order to determine whether loading or unloading takes place, and then in order to establish whether any cracks close or form. Depending on the results of the previous checks, changes are introduced to the stress–strain matrices of the individual FE's and, consequently, to the stiffness matrix of the structure. Based on these modified matrices, deformation, strain and stress corrections are evaluated. During this process convergence is checked locally at each gauss point; this involves the use of the constitutive relations for the calculation of the stress increments which correspond to the estimated values of the strain increments. Once the values of the strain and the corresponding stress increments become less than a small predefined value then convergence is accomplished; on the other hand, when this is not achieved, the residual stresses are used to calculate the residual forces which are then re-imposed onto the FE mesh used to model the RC form investigated until convergence is finally achieved.

Once convergence is accomplished for the case of the equivalent static problem and based on the values of displacement increments evaluated, the values of the velocity and acceleration are corrected. At this stage, and making use of the equation of motion (Eq. (2) in Sect. 5.1), convergence is now checked at each node of the FE mesh. If an imbalance exists between the internal and external actions then this imbalance takes the form of a residual load which is re-imposed onto the structure. This results in the formulation of a new equivalent static problem and the repetition of the procedure described above.

The characteristic features of the procedure outlined above are as follows.

5.1 Numerical Solution of the Equation of Motion

Within the framework of the FE method and through the use of the Newmark family of approximations [32], the equation of motion

$$M \cdot \ddot{u}(t) + C \cdot \dot{u}(t) + K(t) \cdot u(t) = F_{ext}(t) \tag{1}$$

where M, C and K the element mass, damping and stiffness matrices; u, $\dot{u}$ and $\ddot{u}$ the displacement, velocity and acceleration matrices; and F_{ext} the applied load.

is transformed into its static equivalent

$$K^* \cdot \Delta u = \Delta F^* \tag{2}$$

with $\Delta u = {}^{t+\Delta t}u^{i+1} - {}^{t}u$ the incremental change of displacement at $t + \Delta t$ at iteration $i + 1$, whereas K^*, the effective stiffness, and ΔF^*, the effective load vector, are given by

$$K^* = M \cdot \frac{1}{\beta \cdot \Delta t^2} + C \cdot \frac{\gamma}{\beta \cdot \Delta t} + K \tag{3}$$

$$\begin{aligned}\Delta F^* = \Delta F + C \cdot \Bigg[& \frac{\gamma}{\beta \cdot \Delta t^2} \left({}^{t}u - {}^{t-\Delta t}u \right) + \left(\frac{\gamma}{\beta} - 1 \right) \left({}^{t}\dot{u} - {}^{t-\Delta t}\dot{u} \right) \\ & + \Delta t \cdot \left(\frac{\gamma}{2\beta} - 1 \right) \cdot \left({}^{t}\ddot{u} - {}^{t-\Delta t}\ddot{u} \right) \Bigg] + M \cdot \Bigg[\frac{1}{\beta \cdot \Delta t^2} \left({}^{t}u - {}^{t-\Delta t}u \right) \\ & + \frac{1}{\beta \cdot \Delta t} \left({}^{t}\dot{u} - {}^{t-\Delta t}\dot{u} \right) + \left(\frac{1}{2 \cdot \beta} - 1 \right) \cdot \left({}^{t}\ddot{u} - {}^{t-\Delta t}\ddot{u} \right) \Bigg]\end{aligned} \tag{4}$$

where i the number of the iteration; γ, β the Newmark constants (for the unconditionally stable solution adopted $\beta = 1/4$ and $\gamma = 1/2$ (Bathe 1996)); ${}^{t}u$ and ${}^{t-\Delta t}u$, ${}^{t}\dot{u}$ and ${}^{t-\Delta t}\dot{u}$, and ${}^{t}\ddot{u}$ and ${}^{t-\Delta t}\ddot{u}$ the values of displacement, velocity and acceleration predicted in two previous time steps Δt [32].

Equation (2) can be easily solved, the change in displacement that occurs during iteration $i + 1$ is readily defined, and from this the values of stresses and strains also follow.

It should be noted that the damping forces ($F_d = C \cdot \dot{u}$) are not explicitly used, as it is considered that the action of F_d is taken into consideration by the constitutive models adopted for the description of the nonlinear behaviour of the materials. Moreover, since, in contrast with its stability, the accuracy of the solution obtained is dependent on the size of the time step, it is considered that one-tenth of the period that corresponds to the largest eigenvalue (frequency) of the structure investigated may be selected as an initial value in a series of test runs, each time using a smaller time step, until the solutions obtained converge.

5.2 Nonlinear Procedure

The proposed strategy was implemented into the nonlinear analysis so as to form part of an iterative procedure based on the Newton–Raphson method. The total load is imposed incrementally, with each load increment being up to approximately between 5% and 10% of the estimated ultimate load of the structure. Once the load increment is imposed, the iterative procedure commences. At first, every Gauss point is checked in order to determine whether loading or unloading is taking place. Then, a number of checks are carried out to determine if any cracks close or open, or if any steel members yield or even fail. Depending on the results of the previous checks, changes are introduced to the stress–strain matrices D of the individual FE's and, consequently, to the stiffness matrix K of the structure. Based on these modified matrices, deformation, strain and stress corrections are evaluated. Convergence

is accomplished once the above corrections become very small. The scheme used to carry out the above tasks is described in detail elsewhere [24], with the procedure used to take into consideration the nonlinear behaviour of the materials involved being summarized within the space enclosed by the dotted line in Fig. 15. Crucial for avoiding numerical instabilities are the procedures adopted for the closure and formation of cracks outlined in the following:

Crack Closure Procedure During this procedure only Gauss points with cracks formed in previous load steps are checked. In the course of each iteration, the program singles out the crack with the largest compressive strain normal to its plane and closes it. It has been observed that, after the closure of one crack, there is usually a drastic drop in the number of cracks that need to close next. Because of the closure of a crack, changes need to be made to the element stress–strain matrix and, consequently, to the stiffness matrix of the structure, leading to redistribution of the stresses inside the structure. It should be noted that, during the crack-closing procedure, convergence is not checked. This means that the residual stresses and forces are not eliminated during this stage of the iterative procedure but are only calculated and added to those calculated in previous iterations. The crack-closure procedure is repeated until all cracks that fulfil the crack-closure criterion close.

Crack Formation This procedure commences after the completion of the crack-closure procedure. During each iteration of this procedure, all Gauss points are checked in order to determine if any new cracks form. In order to avoid numerical instabilities during the solution of the problem, only a limited number of cracks (no more than three) are allowed to form per iteration. Should the number of cracks that need to open exceed this predefined number, then only the most critical cracks will be allowed to form. As for the case of crack closure, after the formation of the most critical cracks the number of cracks that need to form in the next iteration reduces rapidly due to the redistribution of stress achieved during this process. The formation of a crack leads to the modification of the element stress–strain matrix and the stiffness matrix of the structure, thus causing redistribution of the internal stresses. Unlike the crack-closure procedure, convergence of the residual forces is now checked after all cracks have opened. If the maximum value of the residual forces evaluated is greater than a certain predefined value, then these residual forces are re-imposed onto the structure in the form of an external loading.

5.3 FE Modelling

Concrete is modelled by using 20-node isoparametric or 27-node Lagrangian brick elements whereas, for steel reinforcement, a 3-node isoparametric truss element is adopted. With the use of these elements a mathematical representation of the structure can be achieved with all its essential characteristics, such as geometrical data, material properties and boundary conditions, being contained in matrix form in Eq. (2), in which the effective stiffness matrix K^* connects the external effective loads ΔF^* imposed with the incremental change of displacement Δu.

As regards the mesh size used, the finite elements adopted are kept to sizes such that the space corresponding to a Gauss point is at least two times the size of the maximum aggregate of the concrete used. This is compatible with the investigation stemming from cylinder samples tested for material properties so that the assumption of isotropy is acceptable from an engineering view point [24].

6 FE Predictions of Structural-Concrete Behaviour

The validity of the above nonlinear FE package has been verified by comparing the numerical predictions with experimental data obtained from tests on a wide range of structural members subjected to various regimes of static and dynamic loading. Full details of these comparative studies are given elsewhere [23, 24, 30, 31, 33]. An indication of the predictive capabilities of the package is provided in the following by complementing the above comparative studies with four additional ones, which form part of ongoing research projects on the behaviour of typical structural RC members under loading regimes varying from short-term static to dynamic and short-term static to periodic.

6.1 Hinged Beam Under Static Monotonic Loading

The beam selected for the present case study is the hinged beam C2 tested by Hughes and Speirs [34], since, as discussed in Sect. 5.2, similar beams have also been tested under impact loading. The beam, with a clear span of 2,700 mm and a rectangular cross-section 200 (height) × 100 mm (width), was reinforced with two 12 mm diameter compression bars, two 6 mm diameter tension bars, and 6 mm diameter stirrups at an approximately 180 mm centre-to-centre spacing (see Fig. 16 (top)). The modulus of elasticity (E_S), yield stress (f_y), and ultimate strength (f_u) of both the longitudinal and transverse reinforcement bars used are 206 GPa, 460 MPa and 560 MPa, respectively, with the cylinder compressive strength (f_c) of the concrete used being approximately 45 MPa.

The beam was subdivided into 20 brick elements as shown in Fig. 16 (*bottom*). The line elements representing the steel reinforcement were placed along successive series of nodal points in both vertical and horizontal directions. Since the spacing of these line elements was predefined by the location of the brick elements' nodes, their cross-sectional area was adjusted so that the total amount of both longitudinal and transverse reinforcement to be equal to the design values.

The external load was applied in the form of displacement increments at mid span and the main results obtained are presented in Fig. 17, which shows a close correlation between the predicted load-displacement curve and its experimentally-established counterpart.

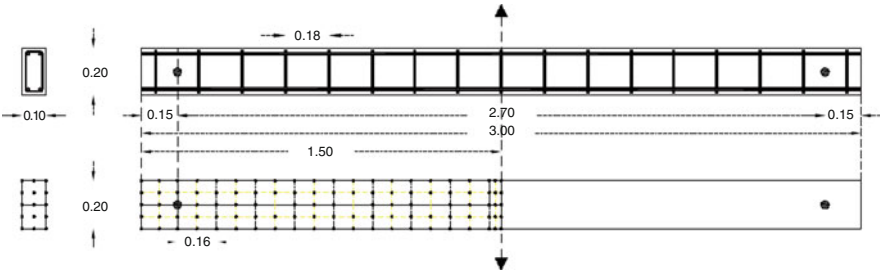


Fig. 16 Design details (*top*) and FE model (*bottom*) hinged beams

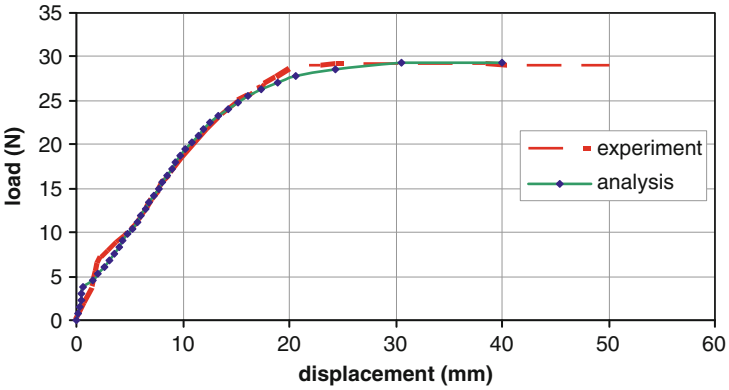


Fig. 17 Experimental and analytical load-deflection curves of beams in Fig. 16 under static monotonic point loading

6.2 Hinged Beam Under Impact Loading

As discussed in the preceding section, beam C2 is typical of a number of beams tested under loading applied at rates which vary from 1 kN/s (static loading) to 10^7 kN/s (impact loading). For the case of impact loading, the load was applied by means of a steel mass left to fall onto the specimen from a certain height, depending on the desired rate of loading [34]. From the measured response, the beam's behaviour is characterised by an increase in load-carrying capacity with increasing loading rate (see Fig. 18). However, it is interesting to note in Fig. 18 the very large scatter exhibited by the test data. The cause of this scatter appears to predominantly reflect the difficulty in establishing experimentally the specimen load-carrying capacity under impact loading, with most values indicated in the figure usually exceeding the "true" load-carrying capacity by a significant margin. Hence, the trends of behaviour described by data such as those in the figure can only provide a qualitative, rather than quantitative, description of structural behaviour.

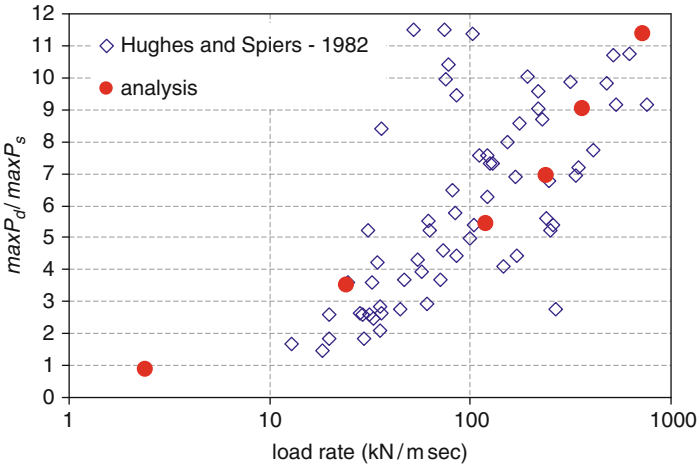


Fig. 18 Experimental and predicted variations of the $maxP_d/maxP_s$ ratio with the rate of loading (where $maxP_d$ and $maxP_s$ are the values of load-carrying capacity under dynamic and static, respectively, loading)

As for the case of static loading, the FE mesh adopted for the analysis is that depicted in Fig. 16, with the results obtained being also presented in Fig. 18, which shows that the analysis is capable of predicting trends of behaviour similar to those experimentally established.

6.3 Beam-Column Joint Under Cyclic Loading

The present case has been extracted from a research programme concerned with an investigation of the validity of the methods currently used to design beam-column joints [35]. It involves an analytical study of the behaviour of one (designated as A2) of the beam-column joint specimens tested under cyclic loading by Shiohara and Kusuhara [36] (see Fig. 19). The specimen was designed so as to exhibit overstrength of the beam-column joint, with the beam attaining its flexural capacity before the column; as a result, the storey shear was expected to reach its peak value when the beam attained its flexural capacity.

The design details of the specimen are shown in Fig. 20. The longitudinal reinforcement in both the beams and the columns comprises 13 mm diameter bars (D13) with a nominal cross sectional area of 139 mm^2 and a yield stress (f_y) of 456.4 MPa, in the beams, and 356.9 MPa in the columns. For both beams and columns, the transverse reinforcement comprises 6 mm diameter stirrups (D6) (nominal cross-sectional area of 32 mm^2 and yield stress of 325.6 MPa) with a spacing of 50 mm. The mean cylinder compressive strength of concrete was 28 MPa. Full design details together with a comprehensive description of the mechanical properties of the

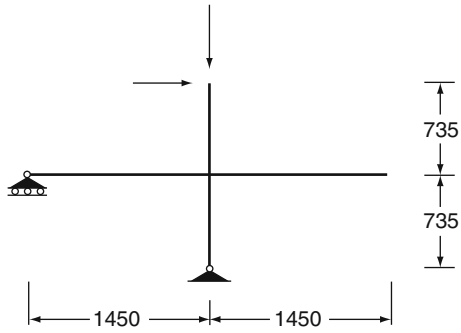


Fig. 19 Beam-column joint element investigated

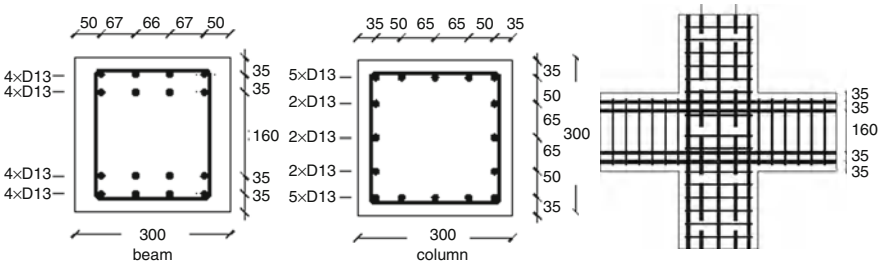


Fig. 20 Design details of beam-column joint element

materials used is provided elsewhere [36]. At the location shown in Fig. 19, the specimen was subjected to the combined action of a constant axial load equal to 216 kN and a lateral displacement which was progressively increased in a cyclic manner to failure.

The beam-column joint was subdivided into 48 elements as shown in Fig. 21. The load was applied through a steel prismatic element monolithically connected to the upper end face of the column element; this steel element was subdivided into $2 \times 1 \times 1 = 2$ brick FE elements, as indicated also in Fig. 21. The line elements representing the steel reinforcement were placed along successive series of nodal points in both vertical and horizontal directions. Since the spacing of these line elements was predefined by the location of the brick elements' nodes, their cross-sectional area was adjusted so that the total amount of both longitudinal and transverse reinforcement to be equal to the design values.

The results of the analysis, expressed in the form of a storey shear vs. drift ratio relationship, are shown in Fig. 22, which, for purposes of comparison, also includes the experimentally-established story shear vs. drift ratio relationship. Although the analysis method adopted does not allow for P-Δ effects (which are clearly present in the case investigated), Fig. 22 indicates that the correlation between analytical and experimental results is realistic, with the area enclosed by the hysteretic loops of the analytically predicted storey shear-drift ratio curve being similar with its experimentally established counterpart.

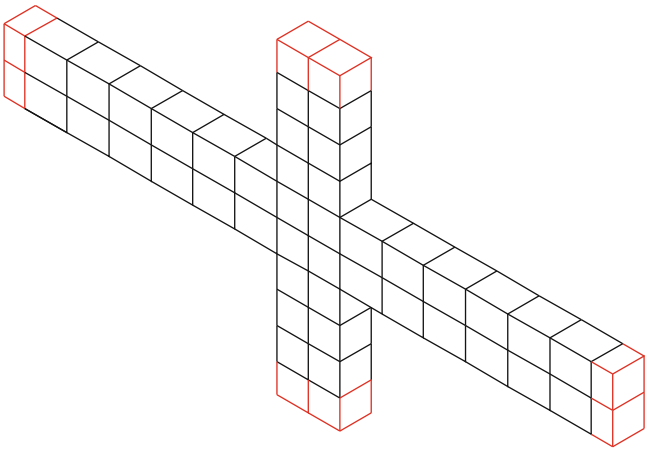


Fig. 21 FE model adopted for the analysis of the beam-column joint element

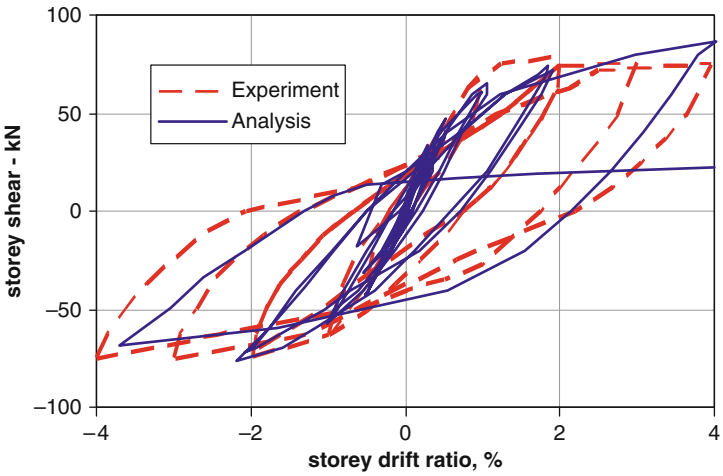


Fig. 22 Experimental and analytical storey shear vs. storey drift ratio curves for the beam-column joint element investigated (storey drift ratio is the ratio of the horizontal displacement of the loaded point to the length of the vertical member of the specimen in Fig. 19)

6.4 Three-Storey Structural Wall Under Seismic Excitation

Full details of the specimen and the test arrangement are provided elsewhere [37]. The RC wall had a cross-section of 900 × 100 mm and a height of approximately 4 m. The wall corresponds to a three-story building and along its height three 12 ton masses were attached to it at approximately 1.36 m intervals as schematically shown

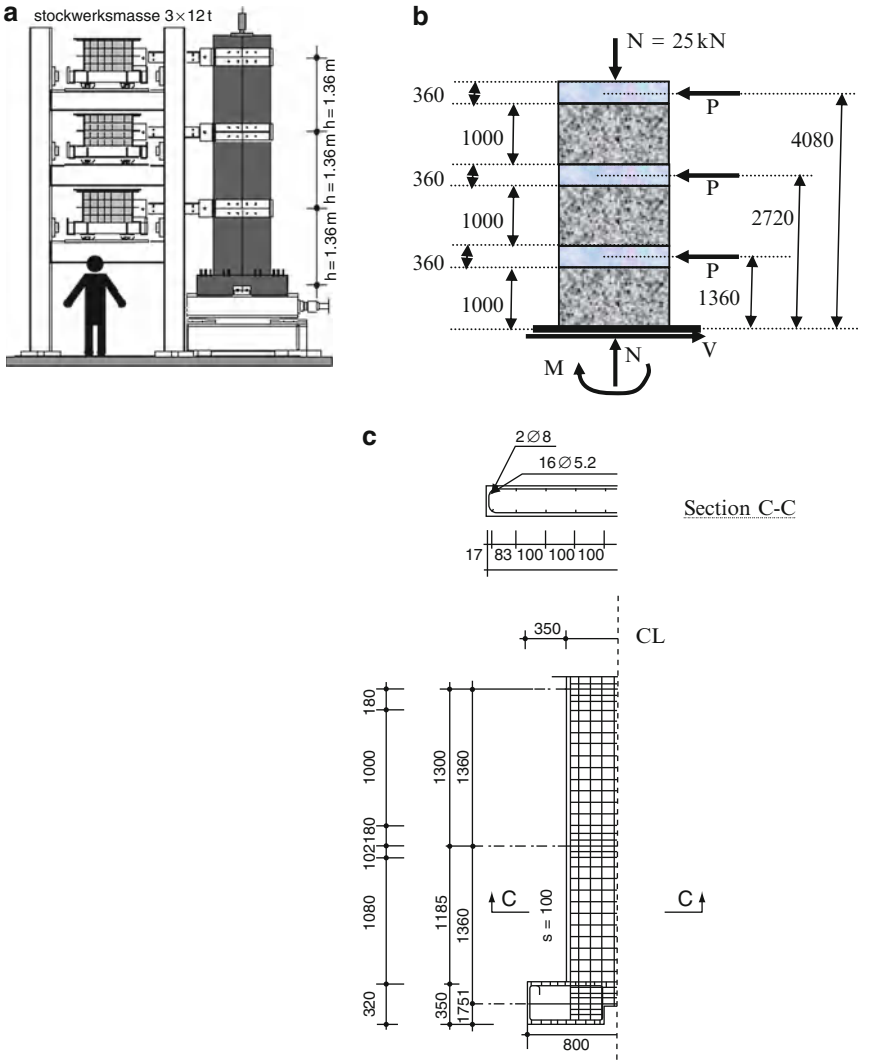


Fig. 23 Details of the RC wall under seismic excitation: (**a**) experimental setup [37]; (**b**) external loading and reactions; (**c**) arrangement of longitudinal and transverse reinforcement (only arrangement for the first two storeys is shown, arrangement for third storey is identical to that of the second) (all dimensions in mm)

in Fig. 23a. Each mass (corresponding to the mass of a floor in the equivalent three-story building) was supported by a separate rigid steel three-story frame and was able to move only in the horizontal direction (so that the inertia of the masses affects only the horizontal motion of the structure). The wall was also subjected to a vertical

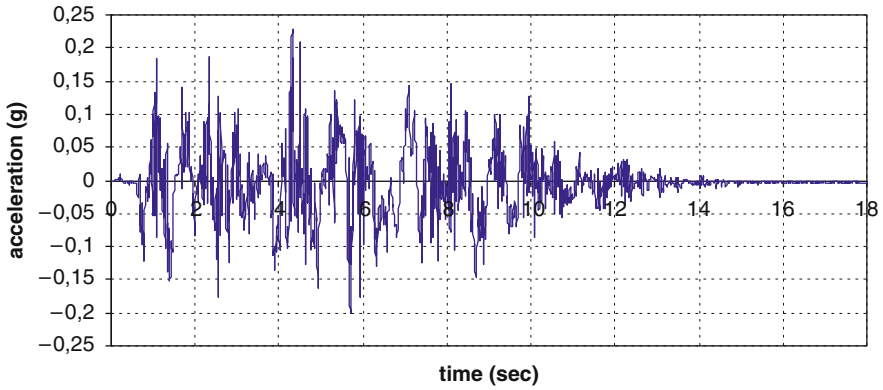


Fig. 24 Acceleration record used in the numerical and experimental investigation of the RC wall specimen in Fig. 23

uniformly distributed compressive stress equal to approximately 30% f_c, with f_c being around 35 MPa. A schematic representation of the RC wall tested and its design details are given in Fig. 23b and c. The values (in MPa) of the yield stress and ultimate strength (in parenthesis) of the reinforcement bars used were 567 (672), 483 (584), and 553 (611) for bar diameters (in mm) 8, 5 and 4, respectively.

Full details of the FE modelling and numerical predictions are given elsewhere [24]. Only the main results are presented herewith in a graphical form. The dynamic load was applied in the form of an acceleration record, which is presented in Fig. 24. The full response of the specimen during the experimental investigation is presented in Figs. 25 and 26 in the form of displacement-time and base shear/moment-time curves, respectively. It can be seen from the figures that the correlation between numerical predictions and measured values is very close in all cases.

7 Concluding Remarks

It appears from the above that nonlinear FE analysis incorporating a brittle, triaxial model of concrete behaviour, load-path and loading-rate independent is capable of yielding realistic predictions for a wide range of structural-concrete configurations subjected to short-term loading conditions ranging from static and impact. Such evidence validates the concepts upon which the FE model's formulation is based and provides an alternative explanation regarding the behaviour of structural concrete and how it should be modelled which contradicts the presently (widely) accepted assumptions adopted by the majority of FE models used to predict structural concrete behaviour.

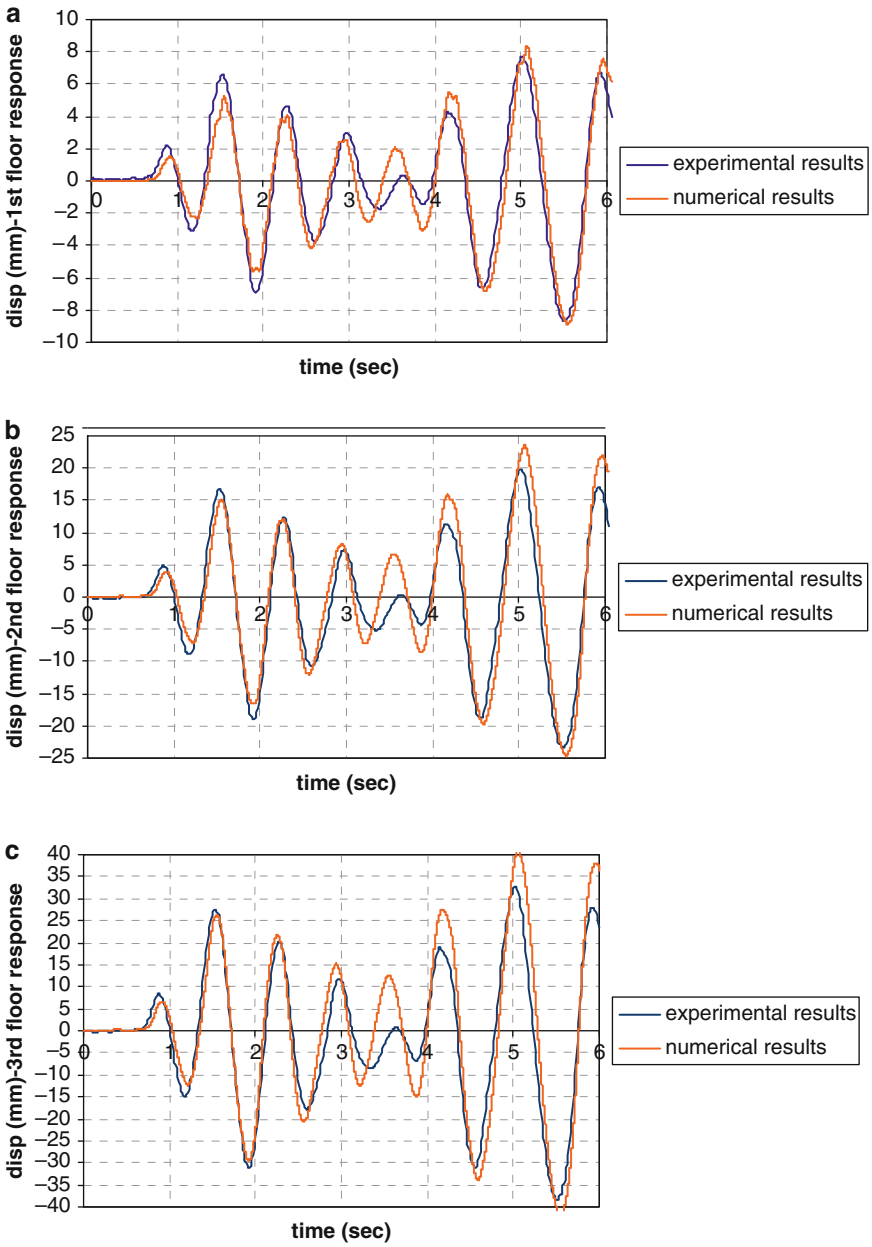


Fig. 25 Numerical and experimental displacement response of (**a**) the first floor (**b**) the second floor and (**c**) the third floor of the RC wall under seismic excitation

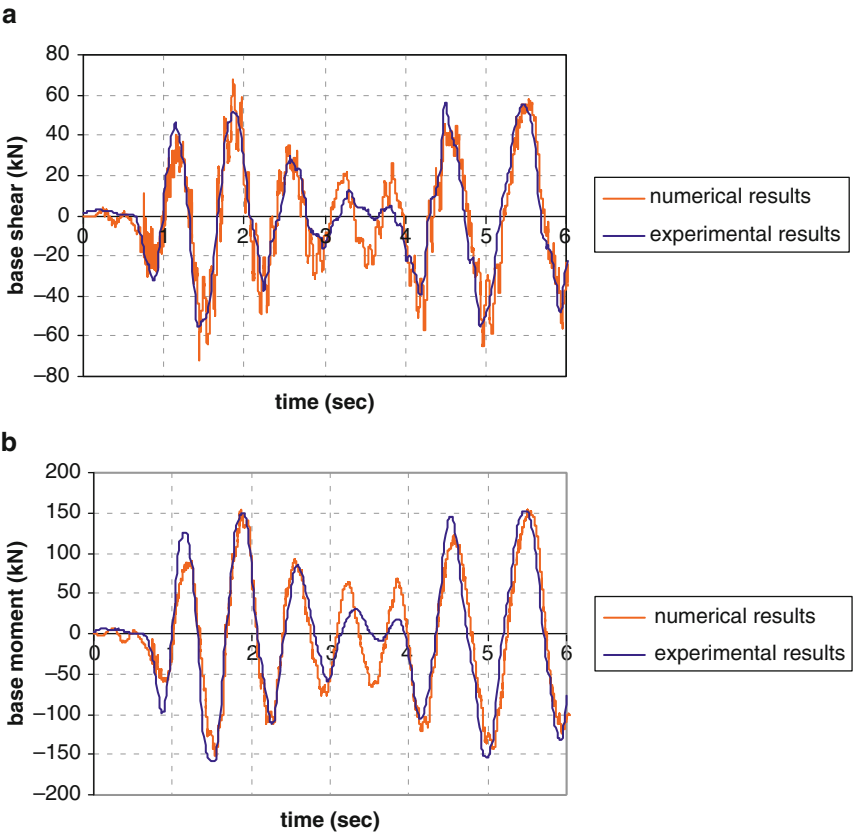


Fig. 26 Numerical and experimental (**a**) base shear and (**b**) base moment of the RC wall under seismic excitation

References

1. Malvar LJ, Crawford JE, Wesevich JW, Simons D (1997) A plasticity concrete material model for DYNA3D. Int J Impact Eng 19:847–873
2. Thabet A, Haldane D (2001) Three-dimensional numerical simulation of the behaviour of standard concrete test specimens when subjected to impact loading. Comput Struct 79:21–31
3. Cela JJL (1998) Analysis of reinforced concrete structures subjected to dynamic loads with a viscoplastic Drucker-Prager model. Appl Math Model 22:495–515
4. Winnicki A, Pearce CJ, Bicanic N (2001) Viscoplasic Hoffman consistency model for concrete. Comput Struct 79:7–19
5. Gomes HM, Awruch AM (2001) Some aspects on three-dimensional numerical modelling of reinforced concrete structures using the finite element method. Adv Eng Softw 32:257–277
6. Georgin JF, Reynouard JM (2003) Modeling of structures subjected to impact: concrete behaviour under high strain rate. Cement Concrete Comp 217:131–143
7. Barpi F (2004) Impact behaviour of concrete: a computational approach. Eng Fract Mech 71:2197–2213

8. Cervera M, Oliver J, Manzoli O (1996) A rate-dependent isotropic damage model for the seismic analysis of concrete dams. Earthquake Eng Struct 25:987–1010
9. Hatzigeorgiou G, Beskos D, Theodorakopoulos D, Sfakianakis M (2001) A simple concrete damage model for dynamic FEM applications. Int J Comput Eng Sci 2:267–286
10. Koh CG, Liu ZJ, Quek ST (2001) Numerical and experimental studies of concrete under impact. Mag Concrete Res 53:417–427
11. Lu Y, Xu K (2004) Modelling of dynamic behaviour of concrete materials under blast loading. Int J Solids Struct 41:131–143
12. Dube JF, Pijaudier-Cabot G, La Borderie C (1996) Rate dependent damage model for concrete in dynamics. J Eng Mech Div ASCE 122:359–380
13. Faria R, Olivera J, Cervera M (1998) A strain-based plastic viscous-damage model for massive concrete structures. Int J Solids Struct 35:1533–1558
14. Agrwal AB, Jaeger LG, Mufti AA (1981) Response of reinforced concrete shear walls under ground motions. J Struct Div ASCE 107:395–411
15. Ile N, Reynouard JM (2000) Nonlinear analysis of reinforced concrete shear wall under earthquake loading. J Earthquake Eng 4:183–213
16. Faria R, Vila Pouca N, Delgado R (2002) Seismic behaviour of a R/C wall: numerical simulation and experimental validation. J Earthquake Eng 6:473–408
17. Mochida A, Mutsuyoshi H, Tsuruta K (1987) Inelastic response of reinforced concrete frame structures subjected to earthquake motion. Concrete Library JSCE 10:125–138
18. Lee H-S, Woo S-W (2002) Seismic performance of a 3-story RC frame in a low-seismicity region. Eng Struct 24:719–734
19. Tedesco JW, Ross AC, Brunair RM (1989) Numerical analysis of dynamic split cylinder tests. Comput Struct 32:609–624
20. Tedesco JW, Ross AC, McGill PB, O'Neil BP (1991) Numerical analysis of high strain rate concrete tension tests. Comput Struct 40:313–327
21. Tedesco JW, Powell JC, Ross AC, Hughes ML (1997) A strain-rate-dependent concrete material model for ADINA. Comput Struct 64:1053–1067
22. Sziveri J, Topping PHV, Ivanyi P (1999) Parallel transient dynamic non-linear analysis of reinforced concrete plates. Adv Eng Softw 30:867–882
23. Kotsovos MD, Pavlovic MN (1995) Structural concrete: finite-element analysis for limit-state design. Thomas Telford, London
24. Cotsovos DM (2004) Numerical investigation of structural concrete under dynamic (earthquake and impact) loading. Ph.D. thesis, University of London, UK
25. Kotsovos MD (1983) Effect of testing techniques on the post-ultimate behaviour of concrete in compression. Mater Struct RILEM 16(91):3–12
26. van Mier JGM (1986) Multiaxial strain-softening of concrete. Mater Struct RILEM 19(111):179–200
27. van Mier JGM, Shah SP, Arnaud M, Balayssac JP, Bassoul A, Choi S, Dasenbrock D, Ferrara G, French C, Gobbi ME, Karihaloo BL, Konig G, Kotsovos MD, Labnz J, Lange-Kornbak D, Markeset G, Pavlovic MN, Simsch G, Thienel K-C, Turatsinze A, Ulmer M, van Vliet MRA, Zissopoulos D (TC 148-SSC: test methods for the strain-softening of concrete) (1997) Strain-softening of concrete in uniaxial compression. Mater Struct RILEM 30(198):195–220
28. Barnard PR (1964) Researches into the complete stress-strain curve for concrete. Mag Concrete Res 16(49):203–210
29. Willam KJ, Warnke EP (1974) Constitutive model for the triaxial behaviour of concrete. Seminar on concrete structures subjected to triaxial stresses, Instituto Sperimentale Modeli e Strutture, Bergamo, May, Paper III-1
30. Kotsovos MD, Spiliopoulos KV (1998) Modelling of crack closure for finite-element analysis of structural concrete. Comput Struct 69:383–398
31. Kotsovos MD, Spiliopoulos KV (1998) Evaluation of structural-concrete design-concepts based on finite-element analysis. Comput Mech 21:330–338
32. Bathe KJ (1996) Finite element procedures. Prentice Hall, New Jersey
33. Jelic I, Pavlovic MN, Kotsovos MD (2004) Performance of structural-concrete members under sequential loading and exhibiting points of inflection. Comput Concrete 1(1):99–113

34. Hughes G, Spiers DM (1982) An investigation on the beam impact problem. Technical Report 546, London: Cement and Concrete Association; 1982. p 117
35. Cotsovos DM, Kotsovos MD (2008) Cracking of rc beam/column joints: Implications for practical structural analysis and design. The Structural Engineer, pp 33–39
36. Shiohara H, Kusuhara F (2006) Benchmark test for validation of mathematical models for nonlinear and cyclic behaviour of R/C beam-column joints. http://www.rcs.arch.t.u-tokyo.ac.jp/shiohara/benchmark/
37. Lestuzzi P, Wenk T, Bachmann H (1999) Dynamic tests of RC structural walls on the ETH earthquake simulator. IBK Report No. 240, Institüt für Baustatik und Konstruktion: ETH, Zurich

Numerical Simulation of Gusset Plate Connection with Rhs Shape Brace Under Cyclic Loading

K.K. Wijesundara, D. Bolognini, and R. Nascimbene

Abstract In concentrically braced frames, gusset plate connections to rectangular hollow section braces are fabricated using welds both on the brace side and to connect the gusset plate to the flanges of the beam and column framing into the brace. The beam-to-column connection at the gusset plate is either welded or bolted. A welded beam-to-column connection could be considered as the best option for braced frame gusset plate connections, because the potentially considerable axial forces developed in the beam must be transferred through this joint. Even when a bolted connection is provided at the face of the column flange, a stiff gusset plate connected to the beam and the column could still provide a fully restrained beam-to-column connection as in the case of the welded connection. The past experimental studies have indicated that undesirable failure modes could occur in the gusset plate even using a linear clearance rule in the design of the gusset plate connection.
For these reasons, this study investigates the local seismic performances of fully restrained gusset plate connections through detailed finite element models of a single storey single bay frame located at the ground floor of the four storey frame using the MIDAS FE program. The main goal of the study on the local performance of the gusset plate connection is to validate the design procedure presented in this chapter, proposing and alternative clearance rule for the accommodation of brace rotation. Finally, local performances of FE models are compared in terms of strain concentrations in gusset plates, beams and columns.

Keywords Concentrically braced frames · Rectangular hollow section · Special concentrically braced frames · Finite element models · Yield mechanism · Equivalent plastic strain · Local buckling

K.K. Wijesundara
European School for Advanced Studies in Reduction of Seismic Risk, IUSS (ROSE School)
Via Ferrata 1, 27100 Pavia, Italy
e-mail: kwijesundara@roseschool.it

D. Bolognini and R. Nascimbene (✉)
European Centre for Training and Research in Earthquake Engineering (EUCENTRE),
Via Ferrata 1, 27100 Pavia, Italy
e-mail: davide.bolognini@eucentre.it; roberto.nascimbene@eucentre.it

M. Papadrakakis et al. (eds.), *Computational Methods in Earthquake Engineering*,
Computational Methods in Applied Sciences 21, DOI 10.1007/978-94-007-0053-6_8,
© Springer Science+Business Media B.V. 2011

1 Introduction

Concentrically braced frames (CBFs) are commonly used for seismic design in high seismic areas due to their high stiffness and strength that they exhibit when compared to moment resisting frames. In the current design practise, CBFs are designed and detailed to dissipate energy through brace yielding in tension and inelastic buckling in compression under the strong shaking of an earthquake. In order to dissipate energy through these yield mechanisms, it is essential to ensure that the premature failures in the connections are prevented. It is important to note that this study is limited to rectangular hollow section (RHS) braces with gusset plate connections.

To ensure the yielding of brace in tension, the current seismic provisions require that the axial capacity of the gusset plate connection must exceed the axial capacity of the brace. The EC8 [4] provisions do not provide any suggestion as to the detailing of the clearance at the gusset plate connection so that the brace can accommodate buckling in the out-of-plane direction by forming the plastic hinges at the gusset plates rather than at the brace ends. To investigate the performance of a gusset plate connection without any clearance under the out-of-plane buckling of the brace, this study develops a FE model referred as Model 1. AISC [1] provisions, on other hand, require for special concentrically braced frames (SCBFs), a 2t clearance to be provided at the end of the brace in order to accommodate the out-of-plane brace buckling and to form the plastic hinge in the gusset plate, where t is the gusset plate thickness. Hence, when the brace buckles in the out-of-plane direction, it is expected to reduce the additional demand to welds due to the excessive rotation of the gusset plate. Such a clearance rule results in relatively large gusset plates causing the gusset plate connection to be potentially uneconomical. Furthermore, when, due to lateral loading, a braced frame bay with larger gusset plates deforms horizontally due to the lateral loading into a parallelogram where the beams remain horizontally and the columns bend, the tension brace gusset plates could undergo compression buckling due to the decreases of the angle between the beam and the column leading to potential tension tearing of the gusset plate.

The studies by Roeder et al. [12] and Lehman et al. [7] have indicated that relatively large and thick gusset plates concentrate the cyclic strain demand in the middle of the brace, thereby reducing the deformation capacity of the brace itself. The study by Lehman et al. [7] proposed to use elliptical clearance rule in designing the gusset plate connection to accommodate the brace end rotation, resulting in more compact rectangular gusset plates. In the present study, two different models are designed and analysed, one of a tapered gusset plate connection with 2t clearance and the other of a rectangular gusset plate connection with sufficient clearance to form a tri-linear yield mechanism. The finite element (FE) models developed in this study with linear and tri-linear clearance in the gusset plate are referred as Model 2 and 3, respectively.

Furthermore, to investigate the effects of weld size, beam-to-column connection and loading history on the performance of the gusset plate connection, four more models have been designed. The gusset plate connections in each model have been designed according to the proposed procedure developed based on the performance

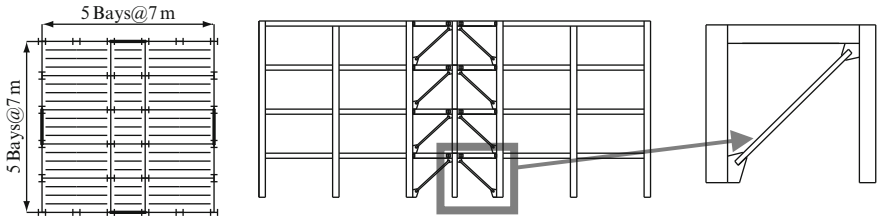


Fig. 1 Selection of half bay single storey model

based seismic design (PBSD) procedure used by Roeder et al. [12]. This design procedure was developed to ensure the occurrence of desirable yield mechanisms, and to prevent undesirable failure modes, thereby achieving the desired seismic performance.

Each of the FE models, including the beam, two gusset plate connections at each end of the brace and two columns as shown in Fig. 1, represents half of the braced bay at the ground floor of the four storey CBF building designed for a 475-year return period of earthquake with a PGA of 0.3 g. To analyze the performance of gusset plate connections, FE models are developed using the MIDAS FEA Program [10].

2 Validation of the Equivalent Plastic Strain Range for the Crack Initiation at the Mid Region of the Brace

In this study, ranges of equivalent plastic strains specified for the different failure modes were obtained from experimental and numerical studies by Lehman et al. [7] and Yoo et al. [16–18]. In the study by Lehman, 13 sub-assemblages (each sub-assemblage includes the beam, columns, and an RHS brace with gusset plate connections) were tested for the applied displacement history. In the study by Yoo, FE models were developed for each of the tested sub-assemblages and further analyzed for the same displacement history. The strain ranges for different failure modes were specified in terms of equivalent plastic strains obtained from FE models at the displacement level which corresponded to the failure mode observed in the test specimen. Thus, the specified ranges of equivalent plastic strain values could vary in different FE mesh size, crack location and the condition. The main objective of this section of the paper is to validate the applicability of the proposed range of equivalent plastic strains on systems other than those used for the calibration. Thus, four RHS shape single brace specimens made in different steel standard, including different width-to-thickness ratios and imposing different end restraint conditions to brace were selected from two different experimental programs by Shaback [13] and Walpole [15] to validate the equivalent plastic strain range at the fracture of the brace in mid region. Unfortunately, the authors were unable to collect well-documented experimental results of sub-assemblages including gusset plate connections other than the configurations used in the calibration by Lehman et al. [7].

Based on the results presented in this section, it seems to appropriate to use of the proposed equivalent plastic strain ranges proposed by Yoo et al. [17] at least for the sub-assemblages which include the RHS shape braces. Table 1 gives the reference test program, the test ID, the member size, the steel grade, the nominal yield stress $F_{y,nom}$, the actual yield stress of the steel F_y, the total length L, the specimen length L_s, the gross cross-section area of brace A_{gB}, Young's modulus of steel E, the initial buckling load N_b, the non-dimensional slenderness ratio λ, the axial yield displacement δ_y, the end restrained condition and the class of the section of each specimen. All brace models were developed using shell elements available in MIDAS FEA programme. The shell elements are capable of taking into account the in-plane deformation (membrane) and the out-of-plane deformation (bending and shear). Mainly, four nodes shell elements are used due to the fact that four-node shell elements generally lead to accurate estimation of both displacement and stresses. An approximate mesh size of 25 × 25 mm was used at the midspan of the brace and for the gusset plates where more severe inelasticity was expected. A coarser mesh size of 50 × 25 mm was used in regions where limited inelasticity was expected. The Von Mises yield criterion was adopted with bilinear isotropic hardening to represent the material non linearity. The parameters for the model were obtained from results of small scale coupon tests in technical reports [13, 15]. Since each brace model undergoes large in-plane and out-of-plane deformation, the geometrical shape of the brace will change. As a result of that the relationship between the strain and the displacement will not remain linear. Hence, in these analyses, geometric nonlinearity was included together with material nonlinearity. The geometrically nonlinear analysis uses an updated Lagrangian formulation expressing the stress and strain using Cauchy stress and the incremental linear Eulerian strain. All translational and rotational degrees of freedoms at one end of the gusset plate were restrained whereas two translational (perpendicular direction to the brace axis and the out-of-plane direction) and all rotational degrees of freedoms at the other end of the brace were restrained. The corresponding displacement history as specified in the technical reports [13, 15] was applied in the direction of the free translational degree of freedom. The initial deformed shape was prescribed in the out-of-plane direction having a mid displacement of $L_s/700$ (where L_s is the specimen length) to represent the geometric imperfection and the residual stress distribution after the manufacturing process.

Figure 2 shows the out-of-plane bucked shape of the FE model of the RHS single brace specimen (1B) and the enlarged view of the mid region of the brace model. The enlarged view clearly illustrates that the local buckling has formed in the mid region after the significant out-of-plane deformation of the brace. Furthermore, Fig. 2 shows that locations of strain concentrations in the FE model are similar to those observed in the experiment.

Figure 3 shows the comparison of the numerical axial force-displacement hysteretic curves of specimens 1B and 2A with the experimental data. The comparison clearly illustrates the capability FE model developed with shell elements to predict the axial force-displacement response accurately. It also validates the use of the initial imperfection of Ls/700 to accurately predict the initial buckling load [11, 14].

Table 1 Characteristics of the specimens

Study	Test ID	Size	Standard	$F_{y,nom}$ (MPa)	F_y (MPa)	L (mm)	L_S (mm)	$(c/t)/(c/t)_{Limit}$	A_{gB} (mm^2)	E (GPa)	N_b (kN)	λ	δ_y (mm)	End restraint	Cross section class	Dis. history
1	1B	127 × 127 × 8.0	CSA-G40.21–350W	350	425	3,401	3,050	0.54	3,620	191	1,156	0.805	7.4	GE (3)	Class 1	NS
	2A	152 × 152 × 8.0	CSA-G40.21–350W	350	442	3,995	3,600	0.68	4,430	202	1,507	0.794	8.6	GE (3)	Class 1	NS
	2B	152 × 152 × 9.5	CSA-G40.21–350W	350	442	3,989	3,600	0.56	5,210	196	1,721	0.792	8.9	GE (3)	Class 1	NS
2	RHS3	150 × 100 × 6.0	AS 1163, gr. C350	350	432	2,704	2,704	0.93	2,730	200	1,032	0.603	6.1	Fix-Fix	Class 1	S

Study no. 1 and 2 refer experimental reports by Shaback [13] and Walpole [15] respectively.
GE stands for gusset ends and "Fix-Fix" means the fix-ended restrained condition provided to the brace.
S, NS, and HUS stand for symmetrical displacement history, nearly symmetrical displacement history, and highly unsymmetrical displacement history respectively.
$(c/t)_{Limit}$ is defined as specified in EC3 [3] for the section class 1.

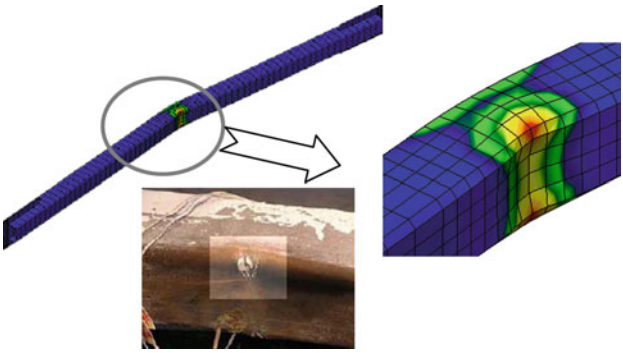


Fig. 2 Typical buckled shape of the brace and the locally buckled region

Furthermore, it is important to note that the imperfection within the cross section was not specified in this study.

As observed in the FE results, it is not possible to completely remove the lateral deformation due to the inelastic buckling of the brace by applying a subsequent tensile loading. Hence, upon reloading in compression, the brace behaves as a component with an initial mid-length deflection, resulting in a lower buckling capacity than the original. Furthermore, the initiation of local buckling in the FE brace model is observed in the same compression cycle in which the initiation of local buckling is observed during the experiments. Since the FE model can predict the local buckling by taking into account the large deformations, it can also predict the compression resistance well in the post buckling phase. The hysteretic curves are highly unsymmetrical due the global buckling of the brace in the out-of-plane direction.

The Main objective of this part of the is to validate the applicability of the range of equivalent plastic strains proposed by Yoo et al. [17] in order to predict the crack initiation in the midspan region of the RHS shape brace. The threshold values of the equivalent plastic strain, ε_{eqv}^{pl} are obtained from the plastic strain component using the general Von Mises equation:

$$\varepsilon_{eqv}^{pl} = \frac{1}{\sqrt{2}(1+\upsilon)}\left[(\varepsilon_x^{pl}-\varepsilon_y^{pl})^2+(\varepsilon_y^{pl}-\varepsilon_z^{pl})^2+(\varepsilon_z^{pl}-\varepsilon_x^{pl})^2 + \frac{2}{3}((\gamma_{xy}^{pl})^2+(\gamma_{yz}^{pl})^2+(\gamma_{zx}^{pl})^2)\right]^{1/2} \quad (1)$$

where ε_x^{pl}, ε_y^{pl}, ε_z^{pl}, γ_{xy}^{pl}, γ_{yz}^{pl} and γ_{zx}^{pl} are the components of the plastic strain and υ is the Poisson ratio. The threshold values highlighted in Fig. 4 are the equivalent plastic strain values which are obtained at the peak compression deformation during the last compression cycle. The last compression cycle is defined as the cycle which causes severe local buckling in the middle of the brace followed by fracture of the brace in the subsequent tensile loading cycle. Figure 4 shows the variation of peak equivalent plastic strain at the mid region of the brace against the ratio of δ/δ_y

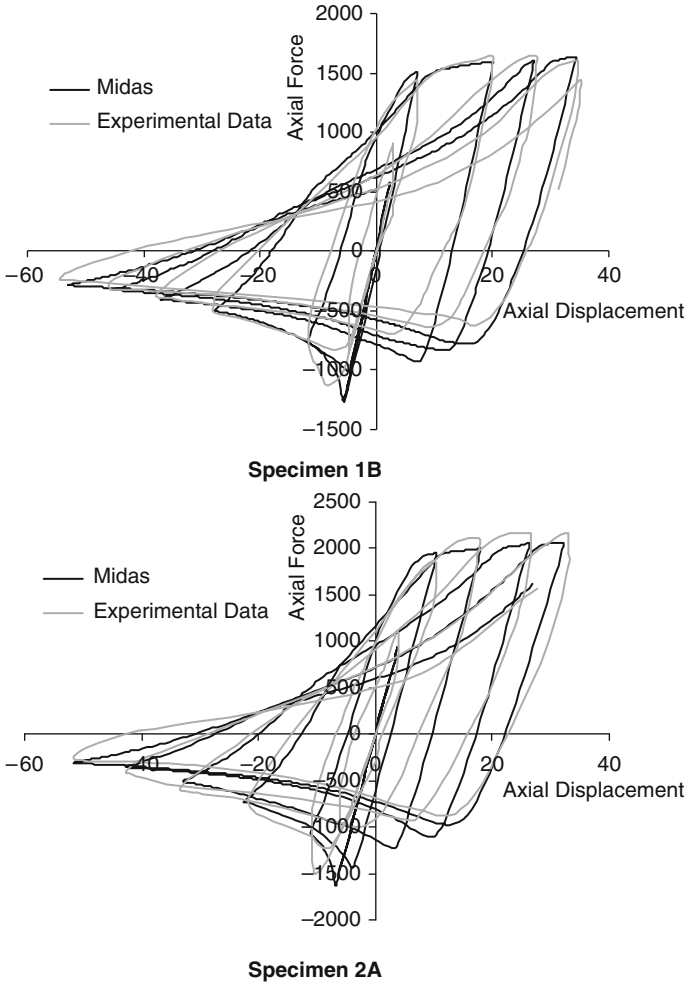


Fig. 3 Axial force-displacement hysteretic curves

of four specimens selected from the experimental programs by Shaback [13] and Walpole [15]. It is important to note that δ is the axial deformation of the brace and δ_y is the yield deformation of the brace calculated as:

$$\delta_y = \frac{F_y L_s}{E} \tag{2}$$

The threshold equivalent plastic strains for the crack initiation at the mid region of the brace of the four specimens are in the range of 0.271–0.306 as specified in Yoo et al. [17]. Thus, the proposed equivalent plastic strain ranges of 0.271–0.306,

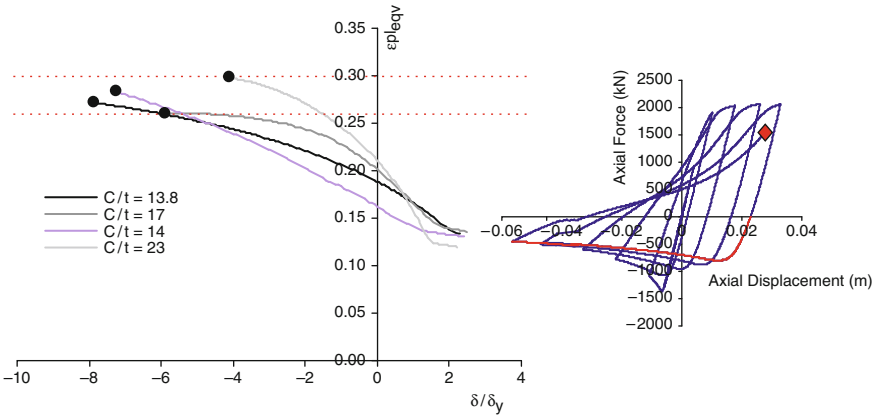


Fig. 4 Variation of Von Mises equivalent plastic strain against the ductility ratio

0.054–0.065 and 0.033–0.055 can be used to predict crack initiation in the mid region of the brace, at the weld of the gusset plate to the column and at the weld of the gusset plate to the beam, respectively.

3 Design of Gusset Plate Connections

In a gusset plate connection of RHS brace in CBF, the slotted brace is welded to the gusset plate and subsequently, the gusset plate is also welded to the beam and the column using fillet weld lines. The beam is either welded or bolted to the face of the column flange. In this study, the gusset plate connections were designed according to the performance based seismic design (PBSD) as proposed by Roeder et al. [12]. The design procedure was developed to ensure the desirable yield mechanisms by preventing the undesirable failure modes and, thereby achieving the desired seismic performance. The formation of a yield mechanism provides the inelastic deformation of the structure without significant strength reduction. The formation of a failure mode could lead to the fracture, the loss of strength or deformation capacity. A single failure mode of the connection will produce a considerable reduction in strength or deformation capacity of the system whereas the multiple failure modes generally result to complete failure of the connection. Figure 5 illustrates possible yield mechanisms and failure modes which could be developed in CBFs under different performance levels.

As shown in Fig. 5, primary or favourable yield mechanisms in CBFs are expected to be the inelastic shortening due to the post-buckling behaviour of the brace and the tensile yielding of the brace. Secondary or less favourable yield mechanisms are expected to be yielding of the gusset plate under the combined actions of axial, moment and shear forces, and the yielding of the beam and the column adjacent to the re-entrant corners of the gusset plate. The possible failure modes of the brace in CBF are fracture of the brace at the mid region due to the excessive

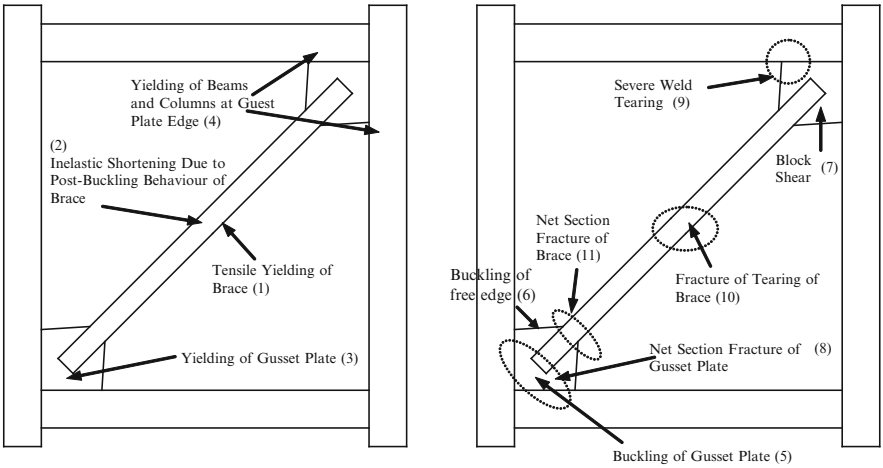


Fig. 5 Yield mechanisms and the failure modes [12]

local deformation and the net section fracture at the slotted brace end. Severe weld tearing, the block shear, the net section fracture and the buckling just beyond the brace end are failure modes of the gusset plate.

Primary yield mechanisms should have smaller resistances than secondary mechanisms and all failure modes. This requirement makes the connection strength and stiffness able to ensure the immediate occupancy performance level. Once this connection strength and stiffness are provided, the connection deformation capacity becomes the dominant concern with the life safety and the collapse prevention performance levels. According to the performance based design strategy, the brace buckling and the incipient of the brace yielding are expected in the immediate occupancy whereas the brace yielding and the incipient of yielding of the gusset plate are expected in the life safety performance level. Due to significant out-of-plane buckling of the brace in the life safety performance level, the gusset plate could subject to significant rotation and subsequently, yielding of the gusset plate initiates under the combined actions of the moment and the axial load. In the collapse prevention performance level, the excessive out-of-plane deformation is expected. Due to the excessive out-of-plane deformation, incipient of the brace fracture and significant yielding in the gusset plate are expected but improperly detailed connection could lead to either the fracture of the net section of the gusset plate or weld tearing of the gusset plate connection.

4 Description of Parametric Study

In this parametric study, the effects of the clearance provided in the gusset plate, the weld size, the beam-to-column connection and the displacement history on the performance of the gusset plate connection were investigated. For these purposes,

the half bay single storey models were selected from the ground floor of four storeys CBF of inverted V configuration with the middle column linking all brace-to-beam intersection points to the ground as shown in Fig. 1. This frame was designed according to the force based design (FBD) procedure with the q factor of four for the event of the 475 year return period earthquake with the PGA of 0.3 g [5]. The resultant brace size of each model was 203 × 203 × 9.5 mm (width x depth x thickness in millimetres) square hollow section (SHS) shape and the beam and columns were wide-flange sections of W360 × 237 and W360 × 101 respectively.

Four different types of brace-beam-column connections as shown in Fig. 6 were designed using aforementioned procedure. Model 1 and 3 were provided the clearance in the gusset plate to facilitate for the brace end rotation when the brace buckles in out-of-plane direction in forming tri-linear yield lines whereas Model 2 and 4 were provided the linear clearance between the brace end and the line which connects the re-entrant corners of the gusset plate as shown in Fig. 7a of two times the gusset plate thickness (2t) as specified in AISC [1]. The difference between Model 1 and 3 is the angle between the vertical line and the line which connects the brace and the re-entrant corner of the gusset plate. This angle is 15° for Model 1 and 30° for Model 3. Furthermore, authors have indicated the clearance provided in Model 3 in Fig. 7b.

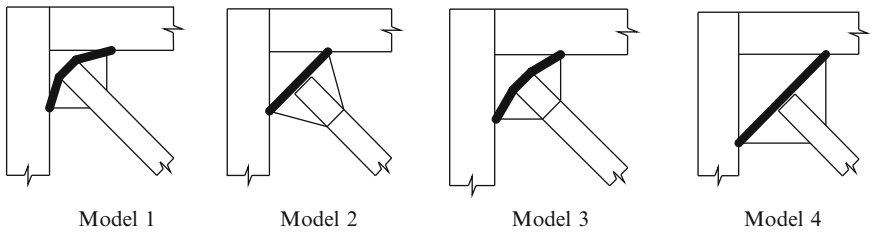


Fig. 6 Expected yield line formed in the gusset plate of different models

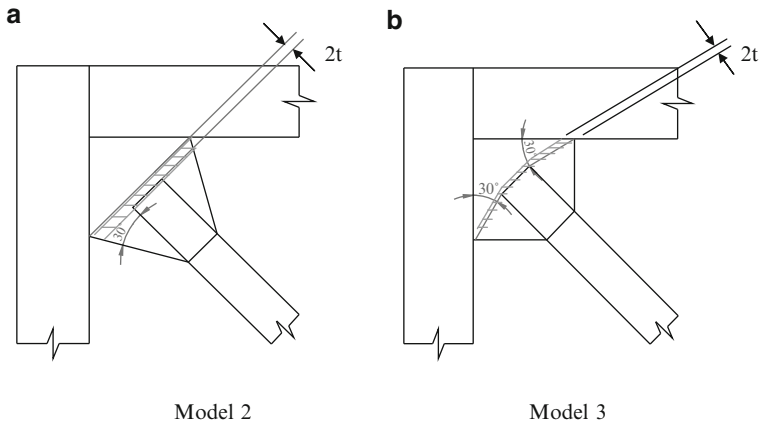


Fig. 7 Connection details of **(a)** Model 2 and **(b)** Model 3

As listed in Table 2, when the 2t linear clearance rule was used to design the gusset plate in rectangular shape, relatively large and thick gusset plate was resulted compared to other models. Relatively long length beyond the brace end in the gusset plate required thick gusset plate to prevent the buckling of the gusset plate under the direct compression load. The experimental studies by Lehman et al. [7] and numerical studies by Yoo et al. [17] have clearly indicated that relatively large and thick gusset plate concentrates the cyclic strain demand in the middle of the brace, thereby reducing the deformation capacity of the brace. Hence, this numerical study is limited to Model 1–3 in order to investigate alternative proposals to improve the performance of the system.

In Model 3 to form a tri-linear yield line in the gusset plate as proposed in the present study, the angle between the line which connects the brace end and the re-entrant corner, and the vertical line should be equal to 30° as shown in Fig. 7b. The purpose to select 30° angle is to use the maximum possible effective width of the gusset plate in resisting the direct axial tensile load developed in the brace when rectangular gusset plate is used. If the angle is less than 30° as in the case of Model 1, higher strain concentration is observed just beyond the brace end due to the reduced effective width when full tensile strength or excessive rotation is developed in the brace.

Furthermore, tri-linear clearance rule results more compact gusset plate in rectangular shape with leg lengths along the column and the beam similar to Model 2 of tapered connection. The controlling yield mechanism of Model 3 is the yielding of the effective width or Whitmore's section of the gusset plate under the direct tension. Model 1–3 are further analysed for different (1) weld sizes (2) beam-to-column connections and (3) loading histories as:

1. **Weld size:** In order to investigate the effects of weld size to the performance of the gusset plate connection, two different sets of fillet weld lengths along the brace-to-gusset plate and gusset plate-to-beam/column connections were designed using different size of weld throats. The fillet weld lengths at the brace-to-gusset plate and the gusset plate-to-beam/column connections in Model 1–3 were designed for the weld throat sizes of 8 and 11 mm respectively. To analyse the effect of short weld lengths, thereby resulting more compact gusset plate, the weld lengths in Model 1C, 2C and 3C were designed using relatively large fillet weld throats of 11 and 15 mm. Resulting in using larger throat sizes, the weld lengths were short and subsequently, the gusset plate was more compact compared to Model 1–3.
2. **Beam-to-column connection:** In the gusset plate connection, the beam is either welded or bolted to the face of the column flange. Welded beam-to-column connections could be considered as the best option to the gusset plate connections in the braced frame, because axial forces developed in beams must be transferred through these joints. But welded connections are comparatively uneconomical and hence, shear plate bolted connections are often provided at the face of column flange. This study developed a model called Model 3PR to investigate the effect of beam-to-column connection provided at the re-entrant corner of the gusset plate to the local performance of the gusset plate with tri-linear clearance.

Table 2 Connection details

Model	Free space	Beam-to column connection	Gusset plate type	Weld length (mm) (beam-column-gusset plate)	Weld length (MM) (brace-gusset plate)	Thickness of gusset plate	Loading history
Model-1	–	Welded	Rectangular	580	535	20	NS
Model-2	Linear	Welded	Tapered	580	420	20	NS
Model-3	Tri-linear	Welded	Rectangular	580	420	20	NS
Model-4	Linear	Welded	Rectangular	770	420	25	-
Model-1C	–	Welded	Rectangular	470	480	20	NS
Model-2C	Linear	Welded	Tapered	470	420	20	NS
Model-3C	Tri-linear	Welded	Rectangular	470	420	20	NS
Model-3PR	Tri-linear	Bolted	Rectangular	580	420	20	NS
Model-1CU	–	Welded	Tapered	470	480	20	US
Model-2CU	Linear	Welded	Rectangular	470	420	20	US
Model-3CU	Tri-linear	Welded	Rectangular	470	420	20	US

It should be noted that the sizes of brace, beam and the columns of each of the model are 203 × 203 × 9.5 mm (width × depth × thickness) in square shape, W360 × 122 and W360 × 237 respectively. *NS* nearly symmetrical, *US* unsymmetrical.

3. **Loading history:** For this study, nearly symmetrical and highly unsymmetrical displacement histories were chosen from the past experimental programme by Shaback [13] and Lee and Geol [6]. Model 1, 2, 3, 1C, 2C, 3C and 3PR were applied the nearly symmetrical displacement history while Model 1CU, 2CU and 3CU were applied highly unsymmetrical displacement history. Table 2 presents the type of free space provided in the gusset plate, the beam-to-column connections, weld lengths, size of the gusset plates and loading history of different models used in this parametric study.

5 Finite Element Model

Ten different FE models were developed in MIDAS FEA programme to simulate the behaviour of the gusset plate connection in CBF. Each model represents the sub-assemblage of the half bay width of the braced bay at the ground floor of the four storey CBF. The bay width and the storey height of the braced frame are 7 and 3.5 m respectively. The sub-assemblage included a brace, top beam, two columns and two gusset plates as shown in Fig. 8. The brace was $203 \times 203 \times 12.5$ HSS shape while the beam and the columns were wide-flange section of W360 $\times$ 237 and W360 $\times$ 101 respectively.

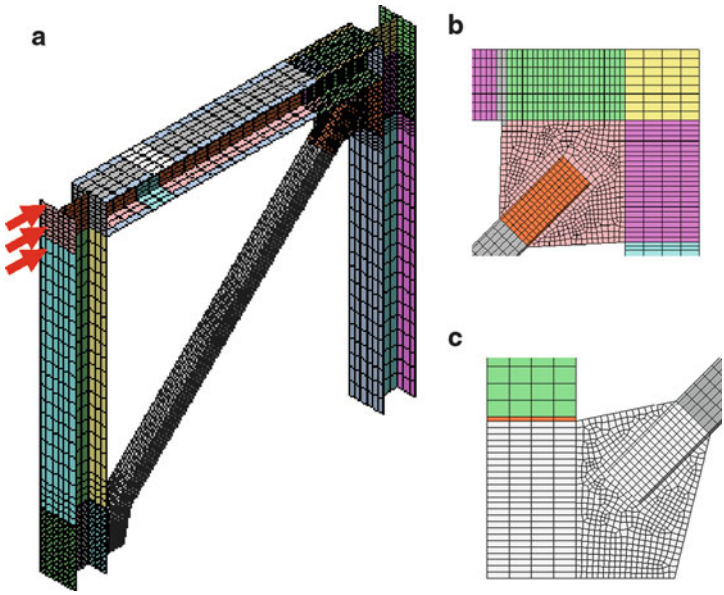


Fig. 8 (**a**) Half bay single storey model (**b**) enlarged view of top gusset plate connection (**c**) enlarged view of bottom gusset plate

All elements in the sub-assembly were also developed in four node shell elements available in MIDAS FEA programme. As it is discussed before, shell elements are capable of taking into account for the in-plane deformation (membrane) and the out-of-plane deformation (bending and shear). The Von Mises yield criterion was adopted with bilinear isotropic hardening to represent the material non linearity. Parameters for the model were adopted in the coupon test results from the experimental program by Walpole [15]. The nominal yield strength is 350 MPa for the grade 350 steel but yield stress specified in the numerical model is the stress that obtained from 0.2% offset method using the coupon testing of the bracing member and subsequently, the hardening function is assumed to be bilinear with 1% hardening till the strain is 0.035 and beyond that the platue is specified with the stress is equal to 490 MPa.

Since large in-plane and out-of-plane deformations were also expected in these analyses, geometric nonlinearity was included together with material nonlinearity. The initial imperfection ratio of $\mathbf{L}_s/700$ at the middle of the brace in the direction of out-of-plane was prescribed in each model. Figure 8 shows typical FE model of the subassembly and refined meshes at top and bottom gusset plate connections. In all models, an approximate mesh size of 25 × 25 mm was used in the mid region of the brace and gusset plates where significant inelastic deformation was expected and the rest was modelled with the coarse mesh. The weld lines were modelled with shared nodes along lines of welds. Welded beam-to-column connections were also modelled with sheared nodes along weld lines. Shear plate bolted connections in Model 3PR were modelled with series of springs and their stiffness was calibrated with experimental data by Astaneh-Asl [2] and others [8, 9]. The out-of-plane deformation of the top flange of the beam was restrained at 300 mm interval in order to provide the restrained to the top flange of the beam. All translational degrees of freedoms at base nodes of each model were restrained. The displacement history was applied to the column flange as shown in Fig. 8a.

6 Results and Discussion

6.1 Free Space in Gusset Plate

The strain distributions at the gusset plates and the midspan regions of the braces of Model 1–3 at ductility levels (δ/δ_y) of 6 in tension and 11 in compression are presented in Figs. 9 and 10. It is important to note that comparisons are made for surface strains those demonstrate the greatest magnitude of the local strain states. In Model 1, higher strain concentrations are developed just beyond the brace end and re-entrant corners of the gusset plate at both ductility levels, compared with Model 2 and 3. Furthermore, significant yielding in the beam and columns adjacent to re-entrant corners of the gusset plate are observed without local buckling in the compression flanges in the beam and the column.

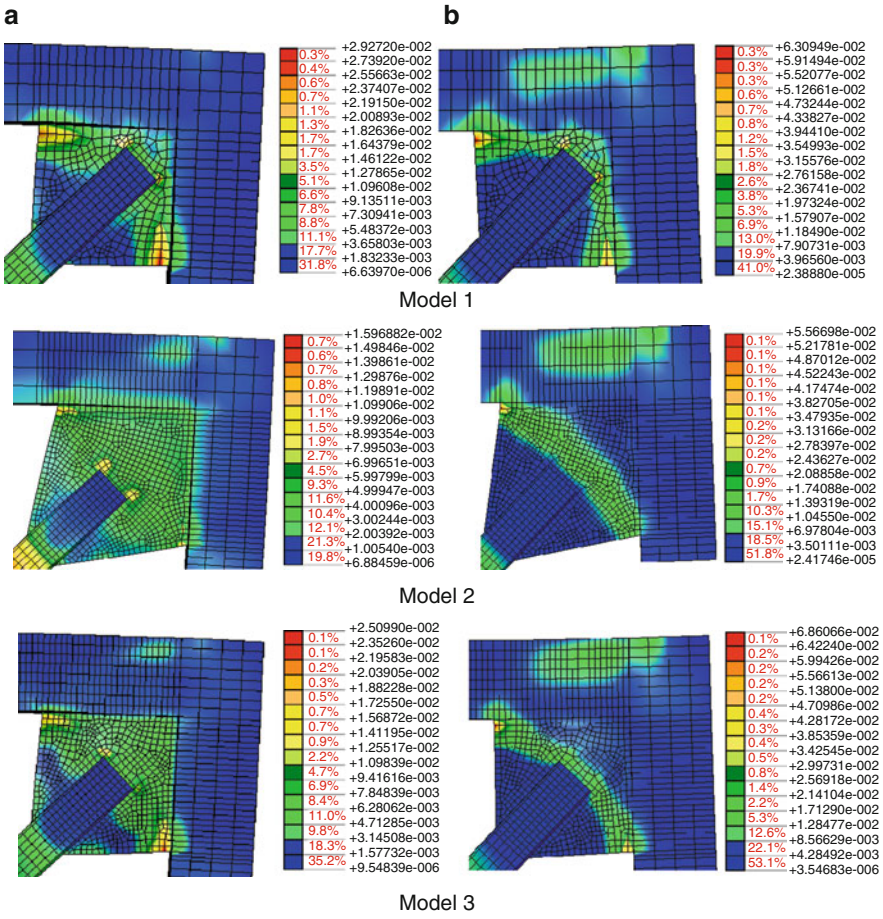


Fig. 9 Equivalent Von Mises strain distributions at the deformation of (**a**) $\delta/\delta_y = 6$ in tension (**b**) $\delta/\delta_y = 11$ in compression

In Model 2, significant yielding is developed beyond the brace end in the gusset plate under the combined actions of axial, moment and shear forces at considered tension and compression ductility levels but, there is no sign of high strain concentrations as observed in Model 1.

It is also observed that linear yield line is formed in the gusset plate when the excessive out-of-plane deformation is occurred in the brace. However, high strain concentrations at corners of the gusset plate are observed. No local buckling is formed in the gusset plate beyond brace ends, free edges of the gusset plate, column and beam flanges.

Similar to Model 2, significant yielding is observed in Model 3 just beyond the brace end in the gusset plate under the combined actions of axial, moment and shear forces at specified ductility levels. Furthermore, tri-linear yield line is formed in

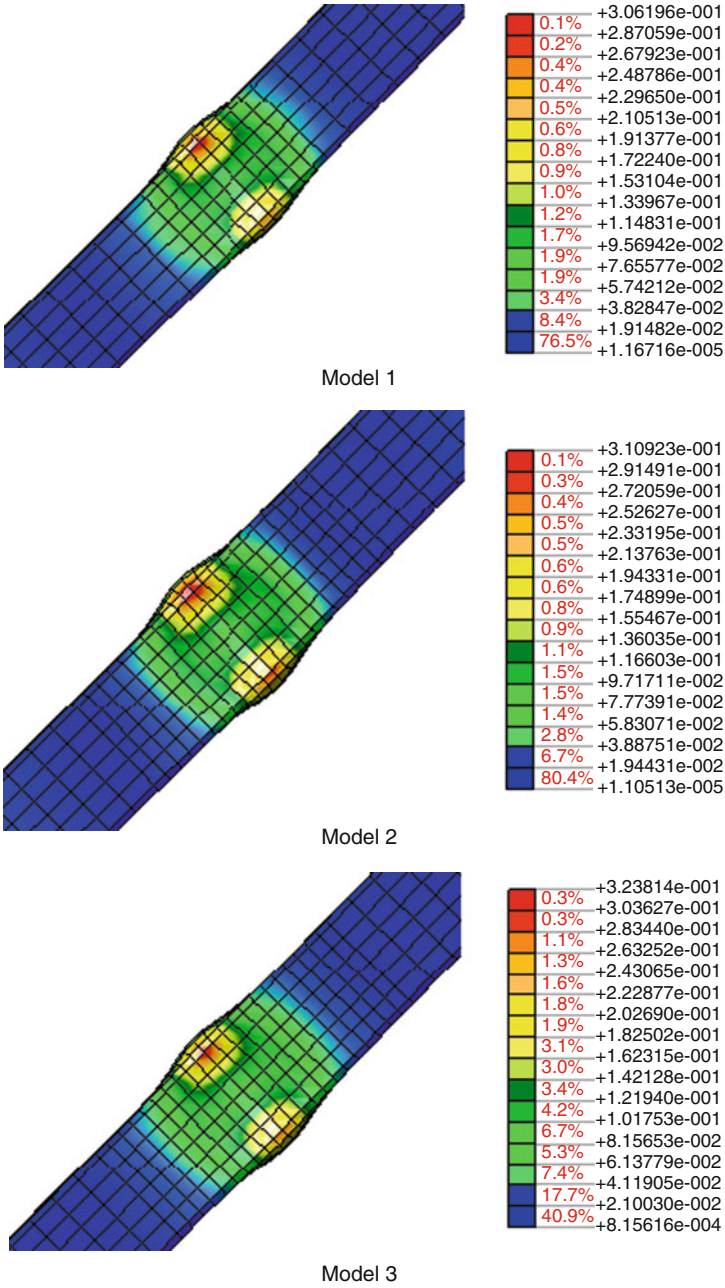


Fig. 10 Equivalent Von Mises strain distributions at the deformation of $\delta/\delta_y = 11$ in compression

the gusset plate when excessively large out-of-plane buckling occurred in the brace without highly concentrating the strain just beyond the brace end in the gusset plate. Again similar to Model 2, high strain concentrations at corners of the gusset plate are observed and no local buckling is formed in the gusset plate beyond brace ends, free edges of the gusset plate, column and beam flanges.

Figure 10 illustrates the peak equivalent strain distributions in mid regions of braces in Model 1–3 at the compression ductility level of 11. At this ductility level, local buckling is formed in the mid region of the brace in each model. Formation of local buckling develops extremely high strain concentrated regions in the midspan of the brace. The high concentration may lead to initiate the fracture at the mid region of the brace. None of the brace model is shown that such high concentration of strain is developed in brace ends even after large out-of-plane buckling was occurred. As shown in Fig. 9, end rotations of the brace are taken place in gusset plates forming plastic hinges. Depending on the free space provided in the gusset plate, the deformation capacity of the gusset plate connection could be limited. In order to better understand yield mechanisms and failure modes of Model 1–3, the distributions of peak equivalent strains at the mid regions of braces, along weld lines and regions just beyond brace ends in gusset plates at the end of each compression cycle are plotted against corresponding drift ratios of the half bay single storey frame models.

Figure 11a illustrates peak equivalent strain distributions in Model 1–3 at locally bucked mid regions of braces against storey drift levels. All three models show very closer strain distributions and hence, it is evident that there is no significant effect of the free space provided in the gusset plate to the strain distribution in the mid region of the brace. Furthermore, Fig. 11a shows that the strain level at the mid region of the brace is increased dramatically after the formation of local buckling. Figure 11b illustrates that considerably increased peak equivalent strain distributions along the weld lines are observed in Model 1 and 3 compared with Model 2. The peak strain values are mostly resulted due to the concentration of strain at the corners of the gusset plate as shown in Fig. 9.

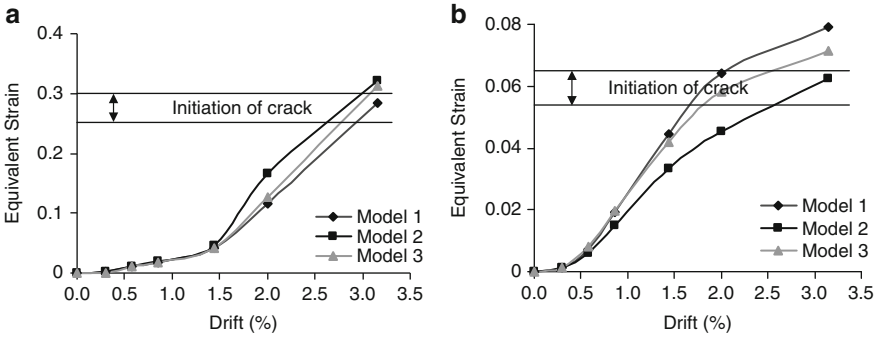


Fig. 11 Strain distribution (**a**) in mid region of the brace (**b**) along the weld lines which connect the gusset plate to beam/column

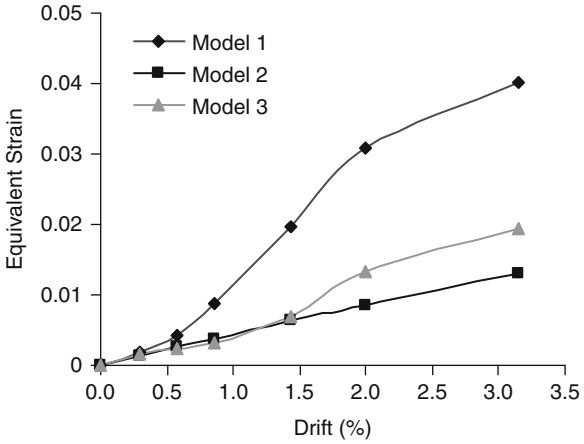


Fig. 12 Strain distribution at the gusset plate

Furthermore, Fig. 12 illustrates peak strain distributions in the regions just beyond the brace ends in the gusset plates. Severely increased strain distribution is observed in Model 1 compared with Model 2 and 3 because of the additional demand imposed due to lack of space provided in the gusset plate for the brace end rotation when it buckles in the out-of-plane direction. From the comparison of Figs. 11 and 12, the immediately occupancy performance level could be achieved in all models, but the achievement of life safety and collapse prevention performance level in Model 1 is raised serious doubt due to the fact that high concentration of strain is developed just beyond the brace end and corners of the gusset plate in the medium level of drift. These high concentrations of strain could lead to either net section fracture of the gusset plate or incipient weld tearing due to excessive brace rotation resulting in the out-of-plane buckling, well before the initiation of brace fracture. Even in Model 2 and 3, collapse prevention performance level could not be achieved because of possible incipient weld tearing before the incipient brace fracture.

6.2 Weld Size

As mentioned before, the use of short weld lengths result more compact gusset plate. Figures 11a and 13a illustrate that such a compact gusset plate is not significantly effect on the strain distribution of the midspan region of the brace. But the comparison of Figs. 11b and 13b show that the more compact gusset plate reduces the strain concentrations at the corners of the gusset plate significantly (Fig. 14).

As a result of that, the dominant failure mode of the system will be the fracture of the brace and hence, collapse prevention performance level is possible to be achieved in designing the connection using more compact gusset plate with the free

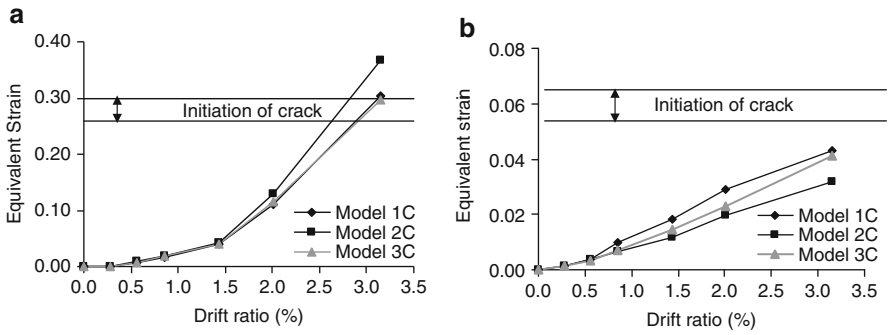


Fig. 13 Strain distributions (**a**) in mid region of brace (**b**) along gusset plate-to-beam/column weld lines

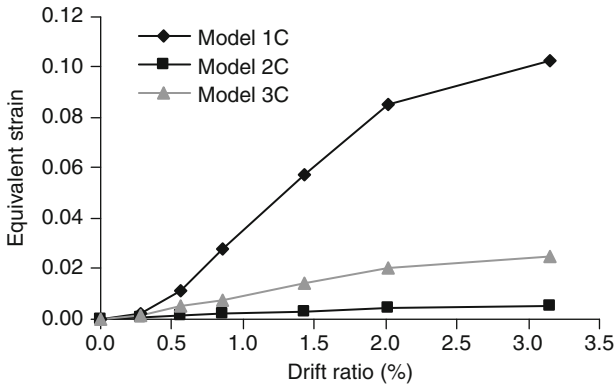


Fig. 14 Strain distribution at the gusset plate

space provided to form the tri-linear yield mechanism. So, this study highlights the importance of the size of welds to strain concentrations at the corners of the gusset plate but more detailed investigations are required to set the limit for the weld length to the gusset plate thickness (L/t) to achieve the collapse prevention performance level.

6.3 Beam-to-Column Connection

Figure 15 shows that the strain distribution at the gusset plate of partially restrained connection is very similar to the distribution that observed at the welded beam-to-column connection.

Figure 16a and b show the variations of equivalent plastic strain against the drift ratio in Model 2, 3 and 3PR. at mid regions of braces and along weld lines. It is clear

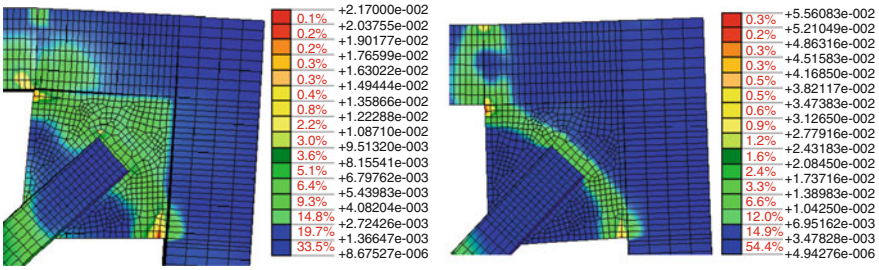


Fig. 15 Equivalent Von Mises strain distributions at the deformation of $\delta/\delta_y = 11$

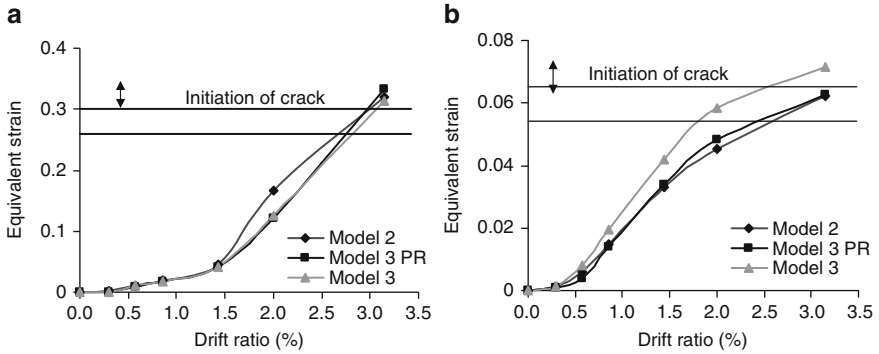


Fig. 16 Strain distributions (**a**) in mid region of the brace (**b**) along the gusset plate-to-beam/column weld lines

that the partial restrained connection at the corner of gusset plate has no influence to strain distribution at the mid region of the brace but there is slight effect on the strain concentrations at corners of the gusset plate.

6.4 Loading History

Figures 17 and 18 illustrate the peak equivalent strain distribution developed at the locally buckled region in the middle of the brace, at the gusset plate and along weld lines resulting in highly unsymmetrical displacement history. In general, distributions of the peak strains against the drift ratios are slightly lower to distributions those are observed from the nearly symmetric displacement history except the strain distribution at the locally buckled region in the middle of the brace. The strain distribution at the mid region of the brace is significantly decreased compared to the distribution resulting in nearly symmetrical displacement history.

Following the compression cycle which causes significant out-of-plane deformation, at the end of the unloading (P = 0) in the tension, the brace retains the

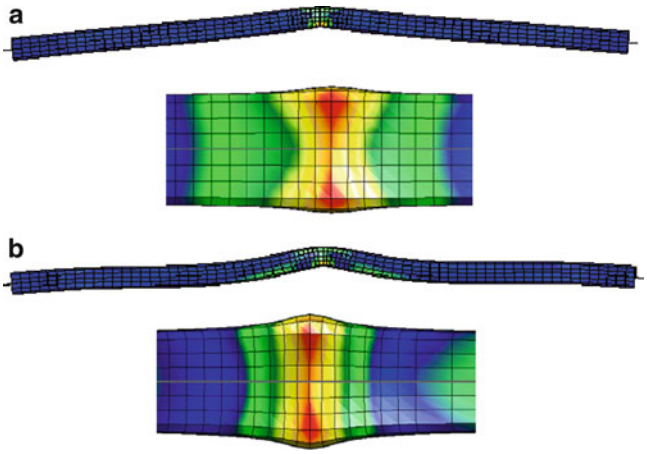


Fig. 17 Global and local buckling mode (**a**) at zero axial displacement (**b**) at the peak displacement of the same tensile cycle with significant tensile yielding

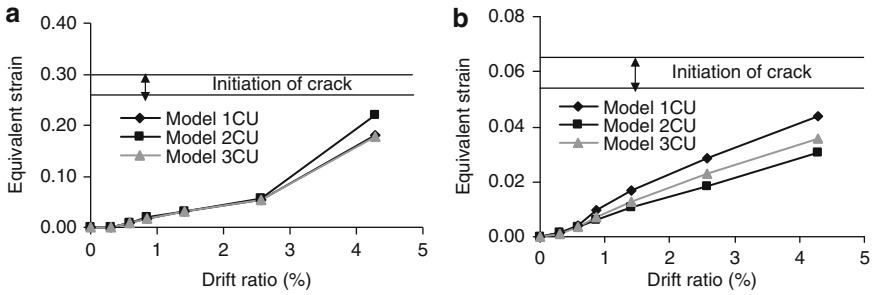


Fig. 18 Strain distributions (**a**) in mid region of the brace (**b**) along the gusset plate-to-beam-column weld lines

residual axial and the transverse deformation being a visible kink in the brace. When the brace is loaded in tension from P = 0, the brace recovers most of the out-of-plane deformation but it is not fully straight as mentioned before even after significant yielding of the brace. Further increasing of axial tension load causes to rotate the locally deformed region in the middle of the brace in the reverse direction of the inelastic buckling during the compression cycle. Eventually the plastic hinge is formed, plastic rotation in the reverse direction lead to effectively reduce the magnitude of the transverse deflection. However, as shown in Fig. 19, significant plastic rotation due to tension yielding in the brace triggers the local buckling in the middle of the brace. As a result of that, larger strain concentration could be observed during the next compression cycle.

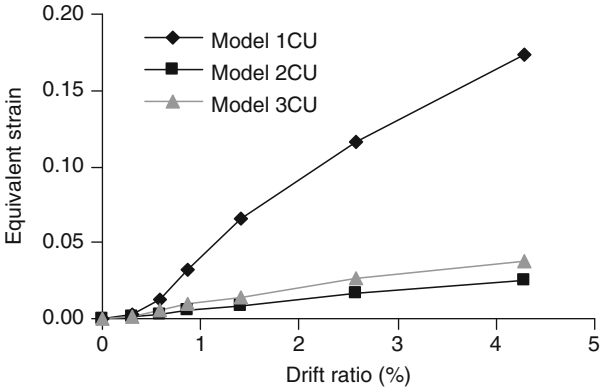


Fig. 19 Strain distribution at the gusset plate

7 Conclusion

From the results of this study, following recommendations for the design of the gusset plate connection and conclusions could be made as:

- Providing a free space in the gusset plate to form tri-linear yield line results more compact gusset plate. Furthermore, it shows that there is no significant difference in the distribution of strains and stresses in the middle of the brace, gusset plate and along the weld lines compared to the current 2t linear clearance model with tapered gusset plate. According to the tri-linear model, it is recommended to insert the brace into the gusset plate till the minimum angle between the line which connects the brace end and the re-entrant corner of the gusset plate and the weld line which connect the gusset plate to the beam or the column, should be 30° as shown in Fig. 7 in order to prevent the highly concentrated stress and strain demands to the weld lines and the gusset plate. Furthermore, it is recommended that when the tapered gusset plate is used, the minimum angle of 30° between the weld line which connects the brace to the gusset plate and the free edge of the gusset plate should be provided.
- Shear plate bolted beam-to-column connection at the corner of the gusset plate rather providing it at the face of the column flange has no significant influence on the local performance of the gusset plate connection. But as discussed in the first part of the study, the bolted beam-to-column connection has significant influence to the global performance.
- The fracture life of the brace greatly depends on the applied loading history. Specially for the loading history which develops the significant tensile yielding in the brace before each of the compression cycle which is capable to develop significant out-of-plane buckling, could cause to reduce the fracture life significantly since inelastic rotation induced in tensile yielding in the brace lead to trigger the local buckling in the middle of the brace.

- Initiation of crack could be developed at re-entrant corners of the weld lines in the gusset plate connection with the free space provided to form either linear or tri-linear yield mechanisms. This could be controlled by designing the weld lengths short, thereby resulting more compact gusset plate. In order to propose the design guidelines to avoid such higher strain concentrations, more parametric studies are required.

References

1. AISC (2005) Seismic provisions for structural steel buildings American Institute of Steel Construction, Inc., Chicago, IL
2. Astaneh-Asl A (2000) Seismic behavior and design of gusset plates for braced frames. Steel Yips, Structural Steel Education Council, Moraga, CA
3. EC3 (2005) ENV 1993-1-1, Eurocode 3: Design of steel structures – Part 1.1: General rules and rules for buildings. European Committee for Standardisation, Brussels
4. EC8 (2005) EN 1998-1, Eurocode 8: Design provisions for earthquake resistance of structures, Part 1: General rules, seismic actions and rules for buildings. European Committee for Standardisation, Brussels
5. Elghazouli AY (2008) Seismic design of steel framed structures to Eurocode 8. Proceedings of the 14th World Conference on Earthquake Engineering, Beijing, China, 12–17 October 2008
6. Lee S, Goel SC (1987) Seismic behavior of hollow and concrete-filled square tubular bracing members. Research Report UMCE 87-11, Department of Civil Engineering, University of Michigan
7. Lehman DE, Roeder CW, Herman D, Johnson S, Kotulka B (2008) Improved seismic performance of gusset plate connections. J Struct Eng ASCE 134(6):890–901
8. Liu J, Astaneh-Asl A (2000) Cyclic testing of simple connections, including effects of the slab. J Struct Eng 126(1):32–39
9. Martinez-Saucedo G, Packer JA, Christopoulos C (2007) Gusset plate connections to circular hollow section braces under inelastic cyclic loading. J Struct Eng ASCE 134(7):1252–1258
10. MIDAS, Nonlinear and detail FE analysis system for civil structures, FEA analysis and algorithm manual
11. OpenSees, Open System for Earthquake Engineering Simulation. Pacific Earthquake Engineering Research Center, University of California, Berkeley, CA
12. Roeder CW, Lehman DE, Yoo JH (2004) Performance based seismic design of braced-frame connections. 7th Pacific Structural Steel Conference, USA, 24–27 March 2004
13. Shaback JB (2001) Behaviour of square HSS braces with end connections under reversed cyclic axial loading. Thesis submitted in partial fulfilment of the requirements for the degree Master of Science, Department of Civil Engineering, University of Calgary, Calgary, Canada
14. Uriz P, Filippou FC, Mahin SA (2008) Model for cyclic inelastic buckling for steel member. J Struct Eng ASCE 134(4):616–628
15. Walpole WR (1996) Behaviour of cold-formed steel RHS members under cyclic loading. Research Report 96-4. Department of Civil Engineering, University of Canterbury, Christchurch, New Zealand
16. Yoo JH, Lehman DE, Roeder CW (2008a) Influence of connection design parameters on the seismic performance of braced frames. J Construct Steel Res 64:608–622
17. Yoo JH, Roeder CW, Lehman DE (2008b) Analytical performance simulation of special concentrically braced frames. J Struct Eng ASCE 134(6):881–889
18. Yoo JH, Roeder CW, Lehman DE (2008c) Simulated behavior of multi-story X-braced frames. J Eng Struct (in press)

Seismic Response of RC Framed Buildings Designed According to Eurocodes

Juan Carlos Vielma, Alex Barbat, and Sergio Oller

Abstract In order to ensure that a structure does not collapse when subjected to the action of strong ground motions, modern codes include prescriptions in order to guarantee the ductile behavior of the elements and of the whole structure. Obviously, it would be of special importance for the designer to know during the design process the extent of damage that the structure will suffer under the seismic action specified by the design spectrum and also the probability of occurrence of different states of behaviour. The incremental nonlinear static analysis procedure used in this paper allows formulating a new, simplified, seismic damage index and damage thresholds associated with five limit states. The seismic behavior of a set of regular reinforced concrete buildings designed according to the EC-2/EC-8 prescriptions for a high seismic hazard level is then studied using the proposed damage index and damage states. Fragility curves and damage probability matrices corresponding to the performance point are calculated for the studied buildings. The obtained results show that the collapse damage state is not reached in the buildings designed according the prescriptions of EC-2/EC-8 and also that the damage does not exceed the irreparable damage limit state.

Keywords Non-linear analysis · Ductility · Overstrength · Objective damage index · Seismic safety

1 Introduction

The main objective of the seismic design is to obtain structures capable to sustain a stable response under strong ground motions. Some of the aspects of the current seismic analysis procedures allow adapting the non-linear features into an

J.C. Vielma (✉)
Lisandro Alvarado University, Decanato de Ingeniería Civil, Av. La Salle, Barquisimeto, Venezuela
e-mail: jcvielma@ucla.edu.ve

A. Barbat and S. Oller
Technical University of Catalonia, c. Gran Capitán s/n 08034, Barcelona, Spain
e-mail: alex.barbat@upc.edu; sergio.oller@upc.edu

M. Papadrakakis et al. (eds.), *Computational Methods in Earthquake Engineering*, Computational Methods in Applied Sciences 21, DOI 10.1007/978-94-007-0053-6_9,
© Springer Science+Business Media B.V. 2011

equivalent elastic analysis and, obviously, the formulation of these procedures is essential in assuring a satisfactory earthquake resistant design. The advances in the field of nonlinear structural analysis and the development of improved computational tools enabled to apply more realistic analysis procedures to new and existent buildings, taking into account the main features of their seismic non-linear behaviour, like constitutive nonlinearities (plasticity and damage) and geometrical nonlinearities (large deformations and displacements). Non linear analysis procedures have been used in previous studies to assess the seismic design of buildings designed according to specific design codes [1–3]. The static incremental non-linear analysis (pushover analysis) can be performed by using a predefined lateral load distribution corresponding to the first mode shape. The dynamic analysis can be applied using a suitable set of records obtained from strong motion databases or from design spectrum-compatible synthesized accelerograms. Recently, Performance-Based Design required the definition of a set of limit states. These limit states are frequently defined by engineering demand parameters, among which the most used are the interstory drift, the global drift and the global structural damage. These parameters define damage thresholds associated with the limit states, which allow calculating fragility curves and the damage probability matrices used in the seismic safety assessment of the buildings. In this work, the seismic safety of regular reinforced concrete framed buildings is studied using both the static and the dynamic nonlinear analysis. The static analysis consisted in using pushover procedure and the dynamic analysis was performed by means of incremental dynamic analysis (IDA). The analyses were performed using the PLCd computer code [4] which allows incorporating the main characteristics of the reinforcement and confinement provided to the cross sections of the structural elements. A set of 16 reinforced concrete framed buildings with plan and elevation regularity was designed according to EC-2 [5] and EC-8 [6]. The results obtained from their non-linear analysis allowed calculating the global ductility, the overstrength and the behaviour factors. The latter were compared with the values prescribed by the EC-8. The global performance of the buildings was evaluated using an objective damage index based on the capacity curve. Finally, with the damage thresholds obtained from non-linear analysis, fragility curves and damage probability matrices were computed.

2 Seismic Response Parameters

Among the seismic response parameters studied in past works, global ductility, overstrength and behaviour factor are the most important; they can be calculated by applying deterministic procedures based the non-linear response of the structures subjected to static or dynamic loads. Although it is difficult to find a method to obtain the global yield and the ultimate displacements [7], a simplified procedure is applied in this work. The non-linear static response obtained via finite element techniques is used to generate the idealized bilinear capacity curve shape shown in Fig. 1, which has a secant segment from the origin to a point that corresponds to

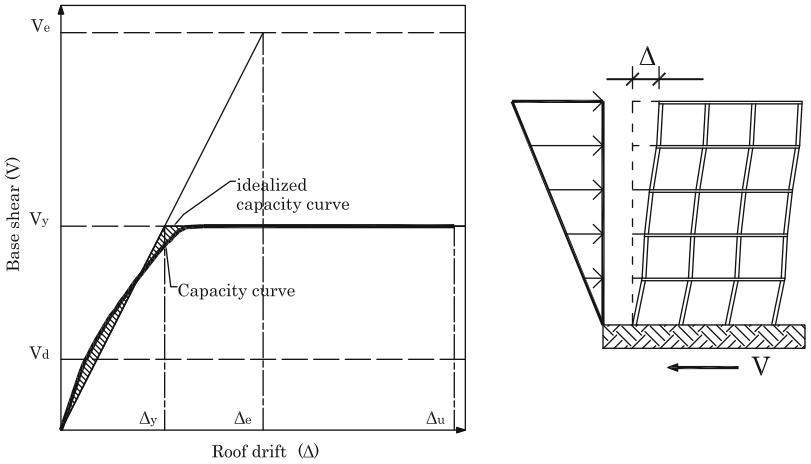


Fig. 1 Scheme for determining displacement ductility and overstrength

a 75% of the maximum base shear [8, 9]. The second segment, which represents the branch of plastic behaviour, was obtained by finding the intersection of the aforementioned segment with another, horizontal segment which corresponds to the maximum base shear. The use this compensation procedure guarantees that the energies dissipated by the ideal system and by the modelled one, are equal (see Fig. 1).

For a simplified non-linear analysis, there are two variables that characterize the quality of the seismic response of buildings. The first is the global ductility μ, defined as

$$\mu = \frac{\Delta_u}{\Delta_y} \tag{1}$$

and calculated based on the values of the yield drift, Δ_y, and of the ultimate drift, Δ_u, which are represented in the idealized capacity curve shown in Fig. 1.

The second variable is the overstrength R_R of the building, which is defined as the ratio of the yielding base shear, V_y to the design base shear, V_d (see Fig. 1)

$$R_R = \frac{V_y}{V_d} \tag{2}$$

3 Local and Objective Damage Index

A local damage index is calculated using the finite element program PLCd with a constitutive damage and plasticity model that enables correlation of damage with lateral displacements [10, 11]

$$D = 1 - \frac{\| P^{in} \|}{\| P_0^{in} \|} \tag{3}$$

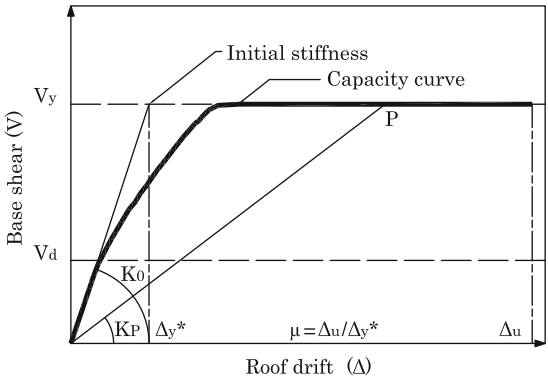


Fig. 2 Parameters for determination of the objective damage-index

where $\|P^{in}\|$ and $\|P_0^{in}\|$ are the norm of current and elastic values of the internal forces vectors, respectively. Initially, the material remains elastic and $D = 0$, but when all the energy of the material has been dissipated $\|P^{in}\| \to 0$ and $D = 1$.

It is important to know the level of damage reached by a structure for a certain demand. This is possible if the damage index is normalized with respect to the maximum damage which can occur in the structure [12]. This objective damage index $0 \leq D_{obj}^{P} \leq 1$ achieved by a structure at any point P is defined as

$$D_{obj}^{P} = \frac{D_P}{D_C} = D_P \frac{\mu}{1-\mu} = \frac{\left(1 - \frac{K_P}{K_0}\right)\mu}{1-\mu} \tag{4}$$

For example, for the point P, which might be the performance point resulting from the intersection between inelastic demand spectrum and the capacity curve (obtained from pu-shover analysis), it corresponds a stiffness K_P. Other parameters are the initial stiffness K_0 and the displacement ductility μ, calculated using the yield displacement Δ_y^* which corresponds to the intersection of the initial stiffness with the maximum shear value (see Fig. 2).

4 Non-linear Response

Non-linear incremental static and dynamic analysis are performed using PLCd finite element code [4,13,14]. PLCd is a finite element code that works with two and three-dimensional solid geometries as well as with prismatic, reduced to one-dimensional members. It provides a solution combining both numerical precision and reasonable computational costs [15,16] and it can deal with kinematics and material nonlinearities. It uses various 3-D constitutive laws to predict the material behaviour (elastic, visco-elastic, damage, damage-plasticity, etc. [17]) with different yield surfaces to control their evolution (Von-Mises, Mohr-Coulomb, improved Mohr-Coulomb, Drucker-Prager, etc. [18]). Newmark's method [10] is used to perform the dynamic analysis. A more detailed description of the code can be found in Mata *et al.*

[15, 16]. The main numerical features included in the code to deal with composite materials are: (1) Classical and serial/parallel mixing theory is used to describe the behaviour of composite components [19]. (2) The Anisotropy Mapped Space Theory enables the code to consider materials with a high level of anisotropy, without the associated numerical problems [20]. (3) The Fiber-matrix debonding, which reduces the composite strength due to the failure of the reinforced-matrix interface, is also considered [21].

Experimental evidence shows that inelasticity in beam elements can be formulated in terms of cross-sectional quantities [22] and, therefore, the beam's behaviour can be described by means of concentrated models, sometimes called plastic hinge models, which localize all the inelastic behaviour at the ends of the beam by means of ad-hoc force-displacement or moment-curvature relationships [23, 24]. But, in the formulation used in this computer program, the procedure consists of obtaining the constitutive relationship at cross-sectional level by integrating on a selected number of points corresponding to the fibers directed along the beam's axis [25]. Thus, the general nonlinear constitutive behaviour is included in the geometrically exact nonlinear kinematics formulation for beams proposed by Simo [26], considering an intermediate curved reference configuration between the straight reference beam and the current configuration. The displacement based method is used for solving the resulting nonlinear problem. Plane cross sections remain plane after the deformation of the structure; therefore, no cross sectional warping is considered, avoiding including additional warping variables in the formulation or iterative procedures to obtain corrected cross sectional strain fields. Thermodynamically consistent constitutive laws are used in describing the material behaviour for these beam elements, which allows obtaining a more rational estimation of the energy dissipated by the structures. The simple mixing rule for composition of the materials is also considered in modelling materials for these elements, which are composed by several simple components. Special attention is paid to obtain the structural damage index capable of describing the load carrying capacity of the structure.

According to the Mixing Theory, in a structural element coexist N different components, all the components undergo same strain; therefore, strain compatibility is forced among the material components. Free energy density and dissipation of the composite are obtained as the weighted sum of the free energy densities and dissipation of the components, respectively. Weighting factors K_q are the participation volumetric fraction of each compounding substance, $K_q = \frac{Vq}{V}$, which are obtained as the quotient between the q-th component volume, V_q, and the total volume, V [13–16].

Discretization of frames was performed with finite elements whose lengths vary depending on the column and beam zones with special confinement requirements. These zones are located near the nodes where the maximum seismic demand is expected, and are designed according to the general dimensions of the structural elements, the diameters of the longitudinal steel, the spans length and the storey heights. Frame elements are discretized into equal thickness layers with different composite materials, characterized by their longitudinal and transversal reinforcement ratio (see Fig. 3). Transverse reinforcement benefits are included by

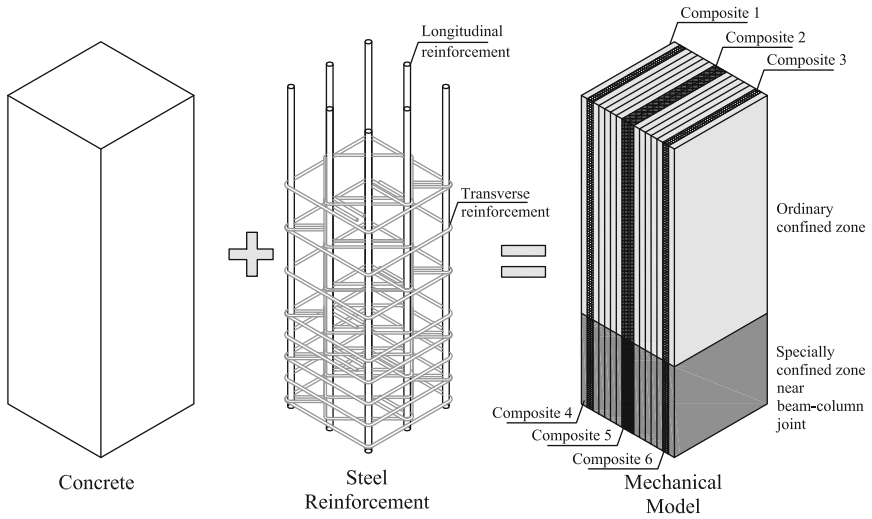


Fig. 3 Discretization of the RC frame's elements

means of the procedure proposed by Mander *et al.* [27]. This procedure consists in improving the compressive strength of the concrete depending on the characteristics of the longitudinal and transversal reinforcement.

5 Design of Buildings

A set of regular reinforced concrete moment-resisting framed buildings (MRFB) designed according to EC-2 and EC-8, characterized by a variable number of storeys (3, 6, 9 and 12) and spans (3, 4, 5 and 6) were selected, in order to cover the low and medium vibration period ranges and also to take into consideration the structural redundancy. Inner and outer frames are defined for each building structure according to the corresponding load ratio (seismic load/gravity load).

The frame members are analyzed designed and detailed following the EC-2 and EC-8 prescriptions for high ductility class (behaviour factor of 5.85). The seismic demand is established for the soil type B (stiff soil) and for a peak ground acceleration of 0.3 g. The geometric characteristics of the typical frames are given in Fig. 4.

5.1 Non-linear Static Analysis

To evaluate the inelastic response of the four structures, pushover analyses were performed applying a set of lateral forces corresponding to seismic actions of the first vibration mode. The lateral forces are gradually increased starting from

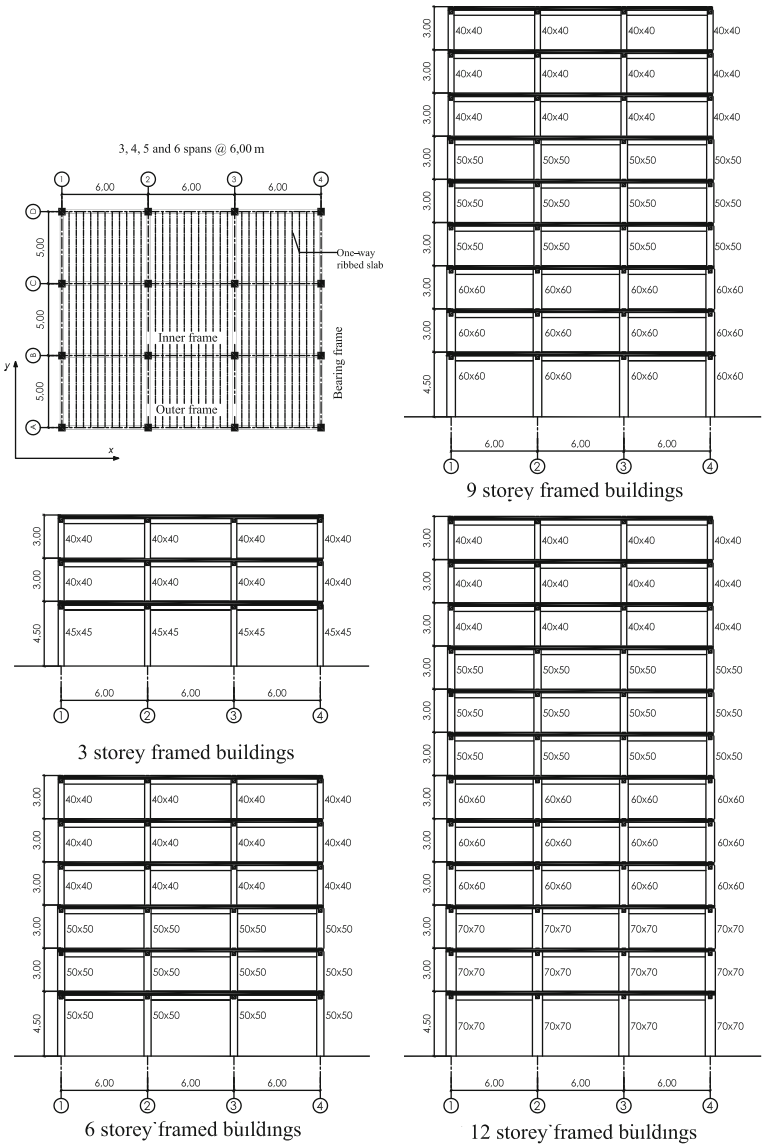


Fig. 4 Plan and elevation view of the framed buildings

zero, passing through the value which induces the transition from elastic to plastic behaviour and, finally, reaching the value which corresponds to the ultimate drift (*i.e.* the point at which the structure can no longer sustain any additional load and collapses). Before the structure is subjected to the lateral loads simulating seismic action, it is first subjected to the action of gravity loads, in agreement with the combinations applied in the elastic analysis. The method applied does not allow for evaluation of torsional effects, being the used model a 2D one.

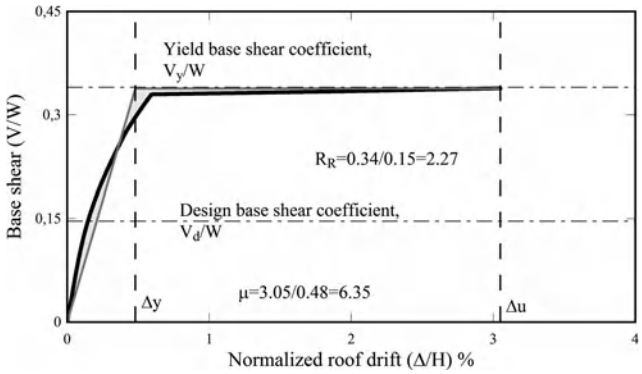


Fig. 5 Typical idealized capacity curve of the studied buildings

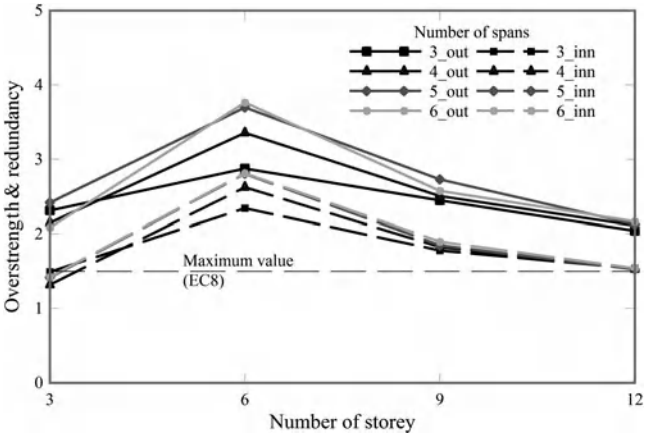


Fig. 6 Overstrength and redundancy vs. the number of storeys of the outer and inner frames

Based on the idealized bilinear curve in Fig. 5, a global ductility of 6.35 is obtained, a higher value than that considered in the EC-8 seismic design code, which is 5.85. From Fig. 5, overstrength is also calculated, obtaining a value of 2.27. This means that the moment resisting buildings designed according to the EC-2 and EC-8 have a ductile response to seismic forces, as well as an adequate overstrength.

Figure 6 shows the computed values of the overstrength for the outer and inner frames of the studied buildings, plotted in function of the number of storeys. The results demonstrate clearly that the influence of the number of spans, equivalent to consider different numbers of resistant lines, is very low, except for the case of the 6 storey buildings. For the other buildings, the overstrength values are closer to each other. It can be also seen that the computed values of the combined overstrength factors are greater than the value which the EC-8 prescribes for the design of ductile framed buildings.

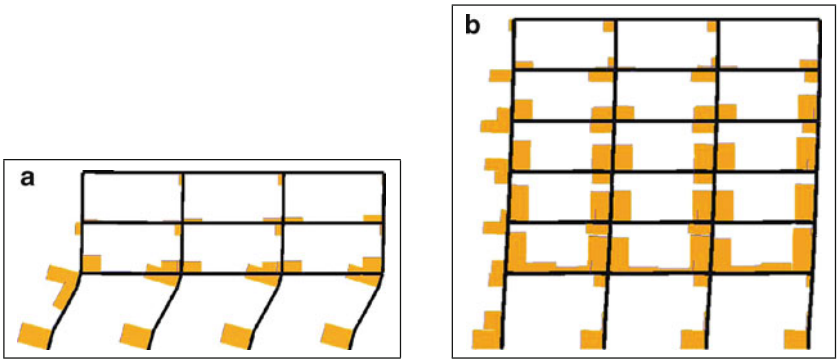


Fig. 7 Distribution of local damage-index at collapse displacement

The local damage index is calculated using Eq. (3) and the results are shown in Fig. 7 for the inner frames of the 3 and 6 storey buildings, for the collapse displacement. In this figure, each rectangle represents the magnitude of the damage reached by the element. It is important to observe that for the low rise buildings (N = 3) the maximum values of the damage corresponds to the elements located at both ends of the first storey columns; this damage concentration corresponds to a soft-storey mechanism. Instead, high rise buildings (N = 6, 9 and 12) show their maximum damage values at low level beams ends, according to the desired objective of the conceptual design which is to produce structures with weak beams and strong columns.

Figure 8 show the interstory drifts at collapse. It is important to note the difference among the interstory values for the three levels building, which reaches very high value at the ground level (Fig. 8a). This feature is a consequence of the soft-story mechanism characterized by the concentration of the damage in the columns of this story. The interstory drifts of the 6, 9 and 12 levels buildings reach values near 4%, without a predominant value in a specific story. From the non-linear static analysis, the objective damage index is computed using Eq. (3).

Figure 9 shows the evolution of the objective damage index respecting the normalized roof drift, computed for all the frames of the 3 storey building. The curves are similar to those obtained for the frames of the same number of stories.

5.2 Non-linear Dynamic Analysis

In order to evaluate the dynamic response of the buildings, IDA (Incremental Dynamic Analysis) procedure was applied [28], which consists in performing time-history analyses for actual ground motion accelerograms or for artificially

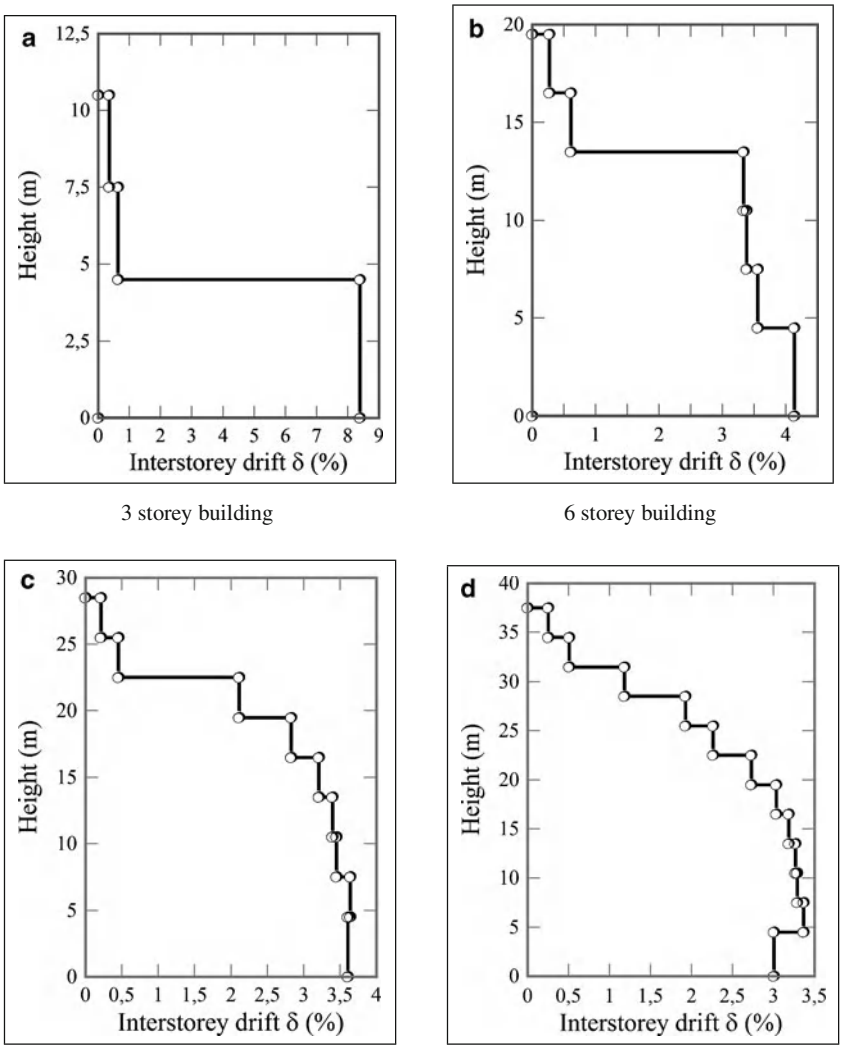


Fig. 8 Interstory drifts at the collapse

synthesized accelerograms scaled in such a way to induce increasing levels of inelasticity in each new analysis. A set of six artificial accelerograms, compatible with the soil type B of EC-8 design spectrum, were generated. Figure 10 shows the elastic design spectrum and the 5% damping response spectra computed from the set of artificial accelerograms.

Peak accelerations equal to the basic design acceleration is assumed in the analysis. From this value, the record is scaled until a plastic response is reached by the structure; this procedure continues until achieving the collapse displacement.

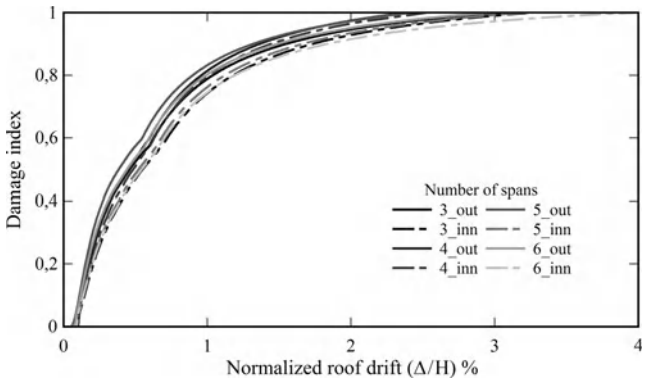


Fig. 9 Evolution of the damage index of the 3 storey inner and outer frames

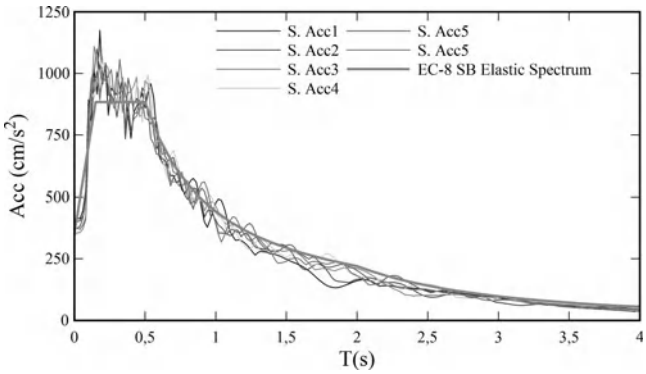
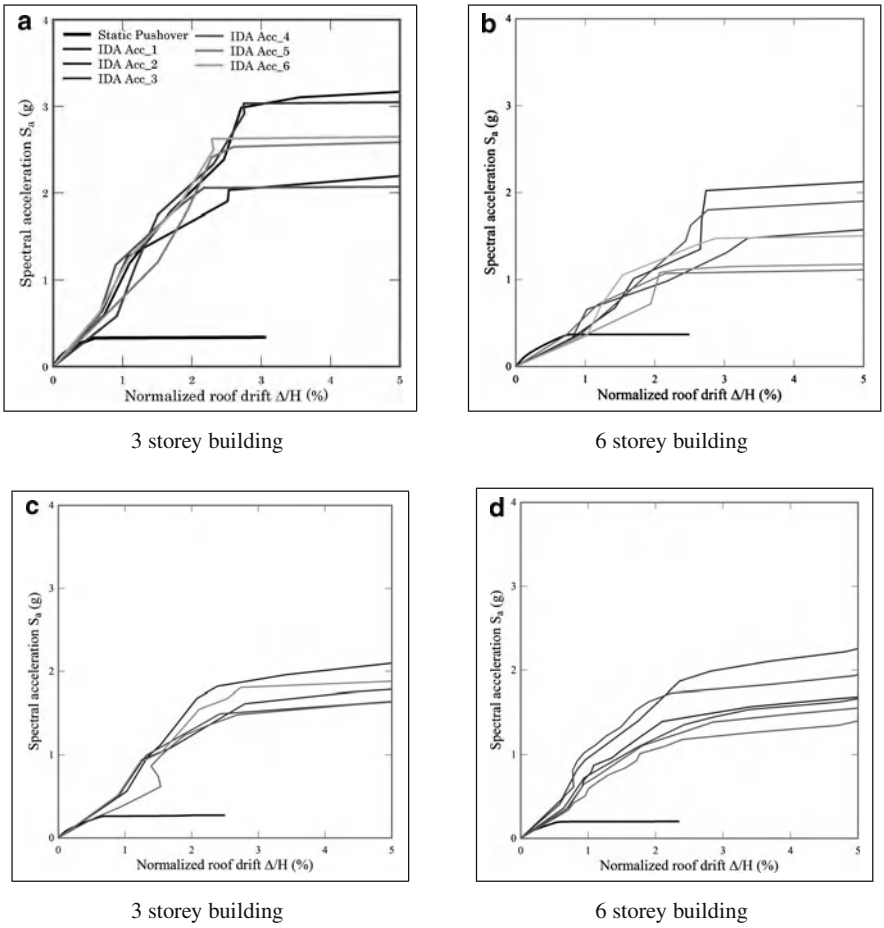


Fig. 10 EC-8 soil type B, elastic design spectrum and response spectra

For each value of scaled acceleration, a maximum value of the structural response is calculated. The IDA curves are obtained by plotting a maximum characteristic of the severity of the earthquake in function of a maximum value of the structural response. In this case, we represented the spectral acceleration for a 5% damping ratio against the roof drift. The collapse is reached when the capacity of the structure drops [29–31]. A usual criterion is to consider that collapse occurs when the slope of the curve is less than the 20% of the elastic slope [28, 31, 32]. Figure 11 show the IDA curves computed for the 3-spans outer frames of the 3, 6, 9 and 12 storey buildings. Note that the collapse points of the frames are closer to the values obtained from the static pushover analysis, validating the collapse threshold values.

Table 1 summarizes the computed average values of the collapse points for all the studied cases, computed by means of the dynamic analysis.



3 storey building

6 storey building

3 storey building

6 storey building

Fig. 11 IDA curves of the outer frames of the buildings

Table 1 Normalized roof displacement (%) at the collapse of the structures

Number of storeys	Static analysis	Dynamic analysis (average)
3	2.51	2.51
6	2.63	2.63
9	2.48	2.62
12	2.35	2.39

The dynamic analysis is useful to assess the collapse point of the buildings. For the behaviour factors q, the following equation has been proposed [2]:

$$q = \frac{a_{g\,(Collapse)}}{a_{g\,(Design-yield)}} \tag{5}$$

Table 2 Computed behaviour factors of the buildings

Number of storeys	$q_{equation}$	q_{code}	$\frac{q_{equation}}{q_{code}}$
3	17.40	5.85	2.97
6	10.79	5.85	1.84
9	15.07	5.85	2.57
12	15.12	5.85	2.58

where $a_{g(Collapse)}$ and $a_{g(Design-yield)}$ are the collapse and the yield design peak ground acceleration, respectively. The former is obtained from the IDA curves and the latter is calculated from the elastic analysis of the building. Average values of the computed behaviour factor q of the studied buildings are show in Table 2; these values correspond to the dynamic response obtained for the set of six synthesized accelerograms, and are compared with behaviour factors prescribed by the design codes.

The computed behaviour factors show that seismic design performed by using the EC-2 and EC-8 leads to structures with satisfactory lateral capacity, when they are subjected to strong motions, regardless of the building height. The relationship between the calculated and the prescribed behaviour factors is close to three for the case of low rise buildings.

6 Seismic Safety of the Buildings

Studying the seismic safety of the buildings designed according to the Eurocodes requires to define and compute the engineering demand measure (EDM). It is usual to select the interstory and the global drifts as EDM; in this article, the latter was selected. In order to assess the seismic safety, the global drifts correspond to the performance point have been determined as described in the following.

6.1 Determination of the Performance Point

In order to evaluate the non-linear behaviour of the buildings, the performance points, which represent the maximum drift of an equivalent single degree of freedom induced by the seismic demand, were calculated. These points have been determined by means of the N2 procedure [33] which requires transforming the capacity curve into a capacity spectrum expressed in terms of the spectral displacement, S_d, and of the spectral acceleration, S_a. The former is obtained by means of the equation

$$S_d = \frac{\delta_c}{MPF} \tag{6}$$

where δ_c is the roof displacement. The term MPF term is the modal participation factor calculated from the response in the first mode of vibration.

$$MPF = \frac{\sum_{i=1}^{n} m_i \phi_{1,i}}{\sum_{i=1}^{n} m_i \phi_{1,i}^2} \tag{7}$$

Spectral acceleration S_a is calculated by means of:

$$S_a = \frac{\frac{V}{W}}{\alpha} \tag{8}$$

where V is the base shear, W is the seismic weight and α is a coefficient obtained as

$$\alpha = \frac{\left(\sum_{i=1}^{n} m_i \phi_{1,i}\right)^2}{\sum_{i=1}^{n} m_i \phi_{1,i}^2} \tag{9}$$

Figure 12 shows a typical capacity spectrum crossed with the corresponding elastic demand spectrum. Idealized bilinear shape of the capacity spectra is also shown.

The values of the spectral displacements corresponding to the performance point are shown in Table 3. An important feature which influences on the non linear

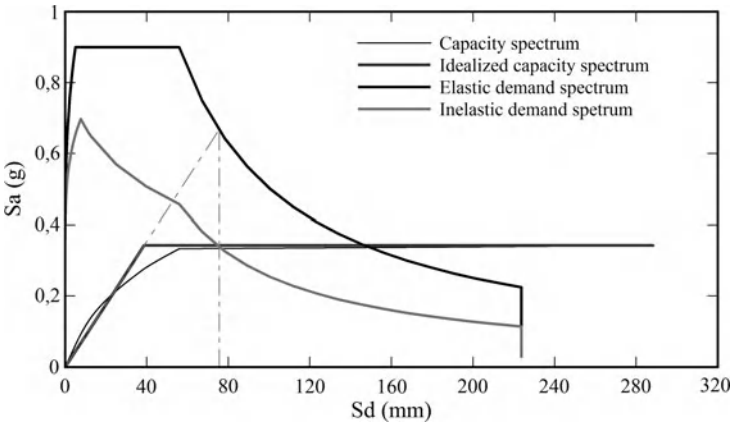


Fig. 12 Determination of the performance point according to N2 procedure

Table 3 Roof drift of performance points of the studied buildings

	Normalized roof drift			Ratio	
Number of stories	Performance point (%)	Static analysis	Dynamic analysis (average)	Static analysis	Dynamic analysis (average)
3	0.80	3.02	2.51	0.26	0.32
6	0.51	2.48	2.63	0.20	0.19
9	0.39	2.48	2.62	0.16	0.15
12	0.21	2.34	2.39	0.09	0.09

response of the buildings is the ratio between the performance point displacement and the collapse displacement. This ratio indicates whether the behaviour of a structure is ductile or fragile. The lower values correspond to the 12 storey buildings, which have a weak-beam strong column failure mechanism.

6.2 Fragility Curves and Damage Probability Matrices

The damage thresholds are determined using the VISION 2000 procedure [34], in which they are expressed in function of interstory drifts. In this article, five damage states thresholds are defined from both the interstory drift curve and the capacity curve [35]. For the slight damage state, the roof drift corresponding to the first plastic hinge is considered. The moderate damage state corresponds to the roof drift for which an interstory drift of 1% is reached in almost all the storeys of the structure. The repairable damage state is defined by an interstory drift of 2%. The severe damage state is identified by a roof drift producing a 2,5% of interstory drift at each level of the structure. Finally, the total damage state (collapse) corresponds to the ultimate roof displacement obtained from the capacity curve. Mean values and standard deviation were computed from the non linear response of the buildings with the same geometry and structural type, varying the number of spans from 3 to 6 [36].

Fragility curves are obtained by using the spectral displacements determined for the damage thresholds and considering a lognormal probability density function for the spectral displacements which define the damage states [37–40]

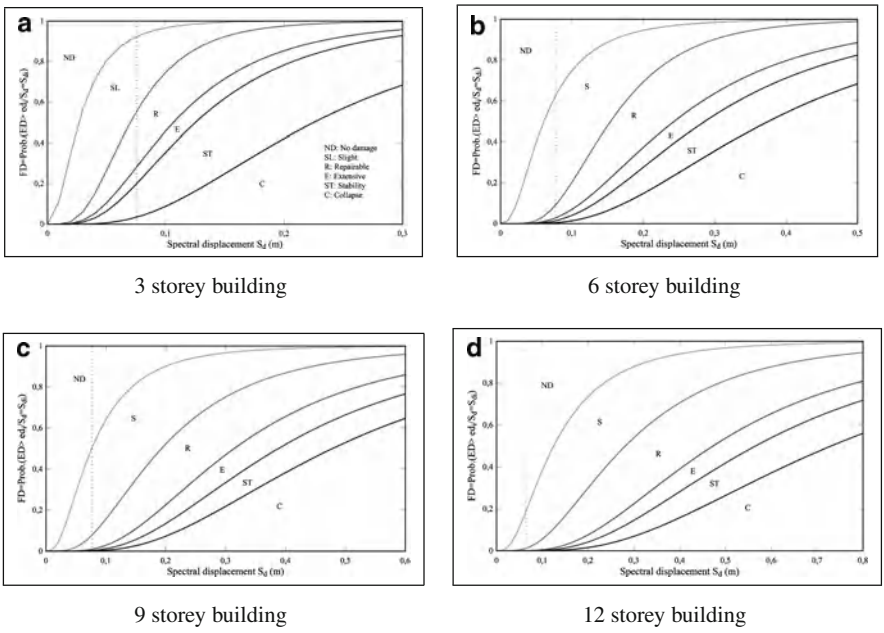
$$F(S_d) = \frac{1}{\beta_{ds} S_d \sqrt[n]{2\pi}} \exp\left[-\frac{1}{2}\left(\frac{1}{\beta_{ds}} \ln \frac{S_d}{\bar{S}_{d,ds}}\right)^2\right] \tag{10}$$

where $\bar{S}_{d,ds}$ is the mean value of spectral displacement for which the building reaches damage state threshold d_s and β_{ds} is the standard deviation of the natural logarithm of spectral displacement for damage state d_s. The conditional probability $P(S_d)$ of reaching or exceeding a particular damage state d_s, given the spectral displacement S_d, is defined as

$$P(S_d) = \int_0^S F(S_d) dS_d \tag{11}$$

Figure 13 show the fragility curves calculated for the four different heights of buildings considered in the analysis.

Figure 14 shows the damage probability matrices calculated for the performance point achieved for all the studied cases. It is important to note that for frames of the same building, probabilities vary according to the load ratio (seismic load/gravity load).



3 storey building

6 storey building

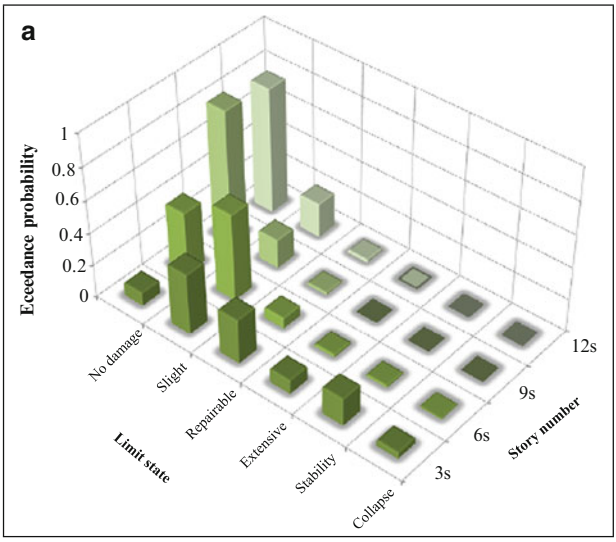
9 storey building

12 storey building

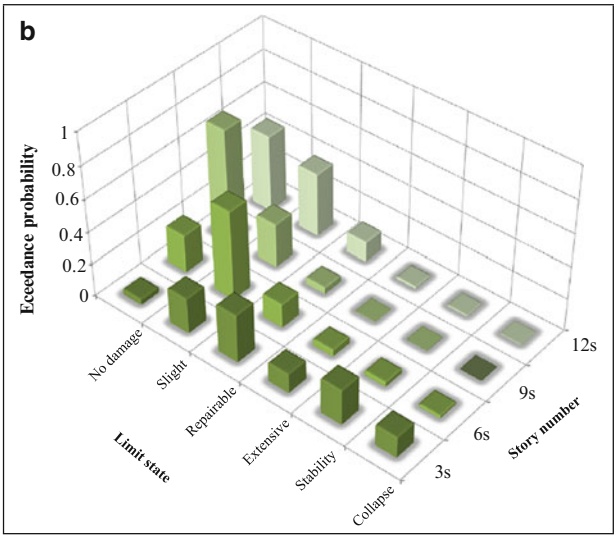
Fig. 13 Fragility curves of the buildings

Another important feature is the increasing values of the probabilities that low rise buildings reach higher damage states; the collapse of these buildings is associated with the soft-storey mechanism, as discussed in previous sections. For example, in the case of the inner frames of the three level building, the probability to reach the collapse is four times higher than in the case of the outer frame of the same building. In contrast, 6, 9 and 12 storey buildings show very low probabilities to reach higher damage states, regardless of the load ratio and of the span number. For these buildings, the predominant damage states are *non-damage* and *slight damage*.

Figure 15 shows the values of the damage index for the performance point of the different frames. These values were obtained using Eq. (3). First of all, it is possible to observe that low rise buildings (three levels) reach higher values of the damage index than the other buildings, as a consequence of the failure mechanism which occurs for this kind of buildings (soft storey mechanism). In contrast, the 12 level buildings exhibits damage indices about 0.3 and 0.35 for the inner and outer frames respectively, values that are consistent with the failure mechanism (strong columns-weak beams). Finally it is important to observe that the values of the damage index obtained for the outer frames are lower than those corresponding to the inner ones, indicating that the damage index depends on the load type ratio [41].



Outer frames



Inner frames

Fig. 14 Damage probability matrices of 3, 6, 9 and 12 storey buildings

7 Concluding Remarks

The proposed objective damage index predicts adequately the state of damage that is achieved by the frames for a specific seismic demand value (displacement of the performance point).

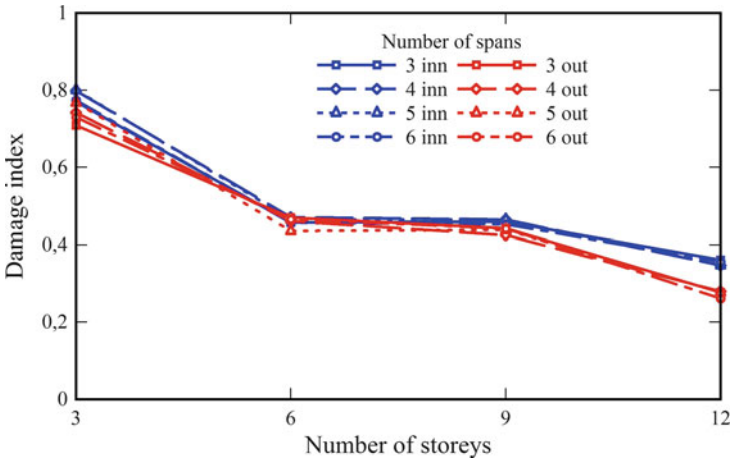


Fig. 15 Damage index computed for the performance point of the 3 storey building frames

The Incremental Dynamic Analysis is useful in order to assess the collapse threshold of the frames. Dynamic results confirm the values obtained from pushover analysis. The dynamic analysis is also suitably to evaluate the behaviour factor q.

In general, the reinforced concrete framed buildings designed according to the Eurocodes for a high ductility class show adequate ductility behaviour, as it is evidenced by the global ductility values and the ratio between the performance point and the ultimate displacement. They also exhibit adequate values of overstrength, which are greater than the code prescribed value (overstrength $= 1.5$). Behaviour factors computed from dynamic analysis are also adequate and reach twice the code values. No influence of the structural redundancy was detected in the procedure applied to evaluate such factors.

The nonlinear response of the buildings depends on the load ratio between the seismic and gravity loads; the inner frames which are designed for lower load ratios have lower overstrength values. Consequently, the seismic safety of the different frames is influenced by this ratio.

The local damage distribution when the buildings reach the collapse threshold, show that low rise buildings (3 storey) have a failure mechanism associated with the formation of the soft storey mechanism. Medium height buildings (6, 9 and 12 storey) exhibit a failure mechanism associated with the conceptual design objective of designing structures with weak-beam and strong column. The interstory drifts of the low rise building show that the damage is concentrated into the ground level, where the interstory drift reached a value greater than 8%. Mid-rise buildings show more uniform values of the interstory drifts and their values are lower than 4%. These results evidenced that the low-rise building collapse corresponds to soft-story mechanism.

References

1. Mwafi AM, Elnashai A (2002) Overstrength and force reduction factors of multistory reinforced-concrete buildings. Struct Des Tall Buil 11:329–351
2. Mwafi AM, Elnashai A (2002) Calibration of force reduction factors of RC buildings. J Earthquake Eng 6(2):239–273
3. Sanchez AM, Plumier L (2008) Parametric study of ductile moment-resisting steel frames: a first step towards Eurocode 8 calibration. Earthquake Eng Struct Dynam 37:1135–1155
4. PLCd (2009) Non-linear thermo mechanic finite element oriented to PhD student education, code developed at CIMNE, Barcelona, Spain
5. Comité Européen de Normalisation (2001) Eurocode 2: Design of concrete structures BS EN 1992, Brussels
6. Comité Européen de Normalisation (2001) Eurocode 8: Design of structures for earthquake resistance EN 2004-1-1, Brussels
7. Priestley MJN, Calvi GM, Kowalsky MJ (2007) Displacement-based seismic design of structures. IUSS Press, Pavia, Italy
8. Park R (1998) State-of-the-art report: ductility evaluation from laboratory and analytical testing. In: Proceedings 9th WCEE. IAEE, Tokyo, Japan
9. Vielma JC, Barbat AH, Oller S (2009) Seismic performance of Waffled-Slab floor buildings. Proc P I Civil Eng Str 16(3):169–182
10. Barbat AH, Oller S, Oñate E, Hanganu A (1997) Viscous damage model for Timoshenko beam structures. Int J Solid Struct 34(30):3953–3976
11. Car E, Oller S, Oñate E (2000) Seismic performance of Waffled-Slab floor buildings. Comput Meth Appl Mech Eng 185(2–4):245–277
12. Vielma JC, Barbat AH, Oller S (2008) An objective seismic damage index for the evaluation of the performance of RC buildings. In: Proceedings 14th WCEE. IAEE, Beijing, China
13. Oller S, Barbat AH (2006) Moment-curvature damage model for bridges subjected to seismic loads. Comput Meth Appl Mech Eng 195:4490–4511
14. Car E, Oller S, Oñate E (2001) A large strain plasticity for anisotropic materials: composite material application. Int J Plast 17(1):1437–1463
15. Mata P, Oller S, Barbat AH (2007) Static analysis of beam structures under nonlinear geometric and constitutive behaviour. Comput Meth Appl Mech Eng 196:4458–4478
16. Mata P, Oller S, Barbat AH (2007) Dynamic analysis of beam structures under nonlinear geometric and constitutive behaviour. Comput Meth Appl Mech Eng 197:857–878
17. Oller S, Oliver J, Oñate E, Lubliner J (1990) Finite element non-linear analysis of concrete structures using a plastic-damage model. Eng Fract Mech 35(1-3):219–231
18. Lubliner J, Oliver J, Oller S, Oñate E (1989) A plastic-damage model for concrete. Int J Solid Struct 25(3):299–326
19. Faleiro J, Oller S, Barbat AH (2008) Plastic-damage seismic model for reinforced concrete frames. Comput Struct 86:581–597
20. Oller S, Car E, Lubliner J (2003) Definition of a general implicit orthotropic yield criterion. Comput Meth Appl Mech Eng 192(7–8):895–912
21. Martinez X, Oller S, Rastellini F, Barbat AH (2008) A numerical procedure simulating RC structures reinforced with FRP using the serial/parallel mixing theory. Comput Struct 86:1604–1618
22. Bayrak O, Sheikh SA (2001) Plastic hinge analysis. J Struct Eng (ASCE) 127:1092–1100
23. Spacone E, El Tawil S (2000) Nonlinear analysis of steel-concrete composite structures: state of the art. J Struct Eng (ASCE) 126:159–168
24. Faleiro J, Oller S, Barbat AH (2010) Plastic-damage analysis of reinforced concrete frames. Eng Computations 27(1):57–83
25. Shao Y, Aval S, Mirmiran A (2005) Fiber-element model for cyclic analysis of concrete-filled fiber reinforced polymer tubes. J Struct Eng (ASCE) 131:292–303
26. Simo JC (1985) A finite strain beam formulation. The three-dimensional dynamic problem Part I. Comput Meth Appl Mech Eng 49:55–70

27. Mander JB, Priestley MJN, Park R (1988) Observed stress-strain behaviour of confined concrete. J Struct Eng (ASCE) 114:1827–1849
28. Vamvatsikos D, Cornell, CA (2002) Incremental dynamic analysis. Earthquake Eng Struct Dynam 31(3):491–514
29. Kunnath, S (2005) Performance-based seismic design and evaluation of buildings structures. In: Chen WF, Lui EM (eds), Earthquake engineering for structural design. CRC, Boca Raton Press
30. Vielma JC, Barbat AH, Oller S (2009) Reserva de resistencia de edificios porticados de concreto armado diseados conforme al ACI-318/IBC-2006. Revista de Ingeniera de la Universidad de Costa Rica 18(1,2):121–131
31. Vielma JC, Barbat AH, Oller S (2010) Seismic safety of low ductility structures used in Spain. Bull Earthquake Eng 8:135–155
32. Han SW, Chopra A (2006) Approximate incremental dynamic analysis using the modal pushover analysis procedure. Earthquake Eng Struct Dynam 35(3):1853–1873
33. Fajfar PA (2000) Nonlinear analysis method for performance based seismic design. Earthquake Spectra 16(3):573–591
34. SEAOC (1995) Vision 2000 report on performance based seismic engineering of buildings. Structural Engineers Association of California, vol I. Sacramento, California
35. Vielma JC, Barbat AH, Oller S (2008) Umbrales de daño para estados lmite de edificios porticados de concreto armado diseados conforme al ACI-318/IBC-2006. Revista Internacional de Desastres Naturales, Accidentes e Infraestructura 8:119–134
36. Vielma JC (2008) Caracterizacin de la respuesta ssmica de edificios de hormign armado mediante la respuesta no lineal, PhD Thesis, Barcelona, Spain
37. Pinto PE, Giannini R, Franchin P (2006) Seismic reliability analysis of structures. IUSS Press, Pavia, Italy
38. Barbat AH, Pujades LG, Lantada N (2008) Seismic damage evaluation in urban areas using the capacity spectrum method: application to Barcelona. Soil Dyn Earthquake Eng 28:851–865
39. Barbat AH, Pujades LG, Lantada N (2006) Performance of buildings under earthquakes in Barcelona, Spain. Comput-Aided Civ Infrastruct Eng 21:573–593
40. Lantada N, Pujades LG, Barbat AH (2009) Vulnerability index and capacity spectrum based methods for urban seismic risk evaluation. A comparison. Nat Hazards 51:501–524
41. Vielma JC, Barbat AH, Oller S (2010) Non-linear structural analysis. Application for evaluating the seismic safety. In: Structural analysis. Nova Science Publishers, New York

Assessment of the Seismic Capacity of Stone Masonry Walls with Block Models

José V. Lemos, A. Campos Costa, and E.M. Bretas

Abstract The application of discrete element models based on rigid block formulations to the analysis of masonry walls under horizontal out-of-plane loading is discussed. The problems raised by the representation of an irregular fabric by a simplified block pattern are addressed. Two procedures for creating irregular block systems are presented, one using Voronoi polygons, the other based on a bed and cross joint structure with random deviations. A test problem provides a comparison of various regular and random block patterns, showing their influence on the failure loads. The estimation of natural frequencies of rigid block models, and its application to static pushover analyses, is addressed. An example of application of a rigid block model to a wall capacity problem is presented.

Keywords Masonry structures · Seismic assessment · Discrete elements · Rigid blocks

1 Introduction

The safety assessment of historical masonry structures under seismic loads requires numerical models with the ability to represent the types of failure modes observed in earthquakes. Laboratory tests provide a controlled environment in which the behavior can be more completely characterized. Block models, based on the discrete element method, are one of the numerical tools available to simulate phenomena such as sliding and separation along joints, which lead to progressive structural damage and collapse. Their application to structural components or monuments of a relatively small size, for which the individual blocks can be numerically represented, poses no major difficulties [1]. The success of this type of application has

J.V. Lemos (✉), A.C. Costa, and E.M. Bretas
LNEC – Laboratório Nacional de Engenharia Civil,
Av. do Brasil 101, 1700-066 Lisboa, Portugal
e-mail: vlemos@lnec.pt; alf@lnec.pt; ebretas@lnec.pt

M. Papadrakakis et al. (eds.), *Computational Methods in Earthquake Engineering*,
Computational Methods in Applied Sciences 21, DOI 10.1007/978-94-007-0053-6_10,
© Springer Science+Business Media B.V. 2011

encouraged the extension of these models to more complex structures, for example, involving masonry walls formed by irregular blocks, or multiple leaf walls, as found in many historical constructions. In these cases, the numerical idealization requires much more drastic simplifications that need to be critically assessed.

The present work addresses the application of rigid block models to analyze the out-of-plane behavior of masonry walls under horizontal loads. The influence of the block patterns on the results is discussed. Block systems based on a simple idealized geometric pattern, typically used in many applications, are compared with randomly generated block systems, using two different procedures. The first is based on Voronoi polygons, which may be representative for some types of masonry, but does not reproduce the laying in courses. The second method is a new proposal based on a bed joint and cross joint structure, but with some degree of randomness applied to joint spacing and orientation.

In these comparative analyses, the seismic action is represented simply as a static horizontal load, which makes the differences in behavior more evident. It should be remarked, however, that the advantages of rigid block models are more significant in dynamic analysis with explicit algorithms, because of the lower run times in comparison with deformable block models. The evaluation of natural frequencies is essential to a correct understanding of the seismic behavior. This may also be done with a rigid block model, by assuming an elastic behavior of all contacts. Since in these models, the system deformability is expressed in terms of joint (or contact) stiffnesses, for which experimental values are often lacking, the knowledge of eigenvalues and eigenmodes is very helpful in calibrating the model parameters, particularly when ambient noise measurements are available, which characterize the global dynamic response in the low level range. A straightforward procedure to calculate natural frequencies for a rigid block system is discussed. An application to the evaluation of the ultimate capacity of a large wall in a historical building is finally presented.

2 Rigid Block Modelling of Masonry Walls

Discrete element models employing polyhedral rigid blocks have proved very effective in the dynamic analysis of structures and monuments composed of blocks of hard rock with dry joints. Classical column-architrave structures are a typical case in which the numerical model may reproduce the individual blocks with reasonable accuracy [2]. The actual position and geometry of each block can be represented, even the existence of broken or damaged blocks.

Modern brick walls, for which unit shapes are known, but not their precise location, may be analyzed with either discontinuum or homogenized continuum models [3]. For large structures, the latter are more straightforward and less time consuming, even if failure modes are more rigorously simulated with the former.

The analysis of a wall formed by coursed or irregular masonry with mortared joints as a continuum appears more natural, since in practice the actual block

geometry is not known. A discrete block model of such a wall is necessarily a simplified representation intended to follow the block pattern, not the exact shapes. The advantages of discrete element models for analyzing failure modes, always involving separation of the wall into blocks, have encouraged research in this area. Several approaches have been attempted, resorting to various levels of geometrical and mechanical complexity. Casolo [4] adopts a very simple block pattern, with continuous orthogonal joints, with all the complexity of masonry behavior being accounted for by elaborate joint constitutive models. At the opposite end, bonded particle models [5] employ large random assemblies of particles to simulate the irregular masonry units and the mortar [6], while relatively simple contact laws are used. In this paper, an intermediate approach is adopted, with polyhedral block systems generated according to various geometrical schemes, involving both regular patterns and systems with various degrees of irregularity and randomness. The mechanical interaction between the blocks is represented by standard Mohr-Coulomb joint models. A similar type of model was employed by De Felice and Giannini [7] to investigate the effect of block size on the out-of-plane resistance of masonry walls.

In a rigid block model, all system deformation is represented by relative movements between the blocks. In the early stages of loading, before the non-elastic behavior becomes dominant, the joint normal and shear stiffness parameters govern the system deformation. Therefore, they must account for both the block deformation and the joint deformation, either in the case of mortared or dry joints. Experimental data on joint stiffness show significant scatter, therefore the global deformability of a rigid block model must always be checked and assessed, to ensure that it is realistic. As block shapes and sizes do not reproduce rigorously the real patterns, some calibration of the stiffness parameters is essential. For dynamic problems, natural frequencies in the linear range can be contrasted with field measurements, providing an important contribution to the model calibration procedure. The ability of rigid block systems, assuming elastic contacts, to supply natural frequencies has been verified by comparison with analytical continuum solutions for walls [8].

3 Analysis of Influence of Block Patterns

The influence of the joint patterns adopted for the rigid block representation of the wall was analyzed with a simple test problem (Fig. 1). The wall was assumed to be simply supported in the out-of-plane direction at both lateral ends, by means of two fixed blocks, representing the effect of cross walls. The wall dimensions are 20×10 m, with 0.80 m thickness. For simplicity, a Coulomb friction model was adopted for the joints, without cohesion or tensile strength. A Young's modulus of 2.5 GPa was assumed. The joint stiffnesses listed in Table 1 correspond to an average joint spacing of 1 m. For other spacings, these values were scaled to maintain an average elastic isotropy. Static analyses were conducted by applying a horizontal

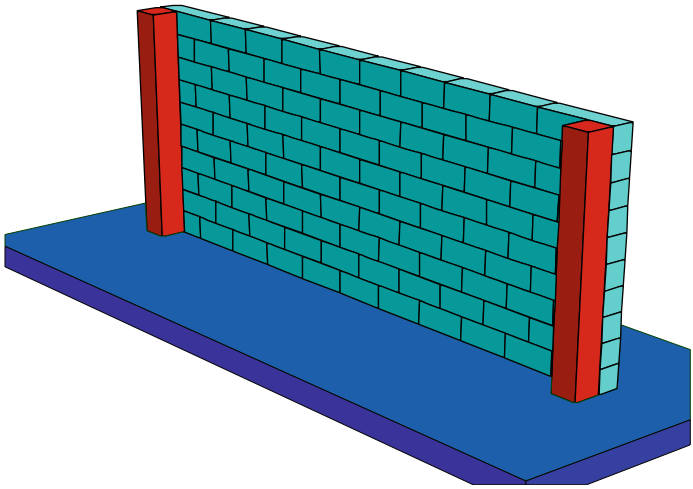


Fig. 1 Test problem (case of vertical joint offset of 1.0)

mass force in the out-of-plane direction. This load was increased in steps until failure. The analyses were performed with the code 3DEC [9].

Table 1 Joint properties for test problem

Joint properties	
Normal stiffness	2.5 GPa/m
Shear stiffness	1.0 GPa/m
Friction angle	35°

3.1 Regular Block Patterns

The model shown in Fig. 1 corresponds to the case of blocks with dimension 2×1 m, with staggered vertical joints with an offset of 1.0 m. For these block dimensions, three other cases were considered: continuous vertical joints (no offset), and staggered vertical joints with offsets of 0.5 and 0.1 m. Figure 2 illustrates the four block patterns analyzed.

A second series of tests were conducted with square blocks, dimensions of 1×1 m. The four block patterns are illustrated in Fig. 3: continuous vertical joints, and three cases of discontinuous joints with offsets 0.5, 0.25 and 0.1 m.

The results for the case of blocks with dimensions 2×1 m are shown in Fig. 4a. The curves represent the out-of-plane displacement of the middle point at the top of the wall (horizontal axis) versus the horizontal gravity force (vertical axis). The horizontal force was incremented in steps of 0.1 g, up to failure. The last point in each curve corresponds to the last equilibrated state. The corresponding curves for the case of blocks 1×1 m are plotted on Fig. 4b.

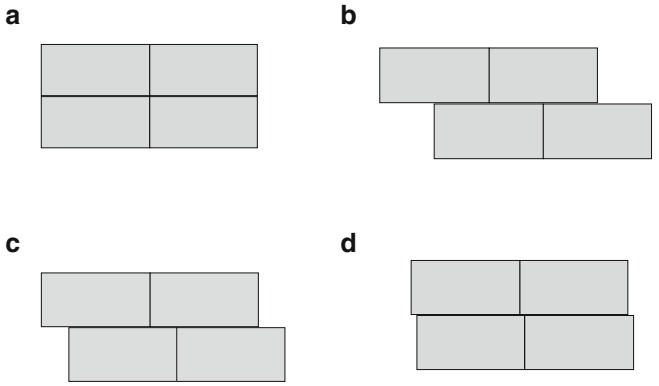


Fig. 2 Block patterns (block dimensions 2 × 1 m): (**a**) no offset; (**b**) offset = 1.0; (**c**) offset = 0.5; (**d**) offset = 0.1

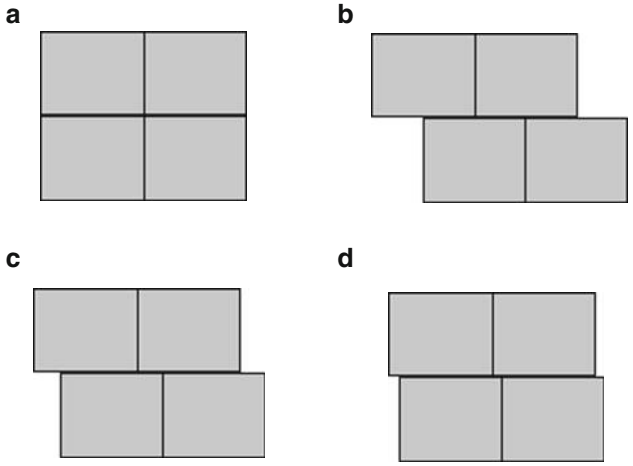


Fig. 3 Block patterns (block dimensions 1 × 1 m): (**a**) no offset; (**b**) offset = 0.5; (**c**) offset = 0.25; (**d**) offset = 0.1

Considering first the case of rectangular blocks (Fig. 4a), it can be seen that the most significant difference is between the case of continuous vertical joints and the models with staggered joints. Even a small offset increases substantially the wall capacity. The chart for the case with square blocks (Fig. 4b) shows that the capacity of the wall with continuous joints is not altered (within the resolution of the load increment used). The staggered joint models display lower strength than those with rectangular blocks. This is related to the fact that the smaller areas of block contact along the horizontal joints lead to a reduced restraint of relative block rotation necessary to create the failure mode. These results show that the typical "brick wall" pattern often used as a representation of an irregular masonry wall may overestimate its strength. This is particularly significant, since numerical models often use larger

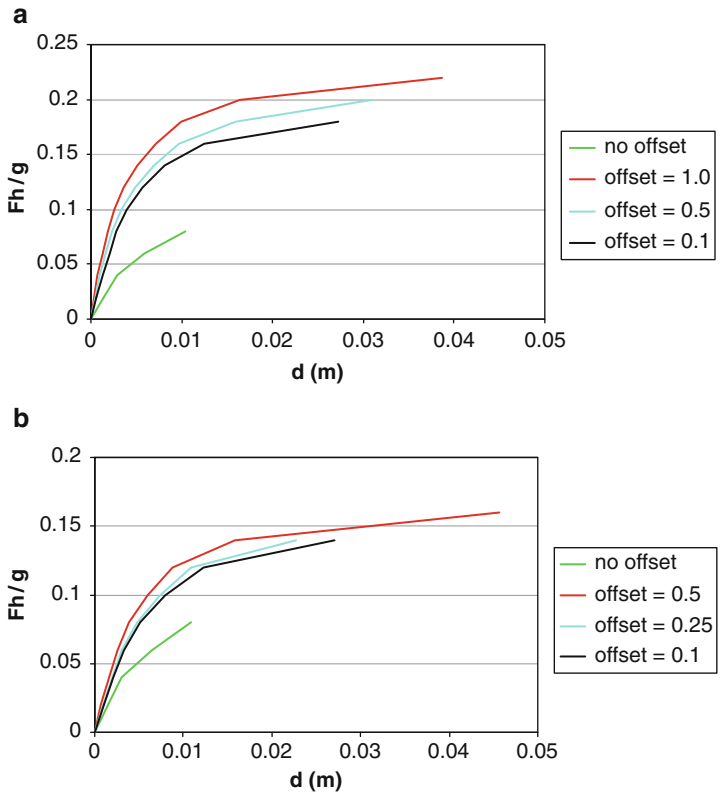


Fig. 4 Horizontal force vs. displacement curves for the four block patterns: (**a**) blocks 2 × 1 m; (**b**) blocks 1 × 1 m

block sizes than the real ones to save computational effort. Therefore the overestimation of the actual imbrication of the wall stones may adversely affect the safety assessment. Considering continuous joints is a rather conservative assumption, as offsets certainly exist, but may be defensible if the actual wall units are much smaller than the numerical blocks.

3.2 Voronoi Block Patterns

The numerical generation of block assemblies that represent correctly the various types of traditional masonry is a topic still demanding more research. Random shape patterns based on Voronoi polygons (or polyhedra) have been found to reproduce the geometries of some natural physical systems. For example, in rock mechanics, these shapes are now used to simulate the grain structure, defining the potential fracture paths [10]. Pina-Henriques and Lourenço [11] also used Voronoi patterns to study the fracture of masonry units in very detailed analyses at the meso-scale.

Herein, Voronoi patterns are used to create the random block pattern of an irregular masonry wall. These models are certainly not realistic for most types of masonry, which display block patterns where horizontal joints are more or less well defined, reflecting the way in which they were built. The block generator presented in the following section will address this point.

In this first study, the block pattern was obtained using a 2D Voronoi polygon generator. An average edge length of 1 m was assumed, to be comparable with the square blocks in the previous section. The 3DEC blocks were created assuming a uniform shape across the wall thickness. Figure 5 shows one the several bock assemblies analyzed. Joint properties were the same as those in Table 1. The results of the simulations with 3 Voronoi block systems are compared in Fig. 6 with two of the square block models presented above (with continuous vertical joints and offset of 0.1 m). First, it is interesting to note that the three randomly generated Voronoi patterns follow fairly similar deformation curves. The initial deformability of the system is close to that obtained with continuous vertical joints. However, the strength is higher, but still below the value obtained with imbricated joints with the

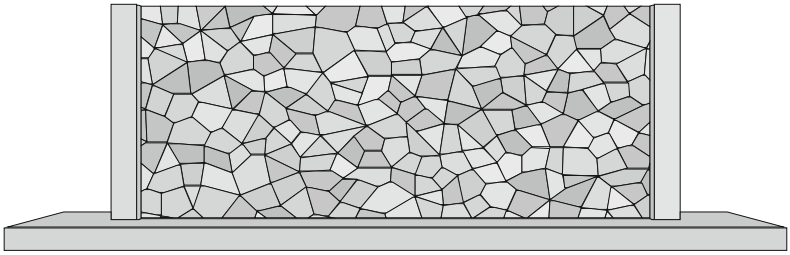


Fig. 5 Model with Voronoi block pattern (case 1)

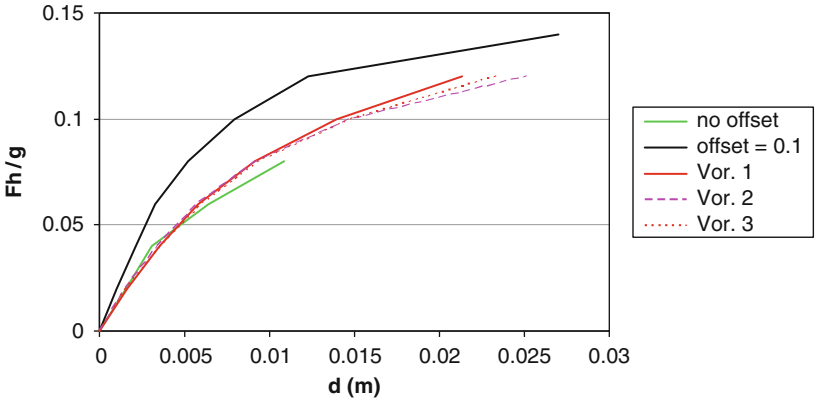


Fig. 6 Horizontal force vs. displacement curves for regular and Voronoi block patterns

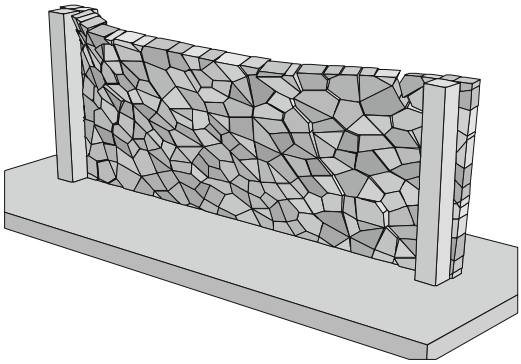


Fig. 7 Failure mode of model with Voronoi block pattern (case 1)

smallest offset. The Voronoi pattern does not create discontinuous joints, so it tends to underestimate the block interlocking. The failure mode of the one of the Voronoi models is illustrated in Fig. 7.

3.3 A Procedure for Generation of Irregular Block Patterns Based on a Bed Joint and Cross Joint Structure

A block generation procedure for use in discrete element models of masonry was developed that is based on a typical bed joint and cross joint structure, but introduces some degree of randomness. In contrast with the Voronoi generator, this method produces a pattern of blocks arranged in courses with different heights and variable cross joint spacing. It is far from reproducing the complexity of masonry construction, but it is a useful tool to assess the influence of geometric variability on the deformation and failure processes.

The procedure starts by generation of continuous bed joints, each one formed by a set of segments (Fig. 8). The geometry of the bed joints defined by the following parameters: spacing (s_m, s_d), segment length (t_m, t_d), vertical deviation (h_m, h_d) from mean trace. Each of these parameters is defined statistically in terms of a mean value (m) and a deviation (d). In the present study a uniform distribution was assumed, for simplicity. For example, for the spacing of bed joints, a random number is generated in the interval $[s_m - s_d, s_m + s_d]$. However, more elaborate distributions may be employed. Cross joints are defining by their spacing (b_m, b_d) and angle deviation from the vertical (a_m, a_d).

The block generation procedure starts by creating the means traces of the bed joints, using the random spacing parameter. Then, each bed joint is created, composed of continuous segments, defined by their length and vertical deviation from mean trace. Finally, the cross joints are inserted, course by course, to form the block structure. This procedure produces blocks with slight concave angles, so an additional step may be taken, in which the concave blocks are split by extra cross joints.

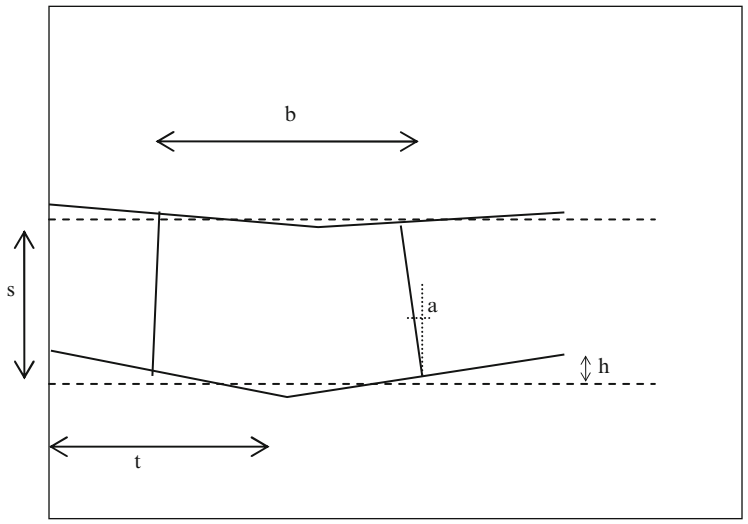


Fig. 8 Definition of geometric parameters in block generation procedure

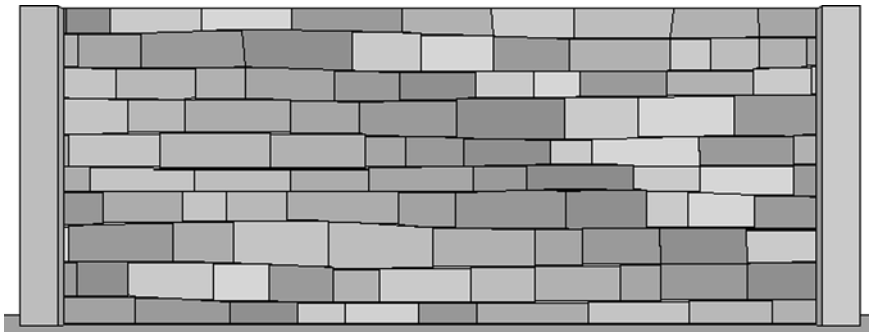


Fig. 9 Block system generated with parameters in Table 2

Table 2 Parameters for irregular block generation

s_m	s_d	t_m	t_d	h_m	h_d	b_m	b_d	a_m	a_d
(m)	**(m)**	**(m)**	**(m)**	**(m)**	**(m)**	**(m)**	**(m)**	(°)	(°)
1	0.1	2	1	0	0.2	1.5	0.5	0	0

In this study, as the degree of irregularity was not large, the concave blocks were retained. Figure 9 shows a system created with the parameters in Table 2.

The system in Fig. 9 is one of three randomly created with the geometric data listed in Table 2. The force-displacement curves obtained with these three models are compared in Fig. 10 with those from regular jointed models already presented (rectangular blocks). It may be seen that the three irregular patters display failure

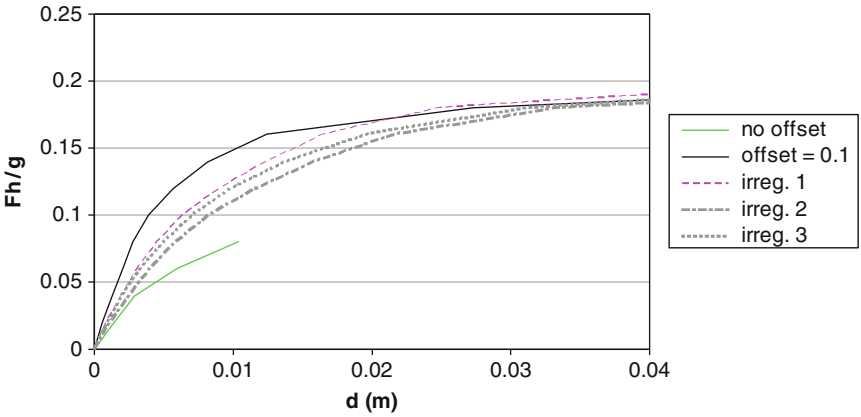


Fig. 10 Horizontal force vs. displacement curves for regular and irregular block patterns

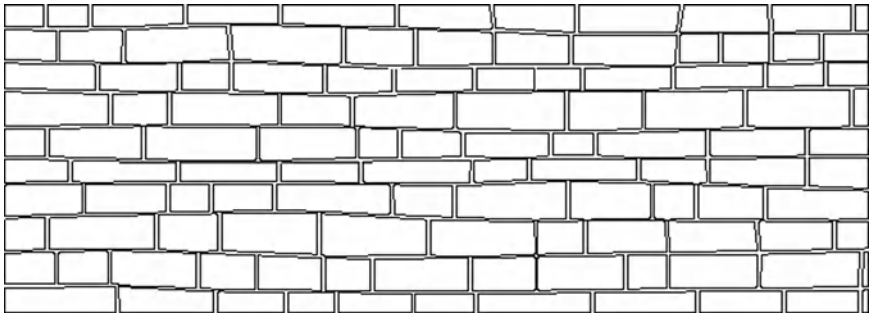


Fig. 11 Block plot displaying mortar thickness

loads in the same range, which are also close to the case of the regular pattern with the smallest offset (0.1), and above the curve for the continuous cross joints.

It should be noted that in this type of model the mortar is not represented, so the stone blocks are extended to include half of the joint height. The mortar properties are taken into account when joint stiffness and strength parameters are assigned. If a mortar thickness is actually plotted, then the system of Fig. 9 would appear somewhat more realistic, as shown in Fig. 11.

4 Natural Frequencies of Rigid Block Systems

Rigid block models are primarily intended for failure analysis. However, there are often situations in which it is useful to analyze its elastic behavior, for example, to verify global deformability or characterize dynamic response. Rigid block codes

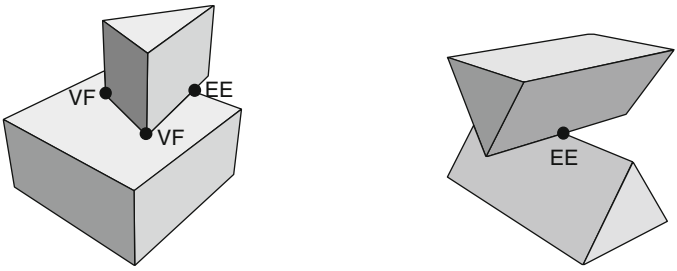


Fig. 12 Representation of block interaction by point contacts in 3DEC

usually employ explicit algorithms in the time domain, so they have no facilities to build stiffness matrices. The procedure employed in the example in the following section is briefly described here.

In 3D a rigid block has 6 degrees of freedom, three translations and three rotations. The stiffness matrix of the elastic rigid block system is defined in terms of these 6 degrees of freedom per free block, and the corresponding forces and moments at the block centroids. The mechanical interaction between two blocks in 3DEC [9] is represented by means of a set of point contacts, which may be of two types, vertex-to-face and edge-to-edge, as shown in Fig. 12.

The contact normal, determined through Cundall's common plane algorithm, corresponds essentially to the normal to the block face or to the plane containing the two edges. Each point contact is assigned an area, which in the case of a face-to-face interaction leads to the actual contact area. For a true point contact (as on the right of Fig. 12), a nominal area is assigned, which physically represents a minimal value of stiffness.

The stiffness matrix of a point contact, a 12×12 matrix, may be numerically built column by column, by prescribing small displacements and rotations of each block, one at a time, in the coordinate directions. The forces and moments originated by these configurations at the two block centroids constitute each matrix column. In this way, in an explicit code, the existing routines for the contact force-displacement laws are directly used to produce the elementary stiffness matrix. The stiffness matrices of all point contacts between a pair of blocks are added, and then these are assembled to get the global system matrix in the usual manner. Eigenvalues and eigenmodes may then be obtained, assuming a diagonal mass matrix.

In this procedure, linear elastic interactions are assumed, in terms of the normal and shear stiffness of joints or contacts. Therefore, the stiffness matrix and natural frequencies depend on the system connectivity. At different stages of the analysis, particular contacts may be separated thus not contributing to the system stiffness. At advanced stages of collapse, loose blocks will render the procedure unfeasible.

The accuracy obtained with rigid block models has been verified against continuum elastic solutions. Comparisons of frequencies and mode shapes for beam and plate bending problems have shown that the rigid block approximation is adequate [8]. For a good representation of the out-of-plane bending, it is recommended that three or more contact points across the thickness of the wall be used.

5 Local Modeling of Wall Failure

The safety assessment of historical buildings usually involves two scales of numerical analysis: global and local. Global models are simplified, not only in terms of geometrical detail, but also in terms of material models, often linear elastic assumptions being adopted. The global dynamic behavior can be calibrated against in situ experiments. The local models are used to assess the safety of critical components, and need to represent the nonlinear behavior, whether pushover methods or dynamic analysis are used. Discrete element models are one of the tools available for this local modeling scale.

The local modeling of a structural component raises the problem of setting adequate boundary conditions, such that the effect of the surrounding structure is satisfactorily represented. In the example presented in this section (Fig. 13), elastic supports are used to provide the support of the wall at both ends, in the two horizontal directions. The stiffness of these elastic supports was calibrated so that the two lowest frequencies and mode shapes matched reasonably well the in situ measurements provided by ambient vibration tests.

The wall shown in Fig. 13 has a maximum height of about 38 m, at the centre, and a thickness varying thickness from 1.6 m at the base to 0.8 m at the top, with thicker buttresses near both ends. The rigid block model adopted a continuous joint pattern, which is a conservative assumption, according to the results discussed before. However, it should be noted that the numerical blocks are much larger than the actual blocks. Therefore, any sizeable offset might overestimate the effects of the actual interlocking, which may be taken into account through the cohesive strength of the vertical joints.

The wall modes were calculated in the assumption of elastic contacts, by the procedure outlined in the previous section. The first two modes are depicted in Fig. 14. This analysis was essential to calibrate the elastic supports on the sides of the model which represent the adjacent structure. The evaluation of the seismic capacity was based on pushover analyses [12, 13]. Unlike the wall test problem,

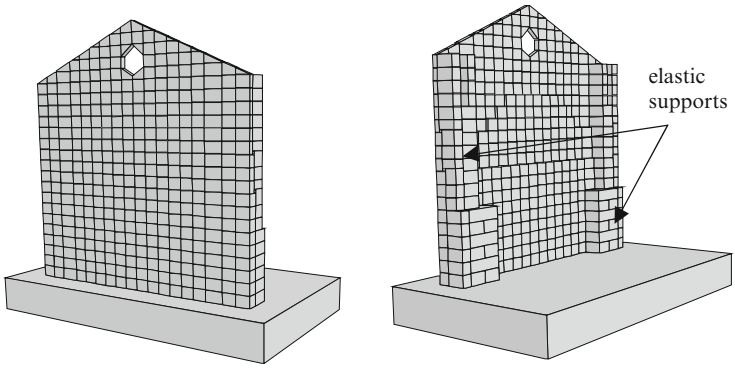


Fig. 13 Rigid block model for local wall failure analysis

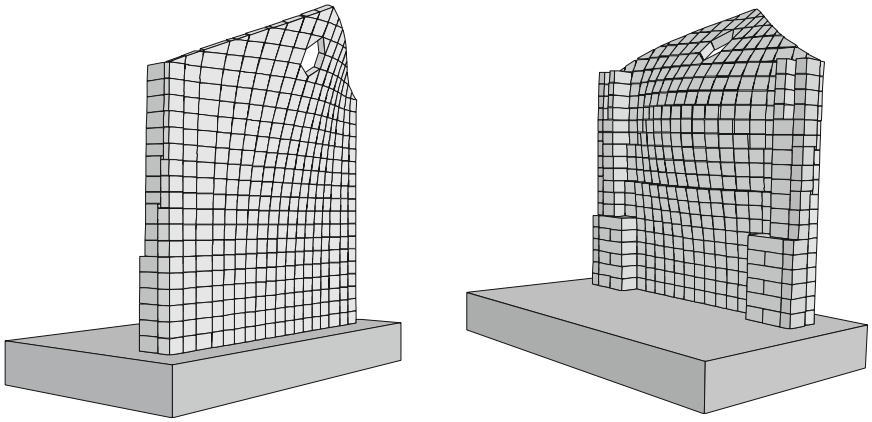


Fig. 14 First and second mode shapes of rigid block model

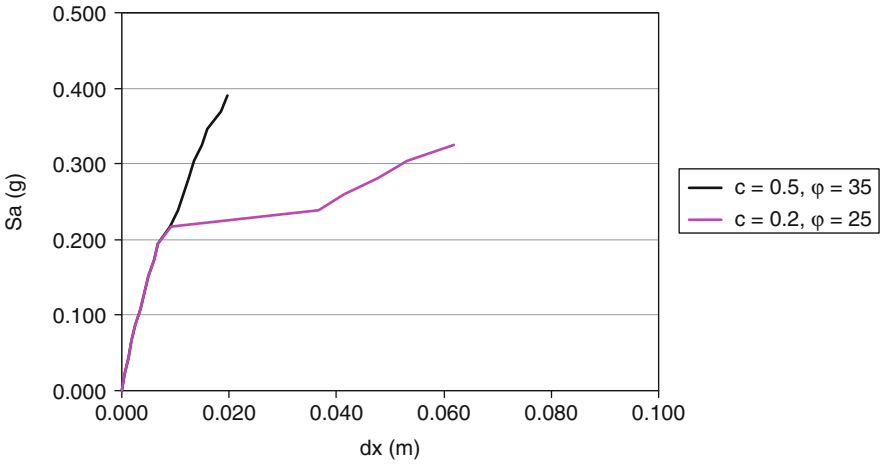


Fig. 15 Spectral acceleration vs. displacement curves for two values of vertical joint strength

the seismic forces acting in the out-of-plane direction were not assumed uniform in height, but were applied to the rigid blocks according to the first mode shape, which dominates the response of the wall.

In the nonlinear analyses, a Mohr-Coulomb model with cohesion and tensile strength was employed. Parametric studies were conducted to assess the influence of the main model parameters. As expected, failure is initiated by sliding and separation on the vertical joints near the thick lateral buttresses. The assumed continuity of these cross joints facilitates this mechanism, which is controlled by the assigned strength. The influence of the shear strength of the vertical joints on the wall capacity is plotted in Fig. 15. The two curves correspond to values of cohesion of 0.5

and 0.2 MPa, and friction angles of 35° and 25°, respectively. In both cases, the joint tensile strength was 0.1 MPa. The lower strength case produces a markedly different behavior from the load level at which substantial shearing develops.

6 Conclusions

Discrete element models provide a powerful tool to analyze the deformation and failure modes of masonry, either in static or dynamic analysis. The successful application of these discontinuous representations involves judicious selection of model geometry and parameters. For simple stone structures, the model may reproduce the actual size and shape of individual blocks, so its generation is straightforward. For large and complex structures, however, the discrete block model is a considerable idealization. The effect of the simplified block patterns on the results needs to be assessed. For masonry walls under horizontal loads, it was shown that indiscriminate use of brick wall patterns with large cross joint offsets may overestimate significantly the wall strength. This is particularly important when the block size in the numerical model is larger than the real one, which is often unavoidable if the computational effort needs to be reduced.

For irregular masonry fabric, the use of random block generators, allows more realistic assemblies, avoiding the bias introduced by simple orthogonal joint sets. Voronoi polygons provide a simple option, but do not represent well the interlocking produced by staggered cross joints. In the test problem, these patterns led to wall strengths of the same order as the regular model with continuous cross joints. The alternative procedure proposed allows a more general class of masonry constructions to be addressed, and it provides a tool to evaluate the influence of irregularity and randomness, but it is still far from reproducing the real patterns. Further research on block generators capable of representing the various types of fabric found in historical masonry remains necessary for an effective application of discontinuous models.

Finally, it should be stressed that even if discontinuous models are mostly intended for collapse analysis, model checking and calibration under assumptions of elastic contact remains an important preliminary step for seismic studies.

References

1. Lemos JV (2007) Discrete element modeling of masonry structures. Int J Archit Heritage 1(2):190–213
2. Psycharis IN, Lemos JV, Papastamatiou DY, Zambas C, Papantonopoulos C (2003) Numerical study of the seismic behaviour of a part of the Parthenon Pronaos. Earthquake Eng Struct Dyn 32:2063–2084
3. Lourenço PB (2002) Computations of historical masonry constructions. Prog Struct Eng Mater 4:301–319

4. Casolo S, Pena F (2007) Rigid element model for in-plane dynamics of masonry walls considering hysteretic behaviour and damage. Earthquake Eng Struct Dyn 36:1029–1048
5. Potyondy DO, Cundall PA (2004) A bonded-particle model for rock. Int J Rock Mech Min Sci 41:1329–1364
6. Lemos JV (2006) Modeling of historical masonry with discrete elements. In: Mota Soares CA, Martins JAC, Rodrigues HC, Ambrósio JAC (eds) Third European conference on computational mechanics solids, structures and coupled problems in engineering, Lisbon, 5–8 June 2006, pp 375–392
7. De Felice G, Giannini R (2001) Out-of-plane seismic resistance of masonry walls. J Earthquake Eng 5(2):253–271
8. Lemos JV (2007) Numerical issues in the representation of masonry structural dynamics with discrete elements. In: Papadrakakis M, Charmpis DC, Lagaros ND, Tsompanakis Y (eds) Compdyn 2007. Rethymno, Crete, Greece, 13–16 June 2007, p 1126
9. 3DEC – Three-dimensional Distinct Element Code (2006). Itasca Consulting Group, Minneapolis
10. Herbst M, Konietzky H, Walter K (2008) 3D microstructural modeling. In: Hart R, Detournay C, Cundall P (eds) Continuum and distinct element numerical modeling in geo-engineering. Itasca Consulting Group, Minneapolis
11. Pina-Henriques J, Lourenço PB (2006) Masonry compression: a numerical investigation at the meso-level. Eng Comput 23(4):382–407
12. Magenes G (2000) A method for pushover analysis in seismic assessment of masonry buildings. In: Twelfth World conference on earthquake engineering, Auckland, New Zealand, p 1866
13. Penna A (2008) Vulnerability assessment of masonry structures using experimental data and simplified models. Short Course on Post-Earthquake Buildings Safety and Damage Assessment, Eucentre, Pavia

Seismic Behaviour of Ancient Multidrum Structures

Loizos Papaloizou and Petros Komodromos

Abstract Strong earthquakes are common causes of destruction of ancient monuments, such as classical columns and colonnades. Ancient columns of great archaeological significance can be found in high seismicity areas in the Eastern Mediterranean. Understanding the behaviour and response of these historic structures during strong earthquakes is useful for the assessment of conservation and rehabilitation proposals for such structures. The seismic behaviour of ancient columns and colonnades involves complicated rocking and sliding phenomena that very rarely appear in modern structures. Analytical study of such multi-block structures under strong earthquake excitations is extremely complicated if not impossible. Computational methods can be used to simulate the dynamic behaviour and seismic response of these structures. The discrete element method (DEM) is utilized to investigate the response of ancient multi-drum columns and colonnades during harmonic and earthquake excitations by simulating the individual rock blocks as distinct rigid bodies.

Keywords Multidrum columns and colonnades · Earthquake engineering · Discrete element methods

1 Introduction

1.1 Motivation

Ancient classical columns and colonnades of great archaeological significance can be abundantly found in the Eastern Mediterranean region. Such columns were once part of entire monuments, usually carrying the load of an entablature (Figs. 1 and 2),

L. Papaloizou and P. Komodromos (✉)
University of Cyprus, Department of Civil and Environmental Engineering, P.O. Box 20537, 1678 Nicosia, Cyprus
e-mail: papaloizou.loizos@ucy.ac.cy; komodromos@ucy.ac.cy

M. Papadrakakis et al. (eds.), *Computational Methods in Earthquake Engineering*, Computational Methods in Applied Sciences 21, DOI 10.1007/978-94-007-0053-6_11,
© Springer Science+Business Media B.V. 2011

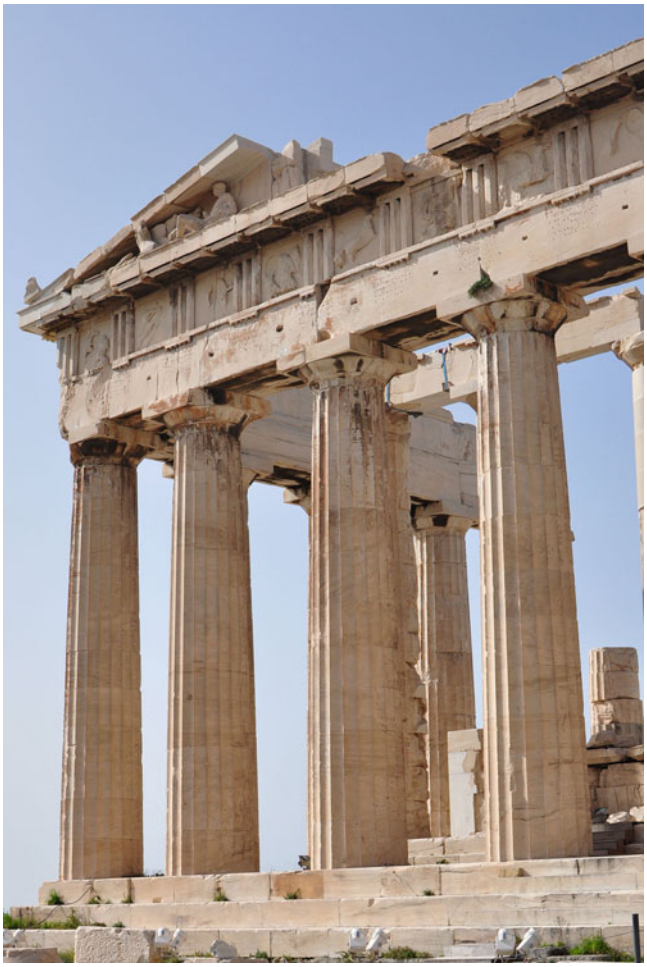


Fig. 1 Ancient columns with an epistyle (Parthenon, Athens)

which is the section of a classical structure that lies between the columns and the roof. Different types of columns can be found in different sizes and with numerous variations of their geometric characteristics. The columns are typically constructed of stone or marble blocks that are placed on top of each other, usually without connecting material between them. Today's remains of such ancient monuments are usually monolithic or multi-drum standalone columns, or series of remaining columns (colonnades), sometimes with epistyles laying on their tops.

Unfortunately, most of these monuments are built in high seismicity areas, where the seismic risk is considerable. Therefore, it is very important to understand the seismic behaviour of these structures so that correct assessments of potential proposals for their structural rehabilitation and strengthening can be made. Moreover, it is very interesting to understand why and how classical columns and colonnades,

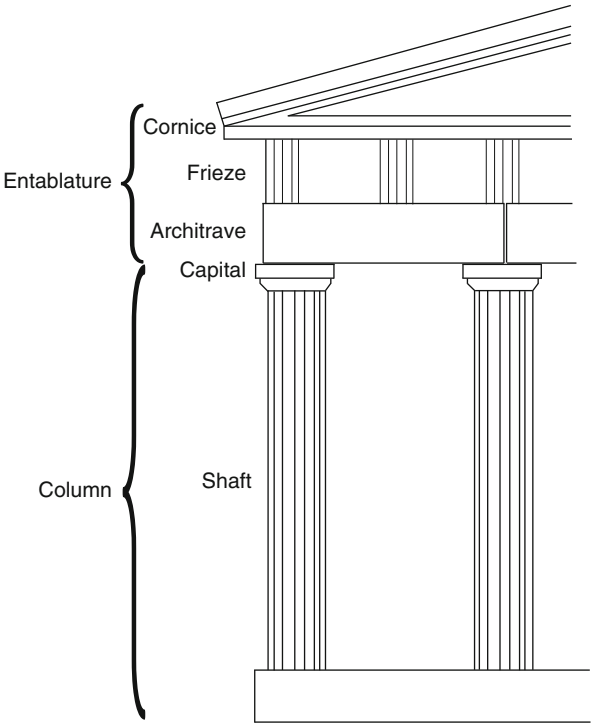


Fig. 2 Architecture of a typical classical monument

which have been exposed to large numbers of very strong earthquakes, throughout the many centuries of their lifetimes, are still standing today. It may also be useful to identify the mechanisms that allow those structural systems to evade structural collapse and destruction after experiencing several strong earthquakes. Furthermore, the investigation of the dynamic response of such monumental structures may uncover certain information from past strong earthquakes that have struck the respective regions.

Multi-drum structures display a very different dynamic response compared to modern structures as they exhibit complex rocking and sliding phenomena among the individual blocks of the structures. The drums can undergo rocking, either individually, or in groups, resulting in several different and alternating shapes of oscillations. This response can be characterized as highly non-linear due to the continuously changing geometry and boundary conditions of the structural system. Considering that analytical study of such multi-block structures under strong ground motions is extremely complicated, if not impossible, for more than a couple of distinct blocks, whereas laboratory experiments are very difficult and costly to perform, numerical methods are employed to simulate their dynamic responses and assess their seismic behaviours.

1.2 Ancient Greek Architecture

In ancient Greece the temples formed the most important class of buildings erected during that era. These monuments can be classified into three "Orders of Architecture", the Doric, Ionic and Corinthian order (Fig. 2). An "order" in Greek architecture consists of the column, including the base and the capital, and the entablature (Fig. 3). The entablature is divided into the epistyle or architrave (lower part), the frieze (middle part) and the cornice (upper part). The differences among these three orders are reflected to the dimensions, proportions, mouldings and decorations of the various parts.

The Doric order, which is the oldest and plainest order, is traced by many to an Egyptian prototype. The column has no base, and stands directly on a stylobate usually of three steps. The stylobate is a flat pavement on which the columns are placed. Including the capital, the column's height is from 4 to 6.5 times the diameter at the base. The entablature was usually about 25% of the total height of the column and the entablature.

The Ionic order is characteristic for its scroll (volute) capital. The earlier findings of Ionic capitals were at Lesbos, Neandra and Cyprus [16]. The columns have

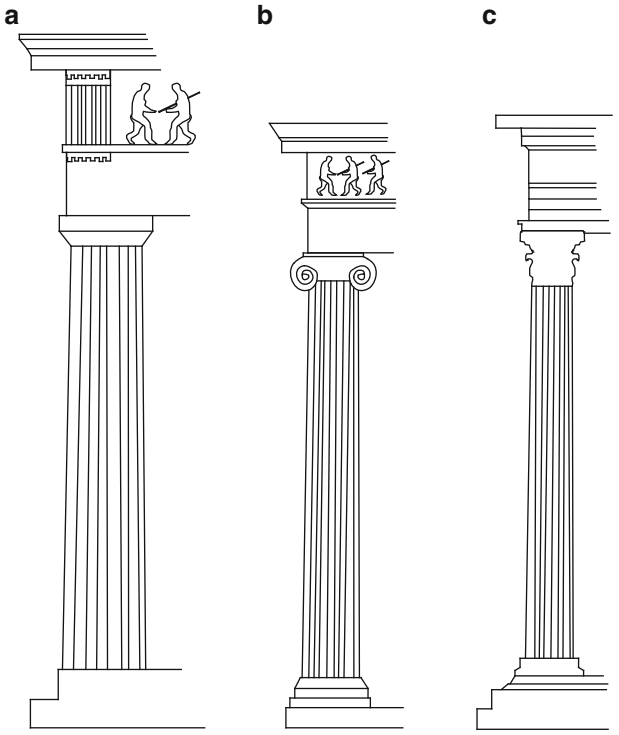


Fig. 3 Greek orders: (**a**) Doric (**b**) Ionic (**c**) Corinthian

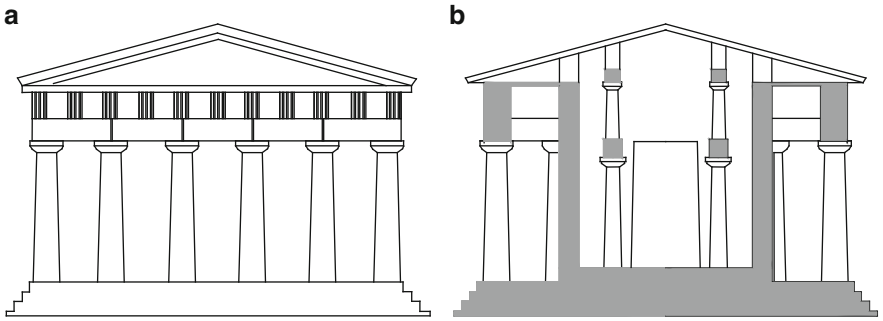


Fig. 4 (**a**) Elevation and (**b**) section illustration of a typical ancient Greek temple

shafts usually about nine times the lower diameter in height, including the capital and the base. The entablature varies in height, but is usually about one-fifth of the whole order.

Finally, the Corinthian order, which is more complex than the Ionic, was modestly used by the Greeks. The column, the base and shaft of which resemble those of the ionic order, is generally about ten times the diameter in height, including the capital, and is placed on a stylobate. The distinctive capital is much higher than the Ionic, being about 100–115% of the diameter in height.

The roof of a temple was constructed of timber and was usually covered with marble slabs. The outer columns of the monument supported the load of the entablature, while the load of the wooden roof was supported by walls, the cella walls. In some large temples there were internal colonnades of columns, placed over each other, to support the roof (Fig. 4).

The main construction material used in such monuments was stone or marble. Columns could be either monolithic (solid) or multi-drum, consisting of a number of drums (blocks). The columns had to be placed comparatively close to each other, since large epistyles were difficult to be constructed in a single monolithic piece. Mortar, was not used as the blocks (drums) of each column were shaped to have very fine surfaces. In some cases iron or wooden cramps were used.

Today, the remains of the majority of these temples are often limited to series of columns with an entablature or only an epistyle, and in some cases only standalone columns (Fig. 1).

2 Literature Review

The dynamic behaviour of rigid blocks under dynamic loading is an extremely complicated phenomenon and can be characterized as highly non-linear, as these systems involve complex rocking and sliding phenomena. Each body can undergo rocking, either individually, or in groups, resulting in several different and alternating

shapes of oscillations of the entire system. Such multi-block systems can represent ancient monumental structures, such as multi-drum classical columns, water tanks, large machinery, containers, electrical equipment or even tombstones.

2.1 Rigid Body Motion

The dynamic response of rigid blocks is complex even for a single rigid body. Figure 5 shows the response of a rigid body left from an initial inclination angle to oscillate freely. The position of the block at different time increments reveals that the motion involves both rocking and sliding motion.

Many researchers have approached the problem of the dynamic response of rigid bodies in different ways. Since 1900, F. Omori [46, 47], one of the first scientists to investigate experimentally the effect of earthquakes on rectangular columns, had stated that the phenomenon is extremely complex and is affected by the input motion. He simplified the problem by focusing on ground motions that had frequency content capable to overturn the columns. A few decades later, other scientists studied the effect of the shape of a rectangular column on its dynamic response, while others, much later, investigated further criteria that affect the overturning of single rigid bodies.

A fundamental analytical study on the rocking response of a rigid block was provided by Housner [18] in 1963. Specifically, Housner considered a rigid body with sufficiently large coefficient of friction so that it can rock, but not slide. Assuming that there is no energy loss during impacts, Housner computed the required time T for a rigid block to complete a full cycle (period) of oscillation, after the rigid body is left to freely oscillate from an initial rotation angle. Furthermore, he computed the reduction of the kinetic energy, during each half-cycle of the oscillation of the body, due to impact.

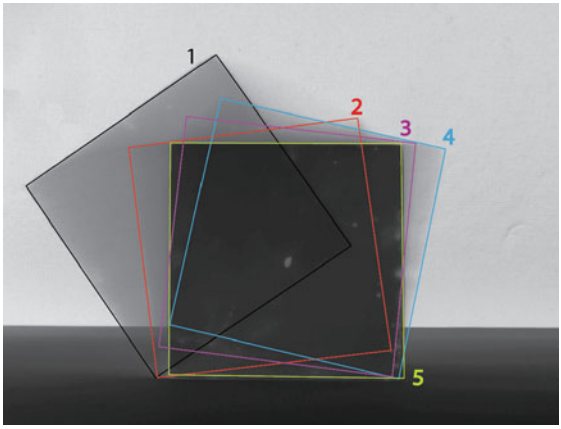


Fig. 5 Motion of a rigid body left to oscillate freely from an initial inclination angle

Aslam et al. [4] studied the rocking and overturning response of rectangular blocks under strong earthquake motions. Aslam et al. suggested that it may be difficult to use data from observations on standing and overturned rigid bodies after an earthquake to provide much useful information on the intensity of the ground motion. They also pointed out the sensitivity of overturning to small changes in the base geometry and the coefficient of restitution as well as to the form of the ground motion.

Ishiyama [19] experimented with motions of rigid bodies on a rigid floor subjected to sinusoidal and earthquake excitations. His study included both experimental and numerical frequency sweep tests, concluding that the horizontal ground velocity, as well as the horizontal ground acceleration must be taken into account as criteria for overturning. He stated that it is possible to estimate the lower limits of the maximum horizontal ground acceleration and velocity needed to overturn rigid bodies.

Psycharis and Jennings [55] studied the dynamic behaviour of a rocking rigid block supported by a flexible foundation that permits uplift, proposing simplified methods of analysis. Moreover, the study showed that, in general, uplift leads to a softer vibrating system that behaves nonlinearly, although the response of such systems is composed of a sequence of linear responses.

Tso and Wong [67, 68] studied both analytically and experimentally the rocking response of rigid bodies. The experiments were conducted using sinusoidal base motions, showing that for each type of steady-state response, the system may respond in either a symmetric or an asymmetric mode.

Spanos and Koh [65] studied in detail the rocking response of free-standing blocks subjected to harmonic steady-state loading, identifying ‘safe’ and ‘unsafe’ regions and developing analytical methods for determining the fundamental and sub-harmonic modes of the system. Hogan [17], extended this study, by expanding the mathematical structure of the problem, introducing the concepts of orbital stability.

Psycharis [53] presented an analysis of the dynamic behaviour of systems consisting of two blocks placed the one on top of the other, free to rock without sliding, stating that during vibration, the system continuously changes from one mode to another, making the response non-linear. The equations of motion for each ‘mode’ of vibration are derived and criteria for the initiation of rocking and the transition between modes are given. This transition between ‘modes’ includes impacts, in which case dissipation of energy occurs and the amount of which depends on the relative velocities and the dimensions of the blocks. The study showed that in most cases, the contribution from the upper block to the system energy increases, which results in a larger and longer response of the top block, compared to the vibration of the lower block.

The impact problem has been also approached by Sinopoli [64] by adopting a unilateral constraint, according to a “kinematic approach”, while the influence of nonlinearities associated with impact on the behaviour of slender rigid objects subjected to horizontal base excitations was studied by Yim and Lin [74].

Furthermore, a general, two-dimensional formulation for the response of free-standing rigid bodies to base excitation was presented by Shenton and Jones [59] to [61]. That formulation assumes rigid body, rigid foundation, and Coulomb friction, while the behaviour was described in terms of the five possible modes of response: rest, slide, rock, slide-rock, and free-flight. Impacts with the foundation were assumed to be perfectly plastic and frictional impulses were included. The study found that periodic solutions exist in general only for relatively high amplitudes of the ground accelerations and coefficients of friction less than the inverse aspect ratio of the block. Also, the rock component of the response is sensitive to changes in the aspect ratio and the coefficients of friction, while it is insensitive to changes of the ground acceleration. The slide component of response is approximately equal to the amplitude of the ground displacement and it is insensitive to changes in the friction and the aspect ratio.

Allen and Duan [3] investigated the reliability of linearizing the equations of motion of rocking blocks. Shi et al. [62] studied the rocking and the overturning of precariously balanced rocks by earthquake, while Scalia and Sumbatyan [58] examined the slide rotation of rigid bodies subjected to a horizontal ground motion.

Zhang and Makris [76] studied the rocking response of a freestanding block to one-sine and one-cosine acceleration pulses. These two trigonometric pulses are physically realizable and resemble in several occasions the fault-parallel and fault-normal component of motions recorded near the source of strong earthquakes (Makris and Roussos [36]). The study showed that under these pulses a free-standing block can overturn by exhibiting one or more impacts, or without exhibiting any impact. The existence of the second mode results in a safe region that is located over the minimum overturning acceleration spectrum. It was found that the shape of this region depends on the coefficient of restitution and is sensitive to the nonlinear nature of the problem. Furthermore, Makris and Zhang [37] investigated the rocking response and the overturning of anchored blocks under pulse-type motions. Pombei et al. [52] also studied the dynamics of a rigid block subjected to a horizontal ground motion, aiming to formulate criteria that separate the various patterns of the motion.

A probabilistic approach to the problem of rocking of rigid blocks was pursued by Yim et al. [75]. In their study a numerical procedure and computer program were developed to solve the non-linear equations of motion that govern the rocking motion of rigid blocks on a rigid base subjected to horizontal and vertical ground motion. The presented response results demonstrate that the response of a block is very sensitive to small changes in its size and slenderness ratio, as well as to the details of ground motion. It was stated that the overturning of a block by a ground motion of particular intensity does not imply that the block will necessarily overturn under the action of more intense ground motion.

Koh and Spanos [23, 24] presented an analysis of random rocking of a block on rigid, as well as on flexible, foundation. Kim et al. [21] investigated experimentally the vibration properties of a rigid body placed on sand ground surface. It was found that the natural vibration period depends not only on the mechanical properties of the rigid body and the ground, but also on the magnitude of the vibration amplitude. This finding suggested the notable effect of nonlinear strain

dependent stiffness of ground material. A physical model with distributed spring-dashpot element was used to model the interactive mechanical behaviour between the rigid body and the ground. The stiffness of the spring-dashpot element was evaluated through modal analysis of observed vibration behaviours. The effects of the base shape, size and pressure on the stiffness of the spring-dashpot element were discussed. The spring-dashpot model was verified with the behaviour observed in forced vibration tests. Finally, Makris [37] stated that the response of a rigid block involves complex dynamics, even with a simple problem of the simplest man-made structures, the free-standing block.

2.2 Dynamic Response of Multi-drum Columns

Experimental research work has been conducted for the investigation of the dynamic behaviour of free standing multi-drum columns and colonnades using metal [14,38], as well as marble [42], small-scale models. However, it has been shown that rocking of rigid bodies is a size dependent phenomenon and, thus, reliable results can be obtained only from tests with real full-scale dimensions and not from models with significantly smaller dimensions. In particular, it has been observed that among multi-block systems with varying sizes, but with the same relative dimensions, the ones with larger absolute dimensions have a larger capacity against overturning, under certain excitations. Therefore, for the response of rocking systems, the experimental results cannot be extrapolated using similarity rules [42].

Nevertheless, certain trends of the seismic response and behaviour of such structures can be qualitatively identified and understood. Physical experiments reveal that the response of multi-drum structures under dynamic loadings is generally affected from the predominant frequency of the ground motion, where rocking dominates the response under earthquakes with low predominant frequency content.

Physical experimental tests of full-scale models are very difficult to perform and monitor. In addition, differences in the response have been observed among experiments with 'identical' models, due to the high sensitivity of the behaviour to slight changes of the geometry or input motion characteristics. Mouzakis et al. [42] conducted an experimental investigation of the earthquake response of a model of a marble classical column. The model was a 1:3 scale replica of a column of the Parthenon on the Acropolis of Athens, made from the same material as the original. The base motion was applied in plane, in one horizontal and the vertical direction, and in space, in two horizontal and the vertical direction, using a shaking table. Several earthquake motions, scaled appropriately in order to cause significant rocking but no collapse of the column, were used as ground excitations. The results showed that the column might undergo large deformations during the shaking. Also, for planar excitations, significant out-of-plane displacements can happen, triggered by the inevitable imperfections of the specimen and that the response is very sensitive, even to small changes of the geometry or the input motion parameters. For this reason, the experiments were not repeatable, while 'identical' experiments produced different results.

Demosthenous and Manos [14, 38], investigated the dynamic response of rigid bodies, representing ancient columns and colonnades, to various types of horizontal base motions. The used rigid bodies were made of steel and were assumed to be small-scale models of prototype structures that were 20 times larger. Two basic configurations were examined: a single steel truncated cone assumed to be a model of a monolithic free-standing column and two steel truncated cones of the same geometry as the first one, supporting a rectangular solid steel and representing the simplest unit of a colonnade. The experimental results were compared with predictions from numerical simulations. More recently, Manos et al. [39] studied the shear transfer mechanism through the horizontal contact surface of two rigid blocks experimentally, as well as numerically using the Finite Element Method (FEM). The experimental sequence included specimens without any connection between the rigid blocks and specimens with poles and empolia connecting the rigid blocks under cyclic loading.

A more realistic, rational and cost-effective approach to investigate the response of multi-drum monuments is through numerical methods, especially since the computing power has been significantly increasing. An extensive overview of the usage of finite and boundary element methods for the analysis of monuments was published by Beskos [7, 8]. However, Finite Element Methods (FEM) are not the most suitable approach for the analysis of multi-block systems that are characterized by continuous changes of their geometry and the contact conditions among individual bodies, although they can be used for the analysis of problems with some discontinuities [40]. Discrete Element Methods (DEM), on the other hand, have been specifically developed for systems with distinct bodies that can move freely in space and interact with each other with contact forces, providing an automatic and efficient recognition of all contacts [5, 10, 15].

The DEM have already been employed, through the usage of commercial general-purpose software in recent publications [2,32,49,50,56], concerning the response of ancient columns. Numerical studies of the earthquake response of ancient columns have been conducted in two dimensions by Psycharis et al. [57], as well as in three dimensions by Papantonopoulos et al. [49], using the commercial software *2DEC* and *3DEC*, respectively. In their work [57], typical sections of two ancient temples were modelled and studied parametrically, in order to identify the main factors affecting their stability and to improve our understanding of the earthquake behaviour of such structures. The analyses showed that, for frequencies usually encountered in earthquakes, free-standing columns can withstand large amplitude harmonic excitations without collapse. The dynamic resistance decreases as the period of the harmonic excitation increases. It was also found that the columns are particularly vulnerable to long-period impulsive earthquake motions. Their study also showed that the response of two columns coupled with an architrave, did not deviate systematically from that of the single multi-drum column or indeed of the equivalent single block. Therefore, a much simpler single block analysis was suggested that can be used to assess the seismic threat to a monument. Furthermore, imperfections, such as initial tilt of the column or loss of the contact area due to edge damage, were also found to reduce the stability of the system significantly.

Psycharis [54] also investigated the seismic response of monuments with fractured structural elements. The distinct element method was used for the analysis of a model that corresponds to a part of the columns of the Olympiou Dios Temple in Athens, Greece. The results indicated that the degree of the crack opening during an earthquake increases almost linearly with the peak velocity of the ground motion and the number of repetitions of the excitation. If significant shear and tensile strength exist at the crack interface, a stronger seismic excitation is, in general, required to cause failure. It was also concluded that cracks at column drums do not endanger the stability of the structure, unless they produce wedge-type pieces, which may slide during the earthquake.

Psycharis et al. [56] reported that the behaviour displayed by the numerical simulations of standalone columns confirms the conclusions drawn from the shaking table tests. A salient feature is the association of drum rocking with movements of twisting of the column around its vertical axis, leading to the patterns of permanent displacements observed in the experiments [42]. They also observed that reinforcement of the column drums, by titanium dowels that offer shear resistance, may reduce the permanent displacements under typical earthquake motions. For more severe base excitations, however, they concluded that their effect is not important due to the uplift that occurs. They suggested that in some cases, the presence of titanium dowels may be unfavourable to the safety of the structure against collapse.

Konstantinidis and Makris [30] also examined the seismic response of multidrum columns and the effect that wooden poles might have in their responses, by using the commercial software *Working Model 2D* [72]. In their work, this specific software was validated by comparing selected computed responses with scarce analytical solutions. The most important conclusion of that paper was that relative sliding between the drums occurs, even when the value of the peak ground acceleration, expressed as a fraction of the gravitational acceleration, is less than the coefficient of friction along the sliding interfaces.

Mitsopoulou et al. [40] investigated numerically the seismic response of multiblock structures by discretizing the blocks in a two dimensional finite element mesh with discrete nodes. The contact interfaces where handled by applying friction. Both monolithic and multi-drum standalone columns were studied, under various seismic and harmonic ground motions, and the computed responses pointed out that the considered monuments were stable under the selected ground motions.

Columns with an architrave (epistyle) were also investigated by Psycharis et al. [56] with the systems displaying considerable stability when the architraves were properly connected by reinforcement elements. Titanium connections, linking the architraves between themselves and with the column capital, showed a good performance under severe seismic excitations. However, they concluded that if the architraves are left free, they are susceptible to falling under input motions lower than those that lead to failures of the columns. Finally, the analyses indicated that the existence of imperfections, such as split drums, reduced sections or asymmetric architrave placement, adversely affect structural safety. They suggested that when it is not possible to eliminate these deviations from the original state, it is important that they are taken into account in the safety assessment models.

The above studies demonstrated that the DEM can be used, although a sensitivity of the response to small perturbations of the characteristics of the structure or the excitation has been reported. Nevertheless, such sensitivities have also been observed in experimental investigations of multi-drum columns and colonnades.

In order to investigate parameters that affect the response of such multi-drum structures, it is necessary to efficiently perform large numbers of numerical simulations, where earthquake characteristics and design parameters are varied [26]. In this research work a custom-made DEM software has been specifically designed and implemented to efficiently and effectively perform large numbers of numerical simulations with varying parameters, modelling the individual rock blocks as distinct bodies. The theory, methodology, as well as assumptions and limitations used to implement the custom-made application are explained in the following sections.

3 Formulation of the Physical Problem

3.1 Discrete Element Methods

The DEM were originally proposed in 1971 for the solution of problems of rock mechanics [11], where distinct elements were used to simulate rock masses. According to the DEM, each distinct body has its own geometric boundaries that separate it from all other bodies. The distinct bodies are usually assumed infinitely rigid, although it is possible to consider them deformable. Contact forces are applied only when a contact between two bodies is detected. The interactions between two bodies can be due to recently detected contacts, existing contacts, or relative displacements and rotations between bodies that are already in contact.

3.2 Contact Modelling

In order to simulate multi-body structural systems, the contact model must have the ability to automatically recognize the existence of any contacts between any discrete bodies of the system. Relevant numerical methods are classified into two groups according to the way with which they treat the contact behaviour in the normal direction of motion at the points of contacts. The first group uses a "soft-contact approach", where, a finite normal stiffness is taken into account to represent the local deformability that exists at a contact, allowing some slight overlapping of colliding bodies. The second group uses a "hard-contact approach", with which, any interpenetration of the two bodies that are in contact is prevented by enforcing certain constraints, which increase substantially the computational cost. The choice of the contact assumption to be used is usually made on the basis of the physical problem under consideration, depending on the circumstances that are involved, the requirements of the analysis and the numbers of the simulated distinct bodies.

The soft contact approach is selected to be used since it is more efficient for the simulation of large number of colliding discrete bodies.

The contact location is an important factor that must also be taken into account. For point contacts, the location of the resultant force vector clearly is at the point of contact. But, where contact conditions exist over a finite surface area on both bodies, the exact point where the contact force should be applied is not so obvious. It is reasonable to assume that the resultant force acts at the centre of the interpenetration volume or area. Cundall [11] suggested that the location should be regarded as an independent constitutive property, depending on the relative rotation of the two surfaces in contact. Even if a computer program can relate force location to geometric variables, there is, at present, very little data from physical tests to substantiate any physical assumption [20].

For the specific problem of the dynamic response of ancient columns and colonnades under dynamic loading, the contact forces are computed based on the overlapping region of the bodies in contact. The contact forces in the normal and tangential contact planes are assumed to act on the centroid of the overlapping region, and applied at the corresponding position of the bodies in contact.

3.3 Block Deformability

There are two approaches for modelling the mechanical behaviour of the solid discrete bodies of a discontinuous system. The simulated discrete bodies can be considered to be either infinitely rigid, i.e. without any deformations, or deformable. Either of the two approaches can be used according to the details of the specific problem under investigation and the response quantities that need to be computed.

If the deformation of each solid discrete body cannot be neglected, two main methods can be used to take into account its deformability. In the direct method of introducing deformability, each discrete body is subdivided internally into finite or boundary elements in order to consider its internal deformations. Due to the large displacements of the simulated bodies, a nonlinear formulation should be used to express the equations of motion on the deformed rather than the initial undeformed configuration of the system. In addition to the geometric nonlinearities due to the large displacements, the deformations of each body may be substantial, requiring a nonlinear constitutive law to consider the large strains. Another difficulty of this approach is that a body of complex shape must necessarily be subdivided into many zones, even if only a simple deformation pattern is required [20].

An alternative scheme to consider the deformability of the individual bodies was devised by Shi [63] in his "Discontinuous Deformation Analysis" (DDA). According to that approach a series of approximations are used to supply an increasingly complex set of strain patterns that are superimposed for each block. However, Williams and Mustoe [71] noted that the use of direct strain modes may be inconsistent.

The assumption that the material of each discrete body is infinitely rigid is appropriate when most of the overall deformations in a physical system are due to movements on discontinuities and rearrangements of the individual bodies rather than due to internal deformations of the simulated discrete bodies. Such a condition applies, for example, in an unconfined assembly of rock blocks at low stress levels. In that case, the deformations of the simulated system are due to the movements that are caused mainly due to sliding and rotation of the individual blocks, as well as, due to the opening and interlocking of interfaces, but not due to internal deformations of the individual bodies.

For the dynamic analyses of ancient columns and colonnades the bodies are assumed infinitely rigid, considering that the overall deformation of a system with distinct bodies is due to the relative displacements and rearrangements of the simulated bodies rather than due to the deformations of the individual bodies. The system is dominated by discontinuities between the drums of the columns and consequently, the material is assumed to be infinitely rigid and its elastic properties are taken into account only indirectly through the stiffness of the corresponding contact springs. The basic formulation for infinitely rigid blocks was given by Cundall et al. [13], where the medium is dealt as a set of distinct blocks that do not change their geometry as a result of the applied loadings.

3.4 Contact Interactions

The contact interactions between colliding bodies constitute an extremely complicated phenomenon that involves stress and strain distributions within the colliding bodies, thermal, acoustical and frictional dissipation of energy due to contacts, as well as plastic deformations. In our simulations, the contact interactions are modelled using soft contact springs and dashpots to evaluate the contact and damping forces based on the interpenetration between bodies in contact. A unique ability of the DEM is the automatic and efficient recognition of contacts between simulated bodies, as well as detachments of bodies that were previously in contact.

In particular, the interactions between two rigid distinct bodies in contact are automatically generated in the DEM as soon as a contact is detected, kept as long as the bodies remain in contact and removed as soon as the bodies are detached from each other (Fig. 6a). In order to be able to consider potential sliding according to the Coulomb law of friction, normal and tangential directions are considered during contact. The normal and tangential directions are based on a contact plane, which is determined at each simulation step (Fig. 6b). The bodies may slide along the contact plane relatively to each other, when the tangential force reaches the maximum allowable force in that direction, as computed by the Coulomb Law of Friction.

At any simulation step, when two bodies come in contact, equivalent springs and dashpots are automatically generated, in the normal and tangential directions, to estimate the respective contact forces that are applied to the bodies pushing them apart

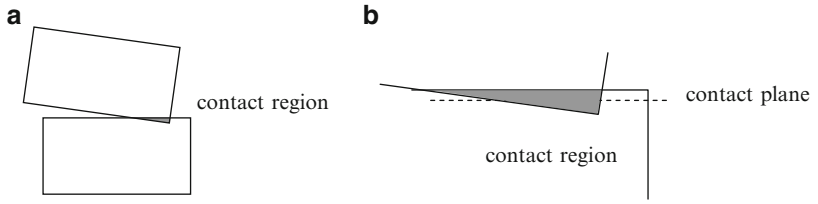


Fig. 6 Contact between two bodies: (**a**) contact region and (**b**) contact plane

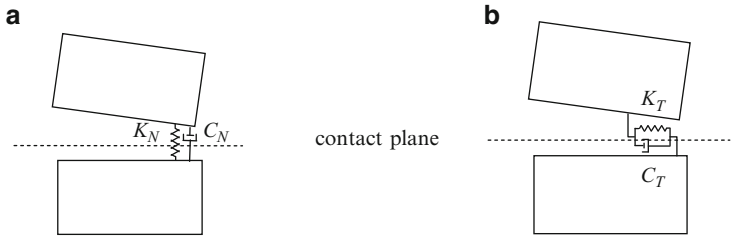


Fig. 7 Contact springs and dashpots: (**a**) in the normal and (**b**) tangential directions

(Fig. 7). Some overlapping of the bodies in contact is allowed, which is justified by the deformability at the vicinity of the contact. The interactions between bodies may involve new contacts, renewed contacts, slippages and complete detachments from other bodies with which they were, until that time, in contact.

3.5 Simulating Discontinuous Systems

Many software applications are based on a continuum mechanics formulation, such as the finite element methods and the Lagrangian finite-differences method, that can simulate the variability in material types and nonlinear constitutive behaviour. However, the representation of discontinuities requires a discontinuum-based formulation. There are several finite element, boundary element and finite difference general purpose programs available that have interface elements or "slide lines", which enable them to model a discontinuous material to some extent. Their formulation is usually restricted in one or more of the following ways. Firstly, the logic may break down when many intersecting interfaces are used. Secondly, there may not be an automatic scheme for recognizing new contacts and thirdly, the formulation may be limited to small displacements and rotation. Finally and most importantly the computational cost of contact problems is substantial, not allowing simulations of more than a couple of distinct bodies.

Computer programs described as *discrete element* codes provide the capability of analyzing the motion of multiple, intersecting discontinuities explicitly. Cundall and Hart [12, 20] provided the following definition of a discrete element method, where the name "discrete element" applies to a computer program *only* if:

1. It allows finite displacements and rotations of discrete bodies, including complete detachments.
2. It recognizes new contacts automatically as the calculation progresses.

A discrete element code typically embodies an efficient algorithm for detecting and classifying contacts. It maintains a data structure and a flexible memory allocation scheme that can handle many hundreds or thousands of discontinuities. Cundall and Hart [12, 20] also identified the following four main classes of codes that conform to the definition of a discrete element method.

1. Distinct element programs use an explicit time-marching scheme to solve the equations of motion directly. Bodies may be rigid or deformable.
2. Modal methods are similar to the distinct element method in the case of rigid blocks but, for deformable bodies, modal superposition is used.
3. Discontinuous deformation analysis assumes that contacts are infinitely rigid. The simulated bodies may be rigid or deformable.
4. Momentum-exchange methods assume that both the contacts and the bodies are infinitely rigid. Friction sliding can be represented.

Another class of codes, defined as limit equilibrium methods, can also model multiple intersecting discontinuities, but does not satisfy the requirements for a discrete element code. These codes use vector analysis to establish whether it is kinematically possible for any block in a multi-body system to move and become detached from the system. This approach does not examine subsequent behaviour of the system of blocks or redistribution of loads, while all blocks are assumed rigid.

3.6 Contact Forces

When damping is taken into account the increment of the contact forces consists of two parts, the elastic and the damping force increments. The elastic and damping contact forces in the normal (N) and tangential (T) directions are computed in terms of the elastic and the damping force components, using the following equations, respectively, based on the area of the overlap region and considering the interpenetrations and the relative velocities, in both directions, between the colliding bodies:

$$ {}^{t+\Delta t}F_N = {}^{t+\Delta t}F_N^{elastic} + {}^{t+\Delta t}F_N^{damp} = {}^{t}A_c \cdot K_N + V_N^{rel} \cdot C_N \tag{1} $$

$$ {}^{t+\Delta t}F_T = {}^{t+\Delta t}F_T^{elastic} + {}^{t+\Delta t}F_T^{damp} = {}^{t}F_T^{elastic} + V_T^{rel} \cdot \Delta t \cdot K_T + V_T^{rel} \cdot C_T \tag{2} $$

Similarly, the indices N and T in the above equations, indicate the normal and the tangential directions, respectively. K_N and K_T are the stiffnesses in the normal and tangential directions, respectively. A_c is the area of the contact region, V_N^{rel}, V_T^{rel}, C_N and C_T are the relative velocities and the damping coefficients in the normal and tangential directions, respectively. Damping is velocity-proportional

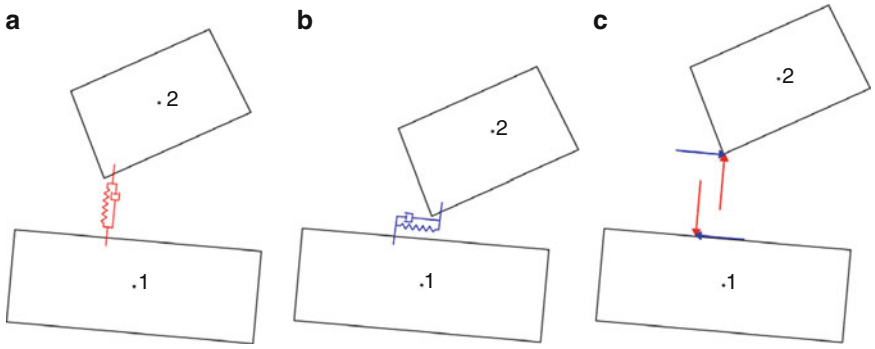


Fig. 8 Contact springs and dashpots: (**a**) in the normal direction and (**b**) in the tangential direction and (**c**) contact forces

and the magnitude of the damping force is proportional to the corresponding relative velocity of the rigid blocks that are in contact.

The Coulomb friction law is used to limit the tangential contact force, ${}^{t+\Delta t}F_T$, below a certain magnitude taking into account the magnitude of the normal contact force, ${}^{t+\Delta t}F_N$, and the minimum of the coefficients of friction, μ, of the bodies in contact.

$$\left|{}^{t+\Delta t}F_T\right| \leq \left|{}^{t+\Delta t}F_N \cdot \mu\right| \tag{3}$$

Damping is velocity-proportional and the magnitude of a damping contact force is proportional to the relative velocity of the rigid blocks that come in contact, representing the dissipation of energy during contacts. In the way the energy dissipation is modelled, velocity-proportional contact dampers are automatically generated and act between bodies that are in contact (Fig. 8). The coefficient of damping for the velocity-proportional contact dampers has *Ns/m* units, so that when multiplied with the relative velocity between the bodies in contact to derive the corresponding contact damping force.

3.7 Equations of Motion

The contact forces, which are applied at the corresponding contact points during impact, are taken into account, together with the gravity or any other forces, in the formulation of the equations of motion. The contact forces from each contact point as well as any other forces acting on each body are then transformed to the centre of mass of the body, as shown in Fig. 9.

The motion of a discrete body at time $t + \Delta t$ is determined from the dynamic equilibrium equations at time t, which are integrated using an explicit direct integration numerical method (Bathe [6]). In particular, the equations of motion are

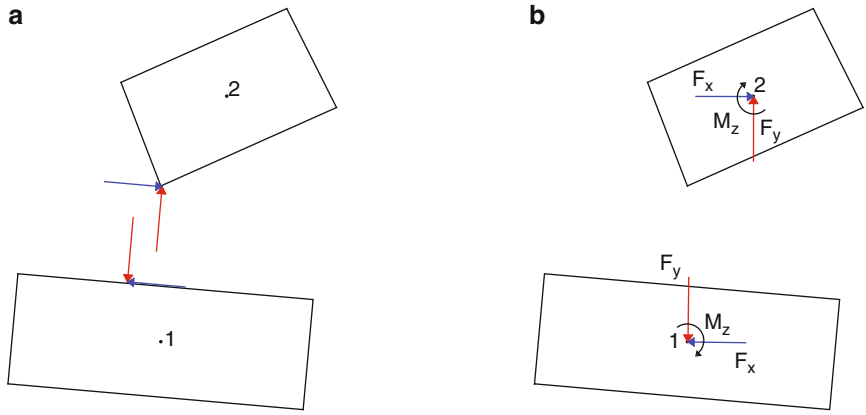


Fig. 9 Transformation of the contact forces to the centre of mass of each rigid body

numerically integrated using the Central Difference Method (CDM) computing the displacements at time $(t + \Delta t)$ from the following equations:

$$U_x\,(t+\Delta t) = \frac{\Delta t^2}{m} \cdot \left\{ F_x - \frac{m}{\Delta t^2} U_x\,(t-\Delta t) + \frac{2m}{\Delta t^2} U_x\,(t) \right\} \tag{4}$$

$$U_y\,(t+\Delta t) = \frac{\Delta t^2}{m} \cdot \left\{ F_y + m \cdot g - \frac{m}{\Delta t^2} U_y\,(t-\Delta t) + \frac{2m}{\Delta t^2} U_y\,(t) \right\} \tag{5}$$

$$\Theta_z\,(t+\Delta t) = \frac{\Delta t^2}{I_o} \cdot \left\{ M_z - \frac{I_o}{\Delta t^2} \Theta_z\,(t-\Delta t) + \frac{2I_o}{\Delta t^2} \Theta_z\,(t) \right\} \tag{6}$$

In the above equations of motion, U_x and U_y are the displacements at the X and Y directions, respectively, while Θ_z is the rotation about the Z axis. Similarly, F_x and F_y are the forces acting on the body at the centre of mass in the X and Y directions, respectively, and M_z is the moment acting on the body about the Z axis. The time step, Δt, is selected to be sufficiently small to satisfy the stability requirements of the numerical method accurately and to capture all contact interactions. Finally, m and I_o are the mass and the rotational inertia at the centre of mass of the body, respectively. This process is iteratively repeated with new cycles of contact detection, contact resolution and numerical solution of the formed equations of motion until the simulation procedure ends.

The numerical analysis is based on the assumption that velocities and accelerations are constant within each time step. The motion of each individual body is computed using the CDM, which is an explicit time stepping integration method, based on the following approximations for the velocity:

$$\dot{\underline{U}}(t + \Delta t/2) = \frac{\underline{U}(t+\Delta t) - \underline{U}(t)}{\Delta t} \tag{7}$$

therefore,

$$\dot{\underline{U}}(t - \Delta t/2) = \frac{\underline{U}(t) - \underline{U}(t - \Delta t)}{\Delta t} \tag{8}$$

where,

$$\underline{U}(t) = \begin{bmatrix} U_x(t) \\ U_y(t) \\ \Theta_z(t) \end{bmatrix} \tag{9}$$

Accordingly the acceleration can be computed by the equations:

$$\ddot{\underline{U}}(t) = \frac{\dot{\underline{U}}(t + \Delta t/2) - \dot{\underline{U}}(t - \Delta t/2)}{\Delta t^2} \tag{10}$$

$$\ddot{\underline{U}}(t) = \frac{\underline{U}(t + \Delta t) - 2\underline{U}(t) + \underline{U}(t - \Delta t)}{\Delta t^2} \tag{11}$$

Considering the equations of motion, the displacements, including the two translational and the rotational degrees of freedom, at time $t + \Delta t$ can be derived:

$$\underline{F}(t) = \underline{M} \cdot \ddot{\underline{U}}(t) = \underline{M} \frac{\underline{U}(t + \Delta t) - 2\underline{U}(t) + \underline{U}(t - \Delta t)}{\Delta t^2} \tag{12}$$

Therefore,

$$\underline{U}(t + \Delta t) = \Delta t^2 \cdot \underline{M}^{-1} \cdot \underline{F}(t) + 2 \cdot \underline{U}(t) - \underline{U}(t - \Delta t) \tag{13}$$

The matrix $\underline{M}$ is diagonal and has the following form for a planar body of mass m and rotational inertia I_0:

$$\underline{M} = \begin{bmatrix} m & & \\ & m & \\ & & I_o \end{bmatrix} \tag{14}$$

The DEM are based on the concept that the time step Δt is sufficiently small so that during a single step, disturbances cannot propagate between one discrete element and its immediate neighbours. Therefore, very small time steps are used, of the order of 1E-6 s, so as to satisfactorily capture the collisions and contacts among the individual discrete bodies of the simulated system. Such small time step satisfies both the stability and the accuracy requirements of the CDM.

After computing the displacements and rotations of all bodies, for each time step, their corresponding positions and orientations are determined and updated. Then, a new cycle of contact detection, contact resolution, application of forces and solution of the equations of motion follows, based on the updated positions of the bodies. This iterative procedure continues until the end of the simulation.

3.8 Analysis Procedure

During the analysis, at each simulation step, all of the bodies are checked with each other for contact. If no contact for a body is detected, gravitational, or any other surface or body, forces are applied on the body.

If contact is detected, the contact area and contact planes are determined and the relative velocities of the bodies in contact are computed. Using the contact springs and dashpots, the contact area and planes and the relative velocities, the contact forces are calculated and applied at each body, in addition to any other forces acting on the bodies.

Taking into account all forces and moments applied at the centroid of each body, the equations of motion are formed and numerically solved using the CDM. After computing the displacements and rotations of all bodies, for each time step, their corresponding positions and orientations are determined. Then, a new cycle of contact detection, contact resolution, application of forces and numerical solution of the equations of motion follows, based on the updated positions of the bodies. This iterative procedure, which is shown graphically in Fig. 10, continues until the end of the simulation.

4 Software Development

Performing large numbers of dynamic simulations of columns with varying mechanical and geometrical characteristics of drums and columns under the action of various harmonic oscillations and earthquake excitations provides an insight into the behaviour of these structures during strong earthquakes. The custom-made software application that has been developed facilitates the specific needs of this work, without being limited to the general capabilities of a commercial general-purpose DEM program.

The DEM software application, which is used in the simulations, has been specifically designed and implemented to enable efficient performance of two-dimensional (2D) seismic simulations of multi-block structures, while maintaining extensibility towards future spatial (3D) capabilities. The developed DEM software has the capability of enforcing displacements of the support base in order to simulate harmonic and seismic excitations of the latter. In addition, customized distinct elements and the respective contact detection algorithms are used for the modelling of ancient columns and colonnades.

A major requirement for the developed software is the ability to perform effectively and efficiently large numbers of dynamic simulations and parametric studies of monolithic or multi-drum columns and colonnades with an epistyle, with varying mechanical and geometrical characteristics, under the action of earthquake excitations. Modern object-oriented design and programming approaches have been employed using Java technologies, in order to benefit from the significant advantages that these technologies offer to modern engineering software.

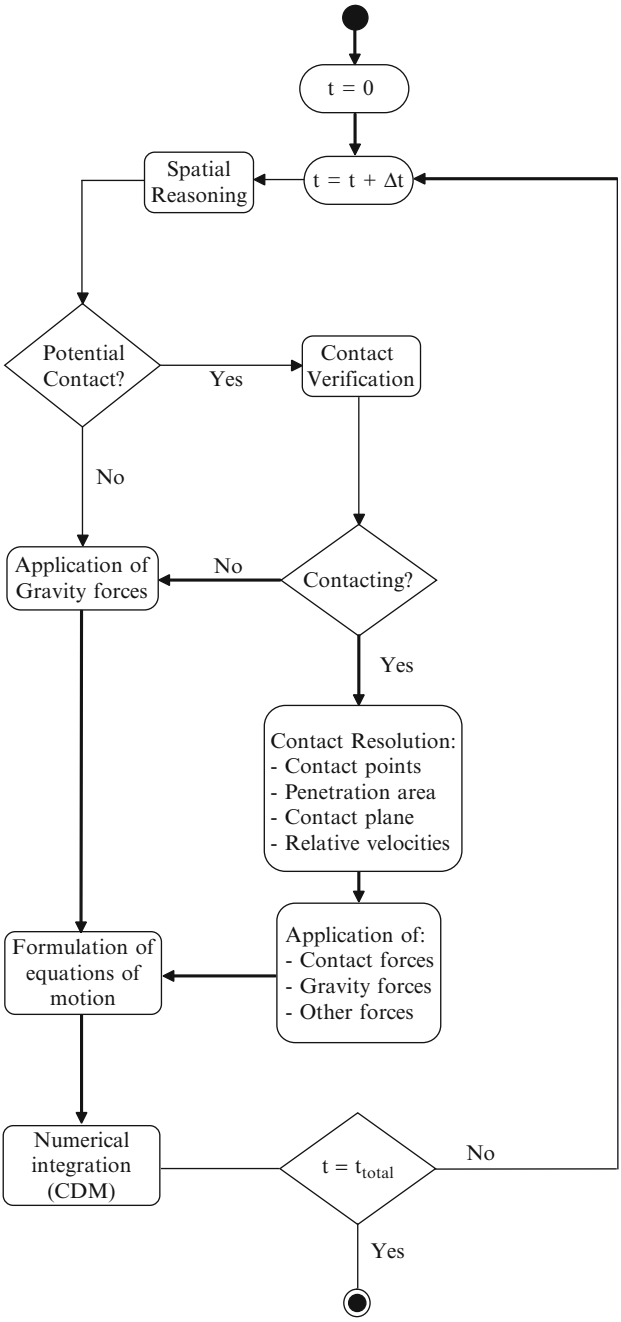


Fig. 10 Flow of control of the developed algorithms

4.1 Limitations of the Two Dimensional Analysis

The developed software application has been specifically designed and implemented to enable efficient performance of 2D seismic simulations of multi-block structures, while maintaining extensibility towards future spatial (3D) capabilities. It is well known that the results obtained by 2D dynamic analysis of rigid block assemblies are not capable of providing phenomena that may appear in the actual 3D response of such systems, such as off-plane movements and oscillations. Numerical studies of the earthquake response of ancient columns by Papantonopoulos et al. [56], using commercial 3D software, reported significant differences in the response of 2D and 3D analysis, even for plane excitations, although the models used were symmetrical about the vertical axis. The researchers also observed that very small disturbances, in the direction normal to the plane of rocking, may cause significant amplification of the response and that 2D analysis may underestimate the response, predicting greater stability. In addition, the collapse mechanisms of colonnades in many cases appear in the out-of-plane direction. Experimental work regarding the response of a scaled model of a marble classical column, presented by Mouzakis et al. [42], also reported this '3D sensitivity' inherent in the rocking phenomenon.

Nevertheless, numerical studies by Psycharis [57] and Konstantinidis [30] showed that 2D analysis can be used to capture the overall phenomenon and various parameters that affect the seismic response of multi-drum columns. Moreover, 2D can be used more efficiently and effectively when it is necessary to perform large numbers of simulations in order to study the effect of various parameters and characteristics, as 2D idealizations analysis is much more time efficient and is less sensitive to the selection of the values of the contact parameters.

5 Numerical Simulation of Colonnades with an Epistyle

In order to investigate various parameters that may affect the seismic response of multi-drum colonnade systems with epistyles, a large number of simulations has been conducted using the developed software application, under both harmonic and earthquake excitations. Here, we indicatively show some selected results from simulations of colonnades with base width of $1\,m$ and total height of $6\,m$ under earthquake excitations.

In particular, Figs. 11–16 show snapshots from the computed time–history responses of multi-drum colonnades with epistyles for the Athens, Kalamata and Mexico City earthquakes, scaled appropriately to cause failure to the simulated structures.

The response of multi-drum colonnades with an epistyle exhibits important similarities with the response of standalone multi-drum columns [48]. For earthquakes with higher predominant frequencies, the response contains both sliding and rocking phenomena. For the Mexico City Earthquake, which has lower predominant frequencies, rocking dominates the seismic response. Moreover, earthquakes

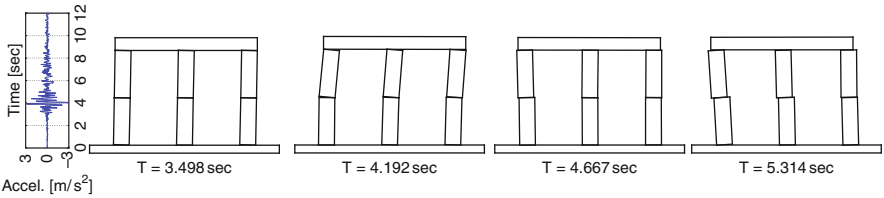


Fig. 11 Time–history response of a colonnade with two drums under an accelerogram from the Athens Earthquake scaled to a PGA of 32.21 m/s^2

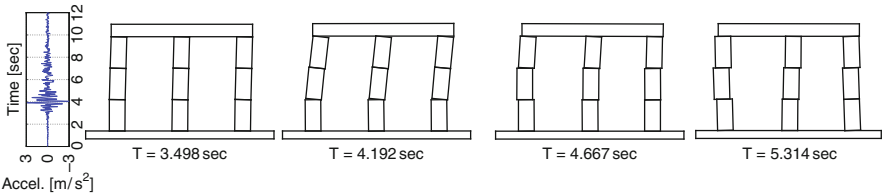


Fig. 12 Time–history response of a colonnade with three drums under an accelerogram from the Athens Earthquake scaled to a PGA of 32.21 m/s^2

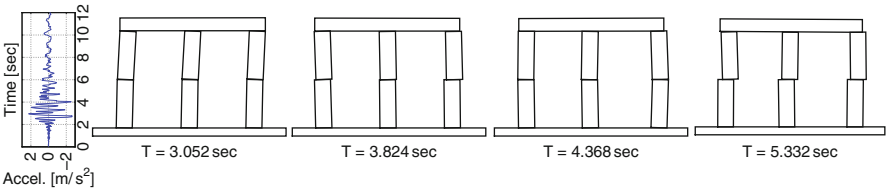


Fig. 13 Time–history response of a colonnade with two drums under an accelerogram from the Kalamata Earthquake scaled to a PGA of 17.35 m/s^2

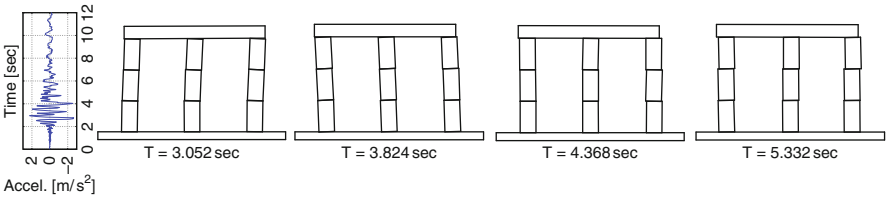


Fig. 14 Time–history response of a colonnade with three drums under an accelerogram from the Kalamata Earthquake scaled to a PGA of 17.35 m/s^2

with relatively low predominant frequencies require lower acceleration to overturn the colonnades than earthquakes with higher predominant frequencies.

As observed in the response of standalone columns [26, 48], in cases of low predominant frequency earthquakes, like the Mexico City Earthquake, the number of drums that assemble a colonnade does not affect the seismic response of the

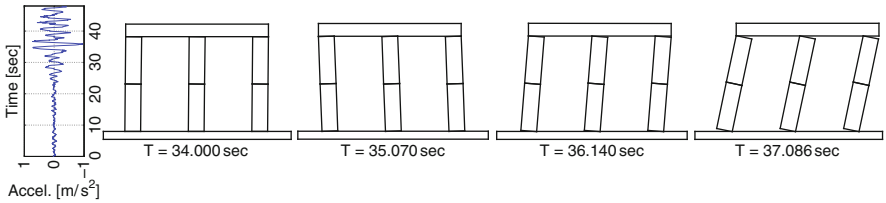


Fig. 15 Time–history response of a colonnade with two drums under an accelerogram from the Mexico City Earthquake scaled to a PGA of $2.45\,\mathrm{m/s^2}$

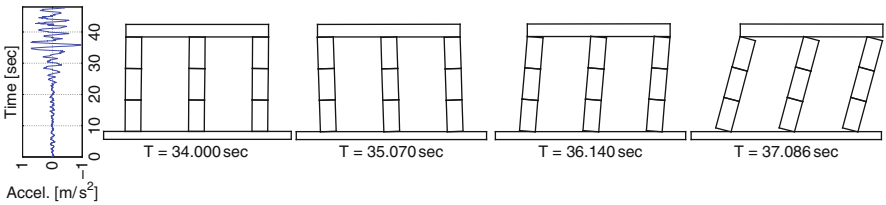


Fig. 16 Time–history response of a colonnade with three drums under an accelerogram from the Mexico City Earthquake scaled to a PGA of $2.45\,\mathrm{m/s^2}$

system, since all of the drums of the columns tend to rotate in a single group, similar to a monolithic column. Therefore no seismic energy is dissipated at the interfaces between each block, since no sliding occurs between adjacent discrete bodies.

6 Concluding Remarks

The dynamic behaviour of rigid blocks under dynamic loading is an extremely complicated phenomenon and can be characterized as highly non-linear, as these systems involve complicated rocking and sliding phenomena. In order to investigate parameters that affect the response of multi-drum structures, it is necessary to efficiently perform large numbers of numerical simulations, where earthquake characteristics and design parameters are varied. Modern object-oriented design and programming approaches can be employed in order to benefit from the significant advantages that these technologies offer to modern engineering software.

The DEM has been utilized to investigate the response and behaviour of ancient columns and colonnades under various ground excitations, by simulating the individual rock blocks as distinct rigid bodies. A specialized software application has been designed and developed, using modern object-oriented technologies to perform efficient seismic simulations of multi-block structures. The numerical simulations and parametric analyses that have been conducted, show that the methodology described as well as the developed software can be effectively used to evaluate the response of multi-drum column systems, which have a great archaeological significance.

The dynamic behaviour of multi-drum colonnades with epistyles under earthquake excitations is examined through planar numerical simulations using the developed application. Analyses conducted with the developed software show that colonnades with epistyles, exhibit very complicated seismic responses that involve rocking and sliding behaviour, depending on certain influencing parameters. The analysis results indicate that the predominant frequencies significantly affect the seismic response. Multidrum columns and colonnades are much more vulnerable to earthquakes with relatively low predominant frequencies than earthquakes with higher predominant frequencies, such as the ones that usually occur in the Eastern Mediterranean region.

References

1. Alexander C, Ishikawa S, Silverstein M (1977) A pattern language: towns, buildings, construction. Oxford University Press, New York
2. Alexandris A, Psycharis IN, Protopapa EA (2001) The collapse of the Temple of Zeus at Olympia. Back analysis using the distinct element method. In: Proceedings of the second Greek national conference on earthquake engineering and seismology, vol 1, Greece, pp 297–306
3. Allen R, Duan X (1995) Effects of linearizing on rocking block. J Struct Eng 12(7):1146–1149
4. Aslam M, Godden W, Scalise D (1980) Earthquake rocking response on rigid bodies. J Struct Div ASCE 106(ST2):377–392
5. Barbosa R, Ghaboussi (1989) Discrete finite element method. In: Proceedings of the 1st U.S. conference on discrete element methods, Golden, CO
6. Bathe KJ (1996) Finite element procedures. Prentice-Hall Inc., Englewood Cliffs, NJ
7. Beskos D (1993/4) Use of finite and boundary elements in the analysis of monuments and special structures. Bulletin of the association of civil engineers of Greece, No. 216 [in Greek]
8. Beskos D (1993/4) Use of finite and boundary elements in the analysis of monuments and special structures. Bulletin of the association of civil engineers of Greece, No. 217 [in Greek]
9. Cook BK, Jensen RP (eds) (2002) Discrete element methods: numerical modelling of discontinua. In: Proceedings of the third international conference on discrete element methods, Santa Fe, NM
10. Connor R, Gill MJ, Williams J (1993) A linear complexity contact detection algorithm for multi-body simulations. In: Proceedings of the 2nd international conference on discrete element methods, Boston, MA, pp 53–64
11. Cundall PA (1971) A computer model for simulating progressive large scale movements in block rock systems. In: Proceedings of the symposium of international society of rock mechanics, 1, paper II-8, Nancy, France
12. Cundall PA, Hart RD (1992) Numerical modelling of discontinua. Eng Comp 9(2):101–113
13. Cundall PA, Marti J, Beresford P, Last NC and Asgian MI (1978) Computer modeling of jointed rock masses. U.S. Army Engineer Waterways Experiment Station, Vicksburg, Mississippi, Tech. Report N-78-4
14. Demosthenous M, Manos GC (1996) Study of the dynamic response of models of ancient columns or colonnades subjected to horizontal base motions. Struct Dyn-EURODYN
15. Feng YT, Owen DRJ (2002) Discrete element methods: numerical modelling of discontinua. In: Proceedings of the third international conference on discrete element methods, Santa Fe, NM, pp 32–41
16. Fletcher B (1905) A history of architecture on the comparative method for the student, craftsman, and amateur. Charles Scribner's Sons, New York
17. Hogan S (1990) The many steady state responses of a rigid block under harmonic forcing. Earthquake Eng Struct Dyn 19:1057–1071

18. Housner GW (1963) The behaviour of inverted pendulum structures during earthquakes. Bull Seismol Soc Am 53:403–417
19. Ishiyama Y (1982) Motions of rigid bodies and criteria for overturning by earthquake excitations. Earthquake Eng Struct Dyn 10(5):635–650
20. Itasca Consulting Group Inc. (2004) UDEC-Universal Distinct Element Code version 4.0. Theory and Background Manual, Minnesota, MN
21. Kim, Y-S, Miura K, Miura S, Nishimura M (2001) Vibration characteristics of rigid body placed on sand ground. Soil Dyn Earthquake Eng 21(1):19–37
22. Kimura H, Iida K (1934) On rocking of rectangular columns (I&II) (in Japanese). J Seismol Soc Jpn 6:125–149 & 165–212
23. Koh AS, Spanos PD, Roesset J (1986) Harmonic rocking of rigid body block on flexible foundation. J Eng Mech, ASCE, 112(11):1165–1180
24. Koh AS, Spanos PD (1986) Analysis of block random rocking. Soil Dyn Earthquake Eng 5:178–183
25. Komodromos P (2005) A simplified updated Lagrangian approach for combining discrete and finite element methods. Comput Mech 35(4):305–313
26. Komodromos P, Papaloizou L, Polycarpou P (2008) Simulation of the response of ancient columns under harmonic and earthquake excitations. Eng Struct 30(8):2154–2164
27. Komodromos P, Papaloizou L, Polycarpou P, Mavronicola E (2007) Modern object-oriented design of structural engineering software. In: Proceedings of the eleventh international conference on civil, structural and environmental engineering computing, St. Julians, Malta
28. Komodromos P, Williams J (2002) Utilization of Java and Database Technology in the development of a combined discrete and finite element multibody dynamics simulator. In: Proceedings of the 3rd international conference on discrete element methods, Santa Fe, NM, ASCE Geotechnical Special Publication, 117, pp 118–124
29. Komodromos PI, Williams JR (2004) Dynamic simulation of multiple deformable bodies using combined discrete and finite element methods. Eng Comput (Swansea, Wales), 21(2–4):431–448
30. Konstantinidis D, Makris N (2005) Seismic response analysis of multidrum classical columns. Earthquake Eng Struct Dyn 34:1243–1270
31. De Lorenzis L, DeJong M, Ochsendorf J (2007) Failure of masonry arches under impulse base motion. Earthquake Eng Struct Dyn 36 (14):2119–2136
32. Lemos JV (2007) Discrete element modelling of masonry structures. J Architectural Heritage 1:190–213
33. Liu XL, Lemos JV (2001) Procedure for contact detection in discrete element analysis. J Adv Eng Softw 32:409–415
34. Mackie RI (1992) Object-oriented programming of the finite element method. Int J Num Methods Eng (35):425–436
35. Madan A (2004) Object-oriented paradigm in programming for computer-aided analysis of structures. J Comput Civil Eng 18(3):226–236
36. Makris N, Roussos YS (2000) Rocking response of rigid blocks under near-source ground motions. Geotechnique 50 (3):243–262
37. Makris N, Zhang J (2001) Rocking response of anchored blocks under pulse-type motions. J Eng Mech 127:484–493
38. Manos GC, Demosthenous M, Kourtides V, Hatzigeorgiou A (2001) Dynamic and earthquake behaviour of models of ancient columns and colonnades with or without energy absorptions systems. In: Proceedings of second Greek national conference on earthquake engineering and seismology, vol 1. Thessaloniki, Greece, pp 257–276
39. Manos GC, Kourtides V, Demosthenous M, Tsakmakides E (2007) Experimental and numerical investigation of the sliding behaviour of a set of two rigid blocks subjected to cyclic shear-type loads. WIT Trans Built Environ 95:633–643
40. Mitsopoulou E, Doudoumis IN, Paschalidis V (1998) Numerical analysis of the dynamic seismic response of multi-block monumental structures. In: Proceedings of the eleventh European conference on earthquake engineering. A.A. Balkema, Rotterdam

41. Mitsopoulou E, Papaloizou L (2006) Evaluation of the response of a stone-masonry building using inelastic analysis procedure. In: Second international conference on nonsmooth/nonconvex mechanics with applications in engineering (II. NNMAE), Thessaloniki
42. Mouzakis H, Psycharis I, Papastamatiou D, Carydis P, Papantonopoulos C, Zambas C (2002) Experimental investigation of the earthquake response of a model of a marble classical column. Earthquake Eng Struct Dyn 31:1681–1698
43. Mustoe G, Henriksen M, Huttelmaier H (eds) (1989) Proceedings of the first U.S. conference on discrete element methods. Colorado School of Mines, Golden, CO
44. Newmark NM (1965) Effects of earthquakes on dams and embankments. Fifth Rankine lecture. Geotechnique 15:139–160
45. O'Connor M. Ruaidhri (1996) A distributed discrete element modelling environment – algorithms, implementation, and applications. Ph.D. thesis, Department of Civil and Environmental Engineering, MIT
46. Omori F (1900) Seismic experiments on the fracturing and overturning of columns. Publications Earthquake Investigation Committee in Foreign Language 4:69–141
47. Omori F (1902) On the overturning and sliding of columns. Publications of the Earthquake Investigation Committee in Foreign Language 12:8–27
48. Papaloizou L, Komodromos P (2009) Planar investigation of the seismic response of ancient columns and colonnades with epistyles using a custom-made software. Soil Dyn Earthquake Eng 29(11–12):1437–1454
49. Papantonopoulos C, Psycharis I, Papastamatiou D, Lemos J, Mouzakis H (2002) Numerical prediction of the earthquake response of classical columns using the distinct element method. Earthquake Eng Struct Dyn 31:1699–1717
50. Papastamatiou D, Psycharis I (1993) Seismic response of classical monuments. A numerical perspective developed at the temple of Apollo in Bassae. Greece, Terra Nova 5:591–601
51. Peña F, Prieto F, Lourenco PB, Campos Costa A, Lemos JV (2007) On the dynamics of rocking motion of single rigid-block structures. Earthquake Eng Struct Dyn 36(15):2383–2399
52. Pombei A, Scalia A, Sumbatyan MA (1998) Dynamics of rigid block due to horizontal ground motion. J Eng Mech ASCE 124(7):713–717
53. Psycharis I.N (1990) Dynamic behaviour of rocking two-block assemblies. Earthquake Eng Struct Dyn 19(4):555–575
54. Psycharis IN (2006) Applications in the restoration of ancient monuments. In: Chapter 4.4 Fracture and failure of natural building stones. Springer, The Netherlands
55. Psycharis I, Jennings P (1983) Rocking of slender rigid bodies allowed to uplift. Earthquake Eng Struct Dyn 11:57–76
56. Psycharis I, Lemos J, Papastamatiou D, Zambas C, Papantonopoulos C (2003) Numerical study of the seismic behaviour of a part of the Parthenon Pronaos. Earthquake Eng Struct Dyn 32:2063–2084
57. Psycharis IN, Papastamatiou DY, Alexandris AP (2000) Parametric investigation of the stability of classical columns under harmonic and earthquake excitations. Earthquake Eng Struct Dyn 29:1093–1109
58. Scalia A, Sumbatyan MA (1996) Slide rotation of rigid bodies subjected to a horizontal ground motion. Earthquake Eng Struct Dyn 25:1139–1149
59. Shenton H, Jones N (1991) Base excitation of rigid bodies. 1: Formulation. J Eng Mech ASCE 117(EM10):2286–2306
60. Shenton H, Jones N (1991) Base excitation of rigid bodies. 2: Periodic slide-rock response. J Eng Mech ASCE 117(EM10):2307–2328
61. Shenton H (1996) Criteria of initiation of slide, rock, and slide-rock rigid-body modes. J Eng Mech, ASCE 122:690–693
62. Shi B, Anooshehpoor A, Zeng Y, Brune JN (1984) Rocking of rigid blocks due to harmonic shaking. J Eng Mech 110:1627–1642
63. Shi GH (1989) Discontinuous deformation analysis – a new numerical model for the statics and dynamics of block systems. Lawrence Berkeley Laboratory, Report to DOE OWTD, Contract AC03-76SF0098, September 1988; also Ph.D. Thesis, University of California, Berkeley, CA

64. Sinopoli A (1990) Dynamics and impact in a system with unilateral constraints. The relevance of dry friction. J Italian Assoc Theoretical Appl Mech 22:210–215
65. Spanos PD, Koh AS (1984) Rocking of rigid blocks due to harmonic shaking. J Eng Mech 110:1627–1642
66. Spanos PD, Roussis PC, Politis NPA (2001) Dynamic analysis of stacked rigid blocks. Soil Dyn Earthquake Eng 21(7):559–578
67. Tso W, Wong C (1989) Steady state rocking response of rigid blocks. Part 1: Analysis. Earthquake Eng Struct Dyn 18:89–106
68. Tso W, Wong C (1989) Steady state rocking response of rigid blocks. Part 2: Experiment. Earthquake Eng Struct Dyn 18:107–120
69. Williams J Mustoe G (eds) (1993) Proceedings of the 2nd international conference on discrete element methods. Department of Civil and Environmental Engineering, Massachusetts Institute of Technology, IESL Publications, Boston, MA
70. Williams J (1988) Contact analysis of large numbers of interacting bodies using discrete modal methods for simulating material failure on the microscopic scale. Eng Comput 5(3): 198–209
71. Williams JR, Mustoe GGW (1987) Modal methods for the analysis of discrete systems. Comp Geotech 4:1–19
72. Working Model (2000) User's manual. MSC Software Corporation, San Mateo, CA
73. Younis C, Tadjbakhsh G (1984) Response of sliding rigid structure to base excitation. J Eng Mech ASCE 110(3):417–432
74. Yim CS, Lin H (1991) Nonlinear impact and chaotic response of slender rocking objects. J Eng Mech, ASCE 117(9):2079–2100
75. Yim CS, Chopra A, Penzien J (1980) Rocking response of rigid blocks to earthquakes. Earthquake Eng Struct Dyn 8(6):567–587
76. Zhang J, Makris N (2001) Rocking response of free-standing blocks under cycloidal pulses. J Eng Mech ASCE 127(5):473–483
77. Zimmerman T, Bomme P, Eyheramendy D, Vernier L, Commend S (1998) Aspects of an object-oriented finite element environment. Comput Struct 68:1–16

Seismic Behaviour of the Walls of the Parthenon A Numerical Study

Ioannis N. Psycharis, Anastasios E. Drougas, and Maria-Eleni Dasiou

Abstract A numerical study of the behaviour of the walls of the Cella of Parthenon subjected to seismic loading is presented. Commonly used numerical codes for masonry structures based on continuum mechanics are unable to handle the behaviour of discontinuous walls of ancient monuments, in the same way as continuum models cannot capture the behaviour of drum-columns. In this analysis, the discrete element method was used, which has been proven, in previous research, capable to accurately predict the response of discontinuous structural systems. The marble structural stones of the walls were modeled as rigid blocks with frictional joints between them. Two types of models were used in the analyses: (i) a sub-assembly consisting of only a section of the wall of limited length, either as it is in-situ (partially collapsed) or with its full height (restored) and (ii) considering the whole structure partially restored. In one of the models of type (i), the existing damage of the stones was also implemented. Analyses were performed with and without considering the metallic elements (clamps and dowels) that connect adjacent stones. The numerical models represented in detail the actual construction of the monument. The assemblies considered were subjected to all three components of four seismic events recorded in Greece. Time domain analyses were performed in 3D, considering the non-linear behaviour at the joints. The general response profile was examined, as manifested by rocking and sliding of individual stones or groups of stones. The effect of several parameters was investigated including: the coefficient of friction at the joints, the imperfections of the blocks, the existence or not of connectors between adjacent blocks and the seismic motion characteristics. The results of the sub-assembly models and the full-structure model were compared in order to estimate the accuracy of the sub-structuring technique. The effect of the restoration of the wall to its original height was also examined. Conclusions were drawn based on the maximum displacements induced to the structure during the ground excitation and the residual deformation at the end of the seismic motion.

I.N. Psycharis (✉), A.E. Drougas, and M.-E. Dasiou
School of Civil Engineering, National Technical University of Athens,
9, Heroon Polytechneiou Str., Zografos, GR15780, Athens, Greece
e-mail: ipsych@central.ntua.gr; a_drougas@yahoo.gr; medasiou@yahoo.com

M. Papadrakakis et al. (eds.), *Computational Methods in Earthquake Engineering*,
Computational Methods in Applied Sciences 21, DOI 10.1007/978-94-007-0053-6_12,
© Springer Science+Business Media B.V. 2011

Keywords Monuments · Masonry · Restoration · Rocking · Sliding · Earthquake response

1 Introduction

The restoration of classical monuments is a complicated and difficult task, first because any intervention should take under consideration the historical, aesthetical and archaeological values of the structure, and second because the structural analysis is quite complicated due to the spinal construction of classical monuments, which are comprised of massive, carefully fitted stone blocks without the use of mortar. Under static loading, the resulting stresses usually do not exceed 15% of the material's strength, owing to their large member sections. This percentage is further decreased in monuments of ruinous nature and thus, failure parameters and criteria should be based on member displacements rather than material failure.

During strong seismic events, the response is dominated by the rocking and the sliding of the structural elements. This behaviour, which is highly non-linear and complicated, is practically impossible to be treated in an analytical manner and can only be handled numerically. So far, a number of numerical studies [1–7] or experimental investigations [8–10] on drum-columns, either free-standing or connected with architraves, have been presented. Comparison of numerical results with shake table experimental data on drum-column marble models [2, 6] showed that the distinct element method and especially the code 3DEC of Itasca Consulting Group, Inc [11] can predict reasonably well the response of such structures, despite the sensitivity of the behaviour to even trivial changes of the parameters.

The earthquake response of walls of classical monuments is different than the response of multi-drum columns, because the structural blocks are interlocked from the way that the masonry is constructed and, usually, they are connected with metallic elements. The dynamic response of columns is prevailed by rocking while in walls, the response is governed mainly by sliding and less by rocking, which can only occur in the out-of-plane direction. However, since the discrete element method can consider both sliding and rocking, it can be applied for the assessment of the earthquake response of stone masonry.

In this paper, an investigation of the seismic behaviour of the walls of the Cella of the Parthenon on the Acropolis of Athens, Greece is presented. Four ground motions, recorded during recent earthquakes in Greece, were used as base excitations. Two series of analyses were performed: (i) using sub-assembly models consisting of only a section of the wall of length equal to 4.88 m at its base (four stones), either as it is in-situ (partially collapsed) or restored to its full height and (ii) considering the whole structure, partially restored compared to its present condition. In both cases, analyses were performed with and without considering the connections between the stones. In case (i), the major structural imperfections due to damage were also considered in some runs.

2 Discrete Element Modeling of Stone Masonry

During the seismic response of discontinuous block assemblages, the deformation and failure is dominated by the movement between individual blocks. Resultantly, continuum models, based primarily on the finite element method, may not be appropriate numerical tools for identifying key features of the response or efficiently handling significant sliding along joints. Instead, discontinuous modelling via the discrete element method tends to function better in that role.

In this paper, the code 3DEC [11] that is based on the discrete element method was used in the analyses. In the distinct (or discrete) element method (Cundall [12]), the system is represented as an assembly of discrete blocks. Joints are viewed as interfaces between distinct bodies, allowed to undergo unlimited translation and rotation including complete detachment from adjacent blocks. New contacts are automatically recognized as the calculation progresses. At each contact surface, relationships are established that associate the normal and the shear forces to displacements. The method is usually applied to systems in which the behaviour is dominated by discontinuities and the material elastic properties may be ignored. It is possible, however, to consider deformable blocks, which are further discretised in finite elements.

The dynamic response is calculated using a time-stepping algorithm. The time-step should be sufficiently small, so that disturbances cannot propagate between adjacent discrete elements during a single step. The required time-step is defined by the mass of the blocks and the stiffness and damping at the contacts. The solution scheme is identical to that used by the explicit finite difference method for continuum analysis.

3 Description of the Monument

The walls of the Cella of the Parthenon are comprised of the row of the orthostates, situated at the base (in effect a row of stretcher stones of 1.16 m in height), followed by 17 alternating rows of header and stretcher stones (Fig. 1a). The width of the header stones is 1.14 m, equal to the width of the wall, and that of the stretcher stones 0.55 m, which, consequentially, leaves a horizontal transverse gap of 4.0 cm width between the stretcher stones of the same row. The orthostate stones have also a width of 0.55 m and protrude outwards by 7 mm. All stones are approximately 1.22 m in length. Both header and stretcher stones are 0.52 m in height, resulting to a total height of the wall, in its original state, just over 10 m without including the architraves, i.e. the upper row of larger size stones.

Due to the absence of mortar, iron elements were initially used to connect structural members. Two types of connections were applied (Fig. 1b): tensile clamps, placed at the top of each stone across vertical joints, and shear dowels, located at the base of each stone.

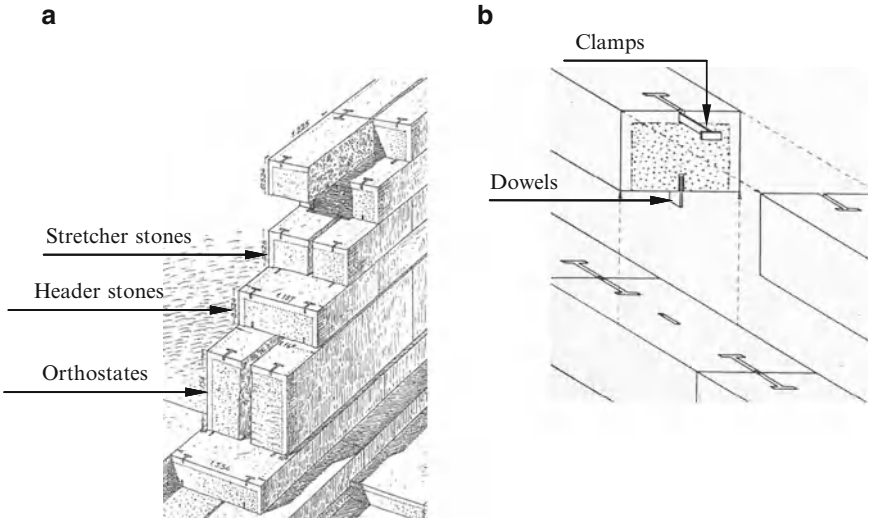


Fig. 1 (**a**) Cross-section of the Parthenon walls (Reproduced from [13]); (**b**) Layout of the connecting elements (Reproduced from [14])

Today, only the W wall is in good condition, while the N, E and S walls are partially collapsed. Also, only small portions of the inner wall, at the places where it was connected to the N and S walls, are still standing. Most of the damage was caused during a large explosion that occurred in the interior of the monument in 1687. The inner side is heavily damaged and most stones suffer from cut-offs and wedge shaped notches, while many have been lost altogether. The detrimental effect of cut-offs to the stability of classical monuments has been previously investigated [3, 5]. However, the properties of the material, for instance its high compressive strength and modulus of elasticity, remain largely unaffected.

4 Numerical Models

4.1 General Assumptions

Two series of analyses were performed: in the first series, the model was based on a sub-assembly section of the wall with length at its base corresponding to four stones; in the second series, the whole structure, partially restored, was modelled. In both cases, analyses with and without considering the connecting elements between the stones were performed.

In all models, each stone was represented by a convex rigid block. For masonry structures composed of stones of hard material, as marble, the deformation of the

system occurs mainly at the joints. Thus, it is reasonable to consider rigid blocks instead of deformable ones in order to reduce the run-times.

A Mohr-Coulomb constitutive model was adopted for the mechanical behaviour of the joints. No tensile strength was considered in the normal direction, in which the joint behaviour was governed by the normal stiffness coefficient that related the contact stress with the normal contact displacement. In the shear direction, an elasto-plastic stress-displacement law was assumed: the elastic range was characterized by the shear stiffness, while the shear strength was governed by the Coulomb friction coefficient with no cohesive strength component. For the normal and the shear stiffness, typical values for marble [2,6] were used, while three values of friction coefficient were considered: $\mu = 0.75$, 1.0 and 1.15. The joint properties used in the analyses are listed in Table 1.

The clamps and dowels were considered as elasto-plastic elements with the properties shown in Table 2. These values were derived from the dimensions of the cross section of the connecting elements and the elastic properties of the material. In the prototype structure, the clamps and dowels were made of iron. However, for the part that will be restored, titanium connecting elements will be used. For this reason, the elastic properties of titanium were used in Table 2.

No damping was considered during the first 20 s of the response, which cover the duration of the strong ground motion for all records, as proposed by Papantonopoulos et al. [2]. However, mass proportional damping with a value of 20% of critical at 0.3 Hz was applied to the remainder of the response, in order to attenuate faster the motion of the structure after the earthquake and, thus, facilitate the determination of the residual displacements.

Table 1 Mechanical properties of the joints

Parameter	Value
Normal stiffness (compressive)	1×10^6 KPa/m
Normal stiffness (tensile)	0
Shear stiffness (elastic branch)	1×10^6 KPa/m
Friction coefficient	0.75, 1.00, 1.15
Cohesion	0

Table 2 Properties of the connecting elements

Parameter	Clamps	Dowels
Axial stiffness	7×10^6 KN/m	–
Axial yield force	50 KN	–
Ultimate axial strain	20%	–
Shear stiffness	2.87×10^6 KN/m	1.3×10^6 KN/m
Shear yield force	25 KN	15 KN

4.2 Sub-Assembly Models of a Section of the N Wall

Three different geometrical models were considered for a sub-assembly section of the N wall, namely: (a) the in-situ, partially collapsed portion of the easternmost surviving part of the N wall with stones without imperfections, as in their initial, intact state (Fig. 2a); (b) the same in-situ part, but taking into account all major structural imperfections due to the existing damage (Fig. 2b); and (c) the same part of the wall fully restored to its original height, without imperfections (Fig. 2c).

The height of the in-situ segment was 4.80 m, its width 1.14 m and its length 4.88 m at the base. For the model with imperfections, cut-offs were considered on selected stones, simulating the existing damage. The fully restored wall segment had a height of 10.0 m, width of 1.14 m and the same length with the in-situ model, equal to 4.88 m.

For the sub-structure models, the connections between the blocks, when considered, were applied using a simplified assumption: since the connecting elements are evenly distributed, their influence was considered by modifying the joint properties instead of accurately modelling each one of them. Thus, in order to count for the longitudinal strength of the clamps, normal tensile strength was added to the vertical joints, equal to the total tensile strength of the clamps connected to each joint. The shear strength of the dowels and the clamps was considered by adding cohesion to the joints, equal to the total shear strength of the corresponding elements divided by the area of the contact surface. The accuracy of this simplified approach was verified, for selected cases, through a comparison with the results of the corresponding model with the actual connecting elements. Such comparisons showed that the maximum displacements during the strong ground motion were almost identical and that the residual deformations were similar.

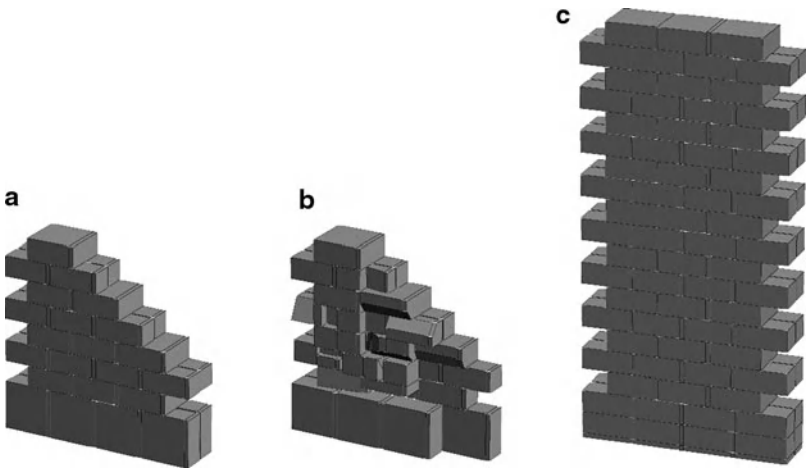


Fig. 2 Sub-assembly section models: (**a**) in-situ part without imperfections; (**b**) in-situ part with imperfections; (**c**) fully restored

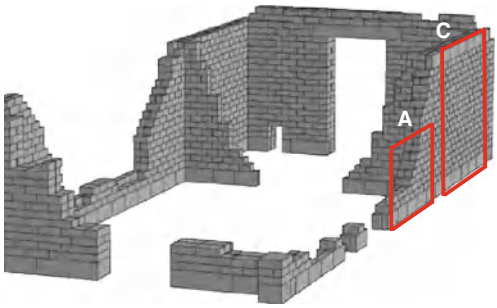


Fig. 3 Full model of the partially restored structure. The boxes A and C correspond to the sub-assembly section models (**a**) and (**c**) of Fig. 2, respectively

4.3 Full Model of the Partially Restored Structure

The model of the full structure (Fig. 3) was based on a restoration scenario, according to which the monument is partially restored. In this model, all the geometrical details of the prototype and an exact representation of the connecting elements were implemented. All the stones were assumed intact, without damage. The parts of this model that are marked with the boxes A and C in Fig. 3 can be assumed representative of the sub-assembly models (a) and (c) of Fig. 2, respectively; thus, comparison of the results is possible.

5 Seismic Input

All the analyses were performed in 3-D, applying all three components of each seismic motion at the base of the models. Four records of recent strong earthquakes in Greece were used (Fig. 4 and Table 3):

- The Kalamata, 1986 (Ms = 6.2) accelerogram that was recorded on stiff soil at a distance of about 9 km from the epicentre. The record samples the near-field strong motion characteristics that caused considerable damage to the buildings of the city of Kalamata. The duration of the strong motion is about 6 s.
- The Aigio, 1995 (Ms = 6.2) accelerogram that was recorded 18 km away from the epicentre. The record was obtained at the basement of a two-storey building on rather soft soil and it is dominated by a 0.5 s period pulse of approximately 0.53 g amplitude in the main horizontal direction.
- The Athens, 1999 earthquake (Ms = 5.9), that was recorded at the Metro station at Syntagma, on firm soil (schist) at a depth of approximately 7.0 m below the ground surface. The site was about 20 km away from the epicentre and located close to the Parthenon, in a distance of less than 1 km.
- The Lefkada, 2003 (Ms = 5.8) accelerogram that was recorded near the causative fault on rather soft soil. The record was influenced by near-field effects of backward directivity, showing a long duration of about 10 s.

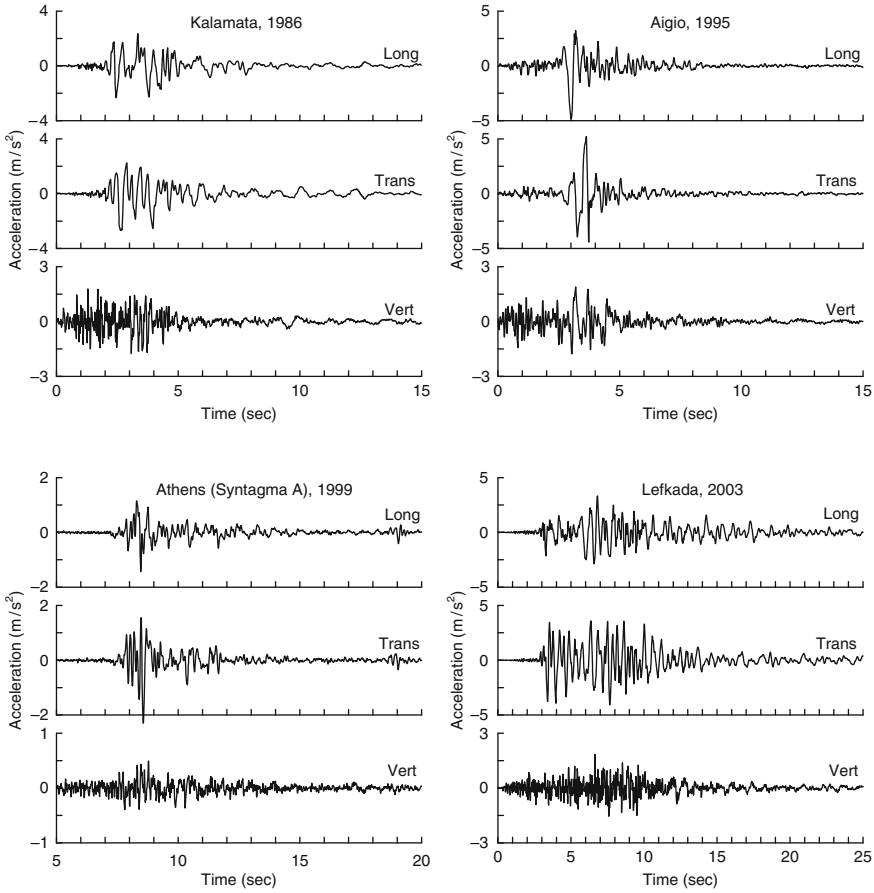


Fig. 4 Earthquake records considered in the analyses

Table 3 Peak ground accelerations and velocities of the two horizontal components of the earthquake records considered in the analyses

	Longitudinal direction		Transverse direction	
Earthquake	PGA (g)	PGV (m/sec)	PGA (g)	PGV (m/sec)
Kalamata, 1986	0.24	0.32	0.27	0.24
Aigio, 1995	0.49	0.44	0.53	0.46
Athens, 1999	0.15	0.13	0.23	0.14
Lefkada, 2003	0.34	0.30	0.42	0.31

In all the analyses, the stronger horizontal component of each earthquake was applied to the normal direction of the long walls (N–S direction).

The results obtained using the Athens record showed significantly smaller deformations compared to the other earthquakes. For this reason, they are not presented

in the following. It should be noted that such small deformations were expected for this record, because the displacements that occurred at the monument, during the actual seismic event, were indeed small.

6 Presentation of the Results

6.1 In-Plane Versus Out-of-Plane Response

Figures 5 and 6 show a comparison between the in-plane and the out-of-plane maximum (during the ground shaking) and residual displacements along the height of the wall, respectively. These results correspond to position C and were obtained using the full-structure model of Fig. 3 for the Lefkada record, normalized to pga = 0.20 g. It can be observed that the residual displacements are similar in both directions, but the maximum displacements are significantly larger in the out-of-plane direction. For this reason, only results in the out-of-plane direction are presented in the following.

6.2 Effect of Friction Coefficient

Previous experimental investigation on shear cyclic tests of marble joints [15] showed that there is a dependence of the friction coefficient on the vertical load

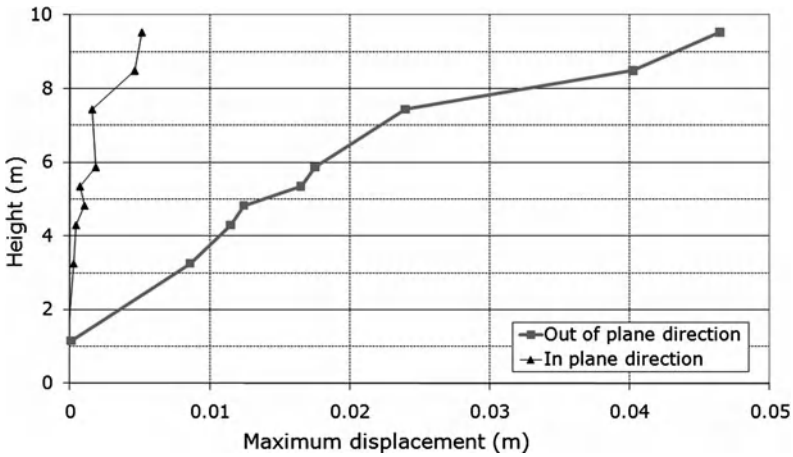


Fig. 5 Maximum displacements along the height of the full-structure model at position C (Lefkada earthquake normalized to pga = 0.20 g)

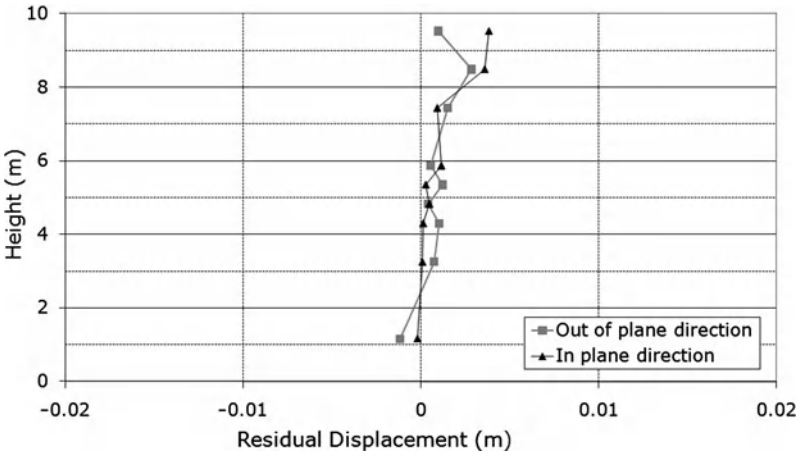


Fig. 6 Residual displacements along the height at position C of the full-structure model (Lefkada earthquake normalized to pga = 0.20 g)

and on the velocity of application of the shear displacement. These experiments were performed using specimens made of Dionysos marble, the same material of which the Parthenon is constructed. The values obtained for the residual friction coefficient were varying from 0.7 to 1.2, approximately, showing the uncertainty that exists concerning the appropriate value that should be used in the analysis. For this reason, a parametric investigation was performed for three values of the friction coefficient, namely: $\mu = 0.75$, 1.00 and 1.15.

In Figs. 7 and 8, the maximum displacements and the residual deformation, respectively, in the out-of-plane direction along the height of the wall of the sub-assembly models of Fig. 2, without connections, are ploted. The displacements shown are relative to the base, thus any base dislocation has been subtracted. Concerning the maximum displacements during the ground shaking, it seems that, practically, friction does not influence the response. For the permanent displacements, the effect of friction is not monotonic and changes with the earthquake characteristics: for the Kalamata earthquake, an increase in the friction coefficient generally decreases the residual displacement at the top of the structure but it increases the deformation at lower positions while for the Lefkada earthquake the opposite behaviour is observed.

Similar results were obtained for the full-structure model of Fig. 3. The top maximum and the residual displacements in this case are given in Tables 4 and 5, respectively.

It should be noted that, according to the results presented in [15], the value of $\mu = 0.75$ is approximately the average residual friction for a wide range of expected velocities. Also, comparison of numerical results with experimental data for the seismic response of marble multi-drum model columns, presented in [2] and [6], showed that good agreement could be obtained if a friction coefficient around 0.75

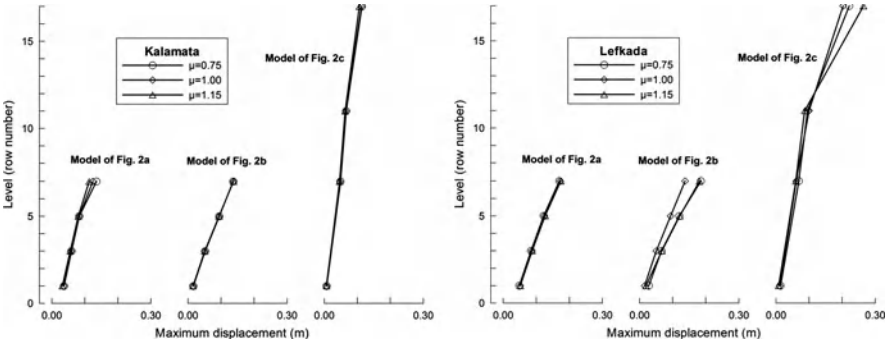


Fig. 7 Effect of friction coefficient to the maximum displacements in the out-of-plane direction

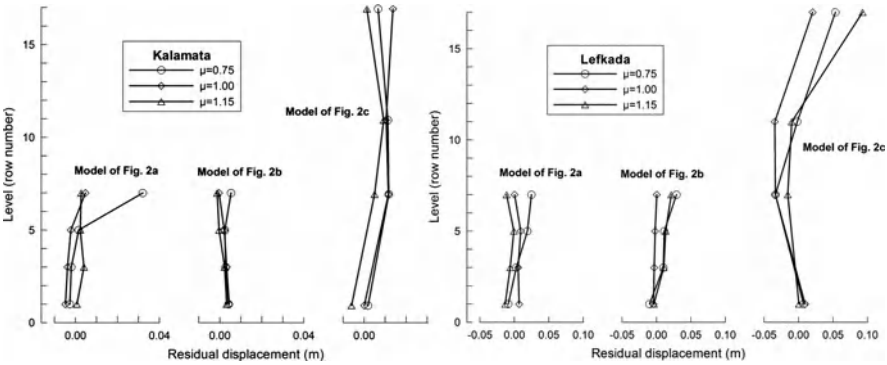


Fig. 8 Effect of friction coefficient to the residual deformation in the out-of-plane direction

Table 4 Top maximum displacements (m) in the out-of-plane direction at positions A and C of the full-structure model (Fig. 3)

	Position A		Position C	
Earthquake	$\mu = 0.75$	$\mu = 1.00$	$\mu = 0.75$	$\mu = 1.00$
Kalamata	0.026	0.028	0.095	0.102
Aigio	0.056	0.057	0.092	0.092
Lefkada	0.076	0.062	0.116	0.125

Table 5 Top residual displacements (m) in the out-of-plane direction at positions A and C of the full-structure model (Fig. 3)

	Position A		Position C	
Earthquake	$\mu = 0.75$	$\mu = 1.00$	$\mu = 0.75$	$\mu = 1.00$
Kalamata	0.007	0.008	0.014	0.013
Aigio	0.013	0.018	0.068	0.043
Lefkada	0.028	0.024	0.050	0.062

was considered. Based on these observations and the relatively small dependence of the response on the friction coefficient, results for only $\mu = 0.75$ are presented in the following.

6.3 Comparison of the Sub-Assembly Models with the Full-Structure Model

The results obtained with the simplified sub-assembly models of Fig. 2 were compared to the corresponding results for positions A and C (Fig. 3) of the full-structure model. The simplified model gave, in all cases, larger maximum top displacements. This was expected, since the section of the wall considered in the sub-assembly models behaves as a free-standing cantilever, being, thus, more flexible than the corresponding part of the whole structure, where the contribution of the transverse walls increases the stiffness and rather prevents rocking.

In Fig. 9, the time-history of the top displacement of model (c) of Fig. 2 and the corresponding one at position C of the model of Fig. 3 are presented for the Lefkada earthquake. The long-period vibrations of the simplified model, which are evident after the strong part of the ground shaking, imply that the motion is governed by rocking. In the contrary, the response of the full-structure model shows high frequency characteristics; in this case, sliding seems to be the prevailing deformation mode.

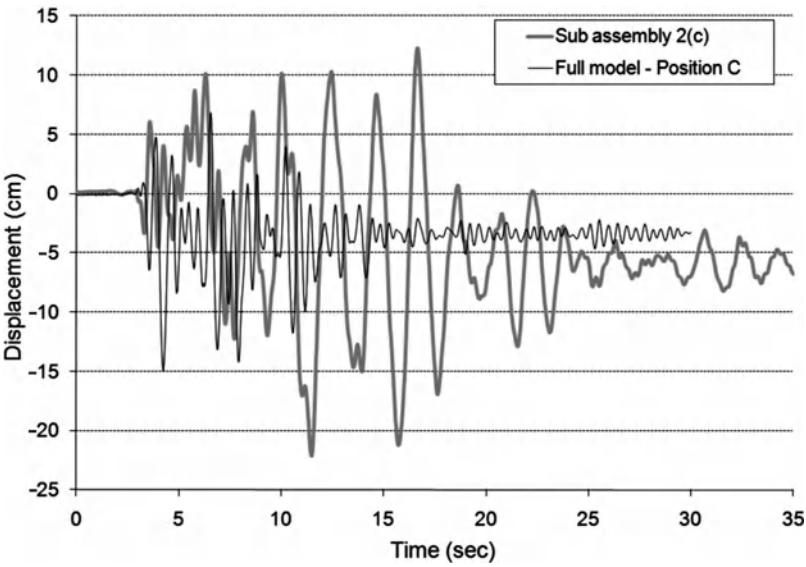


Fig. 9 Time history of the top displacement in the out-of-plane direction of model (**c**) of Fig. 2 and at position C of the full-structure model (Fig. 3) for the Lefkada earthquake

For the sub-assembly model, the predominant role of rocking was also verified from the fact that the out-of-plane displacements of the stones were increasing monotonically with the height and the maximum displacements occurred simultaneously for all blocks. In the contrary, the residual displacements, which are caused mainly by the sliding of the stones, did not show a monotonic pattern with height and displacements of opposite signs were recorded.

It should be noted that, in most cases, the residual displacements of the full-structure model were larger than the corresponding ones of the simplified sub-assembly models. This is in accordance with the above drawn conclusion that the full-structure model responds more in sliding and less in rocking.

6.4 Effect of Connections

Tables 6 and 7 summarize the results of the full-structure model with and without connections. It is interesting to note that, in many cases, the maximum top displacement in the out-of-plane direction was larger if the blocks were connected with clamps and dowels than if not. This should be attributed to the fact that connections force the walls to respond more in rocking and less in sliding, increasing thus the displacements. The rocking that occurs at position C when the blocks are connected is evident in Fig. 10 from the large vibrations that are observed after the end of the strong ground shaking. This phenomenon was pronounced more at the full-height part of the wall (position C) and less at parts of small height (e.g. position A).

Concerning the residual displacements, connections reduce them significantly resulting, in some cases, in values less than one half of the corresponding ones without connections.

Table 6 Top maximum displacements (m) in the out-of-plane direction at positions A and C of the full-structure model (Fig. 3)

	Position A		Position C	
Earthquake	With connections	Without connections	With connections	Without connections
Kalamata	0.040	0.026	0.064	0.095
Aigio	0.052	0.056	0.151	0.092
Lefkada	0.063	0.076	0.149	0.116

Table 7 Top residual displacements (m) in the out-of-plane direction at positions A and C of the full-structure model (Fig. 3)

	Position A		Position C	
Earthquake	With connections	Without connections	With connections	Without connections
Kalamata	0.008	0.007	0.006	0.014
Aigio	0.005	0.013	0.025	0.068
Lefkada	0.011	0.028	0.033	0.050

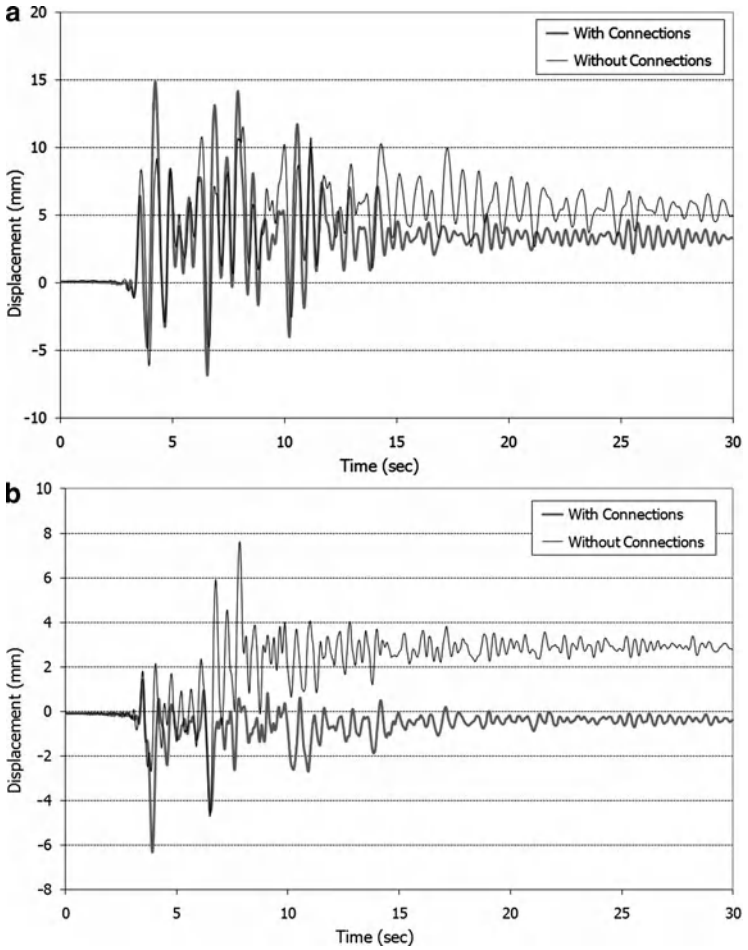


Fig. 10 Time histories of the top displacement in the out-of-plane direction at positions C (**a**) and A (**b**) of the full-structure model, with and without connections, for the Lefkada earthquake

6.5 Effect of Imperfections

Imperfections were considered only in the simplified sub-assembly model (b) of Fig. 2. They consisted of missing stones, blocks of reduced width and corner cut-offs. The results showed that, compared to the corresponding structure without imperfections (Fig. 2a), the maximum displacements in the out-of-plane direction during the seismic motion are, in general, larger, while the residual ones are smaller, as shown in Table 8. This behaviour is attributed to the fact that model (b) responds more in rocking and less in sliding in the normal to the wall direction, compared to model (a). This is also evident from the time-histories of the top response for the Lefkada earthquake presented in Fig. 11.

Table 8 Top displacements in the out-of-plane direction of the model of Fig. 2a without imperfections and the one of Fig. 2b with imperfections

	Residual displacement (cm)			Maximum displacement (cm)		
Model	Kalamata	Aigio	Lefkada	Kalamata	Aigio	Lefkada
Without imperfections [model (a)]	3.2	5.7	2.5	13.3	12.6	16.8
With imperfections [model (b)]	0.5	3.2	2.9	13.4	16.1	18.3

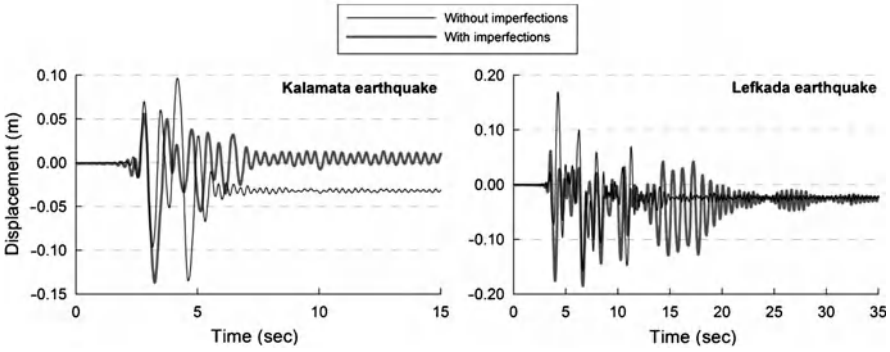


Fig. 11 Time histories of the top displacement in the out-of-plane direction of the model of Fig. 2a without imperfections and of Fig. 2b with imperfections for the Kalamata and the Lefkada earthquakes

It should be noted that commonly encountered imperfections at walls are not as detrimental to the safety against collapse as they are when exist at columns [3], because their effect is less pronounced, as damage is usually diffused on the wall's surface.

The reduced height of some sections of the walls, caused by partial collapse, can also be considered as an imperfection. Thus, the effect of restoring the wall to its full height was examined. As can be seen from Figs. 7 and 8, this intervention reduces the maximum displacements and the relative slip between adjacent rows of stones. However, the residual displacements are not affected significantly and, in some cases, might be even larger at the restored wall than at the partially collapsed one.

In Fig. 12, the time histories of the displacement in the out-of-plane direction at the level of row 7 of the models (a) and (c) of Fig. 2 are presented for the Kalamata and the Lefkada earthquakes. Row 7 corresponds to the top of model (a) and to almost the mid-height of model (c). It is evident that the displacements are smaller at the full-height model (c), but rocking is also much more pronounced.

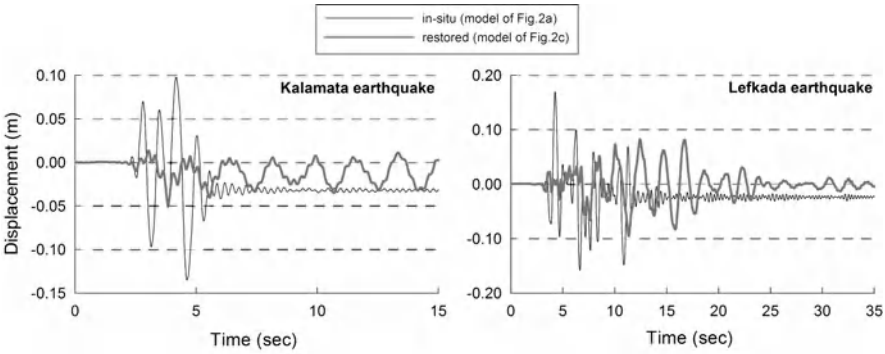


Fig. 12 Time histories of the displacement at level of row 7 in the out-of-plane direction of the model of Fig. 2a (in-situ) and of Fig. 2c (restored) for the Kalamata and the Lefkada earthquakes

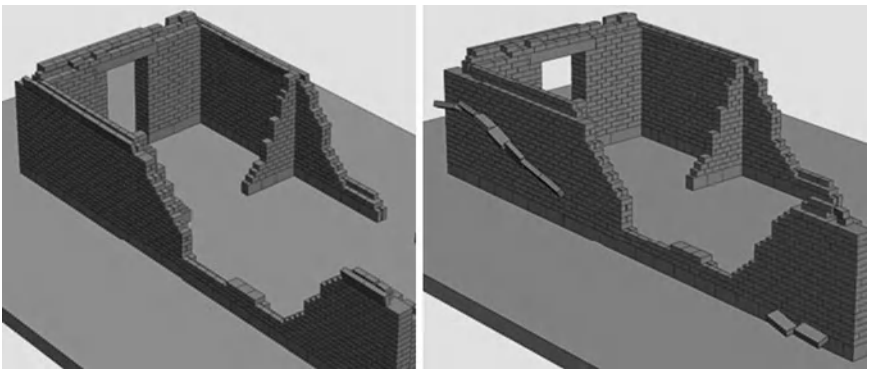


Fig. 13 Snapshots of the collapse of the architraves of S wall for the Aigio earthquake

6.6 Collapse Mechanism

For strong ground shaking, collapse of some stones might happen. For the seismic motions considered in this analysis, collapse occurred only at the full-structure model and for the Aigio earthquake and concerned the outermost upper row of stones (architraves), which are larger in size than the other stones of the walls. Two snapshots of the collapse of the architraves of the S wall are shown in Fig. 13. Note that, for the Aigio record, collapse occurred in both cases, with and without connections.

Similar results were obtained from additional runs with other models of restoration scenarios and other seismic excitations not presented in this analysis. In all cases, collapse initiated from the architraves of the walls, which seem to be the most vulnerable part of the structure.

6.7 *Effect of the Seismic Motion Characteristics*

With the exception of the Athens record, that caused small displacements to the structure, the rest three seismic motions considered in the analyses produced significant deformations, not only during the ground shaking but also residual ones after the end of it.

In general, the displacements were larger for the Lefkada earthquake, which can be attributed to the long duration of this record. In many cases, Lefkada resulted to more than double the displacements caused by the other earthquakes.

Among Aigio and Kalamata records, the Aigio earthquake produced, in general, larger displacements. It should be noted that Aigio contains a strong motion part of smaller duration compared to Kalamata, but with larger peak acceleration. Also, the Aigio record contains a clear, almost sinusoidal pulse with a period of 0.5 s, which seemingly played an important role to the response. It is reminded that, for the full-structure model, collapse of the architrave stones occurred only for the Aigio earthquake.

These results show that the ground motion characteristics influence significantly the response. For classical multi-drum columns, it is known that long-period ground motions are much more destructive than high-frequency ones [1]. However, the response of columns is dominated by the rocking, while for walls, rocking and sliding might be equally important. Thus, conclusions concerning columns cannot be directly applied to walls. Further research is needed on this subject.

The effect of repeated earthquake excitations was also examined for the restored sub-assembly model of Fig. 2c. To this aim, three consecutive ground motions (Kalamata record) were applied to the structure with the residual displacements caused by the previous earthquake being considered as initial conditions for the next one. The results obtained are shown in Fig. 14 and show that the residual deformation increases exponentially with the number of repetition of the ground motion. However, this conclusion cannot be generalized, since, due to the nonlinearity of

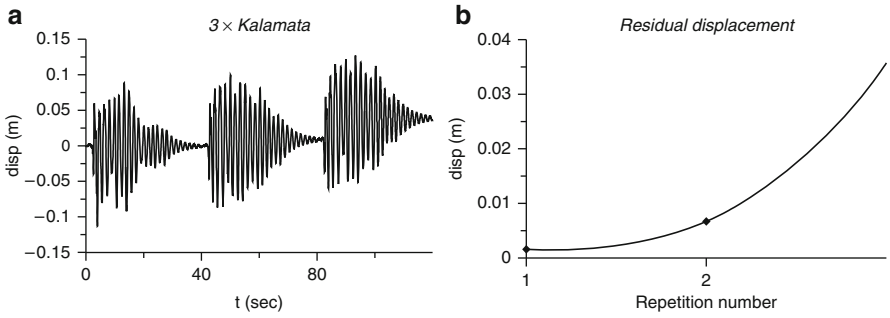


Fig. 14 Top displacement in the out-of-plane direction of model of Fig. 2c for three consecutive applications of the Kalamata earthquake: (**a**) time history of the response; (**b**) increase of the residual displacement with the number of repetitions of the ground motion

the response, the opposite phenomenon may occur in some cases, i.e. a seismic excitation might reduce the deformation caused by a previous ground motion. This behaviour was observed for classical columns [16].

7 Conclusions

- Maximum displacements in the in-plane direction of the walls are much smaller than in the out-of-plane direction. However, residual displacements are of similar magnitude.
- The friction coefficient does not influence, practically, the maximum displacements. Its effect to the residual displacements depends on the characteristics of the ground motion.
- The sub-assembly models overestimate the maximum displacements, compared to the full-structure model, because the stiffness offered by the transverse walls is neglected and the structure responds with pronounced rocking. For the full-structure model, sliding seems to be more intense and, for this reason, the residual deformation is, in general, larger compared to the simplified sub-structure models.
- The metallic connections between the stones decrease significantly the residual deformation. However, the maximum displacements might be larger in some cases, because connections result in more intense rocking response, especially at the full-height parts of the walls.
- Imperfections at the blocks due to existing damage result in more intense rocking and less sliding. Thus, the maximum displacements increase, while the residual ones generally decrease.
- Restoration of a partially collapsed part of the wall to its full height reduces the maximum displacements, while the residual displacements are not affected significantly.
- For strong seismic motions, collapse of some parts of the walls might occur. Collapse starts from the architrave stones.
- The characteristics of the base excitation influence significantly the response, but further research is needed on this subject.
- The repetition of the seismic motion might increase significantly the residual deformation produced by previous earthquakes.

Acknowledgments Part of the research presented in this paper was funded by the Committee for the Preservation of the Acropolis Monuments (YSMA), which also provided the restoration scenario that was used for the full-structure model of Fig. 3. Special thanks are due to A. Vrouva, civil engineer with YSMA and N. Toganidis, architect with YSMA, for their help with the construction details of the monument.

References

1. Psycharis IN, Papastamatiou DY, Alexandris AP (2000) Parametric investigation of the stability of classical columns under harmonic and earthquake excitations. Earthq Eng Struct Dynam 29:1093–1109
2. Papantonopoulos C, Psycharis IN, Papastamatiou DY, Lemos JV, Mouzakis H (2002) Numerical prediction of the earthquake response of classical columns using the distinct element method. Earthq Eng Struct Dynam 31:1699–1717
3. Psycharis IN, Lemos JV, Papastamatiou DY, Zambas C, Papantonopoulos C (2003) Numerical study of the seismic behaviour of a part of the Parthenon Pronaos. Earthq Eng Struct Dynam 32:2063–2084
4. Konstantinidis D, Makris N (2005) Seismic response analysis of multidrum classical columns. Earthq Eng Struct Dynam 34:1243–270
5. Psycharis IN (2006) Seismic response of classical monuments with fractured structural elements. 16th European conference of fracture (ECF16) – Symposium on Fracture and failure of natural building stones – application in the restoration of ancient monuments. Alexandroupolis, Greece, 3–7 July 2006
6. Dasiou ME, Psycharis IN, Vayas I (2009)Verification of numerical models used for the analysis of ancient temples. Prohitech conference. Rome, Italy, 21–24 June 2009
7. Dasiou ME, Psycharis IN, Vayas I (2009) Numerical investigation of the seismic response of Parthenon, Greece. Prohitech conference. Rome, Italy, 21–24 June 2009
8. Manos GC, Demosthenous M (1992) Dynamic response of rigid bodies subjected to horizontal base motion. In: Tenth World conference on Earthquake engineering. Madrid, Spain, pp 2817–2821
9. Mouzakis H, Psycharis IN, Papastamatiou DY, Carydis PG, Papantonopoulos C, Zambas C (2002) Experimental investigation of the earthquake response of a model of a marble classical column. Earthq Eng Struct Dynam 31, 1681–1698
10. Dasiou ME, Mouzakis HP, Psycharis IN, Papantonopoulos C, Vayas I (2009) Experimental investigation of the seismic response of parts of ancient temples. Prohitech conference. Rome, Italy, 21–24 June 2009
11. 3DEC: 3-Dimensional Distinct Element Code (1998) Theory and background. Itasca Consulting Group, Inc., Minneapolis, MN
12. Cundall PA (1988) Formulation of a three-dimensional distinct element model - Part I: a scheme to detect and represent contacts in a system composed of many polyhedral blocks. Int J Rock Mech Min Sci 25:107–116
13. Orlandos A (1977) The architecture of parthenon, vol A and B (in Greek)
14. Zambas C (1994) Structural problems of the restoration of the Parthenon. Study for the Restoration of the Parthenon 3B:153–180 (in Greek)
15. Papadopoulos CT, Basanou ME, Vardoulakis IP, Boulon M, Armand G (1998) Mechanical behavior of Dionysos marble smooth joints under cyclic loading: II Constitutive modeling. 3rd International conference on Mechanics of jointed and faulted rock: MJFR-3, Vienna, Austria, 6–9 April
16. Psycharis IN (2007) A probe into the seismic history of Athens, Greece from the current state of a classical monument. Earthq Spect 23(2):393–415

Estimation of Seismic Response Parameters Through Extended Incremental Dynamic Analysis

Matjaz Dolsek

Abstract Explicit determination of seismic risk is a complex problem, and the subject of many uncertainties, but it also brings new information which could help to reduce losses caused by future earthquakes. Although estimation of seismic hazard and the selection of ground motion records probably represent the main sources of uncertainty, it is also important to consider modelling and physical uncertainties, which can significantly affect the seismic response. Recently Incremental Dynamic Analysis (IDA) has been extended by introducing a set of structural models, in addition to the set of ground motion records which is employed in IDA analysis in order to capture record-to-record variability. The set of structural models reflects epistemic (modelling) uncertainties, and is determined by utilizing the Latin Hypercube Sampling (LHS) method. The effects of both aleatory and epistemic uncertainty on seismic response parameters are therefore considered in the extended IDA analysis, which was performed for a reinforced concrete frame. The results showed that the modelling uncertainties can reduce spectral acceleration capacity and significantly increase dispersion.

Keywords Performance-based earthquake engineering · Extended incremental dynamic analysis · Uncertainty · Epistemic · Aleatory · Latin hypercube sampling

1 Introduction

The modelling of seismic response of structures is a subject of many modelling and physical uncertainties. These uncertainties can affect the seismic response of structure to the same extend than the aleatory uncertainties (e.g. record-to-record variability). In general, the predicted seismic risk is underestimated, if the epistemic uncertainties are not considered in the process of seismic risk estimation. Therefore, it is equally important that the epistemic uncertainties are also included in the seismic risk assessment procedure.

M. Dolsek (✉)
University of Ljubljana, Faculty of Civil and Geodetic Engineering, Jamova 2, SI 1000 Ljubljana
e-mail: mdolsek@ikpir.fgg.uni-lj.si

M. Papadrakakis et al. (eds.), *Computational Methods in Earthquake Engineering*,
Computational Methods in Applied Sciences 21, DOI 10.1007/978-94-007-0053-6_13,
© Springer Science+Business Media B.V. 2011

Different methods are available for studying the influence of epistemic uncertainties on the seismic response parameters. For example, a study of the sensitivity of the seismic response parameter to a single input variable is the simplest approach for estimating the importance of the epistemic uncertainty [1]. The results of sensitivity analysis can be used for first-order second-moment (FOSM) reliability analysis, in order to estimate the effects of several modelling uncertainties on the structural response parameters. FOSM reliability analysis was used by Haselton [2] in his study of the effects of modelling uncertainties on the collapse capacity of reinforced concrete frames designed for a highly seismic region in California, and also for example, by Lee and Mosalam [3]. The later authors studied the sensitivity of seismic demand to possible future earthquakes for a reinforced concrete shear-wall building, using FOSM method in combination with Monte Carlo simulation. On the other hand, Baker [4] used FOSM method in combination with numerical integration for the propagation of uncertainties in probabilistic seismic loss estimation. Unfortunately, the FOSM method may become inaccurate for highly nonlinear problems [5]. The alternative in such cases is Monte Carlo simulation, which is computationally extremely demanding, but has the advantage of being able to incorporate modelling uncertainty directly into the problem. Recently, incremental dynamic analysis [6] has been extended by introducing a set of structural models [7, 8]. The set of structural models are determined by utilizing the Latin Hypercube Sampling (LHS) method [9, 10]. A similar approach, among other approaches, was used to estimate the seismic response parameters of a nine-storey steel frame by assuming non-deterministic beam-hinge properties [11].

In this work extended IDA (EIDA) [8] is summarized and has been applied to an eight-storey reinforced concrete non-ductile frame. The results of such an analysis are the EIDA curves, which are determined for a set of models, and not only for a best-estimate model as in the case of IDA analysis. The summarized EIDA curves incorporate the effects of both aleatory and epistemic uncertainty.

2 Summary of Extended IDA

Recently incremental dynamic analysis (IDA) [6] has been extended by introducing a set of structural models, in addition to the set of ground motion records which is employed in IDA analysis in order to capture record-to-record variability. The set of structural models reflects epistemic (modelling) uncertainties, and is determined by utilizing the Latin Hypercube Sampling (LHS) method. Herein the extended IDA analysis is summarized. More details can be found in [8].

The main steps of the extended IDA analysis are presented in Fig. 1. Extension of the IDA analysis is straightforward since the only new step in the extended IDA analysis in comparison to the IDA analysis introduced by Vamvatsikos and Cornell [6] is the determination of the set of structural models. For this reason only this step will be described here. However, once the set of structural models is determined, the single-record IDA curves can be calculated for each ground motion record and for

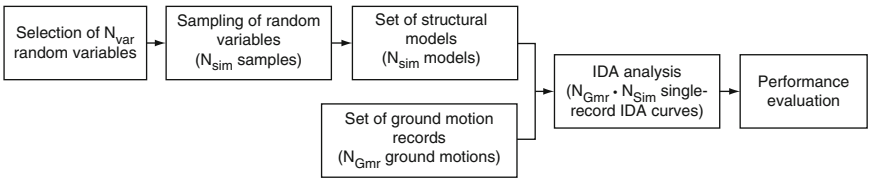


Fig. 1 The main steps of the extended IDA analysis

each structural model defined, respectively, by the set of ground motion records and the set of structural models. Note that exactly the same algorithms as suggested by Vamvatsikos and Cornell [6] can be used to determine the single-record IDA curves. The extended IDA analysis is therefore more time-consuming since the IDA curves are calculated not only for the different ground motion records, but also for a predefined set of structural models. However, it is still less computationally demanding than a corresponding Monte Carlo simulation.

The first step in the process of the determination of the set of structural models is the identification of the sources of epistemic uncertainty. Basically, it is possible to include all types of epistemic uncertainties, which can be described by means of random variables. However, it is practical to consider only a limited number N_{Var} of the random variables X_i, i.e., only those which have a significant influence on the seismic response of the structure, in order to reduce the size of the set of structural models, usually referred to by the number of simulations N_{Sim}. First, each random variable X_i is sampled using N_{Sim} values. The most common strategy used in order to determine the samples of random variables is:

$$x_{j,i} = F_i^{-1}\left(p_{j,i}\right) = F_i^{-1}\left(\frac{j-0.5}{N_{Sim}}\right), \quad i = 1,\ldots,N_{Var}, \quad j = 1,\ldots,N_{Sim} \tag{1}$$

where $x_{j,i}$ is the j-th sample value of the i-th random variable X_i, $p_{i,j}$ is the probability that the random variable X_i is less or equal to $x_{j,i}$ and $F_i^{-1}\left(p_{j,i}\right)$ is the inverse of the cumulative distribution function of the random variable X_i evaluated at probability $p_{j,i}$.

During the sampling of each random variable X_i, an undesired correlation between the different random variables is usually introduced. This problem can be successfully solved by the stochastic optimization method called Simulated Annealing [9, 10], which was also employed in the extended IDA analysis. For this purpose the norm E, which is a measure for difference between the generated and the prescribed correlation matrix, is defined:

$$E = \frac{2}{N_{Var}\left(N_{Var}-1\right)}\sqrt{\sum_{i=1}^{N_{Var}-1}\sum_{j=i+1}^{N_{Var}}\left(S_{i,j}-K_{i,j}\right)^2} \tag{2}$$

where $S_{i,j}$ and $K_{i,j}$ are, respectively, generated and prescribed correlation coefficients between the random variables X_i and X_j, and N_{Var} is the number of random

variables. The norm E takes into account the deviations between all the correlation coefficients and is normalized with respect to the total number of all correlation coefficients. It therefore represents a good measure when examples with a different number of random variables are compared. The norm E is then minimized by stochastic optimization method Simulated Annealing. Result of the optimization is the optimized sample matrix $\mathbf{X}$ with N_{Sim} rows and N_{Var} columns, for which the correlation matrix is close to the target correlation matrix. More details can be found in Vorechovsky and Novak [9, 10].

The set of structural models is then simply determined by employing the optimized sample matrix $\mathbf{X}$. For example, the j-th structural model from the set of structural models is determined based on the sample values defined in the j-th row of the optimized sample matrix $\mathbf{X}$. Since the number of rows of the sample matrix $\mathbf{X}$ is equal to N_{Sim}, the same number of structural models, which form a set of structural models, has to be generated.

Since the determination of the set of structural models is based on the LHS method, the simple approach to determine the sensitivity of the EDP to the input random variables, which has been used and explained more in greater detail elsewhere [9, 12], is based on the Spearman rank-order correlation coefficient ρ, which for the i-th input random variable, is defined as:

$$\rho_i = 1 - \frac{6 \sum_{j=1}^{N_{Sim}} \left(r\left(x_{j,i}\right) - r\left(EDP_j\right) \right)^2}{N_{Sim}\left(N_{Sim}^2 - 1\right)} \tag{3}$$

where $x_{j,i}$ is the value of the random variable X_i for the j-th simulation, taken from the optimized sample matrix $\mathbf{X}$, EDP_j is the engineering demand parameter for the j-th simulation, e.g. maximum storey drift, top displacement, an intensity measure corresponding to a given limit state, or other, N_{Sim} is the number of structural models used in the extended IDA analysis, and r denotes the rank of the j-th sample value of the input random variable or response variable (EDP). The parameter ρ may assume values between 1 and -1. If ρ has value close to 1 it means that the response variable EDP has a strong positive dependence on the selected input random variable, or vice versa, if ρ is close to -1. On the other hand, the input random variable does not have an influence on the response variable when ρ has a value close to 0.

3 Example: An Eight-Storey RC Frame

3.1 Description of Structure and Structural Model

An eight-storey reinforced concrete frame, which had been designed for gravity loads only, is used for demonstration of the extended IDA. The elevation and the typical reinforcement in columns and beams are presented in Fig. 2. Columns in the

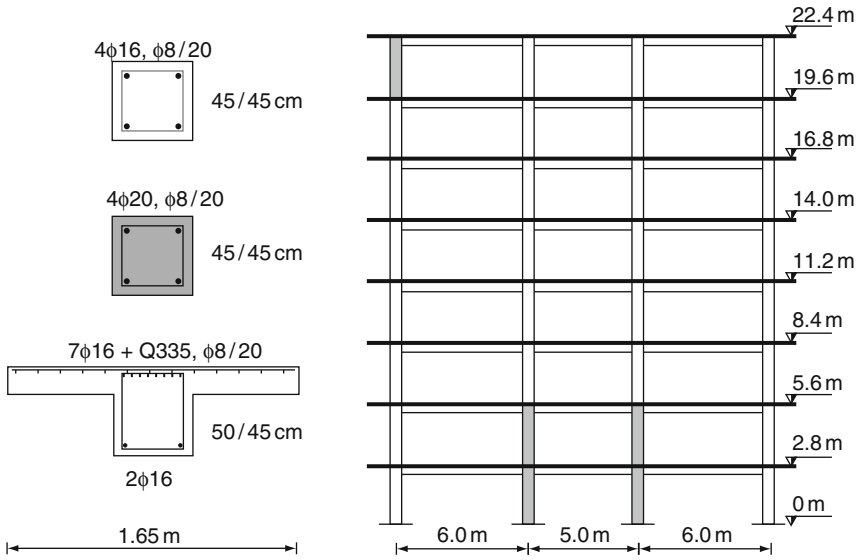


Fig. 2 The view and the reinforcement of the eight-storey RC frame. Note that the grey cross-section corresponds to the columns which are also shown in grey, while other two sections represent reinforcement in beams and remaining columns

middle of frame in the bottom two stories and exterior columns at the top (Fig. 2) are reinforced with four ϕ20 mm bars, while in all other columns the longitudinal reinforcement consists of four ϕ16 mm. All the beams are 0.45 m wide and 0.50 m deep. The bottom longitudinal reinforcement in the beams consists of two ϕ16 mm bars. Seven ϕ16 mm bars are used for the top longitudinal reinforcement of beams. The slabs are 0.15 m thick, and reinforced with steel mesh reinforcement Q335 (ϕ8 mm/15 cm).

In the design mean strength of the concrete amounted to 25 MPa, and the mean yield strength of the steel amounted to 400 MPa. The ratio between maximum base shear and weight of structure amounts to about 5%.

The beams and columns of the structure were modelled with one-component lumped plasticity elements. The schematic moment-rotation envelopes of the inelastic rotational hinges are shown in Fig. 3. The yield and the maximum moment in the columns were calculated taking into account the axial forces due to the vertical loading on the frame. The effective beam width of 165 cm was assumed for the short and long beams.

The characteristic rotations, which describe the moment-rotation envelope of a plastic hinge, were determined according to the procedure described by Fajfar et al. [13]. The zero moment point was assumed to be at the mid-span of the columns and beams. The ultimate rotation Θ_u in the columns at the near collapse (NC) limit state, which corresponds to a 20% reduction in the maximum moment, was estimated by

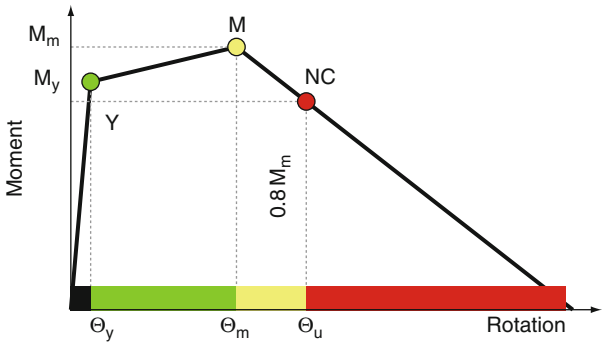


Fig. 3 Schematic moment-rotation relationship of a plastic hinge (Y-yield, M-maximum, NC-near collapse)

means of the Conditional Average Estimate (CAE) method [14]. For the beams, the EC8-3 [15] formulas were used, the parameter γ_{el} being assumed to be equal to 1.0. Due to the absence of seismic detailing, the ultimate rotations were multiplied by a factor of 0.85 [15]. All analyses were performed with OpenSees [16] in combination with OS Modeler [17].

3.2 Sets of Ground Motion Records

Extended incremental dynamic analysis was performed for two sets of ground motion records. The ten ground motions of the first set (Table 1) were selected from the European Strong Motion Database [18]. All the records of the first set were recorded on stiff soil, and the peak ground accelerations exceeded 0.1 g. The second set of twenty records (Table 2) was adopted from previous study [19]. The acceleration spectra for each ground motion record and the mean spectrum are presented in Fig. 4. The mean acceleration spectrum is compared to the EC8 spectrum for a soil class B ($T_B = 0.15$ s, $T_C = 0.5$ s) and assumed soil factor $S = 1$. It can be observed that the EC8 spectrum and the mean spectra of the two sets of ground motions are similar for periods higher than the first period ($T_1 = 1.65$ s) of the eight-storey frame. However, the mean spectra of the sets of records exceed the EC8 spectrum for interval of periods, which are lower than the first period of structure. For that reason the two sets of ground motion records may not have been sufficient for the site-specific seismic hazard, which, however, was not the primary goal of this study. Also, the two sets of ground motion records are not comparable since they consist of different types of ground motion records. Therefore it is not expected that both sets of ground motions will produce similar seismic response of the eight-storey structure.

Table 1 The first set of ten ground motion records selected from EESD [17]

Earthquake	ID	Ground motion records	a_g (g)
Montenegro 1979	196x	Petrovac NS	0.45
	196y	Petrovac EW	0.31
	197x	Ulcinj-Olimpic NS	0.29
	197y	Ulcinj-Olimpic EW	0.24
	199x	Bar NS	0.38
	199y	Bar EW	0.36
Campano Lucano 1980	291y	Calitri NS	0.16
	291x	Calitri EW	0.18
Kalamata 1986	413x	Kalamata-Pre. N265	0.21
	414x	Kalamata-OTE N80E	0.24

Table 2 The second set of twenty ground motion records also used by Fajfar et al. [19]. Note that two components of ground motions were used from each record

Region	Ground motion records	a_g (g)
California	El Centro 1934 S00W (S90W)	0.16 (0.18)
	El Centro 1940 S00E (S90W)	0.35 (0.21)
	Olympia 1949 N04W (N86W)	0.17 (0.28)
	Taft 1952 N21E (S69E)	0.16 (0.18)
	Castaic 1971 N21E (N69E)	0.32 (0.27)
Montenegro 1979	Bar NS (EW)	0.36 (0.36)
	Petrovac NS (EW)	0.44 (0.30)
	Ulcinj-Olimpic NS (EW)	0.24 (0.28)
	Ulcinj-Albatros NS (EW)	0.22 (0.17)
	Hercegnovi NS (EW)	0.23 (0.21)

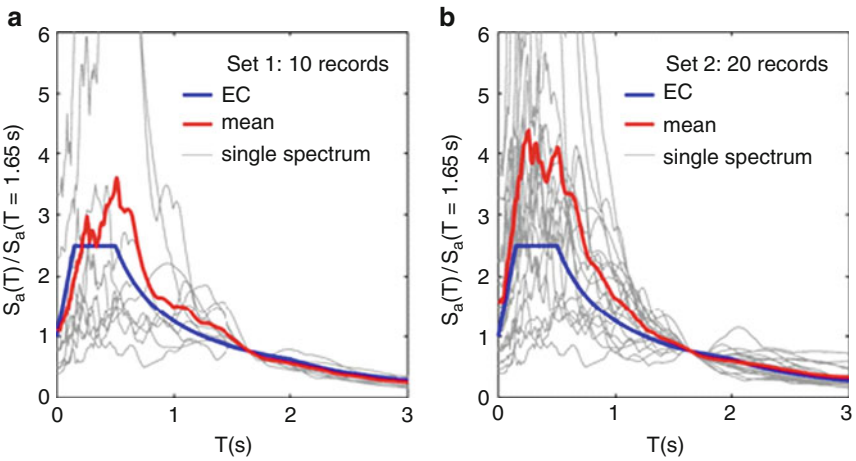


Fig. 4 The elastic response spectra and mean spectrum compared to EC8 spectrum for (**a**) first and (**b**) second set of ground motion records

3.3 Incremental Dynamic Analysis

A hunt and fill tracing algorithm was used to calculate the IDA curves for both sets of ground motions. The intensity measure, which corresponds to dynamic instability ("collapse" of structure), was determined with a tolerance of 0.01 g.

Four limit states were defined to quantify seismic response parameters at different damage levels. The first three limit states, i.e., limit state of damage limitation (DL), of significant damage (SD) and of near collapse (NC), were defined similarly as in the European standard EC8-3 [15]. At the element level, the three limit states can be defined by the rotations in the moment–rotation relationship of the plastic hinge. However, simplifications were made in order to define the limit state at structural level. Therefore it was assumed that DL limit state appears when reinforcement in all columns at the bottom starts to yield. It was further assumed that SD and NC limit state are controlled with the first column if the moment exceeds the maximum moment or rotation exceeds the ultimate rotation, respectively (see Fig. 3). It was also defined that the most severe limits state, collapse limit state (C), appear at global dynamic instability of structure.

The single-record IDA curves together with summarized (16%, 50% and 84% fractile) IDA curves are presented in Fig. 5. Spectral acceleration at period 1.65 s and the maximum drift was selected for intensity measure and engineering demand parameter, respectively. Note that T = 1.65 s corresponds to the most important (first) mode shape of the structure. In addition to the IDA curves also points on the single-record IDA curve, which correspond to damage limitation (DL), significant damage (SD), near collapse (NC) and collapse (C) are also presented. The median spectral acceleration, which causes different limit states ($S_{a,LS}$), was calculated based on

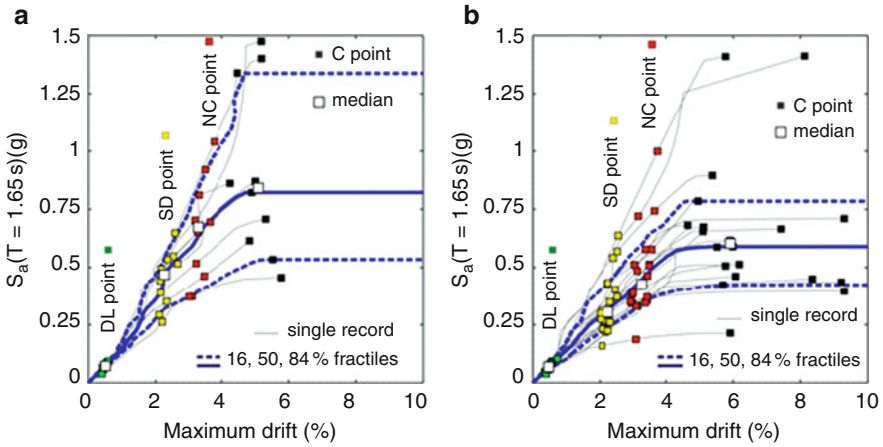


Fig. 5 The single-record IDA curve, summarized IDA curves, both presented in term of spectral acceleration at T = 1.65 s versus maximum drift, and points indicating DL, SD, NC and C limit states as well as the corresponding median values for (**a**) first and (**b**) second set of ground motions

presented LS points on IDA curves (Fig. 5a), and is equal to 0.07, 0.47, 0.67 and 0.84 g for DL, SD, NC and C limit state, respectively. These results correspond to the first set of ground motion records, while for the second set of ground motions structural "capacity" in terms of median spectral acceleration is smaller for more severe limit states, and corresponds to 0.07, 0.30, 0.43 and 0.60 g for DL, SD, NC and C limit state, respectively.

The dispersion for randomness in $S_{a,LS}$ was defined as the standard deviation of the natural logarithm, which was calculated as the average value of the $\beta_{16} = \log(y_{50}/y_{16})$ and $\beta_{84} = \log(y_{84}/y_{50})$, where y_{16}, y_{50}, y_{84} represent the counted 16%, 50% and 84% fractile in terms of spectral acceleration for a given limit state.

Dispersion of spectral acceleration, which causes defined limit states, in general increases with the more severe limit state, but the magnitude of dispersion depends also on the ground motion sets and the definition of limit state. For example, dispersion for randomness in $S_{a,LS}$ ($\beta_{DR,LS}$), corresponding to DL, SD, NC and C limit state and the first set of ground motions, amount to 0.21, 0.30, 0.44 and 0.47, respectively. The dispersions $\beta_{DR,NC} = 0.31$ and $\beta_{DR,C} = 0.32$ of the second set of ground motion records are less than those observed for the first set of ground motions, while dispersions for other less severe limit states (DL and SD) are higher ($\beta_{DR,DL} = 0.25$, $\beta_{DR,SD} = 0.36$) for the second set of ground motions.

Note that only in-cycle deterioration was considered in the model of beam/column hinges (Fig. 3). Therefore the spectral acceleration, which causes the collapse of the structure, may be overestimated, especially, because the period of the structure is quite high. In the case if the period of structure is short usually structure collapse in one cycle if in this cycle strength of structure starts to deteriorate. This is not the case for moderate- or long-period structures. Similar can be observed for our case since the summarized IDA curves are more or less straight lines until the global dynamic instability. It means that inelastic displacement demand is practically the same as the elastic displacement demand even if strength starts to deteriorate. In the interval above the SD points (Fig. 5) strength in the plastic hinges starts to deteriorate.

3.4 Extended Incremental Dynamic Analysis

The set of structural models has to be defined before performing extended IDA analysis (EIDA). First, different sources of uncertainties were assumed in the process of defining the set of structural models but the spatial variability of uncertainties was neglected in the analysis. Actually, the same sources of uncertainty were taken into account as in [8]. Mean/median values of uncertain parameters, corresponding coefficient of variation as well as assumed distributions are presented in Table 3. The first five random variables, storey masses, material strengths, effective slab width, and damping, were assumed uncorrelated. Other random variables, which were defined in Sect. 3.1, indicate error in prediction of yield and ultimate rotation of beams and columns. For these variables the highest value of coefficient of variation (0.6) was

Table 3 The statistical characteristics of the input random variables

No	Name		Mean or median	COV	Distribution
1	Mass at top/other stories	m	121/115 t	0.1	Normal
2	Damping	ξ	2	0.4	Normal
3	Concrete strength	f_{cm}	25 MPa	0.2	Normal
4	Steel strength	f_y	400 MPa	0.05	Lognormal
5	Effective slab width	b_{eff}	165 cm	0.2	Normal
6	Initial stiffness of the columns	$\Theta_{y,c}$	1 · computed	0.36	Normal
7	Initial stiffness of the beams	$\Theta_{y,b}$	1 · computed	0.36	Normal
8	Ultimate rotation of the columns	$\Theta_{u,c}$	1 · computed	0.4	Normal
9	Ultimate rotation of the beams	$\Theta_{u,b}$	1 · computed	0.6	Normal

adopted for the prediction of the ultimate rotations in the beams. This is a rounded value of that reported by Panagiotakos and Fardis: 0.64 [20]. A smaller value was used for the coefficient of variation of the ultimate rotation in the columns (0.4). Such assumption is the consequence of more reliable model which was used to determine the ultimate rotation of the columns [14]. Quite high value for the coefficient of variation was also adopted for the initial stiffness of the beams and columns [20]. It was further assumed that the yield and ultimate rotation of the columns and that of beams are correlated with coefficient of variation equal to 0.8.

All random variables were then sampled with the procedure described in the Sect. 2. Based on the previous study [8] it was assumed that the number of simulations is 20 ($N_{Sim} = 20$). In general it is not known in advance which size of sample is appropriate for further analysis. However, the appropriate size of the sample N_{Sim}, which is equal to the size of the set of structural models, can be based on the acceptable norm E (Eq. 2) [8]. In our case ($N_{Sim} = 20$) the norm $E = 0.0011$ and the maximum and average difference between the actual and target correlation coefficient is only 0.02 and 0.005, respectively.

For example, the relationship between the sample values of selected random variables before and after optimization is presented in Fig. 6. It can be observed that the optimization of the sample matrix was sufficient since the correlation coefficients between the two samples are very close to the target correlation coefficient. The correlation coefficient between the sample values of yield strength and storey mass is −0.006, close to the target correlation, which was assumed to be 0. Similar was observed for other samples where the target correlation coefficient was assumed 0. Even if two random variables were considered correlated, the correlation coefficient between the optimized samples of two random variables is close to target value 0.8.

Optimized sample matrix represents input data for defining the set of structural models. However, it is important to be consistent when creating a structural model, since one random variable may affect more than one parameter in the structural model. For example, if mass is simulated with a random variable, it affects not only the mass but also the vertical loads, or, if the slab effective width is modeled with a

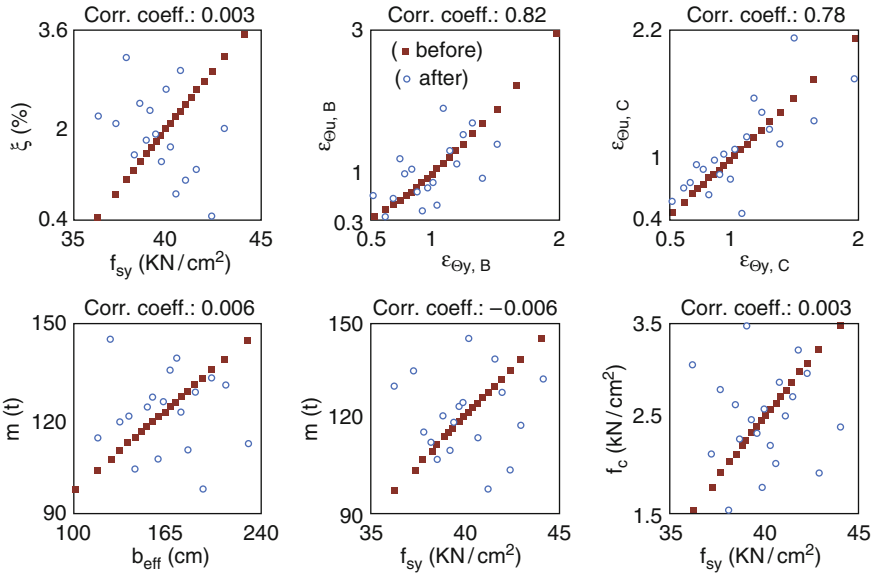


Fig. 6 Comparison between sample values of selected random variables before and after the optimization of the sample matrix **X**

random variable, it has influence on the moment of inertia of the beam and also on the moment-rotation relationship of the plastic hinge of the beam.

Two sets of 20 structural models were created. For the first set only first five variables from Table 3 were considered uncertain while the second set of structural models was defined by considering all random variables presented in Table 3. The first set of models was used only for comparison reasons in order to explore the difference in seismic response parameters if determined based on selected or all random variables from a list of random variables (Table 3). Extended IDA (EIDA) was therefore performed for three different cases:

- First set of ground motions (G1) and first set of models (M1) ($N_{Gmr} = 10$, $N_{Sim} = 20$, 200 EIDA curves)
- First set of ground motions (G1) and second set of models (M2) ($N_{Gmr} = 10$, $N_{Sim} = 20$, 200 EIDA curves)
- Second set of ground motions (G2) and second set of models (M2) ($N_{Gmr} = 20$, $N_{Sim} = 20$, 400 EIDA curves)

The results of EIDA for first set of ground motions and both sets of structural models are presented in Figs. 7 and 8. In Fig. 9 results of EIDA for the second set of ground motions and the second set of models are also presented. In each figure summarized EIDA curves are presented with highlighted different LS points for a given ground motion record and structural model. In the case of EIDA for the first set of ground motions it can be observed that the scatter of LS points is higher for a second set of structural models, since in this case all uncertainties were considered

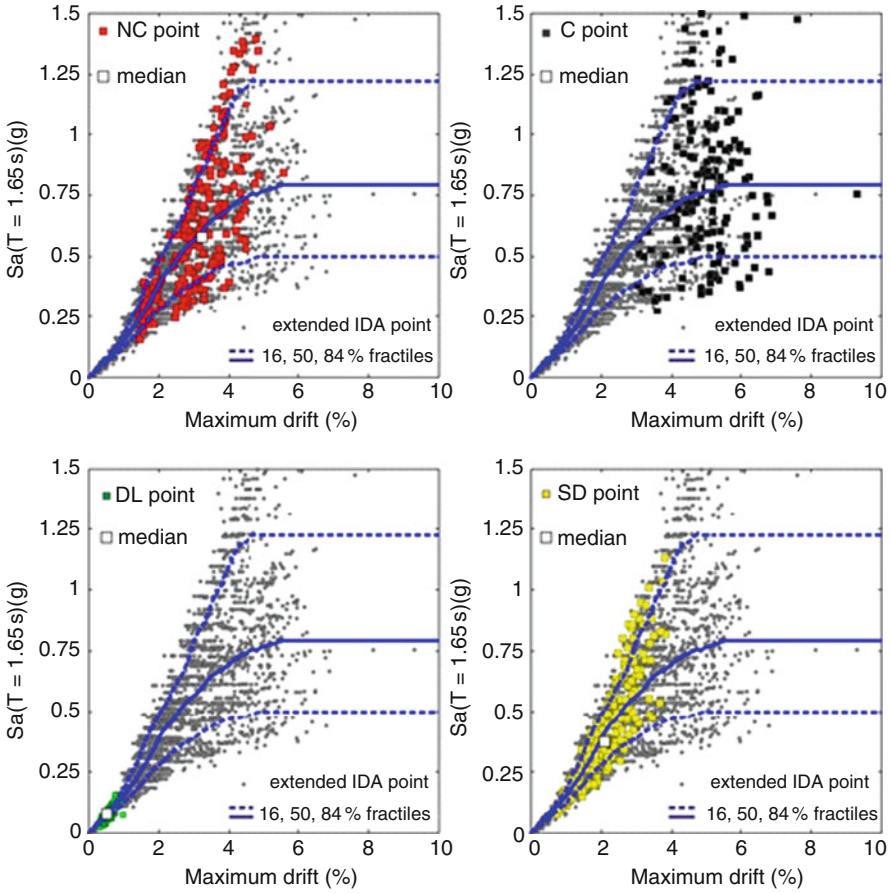


Fig. 7 The extended IDA for the first set of ground motions and structural models (selected random variables). In addition to the EIDA points and summarized EIDA curves also the LS points, which correspond to different limit states for a given ground motion record and structural models, are presented

in the analysis. However, the higher scatter is observed only in terms of maximum drifts, while in terms of spectral acceleration it remains practically unchanged if LS points based on first and second set of structural models are compared. Results in Figs. 8 and 9 presents the EIDAs for the seconds set of structural models and for both set of ground motions. Note that spectral acceleration, which corresponds to global dynamic instability, is smaller for the second set of ground motion records.

In Table 4 the median $S_{a,LS}$ is presented for different limit states, for all three EIDAs, and for comparison reasons also for both IDAs. Note that median $S_{a,LS}$ is calculated from LS points (Figs. 7–9). Substantial decrease can be observed for $S_{a,LS}$ corresponding to SD, NC and C limit state, if results of EIDA are compared

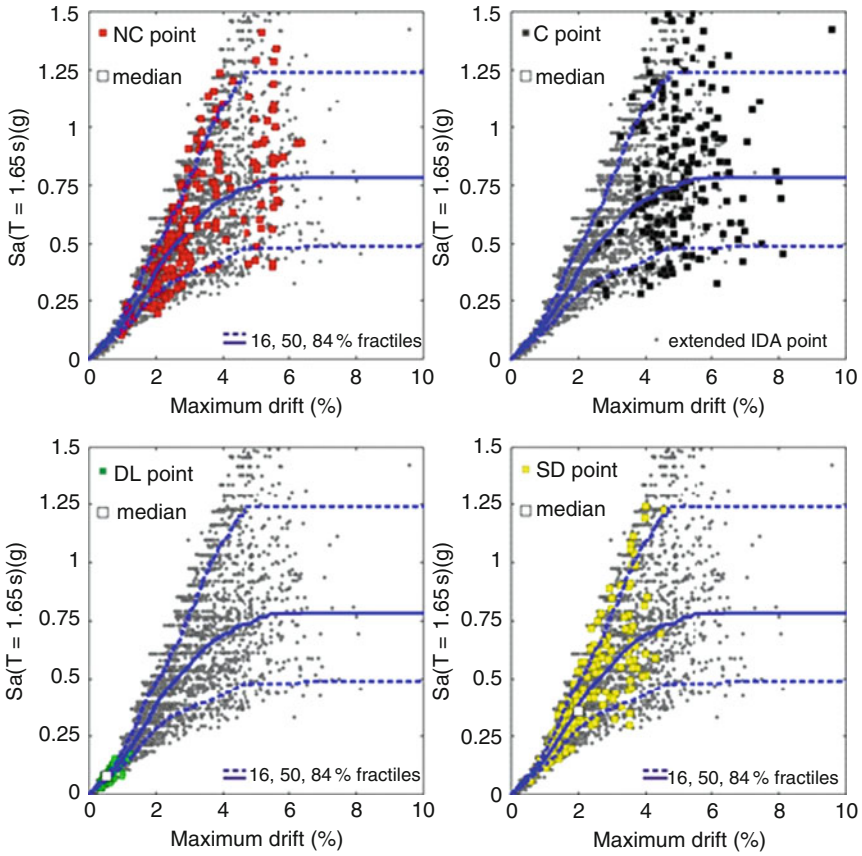


Fig. 8 The extended IDA for the first set of ground motions and the second set of structural models (all random variables). In addition to the EIDA points and summarized EIDA curves also the LS points, which correspond to different limit states for a given ground motion record and structural models, are presented

with results of IDA analysis. The maximum decrease, about 20%, is observed for $S_{a,SD}$. Only for the case of the DL limit state is observed the opposite, since the $S_{a,DL}$ obtained from EIDA for a first set of structural models is slightly increased in comparison to that calculated from results of IDA. The difference between the results of the two EIDAs for the first set ground motions is negligible.

Comparison between the summarized IDA curves and the summarized EIDA curves (16%, 50% and 84% fractiles) is presented in Fig. 10. Similarly as in the previous study [8] it can be observed that the summarized EIDA curves practically do not deviate from the summarized IDA curves, which are determined by employing the deterministic model. This observation is valid within a limited range of intensity measure. It can be concluded that the epistemic uncertainties do not significantly influence the summarized seismic response parameters. However, median collapse

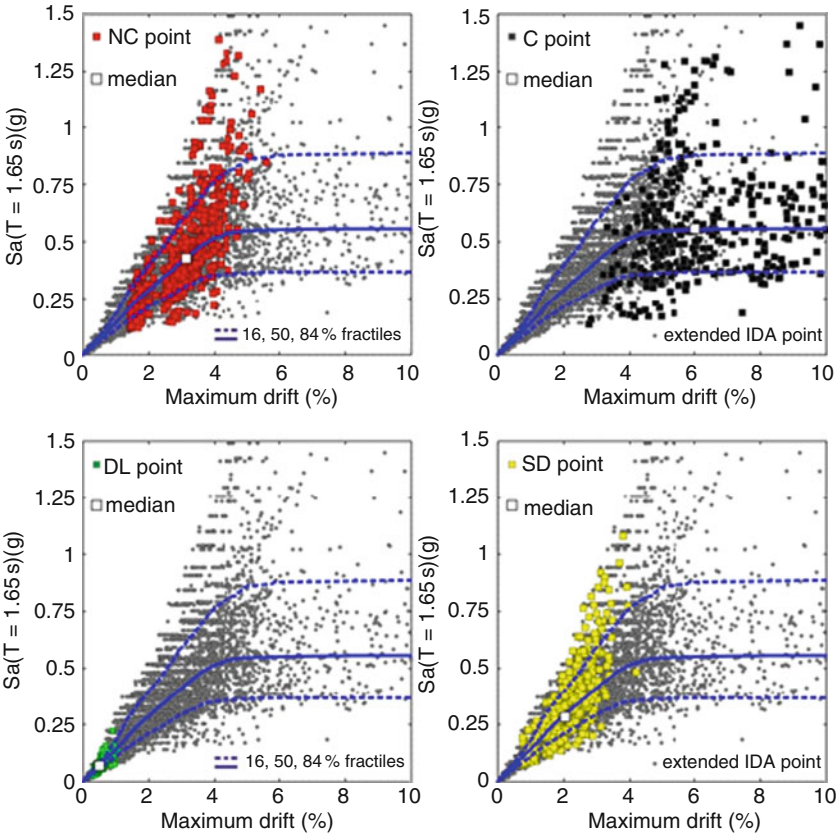


Fig. 9 The extended IDA for the second set of ground motions and the second set of structural models (all random variables). In addition to the EIDA points and summarized EIDA curves also the LS points, which correspond to different limit states for a given ground motion record and structural models, are presented

Table 4 The median $S_{a,LS}$ for different limit states determined from results of IDA for first and second set of structural models and the three EIDAs

	$S_{a,LS}$ (g)			
Analysis/LS	DL	SD	NC	C
IDA G1	0.07	0.47	0.67	0.84
EIDA G1-M1	0.08	0.37	0.58	0.79
EIDA G1-M2	0.08	0.36	0.57	0.79
IDA G2	0.07	0.30	0.43	0.60
EIDA G2-M2	0.07	0.28	0.43	0.56

capacities ($S_{a,C}$) determined with EIDAs is reduced for about 10% if compared to median collapse capacities determined with IDAs. Similarly may be observed for other fractiles with exception of 84% fractile, which corresponds to EIDA performed for the second set of ground motions and structural models.

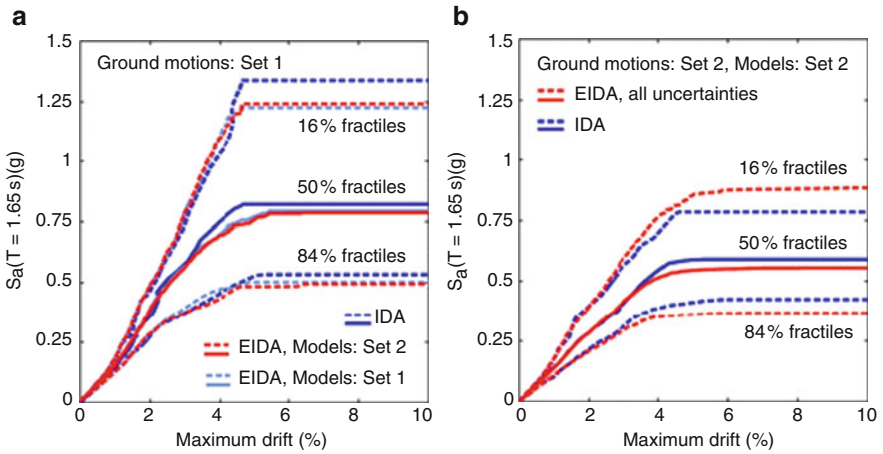


Fig. 10 (**a**) 16%, 50% and 84% fractiles of IDA for the first set of ground motions and of corresponding EIDAs for both sets of structural models, (**b**) 16%, 50% and 84% fractiles of IDA and EIDA for the second set of ground motions

3.5 Dispersion Measures and the Sensitivity of $S_{a,LS}$ to Random Variables

An important result of EIDA consists of the dispersion measures and the sensitivity of the seismic response parameters (e.g. engineering demand parameters, intensity measures corresponding to different limit states) to the input random variables used in the analysis. The dispersion measures which are presented here, were calculated from the LS points obtained from the three EIDAs and compared to the dispersion measures calculated from the results of the IDA performed for the first and second set of ground motions. The same procedure as described in Sect. 3.3 was used for determination of the dispersion measures based on EIDA. Since the EIDA is performed for a set of structural models and for a set of ground motion records makes it possible to determine the dispersion measures which reflect randomness and uncertainty (RU), and also the dispersion measures which are caused only by the uncertainties (U). In the latter case, the dispersion measures are calculated on the basis of seismic response for the different structural models given the ground motion record. They therefore differ from record to record as shown in Fig. 11, where $\beta_{Sa,LS,U}$ is presented as a function of ground motion records for different limit states (DL, SD, NC, C), for the second set of structural models (all random variables) and for both sets of ground motions. The variability of $\beta_{Sa,LS,U}$ due to the ground motions is not negligible. In Table 5 the coefficient of variation for $\beta_{Sa,LS,U}$ for the two EIDAs and DL,SD, NC and C limit state is presented. For example, the highest coefficient of variation for $\beta_{Sa,LS,U}$ (0.39) is observed for the DL limit state, while for others limit states coefficient of variation is less and varies from 0.13 to 0.26. Further research

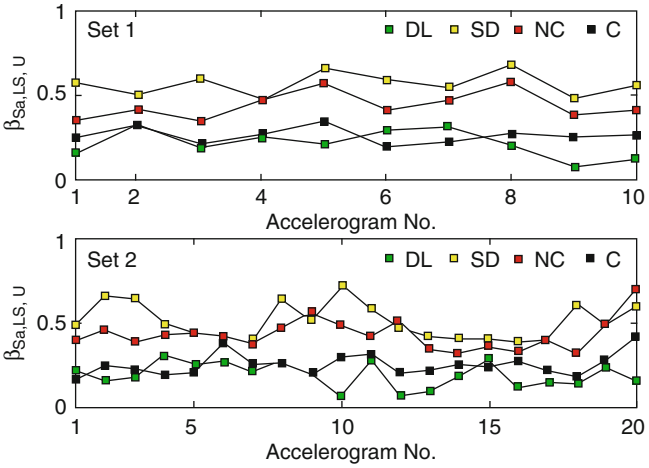


Fig. 11 The dispersion measure for uncertainty $\beta_{Sa,LS,U}$ presented as a function of ground motion records for different limit states (DL, SD, NC, C), for the second set of structural models (all random variables) and for both sets of ground motions

Table 5 The coefficient of variation for $\beta_{Sa,LS,U}$ for the three EIDAs and DL,SD, NC and C limit state

	R-randomness	Coefficient of variation for $\beta_{Sa,LS,U}$			
Analysis	U-uncertainty	DL	SD	NC	C
EIDA G1-M2	U	0.39	0.13	0.19	0.18
EIDA G2-M2	U	0.39	0.21	0.22	0.26

Table 6 The dispersion measure for $S_{a,LS}$ for the IDA and EIDA for the first and second set of structural models

	R-randomness	$\beta_{Sa,LS}$			
Analysis	U-uncertainty	DL	SD	NC	C
IDA G1	R	0.21	0.30	0.44	0.47
EIDA G1-M1	U	0.17	0.56	0.43	0.24
EIDA G1-M1	RU	0.30	0.61	0.53	0.45
EIDA G1-M2	U	0.21	0.56	0.44	0.25
EIDA G1-M2	RU	0.33	0.63	0.55	0.47
IDA G2	R	0.25	0.36	0.31	0.32
EIDA G2-M2	U	0.19	0.51	0.44	0.25
EIDA G2-M2	RU	0.31	0.59	0.53	0.44

is needed in order to detect in advance which ground motions cause high and which low dispersion for uncertainty.

The mean values of the dispersion $\beta_{Sa,LS,U}$ are presented with other dispersions ($\beta_{Sa,LS,R}$, $\beta_{Sa,LS,RU}$) in Table 6 for all IDAs and EIDAs and for all four limit states.

The dispersion for randomness and uncertainty (RU) in $S_{a,LS}$ is based on the EIDA analysis and exceeds dispersion for randomness (R), which was determined based on the results of IDA analysis. It can be observed that the difference between the $\beta_{Sa,LS,RU}$ and $\beta_{Sa,LS,R}$ are the most evident for DL, SD and NC limit state, while for the limit state C the difference is small, especially for the case of second set of ground motions. For example, dispersion $\beta_{Sa,C,RU}$ amounts to about 0.45. It can be observed that the highest dispersion is not obtained for collapse limit state (C) but for limit state of significant damage (SD) ($\beta_{Sa,SD,RU} \approx 0.60$), which appears, when the rotation in the first column exceeds the rotation at maximum moment. Such a high dispersion is probably the consequence of the small correlation between the maximum drift representing EDP and the defined SD limit state.

The dispersion for uncertainty (U) for the SD and NC limit state are larger or at least the same as dispersions for randomness (R) (Table 6). The opposite trend can be observed for the DL and C limit state.

It is interesting that the dispersion measures $\beta_{Sa,LS,RU}$ practically do not differ if comparison is made between the three EIDAs. However, this is not generally true since the opposite was observed in the previous study [8]. Therefore it can be concluded that one source of uncertainty, which is important for one structure, can be less important for other structure and vice versa. This statement can be strengthen if the sensitivity of $S_{a,LS}$ to random variables is determined. In our case this sensitivity was estimated with the Spearman rank correlation coefficient (Eq. 3). The results are presented in Fig. 12 for EIDA performed for first set of ground motions and second set of structural models. Each chart in Fig. 12 corresponds to particular limit state. It can be observed that $S_{a,LS}$ is the most sensitive to the uncertainty in concrete strength although the coefficient of variation for concrete strength was much smaller in comparison to that assumed for damping or ultimate rotation in beams. Again this observation is different from conclusions in the previous study [8].

The fact that uncertainty in concrete strength is important was partly expected, since the amount of reinforcement in columns is very small and the concrete strength has an important influence on the strength of the structure. From the moment-rotation envelope of the middle column at the bottom it was found that the maximum value of the maximum (M) moment (see Fig. 3) was obtained for the maximum value of the concrete strength from the sample values and the minimum value of the maximum moment corresponds to the minimum value of the concrete strength. The difference between the minimum and the maximum value of the maximum moment for the middle column is about 100%. The concrete strength does not influence only on the strength of the structure, but also on the deformation capacity of the structure, which is even more evident. For example, deformation along the height of the frame and at the top displacement (D_t) measured in the degrading part of the pushover curve, which corresponds to 20% reduction of the maximum base shear, is presented in Fig. 13 for the deterministic model employed in the IDA, and the two selected models used in EIDA for the seconds set of structural models. These models, model No. 18 and 15, correspond to the minimum and the maximum strength of concrete obtained from the sample values, respectively. It can be observed that the deformations along the height of the frame, the damage in the plastic hinges,

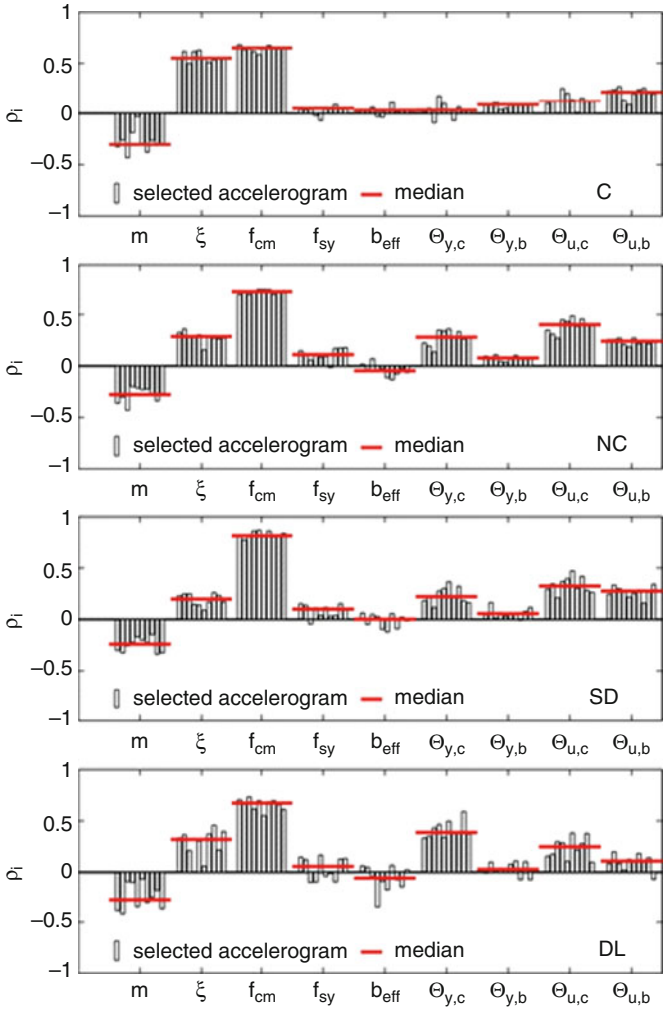


Fig. 12 The Spearman rank correlation coefficient for the $S_{a,LS}$ and the different random variables presented in Table 1. Results are presented for each ground motion records and median values

as well as the top displacements are significantly different for the three presented cases (Fig. 13). The strength of the frame for the model No. 15 is reduced for 20% at $D_t = 38.7$ cm, while for the model No. 18 corresponding D_t is significantly less (15.9 cm) although in model No. 15 the damage in plastic hinges never exceeds NC limit state.

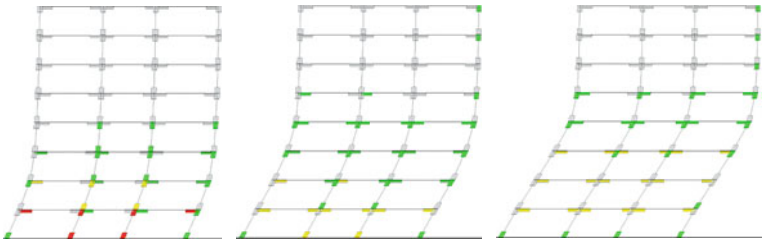


Fig. 13 The damage in the plastic hinges from a pushover analysis at the top displacement in the degrading part of the pushover curve (20% reduction of maximum strength) for two models from the second set of structural models and for the deterministic models used in IDA analysis

4 Conclusions

Extended incremental dynamic analysis has been briefly summarized, and its use has been demonstrated on an example of an eight-storey reinforced concrete frame. The extended IDA was performed for two sets of ground motion records and two sets of structural models. In the first set of structural models, only selected sources of uncertainty were taken into account, whereas in the second set of structural models all the sources of uncertainty were considered in this study.

Similarly as in the previous study [8], it was shown that, within the range far from collapse, epistemic uncertainty does not significantly affects the median seismic response parameters. However, epistemic uncertainties can have an important influence on the dispersion and on the spectral acceleration capacity, which corresponds to global dynamic instability. The results of the sensitivity study showed that the greatest effect on the response parameters do not have the random variables, which have a high coefficient of variation, as observed in the previous study [8], but the concrete strength, which has a moderate coefficient of variation and significantly affects the strength and available ductility of the structure. In the presented example, the initial stiffness and ultimate rotation in the columns and beams had only a minor influence on the seismic response.

It was shown that extended IDA is a simple yet efficient method for estimating the seismic response parameters, while taking into account the modelling uncertainties. The results can be used directly for the determination of the probability of exceeding a given limit state since the seismic response parameters are determined with consideration of both sources of uncertainties. However, the increased price for the additional information is the longer computational time in comparison to the computational time needed for IDA.

Acknowledgments The results presented in this paper are based on work supported by the Slovenian Research Agency. This support is hereby gratefully acknowledged.

References

1. Porter KA, Beck JL, Shaikhutdinov RV (2002) Investigation of sensitivity of building loss estimates to major uncertain variables for the Van Nuys testbed, California Institute of Technology. PEER Report 2002/2003. Pacific Earthquake Engineering Research Center, University of California, Berkeley, CA
2. Haselton CB (2006) Assessing seismic collapse safety of modern reinforced concrete moment frame buildings. Ph.D. dissertation, Stanford University, Stanford
3. Lee T-H, Mosalam KM (2005). Seismic demand sensitivity of reinforced concrete shear-wall building using FOSM method. Earth Eng Struct Dyn 34:1719–1736
4. Baker JW, Cornell CA (2008) Uncertainty propagation in probabilistic seismic loss estimation. Struct Safety 30:236–252
5. Liel AB, Haselton CB, Deierlein GG, Baker JW (2009) Incorporating modeling uncertainties in the assessment of seismic collapse risk of buildings. Struct Safety 31(2):197–211
6. Vamvatsikos D, Cornell CA (2002) Incremental dynamic analysis. Earth Eng Struct Dyn 31:491–514
7. Dolsek M (2007) Influence of the epistemic uncertainty on the probabilistic seismic assessment of the four-storey reinforced concrete frame. In: Proceedings of 8th Pacific conference on earthquake engineering, Paper No. 194, Singapore
8. Dolsek M (2009) Incremental dynamic analysis with consideration of modeling uncertainties. Earth Eng Struct Dyn 38(6):805–825
9. Vorechovsky M, Novak D (2003) Statistical correlation in stratified sampling. In: Der Kiureghian A, Madant S, Pestana JM (eds) ICAPS 9. Proceedings of International conference on applications of statistics and probability in civil engineering. Millpress, Rotterdam, San Francisco, CA pp 119–124
10. Vorechovsky M, Novak D (2009) Correlation control in small-sample Monte Carlo type simulations I: a simulated annealing approach. Probab Eng Mech 24:452–463
11. Vamvatsikos D, Fragiadakis M (2009) Incremental dynamic analysis for estimating seismic performance sensitivity and uncertainty. Earth Eng Struct Dyn Early View. doi: 10.1002/eqe.935
12. Kala Z (2005) Sensitivity analysis of the stability problems of thin-walled structures. J Construct Steel Res 61:415–422
13. Fajfar P, Dolšek M, Marušić D, Stratan A (2006) Pre- and post-test mathematical modelling of a plan-asymmetric reinforced concrete frame building. Earth Eng Struct Dyn 35:1359–1379
14. Peruš I, Poljanšek K, Fajfar P (2006) Flexural deformation capacity of rectangular RC columns determined by the CAE method. Earth Eng Struct Dyn 35:1453–1470
15. CEN (2005). Eurocode 8: design of structures for earthquake resistance. Part 3: strengthening and repair of buildings. *EN 1998–3*, Euro. Commit. for Stand., Brussels, March 2005
16. McKenna F, Fenves GL (2004) Open system for earthquake engineering simulation, Pacific Earthquake Engineering Research Center, Berkeley, CA, http://opensees.berkeley.edu/
17. Dolšek M (2008) OS modeler user's manual, Version 1, University of Ljubljana
18. Ambraseys N, Smith P, Bernardi R, Rinaldis D, Cotton F, Berge-Thierry C (2000) Dissemination of European strong-motion data. CD-ROM collection. European Council, Environment and Climate Research Programme
19. Fajfar P, Vidic T, Fischinger M (1989) Seismic demand in medium-and long-period structures. Earth Eng Struct Dyn 18:1133–1144
20. Panagiotakos TB, Fardis MN (2001) Deformations of reinforced concrete at yielding and ultimate. ACI Struct J 98(2):135–147

Robust Stochastic Design of Viscous Dampers for Base Isolation Applications

Alexandros A. Taflanidis

Abstract Over the last decades, there has been a growing interest in the application of base isolation techniques to civil structures. Of the many relevant research topics, the efficient design of additional dampers, to operate in tandem with the isolation system, has emerged as one of the more important. One of the main challenges of such applications has been the explicit consideration of the nonlinear behavior of the isolators or the dampers in the design process. Another challenge has been the efficient control of the dynamic response under near-field ground motions. A framework is discussed in this chapter that addresses both these challenges. A probability logic approach is adopted for addressing the uncertainties about the structural model as well as the variability of future excitations. In this stochastic setting, a realistic model for the description of near-field ground motions is discussed. The design objective is then defined as the maximization of structural reliability. A simulation-based approach is implemented for evaluation of the stochastic performance and an efficient framework is discussed for performing the associated challenging design optimization and for selecting values of the controllable damper parameters that optimize the system reliability.

1 Introduction

Over the last decades, there has been a growing interest in the application of base isolation techniques for buildings (Fig. 1) and bridges in seismic regions. The potential advantages of seismic isolation and the recent advancements in isolation-system products have led to the design and construction of a constantly increasing number of seismically isolated buildings and bridges worldwide [1]. Apart from new constructions, seismic isolation is extensively used for seismic retrofitting of existing building. Also, base isolation concepts are utilized for the protection from shock and vibration of sensitive components of critical facilities such as nuclear reactors, internet collocation facilities, or data storage facilities.

A.A. Taflanidis (✉)
Department of Civil Engineering and Geological Sciences, University of Notre Dame, Notre Dame
e-mail: a.taflanidis@nd.edu

M. Papadrakakis et al. (eds.), *Computational Methods in Earthquake Engineering*,
Computational Methods in Applied Sciences 21, DOI 10.1007/978-94-007-0053-6_14,
© Springer Science+Business Media B.V. 2011

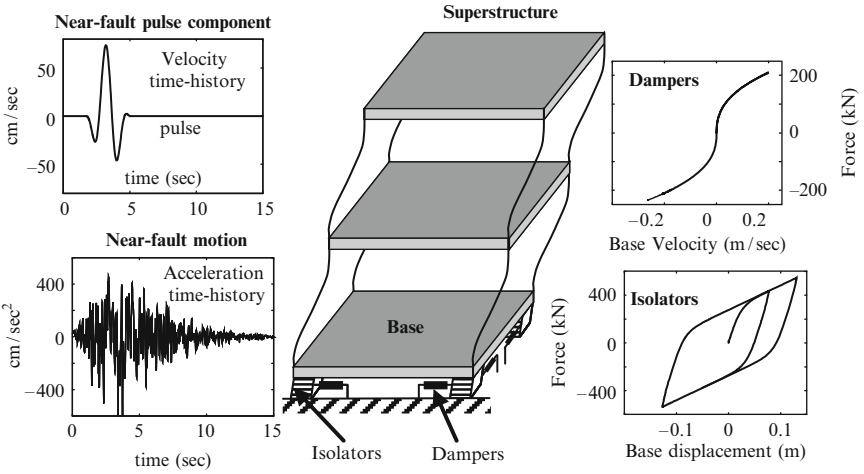


Fig. 1 Base-isolated structure with viscous dampers

One of the current challenges in design of base-isolation systems has been recognized to be the reduction of base displacements under near-fault ground motions. Such motions frequently include a strong longer period pulse (illustrated in the velocity time history in (Fig. 1) that has important implications for flexible structures [2]. Proper characterization and study of their effects on engineering structures is currently an active research topic for seismologists and earthquake engineers [3–5]. For base isolated systems these ground motions may lead to excessive base displacements and thus pounding to the seismic stoppers and neighboring structures, when separation gap is inadequate, with important implications for the superstructure integrity. This realization led engineers to suggest supplemental dampers for protection of base-isolated structures [6–8].

One of the main challenges of such applications has been the explicit consideration of the nonlinear behavior of the isolators and the dampers in the design process. Linearization techniques are frequently adopted for the coupled isolation/damper system. This simplifies the analysis, but there is great doubt [9] if it can accurately predict the combined effect of the non-linear viscous damping, provided by the dampers, along with the non-linear hysteretic damping, provided by the isolators. Another challenge has been the efficient control of the dynamic response under future near-field ground motions considering the potential variability of these motions as well as competing objectives related to (i) the protection of the superstructure and its contents (minimization of drifts and absolute accelerations, respectively), and (ii) the avoidance of seismic pounding (minimization of base displacements).

The current work proposes a framework for design of viscous dampers for base isolation applications which address both these challenges. A probability logic approach is adopted for addressing the uncertainties about the structural model as well as the variability of future excitations. This is established by characterizing the relative plausibility of different properties of the system and future excitations by probability models. In this stochastic setting, a realistic model [10] for

the description of near-field ground motions is discussed. This model establishes a direct link, in a probabilistic sense, between our knowledge about the characteristics of the seismic hazard in the structural site and future ground motion time histories. The design objective is then defined as the maximization of structural reliability, quantified as the probability that the response quantities of interest, for example, drifts, base displacement and accelerations, will not exceed acceptable performance bounds. A simulation-based approach is implemented for evaluation of the stochastic performance of the base isolated structure. This approach explicitly takes into account all non-linear characteristics of the structural response in the design process and allows for complex characterization for the system and excitation models. An efficient framework [11] is discussed for performing the associated challenging design optimization. This approach also allows for a sensitivity analysis for the influence of the uncertain model parameters on the stochastic performance.

2 Structural Model

For simplicity of the presentation, we will assume a planar model for the structural system and a linear model for the superstructure. The ideas discussed here, though, can be directly extended to more complex cases, for example to nonlinear models for the superstructure, or asymmetric buildings. Reference [10] provides a detailed discussion about the latter case.

Let $\mathbf{x}_s$ be the vector of absolute displacements for the superstructure with respect to the base and $\mathbf{M}_s$, $\mathbf{C}_s$, and $\mathbf{K}_s$ be the corresponding mass, damping and stiffness matrices. Also let $\mathbf{R}$ denote the vector of earthquake influence coefficients, m_b the mass of the base and x_b the base displacement. The equation for the base isolated structure is then:

$$\begin{aligned} &\mathbf{M}_s\ddot{\mathbf{x}}_s + \mathbf{M}_s\mathbf{R}\ddot{x}_b + \mathbf{C}_s\dot{\mathbf{x}}_s + \mathbf{K}_s\mathbf{x}_s = -\mathbf{M}_s\mathbf{R}a_g \\ &\mathbf{R}^T\mathbf{M}_s\ddot{\mathbf{x}}_s + (\mathbf{R}^T\mathbf{M}_s\mathbf{R} + m_b)\ddot{x}_b + f_{is} + f_d = -(\mathbf{R}^T\mathbf{M}_s\mathbf{R} + m_b)a_g \end{aligned} \quad (1)$$

where a_g is the ground acceleration; f_{is} corresponds to the isolator forces and f_d to the damper forces. For passive viscous dampers the latter may be modeled by [12]:

$$f_d = c_d \,\mathrm{sgn}(\dot{x}_b)|\dot{x}_b|^{a_d} \quad (2)$$

where c_d is the damping coefficient, a_d an exponent parameter and sgn(.) the sign function. For $a_d = 1$ the above relationship corresponds to a linear viscous damper. The hysteretic behavior of the isolators may be characterized by a Bouc-Wen model [7]:

$$U^y\dot{z} = \alpha_{is}\dot{x}_b - z^2(\gamma_{is}\mathrm{sgn}(\dot{x}_b z) + \beta_{is})\dot{x}_b \quad (3)$$

where z is a dimensionless hysteretic variable that is constrained by values ± 1, U^y is the yield displacement, and α_{is}, β_{is}, and γ_{is} are dimensionless quantities that characterize the properties of the hysteretic behavior. Typical values for these parameters are $\alpha_{is} = 1$, $\beta_{is} = 0.1$, and $\gamma_{is} = 0.9$ [10]. The isolator forces may be then described based on the variable z and the base displacement x_b. For example, for friction-pendulum isolators and lead-rubber bearings we have, respectively:

$$f_{is} = k_p x_b + \mu N_t z \tag{4}$$

$$f_{is} = k_p x_b + (k_e - k_p) U^y z \tag{5}$$

where k_p is the post yield stiffness, N_t the average normal force at the bearing, μ is the coefficient of friction, k_e the pre yield stiffness. For asymmetric buildings, the biaxial interaction, because of the asymmetric motion of the base in its two principal directions, can be accounted for by the modified Bouc-Wen model proposed by Park et al. [13].

3 Near Fault Stochastic Excitation Model

The design of any seismic protection system needs to be performed considering potential damaging future ground motions. As discussed before, for the applications consider here this translates to consideration of near-fault ground motions. A stochastic model for such excitations is discussed next. This model was initially presented in [10] and is based on the methodologies developed by Mavroeidis and Papageorgiou [3] and Boore [14]. The low-frequency (long period) and high-frequency components of the ground motion are independently modeled, according to these approaches, and then combined to form the acceleration time history.

3.1 High-Frequency Component

The fairly general, point source stochastic method is selected for modeling the higher-frequency (>0.1–0.2 Hz) component of ground motions. The stochastic method is based on a parametric description of the ground motion's radiation spectrum $A(f; M, r)$, which is expressed as a function of the frequency, f, for specific values of the earthquake magnitude, M, and epicentral distance, r. This spectrum consists of many factors which account for the spectral effects from the source (source spectrum) as well as propagation through the earth's crust. The duration of the ground motion is addressed through an envelope function $e(t; M, r)$, which again depends on M and r. These frequency and time domain functions, $A(f; M, r)$ and $e(t; M, r)$, completely characterize the model. More details on them are provided next, in Sect. 3.4. Particularly, the two-corner point-source model

by Atkinson and Silva [15] can be selected for the source spectrum because of its equivalence to finite fault models. This equivalence is important because of the desire to realistically describe near-fault motions and adaptation of a point-source model might not efficiently address the proximity of the site to the source [3]. The spectrum developed by Atkinson and Silva [15] has been reported in their studies to efficiently address this characteristic.

The time-history (output) for a specific event magnitude, M, and source distance, r, is obtained according to this model by modulating a white-noise sequence $\mathbf{Z}_w = [Z_w(i\,\Delta t) : i = 1, 2, \ldots, N_T]$ by $e(t; M, r)$ and subsequently by $A(f; M, r)$ through the following steps:

1. The sequence $\mathbf{Z}_w$ is multiplied by the envelope function $e(t; M, r)$
2. This modified sequence is then transformed to the frequency domain
3. It is normalized by the square root of the mean square of the amplitude spectrum
4. The normalized sequence is multiplied by the radiation spectrum $A(f; M, r)$ and finally
5. It is transformed back to the time domain to yield the desired acceleration time history

Assuming that the local site conditions are known, the model parameters consist of the seismological parameters, M and r, and the white-noise sequence $\mathbf{Z}_w$. Figure 2 shows functions $A(f; M, r)$ and $e(t; M, r)$ for different values of M and r. It can be seen that as the moment magnitude increases the duration of the envelope function also increases and the spectral amplitude becomes larger at all frequencies with a shift of dominant frequency content towards the lower-frequency regime. As the epicentral distance increases, the spectral amplitude decreases uniformly and the envelope function also decreases, but at a relatively smaller amount. Figure 2c includes the radiation spectrum $A(f; M, r)$ with the Fourier amplitude and the time history of a sample ground motion generated according to this model.

3.2 Long Period Pulse

For describing the pulse characteristic of near-fault ground motions, the simple analytical model developed by Mavroeidis and Papageorgiou [3] is selected. This model is based on an empirical description of near-fault ground motions and has been calibrated using actual near-field ground motion records from all over the world. According to it, the pulse component of near-fault motions is described through the following expression for the ground motion velocity pulse (the pulse is also illustrated in Fig. 1 earlier):

$$V(t) = \frac{A_p}{2}\left[1 + \cos\left(\frac{2\pi f_p}{\gamma_p}(t - t_o)\right)\right]\cos[2\pi f_p(t - t_o) + \nu_p];$$

$$t \in \left[t_o - \frac{\gamma_p}{2f_p}, t_o + \frac{\gamma_p}{2f_p}\right] = 0; \text{otherwise} \tag{6}$$

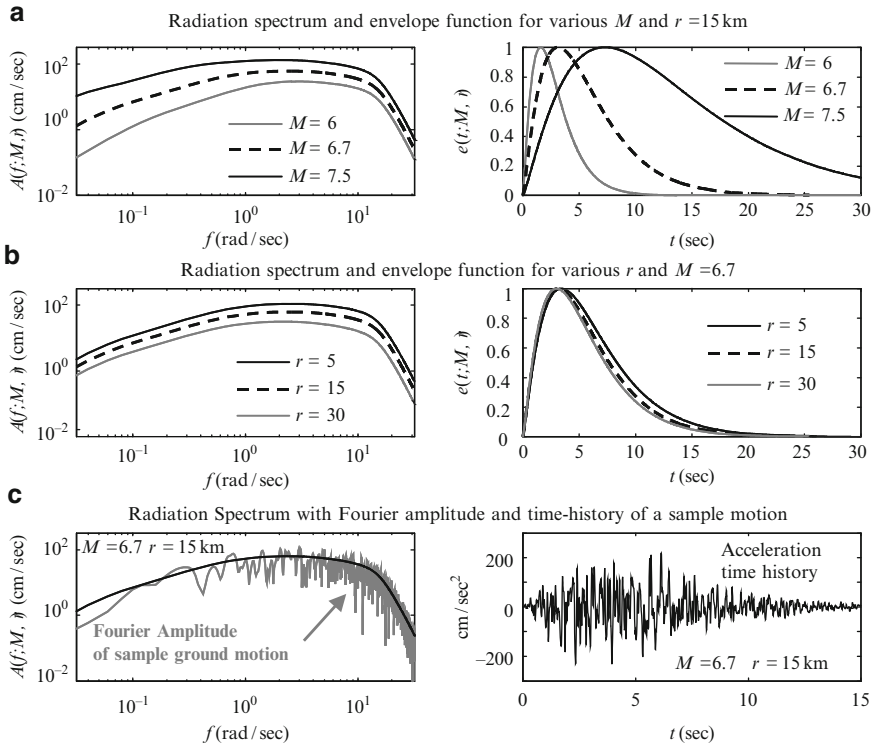


Fig. 2 Radiation spectrum, envelope function, and sample excitation

where A_p, f_p, ν_p, γ_p, and t_o describe the signal amplitude, prevailing frequency, phase angle, oscillatory character (i.e., number of half cycles), and time shift to specify the epoch of the envelope's peak, respectively. Note that all parameters have an unambiguous physical meaning. In response to the recent realization of the importance of near-fault motions to the structural performance a number of studies [3,4,16] have been directed towards developing predictive relationships that connect these pulse characteristics to the seismic hazard of a site. These studies link the amplitude and frequency of near-fault pulses to the moment magnitude and epicentral distance of seismic events, but they also acknowledge that significant uncertainty exists in such relationships. This indicates that a probabilistic characterization, as will be discussed later on, is more appropriate. For the rest of the pulse parameters, no clear link to the seismic hazard of the structural site has been yet established. They need to be considered as independent model parameters.

3.3 Near-Fault Ground Motion

The *stochastic model* for near-fault motions is finally established by combining the above two components. The model parameters consist of the seismological parameters M and r, the additional parameters for the velocity pulse, A_p, f_p, ν_p, γ_p, and the white noise sequence $\mathbf{Z}_w$. The following procedure, which is equivalent to the methodology in [3], describes the model:

1. Apply the stochastic method to generate an acceleration time history.
2. Generate a velocity time history for the near-field pulse using Eq. 6. The pulse is shifted in time to coincide with the peak of the envelope $e(t; M, r)$. This defines the value of the time shift parameter t_o. Differentiate the velocity time series to obtain an acceleration time series.
3. Calculate the Fourier transform of the acceleration time histories generated in steps 1 and 2.
4. Subtract the Fourier amplitude of the time series generated in step 2 from the spectrum of the series generated in 1.
5. Construct a synthetic acceleration time history so that its Fourier amplitude is the one calculated in step 4 and its Fourier phase coincides with the phase of the time history generated in step 2.
6. Finally superimpose the time histories generated in steps 2 and step 5.

This process defines finally the earthquake ground motion a_g. Figure 3 illustrates a synthetic near-fault ground motion sample. Both the acceleration and velocity time histories of the synthetic ground-motion are presented. The existence of the near-fault pulse is evident when looking at the velocity time history.

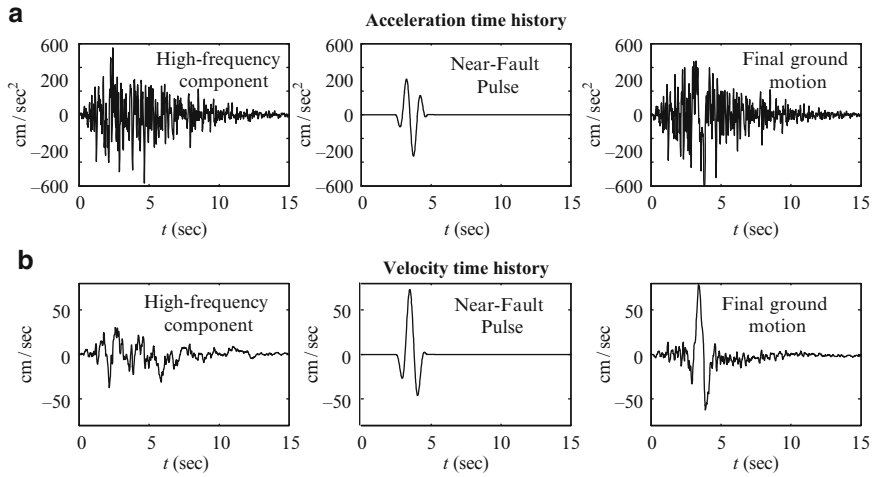


Fig. 3 Sample near-fault ground motion; acceleration and velocity time histories

3.4 Characteristics for Amplitude Spectrum and Envelope Function for Ground Motion Modeling

The characteristics for the functions $A(f;M,r)$ and are briefly summarized here. The total spectrum $A(f;M,r)$ for the acceleration time history is expressed as a product of the source, path and site contributions as [14]

$$A(f;M,r) = (2\pi f)^2 S(f;M)\frac{1}{R}\exp[-\pi f R/(Q(f)\beta_s)]\frac{\exp(-\pi k_o f)}{\sqrt{1+\left(\frac{f}{f_{\max}}\right)^8}}A_m \quad (7)$$

Here $S(f;M)$ is the "equivalent two point-source spectrum" given by [15]:

$$S(f;M) = CM_w\left[\frac{1-e}{1+(f/f_a)^2}+\frac{e}{1+(f/f_b)^2}\right] \quad (8)$$

where M_w is the seismic moment (in dyn-cm) which is connected to the moment magnitude, M, by the relationship $M_w = 10^{1.5(M+10.7)}$ and the constant C is given by $C = 10^{-20}R_\Phi VF/(4\pi R_o\rho_s\beta_s^3)$; $R_\Phi = 0.55$ is the average radiation pattern, $V = 1/2^{(1/2)}$ represents the partition of total shear-wave velocity into horizontal components, $F = 2$ is the free surface amplification, $\rho_s = 2.8\,\mathrm{g/cm^3}$ and $\beta_s = 3.5\,\mathrm{km/s}$ are the density and shear-wave velocity in the vicinity of the source, $R_o = 1\,\mathrm{km}$ is a reference distance, and factor 10^{-20} is needed for consistency of units. The frequencies f_a and f_b in (8) are given by $f_a = 10^{2.181-0.496M}$ and $f_b = 10^{2.41-0.408M}$, respectively, and e is a weighting parameter described by the expression $e = 10^{0.605-0.255M}$. For the rest of the parameters in (7) the term $1/R$ is the geometric spread factor, where $R = [h^2+r^2]^{1/2}$ is the radial distance from the earthquake source to the site, with $h = 10^{0.15M-0.05}$ representing a moment dependent, nominal "pseudo-depth". Term $\exp[-\pi f R/(Q(f)\beta_s)]$ accounts for elastic attenuation through the earth's crust with $Q(f)$ corresponding to a regional quality factor. In this study the latter is chosen $Q(f) = 180f^{0.45}$, which is representative of the California region [15]. The quotient factor in (7) is related to near-surface attenuation, and the parameters chosen in this study are $f_{\max} = 10$ and $k_o = 0.03$, which are again common for California. Finally A_m is a near-surface amplification factor which is described through the empirical curves for generic rock sites [17]. An alternative approach (instead of using the empirical curves) would be to set A_m to an average constant value equal to 2 [30].

The envelope function $e(t;M,r)$ for the excitation is represented by [14]:

$$e(t;M,R) = a(t/t_n)^b\exp(-c(t/t_n)) \quad (9)$$

where a, b and c are chosen so that $e(t;M,r)$ has a peak equal to unity when $t = \lambda t_n$, and $e(t;M,r) = \eta$ when $t = t_n$. This leads to selection $b = -\lambda\ln(\eta)/[1+\lambda(\ln(\lambda)-1)]$, $c = b/\lambda$, $a = [\exp(1)/\lambda]^b$ with values chosen in this study as $\lambda = 0.2$, $\eta = 0.05$, according to the recommendation in [14]. The time t_n corresponds to the duration of strong excitation and is selected here as $t_n = 0.1R + 1/f_a$ [14].

4 Robust Reliability Based Design

The characteristics of the models for the base isolated system and the near-fault excitations, described, respectively, in Sect. 2 and 3 are not known with absolute certainty. Uncertainties may pertain to (i) the properties of the structural system, for example, related to natural periods or damping characteristics; to (ii) the variability of future seismic events, i.e., the moment magnitude or the epicentral distance; or even (iii) to the predictive relationships about the near-fault pulse characteristics. A probability logic approach provides a rational and consistent framework for quantifying all these uncertainties. In this approach, probability can be interpreted as a means of describing the incomplete or missing information [18] about the system under consideration and its environment (representing seismic hazard) though the entire life-cycle [19].

To formalize these ideas let the vector of controllable system parameters, referred to herein as *design variables*, be $\boldsymbol{\varphi} \in \Phi \subset \Re^{n_\varphi}$, where Φ denotes the admissible design space with volume V_Φ. These variables are related to the characteristics of the viscous dampers. Also let $\boldsymbol{\theta} \in \Theta \subset \Re^{n_\theta}$ denote the augmented vector of model parameters for the structural system, $\boldsymbol{\theta}_s$, and the excitation, $\boldsymbol{\theta}_q$, models, where Θ denotes the space of possible model parameter values. A PDF (probability density function) $p(\boldsymbol{\theta})$, which incorporates available knowledge about the system, is assigned to $\boldsymbol{\theta}$. Non-parametric modeling uncertainty may be addressed by introducing a model prediction error, i.e. an error between the response of the actual system and the response of the model adopted for it. This prediction error may be modeled probabilistically and augmented into $\boldsymbol{\theta}$, along with the characteristics of its probability model (if considered uncertain), to form an uncertain parameter vector composed of the system and excitation model parameters as well as the model prediction-error and its properties.

In this stochastic setting, the concept of *robust reliability* [20] may be used to quantify the stochastic performance of the engineering system under design. This performance is characterized by the *robust probability of failure* which provides a measure of the plausibility of the occurrence of unacceptable behavior of the system ("failure"), based on the available information and is given by:

$$P_F(\boldsymbol{\varphi}) \triangleq P(F|\boldsymbol{\varphi}) = \int_\Theta I_F(\boldsymbol{\varphi}, \boldsymbol{\theta}) p(\boldsymbol{\theta}) d\boldsymbol{\theta} \tag{10}$$

where $I_F(\boldsymbol{\varphi}, \boldsymbol{\theta})$ is the indicator function, which equals one if the system that corresponds to $(\boldsymbol{\varphi}, \boldsymbol{\theta})$ fails, i.e., performs unacceptably, and zero if it does not. The failure event F for the system is typically described by a limit state function $g(\boldsymbol{\varphi}, \boldsymbol{\theta})$ and the following convention is assumed herein:

$$F \Leftrightarrow g(\boldsymbol{\varphi}, \boldsymbol{\theta}) > 0 \tag{11}$$

The robust reliability-based design is finally established by selecting the design variables that minimize this failure probability, i.e., maximize the reliability of the system:

$$\boldsymbol{\varphi}^* = \arg\min_{\boldsymbol{\varphi}\in\Phi} \{P_F(\boldsymbol{\varphi}) | \mathbf{f}_c(\boldsymbol{\varphi}) \geq 0\} \tag{12}$$

where $\mathbf{f}_c(\boldsymbol{\varphi})$ is a vector of deterministic constraints, related, for example, to location or space constraints. These constraints may be incorporated into the definition of admissible design space Φ, which leads to the simplified optimization expression:

$$\boldsymbol{\varphi}^* = \arg\min_{\boldsymbol{\varphi}\in\Phi} P_F(\boldsymbol{\varphi}) \tag{13}$$

5 Stochastic Analysis and Optimization

Since the models considered are complex and include a large number of uncertain model parameters the multi-dimensional reliability integral in (10) cannot be calculated, or even accurately approximated, analytically. Many specialized approaches have been proposed for approximating this integral for reliability optimizations. These approaches include, for example, use of some proxy for the failure probability, e.g., reliability index obtained through first-order or second-order analysis (e.g. [21]), decoupling methodologies [22], and response surface approximations to the limit state function defining the model's failure (e.g. [23]). These approximations may work satisfactorily under certain conditions, but they are not guaranteed to converge to the solution of the original optimization problem. Additionally, these specialized approaches might impose implicit or explicit restrictions on the degree of model complexity. An efficient alternative approach is to estimate the integral by *stochastic simulation* [24]. The recent advances in computer hardware and simulation algorithms have reduced the computational cost associated with stochastic simulations. This feature, along with the potential for high-accuracy estimations for the probability of failure and thus solution to the associated optimization problem, have made algorithms based on stochastic simulation an attractive alternative to specialized techniques for reliability-based optimal design applications. This is the approach adopted here. In this case using a finite number, N, of samples of $\boldsymbol{\theta}$ drawn from some importance sampling density $p_{is}(\boldsymbol{\theta})$, an estimate for $P_F(\boldsymbol{\varphi})$ is given by the *stochastic analysis*:

$$\hat{P}_F(\boldsymbol{\varphi}) \triangleq \frac{1}{N}\sum_{i=1}^{N} \boldsymbol{I}_F(\boldsymbol{\varphi}, \boldsymbol{\theta}_i)\frac{p(\boldsymbol{\theta})}{p_{is}(\boldsymbol{\theta})} \tag{14}$$

where vector $\boldsymbol{\theta}_i$ denotes the sample of the uncertain parameters used in the ith simulation. As $N \to \infty$, then $\hat{P}_F \to P_F$ but even for finite, large enough N (14) gives a good approximation for (10). The Importance Sampling (IS) density $p_{is}(\boldsymbol{\theta})$ may be used to improve the efficiency of this estimation. This is established by focusing on regions of the Θ space that contribute more to the integrand of the stochastic integral $P_F(\boldsymbol{\varphi})$ [24]. If $p_{is}(\boldsymbol{\theta}) = p(\boldsymbol{\theta})$ then the approach corresponds to direct Monte Carlo Simulation (MCS).

The optimal design choice is finally given by the *stochastic optimization*:

$$\boldsymbol{\varphi}^* = \arg\min_{\boldsymbol{\varphi}\in\Phi} \hat{P}(\boldsymbol{\varphi}) \tag{15}$$

The estimate for the objective function for this optimization involves an unavoidable estimation error and significant computational cost (since N evaluations of the model response are needed for each stochastic analysis), which make the optimization problem challenging. Many numerical techniques and optimization algorithms have been developed to address such challenges in stochastic optimization problems (e.g. [25–27]). Such approaches may involve one or more of the following strategies: (i) use of common random numbers, i.e. using the same sample sets when estimating (14), to reduce the relative importance of the estimation error when comparing two design choices that are "close" in the design space; (ii) application of exterior sampling techniques which adopt the same stream of random numbers throughout all iterations in the optimization process, thus transforming the stochastic problem (15) into a deterministic one; (iii) simultaneous perturbation stochastic search techniques, which approximate at each iteration the gradient vector by performing only two evaluations of the objective function in a random search direction; and (iv) gradient-free algorithms (such as evolutionary algorithms, or objective function approximation methods) which do not require derivative information. Taflanidis and Beck [11] provide a detailed discussion about algorithms appropriate for stochastic optimization problems like (15). All of these algorithms involve, though, a significant computational cost, especially for design problems for which little information is available a priori about the sensitivity of the objective function to the design variables; such information, if available, is valuable for selecting the parameters (fine-tuning) of the chosen optimization algorithms. An efficient framework is discussed here, based on the novel algorithm developed recently by Taflanidis and Beck [28, 29], called Stochastic Subset Optimization (SSO). Initially this algorithm is briefly reviewed.

5.1 Stochastic Subset Optimization

The basic idea in SSO is the formulation of an augmented stochastic problem where the design variables are artificially considered as uncertain with uniform distribution $p(\boldsymbol{\varphi})$ over the initial design space Φ. The failure probability $P(F|\boldsymbol{\varphi})$ may then be expressed using Bayes' Theorem as:

$$P_F(\boldsymbol{\varphi}) \triangleq P(F|\boldsymbol{\varphi}) = \frac{p(\boldsymbol{\varphi}|F)}{p(\boldsymbol{\varphi})} P(F) \tag{16}$$

where $p(\boldsymbol{\varphi}|F)$ is the PDF for $\boldsymbol{\varphi}$ conditioned on the failure event, and $P(F)$ is the failure probability of the augmented reliability problem. This probability is simply a normalization constant and it is not required in the analysis.

Since $P(F)$ and $p(\boldsymbol{\varphi})$ are constants, the conditional PDF $p(\boldsymbol{\varphi}|F)$ expresses the sensitivity of the objective function $P_F(\boldsymbol{\varphi})$ with respect to the design variables. Samples from this PDF are readily obtained by a simulation-based failure analysis. Such an analysis will give *failure samples* of $[\boldsymbol{\varphi}, \boldsymbol{\theta}]$, i.e. simulation samples that lead to system failure. These failure samples are distributed according to $p(\boldsymbol{\varphi}, \boldsymbol{\theta}|F)$ and their $\boldsymbol{\varphi}$ component corresponds to samples from the conditional PDF $p(\boldsymbol{\varphi}|F)$. Direct Monte Carlo simulation (MCS) may be used to obtain these samples. If $P(F)$ is small, however, then MCS is not computationally efficient since $1/P(F)$ trials are needed on the average in order to obtain one failure sample. Other techniques, for example, Subset Simulation [30] which implements Markov Chain Monte Carlo (MCMC) sampling [31], can be used in such cases.

A sensitivity analysis can be efficiently performed by exploiting the information in these samples, This is established in SSO by focusing on subsets in the design variable space, rather than trying to estimate $p(\boldsymbol{\varphi}|F)$ based on the available samples. The average value of the failure probability over any such subsets $I \subset \Phi$ with volume V_I may expressed using (16) as

$$\begin{aligned} &\int_{\mathbf{I}} P(F|\boldsymbol{\varphi}) d\boldsymbol{\varphi} / V_{\mathbf{I}} = P(F) \frac{V_{\Phi}}{V_{\mathbf{I}}} P(\boldsymbol{\varphi} \in \mathbf{I}|F) \\ &\text{where } P(\boldsymbol{\varphi} \in \mathbf{I}|F) \triangleq \int_{\mathbf{I}} p(\boldsymbol{\varphi}|F) d\boldsymbol{\varphi} \end{aligned} \tag{17}$$

The ratio of average values in I and Φ can be then defined as:

$$H(I) \triangleq \frac{\int_I P(F|\boldsymbol{\varphi}) d\boldsymbol{\varphi} / V_I}{\int_{\Phi} P(F|\boldsymbol{\varphi}) d\boldsymbol{\varphi} / V_{\Phi}} = \frac{V_{\Phi}}{V_I} P(\boldsymbol{\varphi} \in I|F) \tag{18}$$

This ratio expresses the average relative sensitivity of $P(F|\boldsymbol{\varphi})$ to $\boldsymbol{\varphi}$ within the set I. Greater sensitivity means a bigger contrast in the average values over I and Φ, which corresponds to smaller values for $H(I)$. An estimate for $H(I)$ based on samples from $p(\boldsymbol{\varphi}|F)$ may be finally computed as follows:

$$\hat{P}(\boldsymbol{\varphi} \in I|F) = \frac{N_I}{N_{\Phi}} \Rightarrow \hat{H}(I) = \frac{N_I}{V_I} \Big/ \frac{N_{\Phi}}{V_{\Phi}} \tag{19}$$

where N_I and N_{Φ} denote the number of samples from $p(\boldsymbol{\varphi}|F)$ belonging to the sets I and Φ, respectively. The coefficient of variation (c.o.v.) for the estimate $H(I)$ depends on the simulation technique used to obtain the samples from $p(\boldsymbol{\varphi}|F)$. For a broad class of sampling algorithms this c.o.v. may be expressed as:

$$\text{c.o.v.}\hat{H}(I) = \sqrt{\frac{1 - P(\boldsymbol{\varphi} \in I|F)}{\mathrm{N}_s \cdot P(\boldsymbol{\varphi} \in I|F)}} \approx \sqrt{\frac{1 - N_I/N_{\Phi}}{\mathrm{N}_s \cdot N_I/N_{\Phi}}} \tag{20}$$

where $N_s = N_{\Phi}/(1+\gamma)$, $\gamma \geq 0$, is the effective number of independent samples. For example, if direct Monte Carlo techniques are used then $\gamma = 0$, but if Markov

Chain Monte Carlo (MCMC) sampling is selected then $\gamma > 0$ because of the correlation of the generated samples. The reference by Berg [31] provides more details, including methodologies for estimating γ.

A subset sensitivity analysis can be performed by the *stochastic subset optimization*

$$\hat{I} = \arg\min_{I \in A} \hat{H}(I) = \arg\min_{I \in A} N_I / V_I \tag{21}$$

where A is a family of admissible subsets of Φ defined by each subset having to satisfy a specified geometrical shape and some size constraint. Optimization (21) identifies the subset, within the admissible subsets A, that has the highest plausibility, in terms of the information available through the obtained samples, of including $\boldsymbol{\varphi}^*$. This plausibility defines the quality of the identification and depends on $H(I)$; taking into account the fact that the average value of $P(F|\boldsymbol{\varphi})$ in the neighborhood of the optimal solution is the smallest in Φ, it is evident that smaller values of $H(\hat{I})$ (i.e., smaller than one) correspond to greater plausibility for the set $\hat{I}$ to include $\boldsymbol{\varphi}^*$. On the other hand, a value for $H(\hat{I})$ close to unity implies nearly the same average value for the objective function for subsets I and Φ; this case indicates that the search for the optimal I is challenging because the objective function is insensitive to the selection of I.

The stochastic subset optimization (21) is equivalent to identifying the subset, within A, that has the smallest density of samples of $p(\boldsymbol{\varphi}|F)$. This size of that subset is a compromise between (a) the resolution of $\boldsymbol{\varphi}^*$ and (b) the accuracy information about $H(I)$ that is extracted from the available samples. This accuracy is determined by the number of samples included in the identified subset as indicated by (20). Instead of trying to identify a small subset $\hat{I}$ in a single an iterative approach provides greater efficiency [29]. At iteration k, Markov Chain Monte Carlo (MCMC) simulation is implemented in order to obtain additional failure samples in $\hat{I}_{k-1}$ (where $\hat{I}_0 = \Phi$) that are distributed according to $p(\boldsymbol{\varphi}, \boldsymbol{\theta}|F)$, based on the existing samples in $\hat{I}_{k-1}$ from the previous step which are used as seeds for the Markov Chains. A region $\hat{I}_k \subset \hat{I}_{k-1}$ for the optimal design parameters is then identified as before, with the only difference that the search has been restricted within $\hat{I}_{k-1}$. An appropriate MCMC is given later in Sect. 5.3. The samples that are already available from the previous iteration of SSO may be used to form better proposal densities in the MCMC approach and increase the efficiency of the sampling process. Stopping criteria for the iterative process are established with respect to the value of $H(\hat{I})$, which is an indicator, as discussed earlier, of the quality of identification.

For the efficiency of the subset stochastic optimization (21) proper selection of the geometrical shape and size of the admissible sets is important. The geometrical shape should be chosen so that this optimization can be efficiently solved while the sensitivity of the objective function to each design variable is fully explored. For example, a hyper-ellipse is typically an appropriate choice. The size of admissible subsets is determined by incorporating a constraint for the number of samples ratio $\rho = N_I / N_\Phi$. This choice allows for directly controlling the coefficient of variation

(see (20)) and thus the accuracy of information that is extracted from the samples. The definition of A at the k iteration is then

$$A \triangleq A_\rho = \left\{ I \subset \hat{I}_{k-1}, I : \text{hyper} - \text{ellipse} | \rho = N_I / N_{\hat{I}_{k-1}} \right\} \tag{22}$$

The volume (size) of the admissible subsets in this scheme is adaptively chosen so that the ratio of samples in the identified set equals ρ.

Figure 4 illustrates some of these concepts for a two dimensional design application when the shape of admissible subsets is chosen as ellipses. X in these plots corresponds to $\boldsymbol{\varphi}^*$. In this example, SSO converges in only three iterations in a subset much smaller than the initial design space (look at part (f) of plot) that includes the optimal design variables. This also demonstrates the dependence of the quality of the identification on the value of $H(\hat{I}_k)$ for a two-dimensional example. This ratio expresses the difference in volume density of the samples inside and outside the identified set $\hat{I}_k$. In the first iteration, this difference is clearly visible. As SSO evolves and converges to subsets with smaller sensitivity to the objective function, the difference becomes smaller and by the last iteration (Fig. 4e), it is difficult to visually discriminate which region in the set has smaller volume density of failure samples. This corresponds to a decrease in the quality of the identification and is indication that SSO has reached an optimal candidate subset with small sensitivity and the iterative process should be stopped. More details about SSO, including

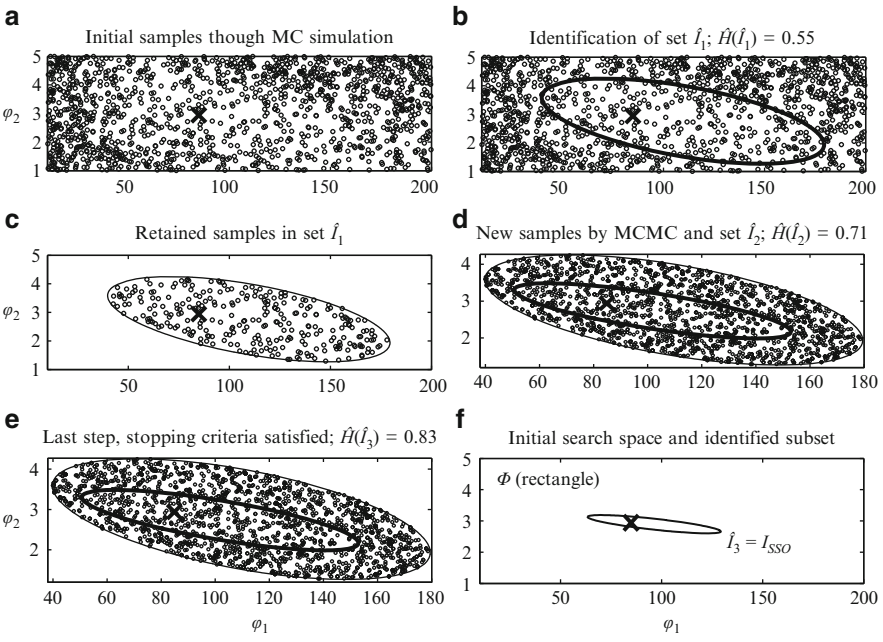


Fig. 4 Illustration of SSO process

a discussion on different stopping criteria for the iterative process, and topics on efficiently performing optimization (21) are discussed in detail in [29].

The SSO setting can be also used to obtain information about the sensitivity of the performance of the system to the model parameters [29]. The concept is similar to the sensitivity analysis for the design variables that was described; the difference is that the samples from $p(\boldsymbol{\varphi}, \boldsymbol{\theta}|F)$ are projected in this case onto the space Θ of the model parameters. The distribution of these samples compared to the prior distribution $p(\boldsymbol{\theta})$ expresses the sensitivity of the performance measure to the specific model parameters; bigger discrepancies between the distributions indicate greater importance of the corresponding model parameters in affecting the system performance. This can also be performed for each model parameter separately or for some selected group of the model parameters. Such information is important for understanding the influence of the model parameters on the system model performance and can be exploited in various ways, for example for establishing importance sampling densities, as will be discussed later.

5.2 Stochastic Optimization Framework

In a small number of iterations, the SSO algorithm will adaptively converge to a sub-region I_{SSO} containing $\boldsymbol{\varphi}^*$ that has small sensitivity with respect to all design variables. Note that for each iteration of the SSO algorithm, a single stochastic analysis is required. This means that SSO explores the sensitivity of the objective function in a highly efficient manner while identifying a smaller sub-region for the optimal design variables. SSO also gives information about the local behavior of the objective function. As long as the shape of the admissible subsets is close to the contours of the objective function near the optimal design point, the subset identified in the last stage of SSO provides a good estimate for these contours.

It is important to note that when SSO has converged, all designs in that set, denoted herein I_{SSO}, give nearly the same value of $P(F|\boldsymbol{\varphi})$ (because of the small sensitivity within I_{SSO}) and so can be considered near-optimal. It is noted though that there is no rigorous measure of the quality of the identified solution, i.e. how close $\boldsymbol{\varphi}_{SSO}$ is to $\boldsymbol{\varphi}^*$. If higher accuracy is required for the optimal design variables than given by $\boldsymbol{\varphi}_{SSO}$ at the center of I_{SSO}, a second optimization can be performed for pinpointing more precisely the optimal solution. Problem (15) is solved in this second stage exploiting *all information* available from SSO about the sensitivity with respect to *both* the design variables as well as the uncertain model parameters. The specific algorithm selected for the second stage determines the level of quality that should be established in the SSO identification. If a method is chosen that is restricted to search only within I_{SSO} (typically characteristic of gradient-free methods), then better quality is needed. The iterations of SSO should stop at a larger size set, and establish greater plausibility that the identified set includes the optimal design point. The efficiency of stochastic optimization (in the second stage) is influenced by (a) the size of the search space (defined by its volume), and, depending

on the characteristics of the algorithm chosen, by (b) the initial point $\boldsymbol{\varphi}_1$ at which the algorithm is initiated, and (c) the knowledge about the local behavior of the objective function in the search space. The SSO stage gives valuable insight for all these topics and can, therefore, contribute to increasing the efficiency of convergence to the optimal solution $\boldsymbol{\varphi}^*$ in the second stage. The set I_{SSO} has smaller size (volume) than the original design space Φ. Also, it is established that the sensitivity of the objective function with respect to all components of $\boldsymbol{\varphi}$ is small and, depending on the selection of the shape of admissible subsets, the correlation, or interaction, between the design variables may be identified by the orientation and relative size of I_{SSO} in Φ. This allows for efficient normalization of the design space (in selecting step sizes and blocking criteria), selection of the starting point for iterative algorithms (the center $\boldsymbol{\varphi}_{SSO}$ can be selected for this purpose), or choice of interpolating functions (for example, for objective function approximation methods). The study by Taflanidis and Beck [11] provides details on how SSO can be efficiently combined with the Simultaneous Perturbation Stochastic Approximation (SPSA) which has been proven efficient for simulation-based optimizations [26].

The results available from SSO for the sensitivity analysis with respect to the model parameters can be exploited to reduce the variance of the stochastic-simulation based estimate for the objective function by using Importance Sampling (IS) [24]. The *failure* samples available for the model parameters from the last iteration of the SSO stage are distributed proportional to the integrand in (10) and thus can be readily used to create efficient importance sampling densities $p_{is}(\boldsymbol{\theta})$. Since the set I_{SSO} is relatively small, it is anticipated that the different system designs will be close and thus the suggested IS densities will be efficient for all of them, i.e. for all $\boldsymbol{\varphi}$ in I_{SSO}. Au and Beck [32] provide a method for creating such adaptive IS densities using samples of the model parameters. For problems with a high-dimensional vector $\boldsymbol{\theta}$, IS densities should be formulated only for the set of the influential model parameters, to circumvent problems that might appear when applying IS in high-dimensional reliability problems [33, 34].

5.3 Markov Chain Monte Carlo Sampling Within SSO

The Metropolis-Hastings algorithm [25, 30] (which belongs to the MCMC family of algorithms) can be used for simulating conditional samples according to $p(\boldsymbol{\varphi}, \boldsymbol{\theta}|F)$ when samples that follow this distribution are already available. Assume there are N_a samples $[\boldsymbol{\varphi}, \boldsymbol{\theta}] \in F$ that lead to failure, available from the previous iteration of SSO, and a total $N > N_a$ are desired. Using each of the N_a original samples as a seed for a Markov Chain, additional $\text{int}[N/N_a] - 1$ failure samples are generated for each chain as follows:

1. Generate a candidate state $[\tilde{\boldsymbol{\varphi}}_{k+1}, \tilde{\boldsymbol{\theta}}_{k+1}]$ using a proposal PDF $q(\tilde{\boldsymbol{\varphi}}_{k+1}, \tilde{\boldsymbol{\theta}}_{k+1}|\boldsymbol{\varphi}_k, \boldsymbol{\theta}_k)$.

2. Compute the acceptance ratio

$$r_{k+1} = \frac{q\left(\boldsymbol{\varphi}_k, \boldsymbol{\theta}_k | \tilde{\boldsymbol{\varphi}}_{k+1}, \tilde{\boldsymbol{\theta}}_{k+1}\right) p\left(\tilde{\boldsymbol{\varphi}}_{k+1}, \tilde{\boldsymbol{\theta}}_{k+1}\right)}{q\left(\tilde{\boldsymbol{\varphi}}_{k+1}, \tilde{\boldsymbol{\theta}}_{k+1} | \boldsymbol{\varphi}_k, \boldsymbol{\theta}_k\right) p\left(\boldsymbol{\varphi}_k, \boldsymbol{\theta}_k\right)} \tag{23}$$

and set

$$[\boldsymbol{\varphi}_{k+1}, \theta_{k+1}] = \begin{cases} [\tilde{\boldsymbol{\varphi}}_{k+1}, \tilde{\theta}_{k+1}] \text{ with probability } \min(1, r_{k+1}) \\ [\boldsymbol{\varphi}_k, \theta_k] \text{ with probability } 1 - \min(1, r_{k+1}) \end{cases} \tag{24}$$

3. Perform a system analysis. If $[\boldsymbol{\varphi}_{k+1}, \boldsymbol{\theta}_{k+1}] \in F$ accept it as the next state; otherwise reject it and set $[\boldsymbol{\varphi}_{k+1}, \boldsymbol{\theta}_{k+1}] = [\boldsymbol{\varphi}_k, \boldsymbol{\theta}_k]$.

Since the initial samples are distributed according to $p(\boldsymbol{\varphi}, \boldsymbol{\theta} | F)$, the Markov Chain generated in this way is always in stationary state and all samples follow the target distribution, thus no burn-in period is needed. The efficiency of the algorithm depends on the selection of proposal densities $q(\tilde{\boldsymbol{\varphi}}_{k+1}, \tilde{\boldsymbol{\theta}}_{k+1} | \boldsymbol{\varphi}_k, \boldsymbol{\theta}_k)$. A detailed discussion on this topic is provided in [31].

For applications with high-dimensional vector $[\boldsymbol{\varphi}\boldsymbol{\theta}]^T$, like the example discussed in this chapter, the modified Metropolis-Hastings algorithm [30] could be used. The modified algorithm differs from the original in the way that the candidate state is generated in steps 1 and 2. In the modified version the parameters in $[\boldsymbol{\varphi}\boldsymbol{\theta}]^T$ are divided into groups and steps 1 and 2 are applied for each group separately. A detailed discussion on grouping guidelines, choice of proposal PDFs along with some other key issues for efficient MCMC simulation is presented in [30]. In the example in the current study, the design variables $\boldsymbol{\varphi}$ are grouped as a separate set and a *global uniform proposal* PDF $q(\tilde{\boldsymbol{\varphi}}_{k+1})$ is chosen. Such a global proposal PDF avoids rejecting samples due to their $\boldsymbol{\varphi}$ component, in the candidate sampling step, falling outside the given search space, which can occur with a local random walk proposal density, and which increases the correlation in the generated Markov Chain. Grouping of the uncertain parameters and selection of proposal densities follows the guidelines given in detail in [30] for earthquake engineering problems.

6 Illustrative Example

The design of passive protective devices for a three-story base isolated building is considered. The base-isolation system consists of lead-rubber bearings modeled by Eq. 5. The passive viscous dampers are modeled by Eq. 2 with a_d and c_d corresponding to the design variables for the problem. The initial design space for each of them is defined as $a_d \in [0.1, 2]$ and $c_d \in [0.1, 10]$MN s/m. A second design problem is also discussed, where a maximum forcing capacity equal to 1,250 kN is considered for the viscous dampers. This is incorporated in the model as a saturation of the damper force. This second design problem is denoted by D_2 and the initial one by D_1.

6.1 System and Excitation Models

The superstructure is modeled as a planar shear building with uncertain inter-story stiffness and uncertain classical modal damping. The lumped mass of the top story is 636 t while it is 817 t for the bottom two. The mass of the base is 999 t and the characteristics of the isolation system are selected as $k_p = 17.9\text{MN/m}$, $k_e = 119.26\text{MN/m}$, $U^y = 2\,\text{cm}$. These choices correspond to a natural period of 2.25 s for a reference base displacement of 0.3 m. The inter-story stiffnesses k_i of all the stories are parameterized by $k_i = \theta_{k,i}\hat{k}_i, i = 1, 2, 3$, where $[\hat{k}_i] = [633.9, 443.7, 253.6]\text{MN/m}$ are the most probable values for the inter-story stiffness, and $\theta_{k,i}$ are non-dimensional uncertain parameters, assumed to be correlated Gaussian variables with mean value one and covariance matrix $\mathbf{\Sigma}_{ij} = (0.1)^2\exp[-(i-j)^2/2^2]$, that roughly imply significant correlation between inter-story stiffnesses within two stories apart and a coefficient of variation (c.o.v) of 10%. The damping ratios for the modes are modeled as independent Gaussian variables with mean value 5% and coefficient of variation 10%.

In order to estimate the structural system reliability, probability models are established for the seismic hazard at the structural site. The uncertainty in moment magnitude for seismic events, M, is modeled by the Gutenberg-Richter relationship truncated to the interval $[M_{min}, M_{max}] = [6, 8]$, which leads to the PDF:

$$p(M) = \frac{b\exp(-bM)}{\exp(-bM_{\min}) - \exp(-bM_{\max})} \tag{25}$$

with regional seismicity factor selected as $b = 0.8\log_e(10)$. For the uncertainty in the event location, the logarithm of the epicentral distance, r, for the earthquake events is assumed to follow a Gaussian distribution with mean log(8) km and standard deviation 0.5. For the near-field pulse, the pulse frequency f_p and the peak ground velocity A_v are selected according to the probabilistic models for the characteristics of near-field pulses in rock sites given in [4]; the logarithms for f_p and the peak ground velocity A_v are modeled as Gaussian variables with standard deviation 0.39 and 0.4, respectively, and mean values:

$$\begin{aligned} \ln \hat{f}_p &= 8.60 - 1.32M \\ \ln \hat{A}_v &= 4.46 + 0.34M - 0.58\ln(r^2 + 7^2) \end{aligned} \tag{26}$$

The probability models for the number of half cycles and phase are chosen, respectively, as Gaussian with mean 1.8 and standard deviation 0.3, and uniform in the range $[-\pi/2, \pi/2]$. These probability models are based on the values reported in [3] when tuning the analytical relationship (6) to a wide range of recorded near-fault ground motions.

Failure, i.e., unacceptable performance, for the *system* is defined to be that any of the inter-story drifts, base displacement, or absolute floor accelerations exceed the thresholds 0.011m, 0.3m and $0.6g$, respectively. The limit state function, $\tilde{g}$,

quantifying the performance of the *system model* is expressed as the logarithm of the maximum over the excitation duration of these performance variables (normalized by their respective threshold). A small model prediction error ε is then assumed that is Gaussian with mean 0 and standard deviation 0.05 and has an additive influence on $\tilde{g}(\boldsymbol{\varphi}, \boldsymbol{\theta})$. Failure for the system is thus defined by the limit state function $g(\boldsymbol{\varphi}, \boldsymbol{\theta}) = \tilde{g}(\boldsymbol{\varphi}, \boldsymbol{\theta}) + \varepsilon$.

The uncertain model parameter vector in this design problem consists of the prediction error ε, the structural model parameters $\boldsymbol{\theta}_s$, the seismological parameter $\boldsymbol{\theta}_g = [M, r]$, the additional parameters for the near-fault pulse $\boldsymbol{\theta}_p = [A_p, f_p, \gamma_p, \nu_p]$ and the white-noise sequence, $\mathbf{Z}_w$, so $\boldsymbol{\theta} = [\varepsilon, \boldsymbol{\theta}_s, \boldsymbol{\theta}_g, \boldsymbol{\theta}_g, \boldsymbol{\theta}_p, \mathbf{Z}_w]$. Denoting the vector of model parameters without the prediction error by $\boldsymbol{\theta}_t = [\boldsymbol{\theta}_s, \boldsymbol{\theta}_g \boldsymbol{\theta}_g, \boldsymbol{\theta}_p, \mathbf{Z}_w]$ the probability of failure in (10) could be simplified

$$P(F|\boldsymbol{\varphi}) = \int_{\Theta} I_F(\boldsymbol{\varphi}, \boldsymbol{\theta}) p(\boldsymbol{\theta}) d\boldsymbol{\theta} = \int_{g(\boldsymbol{\varphi}, \boldsymbol{\theta}) > 0} p(\boldsymbol{\theta}) d\boldsymbol{\theta} = \int_{\varepsilon + \tilde{g}(\boldsymbol{\varphi}, \boldsymbol{\theta}) > 0} p(\boldsymbol{\theta}) d\boldsymbol{\theta}$$
$$= \int \int_{\varepsilon > -\tilde{g}(\boldsymbol{\varphi}, \boldsymbol{\theta})} p(\varepsilon) p(\boldsymbol{\theta}_t) d\varepsilon d\boldsymbol{\theta}_t = \int_{\Theta_t} P_{\varepsilon}\left(\tilde{g}(\boldsymbol{\varphi}, \boldsymbol{\theta})\right) p(\boldsymbol{\theta}_t) d\boldsymbol{\theta}_t \quad (27)$$

where $P_{\varepsilon}(.)$ corresponds to the cumulative distribution function for the model prediction error. The fact that the probability model for ε is symmetric was used in deriving the last equality. As will be discussed next this expression for the objective function will de preferred in the second stage of the optimization framework.

6.2 Stochastic Optimization Results

The two-stage framework discussed in Sect. 5.2 is implemented for the design optimization. Cumulative results are reported in Table 1. V_{Φ} in this table denotes the size (area for our two-dimensional application) of the initial design space and V_{Isso} the area of the set identified by SSO. SSO was used first to perform a global sensitivity analysis for $\boldsymbol{\varphi}$ and $\boldsymbol{\theta}$ with choice for the shape of the admissible subsets as hyper-ellipses, parameter selection $\rho = 0.2$ and simulation of $N = 3{,}000$ failure samples at each stage of the optimization. In both problems SSO converged in just two iterations to a subset with small sensitivity to the design variables, consisting of near-optimal solutions. Small here is quantified as $H(\hat{I}_k) > 0.8$.

Table 1 Cumulative results for the stochastic optimization

∼	∼	$\boldsymbol{\varphi}_{SSO}$	$P_F(\boldsymbol{\varphi}_{\mathrm{SSO}})$	Φ^*	$P_F(\boldsymbol{\varphi}^*)$	$\sqrt[n_{\varphi}]{\frac{V_{ISSO}}{V_{\Phi}}}$
D_1	c_d(MN s/m)	3.52	0.0745	3.26	0.0728	0.29
	a_d	0.92		0.85		
D_2	c_d(MN s/m)	5.65	0.0835	5.41	0.0794	0.28
	a_d	0.89		0.82		

A second optimization stage was then implemented to pinpoint the exact optimal solution $\boldsymbol{\varphi}^*$; the algorithm selected for this stage is the stochastic perturbation stochastic approximation (SPSA) [26]. In this case use of Common Random Numbers (CRN) is adopted and the expression of the objective function in (23) is selected. This choice is motivated by the fact that contrary to the discontinuous indicator function, the CDF $P_\varepsilon(.)$ in (23) is smooth and thus it facilitates a better implementation of CRN. A detailed discussion on efficiency of CRN is provided in [11]. A sample size of $N = 1{,}000$ was used for each evaluation of the objective function (note that two evaluations are required per iteration) and importance sampling densities were established for the influential model parameters (see discussion later on) using information from the last stage of SSO.

The results in Table 1 indicate that SSO efficiently identifies the set I_{SSO} containing $\boldsymbol{\varphi}^*$ and leads to a significant reduction of the size of the search space; the mean reduction per design variable (last column of Table 1) is close to 72%. Additionally, the converged optimal solution in the second stage, $\boldsymbol{\varphi}^*$, is close to the center, $\boldsymbol{\varphi}_{SSO}$, of the set that is identified by SSO and the objective function at that point, $P_F(\boldsymbol{\varphi}_{SSO})$, is not significantly different from the optimal value $P_F(\boldsymbol{\varphi}^*)$. Thus, although selection of $\boldsymbol{\varphi}_{SSO}$ as the design choice would lead to a sub-optimal design, it is close to the optimal one in terms of both the design vector values and its corresponding performance. These characteristics, along with the small computational burden needed to converge to I_{SSO}, illustrate the effectiveness and quality of the set identification in SSO.

6.3 Sensitivity for the Model Parameters

SSO gives additionally information about the sensitivity of the stochastic performance with respect to the uncertain model parameters. This is established by looking at the distribution of the failure samples available for $\boldsymbol{\theta}$ (these samples correspond to samples from $p(\boldsymbol{\theta}|F)$). Since the number of these parameters is large we will discuss in detail only the important results.

For the structural model parameters, $\boldsymbol{\theta}_s$, this distribution, $p(\boldsymbol{\theta}_s|F)$, does not differ significantly from their prior distribution $p(\boldsymbol{\theta}_s)$; only a small (almost -10%) shift of the mean value was found. This means that these model parameters have only a small influence to the structural performance. The same pattern applies to the model prediction error because this error was selected to be relatively small and thus it cannot have a dominant influence on the system failure, compared to the rest of the model parameters.

The results for the stochastic excitation model present more interesting characteristics. First of all, the white noise input $\mathbf{Z}_w$ was found to have no significant influence on the structural performance. The comparison was established here by looking at the frequency content of the sequence $\mathbf{Z}_w$; the spectral content for samples from $p(\mathbf{Z}_w|F)$ was found to be similar to their original (flat) spectrum. The same general remark applies to the phase of the near field pulse v_p for which the samples

from $p(v_p|F)$ had distribution similar to $p(v_p)$. The five remaining excitation model parameters, that is, the moment magnitude, M, epicentral distance, r, peak ground velocity, A_v, number of half cycles, γ_p and frequency, f_p, were found to have a more important influence on the model response, with the first three having the most significant impact (distribution of failure samples defers significantly from $p(\boldsymbol{\theta})$). Samples for both $p(\boldsymbol{\theta})$ and $p(\boldsymbol{\theta}|F)$ when $\boldsymbol{\varphi} \in I_{SSO}$ are shown in Fig. 5. The samples are presented for pairs of the model parameters to investigate the correlation between them.

The failure samples for the model parameters M,r and A_v concentrate in regions with smaller epicentral distance and larger magnitude and peak ground velocity. These values for the model parameters correspond to near-source excitations with stronger characteristics that have important bearing on the response of the base-isolated structure (even though such excitations are less likely to occur). With respect to the peak ground velocity A_v, the distribution moves to larger amplitudes,

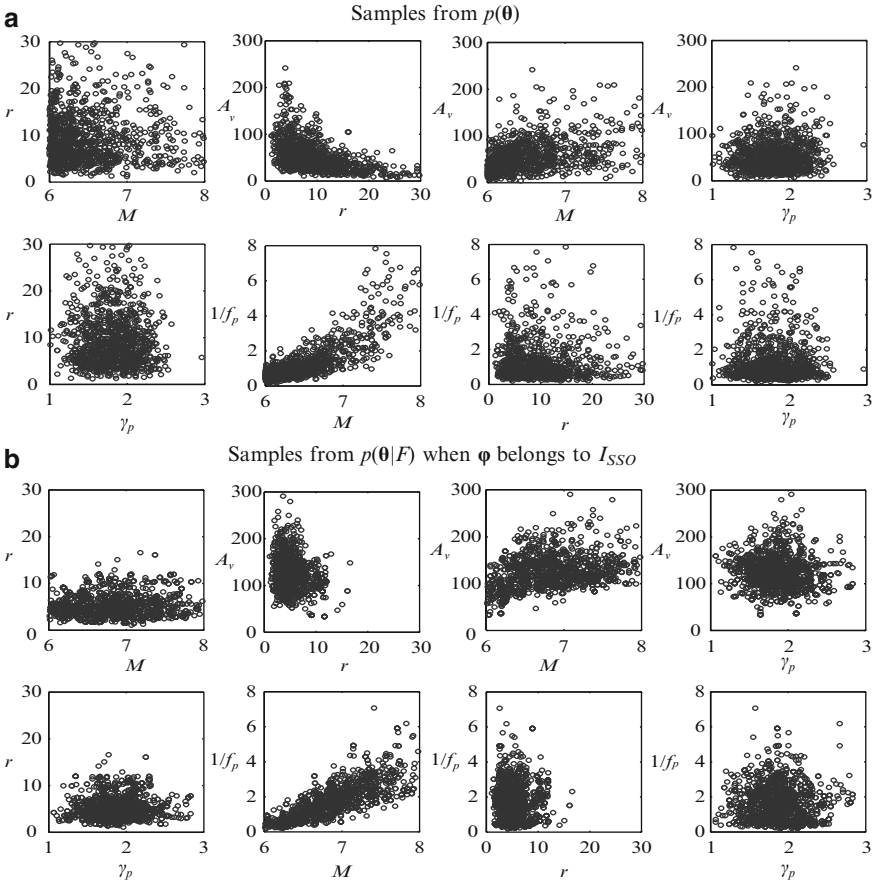


Fig. 5 Samples for eight pairs of the near-fault excitation model parameters M, r (km), A_v (cm/s), γ_p, $1/f_p$(s); samples from both (**a**) $p(\boldsymbol{\theta})$ and (**b**) $p(\boldsymbol{\theta}|F)$ when $\boldsymbol{\varphi} \in I_{SSO}$ are shown

especially for large epicentral distance. This behavior is anticipated since the near-source pulse has smaller amplitude when the epicentral distance is large; for such distances only pulses with stronger characteristics may lead to system failure. This means that the correlation between r and A_v changes from the initial distribution given by Eq. 20. A similar pattern holds here for the relationship of A_v to M but to a smaller degree; this last characteristic can be attributed to the fact that the epicentral distance has greater importance to the pulse amplitude according to the probability models established in this study.

For the two remaining of the model parameters, the distribution for the γ_p failure samples slightly changes, whereas the failure samples for f_p concentrate in regions closer to the natural frequency of the base-isolated structure (unison). This is anticipated, since unison conditions between the isolated structure and the pulse component of the near-fault ground motion lead to significant increase in the dynamic response. The correlation between γ_p or f_p and the other model parameters does not significantly change. There is some degree of correlation between them though; for values of $1/f_p$ close to the fundamental period for the structure the distribution for the failure samples of γ_p moves to larger values, which corresponds to excitations with larger number of pulse cycles and thus greater potential impact on the dynamic behavior. Though the probability of such pulses is low, the unison characteristics of the excitation enhance their effect and increase the overall failure likelihood. It is interesting to note that no such pattern exists between γ_p and any of the other excitation model parameters.

All of the above comments give valuable insight into the influence of the stochastic excitation on the system performance and illustrate that the properties of that excitation are more significant to the system reliability than are the structural system characteristics. This illustrates that greater care should be given to choosing and updating the probability models for the stochastic excitation.

Additionally, since significant differences are exhibited between $p(\boldsymbol{\theta})$ and $p(\boldsymbol{\theta}|F)$ for some of the model parameters, it is anticipated that formulation of IS densities, as discussed in Sect. 5.2, will be beneficial to the accuracy of the objective function evaluation in (14) the second optimization stage. An average reduction of the c.ov. for the estimate of the failure probability by a factor of 3 was reported when using such information to formulate IS densities for all influential model parameters for this specific example. Since this c.o.v varies as $1/N^{1/2}$ [24], the sample size for direct estimation of the failure probability (i.e. without use of IS) with the same level of accuracy as in the case when IS is applied would be approximately nine times larger. This illustrates another benefit of the sensitivity analysis for the model parameters established through SSO.

6.4 Seismic Protection Design Characteristics

The performance of the seismic protection system is reported in Table 2, which includes the failure probability for the base isolated structure with no dampers, as well as for the D_1 and D_2 optimal designs. The partial failure probabilities for each

Table 2 Performance of base-isolated structures

		Partial failure probabilities		
Case	$P_F(\boldsymbol{\varphi})$	Drifts	Base displacement	Acceleration
No Damper	0.1203	0.079	0.117	0.0130
D_1	0.0748	0.063	0.054	0.0098
D_2	0.0794	0.067	0.065	0.0097

of the three groups of performance variables considered (inter story drift, absolute acceleration and base displacement) are also presented.

The probability of failure, given that a near-field earthquake has occurred, is 12% for the base isolated structure. Among the different response quantities the probability that the base displacement will exceed the prescribed acceptable bound is by far the greatest. The addition of the dampers provides a significant improvement in the system reliability. This is established by primarily prioritizing the reduction of the base displacement over the other response quantities. The performance for application D_2 is worse than problem D_1, especially with respect to the base displacement. This is anticipated because of the constraint on the damper forcing capabilities.

It is important to note that the optimal design configuration (reported in Table 1) even for the design problem D_1 corresponds to a nonlinear damper (value for a different than one). Design problem D_2 of course corresponds by default to a nonlinear configuration because of the force saturation. Additionally, note that the optimal damper characteristics for design problem D_2 are different than the ones of problem D_1; this means that the limitation on the damper forcing capabilities has an impact on the optimal design. The overall reliability performance, though, for application D_2 does not significantly differ over D_1 under optimal design. This means that as long as the limited forcing capabilities of the actuators are appropriately accounted for in the design stage they do not impose a big constraint on the optimal performance. All these remarks illustrate the importance of having a design framework that can explicitly account for nonlinearities in the system response.

7 Conclusions

A simulation-based framework for robust stochastic design of viscous dampers for base-isolated applications was discussed. In this framework structural performance is evaluated by nonlinear simulation that can incorporate all important model characteristics and potentially complex performance quantifications. All available information about the structural model and the characteristics of expected future earthquakes are accounted for by appropriate probability models. A realistic excitation model was also discussed for characterizing near-field earthquakes and an efficient approach was presented for performing the associated design optimization and additionally establishing a sensitivity analysis with respect to the uncertain model parameters. This approach is based on the novel algorithm SSO.

The methodology was illustrated through application to a base isolated building with nonlinear viscous dampers. Uncertainty was considered for both the structural model characteristics as well as for the parameters of the near-fault excitation model and the regional seismicity. The design optimization was efficiently performed using SSO. The sensitivity analysis with respect to the uncertain model parameters provided valuable insight into their influence on the stochastic system performance. The parameters of the stochastic excitation were found to have a significantly greater importance, compared to the ones for the structural system. The results also showed that the addition of the optimally designed dampers provides a significant improvement for the seismic performance of the isolated structure and that nonlinearities of the damper behavior are appropriately addressed in the context of the proposed framework.

References

1. Christopoulos C, Filiatrault A (2006) Principles of passive supplemental damping and seismic isolation. IUSS Press, Pavia
2. Hall FF, Heaton TH, Halling MW, Wald DJ (1995) Near-source ground motion and its effects on flexible buildings. Earth Spectra 11:569–605
3. Mavroeidis GP, Papageorgiou AP (2003) A mathematical representation of near-fault ground motions. B Seismol Soc of Am 93:1099–1131
4. Bray JD, Rodriguez-Marek A (2004) Characterization of forward-directivity ground motions in the near-fault region. Soil Dyn Earth Eng 24:815–828
5. Makris N, Black JB (2004) Dimensional analysis of bilinear oscillators under pulse-type excitations. J Eng Mech-ASCE 130:1019–1031
6. Zhang YF, Iwan WD (2002) Protecting base isolated structures from near-field ground motion by tuned interaction damper. J Eng Mech ASCE 128:287–295
7. Narasimhan S, Nagarajaiah S, Gavin HP, Johnson EA (2006) Smart base isolated benchmark building part I: problem definition. J Struct Control Health Monitor 13:573–588
8. Providakis CP (2008) Effect of LRB isolators and supplemental viscous dampers on seismic isolated buildings under near fault excitation. Eng Struct 30:1187–1198
9. Kelly JM (1999) The role of damping in seismic isolation. Earth Eng Struct Dyn 28:3–20
10. Taflanidis AA, Scruggs JT, Beck JL (2008) Probabilistically robust nonlinear design of control systems for base-isolated structures. J Struct Control Health Monitor 15:697–719
11. Taflanidis AA, Beck JL (2008) An efficient framework for optimal robust stochastic system design using stochastic simulation. Comput Method Appl Mech Eng 198:88–101
12. Lee D, Taylor DP (2001) Viscous damper development and future trends. Struct Des Tall Buil 10:311–320
13. Park YJ, Wen YK, Ang AHS (1986) Random vibration of hysteretic systems under bi-directional ground motions. Earth Eng Struct Dyn 14:543–557
14. Boore DM (2003) Simulation of ground motion using the stochastic method. Pure Appl Geophys 160:635–676
15. Atkinson GW, Silva W (2000) Stochastic modeling of California ground motions. B Seismol Soc Am 90:255–274
16. Alavi B, Krawinkler H (2000) Consideration of near-fault ground motion effects in seismic design. In: 12th World conference on earthquake engineering, Auckland, New Zealand
17. Boore DM, Joyner WB (1997) Site amplifications for generic rock sites. B Seismol Soc Am 87:327–341
18. Jaynes ET (2003) Probability theory: the logic of science. Cambridge University Press, Cambridge

19. Taflanidis AA, Beck JL (2009) Life-cycle cost optimal design of passive dissipative devices. Struct Saf 31:508–522
20. Papadimitriou C, Beck JL, Katafygiotis LS (2001) Updating robust reliability using structural test data. Probabilist Eng Mech 16:103–113
21. Enevoldsen I, Sorensen JD (1994) Reliability-based optimization in structural engineering. Struct Saf 15:169–196
22. Royset JO, Der Kiureghian A, Polak E (2006) Optimal design with probabilistic objective and constraints. J Eng Mech ASCE 132:107–118
23. Gasser M, Schueller GI (1997) Reliability-based optimization of structural systems. Math Method Oper Res 46:287–307
24. Robert CP, Casella G (2004) Monte Carlo statistical methods, 2nd edn. Springer, New York
25. Ruszczynski A, Shapiro A (2003) Stochastic programming. Elsevier, New York
26. Spall JC (2003) Introduction to stochastic search and optimization. Wiley-Interscience, New York
27. Royset JO, Polak E (2004) Reliability-based optimal design using sample average approximations. Probabilist Eng Mech 19:331–343
28. Taflanidis AA, Beck JL (2008) Stochastic subset optimization for optimal reliability problems. Probabilist Eng Mech 23:324–338
29. Taflanidis AA, Beck JL (2009) Stochastic subset optimization for reliability optimization and sensitivity analysis in system design. Comput Struct 87:318–331
30. Au SK, Beck JL (2003) Subset simulation and its applications to seismic risk based on dynamic analysis. J Eng Mech ASCE 129:901–917
31. Berg BA (2004) Markov Chain Monte Carlo simulations and their statistical analysis. World Scientific Singapore
32. Au SK, Beck JL (1999) A new adaptive importance sampling scheme. Struct Saf 21:135–158
33. Au SK, Beck JL (2003) Importance sampling in high dimensions. Struct Saf 25:139–163
34. Pradlwater HJ, Schueller GI, Koutsourelakis PS, Champris DC (2007) Application of line sampling simulation method to reliability benchmark problems. Struct Saf 29:208–221

Uncertainty Modeling and Robust Control for Smart Structures

A. Moutsopoulou, G.E. Stavroulakis, and A. Pouliezos

Abstract In this work a robust control problem for smart beams is studied. First the structural uncertainties of basic physical parameters are considered in the model of a composite beam with piezoelectric sensors and actuators subjected to wind-type loading. The control mechanism is introduced and is designed with the purpose to keep the bean in equilibrium in the event of external wind disturbances and in the presence of mode inaccuracies using the available measurement and control under limits. For this model we considered the analysis and synthesis of a H_∞-controller with the aim to guarantee the robustness with respect to parametric uncertainties of the beam and of external loads. In addition a robust m-controller was analyzed and synthesized, using the $D - K$ Iterative method. The results are compared and commented upon using the various controllers.

Keywords Uncertainty · Smart beam · Stochastic load · Robust performance · Robust analysis · Robust synthesis

1 Introduction

The field of smart structures has been an emerging area of research for the last few decades [2–5, 9]. Smart structures (also called smart material structures) can be defined as structures that are capable of sensing and actuating in a controlled manner in response to a stimulus. The development of this field is supported by the development in the field of materials science and in the field of control. In materials science, new smart materials are developed that allow them to be used for sensing and actuation in an efficient and controlled manner. These smart materials are to be integrated with the structures so they can be employed as actuators and sensors

A. Moutsopoulou, G.E. Stavroulakis (✉), and A. Pouliezos
Department of Production Engineering and Management, Technical University of Crete, GR-73100 Chania, Greece
e-mail: amalia@dpem.tuc.gr; gestavr@dpem.tuc.gr; tasos@dpem.tuc.gr

M. Papadrakakis et al. (eds.), *Computational Methods in Earthquake Engineering*, Computational Methods in Applied Sciences 21, DOI 10.1007/978-94-007-0053-6_15,
© Springer Science+Business Media B.V. 2011

effectively. It is also clear that the field of smart structures also involves the design and implementation of the control systems on the structures. A well designed and implemented controller for smart structures is thus desirable.

In this paper we introduce uncertainties in smart structures. The control system aims at suppressing undesirable ones and/or enhancing desirable effects. We study an example of such a structure: an intelligent beam with integrated piezoelectric actuators, the goal of which is to suppress oscillations under stochastic loads. First we examine the H_∞ criterion which takes into account the worst case scenarion of uncertain disturbances or noise in the system. Therefore, it is possible to synthesize a H_∞ controller which will be robust with respect to a predefined number of uncertainties in the model. Then by which among other, may take into account non-linearity of the structure, damage or other changes from the nominal model, a robust m-controller was analyzed and synthesized, using the $D-K$ iterative method. The results are very good: the oscillations were suppressed even for a real aeolian load, with the voltages of the piezoelectric components' lying within their endurance limits.

2 Mathematical Modelling

A cantilever slender beam with rectangular cross-sections is considered. Four pairs of piezoelectric patches are embedded symmetrically at the top and the bottom surfaces of the beam, as shown in Fig. 1. The beam is from graphite-epoxy $T300-976$ and the piezoelectric patches are $PZTG1195N$. The top patches act like sensors and the bottom like actuators. The resulting composite beam is modelled by means of the classical laminated technical theory of bending. Let us assume that the mechanical

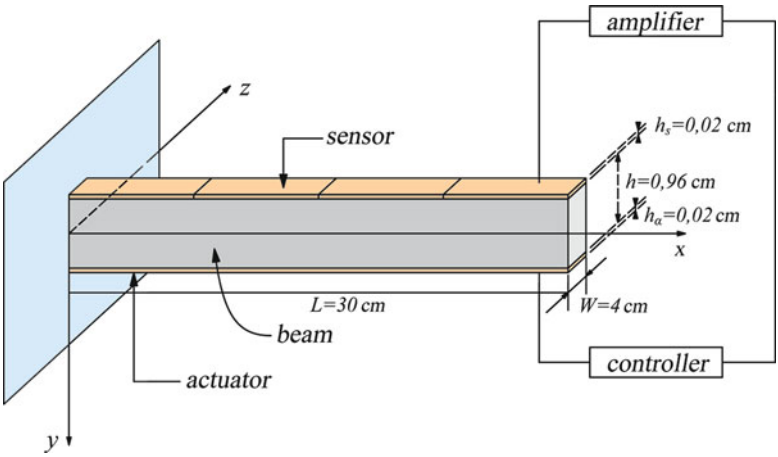


Fig. 1 Beam with piezoelectric sensors/actuators

properties of both the piezoelectric material and the host beam are independent in time. The thermal effects are considered to be negligible as well [9].

The beam has length L, width b and thickness h. The sensors and the actuators have width b_S and b_A and thickness h_S and h_A, respectively. The electromechanical parameters of the beam of interest are given in the table.

Parameters of the Composite Beam

Parameters	Values
Beam length, L	0.3 m
Beam width, W	0.04 m
Beam thickness, h	0.0096 m
Beam density, ρ	1600 kg/m
Youngs modulus of the beam, E	1.5×10^{11} N/m^2
Piezoelectric constant, d_{31}	254×10^{-12} m/V
Electric constant, ξ_{33}	11.5×10^{-3} Vm/N
Young's modulus of the piezoelectric element	1.5×10^{11} N/m^2
Width of the piezoelectric element	$b_S = b_a = 0.04$ m
Thickness of the piezoelectric element	$h_S = h_a = 0.0002$ m

2.1 Piezoelectric Equations

In order to derive the basic equations for piezoelectric sensors and actuators (S/As), we assume that:

- The piezoelectric S/A are bonded perfectly on the host beam;
- The piezoelectric layers are much thinner then the host beam;
- The piezoelectric material is homogeneous, transversely isotropic and linearly elastic;
- The piezoelectric S/A are transversely polarized (in the z-direction) [9].

Under these assumptions the three-dimensional linear constitutive equations are given by [8],

$$\begin{Bmatrix} \sigma_{xx} \\ \sigma_{xz} \end{Bmatrix} = \begin{bmatrix} Q_{11} & 0 \\ 0 & Q_{55} \end{bmatrix} \left(\begin{Bmatrix} \varepsilon_{xx} \\ \varepsilon_{xz} \end{Bmatrix} - \begin{bmatrix} d_{31} \\ 0 \end{bmatrix} E_z \right) \tag{1}$$

$$D_z = Q_{11} d_{31} \varepsilon_{xx} + \xi_{xx} E_z \tag{2}$$

where σ_{xx}, σ_{xz} denote the axial and shear stress components, D_z, denotes the transverse electrical displacement; ε_{xx} and ε_{xz} are a axial and shear strain components; Q_{11}, and Q_{55}, denote elastic constants; d_{31}, and ξ_{33}, denote piezoelectric and dielectric constants, respectively. Equation (1) describes the inverse piezoelectric effect and Eq. (2) describes the direct piezoelectric effect. E_z, is the transverse

component of the electric field that is assumed to be constant for the piezoelectric layers and its components in the xy-plain are supposed to vanish. If no electric field is applied in the sensor layer, the direct piezoelectric Eq. (2) gets the form,

$$D_z = Q_{11} d_{31} \varepsilon_{xx} \tag{3}$$

and it is used to calculate the output charge created by the strains in the beam [7].

2.2 Equations of Motion

We assume that:

- The beam centroidal and elastic axis coincides with the x-coordinate axis so that no bending-torsion coupling is considered;
- The axial vibration of the host beam is considered negligible;
- The displacement field $\{u\} = (u_1, u_2, u_3)$ is obtained based on the usual Timoshenko assumptions [1],

$$\begin{aligned} u_1(x, y, z) &\approx z\phi(x, t) \\ u_2(x, y, z) &\approx 0 \\ u_3(x, y, x) &\approx w(x, t) \end{aligned} \tag{4}$$

where ϕ is the rotation of the beam's cross-section about the positive y-axis and w is the transverse displacement of a point of the centroidal axis ($y = z = 0$).

The strain displacement relations can be applied to Eq. (4) to give,

$$\varepsilon_{xx} = z\frac{\vartheta \phi}{\vartheta x} \quad \varepsilon_{xz} = \phi + \frac{\vartheta w}{\vartheta x} \tag{5}$$

We suppose that the transverse shear deformation ε_{xx} is equal to zero [2].

In order to derive the equations of the motion of the beam we use Hamilton's principle,

$$\int_{t_2}^{t_1} (\delta T - \delta U + \delta W) dt = 0, \tag{6}$$

where T [11] is the total kinetic energy of the system, U is the potential (strain) energy and W is the virtual work done by the external mechanical and electrical loads and moments. The first variation of the kinetic energy is given by,

$$\begin{aligned} \delta T &= \frac{1}{2} \int_V \rho \left\{ \frac{\vartheta u}{\vartheta t} \right\}^r \left\{ \frac{\vartheta u}{\vartheta t} \right\} dV \\ &= \frac{b}{2} \int_0^L \int_{-\frac{h}{2}-h_a}^{\frac{h}{2}+h_s} \rho \left(z\frac{\vartheta \phi}{\vartheta t} \delta \frac{\vartheta \phi}{\vartheta t} + \frac{\vartheta w}{\vartheta t} \delta \frac{\vartheta w}{\vartheta t} \right) dz dx \end{aligned} \tag{7}$$

The first variation of the kinetic energy is given by,

$$\begin{aligned}\delta U &= \frac{1}{2}\int_V \delta\{\epsilon\}^T\{\sigma\}dV \\ &= \frac{b}{2}\int_0^L \int_{-\frac{h}{2}-h_a}^{\frac{h}{2}+h_s}\left[Q_{11}\left(z\frac{\vartheta w}{\vartheta x}\delta\right)\left(z\frac{\vartheta w}{\vartheta x}\right)\right]dzdx\end{aligned} \tag{8}$$

If the load consists only of moments induced by piezoelectric actuators and since the structure has no bending twisting couple then the first variation of the work has the form [11],

$$\delta W = b\int_0^L M^a\delta\left(\frac{\vartheta\phi}{\vartheta x}\right)dx \tag{9}$$

where M^a is the moment per unit length induced by the actuator layer and is given by,

$$M^a = \int_{-\frac{h}{2}-h_a}^{-\frac{h}{2}} z\sigma_{xx}^a dz = \int_{-\frac{h}{2}-h_a}^{-\frac{h}{2}} zQ_{11}d_{31}E_z^a dz\left(E_z^a = \frac{V_a}{h_a}\right) \tag{10}$$

2.3 Finite Element Formulation

We consider a beam element of length L_e, which has two mechanical degrees of freedom at each node: one translational ω_1 (respectively ω_2) in direction y and one rotational ψ_1 (respectively ψ_2), as it is shown in Fig. 2.

The vector of nodal displacements and rotations q_e is defined as [8],

$$q_e = [\omega_1, \psi_1, \omega_2, \psi_2] \tag{11}$$

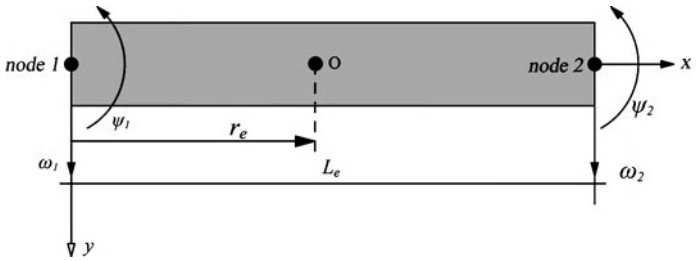


Fig. 2 Beam finite element

The transverse deflection $\omega(x,t)$ and rotation $\psi(x,t)$ along the beam are continuous and they are interpolated by Lagrange linear shape functions H_i^{ω} and H_i^{ψ} as follows [5],

$$\omega(x,t) = \sum_{i=1}^{4} H_i^{\omega}(x) q_i(t)$$
$$\psi(x,t) = \sum_{i=1}^{4} H_i^{\psi}(x) q_i(t) \tag{12}$$

This classical finite element procedure leads to the approximate (discretized) problem. For a finite element the discrete differential equations are obtained by substituting the discretized expressions (12) into Eqs. (7) and (8) to evaluate the kinetic and strain energies. Integrating over spatial domains and using the Hamilton's principle (6) the equation of motion for a beam element are expressed in terms of nodal variable q as follows [2,6,8],

$$M\ddot{q}(t) + D\dot{q}(t) + Kq(t) = f_m(t) + f_e(t) \tag{13}$$

where M is the generalized mass matrix, D the viscous damping matrix, K the generalized stiffness matrix, f_m the external loading vector and f_e the generalized control force vector produced by electromechanical coupling effects. The independent variable vector $q(t)$ is composed of transversal deflections ω_i and rotations ψ_i, i.e., [4]

$$q(t) = \begin{bmatrix} \omega_1 \\ \psi_1 \\ \vdots \\ \omega_n \\ \psi_n \end{bmatrix} \tag{14}$$

where n is the number of nodes used in the analysis. Vectors w and f_m are positive upwards. For the state-space control transformation, let (in the usual manner),

$$\dot{x}(t) = \begin{bmatrix} q(t) \\ \dot{q}(t) \end{bmatrix} \tag{15}$$

Furthermore to express $f_e(t)$ as $Bu(t)$ we write it as $f_e^* u$, where f_e^* is the piezoelectric force for a unit applied on the corresponding actuator, and u represents the voltages on the actuators. Furthermore, $d(t) = f_m(t)$ is the disturbance vector [3]. Then,

$$\dot{x}(t) = \begin{bmatrix} 0_{2n\times 2n} & I_{2n\times 2n} \\ -M^{-1}K & -M^{-1}D \end{bmatrix} x(t) + \begin{bmatrix} 0_{2n\times n} \\ M^{-1} f_e^* \end{bmatrix} u(t) + \begin{bmatrix} 0_{2n\times 2n} \\ M^{-1} \end{bmatrix} \tag{16}$$

$$= Ax(t) + Bu(t) + Gd(t) = Ax(t) + \begin{bmatrix} B & G \end{bmatrix} \begin{bmatrix} u(t) \\ d(t) \end{bmatrix} = Ax(t) + \tilde{B}\tilde{u}(t) \quad (17)$$

The previous description of the dynamical system will be augmented with the output equation (*displacements* only measured) [5],

$$y(t) = [x_1(t) \quad x_3(t) \quad \dots \quad x_{n-1}(t)]^T = Cx(t) \quad (18)$$

In this formulation u is $n \times 1$ (at most, but can be smaller), while d is $2n \times 1$. The units used are compatible for instance m, rad, sec and N [6, 8].

3 Design Objectives and System Specifications

The structured singular value of the transfer function is defined as,

$$\mu(M) = \begin{cases} \frac{1}{\min_{k_m}\{det(I - k_m M\Delta) = 0,\ \bar{\sigma}(\Delta) \leq 1\}} \\ 0, \ \Delta \ det(I - M\Delta) = 0 \end{cases} \quad (19)$$

In words it defines the smallest structured $\mu(M)$ (measured in terms of $\bar{\sigma}(\Delta)$) which makes $det(I - M\Delta) = 0$: then $\mu(M) = \frac{1}{\bar{\sigma}(\Delta)}$. It follows that values of μ smaller than 1 are desired [12].

The design objectives fall into two categories:

1. Stability of closed loop system (plant+controller).
   a. Disturbance attenuation with satisfactory transient characteristics (overshoot, settling time).
   b. Small control effort.
2. Robust performance

Stability of closed loop system (plant+controller) should be satisfied in the face of modelling errors.

In order to obtain the required system specifications with respect to the above objectives we need to represent our system in the so-called - Δ structure. Let us start with the simple typical diagram of Fig. 3 [13, 14].

In this diagram there are two inputs, d and n, and two outputs, u and x. In what follows it is assumed that,

$$\left\| \begin{matrix} d \\ n \end{matrix} \right\|_2 \leq 1, \quad \left\| \begin{matrix} x \\ u \end{matrix} \right\|_2 \leq 1 \quad (20)$$

If that's not the case, appropriate frequency-dependent weights can transform original signals so that the transformed signals have this property. The details of the system are given in Fig. 4.

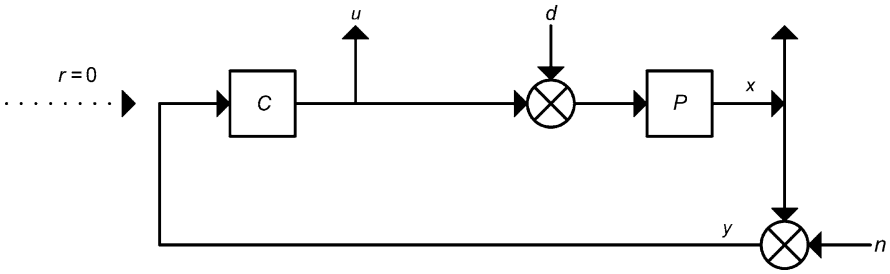


Fig. 3 Classical control block diagram (P: plant dynamical system, C: controller)

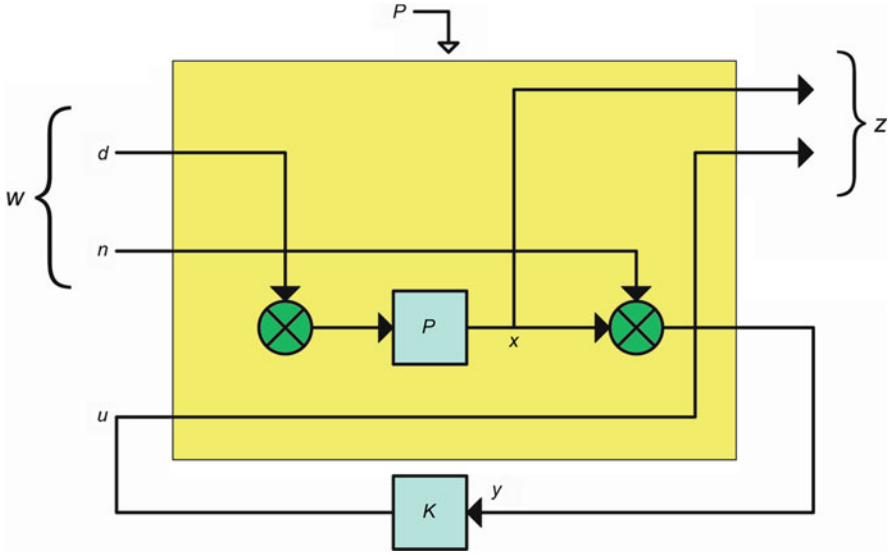


Fig. 4 Detailed two-port diagram (with a linear feedback control K)

In this description,

$$z = \begin{bmatrix} u \\ x \end{bmatrix}, \quad w = \begin{bmatrix} d \\ n \end{bmatrix} \tag{21}$$

where z are the output variables to be controlled, and w the exogenous inputs.

Given that P has two inputs and two outputs it is (Fig. 5), as usual, naturally partitioned as,

$$\begin{bmatrix} z(s) \\ y(s) \end{bmatrix} = \begin{bmatrix} P_{zw}(s) & P_{zu}(s) \\ P_{yw}(s) & P_{yu}(s) \end{bmatrix} \begin{bmatrix} w(s) \\ u(s) \end{bmatrix} = P(s) \begin{bmatrix} w(s) \\ u(s) \end{bmatrix} \tag{22}$$

In addition the controller is written,

$$u(s) = K(s)y(s) \tag{23}$$

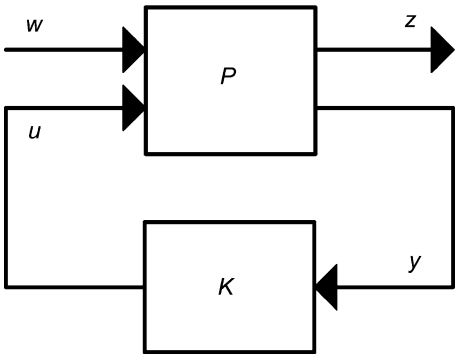


Fig. 5 Two-port diagram

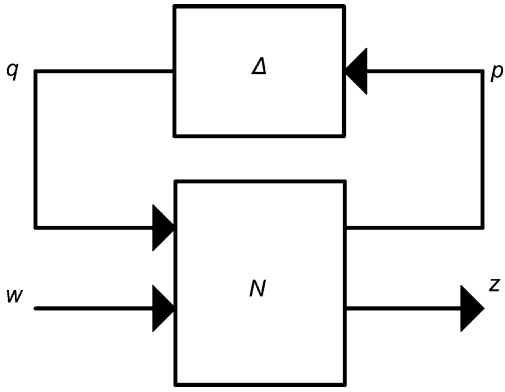


Fig. 6 Two-port diagram with uncertainty

Substituting Eq. (22) in Eq. (23) gives the closed loop transfer function $N_{zw}(s)$,

$$N_{zw}(s) = P_{zw}(s) + P_{zu}(s)K(s)(I - P_{yu}(s)K(s))^{-1}P_{yw}(s) \tag{24}$$

To deduce robustness specifications a further diagram is needed, namely that of Fig. 6: where N is defined by Eq. (24) and the uncertainty modelled in Δ satisfies $||\Delta||_\infty \leq 1$ (details later). Here,

$$z = \mathscr{F}_u(N, \Delta)w = [N_{22} + N_{21}\Delta(I - N_{11}\Delta)^{-1}N_{12}]w = Fw \tag{25}$$

Given this structure we can state the following definitions:

$$\begin{gathered}
\text{Nominal stability } (NS) \Leftrightarrow N \text{ internally stable} \\
\text{Nominal performance } (NP) \Leftrightarrow ||N_{22}(j\omega)||_\infty \leq 1 \ \forall\omega \text{ and } NS \\
\text{Robust stability } (RS) \Leftrightarrow F = \mathscr{F}_u(N, \Delta) \text{ stable } \forall\Delta,\ ||\Delta||_\infty < 1 \text{ and } NS \\
\text{Robust performance } (RP) \Leftrightarrow ||F||_\infty < 1,\ \forall\Delta,\ ||\Delta||_\infty < 1 \text{ and } S
\end{gathered} \tag{26}$$

It has been proved that the following conditions hold in the case of block-diagonal real or complex perturbations Δ:

1. The system is nominally stable if M is internally stable.
2. The system exhibits nominal performance if $\bar{\sigma}(N_{22}(j\omega)) < 1$.
3. The system (M, Δ) is robustly stable if and only if,

$$\sup_{\omega \in \mathbb{R}} \mu_{\Delta}(N_{11}(j\omega)) < 1 \tag{27}$$

   where μ_{Δ} is the structured singular value of N given the structured uncertainty set Δ. This condition is known as the generalized small gain theorem.
4. The system (N, Δ) exhibits robust performance if and only if,

$$\sup_{\omega \in \mathbb{R}} \mu_{\Delta_a}(N(j\omega)) < 1 \tag{28}$$

   where,

$$\Delta_a = \begin{bmatrix} \Delta_p & 0 \\ 0 & \Delta \end{bmatrix} \tag{29}$$

   and Δ_p is full complex, has the same structure as Δ and dimensions corresponding to w, z [15].
   Unfortunately, only bounds on μ can be estimated.

3.1 Controller Synthesis

All the above results support the analysis problem and provide tools to judge the performance of any controller or to compare different controllers. However it is possible to approximately synthesize a controller that achieves given performance in terms of the structured singular value μ.

In this procedure, which is called $(D, G - K)$ iteration [20] the problem of finding an μ-optimal controller K such that $\mu(\mathscr{F}_u(F(j\omega)), K(j\omega)) \leq \beta$, $\forall \omega$ is transformed into the problem of finding transfer function matrices $D(\omega) \in \mathscr{D}$ and $G(\omega) \in \mathscr{G}$, such that,

$$\sup_{\omega} \bar{\sigma} \left[\left(\frac{D(\omega)\mathscr{F}_u(F(j\omega), K(j\omega))D^{-1}(\omega)}{\gamma} - jG(\omega) \right) \left(I + G^2(\omega)\right)^{-\frac{1}{2}} \right] \leq 1, \quad \forall \omega \tag{30}$$

Unfortunately this method does not guarantee even finding local maxima. However for complex perturbations a method known as $D-K$ iteration is available (implemented in MATLAB) [20]. It combines H_{∞} synthesis and μ-analysis and often yields good results. The starting point is an upper bound on μ in terms of the scaled singular value,

$$\mu(N) \leq \min_{D \in \mathscr{D}} \bar{\sigma}(DND^{-1}) \tag{31}$$

The idea is to find the controller that minimizes the peak over the frequency range namely,

$$\min_{K}\left(\min_{D\in\mathscr{D}}||DN(K)D^{-1}||_{\infty}\right) \tag{32}$$

by alternating between minimizing $||DN(|K)D^{-1}||_{\infty}$ with respect to either K or D (while holding the other fixed).

1. **K-step**. Synthesize an $\mathscr{H}_{\infty}$ controller for the scaled problem $\min_K ||DN(K)$ $D^{-1}||_{\infty}$ with fixed $D(s)$.
2. **D-step**. Find $D(j\omega)$ to minimize at each frequency $\bar{\sigma}(DND^{-1}(j\omega))$ with fixed N.
3. Fit the magnitude of each element of $D(j\omega)$ to a stable and minimum phase transfer function $D(s)$ and got to Step 1 [20].

3.2 System Uncertainty

Let us assume uncertainty in the mass M and K matrices of the form,

$$\begin{aligned} K &= K_0(I + k_p I_{2n\times 2n}\delta_K) \\ M &= M_0(I + m_p I_{2n\times 2n}\delta_M) \end{aligned} \tag{33}$$

Alternatively, since in general the Rayleigh damping assumption is,

$$D = aK + \beta M \tag{34}$$

D could be expressed similarly to K, M, as,

$$D = D_0(I + d_p I_{2n\times 2n}\delta_D) \tag{35}$$

In this way we introduce uncertainty in the form of percentage variation in the relevant matrices. Uncertainty is most likely to arise from terms outside the main matrices (since length can be adequately measured).

Here it will be assumed,

$$||\Delta||_{\infty} \stackrel{def}{=} \left\| \left[\begin{array}{c|c} I_{n\times n}\delta_K & 0_{n\times n} \\ \hline 0_{n\times n} & I_{n\times n}\delta_M \end{array}\right] \right\|_{\infty} < 1 \tag{36}$$

hence m_p, k_p are used to scale the percentage value and the zero subscript denotes nominal values. (it is reminded that the norm for a matrix $A_{n\times n}$ is calculated through $||A||_{\infty} = \max_{1\le j\le m}\sum_{j=1}^{n}|a_{ij}|$)

With these definitions Eq. 13 becomes,

$$
\begin{aligned}
&M_0(I + m_p I_{2n\times 2n}\delta_M)\ddot{w}(t) + K_0(I + k_p I_{2n\times 2n}\delta_K)w(t) \\
&\quad + [D_0 + 0.0005[K_0 k_p I_{2n\times 2n}\delta_K + M_0 m_p I_{2n\times 2n}\delta_M]]\dot{w}(t) \\
&= f_m(t) + f_e(t) \\
&\Rightarrow M_0\ddot{w}(t) + D_0\dot{q}(t) + K_0 w(t) = -[M_0 m_p I_{2n\times 2n}\delta_M \ddot{w}(t) \\
&\quad + 0.0005[K_0 k_p I_{2n\times 2n}\delta_K + M_0 m_p I_{2n\times 2n}\delta_M]\dot{w}(t) + K_0 k_p I_{2n\times 2n}\delta_K w(t)] \\
&= f_m(t) + f_e(t) \\
&\Rightarrow M_0\ddot{w}(t) + D_0\dot{w}(t) + K_0 w(t) = \tilde{D}q_u(t) + f_m(t) + f_e(t)
\end{aligned} \tag{37}
$$

where,

$$
q_u(t) = \begin{bmatrix} \ddot{w}(t) \\ \dot{w}(t) \\ w(t) \end{bmatrix} \tag{38}
$$

$$
\begin{aligned}
\tilde{D} &= -\begin{bmatrix} M_0 m_p & K_0 k_p \end{bmatrix} \left[\begin{array}{c|c} I_{2n\times 2n}\delta_M & 0_{2n\times 2n} \\ \hline 0_{2n\times 2n} & I_{2n\times 2n}\delta_K \end{array}\right] \begin{bmatrix} I_{2n\times 2n} & 0.0005 I_{2n\times 2n} & 0_{2n\times 2n} \\ 0_{2n\times 2n} & 0.0005 I_{2n\times 2n} & I_{2n\times 2n} \end{bmatrix} \\
&= G_1 \cdot \Delta \cdot G_2
\end{aligned} \tag{39}
$$

Writing (37) in state space form, gives,

$$
\begin{aligned}
\dot{x}(t) &= \begin{bmatrix} 0_{2n\times 2n} & I_{2n\times 2n} \\ -M^{-1}K & -M^{-1}D \end{bmatrix} x(t) + \begin{bmatrix} 0_{2n\times 2n} \\ M^{-1} f_e^* \end{bmatrix} u(t) + \begin{bmatrix} 0_{2n\times 2n} \\ M^{-1} \end{bmatrix} d(t) \\
&\quad + \begin{bmatrix} 0_{2n\times 6n} \\ M^{-1}F_1 \cdot \Delta \cdot G_2 \end{bmatrix} q_u(t) \\
&= Ax(t) + Bu(t) + Gd(t) + G_u G_2 q_u(t)
\end{aligned} \tag{40}
$$

In this way we treat uncertainty in the original matrices as an extra uncertainty term. To express our system in the form of Fig. 6, consider Fig. 7.

The matrices E_1, E_2 are used to extract,

$$
q_u(t) \overset{def}{=} \begin{bmatrix} \ddot{w}(t) \\ \dot{w}(t) \\ w(t) \end{bmatrix} \tag{41}
$$

Since,

$$
\gamma = \begin{bmatrix} \dot{w}(t) \\ \ddot{w}(t) \end{bmatrix} \qquad \beta = \int \begin{bmatrix} \dot{w}(t) \\ \ddot{w}(t) \end{bmatrix} dt = \begin{bmatrix} w(t) \\ \dot{w}(t) \end{bmatrix} \tag{42}
$$

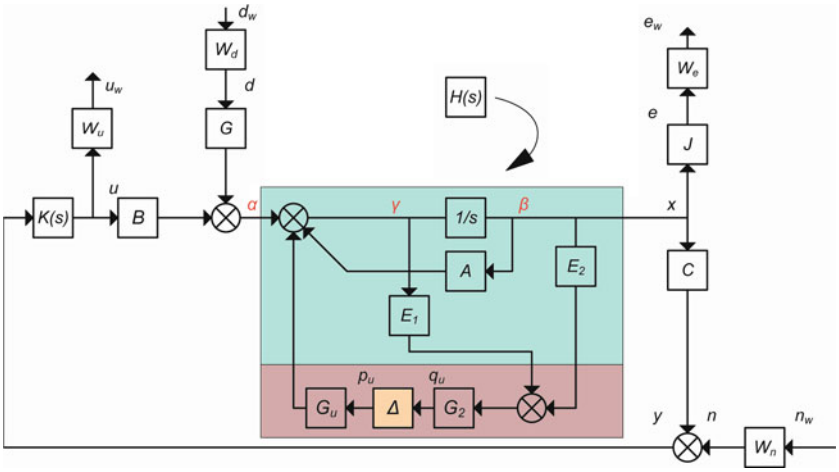


Fig. 7 Uncertainty block diagram

appropriate choices for E_1, E_2 are,

$$E_1 = \begin{bmatrix} 0_{2n\times 2n} & \vdots & I_{2n\times 2n} \\ \cdots & \vdots & \cdots \\ I_{2n\times 2n} & \vdots & 0_{2n\times 2n} \\ \cdots & \vdots & \cdots \\ 0_{2n\times 2n} & \vdots & 0_{2n\times 2n} \end{bmatrix}, \quad E_2 = \begin{bmatrix} 0_{2n\times 2n} & \vdots & 0_{2n\times 2n} \\ \cdots & \vdots & \cdots \\ 0_{2n\times 2n} & \vdots & 0_{2n\times 2n} \\ \cdots & \vdots & \cdots \\ I_{2n\times 2n} & \vdots & 0_{2n\times 2n} \end{bmatrix} \tag{43}$$

The idea is to find an N such that,

$$\begin{bmatrix} q_u \\ \cdots \\ e_w \\ u_w \end{bmatrix} = N \begin{bmatrix} p_u \\ \cdots \\ d_w \\ n_w \end{bmatrix}, \quad N = \begin{bmatrix} N_{p_u q_u} & \vdots & N_{d_w q_u} & N_{n_w q_u} \\ \cdots & \vdots & \cdots & \cdots \\ N_{p_u e_w} & \vdots & N_{d_w e_w} & N_{n_w e_w} \\ N_{p_u u_w} & \vdots & N_{d_w u_w} & N_{n_w u_w} \end{bmatrix} = \begin{bmatrix} N_{11} & N_{12} \\ N_{21} & N_{22} \end{bmatrix} \tag{44}$$

or in the notation of Fig. 6

$$\begin{bmatrix} q_u \\ w \end{bmatrix} = N \begin{bmatrix} p_u \\ z \end{bmatrix} \tag{45}$$

Now $N_{d_w e_w}$, $N_{n_w e_w}$, $N_{n_w u_w}$ are known. For the rest we will use a methodology known as "pulling out the Δ's". To this end, break the loop at points p_u, q_u (which

will be used as additional inputs/outputs respectively) and use the auxiliary signals a, β, γ. To get the transfer function $N_{d_w q_u}$ (from d_w to q_u):

$$q_u = G_2(E_2\beta + E_1\gamma) = G_2\left(E_2\frac{1}{s} + E_1\right)\gamma \tag{46}$$

$$\gamma = GW_d d_w + Bu + A\frac{1}{s}\gamma = GW_d d_w + BKC\frac{1}{s}\gamma + A\frac{1}{s}\gamma \tag{47}$$

$$\Rightarrow \gamma = \left(I - BKC\frac{1}{s} - A\frac{1}{s}\right)^{-1} GW_d d_w \tag{48}$$

Hence,

$$N_{d_w q_u} = G_2\left(E_2\frac{1}{s} + E_1\right)\left(I - BKC\frac{1}{s} - A\frac{1}{s}\right)^{-1} GW_d \tag{49}$$

Now, $N_{p_u q_u}$, $N_{p_u e_w}$, $N_{p_u u_w}$, are similar to $N_{d_w q_u}$, $N_{d_w e_w}$, $N_{d_w u_w}$, with GW_d replaced by G_u, i.e.,

$$\begin{aligned} N_{p_u q_u} &= G_2\left(E_2\frac{1}{s} + E_1\right)\left(I - BKC\frac{1}{s} - A\frac{1}{s}\right)^{-1} G_u \\ N_{p_u e_w} &= W_y JH[I + B[K(I - CHBK)^{-1}CH]]G_u \\ M_{p_u u_w} &= W_u K(I - CHBK)^{-1}CHG_u \end{aligned} \tag{50}$$

Finally to find $N_{n_w q_u}$,

$$q_u = G_2(E_2\beta + E_1\gamma) = G_2\left(E_2\frac{1}{s} + E_1\right)\gamma \tag{51}$$

$$\gamma = Bu + A\frac{1}{s}\gamma = BK(W_n n_w + y) + A\frac{1}{s}\gamma = BKW_n n_w + BKC\frac{1}{s}\gamma + A\frac{1}{s}\gamma \tag{52}$$

$$\Rightarrow \gamma = \left(I - BKC\frac{1}{s} - A\frac{1}{s}\right)^{-1} BKW_n n_w \tag{53}$$

Hence,

$$N_{n_w q_u} = G_2\left(E_2\frac{1}{+}E_1\right)\left(I - BKC\frac{1}{s} - A\frac{1}{s}\right)^{-1} BKW_n \tag{54}$$

Collecting all the above yields N:

$$N = \begin{bmatrix} G_2\left(E_2\frac{1}{s}+E_1\right)\left(I-BKC\frac{1}{s}-A\frac{1}{s}\right)^{-1}G_u & G_2\left(E_2\frac{1}{s}+E_1\right)\left(I-BKC\frac{1}{s}-A\frac{1}{s}\right)^{-1}GW_d & G_2\left(E_2\frac{1}{s}+E_1\right)\left(I-BKC\frac{1}{s}-A\frac{1}{s}\right)^{-1}BKW_u \\ W_e JH\left[I+BK(I-CHBK)^{-1}CF\right]G_u & W_e J(I-HBKC)^{-1}HGW_d & W_e J(I-HBKC)^{-1}HBKW_u \\ W_u K(I-CHBK)^{-1}CFG_u & W_u(I-KCHB)^{-1}KCHGW_d & W_u(I-KCHB)^{-1}KW \end{bmatrix} \tag{55}$$

Having obtained N for the beam problem, all proposed controllers $K(s)$ can be compared using the structured singular value relations [18, 19, 21].

4 Robustness Issues

The superiority of H_∞ control lies in its ability to take explicitly into account the worst effect of unknown disturbances and noise in the system. Furthermore, at least in theory, it is possible to synthesize an H_∞ controller that is robust to a prescribed amount of modeling errors. Unfortunately, this last possibility is not implementable in some cases, as it will be subsequently illustrated [16, 17].

In what follows, the robustness to modeling errors of the designed H_∞ controller will be analyzed. Furthermore an attempt to synthesize a μ-controller will be presented, and comparisons between the two will be made.

In all simulations, routines from Matlab's Robust Control Toolbox will be used. In particular:

1. For uncertain elements,
2. To calculate bounds on the structured singular value,
3. To calculate a μ-controller.

Numerical models used in all simulations, are implemented in three ways:

1. Through Eq. (56)

$$\begin{aligned} K &= K_0(I + k_p I_{2n\times 2n}\delta_K) \\ M &= M_0(I + m_p I_{2n\times 2n}\delta_M) \\ D &= D_0 + 0,0005[K_0 k_p I_{2n\times 2n}\delta_K + M_0 m_p I_{2n\times 2n}\delta_M] \end{aligned} \tag{56}$$

   and subsequent evaluation of matrix N for specific values of k_p, m_p.
2. By use of Matlab's "uncertain element object". As explained, this form is needed in the D-K robust synthesis algorithm.
3. By Simulink implementation of Fig. 8.

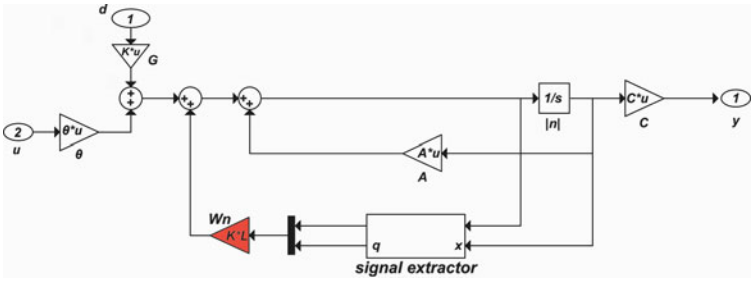


Fig. 8 Simulink diagram of uncertain plant

4.1 Robust Analysis: Results

Robust analysis is carried out through the relations:

$$\sup_{\omega\in\mathbb{R}} \mu_{\Delta}(N_{11}(j\omega)) < 1 \tag{57}$$

for robust stability, and,

$$\sup_{\omega\in\mathbb{R}} \mu_{\Delta_a}(N(j\omega)) < 1 \tag{58}$$

for robust performance.

In all the simulations that follow the disturbance is the first mechanical load, i.e. $10N$ at the free end. For the H_∞ found, robust analysis was performed for the following values of m_p, k_p:

1. $m_p = 0, k_p = 0.9$. This corresponds to a $\pm$ 90% variation from the nominal value of the stiffness matrix K.
   In Fig. 9 are shown the displacement responses for this controller for the first mechanical input. In Fig. 10 are shown the bounds on the μ values. As seen the system remains stable and exhibits robust performance, since the upper bounds of both values remain below 1 for all frequencies of interest. This result is validated in Fig. 11, where the displacement of the free end and the voltage applied are shown at the extreme uncertainty. Comparison with the open loop response for the same plant shows the good performance of the nominal controller.
2. $m_p = 0.9, k_p = 0$. This corresponds to a $\pm$ 90% variation from the nominal value of the mass matrix M.

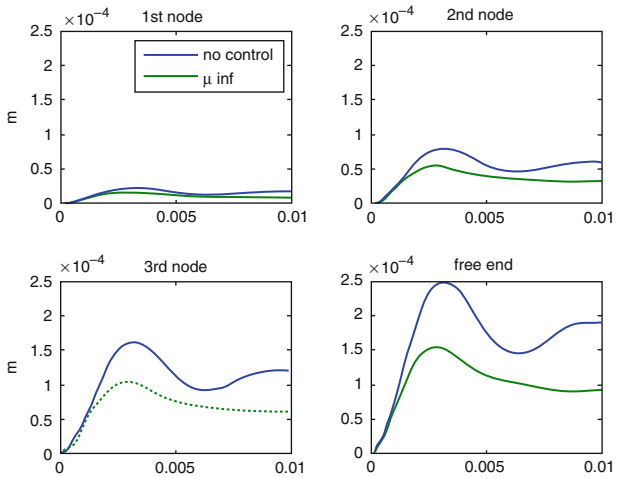


Fig. 9 Displacement response loading equal to 10 N at free end, μ-controller for $m_p = 0, k_p = 0.9$

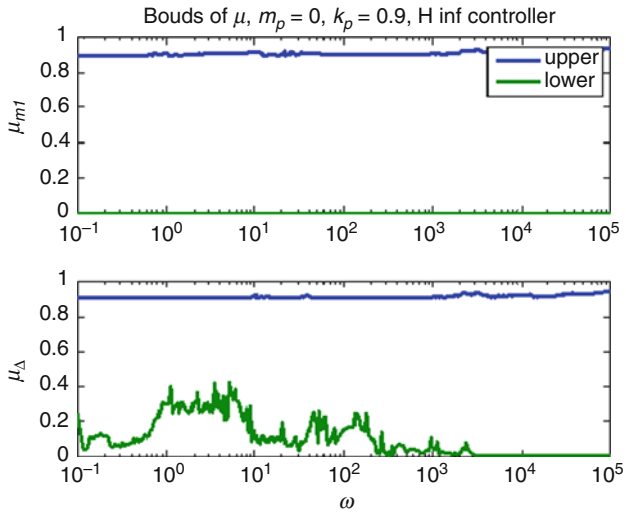


Fig. 10 μ-bounds of the H_∞ controller for $m_p = 0$, $k_p = 0.9$

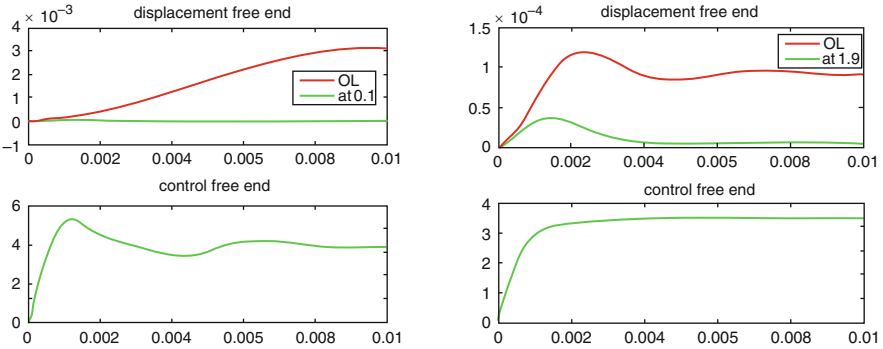


Fig. 11 Displacement and control at free end for the H_∞ controller with $m_p = 0$, $k_p = 0.9$ (extreme values)

In Fig. 12 are shown the bounds on the μ values. As seen the system remains stable and exhibits robust performance, since the upper bounds of both values remain below 1 for all frequencies of interest. This result is validated in Fig. 13, where the displacement of the free end and the voltage applied are shown. Comparison with the open loop response for the same plant shows the good performance of the nominal controller.

3. $m_p = 0.9$, $k_p = 0.9$. This corresponds to a $\pm 90\%$ variation from the nominal values of both the mass and stiffness matrices M, K.

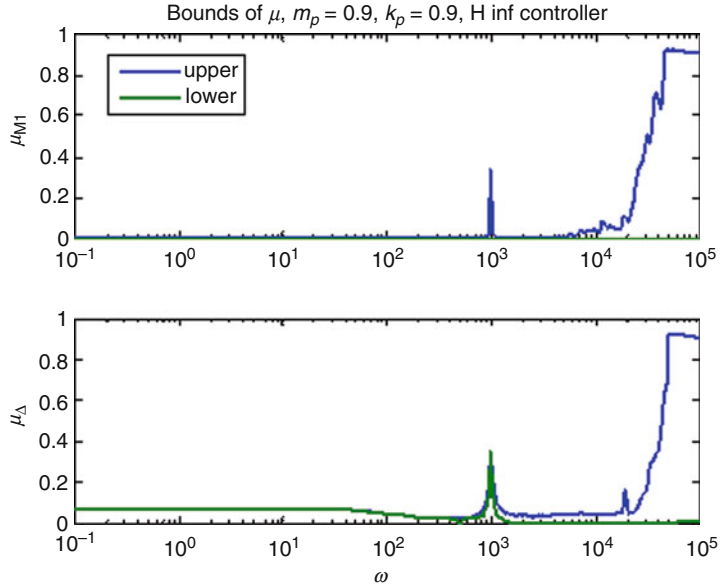


Fig. 12 μ-bounds of the H_∞ controller for $m_p = 0.9$, $k_p = 0$

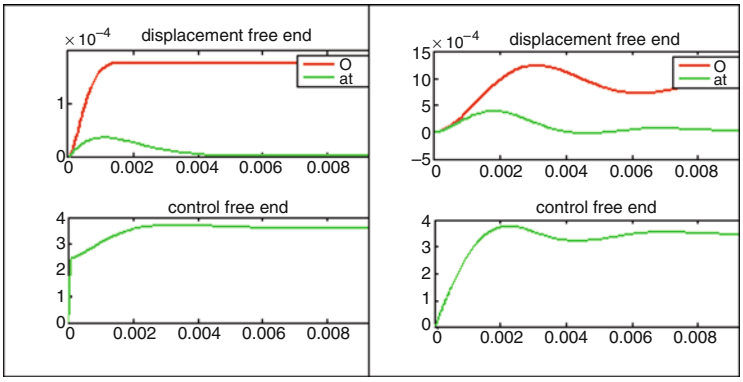


Fig. 13 Displacement and control at free end for the H_∞ controller with $m_p = 0.9$, $k_p = 0$ (extreme values)

In Fig. 14 are shown the bounds on the μ values. As seen the system remains stable and exhibits robust performance, since the upper bounds of both values remain below 1 for all frequencies of interest. This result is validated in Fig. 15, where the displacement of the free end and the voltage applied are shown. Comparison with the open loop response for the same plant shows the good performance of the nominal controller.

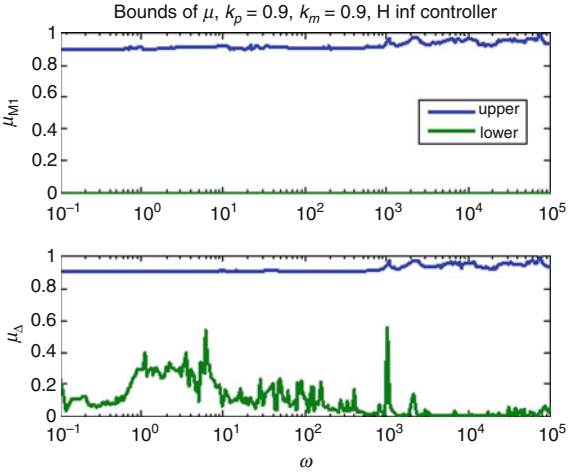


Fig. 14 Displacement and control at free end for the H_∞ controller with $m_p = 0.9$, $k_p = 0$ (extreme values)

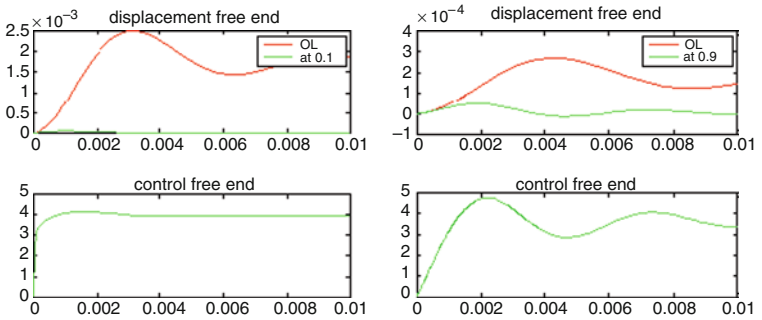


Fig. 15 Displacement and control at free end for the H_∞ controller with $m_p = 0.9$, $k_p = 0$ (extreme values)

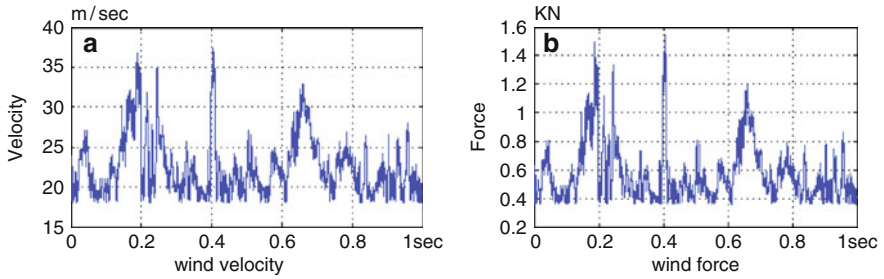


Fig. 16 Wind force and velocity

Concluding, it has been demonstrated that the H_∞ controller found is extremely robust in model variations.

Furthermore, a typical stochastic wind–type load is considered (Fig. 16). We change the mass M, the viscous K and A and B matrices of the system.

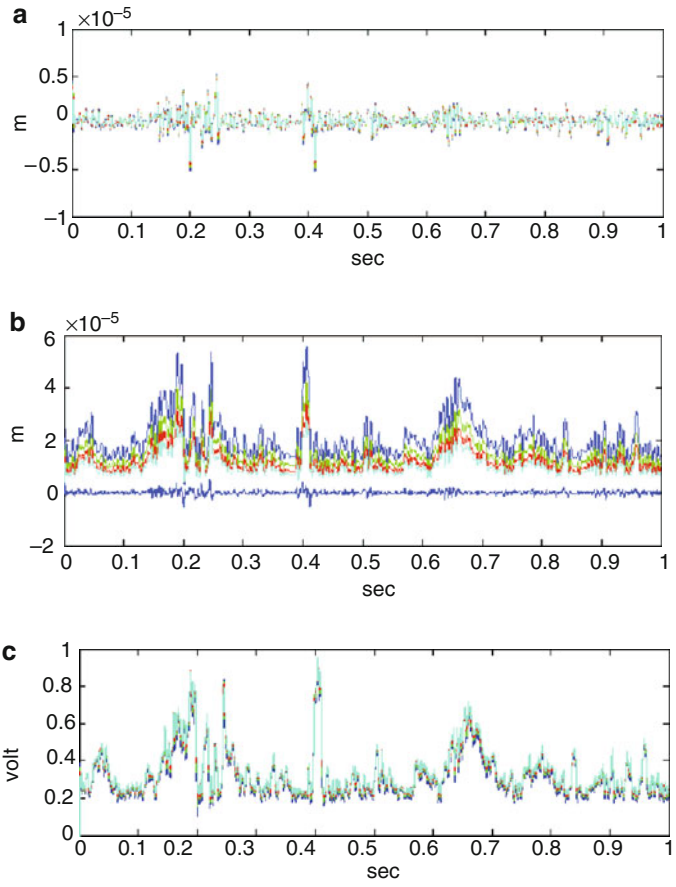


Fig. 17 ± 50% variation from the nominal values of the mass and the viscous matrices (**a**) The displacement of the free end of the beam with control (**b**) The displacement of the free end of the beam with and without control who corresponds to a ± 50% variation from the nominal values of the mass and the viscous matrices (**c**) The applied voltages of the free end

In Fig. 17 are shown the free end of the beam with and without control who corresponds to a ± 50% variation from the nominal value of the mass matrix and the viscous matrix of the beam, and the applied voltages of the free end.

In Fig. 18 are shown the free end of the beam with and without control, who corresponds to a ± 50% variation from the nominal value of the matrix A and B of the beam and the applied voltages of the free end.

The beam with the control keeps in equilibrium and we have zero displacements, event for the changes of the mass, viscous, and the A and B matrices of the system.

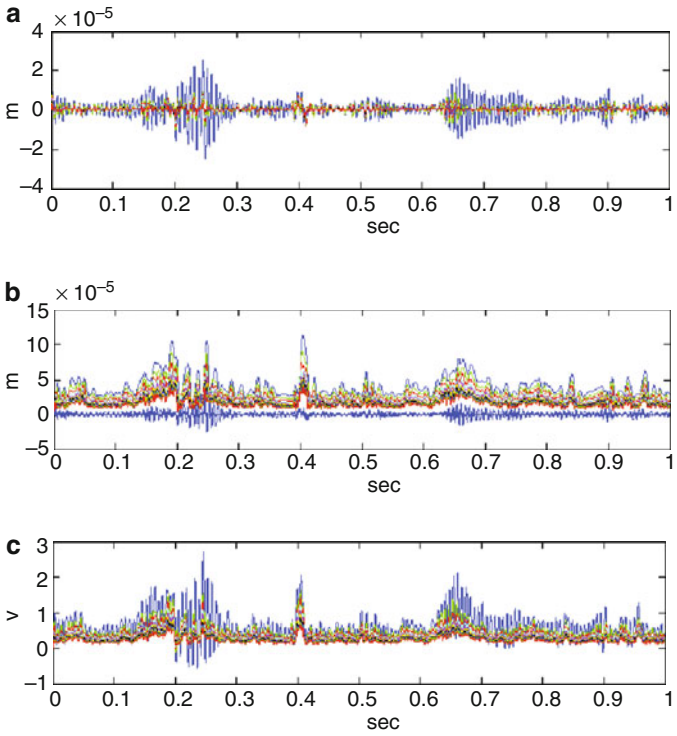


Fig. 18 $\pm$ 50% variation from the nominal values of the A and B (**a**) The displacement of the free end of the beam with control (**b**) The displacement of the free end of the beam with and without control who corresponds to a $\pm$ 50% variation from the nominal values of the matrices A and B of the system (**c**) The applied voltages of the free end

4.2 Robust Synthesis: μ-Controller

A μ-controller can be synthesized via the procedure of D-K μ iteration As explained, this an approximate procedure, providing bounds on the μ-value. To facilitate comparison with the H_∞ controller, similar bounds for the uncertainty will be used.

1. $m_p = 0, k_p = 0.9$. This corresponds to a $\pm 90\%$ variation from the nominal value of the stiffness matrix K.

In Fig. 19 μ-values of the calculated controller are shown. As seen the controller is robust in most frequencies.

In Fig. 20 performance of the μ and H_∞ controllers is compared at the free end (this is indicative of overall performance). As seen the H_∞ controller performs better at the expense of increased control effort. Figure 21 (left window) verifies this result, where it is seen that the H_∞ controller performs better at the extreme value.

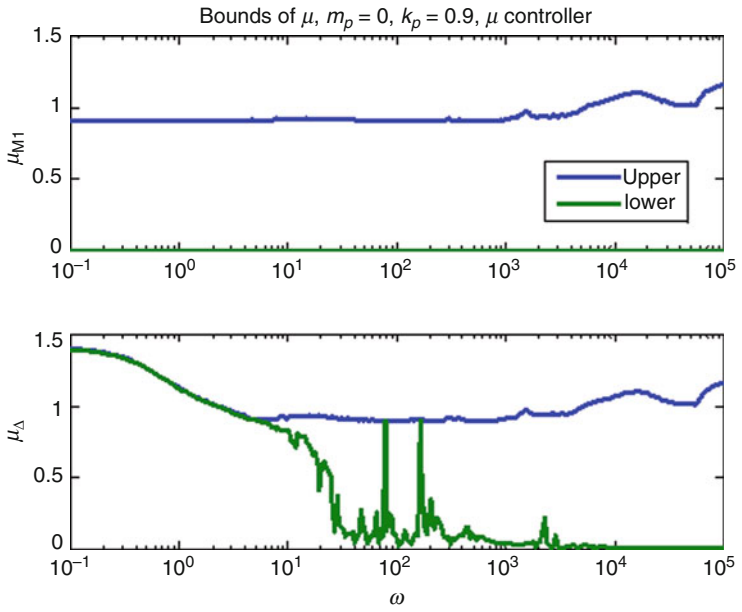


Fig. 19 μ-bounds of the μ-controller for $m_p = 0$, $k_p = 0.9$

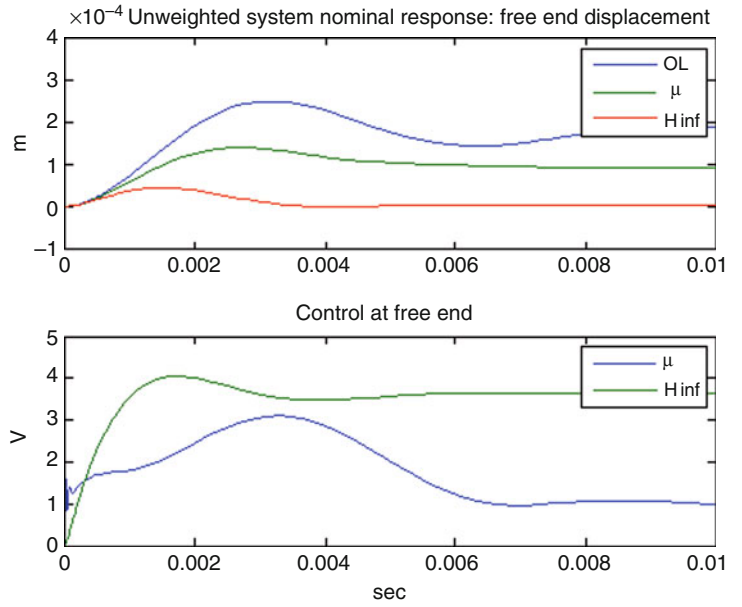


Fig. 20 Comparison of free end data of nominal system for μ-controller ($m_p = 0$, $k_p = 0.9$) and H_∞

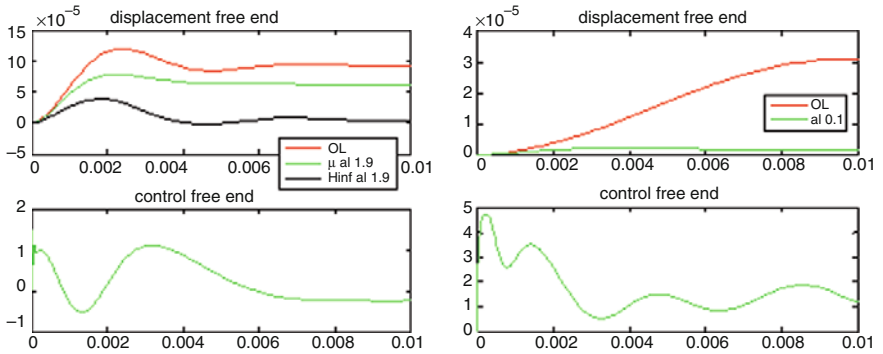


Fig. 21 Displacement and control at free end for the μ-controller with $m_p = 0$, $k_p = 0.9$ (extreme values)

This could be due to numerical difficulties in the calculation of the μ-controller arising from the bad condition number of the plant. It could also be due to the high order of the μ-controller. In any case, further investigation is needed.

5 Reduced Order Control

The H_∞ controller found is of 24th order. Using the Matlab package *HIFOO* we can reduce this controller and stabilize the system with a second order controller without difficulty suggesting explicit formulas for the controller and for the closed loop system.

Furthermore, analytical techniques prove that this controller is locally optimal in the sense that there is no nearby controller with the same order for which the closed loop system has all its poles further left in the complex plane [10, 12].

These approaches can be extended in order to take into account other key quantities of great practical interest, such as optimization of the H_∞ performance. In particular, with the help of a MATLAB toolbox called *HIFOO* (Fixed Order Optimization) we can reduce the order of the controller and have very good results [10].

Figure 22 shows the corresponding control voltages using the 24th order controller for the four nodes of the beam. The beam with H_∞ control keeps in equilibrium and we have zero displacements, as we can see (Fig. 22) the voltage is much lower than 500 V, which is the piezoelectric limit.

Then we use a second order controller for the H_∞ control performance. Figure 23 shows the response of the uncontrolled and controlled beam at the free end, using the second order controller for the stochastic wind load (Fig. 16). Figure 24 shows the corresponding control voltage of the free end. With the help of the controller *HIFOO* we can reduce the order of the system and keep the beam in equilibrium with even lower voltages.

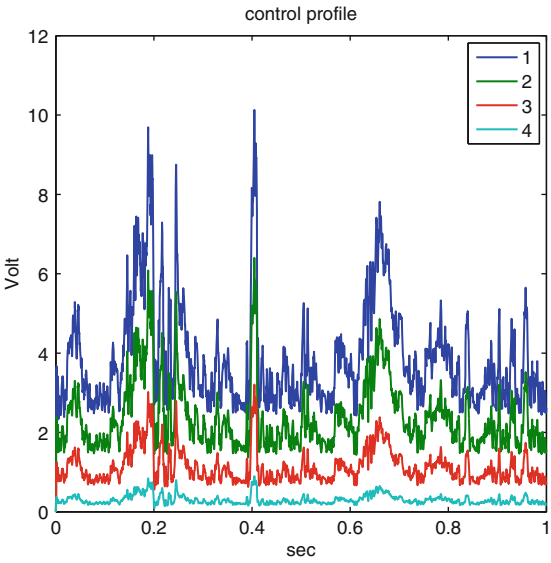


Fig. 22 The control voltages for the four nodes of the beam with the 24th order controller

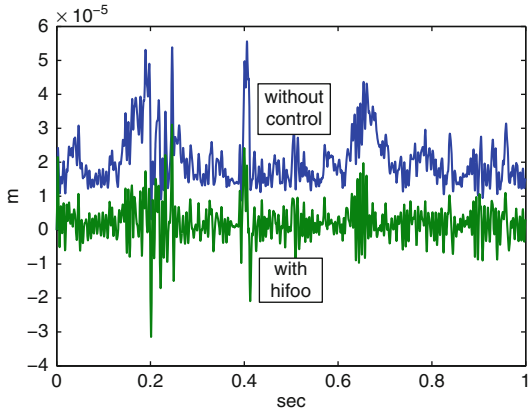


Fig. 23 The displacement of the free end of the beam without and with control with the 2nd order controller

6 Conclusions

A finite element based modelling technique for the determination of the system model of the smart beam was presented. Based on this model an H_∞ and a μ-controller was designed which effectively suppress the vibrations of the smart beam under stochastic wind load.

The advantage of the H_∞ criterion is its ability to take into account the worst influence of uncertain disturbances or noise in the system. It is possible to synthesize a H_∞ controller which will be robust with respect to a prespecified number of errors in the model. Hoping to reduce the model's computational requirements,

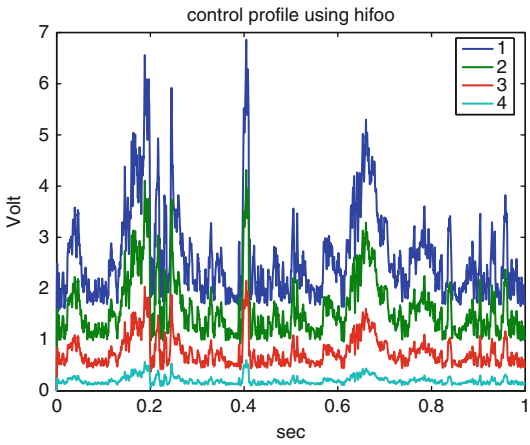


Fig. 24 The control voltages for the four nodes of the beam with the 2nd order controller

the controller's order was reduced, aided by a parametric, nonconvex optimization, and using the *HIFOO* controller. The controller's good performance was maintained even for a much smaller system degree.

Finally taking into account the system's non-linearity which was not considered in the model, our inaccurate knowledge of the model's values and parameters, and their variations over the life of the structure operation, we introduce modeling uncertainties. A robust μ-controller was analyzed and synthesized, using the $D - K$ iterative method. The results are compared and commented upon using the various controllers. The results are very good: the oscillations were suppressed even for a real aeolian load, with the piezoelectric components' voltages within their endurance limits.

References

1. Friedman J, Kosmatka K (1993) An improved two node Timoshenko beam finite element. Comput Struct 47:473–481
2. Foutsitzi G, Marinova D, Hadjigeorgiou E, Stavroulakis G (2003) Robust H2 vibration control of beams with piezoelectric sensors and actuators. Proceedings of physics and control conference (PhyCon03), St. Petersburg, Russia, 20–22 August, vol I, pp 158–163
3. Sisemore C, Smaili A, Houghton R (1999) Passive damping of flexible mechanism system: experimental and finite element investigation. The 10th world congress of the theory of machines and mechanisms, Oulu, Finland, vol 5, pp 2140–2145
4. Zhang N, Kirpitchenko I (2002) Modelling dynamics of a continuous structure with a piezoelectric sensor/actuator for passive structural control. J Sound Vib 249:251–261
5. Miara B, Stavroulakis G, Valente V (eds) (2007) Topics on mathematics for smart systems. Proceedings of the European conference, Rome, Italy, 26–28 October 2006, World Scientific, Singapore
6. Shahian B, Hassul M (1994) Control system design using MATLAB. Prentice-Hall, New Jersey
7. Huang WS, Park HC (1993) Finite element modelling of piezoelectric sensors and actuators. AIAA J 31:930–937

8. Foutsitzi G, Marinova D, Hadjigeorgiou E, Stavroulakis G (2002) Finite element modelling of optimally controlled smart beams. 28th summer school: applications of mathematics in engineering and economics, Sozopol, Bulgaria
9. Stavroulakis GE, Foutsitzi G, Hadjigeorgiou E, Marinova D, Baniotopoulos CC (2005) Design and robust optimal control of smart beams with application on vibrations suppression. Adv Eng Software 36(11–12):806–813
10. Burke JV, Henrion D, Lewis ML (2006) Overton.HIFOO – a MATLAB package for fixed-order controller design and Hinf. optimization. Proceedings of the IFAC symposium on robust control design. Toulouse, France. www.cs.nyu.edu/overton/software/hifoo
11. Tiersten HF (1969) Linear piezoelectric plate vibrations. Plenum Press, New York
12. Burke JV, Henron D, Kewis AS, Overton ML (2006) Stabilization via nonsmooth, nonconvex optimization. Automatic Control IEEE 5(11):1760–1769
13. Bosgra OH, Kwakernaak H (2001) Design methods for control systems. Lecture Notes for a course, Dutch Institute for Systems and Control, The Netherlands, p 69
14. Hou M, Muller PC (1992) Design of observers for linear systems with unknown inputs. IEEE Trans Automat Contr 37:871–875
15. Packard A, Doyle J, Balas G (1993) Linear, multivariable robust control with a μ perspective. ASME J Dyn Syst Meas Contr, 50th Anniversary Issue 115(2b):310–319
16. Pouliezos A (2008) MIMO control systems. Lecture Notes for a course, http://pouliezos.dpem.tuc.gr
17. Marinova D, Stavroulakis GE, Foutsitzi D, Hadjigeorgiou E, Zacharenakis EC (2004) Robust design of smart structures taking into account structural defects. Summer school conference advanced problems in mechanics In: Indeitsev DA (ed) Russian academy of sciences, pp 288–292
18. Tits AL, Yang Y (1996) Globally convergent algorithms for robust pole assignment by state feedback. IEEE Trans Automat Contr 41:1432–1452
19. Ward RC (1981) Balancing the generalized eigenvalue problem. SIAM J Sci Stat Comput 2:141–152
20. Young P, Newlin M, Doyle J (1992) Practical computation of the mixed problem. Proceedings of the American control conference, pp 2190–2194
21. Arvanitis KG, Zacharenakis EC, Soldatos AG, Stavroulakis GE (2003) New trends in optimal structural control. In: Belyaev A, Guran A (ed) Selected topics in structronic and mechatronic system, Chapter 8, World Scientific, Singapore, pp 321–415

Critical Assessment of Penalty-Type Methods for Imposition of Time-Dependent Boundary Conditions in FEM Formulations for Elastodynamics

Christos G. Panagiotopoulos, Elias A. Paraskevopoulos, and George D. Manolis

Abstract Recent work by the authors proposes a methodology that avoids ad hoc procedures and is applicable to both linear as well as nonlinear problems and provides a variationally-consistent way for incorporation of time-dependent boundary conditions in problems of elastodynamics. More specifically, an integral formulation of the elastodynamic problem serves as basis for the imposition of the corresponding constraints, which are enforced via the consistent form of the penalty method, e.g., a form that complies with the norm and inner product of the functional space where the weak formulation is mathematically posed. It is shown that well known and broadly implemented modelling techniques in the finite element method such as "large mass" and "large spring" techniques arise as limiting cases of this penalty formulation. In here, we examine the performance and the characteristics of such techniques through some simple examples.

Keywords Time-dependent boundary conditions · Elastodynamics · Penalty method · Large mass method · Large spring method · Transient dynamics · Non-linear system

1 Introduction

As discussed in recent work by the authors [1], in Newton's principle of determinacy all motions of a system are determined by their initial positions and initial velocities (monogenic systems) [2]. In particular, the initial positions and velocities determine

C.G. Panagiotopoulos (✉)
Group of Elasticity and Strength of Materials, Department of Continuum Mechanics, School of Engineering, University of Seville, Sevilla, ES-41092, Spain
e-mail: cpanagiotopoulos@us.es

E.A. Paraskevopoulos
Department of Mechanical Engineering, Aristotle University, Thessaloniki, GR-54124, Greece
e-mail: eapcivil@yahoo.gr

G.D. Manolis
Department of Civil Engineering, Aristotle University, Thessaloniki, GR-54124, Greece
e-mail: gdm@civil.auth.gr

M. Papadrakakis et al. (eds.), *Computational Methods in Earthquake Engineering*, Computational Methods in Applied Sciences 21, DOI 10.1007/978-94-007-0053-6_16,
© Springer Science+Business Media B.V. 2011

the acceleration, i.e., all forces are dependent on the velocities, positions and time. Therefore, strictly speaking we cannot enforce accelerations but only displacements and velocities at the boundaries. Also, mathematical theory of second order differential equations states that the boundary conditions involve derivatives up to first order [3].

In the regime of elastodynamics there are three general methods for enforcing prescribed motion, namely the direct substitution method (also known as elimination method), the penalty method and Lagrange multipliers.

The most common procedure for the imposition of time dependent boundary conditions is the one originated in [4], which is based on decomposition of the displacement function in such a way that the derived problem is one of homogeneous boundary conditions in time. These methods, which come under the direct substitution classification, were first employed for continuous bodies but later extended for the case of spatially discretized systems (such as finite element systems) and are sometimes known as absolute and relative motion methods, respectively. The above procedure when superposition is used is restricted to problems involving linear operators and can not be utilized in nonlinear problems.

Boundary conditions may also be taken into account by Lagrange multipliers, a procedure that in the elastostatic case (and more general in time-independent problems) is well established [5]. The use of Lagrange multipliers in elastodynamics is outside the scope of this paper.

The penalty method for prescribed kinematical condition enforcement on boundaries is well understood in the case of time independent problems [6]. In the case of elastodynamics, finite elements with penalty function formulation are considered as an extension of elastostatics, by trying to modify the potential energy of the system due to constraints. This formulation is also known as "large stiffness" or "large spring" method in the literature, because it augments the stiffness matrix of the system with a penalty matrix. This method produces very large values for the maximum eigenvalues of the system and should be avoided, especially in conditionally stable time integrations schemes [7]. Another methodology that also falls into the penalty formulation and it is widely used is the so called "large mass" method. Actually this approach is a modelling technique adopted in various commercial finite element codes that is based mainly on physical arguments without (at least to the authors' knowledge) a firm theoretical justification. A common consensus that, *the "large mass" method is not derived from a rigorous mathematical formulation*, is also impressed in [8].

The authors have presented in [1] a general procedure for the imposition of time dependent boundary conditions. In that paper, the prescribed boundary conditions are enforced through a consistent form of the penalty method, e.g., a form that conforms with the norm and inner product of the functional space where the weak formulation is posed. The above results in modification of the potential as well as the kinetic energy of the system due to constraints. It is also shown in that paper that the "large spring" method has no formal mathematical justification and it is only used under certain approximations.

In this work, a survey on penalty type formulations is presented and it is shown under which conditions the "large mass" and "large spring" methods appear as limiting cases of the general consistent penalty method. Also, through some simple examples the characteristics of each method are examined.

2 Governing Equations

The following hyperbolic, initial boundary-value problem serves as starting point for the subsequent developments:

$$(\rho \dot{\boldsymbol{u}}) - \sum_{i=1}^{m} \frac{\partial \boldsymbol{s}^i}{\partial x_i} = \boldsymbol{f}(\boldsymbol{x}, t), \qquad (\boldsymbol{x}, t) \in \boldsymbol{\Omega} \times (0, T] \tag{1}$$

$$\boldsymbol{u}(\boldsymbol{x}, t) = \tilde{\boldsymbol{u}}(\boldsymbol{x},\mathrm{t}), \qquad (\boldsymbol{x}, t) \in \boldsymbol{\Gamma}_u \times (0, T] \tag{2}$$

$$\boldsymbol{s}^i n_i = \tilde{\boldsymbol{t}}(\boldsymbol{x},\mathrm{t}), \qquad (\boldsymbol{x}, t) \in \boldsymbol{\Gamma}_t \times (0, T] \tag{3}$$

$$\boldsymbol{u}(\boldsymbol{x}, 0) = \bar{\boldsymbol{u}}(\boldsymbol{x}), \qquad \boldsymbol{x} \in \boldsymbol{\Omega} \tag{4}$$

$$\dot{\boldsymbol{u}}(\boldsymbol{x}, 0) = \bar{\boldsymbol{v}}(\boldsymbol{x}), \qquad \boldsymbol{x} \in \boldsymbol{\Omega} \tag{5}$$

In Eqs. (1)–(5), the vector $\boldsymbol{x}$ and the scalar t denote spatial coordinates (x^i) and time, respectively. The vector $\boldsymbol{u}$ is the displacement vector with components u_i, while vectors $\boldsymbol{f}$ and $\bar{\boldsymbol{u}}$ are prescribed functions. Vectors $\tilde{\boldsymbol{u}}(\boldsymbol{x}, t)$ and $\tilde{\boldsymbol{t}}(\boldsymbol{x}, t)$ denote time dependent prescribed boundary conditions on the Γ_u and Γ_t parts of the boundary Γ, (see Fig. 1). Furthermore, ρ denotes mass density, and m equals the spatial dimensions of the problem. Also, $\boldsymbol{s}^i$ signify the stress vector and n_i the components of the outward unit normal to Γ_t. Finally, note that since $\tilde{\boldsymbol{u}}(\boldsymbol{x}, t)$ is a prescribed function of time, its derivative with respect to time is also known. Specifically, this is $\tilde{\boldsymbol{v}}(\boldsymbol{x}, t)$, the prescribed velocities on Γ_u.

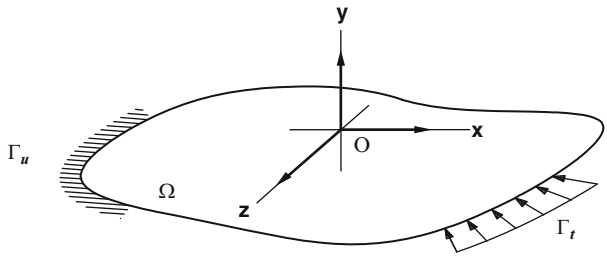


Fig. 1 Reference domain for a solid body with surface $\Gamma_u \bigcup \Gamma_t$

3 Variational Formulation

Multiplying Eq. (1) by an arbitrary function $\boldsymbol{w}$

$$\boldsymbol{w} \in V, \qquad V = \{\boldsymbol{w} \in H^1(\Omega) : \ \boldsymbol{w} = \boldsymbol{0} \text{ on } \Gamma_u\} \tag{6}$$

integrating (in space), applying Green's theorem, and employing the natural boundary conditions of Eq. (3), we obtain

$$\int_\Omega (\rho \dot{\boldsymbol{u}}) \cdot \boldsymbol{w} \, d\Omega + \sum_{i=1}^{m} \int\int_\Omega \boldsymbol{s}^i \cdot \frac{\partial \boldsymbol{w}}{\partial x_i} \, d\Omega - \int_{\Gamma_t} \tilde{\boldsymbol{t}} \cdot \boldsymbol{w} \, d\Gamma_t - \int_\Omega \boldsymbol{f} \cdot \boldsymbol{w} \, d\Omega = 0 \tag{7}$$

Integrating Eq. (7) over the time interval $I \in (0, T]$ and integrating by parts on the first term of the left hand side, yields the weak formulation of Eq. (1). Specifically we find

$$\boldsymbol{u} \in \mathscr{U} = \{\boldsymbol{u} \in L_2(I, H^1(\Omega)) : \ \dot{\boldsymbol{u}} \in L_2(I, H^1(\Omega))\} \tag{8}$$

satisfying the relation

$$\int_0^T \left(\int_\Omega -\rho \dot{\boldsymbol{u}} \cdot \dot{\boldsymbol{w}} \, d\Omega + \sum_{i=1}^{m} \int_\Omega \boldsymbol{s}^i \cdot \frac{\partial \boldsymbol{w}}{\partial x_i} \, d\Omega - \int_{\Gamma_t} \tilde{\boldsymbol{t}} \cdot \boldsymbol{w} \, d\Gamma_t - \int_\Omega \boldsymbol{f} \cdot \boldsymbol{w} \, d\Omega \right) dt = 0$$

where

$$\begin{aligned} \boldsymbol{w} \in \mathscr{W} = \{\boldsymbol{w} \in L_2(I, H^1(\Omega)) : \\ \dot{\boldsymbol{w}} \in L_2(I, H^1(\Omega)), \ \boldsymbol{w}(0) = \boldsymbol{w}(T) = \boldsymbol{0}, \\ \boldsymbol{w} = \dot{\boldsymbol{w}} = \boldsymbol{0} \in \Gamma_u\} \end{aligned} \tag{9}$$

are the essential boundary conditions of Eq. (2) and the initial condition of Eq. (4). Moreover, the aforementioned system of equations is augmented by the constitutive equations and the flow rule in the presence of material nonlinearities.

4 Imposition of Boundary Conditions

Since $\boldsymbol{u}$ belongs to *Sobolev* space $H^1(\Omega)$, the strong time derivative also belongs to the same space. Then, according to the trace theorem the displacements $\boldsymbol{u}|_{\Gamma_u}$ and the velocities $\dot{\boldsymbol{u}}|_{\Gamma_u}$ on the boundaries belongs to $L_2(\Gamma_u)$ [9, 10].

Since $\boldsymbol{u}|_{\Gamma_u}$ and $\dot{\boldsymbol{u}}|_{\Gamma_u}$ should belong to the abstract *Bochner* space $L_2(I, L_2(\Gamma_u))$, it is concluded that the associated norms are the following [11]:

$$||\boldsymbol{u}||_{L_2(I,L_2(\Gamma_u))} = \left(\int_0^T \left(||\boldsymbol{u}||_{L_2(\Gamma_u)} \right)^2 dt \right)^{1/2}$$

$$||\dot{\boldsymbol{u}}||_{L_2(I,L_2(\Gamma_u))} = \left(\int_0^T \left(||\dot{\boldsymbol{u}}||_{L_2(\Gamma_u)} \right)^2 dt \right)^{1/2} \tag{10}$$

The imposition of constraints can be achieved either through the penalty method or via Lagrange multipliers in an appropriate way which complies with the norm and the inner product of the functional space where the weak form has been posed.

4.1 Consistent Penalty Formulation

In the case of prescribed displacements, the time derivative has to be enforced as a constraint in order to guarantee convergence. This complies with the selected norms of Eq. (10). The weak form given by Eq. (9) is associated with the essential boundary conditions of Eq. (2) and is augmented by the variation of the following two terms:

$$\alpha_\kappa \left(\int_0^T \left(||\boldsymbol{u} - \tilde{\boldsymbol{u}}||_{L_2(\Gamma_u)} \right)^2 dt \right) \tag{11}$$

and

$$-\alpha_\mu \left(\int_0^T \left(||\dot{\boldsymbol{u}} - \tilde{\boldsymbol{v}}||_{L_2(\Gamma_u)} \right)^2 dt \right) \tag{12}$$

i.e.,

$$\int_0^T \left(\int_{\Gamma_u} \alpha_\kappa \left(\boldsymbol{u} - \tilde{\boldsymbol{u}} \right) \boldsymbol{w} \; d\Gamma_u \right) dt - \int_0^T \left(\int_{\Gamma_u} \alpha_\mu \left(\dot{\boldsymbol{u}} - \tilde{\boldsymbol{v}} \right) \dot{\boldsymbol{w}} \; d\Gamma_u \right) dt \tag{13}$$

Once more, the test functions $\boldsymbol{w}$ are not restricted to be zero on Γ_u. Note that both α_k and α_μ tend to infinity, while their relative order is further examined in Sect. 5. Physical considerations again led to the presented selection of signs and, more specific, the first term follows the term associated with the strain energy while the second one has the sign of the kinetic energy. From a mathematical point of view, an arbitrary combination of signs yields the same solution. Choosing the same sign for the two terms gives rise to numerical difficulties, because the equations

that derived from the variation of the constrained degrees of freedom will not be hyperbolic in time [12] and thus alter the nature of the problem under consideration.

In the case of prescribed displacements on the boundaries, the weak form in view of Eq. (13) takes the following form:

$$\int_0^T \left(\int_\Omega -\rho \dot{\boldsymbol{u}} \cdot \dot{\boldsymbol{w}} \, d\Omega + \sum_{i=1}^{m} \int_\Omega \boldsymbol{s}^i \cdot \frac{\partial \boldsymbol{w}}{\partial x_i} \, d\Omega - \int_{\Gamma_t} \tilde{\boldsymbol{t}} \cdot \boldsymbol{w} \, d\Gamma_t - \int_\Omega \boldsymbol{f} \cdot \boldsymbol{w} d\Omega \right) dt$$
$$+ \int_0^T \left(\int_{\Gamma_u} \alpha_\kappa \left(\boldsymbol{u} - \tilde{\boldsymbol{u}} \right) \boldsymbol{w} d\Gamma_u \right) dt - \int_0^T \left(\int_{\Gamma_u} \alpha_\mu \left(\dot{\boldsymbol{u}} - \tilde{\boldsymbol{v}} \right) \dot{\boldsymbol{w}} \, d\Gamma_u \right) dt = 0 \tag{14}$$

Integrating by parts (with respect to time) the first term and the penalty term associated with the α_μ coefficient of Eq. (14), we obtain

$$\int_0^T \left(\int_\Omega \rho \, \ddot{\boldsymbol{u}} \cdot \boldsymbol{w} \, d\Omega + \sum_{i=1}^{m} \int_\Omega \boldsymbol{s}^i \cdot \frac{\partial \boldsymbol{w}}{\partial x_i} \, d\Omega - \int_{\Gamma_t} \tilde{\boldsymbol{t}} \cdot \boldsymbol{w} \, d\Gamma_t - \int_\Omega \boldsymbol{f} \cdot \boldsymbol{w} d\Omega \right) dt$$
$$+ \int_0^T \left(\int_{\Gamma_u} \alpha_\kappa \left(\boldsymbol{u} - \tilde{\boldsymbol{u}} \right) \boldsymbol{w} d\Gamma_u \right) dt + \int_0^T \left(\int_{\Gamma_u} \alpha_\mu \left(\ddot{\boldsymbol{u}} - \dot{\tilde{\boldsymbol{v}}} \right) \boldsymbol{w} d\Gamma_u \right) dt = 0 \tag{15}$$

Equation (15) provides a framework for space-time finite elements formulations [13, 14]. Since $\boldsymbol{w}$ is an arbitrary function with respect to time, we obtain the following form, which serves once again as a basis for the derivation of the semi-discrete form of the equation of dynamics, i.e.

$$\int_\Omega \rho \, \ddot{\boldsymbol{u}} \cdot \boldsymbol{w} d\Omega + \sum_{i=1}^{m} \int_\Omega \boldsymbol{s}^i \cdot \frac{\partial \boldsymbol{w}}{\partial x_i} \, d\Omega - \int_{\Gamma_t} \tilde{\boldsymbol{t}} \cdot \boldsymbol{w} \, d\Gamma_t - \int_\Omega \boldsymbol{f} \cdot \boldsymbol{w} d\Omega +$$
$$\int_{\Gamma_u} \alpha_\kappa \left(\boldsymbol{u} - \tilde{\boldsymbol{u}} \right) \boldsymbol{w} d\Gamma_u + \int_{\Gamma_u} \alpha_\mu \left(\ddot{\boldsymbol{u}} - \dot{\tilde{\boldsymbol{v}}} \right) \boldsymbol{w} d\Gamma_u = 0 \tag{16}$$

In the following sections we show that the "large mass" as well as "large spring" methods may obtained as subcases of the general consistent formulation given above.

4.2 Large Mass Method

The standard "large mass" method is obtained from Eq. (16) by omitting terms related to α_k. Therefore, its semidiscrete form is

$$\int_{\Omega} \rho\, \ddot{\boldsymbol{u}} \cdot \boldsymbol{w} d\Omega + \sum_{i=1}^{m} \int_{\Omega} \boldsymbol{s}^{i} \cdot \frac{\partial \boldsymbol{w}}{\partial x_i}\, d\Omega - \int_{\Gamma_t} \tilde{\boldsymbol{t}} \cdot \boldsymbol{w}\, d\Gamma_t - \int_{\Omega} \boldsymbol{f} \cdot \boldsymbol{w} d\Omega + \int_{\Gamma_u} \alpha_{\mu} \left(\ddot{\boldsymbol{u}} - \dot{\tilde{\boldsymbol{v}}} \right) \boldsymbol{w} d\Gamma_u = 0 \qquad (17)$$

Notice that the weak (in time) formulations associated with this approach are obtained from Eqs. (14) and (15) by omitting terms related to α_k. In this case only the penalty term of the velocities in Eq. (12) is enforced.

4.3 Large Spring Method

The so called "large spring" method is obtained from Eq. (16) by omitting terms related to α_m. Therefore, its semidiscrete form is

$$\int_{\Omega} \rho\, \ddot{\boldsymbol{u}} \cdot \boldsymbol{w} d\Omega + \sum_{i=1}^{m} \int_{\Omega} \boldsymbol{s}^{i} \cdot \frac{\partial \boldsymbol{w}}{\partial x_i}\, d\Omega - \int_{\Gamma_t} \tilde{\boldsymbol{t}} \cdot \boldsymbol{w} d\Gamma_t - \int_{\Omega} \boldsymbol{f} \cdot \boldsymbol{w} d\Omega + \int_{\Gamma_u} \alpha_{\kappa} \left(\boldsymbol{u} - \tilde{\boldsymbol{u}} \right) \boldsymbol{w} d\Gamma_u = 0 \qquad (18)$$

Once again and similarly to the previous case, the weak (in time) formulations associated to this approach are obtained from Eqs. (14) and (15) by omitting terms related to α_{μ}. In this case only the penalty term of the displacement Eq. (11) is utilized, which tends to satisfy the condition only in the L_2 norm with respect to time.

5 Selection of Penalty Parameters and Assessment of the Penalty Type Methods

Attention is focused here on appropriate selection of the penalty parameters (α_{μ}, α_{κ}), in such a manner that the associated numerical errors are controlled, utilizing energy-based considerations. Moreover, care is taken to avoid the introduction of additional numerical difficulties. The selection of the penalty parameters could be better described in the case of linear systems. In the presence of nonlinearities the associated linearized system serves as a basis for the selection of penalty parameters. With the aim of clarifying these basic concepts, a single degree of freedom kinematical system is investigated. Furthermore, by exploiting the results of the above mentioned example, extension to more complex multi-degree of freedoms systems is provided.

5.1 Single Degree of Freedom System

A simple, yet instructive case is that of a prescribed single degree of freedom with mass m and stiffness k which is a fully determined kinematical system. Application of the proposed methodology yields the following equation:

$$(m + \alpha_\mu)\, \ddot{u} + (k + \alpha_\kappa)\, u = \alpha_\mu\, \ddot{\tilde{u}} + \alpha_\kappa\, \tilde{u} \tag{19}$$

Since any function may be expressed with any desired accuracy as a linear combination of harmonics, without loss of generality we assume a prescribed harmonic displacement of unit amplitude with the associated initial conditions, i.e.,

$$\begin{aligned} \tilde{u}(t) &= \sin(\bar{\omega} t) \\ \ddot{\tilde{u}}(t) &= -\bar{\omega}^2 \sin(\bar{\omega} t) \end{aligned}$$

Also expressing the ratio of penalty parameters as $c^2 = \frac{\alpha_\kappa}{\alpha_\mu}$, Eq. (19) takes the following form.

$$(m + \alpha_\mu)\, \ddot{u} + (k + \alpha_\kappa)\, u = \alpha_\mu\, (c^2 - \bar{\omega}^2) \sin(\bar{\omega} t) \tag{20}$$

The analytical solution of the above equation is given by

$$u(t) = \frac{\bar{\omega}}{\hat{\omega}} \sin(\hat{\omega} t) + \frac{\alpha_\mu (c^2 - \bar{\omega}^2)}{(\alpha_\mu + m)\hat{\omega}(\hat{\omega}^2 - \bar{\omega}^2)} [\hat{\omega} \sin(\bar{\omega} t) - \bar{\omega} \sin(\hat{\omega} t)]$$

$$\dot{u}(t) = \bar{\omega} \cos(\hat{\omega} t) + \frac{\alpha_\mu (c^2 - \bar{\omega}^2)}{(\alpha_\mu + m)(\hat{\omega}^2 - \bar{\omega}^2)} \bar{\hat{\omega}} [\cos(\bar{\omega} t) - \cos(\hat{\omega} t)]$$

Parameter $\hat{\omega}$, which we call here the augmented frequency, is given as

$$\hat{\omega}^2 = \frac{\alpha_\kappa + k}{\alpha_\mu + m} \tag{21}$$

The total energy of this conservative system

$$E(t) = T(t) + V(t) = \frac{1}{2}(\alpha_\mu + m)\dot{u}^2(t) + \frac{1}{2}(\alpha_\kappa + k)u^2(t)$$

Since $E(t)$ as a function of displacement and velocity defines a norm in the state space [2], it serves as a measure of deviation from the exact solution. More specifically, the expression utilized to measure the error is given as

$$E(t) = \frac{1}{2}(\alpha_\mu + m)(\dot{u}(t) - \dot{\tilde{u}}(t))^2 + \frac{1}{2}(\alpha_\kappa + k)(u(t) - \tilde{u}(t))^2 \tag{22}$$

The above expression degenerates to the one used in elastostatic problems [15], where the velocities are assumed to be zero. The selection of penalty ratio is obtained by minimizing Eq. (22) with respect to c, independently of the prescribed

frequency $\bar{\omega}$ in a requisite bandwidth. This bandwidth is designated as $\bar{\omega} \in [0, \sqrt{\frac{k+\alpha_k}{m}}]$ so as to spread the width of all possible values. The only acceptable solution in the above bandwidth is $c = \hat{\omega}$, which, utilizing Eq. (21), yields

$$c^2 = \frac{k}{m} \tag{23}$$

Notice that the penalty ratio c depends only on the properties of the dynamical system under consideration. Moreover, in the case of a system where forces dependent on displacements are absent ($k = 0$), the consistent penalty formulation leads to the "large mass" method in a natural way. By way of contrast, since we study dynamical systems, very small finite mass values may occur (zero values are unacceptable), which means a large finite value of ratio c. In this case, the consistent penalty formulation tends to the "large spring" method, although emergence of this method (i.e., $c \to \infty$) is not admissible according the physics of the problem under consideration.

5.2 Numerical Implementation in the Case of Single Degree of Freedom Systems

In this section, we present some numerical as well as qualitative results with respect to the performance of the penalty methods in the case of a single degree of freedom system. The respective expressions of the response and the energy of error measure for the case of the "large spring" method is as follows:

$$u(t) = \frac{\bar{\omega}}{\hat{\omega}} \sin(\hat{\omega} t) + \frac{\alpha_\kappa \omega^2}{k\hat{\omega}(\hat{\omega}^2 - \bar{\omega}^2)} (\hat{\omega} \sin(\bar{\omega}) - \bar{\omega} \sin(\hat{\omega}))$$

$$\dot{u}(t) = \bar{\omega} \cos(\hat{\omega} t) + \frac{\alpha_\kappa \omega^2 \hat{\omega}}{k(\hat{\omega}^2 - \bar{\omega}^2)} (\cos(\bar{\omega}) - \cos(\hat{\omega}))$$

Here $\hat{\omega}$ is the augmented frequency for the case of "large spring", i.e.,

$$\hat{\omega}^2 = \frac{\alpha_\kappa + k}{m}$$

while the expression utilized to measure the error is given in this case as

$$E(t) = \frac{1}{2} m (\dot{u}(t) - \dot{\tilde{u}}(t))^2 + \frac{1}{2} (\alpha_\kappa + k)(u(t) - \tilde{u}(t))^2$$

For the "large mass" method similar expressions may obtained and given below.

$$u(t) = \frac{\bar{\omega}}{\hat{\omega}} \sin(\hat{\omega} t) + \frac{\alpha_\mu \bar{\omega}^2}{(\alpha_\mu + m)\hat{\omega}(\hat{\omega}^2 - \bar{\omega}^2)} [\hat{\omega} \sin(\bar{\omega} t) - \bar{\omega} \sin(\hat{\omega} t)]$$

$$\dot{u}(t) = \bar{\omega}\cos(\hat{\omega}t) + \frac{\alpha_\mu \bar{\omega}^2}{(\alpha_\mu + m)(\hat{\omega}^2 - \bar{\omega}^2)}\bar{\hat{\omega}}[\cos(\bar{\omega}t) - \cos(\hat{\omega}t)]$$

Here $\hat{\omega}$ is the augmented frequency for the case of "large mass", i.e.,

$$\hat{\omega}^2 = \frac{k}{\alpha_\mu + m}$$

and also the measure of the error is given in this case as

$$E(t) = \frac{1}{2}(\alpha_\mu + m)(\dot{u}(t) - \dot{\tilde{u}}(t))^2 + \frac{1}{2}k(u(t) - \tilde{u}(t))^2$$

When $\hat{\omega} = \bar{\omega}$ in any of the above three formulations, a resonant response occurs. A noticeable fact is that only in the case of the consistent penalty formulation (as well as only for the $c = \omega$ selection) this phenomenon does not occur. In Figs. 2–4 there are plots of the maximum values of energy error for all three methods near the resonance area. Note that each graph has two ordinates, the upper one shows the ratio $\frac{\hat{\omega}}{\bar{\omega}}$ while the lower one gives the direct value of the $\bar{\omega}$ frequency. The examples depicted here concerned a system of stiffness $k = 100.0$, natural frequency $\omega = 1.0$, and penalty parameters $\alpha_\kappa = 10^6 k$ and $\alpha_\mu = \frac{\alpha_\kappa}{\omega^2}$.

5.3 Multiple Degree of Freedom Systems

Assume an N degree of freedom system with the first B (where $B \leq N$) being prescribed in time following the form described in Eq. (2). According to the proposed formulation, penalty parameters are added to the system's mass as well as to the stiffness matrices only along the main diagonal and in positions corresponding to prescribed degrees of freedom. To be more specific,

$$\begin{aligned} \hat{k}_{ij} &= k_{ij} + c_i^2 \alpha_\mu \delta_{ij} \\ \hat{m}_{ij} &= m_{ij} + \alpha_\mu \delta_{ij} \qquad i, j = 1, ..., B \end{aligned} \tag{24}$$

where δ_{ij} is Kronecker's delta and the value of α_μ may be distinct for each i. Furthermore, $[m_{ij}]$ and $[k_{ij}]$ denote the mass and stiffness matrix, respectively. Also, forcing terms arise in the following form:

$$\hat{f}_i = f_i + \alpha_\mu \ddot{\tilde{u}}_i(t) + \alpha_\kappa \tilde{u}_i(t) \qquad i = 1, ..., B \tag{25}$$

In order to study the response generated by the penalty formulation, we assume $f_i = 0$ and a prescribed harmonic function for the ith displacement amplitude $\bar{u}_i$ and frequency $\bar{\omega}_i$. Forcing terms are as follows:

$$\hat{f}_i = \alpha_\mu \bar{u}_i (c_i^2 - \bar{\omega}_i^2)\sin(\bar{\omega}_i t) \qquad i = 1, ..., B \tag{26}$$

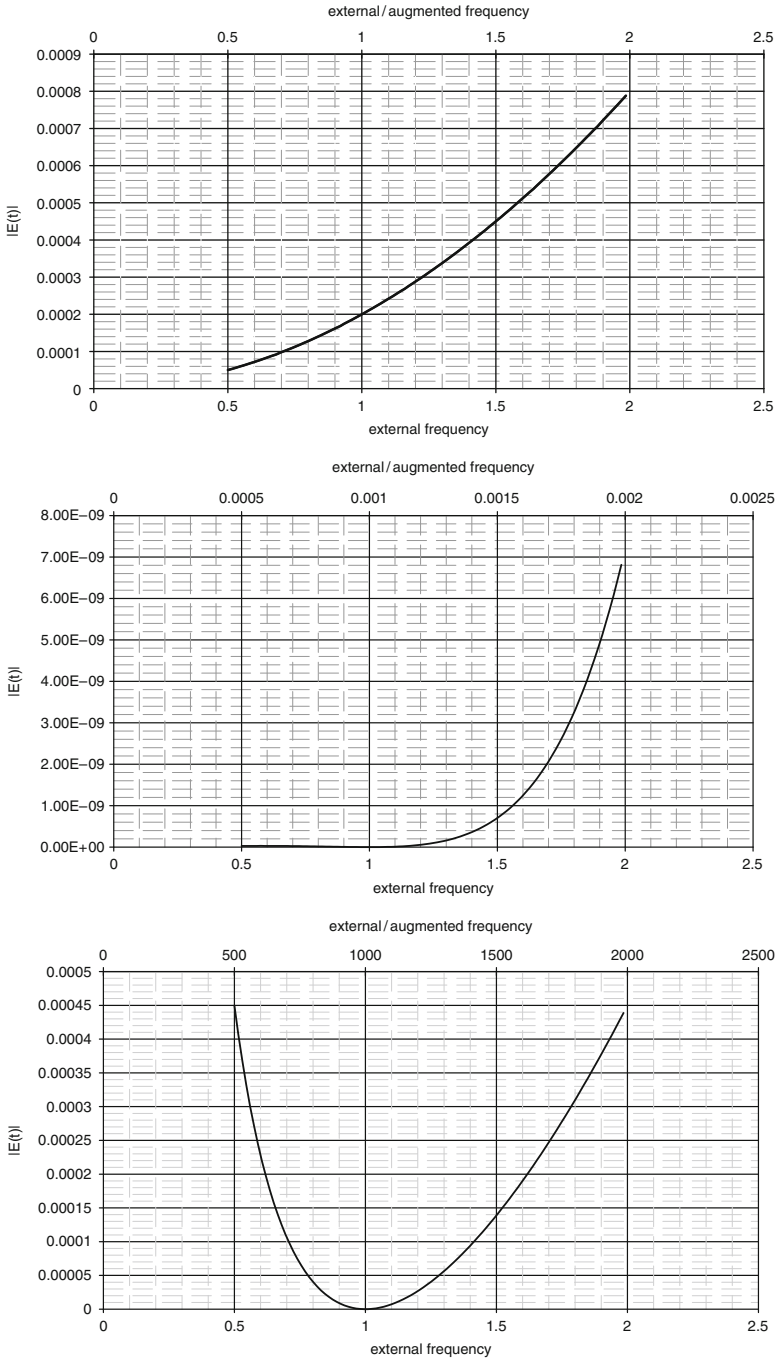


Fig. 2 Energy error spectrum in the consistent formulation resonance area: Upper to lower graphs are the consistent, "large spring" and "large mass" methods

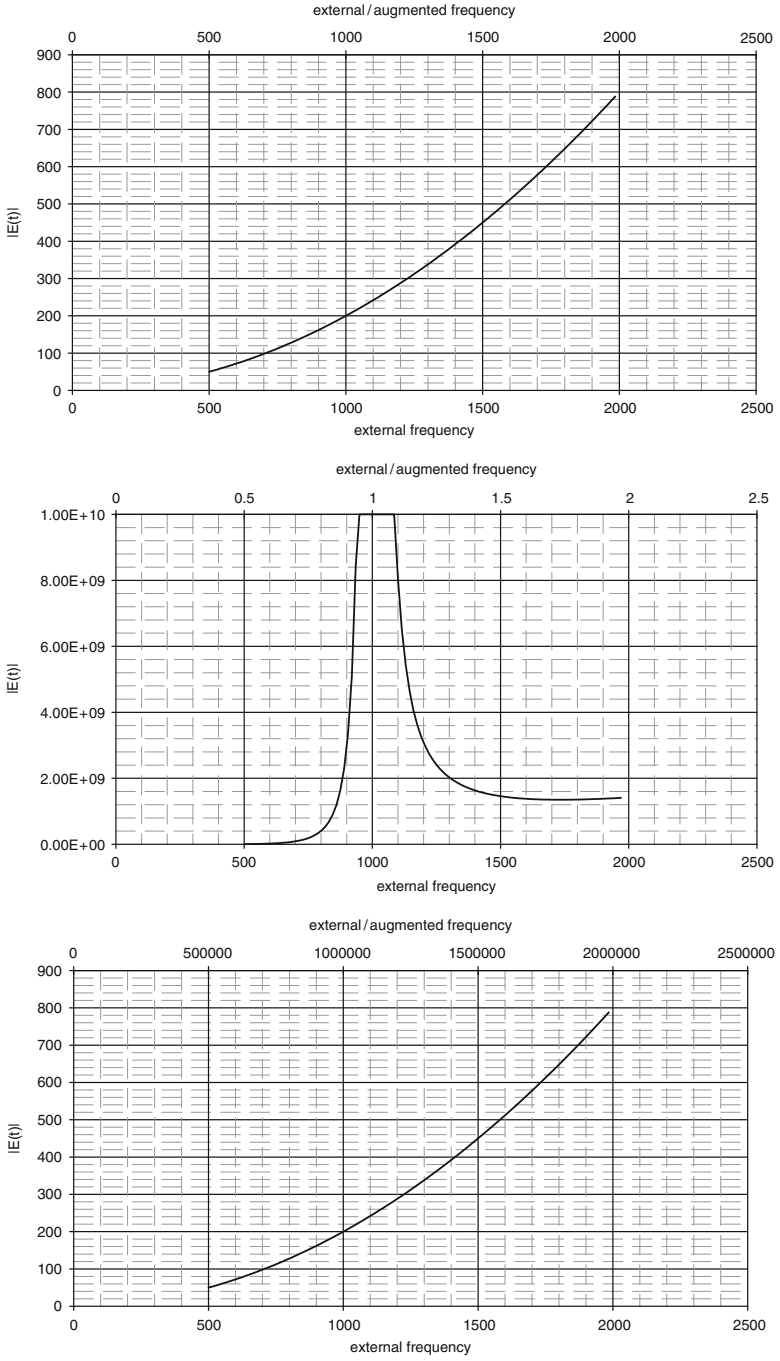


Fig. 3 Energy error spectrum in the "large spring" formulation resonance area: Upper to lower graphs are the consistent, "large spring" and "large mass" methods

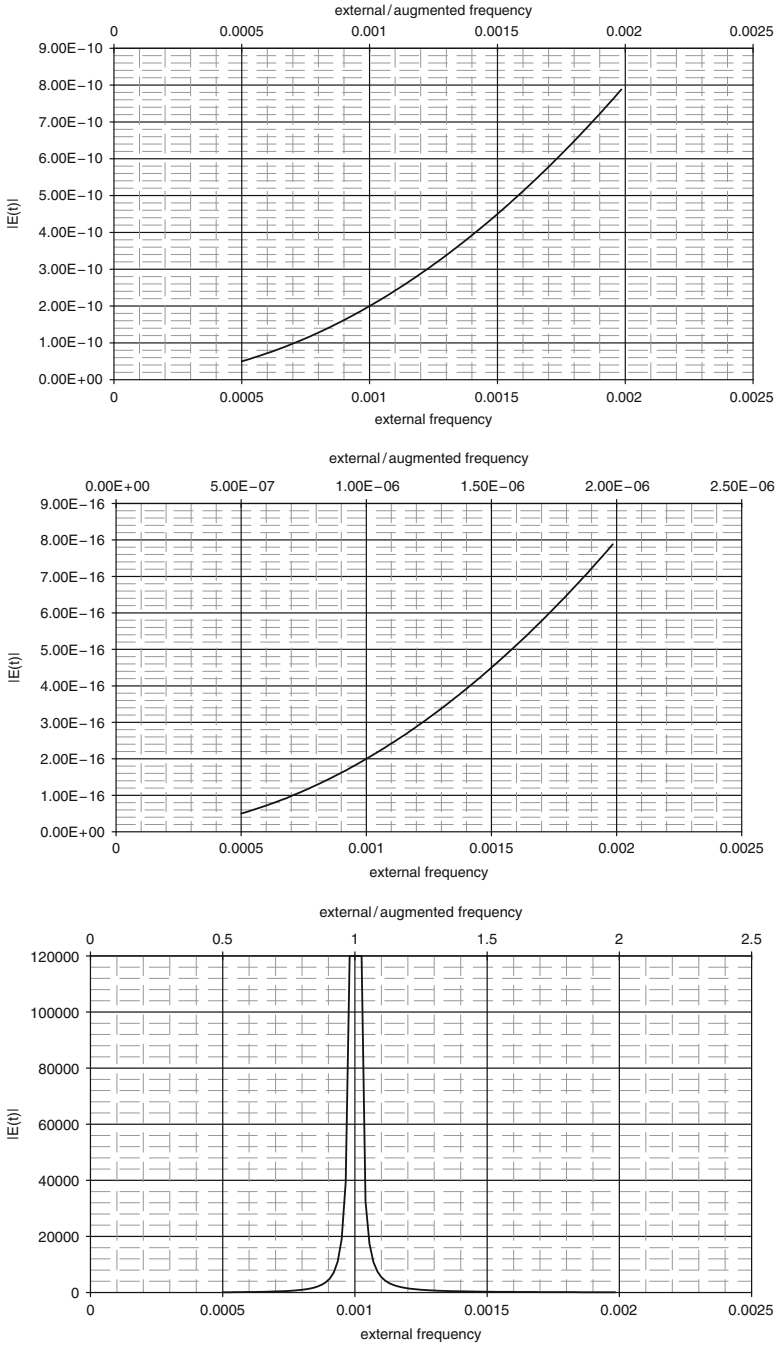


Fig. 4 Energy error spectrum in the "large mass" formulation resonance area: Upper to lower graphs are the consistent, "large spring" and "large mass" methods

Assuming that the penalty parameter α_μ tends to infinity and keeping the leading terms of the total energy, an estimation of c_i ratios is obtained by minimizing the energy related norm as defined in Sect. 5.1. This procedure leads to the following estimation:

$$c_i^2 = \frac{k_{ii}}{m_{ii}} \qquad i = 1, ..., B \tag{27}$$

In numerical implementation of multi degrees of freedom systems, a crucial point, regarding accuracy and stability is the so called *stiffness* of the system of equations ([16, 17]). This is defined as the ratio of the largest eigenfrequency to the smallest one as

$$S = \frac{\omega_{max}}{\omega_{min}} \tag{28}$$

It is shown in [1] that an estimation of the *stiffness* of the modified system is given by

$$\hat{S} = \frac{\hat{\omega}_{max}}{\hat{\omega}_{min}} \leq \sqrt{2}\,\frac{\omega_{max}}{\omega_{min}} = \sqrt{2}\,S \tag{29}$$

Hence, the proposed selection for c_i ratios does not alter the order of the system stiffness and the order of maximum and minimum eigenfrequencies. Contrary to the case of "large spring" method, $\hat{\omega}_{max}$ as well as the system stiffness tend to infinity, requiring a time step in the numerical integration algorithms that tends to zero or the introduction of artificial numerical damping. To be more specific, in the case of conditionally stable algorithms, this requirement arises from stability criteria, whereas in the case of unconditional stability, the same requirement emerges regarding accuracy of the algorithms (numerical integration of high frequencies).

In the context of the "large mass" method, $\hat{\omega}_{min}$ tends to zero and therefore the system stiffness tends to infinity, contrary to the case of "large spring" method. Since $\hat{\omega}_{max}$ does not change, there is no demand for a smaller time step regarding the aforementioned criteria. However, as was shown in this section, in this case the overall accuracy, in terms of the selected norm, is not the optimal one.

5.4 Numerical Implementation in the Case of Multiple Degree of Freedom Systems

The variation of the *stiffness* of a system produced by a simple finite element formulation is examined. The initial *stiffness* of this system is $S = 12.85$ with a minimum eigenvalue $\omega_{min} = 20.62$ and a maximum one $\omega_{max} = 264.93$. As expected, the "large spring" as well as the "large mass" method force the *stiffness* of the system to very large values, while the consistent penalty formulation retains the same order of magnitude as the original system. This behavior is depicted in Fig. 5 where the x-axis represents the penalty method parameter given as $\alpha_\kappa = i \cdot 10^6 \cdot \tilde{k}$ and

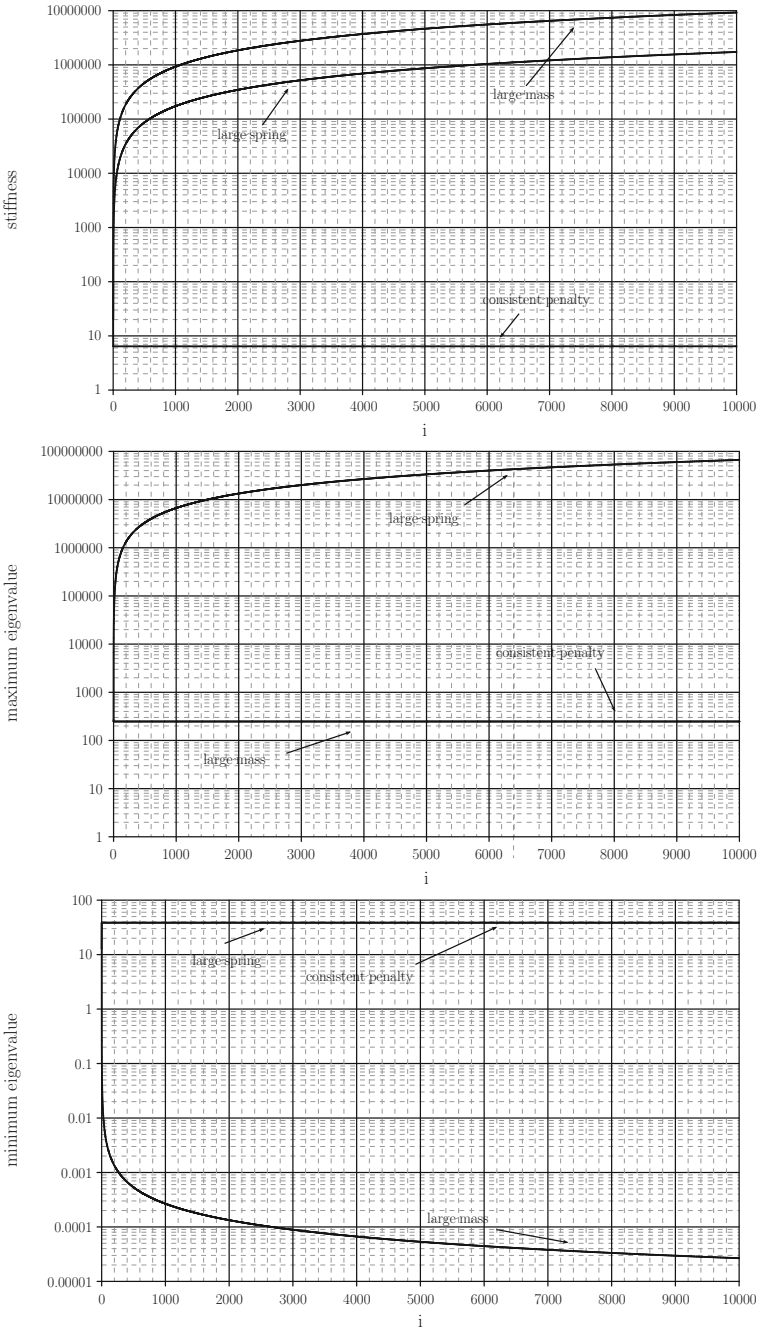


Fig. 5 *Stiffness*, maximum and minimum eigenvalue (upper to lower graphs respectively) variation with increasing values of penalty parameter α_κ

$\tilde{k}$ is the largest value in the stiffness matrix. Furthermore, parameter α_μ is given as $\alpha_\mu = \alpha_\kappa \cdot \frac{\hat{m}}{\hat{k}}$, with $\hat{k}$ and $\hat{m}$ being the stiffness and mass of the associated to boundary condition degree of freedom. Regarding the limiting eigenvalues of the system, the "large spring" tends to lead the maximum eigenvalue to larger values as it increases, while "large mass" retains its order of magnitude. The opposite happens regarding the minimum eigenvalue, where the "large mass" tends to nullify it, while the "large spring" retains its order of magnitude. In all cases, the consistent penalty formulation does not alter the order of the stiffness or the maximum and minimum eigenvalues. Note also that in all three figures, the y-axis is given in a logarithmic scale.

6 A Non-linear Elasticity Example

The proposed methodology is capable of handling problems with non-linearities. In order to demonstrate this capability, we proceed with a simple example shown in Fig. 6. The model problem consists of two masses equal to 10 ton connected by an elastic rod. In order to describe large rigid body motions, the corotational (CR) formulation is exploited [18,19]. The standard β-Newmark time integration method is used. Mass m_1 is constrained to the prescribed motion $u_1(t) = \sin(10\pi)$, with mass m_2 being free to move, while the gravity forces are also considered with a coefficient of gravity $g = 9.81\text{m/s}^2$. The elastic modulus and cross section area product is considered for two distinct values, that of $EA = 10^7\text{kN/m}$ as well as $EA = 10^4\text{kN/m}$ with an initial length $L = 5m$. In order to utilize the consistent penalty method for this problem, a large number for the penalty coefficient a_μ is selected, while the respective value for the a_κ coefficient is computed through the c ratio of Eq. (27) with k_{ii} being the relevant diagonal coefficient of the current tangent stiffness matrix. The same problem is also solved using the reduced two dimensional configuration space that is obtained through explicit incorporation of the prescribed motion, for reasons of comparison. We observe total agreement of the results obtained. The configuration of the rod at various time instances is depicted in Fig. 6.

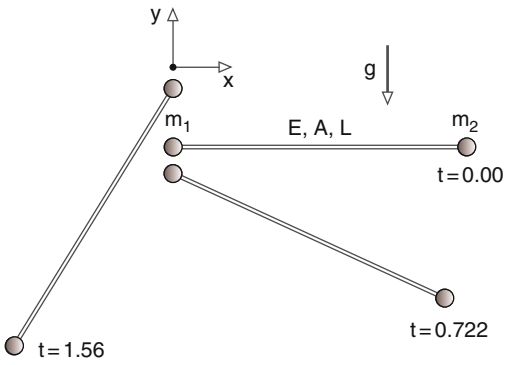


Fig. 6 Model problem of the corotational rod formulation

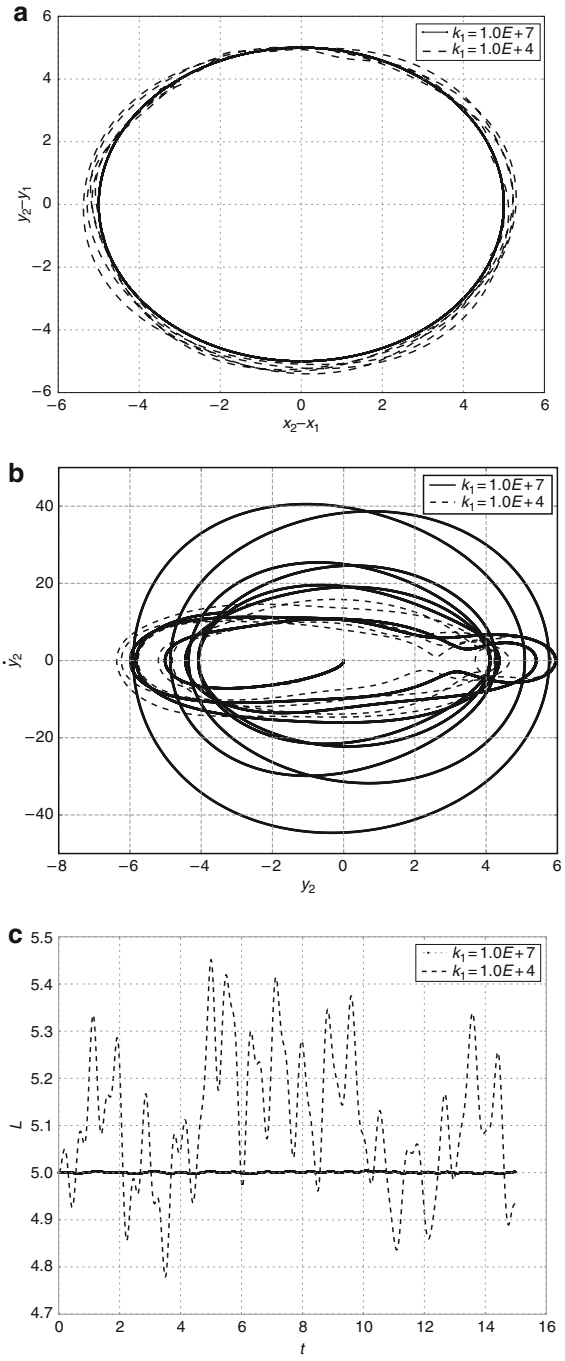


Fig. 7 Rod problem: (**a**) position difference $\Delta x = x_2 - x_1$ and $\Delta y = y_2 - y1$, (**b**) position y_2 of mass m_2 versus velocity $\dot{y}_2$, (**c**) rod deformation L in time t

Also, additional results are given in Fig. 7 where we note the almost rigid body motion of the rod for the first configuration of EA, while a finite deformation for the second configuration coexists with the almost rigid body motion.

7 Concluding Remarks

Based on a variationally consistent methodology, time dependent boundary conditions are incorporated within the context of elastodynamics. The development rests upon a modified weak formulation, which provides a solid basis for reliable imposition of time varying boundary conditions.

The prescribed boundary conditions are enforced via the consistent form of the penalty method, e.g. a form that conforms to the norm and inner product of the functional space where the weak formulation is defined. It is interesting to notice that the penalty parameters proposed depend only on the properties of the specific dynamical system. The derived methodology applies to linear as well as to nonlinear problems.

Also, it is shown that well known and broadly implemented modelling techniques such as the "large mass" and "large spring" methods, arise from the proposed penalty formulation by omitting specific terms. However, it is also shown these selections are not, in the general case, theoretically sound. The consistent penalty formulation is shown not to alter the order of the *stiffness* of the dynamical system under consideration, while the overall accuracy, in terms of a selected appropriate norm, is found to be the optimal one.

An extension of the proposed methodology in generalized weak forms where displacements, velocities and momentum type variables are taken to be independent, is presented in [1]. These formulations serves as a basis for the development of useful approximating schemes, where the embedding of the consistent penalty formulation is not trivial [20].

References

1. Paraskevopoulos EA, Panagiotopoulos CG, Manolis GD (2010) Imposition of time-dependent boundary conditions in FEM formulations for elastodynamics: critical assessment of penalty-type methods. Comput Mech 45:157–166
2. Arnold VI (1988) Mathematical methods of classical mechanics. Springer, New York
3. Stakgold I (1998) Green's functions and boundary value problem. Wiley, New York
4. Mindlin RD, Goodman LE (1950) Beam vibrations with time-dependent boundary conditions. ASME J Appl Mech 17:377–380
5. Babuska I (1973) The finite element method with Lagrangian multipliers. Numer Math 20:179–192
6. Babuska I (1973) The finite element method with penalty. Math Comput 27:221–228
7. Cook RD, Malkus DS, Plesha ME (1989) Concepts and applications of finite element analysis. Wiley, New York

8. Leger P, Idet IM, Paultre P (1990) Multiple-support seismic analysis of large structures. Comput Struct 36:1153–1158
9. Brezis H (1983) Analyse Functionelle, Thèorie et Applications. Masson, Paris
10. Rektorys K (1977) Variational methods in mathematics, science and engineering. D. Reidel Publishing Company, Dordrecht
11. Ženišek A (1990) Nonlinear elliptic and evolution problems and their finite element approximations. Academic, London, p 32
12. Courant R, Hilbert D (1989) Methods of mathematical physics, vol 2. Wiley, Berlin
13. Pitarresi JM, Manolis GD (1991) The temporal finite element method in structural dynamics. Comput Struct 41:647–655
14. Hughes TJR, Hulbert GM (1988) Space-time finite element methods for elastodynamics: formulations and error estimates. Comput Meth Appl Mech Eng 66:339–363
15. Bathe KJ (1995) Finite element procedures. Prentice-Hall, Englewood Cliffs
16. Brenan K, Campbell S, Petzold L (1989) Numerical solution of initial-value problems in differential-algebraic equations. North-Holland, Amsterdam
17. Geradin M, Cardona A (2001) Flexible multibody dynamics: a finite element approach. Wiley, New York
18. Belytschko T, Liu WK, Moran B (2001) Nonlinear finite elements for continua and structures. Wiley, New York
19. Wempner G, Talaslidis D (2003) Mechanics of solids and shells. CRC, Boca Raton
20. Paraskevopoulos EA, Panagiotopoulos CG, Talaslidis DG (2009) Rational derivation of conserving time integration schemes: the moving mass case. In: Papadrakakis M, Charmpis DC, Lagaros ND, Tsompanakis Y (eds) Computational structural dynamics and earthquake engineering. Taylor & Francis, London

Nonlinear Dynamic Analysis of Timoshenko Beams

E.J. Sapountzakis and J.A. Dourakopoulos

Abstract A boundary element method is developed for the nonlinear dynamic analysis of beams of arbitrary doubly symmetric simply or multiply connected constant cross section, undergoing moderate large displacements under general boundary conditions, taking into account the effects of shear deformation and rotary inertia. The beam is subjected to the combined action of arbitrarily distributed or concentrated transverse loading and bending moments in both directions as well as to axial loading. To account for shear deformations, the concept of shear deformation coefficients is used. Five boundary value problems are formulated and solved using the Analog Equation Method, a BEM based method. Application of the boundary element technique yields a nonlinear coupled system of equations of motion. The solution of this system is accomplished iteratively by employing the average acceleration method in combination with the modified Newton Raphson method. The evaluation of the shear deformation coefficients is accomplished from stress functions using only boundary integration. Both free and forced vibrations are examined.

Keywords Nonlinear dynamic analysis · Timoshenko beam · Moderate large displacements · Shear center · Shear deformation coefficients · Boundary element method

1 Introduction

The study of nonlinear effects on the dynamic analysis of structural elements is essential in aerospace, civil and mechanical engineering applications, wherein weight saving is of paramount importance. This nonlinearity results from retaining the square of the slope in the strain–displacement relations (intermediate

E.J. Sapountzakis (✉) and J.A. Dourakopoulos
School of Civil Engineering, National Technical University of Athens, Zografou Campus, GR-157 80 Athens, Greece
e-mail: cvsapoun@central.ntua.gr; jdour@mail.ntua.gr

M. Papadrakakis et al. (eds.), *Computational Methods in Earthquake Engineering*, Computational Methods in Applied Sciences 21, DOI 10.1007/978-94-007-0053-6_17,
© Springer Science+Business Media B.V. 2011

non-linear theory), avoiding in this way the inaccuracies arising from a linearized second – order analysis. Thus, the aforementioned study takes into account the influence of the action of axial, lateral forces and bending moments on the deformed shape of the structural element. Moreover, due to the intensive use of materials having relatively low transverse shear stiffness (high $EI/\kappa AG$) and short span members, as well as the need for beam members with high natural frequencies, the error incurred from the ignorance of the effect of shear deformation may be substantial. The Timoshenko beam theory, which includes shear deformation and rotary inertia effects has an extended range of applications as it allows treatment of deep beams (depth is large relative to length), short and thin-webbed beams and beams where higher modes are excited. However it introduces some complications not found in the elementary Bernoulli-Euler formulation.

When the deflections of the structure are small, a wide range of linear analysis tools, such as modal analysis, can be used, and some analytical results are possible. As the deflections become larger, the induced geometric nonlinearities result in effects that are not observed in linear systems. In such situations the possibility of an analytical solution method is significantly reduced and is restricted to special cases of beam boundary conditions or loading. During the past few years, the nonlinear dynamic analysis of the classical Bernoulli-Euler beam undergoing large deflections has received a good amount of attention in the literature employing semi-analytical solutions [1, 2], an exact successive integration and iteration technique [3, 4], a modeshape technique [5], the Hamilton's principle and a perturbation procedure [6], the Finite Element Method [7–13] and the Boundary Element Method [14, 15].

On the other hand, to the authors' knowledge very little work has been done on the corresponding nonlinear dynamic analysis of beams taking into account the effects of shear deformation and rotary inertia, while most of these research efforts concern only free vibrations of beams with special cases of boundary conditions. More specifically, Rao et al. [16] employing the finite element method and polynomial expressions for the displacement components presented the large amplitude free vibrations of slender beams. Foda [17] utilizing the method of multiple scales, considered the large amplitude free vibration of a simply supported Timoshenko beam. For the same beam Zhong and Guo [18] employed the Differential Quadrature Method, while Guo et al. [19] studied the effects of three cases of boundary conditions. Zhong and Liao [20] using a spline-based differential quadrature method presented the higher-order nonlinear free vibrations of Timoshenko beams with immovable ends, while Liao and Zhong [21] employing the Differential Quadrature Method studied the nonlinear flexural free vibrations of tapered Timoshenko beams with two simply supported or clamped ends. Moreover, the nonlinear dynamic analysis of a flexible Timoshenko beam with geometrical nonlinearities subjected to initial conditions employing the Galerkin's method [22], the Finite Element Method [23], the Lagrange's equation based on the expression of the kinetic and potential energies in terms of generalized coordinates [24, 25] are also presented taking into account or ignoring the axial differential equation of equilibrium. Finally, the effects of shear deformation and rotary inertia have been taken into account in linearized dynamic analysis [26] ignoring the squares of the derivatives of the deflections in

the normal strain component and the axial differential equation of equilibrium. The boundary element method has not yet been used for the nonlinear dynamic analysis of Timoshenko beams.

In this chapter, a boundary element method is developed for the nonlinear dynamic analysis of beams of arbitrary doubly symmetric simply or multiply connected constant cross section, undergoing moderate large deflections under general boundary conditions, taking into account the effects of shear deformation and rotary inertia. The beam is subjected to the combined action of arbitrarily distributed or concentrated transverse loading and bending moments in both directions as well as to axial loading. To account for shear deformations, the concept of shear deformation coefficients is used. Five boundary value problems are formulated with respect to the transverse displacements, to the axial displacement and to two stress functions and solved using the Analog Equation Method [27], a BEM based method. Application of the boundary element technique yields a nonlinear coupled system of equations of motion. The solution of this system is accomplished iteratively by employing the average acceleration method in combination with the modified Newton Raphson method [28, 29]. The evaluation of the shear deformation coefficients is accomplished from the aforementioned stress functions using only boundary integration. The essential features and novel aspects of the present formulation compared with previous ones are summarized as follows.

1. The beam is subjected to an arbitrarily distributed or concentrated transverse loading and bending moments in both directions as well as to axial loading.
2. The beam is supported by the most general nonlinear boundary conditions including elastic support or restraint, while its cross section is an arbitrary doubly symmetric one.
3. Shear deformation effect and rotary inertia are taken into account on the nonlinear dynamic analysis of beams subjected to arbitrary loading and boundary conditions.
4. The proposed model takes into account the coupling effects of bending and shear deformations along the member as well as shear forces along the span induced by the applied axial loading.
5. The shear deformation coefficients are evaluated using an energy approach, instead of Timoshenko's [30] and Cowper's [31] definitions, for which several authors [32, 33] have pointed out that one obtains unsatisfactory results or definitions given by other researchers [34, 35], for which these factors take negative values.
6. The effect of the material's Poisson ratio v is taken into account in the evaluation of shear deformation coefficients.
7. The proposed method employs a BEM approach (requiring boundary discretization) resulting in line or parabolic elements instead of area elements of the FEM solutions (requiring the whole cross section to be discretized into triangular or quadrilateral area elements), while a small number of line elements are required to achieve high accuracy.

Numerical examples are worked out to illustrate the efficiency, the accuracy and the range of applications of the developed method. Both free and forced vibrations are examined.

2 Statement of the Problem

Let us consider a prismatic beam of length l (Fig. 1), of constant arbitrary doubly symmetric cross-section of area A. The homogeneous isotropic and linearly elastic material of the beam cross-section, with modulus of elasticity E, shear modulus G and Poisson's ratio v occupies the two dimensional multiply connected region Ω of the y,z plane and is bounded by the $\Gamma_j (j = 1, 2, \ldots, K)$ boundary curves, which are piecewise smooth, i.e. they may have a finite number of corners. In Fig. 1b Cyz is the principal bending coordinate system through the cross section's centroid. The beam is subjected to the combined action of the arbitrarily distributed or concentrated time dependent axial loading $p_x = p_x(x,t)$, transverse loading $p_y = p_y(x,t)$, $p_z = p_z(x,t)$ acting in the y and z directions, respectively and bending moments $m_y = m_y(x,t)$, $m_z = m_z(x,t)$ along y and z axes, respectively (Fig. 1a).

Under the action of the aforementioned loading, the displacement field of the beam, taking into account shear deformation effect, is given as

$$\overline{u}(x,y,z,t) = u(x,t) - y\theta_z(x,t) + z\theta_y(x,t) \tag{1a}$$

$$\overline{v}(x,t) = v(x,t) \tag{1b}$$

$$\overline{w}(x,t) = w(x,t) \tag{1c}$$

where $\overline{u}$, $\overline{v}$, $\overline{w}$ are the axial and transverse beam displacement components with respect to the Cyz system of axes; $u(x,t)$, $v(x,t)$, $w(x,t)$ are the corresponding components of the centroid C and $\theta_y(x,t)$, $\theta_z(x,t)$ are the angles of rotation due to bending of the cross-section with respect to its centroid.

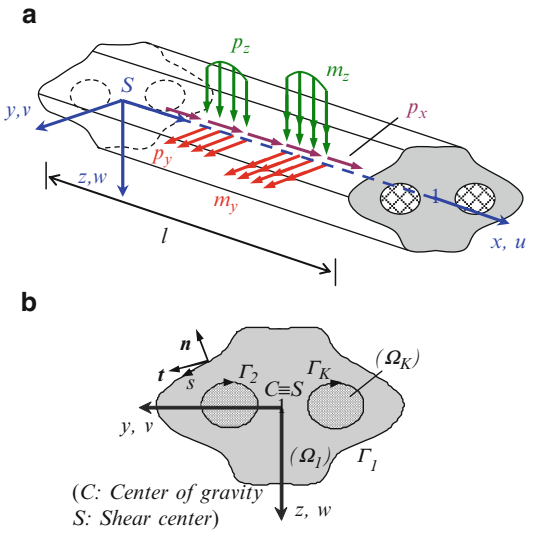


Fig. 1 Prismatic beam in axial – flexural loading (**a**) with an arbitrary doubly symmetric cross-section occupying the two dimensional region Ω (**b**)

Employing the strain-displacement relations of the three - dimensional elasticity for moderate large displacements [36, 37], the following strain components can be easily obtained

$$\varepsilon_{xx} = \frac{\partial \overline{u}}{\partial x} + \frac{1}{2}\left[\left(\frac{\partial \overline{v}}{\partial x}\right)^2 + \left(\frac{\partial \overline{w}}{\partial x}\right)^2\right] \tag{2a}$$

$$\gamma_{xz} = \frac{\partial \overline{w}}{\partial x} + \frac{\partial \overline{u}}{\partial z} + \left(\frac{\partial \overline{v}}{\partial x}\frac{\partial \overline{v}}{\partial z} + \frac{\partial \overline{w}}{\partial x}\frac{\partial \overline{w}}{\partial z}\right) \tag{2b}$$

$$\gamma_{xy} = \frac{\partial \overline{v}}{\partial x} + \frac{\partial \overline{u}}{\partial y} + \left(\frac{\partial \overline{v}}{\partial x}\frac{\partial \overline{v}}{\partial y} + \frac{\partial \overline{w}}{\partial x}\frac{\partial \overline{w}}{\partial y}\right) \tag{2c}$$

$$\varepsilon_{yy} = \varepsilon_{zz} = \gamma_{yz} = 0 \tag{2d}$$

where it has been assumed that for moderate displacements $(\partial\overline{u}/\partial x)^2 << \partial\overline{u}/\partial x$, $(\partial\overline{u}/\partial x)(\partial\overline{u}/\partial z) << (\partial\overline{u}/\partial x) + (\partial\overline{u}/\partial z)$, $(\partial\overline{u}/\partial x)(\partial\overline{u}/\partial y) << (\partial\overline{u}/\partial x) + (\partial\overline{u}/\partial y)$. Substituting the displacement components (1) to the strain-displacement relations (2), the strain components can be written as

$$\varepsilon_{xx}(x, y, z, t) = u' + z\theta_y' - y\theta_z' + \frac{1}{2}(v'^2 + w'^2) \tag{3a}$$

$$\gamma_{xy} = v' - \theta_z \tag{3b}$$

$$\gamma_{xz} = w' + \theta_y \tag{3c}$$

where γ_{xy}, γ_{xz} are the additional angles of rotation of the cross-section due to shear deformation.

Considering strains to be small, employing the second Piola–Kirchhoff stress tensor and assuming an isotropic and homogeneous material, the stress components are defined in terms of the strain ones as

$$\begin{Bmatrix} S_{xx} \\ S_{xy} \\ S_{xz} \end{Bmatrix} = \begin{bmatrix} E & 0 & 0 \\ 0 & G & 0 \\ 0 & 0 & G \end{bmatrix} \begin{Bmatrix} \varepsilon_{xx} \\ \gamma_{xy} \\ \gamma_{xz} \end{Bmatrix} \tag{4}$$

or employing Eqs. (3) as

$$S_{xx} = E\left[u' + z\theta_y' - y\theta_z' + \frac{1}{2}(v'^2 + w'^2)\right] \tag{5a}$$

$$S_{xy} = G \cdot (v' - \theta_z) \tag{5b}$$

$$S_{xz} = G \cdot (w' + \theta_y) \tag{5c}$$

On the basis of Hamilton's principle, the variations of the Lagrangian equation defined as

$$\delta \int_{t_1}^{t_2} (U - K - W_{ext})dt = 0 \tag{6}$$

and expressed as a function of the stress resultants acting on the cross section of the beam in the deformed state provide the governing equations and the boundary conditions of the beam subjected to nonlinear vibrations. In Eq. (6) $\delta(\cdot)$ denotes variation of quantities, while U, K, W_{ext} are the strain energy, the kinetic energy and the external load work, respectively given as

$$\delta U = \int_V (S_{xx}\delta\varepsilon_{xx} + S_{xy}\delta\gamma_{xy} + S_{xz}\delta\gamma_{xz})dV \tag{7a}$$

$$\delta K = \int_V \rho(\dot{\bar{u}}\delta\dot{\bar{u}} + \dot{\bar{v}}\delta\dot{\bar{v}} + \dot{\bar{w}}\delta\dot{\bar{w}})dV \tag{7b}$$

$$\delta W_{ext} = \int_L (p_x\delta u + p_y\delta v + p_z\delta w + m_y\delta\theta_y + m_z\delta\theta_z)dx \tag{7c}$$

Moreover, the stress resultants of the beam are given as

$$N = \int_\Omega S_{xx}d\Omega \tag{8a}$$

$$\mathrm{M}_y = \int_\Omega S_{xx}zd\Omega \qquad \mathrm{M}_z = -\int_\Omega S_{xx}yd\Omega \tag{8b,c}$$

$$Q_y = \int_{A_y} S_{xy}d\Omega \qquad Q_z = \int_{A_z} S_{xz}d\Omega \tag{8d,e}$$

Substituting the expressions of the stress components (5) into Eqs. (8), the stress resultants are obtained as

$$N = EA\left[u' + \frac{1}{2}\left(v'^2 + w'^2\right)\right] \tag{9a}$$

$$M_y = EI_y\theta_y' \qquad M_z = EI_z\theta_z' \tag{9b,c}$$

$$Q_y = GA_y\gamma_{xy} \qquad Q_z = GA_z\gamma_{xz} \tag{9d,e}$$

where A is the cross section area, I_y, I_z the moments of inertia with respect to the principle bending axes given as

$$A = \int_\Omega d\Omega \tag{10}$$

$$I_y = \int_\Omega z^2 d\Omega \qquad I_z = \int_\Omega y^2 d\Omega \tag{11a,b}$$

and GA_y, GA_z are its shear rigidities of the Timoshenko's beam theory, where

$$A_z = \kappa_z A = \frac{1}{a_z} A \qquad A_y = \kappa_y A = \frac{1}{a_y} A \tag{12a,b}$$

are the shear areas with respect to y, z axes, respectively with κ_y, κ_z the shear correction factors and a_y, a_z the shear deformation coefficients. Substituting the stress components given in Eqs. (5) and the strain resultants given in Eq. (3) to the strain energy variation $\delta \mathrm{E}_{\mathrm{int}}$ (Eq. 7a) and employing Eq. (6) the equilibrium equations of the beam are derived as

$$-EA(u'' + w'w'' + v'v'') + \rho \mathrm{A}\ddot{u} = p_x \tag{13a}$$
$$-(Nv')' + \rho \mathrm{A}\ddot{v} - GA_y(v'' - \theta_z') = p_y \tag{13b}$$
$$-EI_z\theta_z'' + \rho I_z\ddot{\theta}_z - GA_y(v' - \theta_z) = m_z \tag{13c}$$
$$-(Nw')' + \rho \mathrm{A}\ddot{w} - GA_z(w'' + \theta_y') = p_z \tag{13d}$$
$$-EI_y\theta_y'' + \rho I_y\ddot{\theta}_y + GA_z(w' + \theta_y) = m_y \tag{13e}$$

Combining Eqs. (13b,c) and (13d,e), the following differential equations with respect to u, v, w are derived

$$-EA(u'' + w'w'' + v'v'') + \rho \mathrm{A}\ddot{u} = p_x \tag{14a}$$

$$EI_z v'''' - \rho I_z\left(\frac{Ea_y}{G} + 1\right)\frac{\partial^2 \ddot{v}}{\partial x^2} + \rho \mathrm{A}\ddot{v} + \frac{EI_z}{GA_y}(Nv')'' - (Nv')' - \frac{\rho I_z}{GA_y}\left(\frac{\partial^2 (Nv')'}{\partial t^2} - \rho A\ddot{v}\right) = p_y - \frac{EI_z}{GA_y}p_y'' + \frac{\rho I_z}{GA_y}\ddot{p}_y - m_z' \tag{14b}$$

$$EI_y w'''' - \rho I_y\left(\frac{Ea_z}{G} + 1\right)\frac{\partial^2 \ddot{w}}{\partial x^2} + \rho \mathrm{A}\ddot{w} + \frac{EI_y}{GA_z}(Nw')'' - (Nw')' - \frac{\rho I_y}{GA_z}\left(\frac{\partial^2 (Nw')'}{\partial t^2} - \rho A\ddot{w}\right) = p_z - \frac{EI_y}{GA_z}p_z'' + \frac{\rho I_y}{GA_z}\ddot{p}_z + m_y' \tag{14c}$$

Equations (14) constitute the governing differential equations of a Timoshenko beam subjected to nonlinear vibrations due to the combined action of time dependent axial, transverse loading and bending moments. These equations are also subjected to the pertinent boundary conditions of the problem, which are given as

$$a_1 u(x,t) + \alpha_2 N(x,t) = \alpha_3 \tag{15}$$

$$\beta_1 v(x,t) + \beta_2 V_y(x,t) = \beta_3 \qquad \overline{\beta}_1\theta_z(x,t) + \overline{\beta}_2 \mathrm{M}_z(x,t) = \overline{\beta}_3 \tag{16a,b}$$

$$\gamma_1 w(x,t) + \gamma_2 V_z(x,t) = \gamma_3 \qquad \overline{\gamma}_1\theta_y(x,t) + \overline{\gamma}_2 \mathrm{M}_y(x,t) = \overline{\gamma}_3 \tag{17a,b}$$

at the beam ends $x = 0, l$, together with the initial conditions

$$u(x,0) = \overline{u}_0(x) \quad \dot{u}(x,0) = \dot{\overline{u}}_0(x) \tag{18a,b}$$

$$v(x,0) = \overline{v}_0(x) \quad \dot{v}(x,0) = \dot{\overline{v}}_0(x) \tag{19a,b}$$

$$w(x,0) = \overline{w}_0(x) \quad \dot{w}(x,0) = \dot{\overline{w}}_0(x) \tag{20a,b}$$

where $\overline{u}_0(x)$, $\overline{v}_0(x)$, $\overline{w}_0(x)$, $\dot{\overline{u}}_0(x)$, $\dot{\overline{v}}_0(x)$ and $\dot{\overline{w}}_0(x)$ are prescribed functions. In Eqs. (16a,b), (17a,b) V_y, V_z and M_y, M_z are the reactions and bending moments at the boundary with respect to y, z axes, respectively, which together with the angles of rotation due to bending θ_y, θ_z are given by the following relations

$$V_y = Nv' - EI_z v''' - \frac{EI_z}{GA_y}\left[Nv''' - \rho A\frac{\partial \ddot{v}}{\partial x}\right] + \rho I_z \ddot{\theta}_z \tag{21a}$$

$$V_z = Nw' - EI_y w''' - \frac{EI_y}{GA_z}\left[Nw''' - \rho A\frac{\partial \ddot{w}}{\partial x}\right] - \rho I_y \ddot{\theta}_y \tag{21b}$$

$$M_z = EI_z v'' + \frac{EI_z}{GA_y}[Nv'' - \rho A\ddot{v}] \tag{21c}$$

$$M_y = -EI_y w'' - \frac{EI_y}{GA_z}[Nw'' - \rho A\ddot{w}] \tag{21d}$$

$$\theta_y = \frac{EI_y}{G^2A_z^2}\left(\rho A\frac{\partial \ddot{w}}{\partial x} - Nw'''\right) - \frac{1}{GA_z}\left(EI_z w''' + \rho I_y \ddot{\theta}_y + GA_z w'\right) \tag{21e}$$

$$\theta_z = \frac{EI_z}{G^2A_y^2}\left(Nv''' - \rho A\frac{\partial \ddot{v}}{\partial x}\right) + \frac{1}{GA_y}\left(EI_z v''' - \rho I_z \ddot{\theta}_z + GA_y v'\right) \tag{21f}$$

Finally, $\alpha_k, \beta_k, \overline{\beta}_k, \gamma_k, \overline{\gamma}_k (k = 1,2,3)$ are functions specified at the beam ends $x = 0, l$. Eqs. (15)–(17) describe the most general nonlinear boundary conditions associated with the problem at hand and can include elastic support or restraint. It is apparent that all types of the conventional boundary conditions (clamped, simply supported, free or guided edge) can be derived from these equations by specifying appropriately these functions (e.g. for a clamped edge it is $\alpha_1 = \beta_1 = \gamma_1 = 1$, $\alpha_2 = \alpha_3 = \beta_2 = \beta_3 = \gamma_2 = \gamma_3 = \overline{\beta}_2 = \overline{\beta}_3 = \overline{\gamma}_2 = \overline{\gamma}_3 = 0 \quad \overline{\beta}_1 = \overline{\gamma}_1 = 1$).

The solution of the initial boundary value problem given from Eqs. (14), subjected to the boundary conditions (15)–(17) and the initial conditions (18)–(20) which represents the nonlinear flexural dynamic analysis of Timoshenko beams, presumes the evaluation of the shear deformation coefficients a_y, a_z, corresponding to the principal coordinate system Cyz. These coefficients are established equating the approximate formula of the shear strain energy per unit length [33]

$$U_{appr.} = \frac{a_y Q_y^2}{2AG} + \frac{a_z Q_z^2}{2AG} \tag{22}$$

with the exact one given from

$$U_{exact} = \int_{\Omega} \frac{(\tau_{xz})^2 + (\tau_{xy})^2}{2G} d\Omega \tag{23}$$

and are obtained as [38]

$$a_y = \frac{1}{\kappa_y} = \frac{A}{\Delta^2} \int_{\Omega} [(\nabla\Theta) - \mathbf{e}] \cdot [(\nabla\Theta) - \mathbf{e}] d\Omega \tag{24a}$$

$$a_z = \frac{1}{\kappa_z} = \frac{A}{\Delta^2} \int_{\Omega} [(\nabla\Phi) - \mathbf{d}] \cdot [(\nabla\Phi) - \mathbf{d}] d\Omega \tag{24b}$$

where $(\tau_{xz})_j, (\tau_{xy})_j$ are the transverse (direct) shear stress components, $(\nabla) \equiv \mathbf{i}_y(\partial/\partial y) + \mathbf{i}_z(\partial/\partial z)$ is a symbolic vector with $\mathbf{i}_y$, $\mathbf{i}_z$ the unit vectors along y and z axes, respectively, Δ is given from

$$\Delta = 2(1+\nu)\mathrm{I}_y\mathrm{I}_z \tag{25}$$

ν is the Poisson ratio of the cross section material, $\mathbf{e}$ and $\mathbf{d}$ are vectors defined as

$$\mathbf{e} = \left(\nu I_y \frac{y^2 - z^2}{2}\right)\mathbf{i}_y + \nu I_y yz\mathbf{i}_z \tag{26a}$$

$$\mathbf{d} = \nu I_z yz\mathbf{i}_y - \left(\nu I_z \frac{y^2 - z^2}{2}\right)\mathbf{i}_z \tag{26b}$$

and $\Theta(y,z)$, $\Phi(y,z)$ are stress functions, which are evaluated from the solution of the following Neumann type boundary value problems [38]

$$\nabla^2\Theta = -2I_y y \qquad \text{in } \Omega \tag{27a}$$

$$\frac{\partial\Theta}{\partial n} = \mathbf{n}\cdot\mathbf{e} \qquad \text{on } \Gamma = \bigcup_{j=1}^{K+1} \Gamma_j \tag{27b}$$

$$\nabla^2\Phi = -2I_z z \qquad \text{in } \Omega \tag{28a}$$

$$\frac{\partial\Phi}{\partial n} = \mathbf{n}\cdot\mathbf{d} \qquad \text{on } \Gamma = \bigcup_{j=1}^{K+1} \Gamma_j \tag{28b}$$

where $\mathbf{n}$ is the outward normal vector to the boundary Γ. In the case of negligible shear deformations $a_z = a_y = 0$. It is also worth here noting that the boundary conditions (27b), (28b) have been derived from the physical consideration that the traction vector in the direction of the normal vector $\mathbf{n}$ vanishes on the free surface of the beam.

3 Integral Representations – Numerical Solution

According to the precedent analysis, the nonlinear flexural dynamic analysis of Timoshenko beams, undergoing moderate large displacements reduces in establishing the displacement components $u(x,t)$ and $v(x,t)$, $w(x,t)$ having continuous derivatives up to the second order and up to the fourth order with respect to x, respectively, and also having derivatives up to the second order with respect to t (ignoring the inertia terms of the fourth order [39]). Moreover, these displacement components must satisfy the coupled governing differential Eqs. (14) inside the beam, the boundary conditions (15)–(17) at the beam ends $x = 0, l$ and the initial conditions (18)–(20). Equations (14) are solved using the Analog Equation Method [27] as it is developed for hyperbolic differential equations [40].

3.1 For the Transverse Displacements v, w

Let $v(x,t)$, $w(x,t)$ be the sought solution of the aforementioned boundary value problem. Setting as $u_2(x,t) = v(x,t)$, $u_3(x,t) = w(x,t)$ and differentiating these functions four times with respect to x yields

$$\frac{\partial^4 u_i}{\partial x^4} = q_i(x,t)(i = 2,3) \tag{29}$$

Equations (29) are quasi-static, that is the time variable appears as a parameter. They indicate that the solution of Eqs. (14b), (14c) can be established by solving Eqs. (29) under the same boundary conditions (16)–(17), provided that the fictitious load distributions $q_i(x,t)(i = 2,3)$ are first established. These distributions can be determined using BEM as follows.

Following the procedure presented in [39] and employing the constant element assumption for the load distributions q_i along the L internal beam elements (as the numerical implementation becomes very simple and the obtained results are of high accuracy), the integral representations of the displacement components $u_i(i = 2,3)$ and their first derivatives with respect to x when applied for the beam ends $(0, l)$, together with the boundary conditions (16)–(17) are employed to express the unknown boundary quantities $u_i(\zeta,t)$, $u_{i,x}(\zeta,t)$, $u_{i,xx}(\zeta,t)$ and $u_{i,xxx}(\zeta,t)$ $(\zeta = 0, l)$ in terms of q_i as

$$\begin{bmatrix} \mathbf{D}_{11} & 0 & \mathbf{D}_{13} & \mathbf{D}_{14} \\ \mathbf{D}_{21} & \mathbf{D}_{22} & \mathbf{D}_{23} & 0 \\ \mathbf{E}_{31} & \mathbf{E}_{32} & \mathbf{E}_{33} & \mathbf{E}_{34} \\ \mathbf{E}_{41} & \mathbf{E}_{42} & \mathbf{E}_{43} & 0 \end{bmatrix} \begin{Bmatrix} \hat{\mathbf{u}}_{2,xxx} \\ \hat{\mathbf{u}}_{2,xx} \\ \hat{\mathbf{u}}_{2,x} \\ \hat{\mathbf{u}}_{2} \end{Bmatrix} = \begin{Bmatrix} \boldsymbol{\beta}_3 \\ \overline{\boldsymbol{\beta}}_3 \\ 0 \\ 0 \end{Bmatrix} + \begin{Bmatrix} 0 \\ 0 \\ \mathbf{F}_3 \\ \mathbf{F}_4 \end{Bmatrix} \mathbf{q}_2 \tag{30a}$$

$$\begin{bmatrix} \mathbf{G}_{11} & 0 & \mathbf{G}_{13} & \mathbf{G}_{14} \\ \mathbf{G}_{21} & \mathbf{G}_{22} & \mathbf{G}_{23} & 0 \\ \mathbf{E}_{31} & \mathbf{E}_{32} & \mathbf{E}_{33} & \mathbf{E}_{34} \\ \mathbf{E}_{41} & \mathbf{E}_{42} & \mathbf{E}_{43} & 0 \end{bmatrix} \begin{Bmatrix} \hat{\mathbf{u}}_{3,xxx} \\ \hat{\mathbf{u}}_{3,xx} \\ \hat{\mathbf{u}}_{3,x} \\ \hat{\mathbf{u}}_{3} \end{Bmatrix} = \begin{Bmatrix} \boldsymbol{\gamma}_3 \\ \overline{\boldsymbol{\gamma}}_3 \\ 0 \\ 0 \end{Bmatrix} + \begin{Bmatrix} 0 \\ 0 \\ \mathbf{F}_3 \\ \mathbf{F}_4 \end{Bmatrix} \mathbf{q}_3 \tag{30b}$$

where $\mathbf{D}_{11}, \mathbf{D}_{13}, \mathbf{D}_{14}, \mathbf{D}_{21}, \mathbf{D}_{22}, \mathbf{D}_{23}, \mathbf{G}_{11}, \mathbf{G}_{13}, \mathbf{G}_{14}, \mathbf{G}_{21}, \mathbf{G}_{22}, \mathbf{G}_{23}$ are 2×2 known square matrices including the values of the functions $\beta_j, \overline{\beta}_j, \gamma_j, \overline{\gamma}_j$ $(j = 1, 2)$ of Eqs. (16)–(17); $\boldsymbol{\beta}_3, \overline{\boldsymbol{\beta}}_3, \boldsymbol{\gamma}_3, \overline{\boldsymbol{\gamma}}_3$ are 2×1 known column matrices including the boundary values of the functions $\beta_3, \overline{\beta}_3, \gamma_3, \overline{\gamma}_3$ of Eqs. (16)–(17); $\mathbf{E}_{jk}$, $(j = 3, 4, k = 1, 2, 3, 4)$ are square 2×2 known coefficient matrices and $\mathbf{F}_j$ $(j = 3, 4)$ are $2 \times L$ rectangular known matrices originating from the integration of kernels on the axis of the beam. Moreover,

$$\hat{\mathbf{u}}_i = \{u_i(0,t)\, u_i(l,t)\}^T \tag{31a}$$

$$\hat{\mathbf{u}}_{i,x} = \left\{ \frac{\partial u_i(0,t)}{\partial x} \; \frac{\partial u_i(l,t)}{\partial x} \right\}^T \tag{31b}$$

$$\hat{\mathbf{u}}_{i,xx} = \left\{ \frac{\partial^2 u_i(0,t)}{\partial x^2} \; \frac{\partial^2 u_i(l,t)}{\partial x^2} \right\}^T \tag{31c}$$

$$\hat{\mathbf{u}}_{i,xxx} = \left\{ \frac{\partial^3 u_i(0,t)}{\partial x^3} \; \frac{\partial^3 u_i(l,t)}{\partial x^3} \right\}^T \tag{31d}$$

are vectors including the two unknown boundary values of the respective boundary quantities and $\mathbf{q}_i = \{q_1^i \, q_2^i \, ... \, q_L^i\}^T$ $(i = 2, 3)$ is the vector including the L unknown nodal values of the fictitious load.

Discretization of the integral representations of the displacement components u_i $(i = 2, 3)$ and their derivatives with respect to x, after elimination of the boundary quantities employing Eqs. (30), gives

$$\mathbf{u}_i = \mathbf{T}_i \mathbf{q}_i + \mathbf{t}_i \quad i = 2, 3 \tag{32a}$$

$$\mathbf{u}_{i,x} = \mathbf{T}_{ix} \mathbf{q}_i + \mathbf{t}_{ix} \quad i = 2, 3 \tag{32b}$$

$$\mathbf{u}_{i,xx} = \mathbf{T}_{ixx} \mathbf{q}_i + \mathbf{t}_{ixx} \quad i = 2, 3 \tag{32c}$$

$$\mathbf{u}_{i,xxx} = \mathbf{T}_{ixxx} \mathbf{q}_i + \mathbf{t}_{ixxx} \quad i = 2, 3 \tag{32d}$$

$$\mathbf{u}_{i,xxxx} = \mathbf{q}_i \quad i = 2, 3 \tag{32e}$$

where $\mathbf{u}_i$, $\mathbf{u}_{i,x}$, $\mathbf{u}_{i,xx}$, $\mathbf{u}_{i,xxx}$, $\mathbf{u}_{i,xxxx}$ are vectors including the values of $u_i(x,t)$ and their derivatives at the L nodal points, $\mathbf{T}_i$, $\mathbf{T}_{ix}$, $\mathbf{T}_{ixx}$, $\mathbf{T}_{ixxx}$ are known $L \times L$ matrices and $\mathbf{t}_i$, $\mathbf{t}_{ix}$, $\mathbf{t}_{ixx}$, $\mathbf{t}_{ixxx}$ are known $L \times 1$ matrices.

In the conventional BEM, the load vectors $\mathbf{q}_i$ are known and Eqs. (32) are used to evaluate $u_i(x,t)$ and their derivatives at the L nodal points. This, however, can not be done here since $\mathbf{q}_i$ are unknown. For this purpose, $2L$ additional equations are derived, which permit the establishment of $\mathbf{q}_i$. These equations result by applying Eqs. (14b), (14c) to the L collocation points, which after ignoring the inertia terms

of the fourth order arising from coupling of shear deformations and rotary inertia [39], lead to the formulation of the following set of $2L$ simultaneous equations

$$\mathbf{M}_2\ddot{\mathbf{q}}_2 + \mathbf{S}_2\dot{\mathbf{q}}_2 + \mathbf{K}_2\mathbf{q}_2 = \mathbf{f}_2 \tag{33a}$$

$$\mathbf{M}_3\ddot{\mathbf{q}}_3 + \mathbf{S}_3\dot{\mathbf{q}}_3 + \mathbf{K}_3\mathbf{q}_3 = \mathbf{f}_3 \tag{33b}$$

where the $\mathbf{M}_2$, $\mathbf{M}_3$, $\mathbf{S}_2$, $\mathbf{S}_3$, $\mathbf{K}_2$, $\mathbf{K}_3$ $L \times L$ matrices and the $\mathbf{f}_2$, $\mathbf{f}_3$ $L \times 1$ vectors are given as

$$\mathbf{M}_2 = \rho A\mathbf{T}_2 - \rho \mathrm{I}_z\left(\frac{Ea_y}{G} + 1\right)\mathbf{T}_{2xx} - \frac{\rho I_z}{GA_y}\left(\mathbf{N}_x\mathbf{T}_{2x} + \mathbf{N}\mathbf{T}_{2xx}\right) \tag{34a}$$

$$\mathbf{S}_2 = -\frac{2\rho I_z}{GA_y}\left(\mathbf{N}_{xt}\mathbf{T}_{2x} + \mathbf{N}_t\mathbf{T}_{2xx}\right) \tag{34b}$$

$$\begin{aligned}\mathbf{K}_2 = {} & \mathbf{E}\mathbf{I}_z - \mathbf{N}_x\mathbf{T}_{2x} - \mathbf{N}\mathbf{T}_{2xx} + \frac{EI_z}{GA_y}(\mathbf{N}_{xxx}\mathbf{T}_{2x} \\ & + 3\mathbf{N}_{xx}\mathbf{T}_{2xx} + 3\mathbf{N}_x\mathbf{T}_{2xxx} + \mathbf{N}) - \frac{\rho I_z}{GA_y}\left(\mathbf{N}_{xtt}\mathbf{T}_{2x} + \mathbf{N}_{tt}\mathbf{T}_{2xx}\right)\end{aligned} \tag{34c}$$

$$\begin{aligned}\mathbf{f}_2 = {} & \mathbf{p}_y - \frac{EI_z}{GA_y}\mathbf{p}_{y,xx} + \frac{\rho I_z}{GA_y}\mathbf{p}_{y,tt} - \mathbf{m}_{z,x} + \mathbf{N}_x\mathbf{t}_{2x} + \mathbf{N}\mathbf{t}_{2xx} - \frac{EI_z}{GA_y}(\mathbf{N}_{xxx}\mathbf{t}_{2x} \\ & + 3\mathbf{N}_{xx}\mathbf{t}_{2xx} + 3\mathbf{N}_x\mathbf{t}_{2xxx}) + \frac{\rho I_z}{GA_y}\left(\mathbf{N}_{xtt}\mathbf{t}_{2x} + \mathbf{N}_{tt}\mathbf{t}_{2xx}\right)\end{aligned} \tag{34d}$$

$$\mathbf{M}_3 = \rho A\mathbf{T}_3 - \rho \mathrm{I}_y\left(\frac{Ea_z}{G} + 1\right)\mathbf{T}_{3xx} - \frac{\rho I_y}{GA_z}\left(\mathbf{N}_x\mathbf{T}_{3x} + \mathbf{N}\mathbf{T}_{3xx}\right) \tag{34e}$$

$$\mathbf{S}_3 = -\frac{2\rho I_y}{GA_z}\left(\mathbf{N}_{xt}\mathbf{T}_{3x} + \mathbf{N}_t\mathbf{T}_{3xx}\right) \tag{34f}$$

$$\begin{aligned}\mathbf{K}_3 = {} & \mathbf{E}\mathbf{I}_y - \mathbf{N}_x\mathbf{T}_{3x} - \mathbf{N}\mathbf{T}_{3xx} + \frac{EI_y}{GA_z}(\mathbf{N}_{xxx}\mathbf{T}_{3x} + 3\mathbf{N}_{xx}\mathbf{T}_{3xx} \\ & + 3\mathbf{N}_x\mathbf{T}_{3xxx} + \mathbf{N}) - \frac{\rho I_y}{GA_z}\left(\mathbf{N}_{xtt}\mathbf{T}_{3x} + \mathbf{N}_{tt}\mathbf{T}_{3xx}\right)\end{aligned} \tag{34g}$$

$$\begin{aligned}\mathbf{f}_3 = {} & \mathbf{p}_z - \frac{EI_y}{GA_z}\mathbf{p}_{z,xx} + \frac{\rho I_y}{GA_z}\mathbf{p}_{z,tt} + \mathbf{m}_{y,x} + \mathbf{N}_x\mathbf{t}_{3x} + \mathbf{N}\mathbf{t}_{3xx} - \frac{EI_y}{GA_z}(\mathbf{N}_{xxx}\mathbf{t}_{3x} \\ & + 3\mathbf{N}_{xx}\mathbf{t}_{3xx} + 3\mathbf{N}_x\mathbf{t}_{3xxx}) + \frac{\rho I_y}{GA_z}\left(\mathbf{N}_{xtt}\mathbf{t}_{3x} + \mathbf{N}_{tt}\mathbf{t}_{3xx}\right)\end{aligned} \tag{34h}$$

where $\mathbf{N}$, $\mathbf{N}_{km}(\mathbf{k}, \mathbf{m} = \mathbf{x}, \mathbf{t})$ are $L \times L$ diagonal matrices containing the values of the axial force and its derivatives with respect to k and m parameters at the L nodal points, $\mathbf{EI}_y$, $\mathbf{EI}_z$ are $L \times L$ diagonal matrices including the values of the corresponding quantities, at the aforementioned points, while $\mathbf{p}_y$, $\mathbf{p}_{y,xx}$, $\mathbf{p}_{y,tt}$, $\mathbf{p}_z$, $\mathbf{p}_{z,xx}$, $\mathbf{p}_{z,tt}$, $\mathbf{m}_{y,x}$ and $\mathbf{m}_{z,x}$ are $L \times 1$ vectors containing the values of the external loading and its derivatives at these points.

3.2 For the Axial Displacement u

Let $u_1 = u(x,t)$ be the sought solution of the boundary value problem described by Eqs. (14a) and (15). Differentiating this function two times yields

$$\frac{\partial^2 u_1}{\partial x^2} = q_x(x,t) \tag{35}$$

Equation (35) indicates that the solution of the original problem can be obtained as the axial displacement of a beam with unit axial rigidity subjected to an axial fictitious load $q_x(x,t)$ under the same boundary conditions. The fictitious load is unknown. Following the same procedure as in previous section, the discretized counterpart of the integral representations of the displacement component u_1 and its first derivative with respect to x when applied to all nodal points in the interior of the beam yields

$$\mathbf{u_1} = \mathbf{T_1 q_1} + \mathbf{t_1} \tag{36a}$$

$$\mathbf{u_{1,x}} = \mathbf{T_{1x} q_1} + \mathbf{t_{1x}} \tag{36b}$$

where $\mathbf{T_1}$, $\mathbf{T_{1x}}$ are known $L \times L$ matrices, similar with those mentioned before for the displacements u_2 u_3. Application of Eq. (14a) to the L collocation points, after employing Eqs. (32), (36) leads to the formulation of the following system of L equations with respect to $\mathbf{q_1}$, $\mathbf{q_2}$ and $\mathbf{q_3}$ fictitious load vectors

$$\begin{aligned}\mathbf{EA q_1} - \rho\mathbf{A T_1}\ddot{\mathbf{q}}_\mathbf{1} = &-\mathbf{p_x} - \mathbf{EA}[(\mathbf{T}_{2xx}\mathbf{q_2} + \mathbf{t}_{2xx})]_{dg}.(\mathbf{T}_{2x}\mathbf{q_2} + \mathbf{t}_{2x}) \\ &-\mathbf{EA}[(\mathbf{T}_{3xx}\mathbf{q_3} + \mathbf{t}_{3xx})]_{dg}.(\mathbf{T}_{3x}\mathbf{q_3} + \mathbf{t}_{3x})\end{aligned} \tag{37}$$

where $\mathbf{EA}$, $\rho\mathbf{A}$ are $L \times L$ diagonal matrices including the values of the corresponding quantities at the L nodal points. Moreover, substituting Eqs. (32) and (36) in Eq. (9a) the discretized counterpart of the axial force at the neutral axis of the beam is given as

$$\begin{aligned}\mathbf{N} = &\mathbf{EA}(\mathbf{T}_{1x}\mathbf{q}_1 + \mathbf{t}_{1x}) + \frac{1}{2}\mathbf{EA}[(\mathbf{T}_{2x}\mathbf{q_2} + \mathbf{t}_{2x})]_{dg}(\mathbf{T}_{2x}\mathbf{q_2} + \mathbf{t}_{2x}) \\ &+\frac{1}{2}\mathbf{EA}[(\mathbf{T}_{3x}\mathbf{q_3} + \mathbf{t}_{3x})]_{dg}(\mathbf{T}_{3x}\mathbf{q_3} + \mathbf{t}_{3x})\end{aligned} \tag{38}$$

Equations (33a), (33b), (37) and (38) constitute a nonlinear coupled system of equations with respect to $\mathbf{q_1}$, $\mathbf{q_2}$, $\mathbf{q_3}$ and $\mathbf{N}$ quantities. The solution of this system is accomplished iteratively by employing the average acceleration method in combination with the modified Newton Raphson method [28, 29].

3.3 For the Stress Functions $\Theta(y,z)$ and $\Phi(y,z)$

The evaluation of the stress functions $\Theta(y,z)$ and $\Phi(y,z)$ is accomplished using BEM as this is presented in Sapountzakis and Mokos [38].

Moreover, since the nonlinear flexural problem of Timoshenko beams is solved by the BEM, the domain integrals for the evaluation of the area, the bending moments of inertia (Eqs. 10) and the shear deformation coefficients (Eqs. 4) have to be converted to boundary line integrals, in order to maintain the pure boundary character of the method. This can be achieved using integration by parts, the Gauss theorem and the Green identity. Thus, the moments, the product of inertia and the cross section area can be written as

$$I_y = \int_\Gamma (yz^2 n_y) ds \tag{39a}$$

$$I_z = \int_\Gamma (zy^2 n_z) ds \tag{39b}$$

$$A = \frac{1}{2} \int_\Gamma (y n_y + z n_z) ds \tag{39c}$$

while the shear deformation coefficients a_y and a_z are obtained from the relations

$$a_y = \frac{A}{\Delta^2} \left((4\nu + 2) I_y I_{\Theta y} + \frac{1}{4} \nu^2 I_{yy}^2 I_{ed} - I_{\Theta e} \right) \tag{40a}$$

$$a_z = \frac{A}{\Delta^2} \left((4\nu + 2) I_z I_{\Phi z} + \frac{1}{4} \nu^2 I_z^2 I_{ed} - I_{\Phi d} \right) \tag{40b}$$

where

$$I_{\Theta e} = \int_\Gamma \Theta(\mathbf{n} \cdot \mathbf{e}) ds \tag{41a}$$

$$I_{\Phi d} = \int_\Gamma \Phi(\mathbf{n} \cdot \mathbf{d}) ds \tag{41b}$$

$$I_{ed} = \int_\Gamma \left(y^4 z n_z + z^4 y n_y + \frac{2}{3} y^2 z^3 n_z \right) ds \tag{41c}$$

$$I_{\Theta y} = \frac{1}{6} \int_\Gamma \left[-2 I_{yy} y^4 z n_z + (3\Theta n_y - y(\mathbf{n} \cdot \mathbf{e})) y^2 \right] ds \tag{41d}$$

$$I_{\Phi z} = \frac{1}{6} \int_\Gamma \left[-2 I_{zz} z^4 y n_y + (3\Phi n_z - z(\mathbf{n} \cdot \mathbf{d})) z^2 \right] ds \tag{41e}$$

4 Numerical Examples

On the basis of the analytical and numerical procedures presented in the previous sections, a computer program has been written and representative examples have been studied to demonstrate the efficiency, the accuracy and the range of applications of the developed method. In all the examples treated the results have been obtained using $L = 41$ nodal points along the beam.

4.1 Example 1

For comparison reasons, the special case of a simply supported beam of a 6×25 mm rectangular cross section subjected to free vibrations has been studied, where the employed initial conditions are represented by the following expression

$$w(x) = w_{\max} \sin(\pi x/L) \tag{42}$$

where $w_{\max}$ is the central beam deflection. In Table 1, the material properties, the geometric and inertia constants as well as the shear deformation coefficients of the examined cross section are presented.

In Figs. 2–4 the obtained results of the period ratios T/T_0 at various amplitude ratios $w_{\max}/r$ for three different cases of beam slenderness l/r are presented as compared with those obtained from a multiple scales solution [17], where T is the nonlinear period of vibration including rotary inertia and taking into account or ignoring shear deformation effect, T_0 is the respective period of the linear vibration ignoring both rotary inertia and shear deformation effect and $r = \sqrt{I_y/A}$ is the radius of gyration. From these figures, the accuracy of the results of the proposed method is verified, while it is easily concluded that the effect of shear deformation is significant for low beam slenderness values. Moreover, in Table 2 the obtained ratios of the nonlinear frequency ω_{NL} over the linear one ω_L at various amplitude ratios $w_{\max}/r$ taking into account both rotary inertia and shear deformation effect, for three different cases of beam slenderness l/r are presented as compared with those obtained from a finite element solution employing polynomial expressions for the displacement components [16]. The accuracy of the results of the proposed method, with the exception of that with $w_{\max}/r = 3$, $l/r = 10$, is remarkable. It is worth noting that for this latter value of the proposed method ($\omega_{NL}/\omega_L = 1.9268$) is in agreement with the corresponding one obtained from [17] (see also Fig. 2).

Table 1 Material properties, geometric, inertia constants and shear deformation coefficients of the rectangular cross section of example 1

$A = 150 \times 10^{-6}\,\mathrm{m}^2$	$\rho = 2{,}700\,\mathrm{kg/m}^3$
$E = 70\,\mathrm{GPa}$	$G = 27\,\mathrm{GPa}$
$I_y = 7812.5 \times 10^{-12}\,\mathrm{m}^4$	$I_z = 450 \times 10^{-12}\,\mathrm{m}^4$
$a_y = 1.74$	$a_z = 1.20$

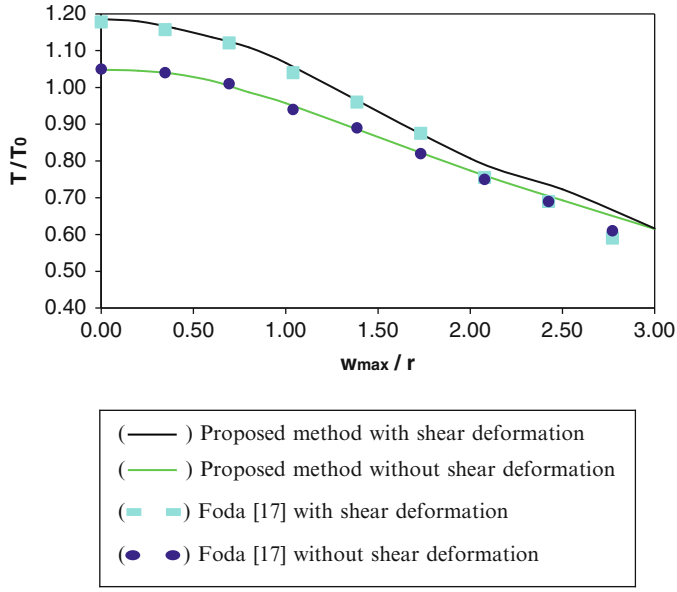


Fig. 2 Free vibration period ratios T/T_0 at various amplitude ratios $w_{\max}/r$ for beam slenderness $l/r = 10$ of the simply supported beam of example 1

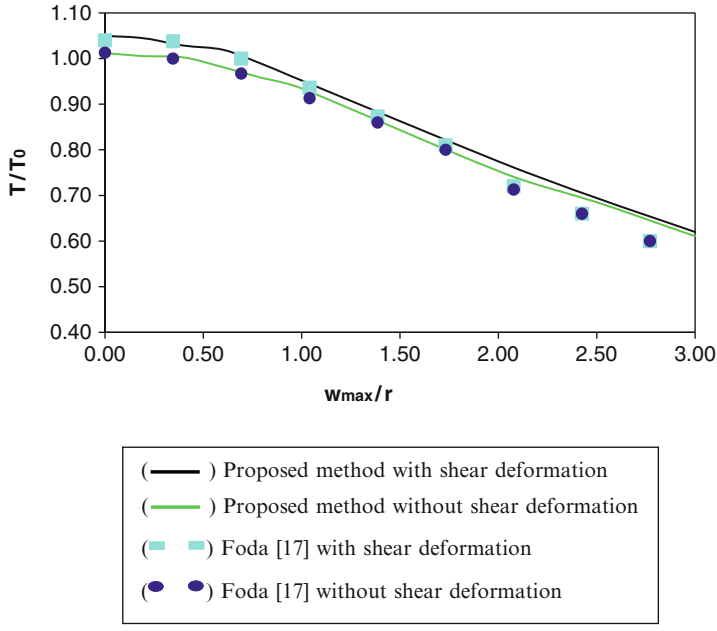


Fig. 3 Free vibration period ratios T/T_0 at various amplitude ratios $w_{\max}/r$ for beam slenderness $l/r = 20$ of the simply supported beam of example 1

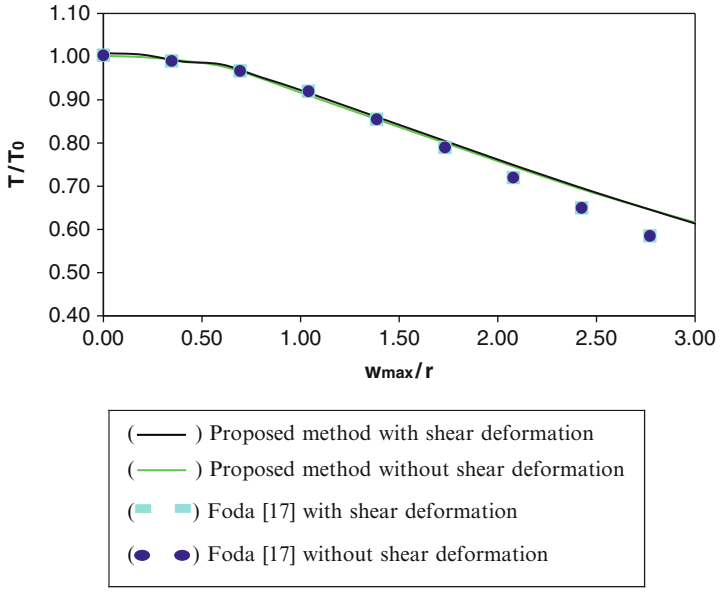


Fig. 4 Free vibration period ratios T/T_0 at various amplitude ratios $w_{\max}/r$ for beam slenderness $l/r = 50$ of the simply supported beam of example 1

Table 2 Frequency ratios ω_{NL}/ω_L at various amplitude ratios $w_{\max}/r$ of the simply supported beam of example 1

	$l/r = 10$		$l/r = 50$		$l/r = 100$	
$w_{\max}/r$	AEM	Rao et al. [16]	AEM	Rao et al. [16]	AEM	Rao et al. [16]
0.4	1.0214	1.0193	1.0198	1.0154	1.0103	1.0149
0.8	1.0694	1.0737	1.0587	1.0585	1.0551	1.0581
1.0	1.1116	1.1116	1.0928	1.0897	1.0920	1.0890
2.0	1.4296	1.3701	1.3230	1.3143	1.3227	1.3125
3.0	1.9268	1.6884	1.6432	1.6052	1.6410	1.6030

4.2 Example 2

For comparison reasons of the forced vibrations case, a clamped beam of length $l = 0.508$ m, having a 2.54×0.3175 cm rectangular cross section and subjected to a suddenly applied concentrated load of $P_z(t) = 2.844$ kN, $(t \geq 0)$ acting at the midspan has been studied. In Table 3, the material properties, the geometric and inertia constants as well as the shear deformation coefficients of the examined cross section are presented.

This problem has been studied by many researchers. More specifically, McNamara [41], based on a central-difference operator, employed five beam bending elements, Mondkar and Powell [42] used five 8-noded plane stress elements to model one half of the beam, Yang and Saigal [9] employed six beam elements,

Table 3 Material properties, geometric, inertia constants and shear deformation coefficients of the rectangular cross section of example 2

$A = 80.645 \times 10^{-6}\,\mathrm{m}^2$	$\rho = 2{,}713\,\mathrm{kg/m}^3$
$E = 207\,\mathrm{GPa}$	$\nu = 0.0$
$I_y = 67.746 \times 10^{-12}\,\mathrm{m}^4$	$I_z = 4335.74 \times 10^{-12}\,\mathrm{m}^4$
$a_y = 1.20$	$a_z = 1.20$

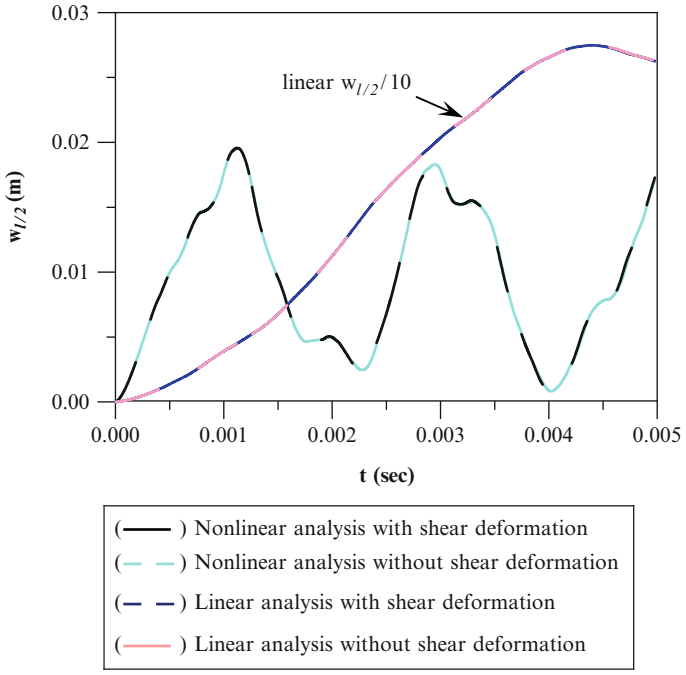


Fig. 5 Time history of the central deflection $w_{l/2}$ of the clamped beam of example 2

Leung and Mao [11] used six beam elements for the one-half of the beam and finally, Katsikadelis and Tsiatas [14] employed a BEM solution using 21 nodal points along the beam. In all of the aforementioned research efforts, the results have been obtained ignoring both rotary inertia and shear deformation effect.

In Fig. 5, the time history of the central deflection $w_{l/2}$ of the beam performing either a linear ($w_{l/2}/10$) or a nonlinear analysis with $\Delta t = 1\,\mu\mathrm{s}$ are presented taking into account or ignoring shear deformation effect. Moreover, in Table 4 the maximum central deflection $w_{\max}$ and period T of the first cycle are presented as compared with those obtained from the aforementioned researchers, ignoring both rotary inertia and shear deformation effect, while in Table 5 the same values obtained from both a linear and a nonlinear analysis are presented including rotary inertia and taking into account or ignoring shear deformation effect. The accuracy of the obtained results is remarkable, while it is obvious that shear deformation effect is negligible in this case, in both the linear and nonlinear analysis and could be ignored.

Table 4 Maximum deflection $w_{\max}(m)$ and period $T(\mu s)$ of the first cycle of the clamped beam of example 2, ignoring both rotary inertia and shear deformation effect

	Nonlinear Analysis					
	Present Study	Katsikadelis and Tsiatas [14]	McNamara [41]	Mondkar and Powell [42]	Yang and Saigal [9]	Leung and Mao [11]
$w_{\max}$	0.01957	0.01960	0.02286	0.01956	0.01956	0.01946
T	2,271	2,275	2,884	2,300	2,300	2,151

Table 5 Maximum deflection $w_{\max}(m)$ and period $T(\mu s)$ of the first cycle of the clamped beam of example 2, including rotary inertia

	Without shear deformation		With shear deformation	
	Linear analysis	Nonlinear analysis	Linear analysis	Nonlinear analysis
$w_{\max}$	0.2748	0.01957	0.2749	0.01958
T	8,781	2,273	8,806	2,273

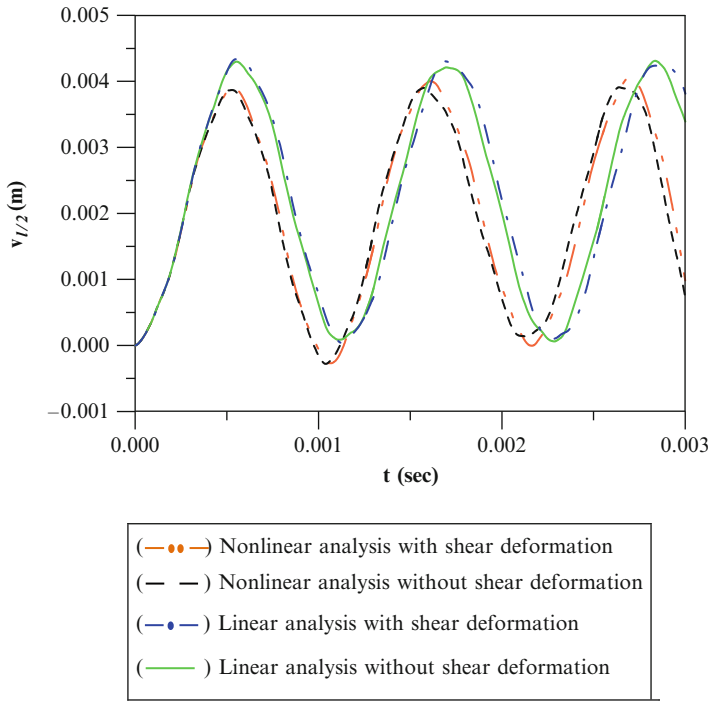


Fig. 6 Time history of the central transverse displacement $v_{l/2}$ of the clamped beam of example 2

Furthermore, the examined beam additionally to the aforedescribed loading $P_z(t) = 2.844\,\text{kN}$, $(t \geq 0)$ is also subjected to a concentrated load of the same value and time history $P_y(t) = 2.844\,\text{kN}$, $(t \geq 0)$, applied to the other direction, parallel to its width. In Fig. 6 the time history of the central transverse displacement $v_{l/2}$ of the beam performing either a linear or a nonlinear analysis with $\Delta t = 1\,\mu\text{s}$ are

Table 6 Maximum central deflections $v_{\max}(m)$, $w_{\max}(m)$ and periods T_y, $T_z(\mu s)$ of the first cycle of the clamped beam of example 2, for external loading in both directions

	Without shear deformation		With shear deformation	
	Linear analysis	Nonlinear analysis	Linear analysis	Nonlinear analysis
$v_{\max}$	0.0043	0.00387	0.00435	0.00392
$w_{\max}$	0.2748	0.01956	0.2749	0.01957
T_y	1,107	1,039	1,135	1,059
T_z	8,781	2,260	8,806	2,263

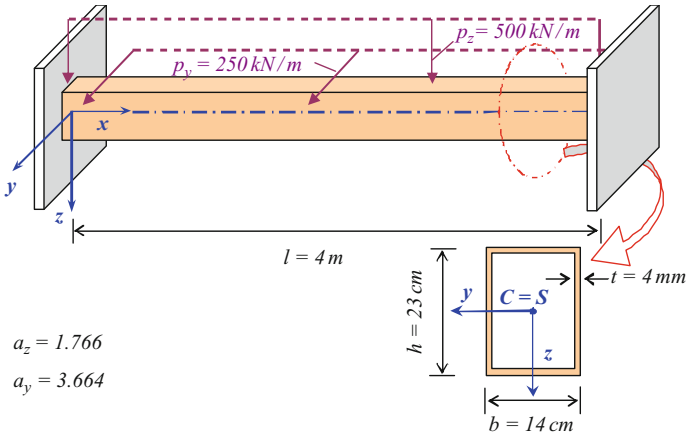


Fig. 7 Clamped beam of hollow rectangular cross section of example 3 subjected to the suddenly applied uniformly distributed loads p_y, p_z

presented, taking into account or ignoring shear deformation effect. Moreover, in Table 6 the maximum values of the central deflections $v_{l/2}$, $w_{l/2}$ and the periods T_y, T_z of the first cycle are presented for the aforementioned cases of analysis, taking into account or ignoring shear deformation effect.

The conclusion already drawn for the influence of the shear deformation effect is also here verified, while it is worth noting that the small discrepancy of the central deflections $w_{l/2}$ between the Tables 5 and 6 is due to the coupling effect of the transverse displacements in y, z directions in the nonlinear analysis.

4.3 Example 3

In order to demonstrate the influence of shear deformation effect in nonlinear dynamic analysis, in our third example a clamped beam of length $l = 4.0\,\text{m}$, having a hollow rectangular cross section ($E = 210\,\text{GPa}$, $\nu = 0.3$, $\rho = 7.85\,\text{tn/m}^3$) subjected to the suddenly applied uniformly distributed loads $p_y(t) = 250\,\text{kN/m}$, $p_z(t) = 500\,\text{kN/m}$, ($t \geq 0$), as this is shown in Fig. 7 has been studied.

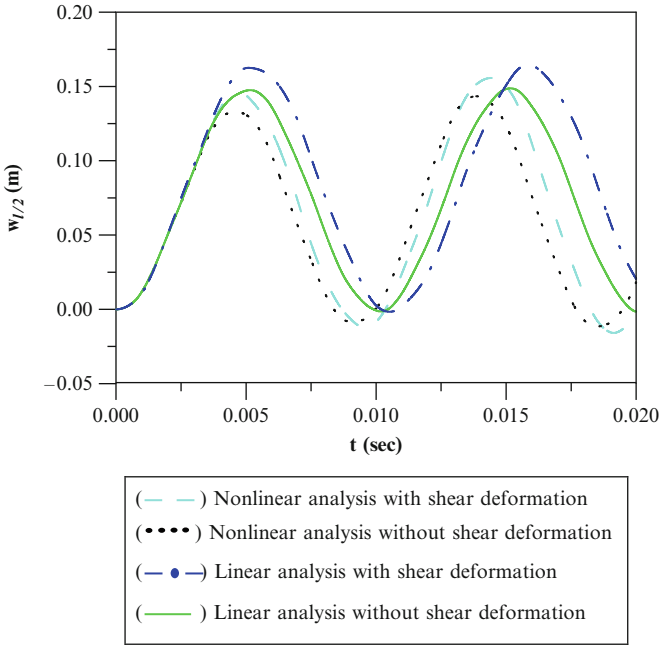


Fig. 8 Time history of the central transverse displacement $w_{l/2}$ of the clamped beam of example 3

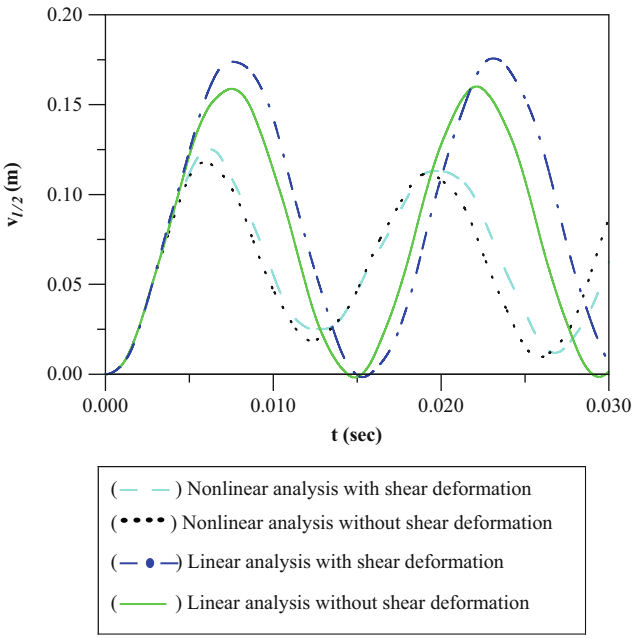


Fig. 9 Time history of the central transverse displacement $v_{l/2}$ of the clamped beam of example 3

Table 7 Maximum central deflections $v_{\max}(m)$, $w_{\max}(m)$ and periods T_y, $T_z(s)$ of the first cycle, of the clamped beam of example 3

	Without shear deformation		With shear deformation	
	Linear analysis	Nonlinear analysis	Linear analysis	Nonlinear analysis
$v_{\max}$	0.1588	0.1180	0.1739	0.1252
$w_{\max}$	0.1476	0.1330	0.1626	0.1460
T_y	0.01483	0.01229	0.01532	0.01240
T_z	0.01019	0.00911	0.01051	0.00958

In Figs. 8–9 the time history of the central transverse displacements $w_{l/2}$, $v_{l/2}$ of the beam performing either a linear or a nonlinear analysis with $\Delta t = 1\,\mu$s are presented taking into account or ignoring shear deformation effect. Moreover, in Table 7 the maximum values of the central deflections $v_{l/2}$, $w_{l/2}$ and the periods T_y, T_z of the first cycle are presented for the aforementioned cases of analysis, taking into account or ignoring shear deformation effect. From the obtained results the significant influence of shear deformation effect is established in both directions of motion. More specifically, shear deformation increases both the maximum central transverse displacements (especially in z direction) and the calculated periods of the first cycle of motion.

5 Concluding Remarks

In this chapter, a boundary element method is developed for the nonlinear dynamic analysis of beams of arbitrary doubly symmetric simply or multiply connected constant cross section, undergoing moderate large displacements under general boundary conditions, taking into account the effects of shear deformation and rotary inertia. The beam is subjected to the combined action of arbitrarily distributed or concentrated transverse loading and bending moments in both directions as well as to axial loading. The proposed model takes into account the coupling effects of bending and shear deformations along the member as well as the shear forces along the span induced by the applied axial loading. The main conclusions that can be drawn from this investigation are

(a) The numerical technique presented in this investigation is well suited for computer aided analysis for beams of arbitrary simply or multiply connected doubly symmetric cross section.
(b) The accuracy of the obtained results for a small number of nodal points along the beam is remarkable.
(c) In some cases, the effect of shear deformation is significant, especially for low beam slenderness values, increasing both the maximum transverse displacements and the calculated periods of the first cycle of motion.
(d) The discrepancy between the results of the linear and the nonlinear analysis is remarkable.

(e) The coupling effect of the transverse displacements in both directions in the nonlinear analysis influences these displacements.

Acknowledgments This work is part of the 03ED102 research project, implemented within the framework of the "Reinforcement Programme of Human Research Manpower" (PENED) and co-financed by National and Community Funds (25% from the Greek Ministry of Development-General Secretariat of Research and Technology and 75% from E.U.-European Social Fund).

References

1. Küpper T, Molitor A (1977) Nonlinear vibrations of simply supported beams. Nonlinear Anal Theor 3(1):45–48
2. Liu JQ (1989) Nonlinear vibration of a beam. Nonlinear Anal Theor 13(25):1139–1148
3. Prathap G, Varadan TK (1978) The large amplitude vibration of hinged beams. Comput Struct l9:219–222
4. Prathap G, Varadan TK (1978) The large amplitude vibration of tapered clamped beams. J Sound Vib 58(1):87–94
5. Sato K (1968) Nonlinear free vibration of beams with clamped ends and with one end clamped, other end simply supported. Bull Jpn Soc Mech Eng 11:1027–1036
6. Rehfield LW (1973) Nonlinear free vibrations of elastic structures. Int J Solids Struct 9:581–590.
7. Mei Ch (1973) Finite element displacement method for large amplitude free flexural vibrations of beams and plates. Comput Struct 3:163–174
8. Bhashyam GR, Prathap G (1980) Galerkin finite element method for non-linear beam vibrations. J Sound Vib 72(2):191–203
9. Yang TY, Saigal S (1984) A simple element for static and dynamic response of beams with material and geometric nonlinearities. Intl J Numer Meth Eng 20:851–867
10. Mei Ch (1986) Discussion of finite element formulations of nonlinear beam vibrations. Comput Struct 22(1):83–85
11. Leung AYT, Mao S.G. (1995) Symplectic integration of an accurate beam finite element in non-linear vibration. Comput Struct 54:1135–1147
12. Chang TP, Liu Y-N (1996) Dynamic finite element analysis of a nonlinear beam subjected to a moving load. Int J Solids Struct 33(12):1673–1688
13. Fotouhi R (2007) Dynamic analysis of very flexible beams. J Sound Vib 305:521–533
14. Katsikadelis JT, Tsiatas GC (2004) Nonlinear dynamic analysis of beams with variable Stiffness. J Sound Vib 270:847–863
15. Katsikadelis JT, Tsiatas GC (2007) Non-linear dynamic stability of damped Beck's column with variable cross-section. Int J Nonlinear Mech 42:164–171
16. Rao GV, Raju IS, Kanaka Raju K (1976) Nonlinear vibrations of beams considering shear deformation and rotary inertia. AIAA J 14(5):685–687
17. Foda MA (1999) Influence of shear deformation and rotary inertia on nonlinear free vibration of a beam with pinned ends. Comput Struct 71:663–670
18. Zhong H, Guo Q (2003) Nonlinear vibration analysis of Timoshenko beams using the differential quadrature method. Nonlinear Dynam 32:223–234
19. Guo Q, Liu LX, Zhong H (2004) Nonlinear vibrations of Timoshenko beams with various boundary conditions. Tsinghua Sci Technol 9(2):125–129
20. Zhong H, Liao M (2007) Higher-order nonlinear vibration analysis of Timoshenko beams by the spline-based differential quadrature method. Shock Vib 14:407–416
21. Liao M, Zhong H (2008) Nonlinear vibration analysis of tapered Timoshenko beams. Chaos Soliton Fract 36:1267–1272

22. Doong JL, Chen CS (1988) Large amplitude vibration of a beam based on a higher-order deformation theory. Appl Acoust 25:281–293
23. Lai S HY (1994) Nonlinear finite element modeling of a high speed rotating Timoshenko beam structure. Int J Mech Sci 36(9):849–861
24. Meek J, Liu H (1995) Nonlinear dynamic analysis of flexible beams under large overall motions and the flexible manipulator simulation. Comput Struct 56(1):1–14
25. Wang RT, Chou TH (1998) Non-linear vibration of Timoshenko beam due to a moving force and the weight of beam. J Sound Vib 218(1):117–131
26. Arboleda-Monsalve LG, Zapata-Medina DG, Darío Aristizabal-Ochoa J (2008) Timoshenko beam-column with generalized end conditions on elastic foundation: dynamic-stiffness matrix and load vector. J Sound Vib 310:1057–1079
27. Katsikadelis JT (2002) The analog equation method. A boundary-only integral equation method for nonlinear static and dynamic problems in general bodies. Theor Appl Mech 27:13–38
28. Chang SY (2004) Studies of Newmark method for solving nonlinear systems: (I) Basic analysis. J Chin Inst Eng 27(5):651–662
29. Isaacson E, Keller HB (1966) Analysis of numerical methods. Wiley, New York
30. Timoshenko SP (1921) On the correction for shear of the differential equation for transverse vibrations of prismatic bars. Philos Mag 41:744–746
31. Cowper GR (1966) The shear coefficient in Timoshenko's beam theory. J Appl Mech ASME 33(2):335–340
32. Schramm U, Kitis L, Kang W, Pilkey WD (1994) On the shear deformation coefficient in beam theory. Finite Elem Anal Des 16:141–162
33. Schramm U, Rubenchik V, Pilkey WD (1997) Beam stiffness matrix based on the elasticity equations. Int J Numer Meth Eng 40:211–232
34. Stephen NG (1980) Timoshenko's shear coefficient from a beam subjected to gravity loading. ASME J Appl Mech 47:121–127
35. Hutchinson JR (2001) Shear coefficients for Timoshenko beam theory. ASME J Appl Mech 68:87–92
36. Ramm E, Hofmann TJ (1995) Stabtragwerke, Der Ingenieurbau. In: Mehlhorn G (ed) Band Baustatik/Baudynamik. Ernst & Sohn, Berlin
37. Rothert H, Gensichen V (1987) Nichtlineare Stabstatik. Springer, Berlin
38. Sapountzakis EJ, Mokos VG (2005) A BEM solution to transverse shear loading of beams. Comput Mech 36:384–397
39. Thomson WT (1981) Theory of vibration with applications. Prentice Hall Englewood-Cliffs,
40. Sapountzakis EJ, Katsikadelis JT (2000) Analysis of plates reinforced with beams. Comput Mech 26:66–74
41. McNamara JE (1974) Solution schemes for problems of nonlinear structural dynamics. J Press Vess Technol 96:147–155
42. Mondkar DP, Powell GH (1977) Finite element analysis of nonlinear static and dynamic response. Int J Numer Meth Eng 11:499–520

Inelastic Analysis of Frames Under Combined Bending, Shear and Torsion

Aristidis Papachristidis, Michalis Fragiadakis, and Manolis Papadrakakis

Abstract The chapter discusses the fiber approach for the inelastic analysis of structures subjected to high shear. The element formulation follows the kinematics of the natural mode method, while the flexibility or force-based approach is adopted to integrate the section forces and deformations. Initially we present the fiber approach within its standard, purely bending, formulation and we then expand it to the case of high shear deformations. The element formulation follows the assumptions of the Timoshenko beam theory. Numerical examples are presented confirming the accuracy and the computational efficiency of the proposed element formulation under monotonic, cyclic and dynamic/seismic loading. Compared to experimental results and the results of detailed finite element models, excellent agreement and efficiency is achieved.

Keywords Fibre beam-column element · Force-based element · Moment-shear interaction · Natural-mode method · Timoshenko beam

1 Introduction

To perform inelastic static or dynamic analysis of frame structures, models that combine accuracy and simplicity are necessary. Such models can be either lumped or distributed plasticity models. When a lumped plasticity model is adopted, the inelastic behavior is concentrated at the ends of otherwise linear-elastic beam elements. This approach is also known as the plastic hinge approach. On the other hand,

A. Papachristidis and M. Papadrakakis
National Technical University of Athens, Institute of Structural Analysis and Seismic Research, Athens, Greece
e-mail: aristidi@central.ntua.gr; mpapadra@central.ntua.gr

M. Fragiadakis (✉)
Department of Civil and Environmental Engineering, University of Cyprus, P.O. BOX 20537, 1678 Nicosia, Cyprus
e-mail: mfrag@mail.ntua.gr

M. Papadrakakis et al. (eds.), *Computational Methods in Earthquake Engineering*, Computational Methods in Applied Sciences 21, DOI 10.1007/978-94-007-0053-6_18,
© Springer Science+Business Media B.V. 2011

distributed plasticity models consider the inelastic stresses and strains in a number of sections along the element which are also divided to monitoring points known as section fibers. The use of fibers allows the accurate representation of the stress level across the sections, while the nonlinearities are monitored in a number of sections along the element. The yield criteria adopted for the plastic hinge approach are expressed in moment-rotation terms, while in the fiber approach they are expressed in the level of stresses and strains. Fiber-based elements offer increased accuracy compared to plastic hinge models at the expense of increased computational cost.

Perhaps the most significant limitation of inelastic fibre beam-column elements is their inability to simulate the response of structural members under high shear. When two or three dimensional finite elements are used, the shear stresses at any point are directly calculated from the element formulation. For beam-column elements, the shear strain is either neglected, according to the Euler–Bernoulli assumption, or following the Timoshenko theory, it is assumed constant along the element length and the cross-section. Given the well-documented limitations of lumped-plasticity elements, a more refined fibre element capable to model the response of members under high shear has always been desirable.

The chapter presents the fiber approach in the context of the natural mode method of Argyris [1]. We provide all the basic equations within its common, purely-bending, format and then our implementation is extended to consistently account for the effect of shear and torsion. The chapter gives emphasis on a consistent formulation where coupling between flexure, shear and torsion exists. A decoupled approach is also discussed as a simplified alternative.

2 Beam Element Formulation

The beam element formulation is based on the natural mode method, developed by Argyris [1,2] and his co-workers. The resulting element is computationally efficient and can be easily combined with the corotational formulation or other procedures to account for mixed type of structures comprising shells and beams in a unified and consistent manner. The element-state determination phase of the proposed natural mode-based beam element is that of the "force-based", or "flexibility-based", approach [3, 4]. Force-based elements perform interpolation on both displacements and forces and have been shown to be advantageous over conventional displacement-based elements [5] since it requires fewer elements per member [6,7].

2.1 The Natural Mode Method

The natural mode concept proposed by Argyris [1] is applicable to beam, plate and shell finite elements. For a 3D beam element with six degrees-of-freedom per node,

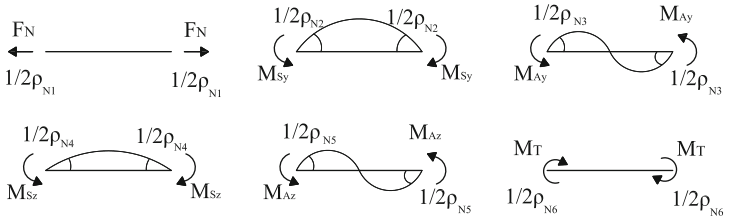


Fig. 1 Natural straining modes and the corresponding natural forces

the element formulation is based on the decomposition of the displacement field to six rigid body modes $\boldsymbol{\rho}_o$ and six straining modes $\boldsymbol{\rho}_N$, grouped in the vector $\boldsymbol{\rho}$ [2]:

$$\boldsymbol{\rho} = [\boldsymbol{\rho}_o \; \boldsymbol{\rho}_N] \tag{1}$$

The rigid body modes do not introduce any straining on the element and thus the element stiffness matrix is derived only from the straining modes. As shown in Fig. 1, the straining mode vector, $\boldsymbol{\rho}_N$, consists of a unit extension mode, ρ_{N1}, two symmetric bending straining modes, ρ_{N2} and ρ_{N4}, two antisymmetric modes, denoted as ρ_{N3} and ρ_{N5} and a twisting mode ρ_{N6}. Thus, the vector of the straining modes is:

$$\boldsymbol{\rho}_N = [\rho_{N1} \; \rho_{N2} \; \rho_{N3} \; \rho_{N4} \; \rho_{N5} \; \rho_{N6}]^T \tag{2}$$

The corresponding, work conjugate natural forces, also shown in Fig. 1, are:

$$\begin{aligned} \mathbf{P}_N &= [P_{N1} \; P_{N2} \; P_{N3} \; P_{N4} \; P_{N5} \; P_{N6}]^T \\ &= \left[F_N \; M_{Sy} \; M_{Ay} \; M_{Sz} \; M_{Az} \; M_T\right]^T \end{aligned} \tag{3}$$

Figure 1 shows that the axial and the symmetric modes are self-equilibrated, but this is not the case for the antisymmetric mode. Assuming that the effect of this inconsistency is not significant, the resulting formulation is equivalent to a beam-column element that follows the Euler–Bernoulli assumption.

The natural modes and the displacement field along the element are related with the following relationship:

$$\begin{bmatrix} u \\ v \\ w \end{bmatrix} = \begin{bmatrix} \frac{1}{2}\xi & 0 & 0 & 0 & 0 & 0 \\ 0 & \frac{L}{8}\left(1-\xi^2\right) & \frac{L}{8}\left(\xi^3-\xi\right) & 0 & 0 & 0 \\ 0 & 0 & 0 & \frac{L}{8}\left(1-\xi^2\right) & \frac{L}{8}\left(\xi^3-\xi\right) & 0 \end{bmatrix} \boldsymbol{\rho}_N \tag{4}$$

where $\xi = 2x/L - 1, \xi \in [-1, 1]$ is the natural coordinate along the element, u is the deformation along the longitudinal axis and v, w are the transverse displacements. The above expression assumes a constant distribution for the axial deformations, a quadratic interpolation for the symmetric bending modes and a cubic interpolation for the antisymmetric bending modes. The relationship between the natural straining modes and the nodal displacements in the element local system, $\boldsymbol{\rho}_{el}$, is:

$$\boldsymbol{\rho}_N = \mathbf{a}_N \boldsymbol{\rho}_{el} \tag{5}$$

The transformation matrix $\mathbf{a}_N$ contains simple algebraic transformations and has the form:

$$\mathbf{a}_N = \begin{bmatrix} -1 & 0 & 0 & 0 & 0 & 0 & 1 & 0 & 0 & 0 & 0 & 0 \\ 0 & 0 & 0 & 0 & 0 & -1 & 0 & 0 & 0 & 0 & 0 & 1 \\ 0 & -\frac{2}{L} & 0 & 0 & 0 & -1 & 0 & \frac{2}{L} & 0 & 0 & 0 & -1 \\ 0 & 0 & 0 & 0 & 1 & 0 & 0 & 0 & 0 & 0 & -1 & 0 \\ 0 & 0 & \frac{2}{L} & 0 & 1 & 0 & 0 & 0 & -\frac{2}{L} & 0 & 1 & 0 \\ 0 & 0 & 0 & -1 & 0 & 0 & 0 & 0 & 0 & 1 & 0 & 0 \end{bmatrix} \quad (6)$$

According to the principle of virtual work, for an individual beam element the external work of the element forces, $\mathbf{P}_{el}$, and the corresponding nodal displacements, $\boldsymbol{\rho}_{el}$, is equal to the work produced by the natural forces $\mathbf{P}_N$ and deformations $\boldsymbol{\rho}_N$:

$$\delta\boldsymbol{\rho}_{el}^T\mathbf{P}_{el} = \delta\boldsymbol{\rho}_N^T\mathbf{P}_N \Leftrightarrow \delta\boldsymbol{\rho}_{el}^T\mathbf{P}_{el} = \delta\boldsymbol{\rho}_{el}^T\mathbf{a}_N^T\mathbf{P}_N \Leftrightarrow \delta\boldsymbol{\rho}_{el}^T\left(\mathbf{P}_{el} - \mathbf{a}_N^T\mathbf{P}_N\right) = 0 \quad (7)$$

If Eq. (7) holds for any arbitrary virtual displacement $\boldsymbol{\rho}_{el}$, then $\mathbf{P}_{el} = \mathbf{a}_N^T\mathbf{P}_N$. In an arbitrary section ξ_0, the section forces are computed from the natural forces with the aid of the interpolation matrix $\mathbf{b}$:

$$\mathbf{D}_{sec} = \mathbf{b}(\xi_0)\,\mathbf{P}_N \Leftrightarrow \begin{bmatrix} N_0 \\ M_{0y} \\ M_{0z} \end{bmatrix} = \begin{bmatrix} 1 & 0 & 0 & 0 & 0 & 0 \\ 0 & -1 & \xi_0 & 0 & 0 & 0 \\ 0 & 0 & 0 & -1 & \xi_0 & 0 \end{bmatrix} \begin{bmatrix} P_{N1} \\ P_{N2} \\ P_{N3} \\ P_{N4} \\ P_{N5} \\ P_{N6} \end{bmatrix} \quad (8)$$

where N_0, M_{0y}, M_{0z} are the axial force and the bending moments at section ξ_0, respectively. Therefore, the distribution of axial forces is constant along the member, while the moments are assumed linear. In addition, $\mathbf{d}_{sec} = [\epsilon_x, \kappa_y, \kappa_z]^T$ is the vector of section deformations that consists of the longitudinal strain ϵ_x and the curvatures κ_y, κ_z.

2.2 Force-Based Fibre Element Formulation

The element follows the force-based theory also known as flexibility formulation [3,4,8,9]. This theory allows the use of a single beam-column element per member, provided that only nodal loads are present. Compared to the commonly adopted displacement-based elements, this approach improves considerably the accuracy and the efficiency of the analysis. Force-based elements, in order to calculate the element resisting forces, introduce an additional iterative process at the element level, known as element-state determination phase.

In the standard stiffness approach (displacement-based approach) the section deformations $\mathbf{d}_{sec}$ can be directly obtained from the natural modes (or the member shape functions), e.g. by differentiating Eq. (4). In a flexibility-based element, however, this task is performed iteratively, using an expression of the form:

$$\begin{aligned} \Delta\mathbf{d}_{sec} &= \mathbf{f}_{sec}\Delta\mathbf{D}_{sec} \Rightarrow \Delta\mathbf{d}_{sec} = \mathbf{f}_{sec}\mathbf{b}(\xi)\Delta\mathbf{P}_N \Rightarrow \\ \Delta\mathbf{d}_{sec} &= \mathbf{f}_{sec}\mathbf{b}(\xi)\mathbf{F}_N\Delta\boldsymbol{\rho}_N \Rightarrow \Delta\mathbf{d}_{sec} = \boldsymbol{\alpha}(\xi)\Delta\boldsymbol{\rho}_N \end{aligned} \tag{9}$$

the equation above relies on the force interpolation function $\mathbf{b}(\xi)$ to obtain the function $\boldsymbol{\alpha}(\xi)$ used for interpolating the displacement field along the member.

According to Petrangelli and Ciampi [8], different element formulations have been proposed, based on Eq. (9), e.g. [3, 9]. The effort is focused on treating the residuals consistently, thus assuring that equilibrium along the element is satisfied. Early efforts were based on different forms of shape functions, with the "variable shape functions" of Zeris and Mahin [9] to be a very accurate approach. However, the use of such shape functions does not satisfy strictly the equilibrium along the beam although the numerical problems that arise are not significant. To overcome this problem, a procedure initially proposed by Ciampi and Carlesimo [10] has been refined by Spacone et al. [3, 4] and has been applied to a fibre-based, beam-column formulation. This approach constitutes the core of our implementation, guaranteeing that equilibrium is always strictly satisfied even for highly nonlinear or softening problems.

The first step of the iterative procedure is to determine the vector of the natural forces from the Cartesian nodal displacements. Then using force interpolation functions, the section forces are obtained and subsequently are corrected according to the constitutive law of the fibres. The residual section forces are then multiplied with the section flexibility and integrated along the element length to obtain the element residual deformations. The iterative process at the element level is terminated when the residual deformations are minimized following an energy convergence criterion. The whole procedure combined with the proposed implementations for accounting shear deformations are presented in the form of a flowchart in Sect. 3.4 of this chapter.

The accuracy of the force-based formulation depends on the force interpolation functions, which are "exact", provided that only nodal loads are present. The element displacement field defined by the natural modes vector, $\boldsymbol{\rho}_N$, is cubic and therefore the curvature distribution is assumed linear along the element. This assumption is not sufficient, since the curvature demand localizes at the plastic zone regions and thus for displacement-based elements a denser mesh at the critical regions is necessary, as will be demonstrated in the first numerical example. On the other hand, the force interpolation functions of matrix $\mathbf{b}$ (Eq. (8)) are always "exact" since the axial forces are considered constant and the bending moments linear. Furthermore, a well-known problem, always encountered on displacement-based Timoshenko beams, is the over-stiffening due to transverse shear locking. The force-based approach avoids this problem, since a flexibility-based integration is adopted for the calculation of the stiffness matrix. This has been demonstrated numerically by Taylor et al. [11].

2.3 Section and Element Stiffness Matrices

The internal work for a single element, in the virtual work principle of Eq. (7), is the integral of the product of the stress and the virtual strains over the element volume, i.e.:

$$\delta\boldsymbol{\rho}_N^T\mathbf{P}_\mathrm{N} = \int_V \delta\boldsymbol{\epsilon}^T\boldsymbol{\sigma}\, dV = \int_L \left(\int_A \delta\boldsymbol{\epsilon}^T\boldsymbol{\sigma}\, dA\right) dL \tag{10}$$

According to Eq. (10) the internal work is calculated by first integrating in the section volume A and then summing along the member length L. Therefore, the strains at any position x,y,z in the member volume are calculated as the product of the section deformations $\mathbf{d}_{sec}$ and of a matrix that represents the strain distribution at the section located at position ξ along the beam axis:

$$\boldsymbol{\epsilon}\,(\xi, y, z) = \mathbf{a}_S\,(y, z)\,\mathbf{d}_{sec}\,(\xi) \tag{11}$$

The section strain distribution matrix $\mathbf{a}_S$ has the form:

$$\mathbf{a}_S\,(y,\, z) = \begin{bmatrix} 1 & -y & z \end{bmatrix} \tag{12}$$

where y and z are the coordinates of an arbitrary point in section A (Fig. 2). Equation (12) implies that the sections remain plane. With the aid of Eq. (11), Eq. (10) becomes:

$$\begin{aligned}\delta\boldsymbol{\rho}_N^T\mathbf{P}_N^T = \int_V \delta\boldsymbol{\epsilon}^T\boldsymbol{\sigma}\, dV &= \int_L \left(\int_A \boldsymbol{\epsilon}^T\boldsymbol{\sigma}\, dA\right) dL \\ &= \int_L \delta\mathbf{d}_{sec}^T \left(\int_A \mathbf{a}_S^T\boldsymbol{\sigma}\, dA\right) dL = \int_L \delta\mathbf{d}_{sec}^T\mathbf{D}_{sec}\, dL\end{aligned} \tag{13}$$

The above expression implies that the section forces $\mathbf{D}_{sec}$ are obtained as:

$$\mathbf{D}_{sec} = \int_A \mathbf{a}_S^T\boldsymbol{\sigma}\, dA \tag{14}$$

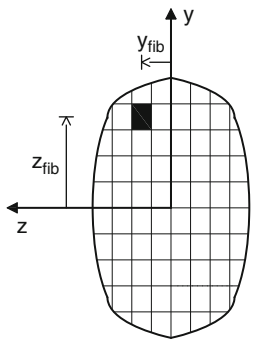


Fig. 2 Discretization of a cross-section to *nfib*-fibres

while, if Eq. (10) holds for every arbitrary $\delta\boldsymbol{\rho}_N$, the natural forces can be obtained as:

$$\begin{aligned}\delta\boldsymbol{\rho}_N^T\mathbf{P}_N &= \int_L \delta\mathbf{d}_{sec}^T\mathbf{D}_{sec}d\xi \Rightarrow \delta\boldsymbol{\rho}_N\mathbf{P}_N = \delta\boldsymbol{\rho}_N^T\int_L \mathbf{b}^T\mathbf{D}_{sec}\,dL \\ \Rightarrow \mathbf{P}_N &= \int_L \mathbf{b}^T\mathbf{D}_{sec}\,dL \Rightarrow \mathbf{P}_N = \int_{-1}^{1}\mathbf{b}^T\mathbf{D}_{sec}d\xi \end{aligned} \tag{15}$$

The section stiffness matrix $\mathbf{k}_{sec}$ is obtained as the partial derivative of the section forces over the corresponding deformations:

$$\begin{aligned}\mathbf{k}_{sec} &= \frac{\partial\mathbf{D}_{sec}}{\partial\mathbf{d}_{sec}} = \frac{\partial\mathbf{D}_{sec}}{\partial\boldsymbol{\epsilon}}\frac{\partial\boldsymbol{\epsilon}}{\partial\mathbf{d}_{sec}} = \int_A \mathbf{a}_S^T\frac{\partial\boldsymbol{\sigma}}{\partial\boldsymbol{\epsilon}}\frac{\partial\boldsymbol{\epsilon}}{\partial\mathbf{d}_{sec}}\,dA \\ &= \int_A \mathbf{a}_S^T\frac{\partial\boldsymbol{\sigma}}{\partial\boldsymbol{\epsilon}}\mathbf{a}_S\,dA = \int_A \mathbf{a}_S^T\mathbf{C}\mathbf{a}_S\,dA \end{aligned} \tag{16}$$

The partial derivative of the stress over the strain in Eq. (16), constitutes the material constitutive matrix, denoted as $\mathbf{C}$. Finally, the element flexibility matrix in the natural system $\mathbf{F}_N$ is obtained as the partial derivative of the natural deformations with respect to the natural forces:

$$\begin{aligned}\mathbf{F}_N &= (\mathbf{K}_N)^{-1} = \frac{\partial\boldsymbol{\rho}_N}{\partial\mathbf{P}_N} = \int_L \mathbf{b}^T(\xi)\frac{\partial\mathbf{d}_{sec}}{\partial\mathbf{D}_{sec}}\bigg|_\xi\frac{\partial\mathbf{D}_{sec}}{\partial\mathbf{P}_N}\,dL \\ &= \int_L \mathbf{b}^T(\xi)\,\frac{\partial\mathbf{d}_{sec}}{\partial\mathbf{D}_{sec}}\bigg|_\xi\mathbf{b}(\xi)dL \Rightarrow \mathbf{F}_N = \int_L \mathbf{b}^T\mathbf{k}_{sec}^{-1}\mathbf{b}\,dL \end{aligned} \tag{17}$$

According to the Euler–Bernoulli theory for beams the stress tensor consists of a single stress value, thus $\boldsymbol{\sigma} = \sigma_x$ and $\boldsymbol{\epsilon} = \epsilon_x$. Therefore, also the constitutive matrix $\mathbf{C}$ is simplified to $\mathbf{C} = C_{11} = E$, where E is the tangent modulus of elasticity.

The element stiffness matrix is calculated numerically at the integration sections along the element. Since the distribution of the normal stress σ_x in the section plane is not known, or cannot be represented by a polynomial of a known order, every section is divided to *nfib* control areas, known as "fibres". The section stiffness of Eq. (16) is therefore calculated as:

$$\begin{aligned}\mathbf{k}_{sec} &= \int_A \mathbf{a}_S^T\mathbf{C}\mathbf{a}_S\,dA = \int_A C_{11}\mathbf{a}_S^T\mathbf{a}_S\,dA \\ &= \int_A C_{11}\begin{bmatrix}1 & -y & z\\ -y & y^2 & -yz\\ z & -yz & z^2\end{bmatrix}dA = \sum_{i=1}^{nfib}E_iA_i\begin{bmatrix}1 & -y_i & z_i\\ -y_i & y_i^2 & -y_iz_i\\ z_i & -y_iz_i & z_i^2\end{bmatrix}\end{aligned} \tag{18}$$

where y_i and z_i is the distance of a fiber from the corresponding axis of the section.

Equation (17) implies that numerical integration is required to obtain the element stiffness matrix, which is the inverse of the sum of section flexibilities.

A Gauss–Lobatto quadrature scheme is preferable since it includes the end sections in the integration where the bending moment takes its maximum and/or minimum value. This integration scheme requires at least three integration sections for a linear curvature distribution, while typically four to six sections are chosen. Alternatively a Gauss quadrature, requiring only two sections can also be used. Experience has shown that the latter scheme is not efficient due to the location of the integration sections that does not include the beam ends [7]. Once the element natural stiffness is obtained, it is augmented with the GJ/L term to introduce the torsion term in the natural stiffness matrix. For a lineal elastic material the constitutive matrix $\mathbf{C}$ will be equal to $\mathbf{C} = E$, where E is the initial elastic tangent modulus of elasticity. In this case, the section stiffness will be:

$$\mathbf{k}_{sec} = diag\left[\, EA \;\; EI_y \;\; EI_z \,\right] \tag{19}$$

and the natural stiffness matrix results to:

$$\mathbf{K}_N = diag\left(\frac{1}{L}\left[\, EA \;\; EI_y \;\; 3EI_y \;\; EI_z \;\; 3EI_z \,\right]\right) \tag{20}$$

2.4 Numerical Examples: Clamped Beam

The first numerical example is the clamped beam of Fig. 3. This example compares the force-based (FB) and the conventional displacement-based (DB) fibre beam-column elements and demonstrates the advantages of the former. The beam-column elements of this comparison follow the Euler–Bernoulli assumption, while more details on the displacement-based formulation can be found in Ref. [7]. In the mid-span of the beam we apply a concentrated load, while a bilinear elastic-perfectly plastic material law with modulus of elasticity $E = 20\,000$ MPa and yield stress $f_y = 100$ MPa is adopted. The beam section is rectangular with dimensions 20×40 cm. The beam is first analysed with ten and fifty displacement-based elements of equal length. The section is divided to ten layers along its height. Figure 4 shows the load-deformation curves for the two meshes. The dashed line denotes the load where, according to plasticity theory, a collapse mechanism is formed. If the plastic capacity of a rectangular section with dimensions b, h is $M_p = bh^2/4$, then the ultimate capacity for the beam of Fig. 3 will be $P_{cr} = 8M_p/L = 1280$ kN. From

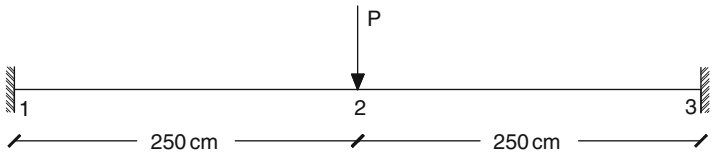


Fig. 3 Clamped beam of 20×40 cm rectangular cross section

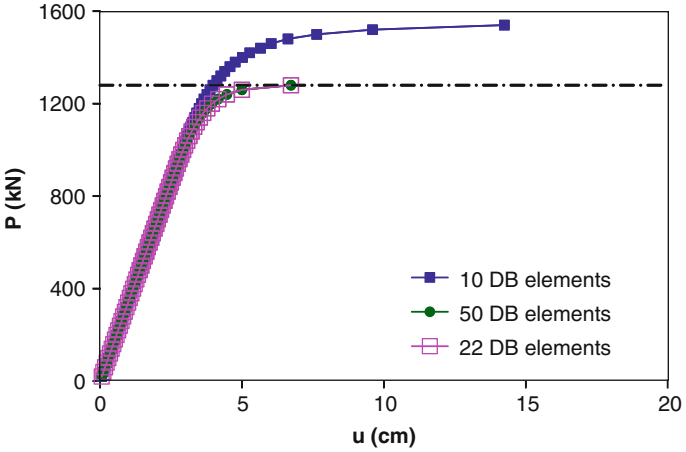


Fig. 4 Load-deformation curves using different discretizations of displacement-based elements

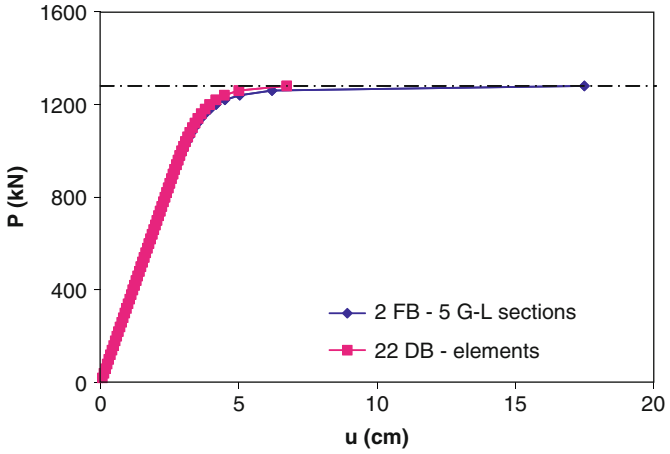


Fig. 5 Load deformation curves for force-based and displacement-based elements

Fig. 4 it is evident that the displacement-based formulation needs approximately 50 equally-spaced elements to capture accurately the collapse load. Also we show the response obtained with a mesh of 22, adaptively-spaced, beam-column elements. This mesh uses a single element for the regions that are expected to remain elastic and a dense mesh at the locations where inelastic deformations are expected.

Contrary to the displacement-based element, the force-based formulation can capture the inelastic response with a single beam element per member. Figure 5 shows a comparison between the two formulations. In Fig. 6 we investigate the sensitivity of the force-based element to the number of integration sections and the numerical integration scheme. When Gauss quadrature is adopted, the force-based element is not able to capture the collapse load, while Gauss–Lobatto quadrature

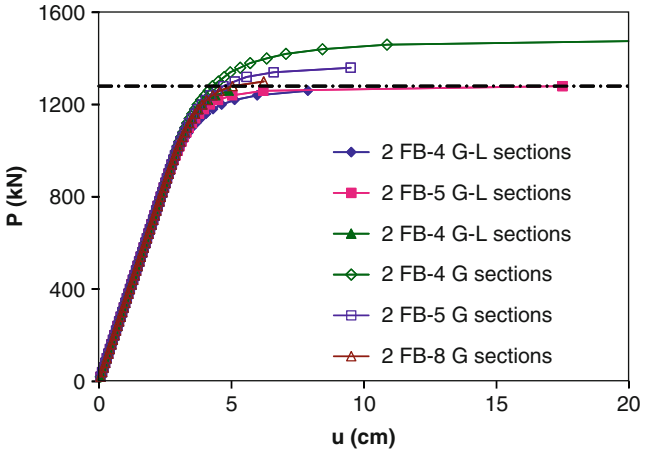


Fig. 6 Load deformation curves showing the influence of the number of integration sections and the numerical integration scheme. (G: Gauss integration, G–L Gauss–Lobatto integration)

always leads to the correct capacity regardless of the number of integration sections. A possible reason is that the Gauss–Lobatto scheme includes the beam ends as sections of integration. The number of sections slightly influences the load-deformation curve, which nevertheless converges to the correct collapse load for the Gauss–Lobatto case. The small differences observed are due to localization issues, which experience has shown that are not significant unless the load-deformation curve exhibits a negative post-elastic slope (softening) [12].

3 Shear-Deformable Fiber Element

A comprehensive review on the progress made in the past years on beam element formulations for members subjected to high shear can be found in [13]. One of the early developments was that of Vecchio and Collins [14] who introduced a "dual-section analysis" procedure where the element is discretized to layers, while iterations are performed for each layer until the internal equilibrium between adjacent sections is satisfied. This approach is limited to 2D problem. Bairan and Mari [15] extended the previous formulation to 3D cases by introducing an asymptotic approximation of the total energy. For RC members, Petrangeli et al. [16] proposed a flexibility-based, shear-deformable beam element where the longitudinal strain, ϵ_x, and the shear strain, τ_{xy}, are obtained from the element kinematics, while the transverse strain, ϵ_y, is calculated through lateral equilibrium between steel and concrete fibres. This formulation is combined with a biaxial law for concrete using the components of the two-dimensional strain tensor. Saritas and Filippou [17] presented a force-based formulation for the seismic assessment of steel structures also

using a multi-dimensional material law, but their study is limited to two-dimensional problems and has been demonstrated on simple academic examples only. Marini and Spacone [18] also presented a flexibility-based, shear-deformable beam element where a separate constitutive law for the shear component was adopted. This is clearly a simplifying assumption but maintains all the advantages of fibre beam elements in terms of robustness and simplicity of the material laws. This approach is also discussed in last part of this chapter to provide a simplified approach to the problem. Finally, Navarro et al. [19] presented a formulation for concrete beams under combined loading.

In the sections that follow we extent the element formulation to account for the effect of shear and torsion. The element formulation is similar to that already discussed, and therefore we focus on the additional terms and equations that we introduce in order to enhance the capacity of the element formulation.

3.1 Element Kinematics

When the moment-shear interaction is expected to be significant, a pair of shear forces, Q, has to be introduced to satisfy equilibrium for the two antisymmetric modes as can be seen from Figs. 1 and 7. If L is the length of the beam, in order to equilibrate the antisymmetric bending moments, M_A, a pair of shear forces, Q, must be applied so that $Q = 2M_A/L$ (Fig. 7). Once the pair of shear forces is introduced, the interpolation **b** matrix of Eq. (8), becomes:

$$\mathbf{D}_{sec} = \mathbf{b}(\xi)\,\mathbf{P}_N \Leftrightarrow \begin{bmatrix} N \\ M_y \\ M_z \\ Q_y \\ Q_z \end{bmatrix} = \begin{bmatrix} 1 & 0 & 0 & 0 & 0 & 0 \\ 0 & -1 & \xi & 0 & 0 & 0 \\ 0 & 0 & 0 & -1 & \xi & 0 \\ 0 & 0 & \frac{2}{L} & 0 & 0 & 0 \\ 0 & 0 & 0 & 0 & \frac{2}{L} & 0 \end{bmatrix} \begin{bmatrix} P_{N1} \\ P_{N2} \\ P_{N3} \\ P_{N4} \\ P_{N5} \\ P_{N6} \end{bmatrix} \tag{21}$$

where N, M_y, M_z are the axial force and the bending moments of the section ξ, respectively and Q_y and Q_z are the section shear forces which remain constant along the element. Moreover, the section deformations with the addition of the shear strains γ_{xy} and γ_{xz} will become: $\mathbf{d}_{sec} = \left[\epsilon_x, \kappa_y, \kappa_z, \gamma_{xy}, \gamma_{xz}\right]$. With the new

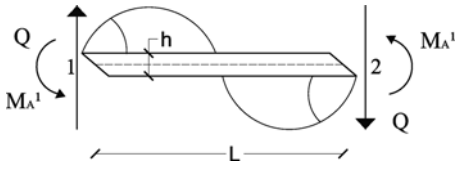


Fig. 7 Imposing transverse shear forces to satisfy equilibrium for the antisymmetric straining mode

definition of **b** and maintaining all equations of the previous sections, the resulting formulation will yield results identical to those of the Timoshenko beam theory.

3.2 Section and Element Stiffness Matrices

For Euler–Bernoulli beams **C** is a scalar equal to the tangent Young modulus of the uniaxial material law, since according to the kinematics of the element: $\boldsymbol{\sigma} = \sigma_x$. After the enhancements towards a shear-deformable formulation the stress and stain tensors contain three parameters: $\boldsymbol{\sigma} = \left[\sigma_x, \tau_{xy}, \tau_{xz}\right]$. In this case, the material constitutive matrix **C** will be a 3×3 matrix, where coupling between the normal and shear stresses and strains exists. Moreover, in order to take into consideration that the shear stresses are not constant in the section, as Timoshenko beam theory assumes, the scaled shear stress distribution factors $q_y(y,z)$, $q_z(y,z)$ are introduced. For simplicity the shear stress distribution factors are also denoted as q_y and q_z in the remainder of the chapter. Therefore, the material matrix **C** will take the form:

$$\mathbf{C} = \frac{\partial \boldsymbol{\sigma}}{\partial \boldsymbol{\epsilon}} = \begin{bmatrix} C_{11} & C_{12} & C_{13} \\ C_{21}\, q_y C_{22} & C_{23} \\ C_{31} & C_{32} & q_z C_{33} \end{bmatrix} \tag{22}$$

Special treatment is also required for the calculation of the section forces $\mathbf{D}_{sec}$, where the shear correction factor is also inserted in the stress vector σ. Thus the section forces $\mathbf{D}_{sec}$ will be:

$$\mathbf{D}_{\text{sec}} = \int_A \mathbf{a}_S^T \boldsymbol{\sigma}\, dA = \int_A \begin{bmatrix} \sigma_{xx} \\ -y\sigma_{xx} \\ z\sigma_{xx} \\ q_y \tau_{xy} \\ q_z \tau_{xz} \end{bmatrix} dA \tag{23}$$

The section strain distribution matrix $\mathbf{a}_S$ of Eq. (12) takes the form:

$$\mathbf{a}_S\,(y,z) = \begin{bmatrix} 1 & -y & z & 0 & 0 \\ 0 & 0 & 0 & 1 & 0 \\ 0 & 0 & 0 & 0 & 1 \end{bmatrix} \tag{24}$$

For coupled bending-shear behaviour the section stiffness is therefore calculated as:

$$\mathbf{k}_{sec} = \int_A \mathbf{a}_S^T \mathbf{C} \mathbf{a}_S\, dA = \sum_{i=1}^{nfib} \begin{bmatrix} C_{11}^i \mathbf{a}_{S,EB}^T \mathbf{a}_{S,EB} & C_{21}^i \mathbf{a}_{S,EB} & C_{31}^i \mathbf{a}_{S,EB} \\ C_{21}^i \mathbf{a}_{S,EB}^T & q_y C_{22}^i & C_{23}^i \\ C_{31}^i \mathbf{a}_{S,EB}^T & C_{32}^i & q_z C_{33}^i \end{bmatrix} \tag{25}$$

where $\mathbf{a}_{S,EB}$ is the section strain distribution matrix of Eq. (12) where the subscript EB is here introduced to avoid confusion with Eq. (24). Once the element natural stiffness is obtained, again has to be augmented with the GJ/L term to introduce the torsion term in the natural stiffness matrix $\mathbf{K}_N$. For a lineal elastic material the constitutive matrix $\mathbf{C}$ will be diagonal and equal to $\mathbf{C}= diag([E, q_y G_{xy}, q_z G_{xz}])$, where E is the modulus of elasticity and G_{xy}, G_{xz} are the shear modulii in the xy and the xz planes, respectively. The section stiffness in this case is given by:

$$\begin{aligned}\mathbf{k}_{sec} &= diag\left[\,\mathbf{k}_{sec}^{EB}\ q_y G_{xy} A\ q_z G_{xz} A\,\right] \\ &= diag\left[\,EA\ EI_y\ EI_z\ q_y G_{xy} A\ q_z G_{xz} A\,\right]\end{aligned} \tag{26}$$

and the natural stiffness matrix will be:

$$\mathbf{K}_N = diag\left[\,\frac{EA}{L}\ \frac{EI_y}{L}\ \frac{3EI_y q_y G_{xy} A}{L^3 q_y G_{xy} A + 12 EI_y/L}\ \frac{EI_z}{L}\ \frac{3EI_z q_z G_{xz} A}{L^3 q_z G_{xz} A + 12 EI_z/L}\,\right] \tag{27}$$

3.3 Modifications to Account for Torsion

The formulation discussed so far assumes that torsional effects are linear. This approach may not be accurate enough for problems where the shear stresses caused by twisting moments are large enough to cause yielding. Our element formulation can be easily extended to also include this effect. To account for the transverse displacements produced by the torsional straining mode, ρ_{N6}, Eq. (28) will become:

$$\begin{bmatrix} u \\ v \\ w \end{bmatrix} = \begin{bmatrix} \frac{1}{2}\xi & 0 & 0 & 0 & 0 & 0 \\ 0 & \frac{L}{8}\left(1-\xi^2\right) & \frac{L}{8}\left(\xi^3-\xi\right) & 0 & 0 & -\frac{1}{2}z\xi \\ 0 & 0 & 0 & \frac{L}{8}\left(1-\xi^2\right) & \frac{L}{8}\left(\xi^3-\xi\right) & \frac{1}{2}y\xi \end{bmatrix} \boldsymbol{\rho}_N \tag{28}$$

Also, the section forces $\mathbf{D}_{sec}$ and the section deformation vector $\mathbf{d}_{sec}$ are expanded to include the torque T and the corresponding twisting curvature κ_x. Therefore, the $\mathbf{b}(\xi)$ and $\mathbf{a}_S(y,z)$ matrices of Eqs. (8) and (12), respectively, are modified as follows:

$$\mathbf{D}_{sec} = \mathbf{b}(\xi_0)\,\mathbf{P}_N \Leftrightarrow \begin{bmatrix} N_0 \\ M_{0y} \\ M_{0z} \\ Q_{0y} \\ Q_{0z} \\ T \end{bmatrix} = \begin{bmatrix} 1 & 0 & 0 & 0 & 0 & 0 \\ 0 & -1 & \xi_0 & 0 & 0 & 0 \\ 0 & 0 & 0 & -1 & \xi_0 & 0 \\ 0 & 0 & 2/L & 0 & 0 & 0 \\ 0 & 0 & 0 & 0 & 2/L & 0 \\ 0 & 0 & 0 & 0 & 0 & 1 \end{bmatrix} \begin{bmatrix} P_{N1} \\ P_{N2} \\ P_{N3} \\ P_{N4} \\ P_{N5} \\ P_{N6} \end{bmatrix} \tag{29}$$

$$\mathbf{a}_S(y,z) = \begin{bmatrix} 1 & -y & z & 0 & 0 & 0 \\ 0 & 0 & 0 & 1 & 0 & y \\ 0 & 0 & 0 & 0 & 1 & -z \end{bmatrix} \tag{30}$$

Following all previous equations the section stiffness matrix and the 6×6 natural stiffness matrix $\mathbf{K}_N$ are calculated. It is evident that this approach does not require augmenting the natural stiffness with the GJ/L term. Finally, the section forces are obtained as:

$$\mathbf{D}_{\text{sec}} = \int_A \mathbf{a}_S^T \boldsymbol{\sigma}\, dA = \int_A \begin{bmatrix} \sigma_{xx} \\ -y\sigma_{xx} \\ z\sigma_{xx} \\ q_y \tau_{xy} \\ q_z \tau_{xz} \\ y q_y \tau_{xy} - z q_z \tau_{xz} \end{bmatrix} dA \tag{31}$$

3.4 Implementation of a 3D Constitutive Relationship on a Beam Element

Any material law that refers to the three dimensional case can be used with the beam element formulation already discussed. Following Eq. (18), the constitutive matrix $\mathbf{C}$ relates the increments of strains and stresses as:

$$\delta\boldsymbol{\sigma} = \mathbf{C}\delta\boldsymbol{\epsilon} \tag{32}$$

For the general 3D case the six components of the stress tensor σ_{3D} corresponds to the 6×6 material matrix, $\mathbf{C}_{3D}$ (Fig. 8). Finite elements that inherently contain special stress constraints, such as plates, shells and beams usually are restricted to simplified one- or two-dimensional constitutive laws. However, complicated materials are often described in the 3D continuum, thus hampering their application to these "structural" type of elements. In order to incorporate a 3D material law in such elements, local or global algorithms have been proposed in the past [20–22]. These algorithms impose a zero-stress condition to the components of the stress tensor that according to the element formulation are, or should be, equal to zero. For a beam

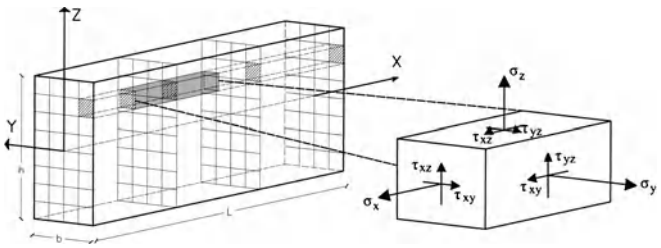


Fig. 8 Definition of stresses on a 3D fibre beam-column element

in space the stress components σ_{yy}, σ_{zz}, τ_{zy} are assumed zero and thus they are considered not active, while $\mathbf{C}$ is a 3×3 matrix corresponding to the active σ_{xx}, τ_{xy}, τ_{xz}. In this study, we adopt a local iteration algorithm so that for every fibre the non-active stresses are always set to zero. The algorithm is local in the sense that iterations are performed on the fibre level until the unknown stresses are set to zero, thus does not require any additional history variables, as opposed to global iteration procedures, such as the one proposed for shell structures [20], which operates on the element level. Clearly local algorithms can be easily implemented within any general-purpose FE code such as beam-column elements, as shown in [22].

For a beam in space, the non-active stresses are σ_{yy}, σ_{zz}, τ_{zy}, while for a 2D problem σ_{yy} is the only non-active stress. The active components are the remaining elements of the 3D tensor. If the non-active components that need to be set to zero are denoted with the subscript n and the active components with m, the incremental relationship of Eq. (32) is partitioned as follows:

$$\delta\boldsymbol{\sigma} = \mathbf{C}_{3D}\,\delta\boldsymbol{\epsilon} \Leftrightarrow \begin{bmatrix} \delta\boldsymbol{\sigma}_m \\ \delta\boldsymbol{\sigma}_n \end{bmatrix} = \begin{bmatrix} \mathbf{C}_{mm} & \mathbf{C}_{mn} \\ \mathbf{C}_{nm} & \mathbf{C}_{nn} \end{bmatrix} \begin{bmatrix} \delta\boldsymbol{\epsilon}_m \\ \delta\boldsymbol{\epsilon}_n \end{bmatrix} \tag{33}$$

According to the local plane stress algorithm the $\mathbf{C}$ constitutive matrix of Eq. (18) is obtained by condensing $\mathbf{C}_{3D}$ to the active stresses:

$$\mathbf{C} = \mathbf{C}_{mm} - \mathbf{C}_{mn}\mathbf{C}_{nn}^{-1}\mathbf{C}_{nm} \tag{34}$$

The algorithm is iterative and refers to every control point or integration-fibre. The constitutive matrix $\mathbf{C}$ is updated using all the components of the strain vector, $\delta\boldsymbol{\epsilon}_m$ and $\delta\boldsymbol{\epsilon}_n$. The component $\delta\boldsymbol{\epsilon}_m$ is directly calculated through the incremental-iterative analysis, while $\delta\boldsymbol{\epsilon}_n$ is obtained from the second equation of Eq. (33), assuming that $\delta\boldsymbol{\sigma}_n = 0$. Thus, for the jth iteration:

$$\boldsymbol{\epsilon}_n^j = \boldsymbol{\epsilon}_n^{j-1} + \delta\boldsymbol{\epsilon}_n^j \tag{35}$$

$$\delta\boldsymbol{\epsilon}_n = -\mathbf{C}_{nn}^{-1}\delta\boldsymbol{\epsilon}_m \tag{36}$$

The steps of the element-state determination phase of the force-based element that includes the local plane stress algorithm are outlined in Fig. 9.

The above algorithm is general in application and can be combined with every material law that refers to the full engineering stress vector. A J_2 plasticity material has been adopted for the implementation of the proposed shear deformable beam-column element of Sect. 3, although any material law that refers to the three dimensional case can be used. For the generalized J_2 plasticity material, the constitutive matrix $\mathbf{C}_{3D}$ can be obtained in a closed form following the work of Yamada et al. [23].

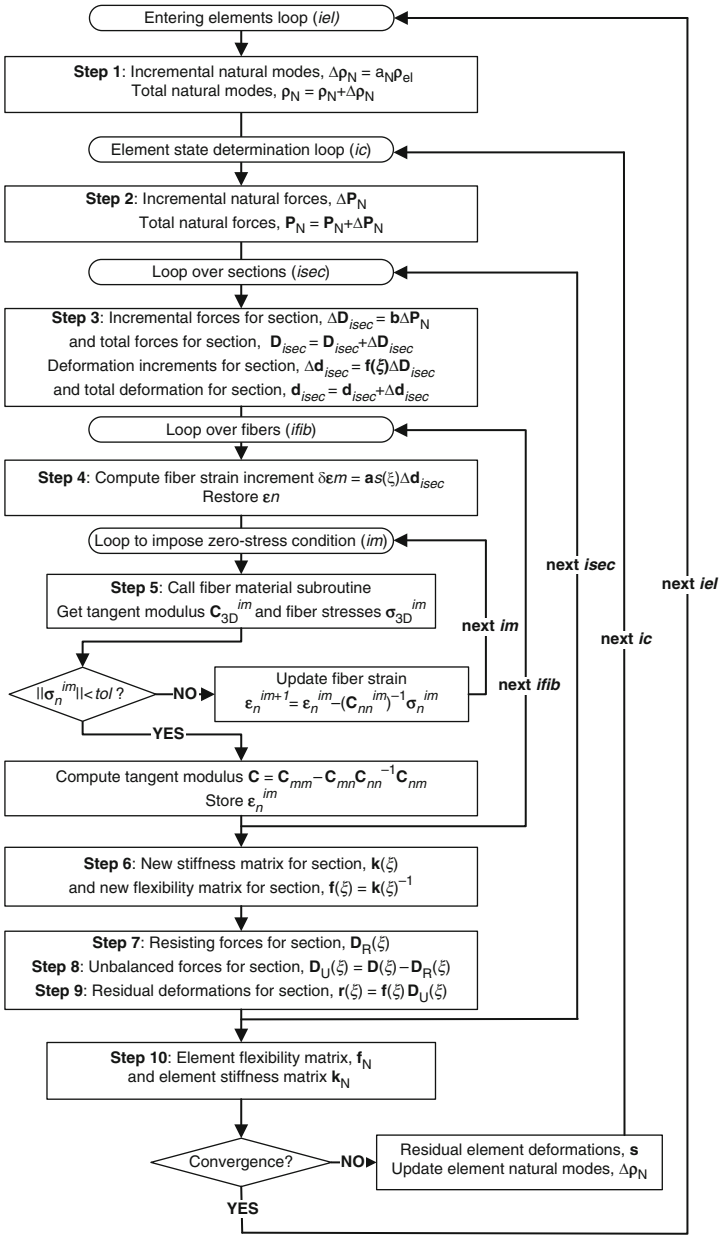


Fig. 9 Flowchart of the element-state determination algorithm

3.5 Numerical Example: Shear Link

The first numerical example is a shear link. The shear link and its FE model are shown in Fig. 10. The steel specified for the link was A572 Gr.50 and the properties of the material model were determined by a coupon test that gave 448 MPa yield stress for the web material and 393 MPa for the flange. We analyse the horizontal member Fig. 10 that is reinforced with four equally-spaced web stiffeners to prohibit local buckling and allow large rotations.

Initially we perform a parametric investigation, adopting three different cross-sections for the link: (a) a tubular section ($h = 152\,\text{mm}, b = 152\,\text{mm}, t_f = 16\,\text{mm}, t_w = 8\,\text{mm}, I_{yy} = 2.48989 \times 10^{-5}\,\text{m}^4$), (b) a slender IPE 330 section, and (c) a rectangular section with dimensions $5 \times 30\,\text{cm}^2$. The results were obtained using a single beam-column element of length equal to 0.50m with four Gauss–Lobatto sections of integration and 50 layers along the height of the section.

Five monotonic curves are shown for each type of cross-section (Fig. 11). The curves correspond to the basic force-based element (Euler–Bernoulli beam) and the proposed shear deformable element with and without considering the shear correction factor. For the shear-deformable formulations, the dashed lines denote the curves obtained using uniaxial stress-strain relationships (Timoshenko beam), while the solid lines correspond to the proposed J_2 plasticity zero stress algorithm.

The difference between the Euler–Bernoulli and the Timoshenko formulation lies on the calculation of the section stiffness using either Eq. (18) or Eq. (25), respectively, while both adopt the same uniaxial material. Furthermore, the dashed lines correspond to the force-deformation curves when the coupling algorithm with the J_2 plasticity law is used instead. It is clear, especially for sections (a) and (b), that both initial stiffness and strength is considerably overestimated when the shear correction is not calculated, while the coupling between bending and shear actions controls primarily the ultimate strength. Comparing the pure bending formulation and the shear-deformable formulation without a shear correction factor, we conclude that for sections (a) and (b) the improvement on the initial stiffness is small and thus we need to proceed to the calculation of the shear correction factor, while for the rectangular section it seems that the results obtained are adequately accurate.

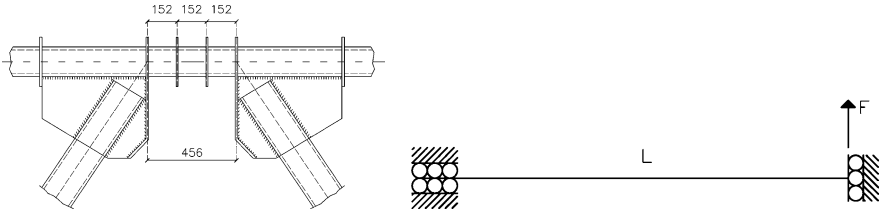


Fig. 10 Shear link. Right: Shear-link modelling

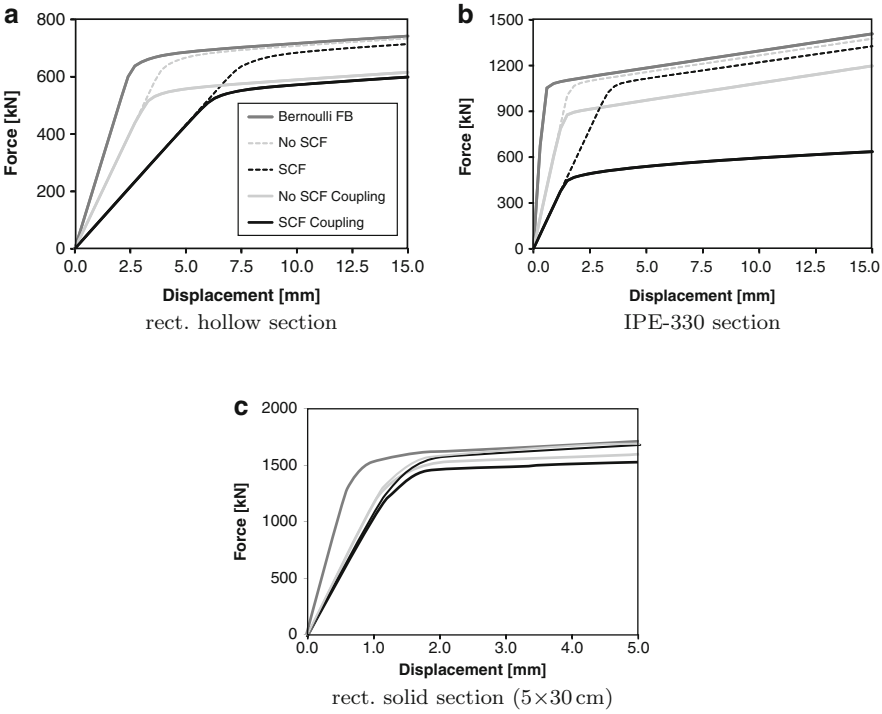
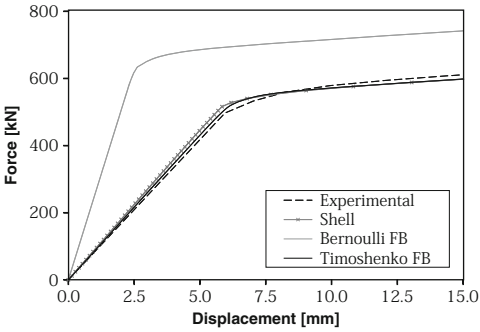


Fig. 11 Force-displacement curves of a shear link when different cross sections are adopted

Fig. 12 Tubular shear link response under monotonically increasing load



To further investigate the performance of the proposed element formulation we adopt the beam with the hollow rectangular section (section (a)), assuming that the link has length equal to 456 mm, corresponding to that studied by Berman and Bruneau [24].

The numerical results obtained with the proposed shear-deformable force-based beam element (*Timoshenko FB*) are shown in Fig. 12 and are compared to: (a) experimental results under monotonic and cyclic loading, as presented in [24],

(b) force-based Euler–Bernoulli fibre element modelling (*Bernoulli FB*) and (c) detailed modelling with shell finite elements. For the force-based model, a single shear-deformable beam element with four Gauss–Lobatto integration sections was adopted for both the Euler–Bernoulli and the Timoshenko formulations. The shear flow function and the corresponding scale factor k_z were obtained with the aid of closed form expressions [25] and k_z was found equal to 0.2880.

Apart from the experimental results, we present as a reference solution the numerical results obtained with a detailed analysis using shell finite element elements. The finite element mesh adopted consists of 2576 quadrilateral shell elements with six degrees of freedom per node (Fig. 13). The boundary conditions at the clamped end do not permit any deformation, while at the other end a master node at the centre of the section is allowed to deform vertically, while all nodes of the section are kinematically constrained to it. The remaining nodes of the section are kinematically restrained from the master according to the plane section assumption. A concentrated force is distributed to the nodes of one beam end. The resulting loading scheme and boundary conditions produce constant shear, two equal bending moments at the ends and no axial forces along the link [26].

Figure 12 shows the comparison of the numerical results with the experimental measurements of Ref. [24] under monotonic loading. The web will yield before the flanges due to the existence of high shear and also because its width is half compared to that of the flange. According to the load-deformation curve, yielding starts to occur when the flanges start to yield (approximately at 500 kN), while the inelastic slope of the curve is stabilized due to the 1% material hardening. It is interesting to note that the CPU time for the shell element formulation was 225 s, using the minimum mesh size to attain the required accuracy, for the *Bernoulli FB* model it was 20 s and approximately 25 s for the proposed element. Thus improved accuracy within an affordable increase of the CPU time has been achieved with the formulation proposed.

Figure 14 compares the shear stress distribution, τ_{xy}, in the middle section of the shear link obtained with the shell FE mesh and the *Timoshenko FB* model for a load increment corresponding to the yield point of Fig. 12. The comparison reveals that a good agreement is also obtained at the stress-strain level. Figure 15 presents the comparison between the hysteretic cyclic response obtained with the proposed

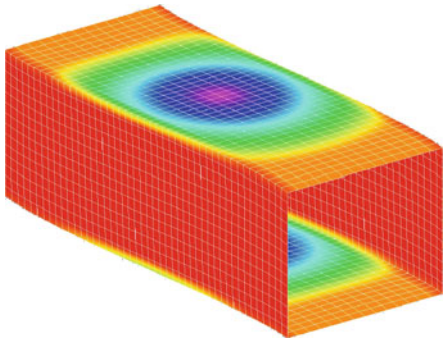


Fig. 13 Detailed finite element mesh of the tubular shear link

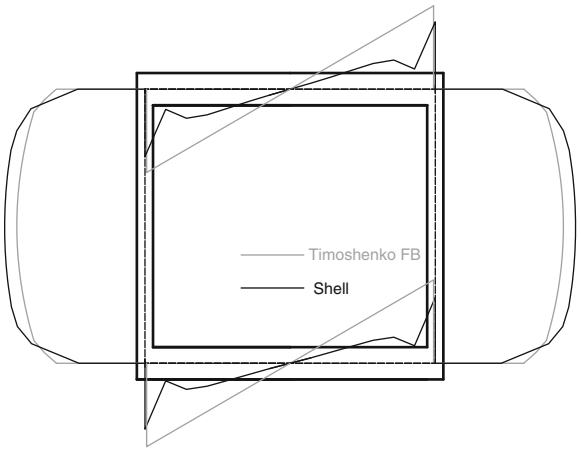


Fig. 14 Shear stress distribution at the yield point

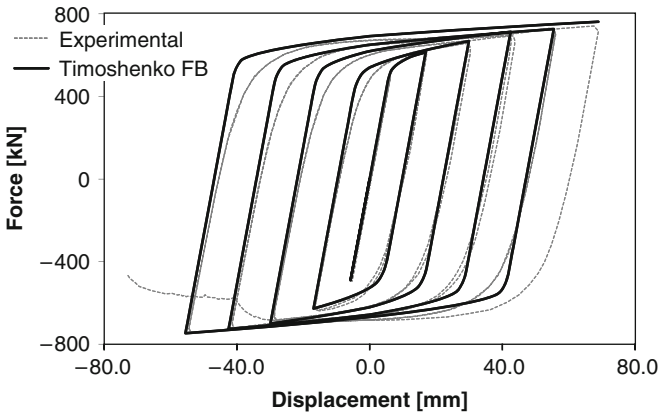


Fig. 15 Tubular shear link response under cyclic load

Timoshenko FB beam-column element against the experimental measurements of Berman and Bruneau [24]. The experimental results of the shear link were obtained with force-control up to the yield point, while beyond the yield point, displacement control was adopted. Very good agreement was also achieved for the cyclic quasi-static case despite the inability of analysis to capture the rapture observed during the test.

The hollow rectangular shear link is subjected to combined bending and twisting moments to demonstrate the efficiency of the equations presented in Sect. 3.3. A twisting moment, equal to $1/6L$ of the moment caused by the shear force is also applied.

Figure 16 shows the results obtained with four modelling schemes. Results have been obtained with the shell FE mesh of Fig. 17 and are shown together with the

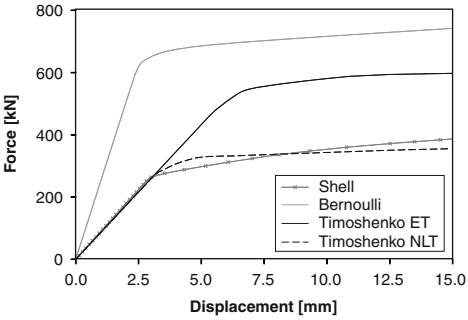


Fig. 16 Force-deformation curve for the tubular shear link under combined shear and torsion

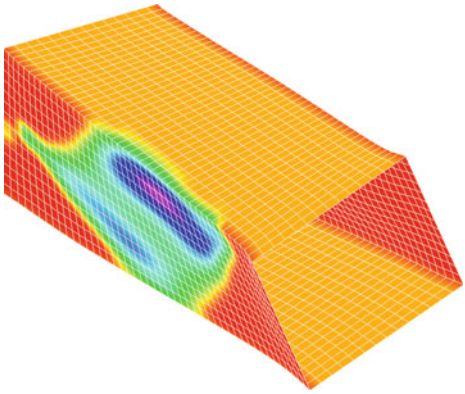


Fig. 17 Detailed finite element mesh of the tubular shear link under torsion

results of the Euler–Bernoulli fibre element and the proposed Timoshenko beam. The results of the Timoshenko beam element are shown with without the modifications for torsional effects. The corresponding curves are denoted as "Timoshenko ET" and "Timoshenko NLT", where ET stands for "elastic torsion" and NLT for "nonlinear torsion". The modifications proposed allow for an accurate representation of the effect of torsion, coincident to that of the analysis with shell elements, while the initial formulation overestimates the capacity since it did not take into account the shear stresses caused by twisting rotations.

4 A Simplified, Decoupled, Shear-Deformable Fiber Element

As a simplified alternative we present a hybrid approach that uses the standard fiber approach for the bending moments and a shear force (V) versus shear strain (γ) relationship for the shear component. The bending part of this approach operates at a stress-strain level, while the shear component is evaluated at the section level. Therefore, this approach combines uniaxial stress-strain laws, typically used with fiber elements and a multilinear V–γ relationship. This idea was initially presented by Marini and Spacone [18].

The section stiffness of Eq. (18) is augment with the slopes of the V–γ relationship in the xy and xz planes, respectively. Therefore, the section stiffness $\mathbf{k}_{sec}$ is obtained as:

$$\mathbf{k}_{sec} = \sum_{i=1}^{nfib} \begin{bmatrix} E_i A_i & -y_i E_i A_i & z_i E_i A_i & 0 & 0 \\ -y_i E_i A_i & y_i^2 E_i A_i & -y_i z_i E_i A_i & 0 & 0 \\ z_i E_i A_i & -y_i z_i E_i A_i & z_i^2 E_i A_i & 0 & 0 \\ 0 & 0 & 0 & \frac{dV_y}{d\gamma_{xy}} & 0 \\ 0 & 0 & 0 & 0 & \frac{dV_z}{d\gamma_{xz}} \end{bmatrix} \tag{37}$$

where $dV/d\gamma$ is the derivative of the shear law, which is equal to the tangent shear stiffness. Vectors $\mathbf{D}_{sec}$, $\mathbf{d}_{sec}$ and $\mathbf{b}$ are similar to that of the coupled case and are given in Sect. 3, while the element natural stiffness is calculated with Eq. (17). Since this is still a force-based formulation, the shear locking problem is avoided.

Compared to common fiber beam-column elements, the only issue that needs special attention is the V–γ relationship to be adopted. If we assume infinite shear capacity, then the slope $dV/d\gamma$ is constant and equal to the product of the shear modulus times the section area, GA. If a uniaxial V–γ relationship is adopted the degradation of the shear capacity strength and stiffness can be accommodated. Such laws can be either a simple bilinear law with negative hardening, or a relationship that consists of a quadrilinear backbone that accounts for pinching and the degradation of stiffness and strength [27]. For reinforced concrete members the backbone of such laws can be obtained using theories for the design to resist shear, such as EC2 [28] or the Modified Compression Field Theory (MCFT) [14]. Due to the damage rules that introduce stiffness and strength deterioration the history of the V–γ relationship is different for every section of integration and thus the shear forces do not remain constant along the beam as the Timoshenko beam theory dictates.

4.1 Numerical Example: Squat Column

A scaled bridge pier, originally examined in [18] is chosen to demonstrate the decoupled element formulation. The V–γ relationship adopted is that of Fig. 18. For the concrete fibers we adopted a modified Kent-Park [29] model and for the steel fibers a bilinear model with pure kinematic hardening. The shear law has a quadrilinear backbone [27] and its properties were obtained following the provisions of EC2, where the maximum shear capacity was considered equal to $V_{max} = 513\,\text{kN}$ and the ultimate capacity was found $V_{min} = 114\,\text{kN}$. The strength degradation parameter was considered equal to 0.90, while no stiffness degradation was assumed. Moreover, the column is preloaded with a constant axial force equal to 507.3 kN and is loaded with a cyclic displacement at the top. The column is modeled with a single beam element that consists of five integration sections. More details regarding section properties, reinforcement and the other parameters can be found in Ref. [18].

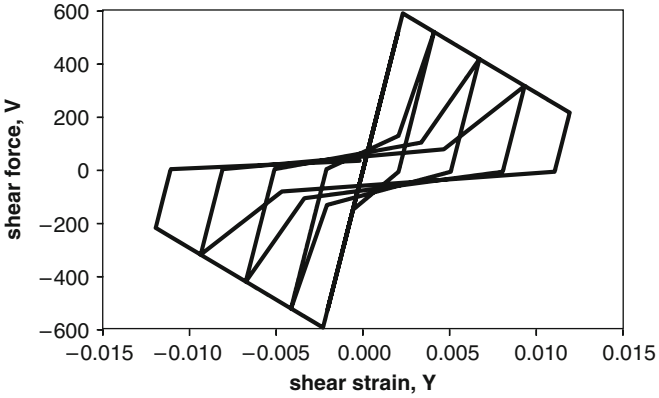


Fig. 18 Shear force versus shear strain ($V-\gamma$) relationship with stiffness and strength degradation, used for the shear component of the decoupled approach

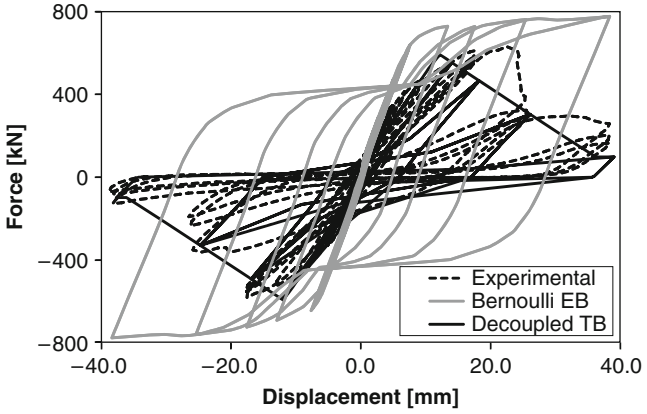


Fig. 19 Force-deformation curve of an RC member under cyclic loading, with and without taking into consideration the shear component

The beam is modeled with and without taking into consideration the shear component and the corresponding hysteretic curves are shown in Fig. 19. When the effect of shear is neglected, the capacity increases happily as the load increases. The response obtained with this formulation is expected to provide sufficient response estimates only for the early cycles of the deformation history, approximately for displacements less than 10 mm. On the other hand, when the shear-deformable formulation is adopted, a gradual loss of the strength is observed. For ultimate deformation equal to 30 mm, the capacity is dropped from the 789 kN of the purely bending case to 209 kN. Therefore, this element formulation is proven robust and maintains all the advantages of common fiber elements. Its only shortcoming is that the effect of shear is taken into consideration phenomenologically.

5 Conclusions

We present the background calculations of fiber-based, beam-column elements suitable for the seismic capacity assessment of frame structures under high shear. Flexure-dominated force-based elements overestimate the capacity of structures designed to yield in shear, especially in the inelastic area where the flexure–shear interaction affects considerably the capacity. The proposed element is based on the natural mode method and adopts a shear-deformable, flexibility-based formulation that allows for an accurate simulation of the inelastic response with the use of a single element for every member of the structure. In order to account for the shear contribution in the elastoplastic range, a local iteration procedure has been introduced, imposing zero stress conditions on the components of the stress tensor that cannot be accounted when uniaxial material laws are adopted. Combined with the proper calculation of the shear correction factor, this procedure allows any two- or three- dimensional constitutive law to be implemented for the monotonic and the cyclic analysis of steel structures. Thus the interaction of axial, bending, shear and torsion within the member is accounted accurately and efficiently.

Acknowledgements The present work was carried out under the wing of the Meter 8.3 of the Operational Programme "Competitiveness" (3rd Community Support Programme) funded by the European Union (75%), the Greek Government [General Secretariat for Research and Technology of the Ministry of Development] (25%) and Private founds. The authors would also like to acknowledge the support of the John Argyris International Centre for Computational Methods in Engineering.

References

1. Argyris JH (1963) Recent advances in matrix methods for structural analysis. In: Progress in Aeronautical Sciences, vol 4, Pergamon Press, New York
2. Argyris J, Tenek L, Mattsson A (1988) BEC: a 2-node fast converging shear-deformable isotropic and composite beam element based on 6 rigid-body and 6 straining modes. Comput Meth Appl Mech Eng 152:281–336
3. Spacone E, Ciampi V, Filippo FC (1996) Mixed formulation of nonlinear beam element. Comput Struct 58:71–83
4. Spacone E, Filippou FC, Taucer FF (1996) Fibre beam-column model for non-linear analysis of R/C frames: Part I. Formulation. Earthquake Eng Struct Dynam 1996; 25:711–725
5. Mata P, Oller S, Barbat AH (2007) Static analysis of beam structures under nonlinear geometric and constitutive behaviour. Comput Meth Appl Mech Eng 196:4458–4478
6. Neuenhofer A, Filippou FC (1997) Evaluation of nonlinear frame finite-element models. J Struct Eng 123:958–966
7. Papaioannou I, Fragiadakis M, Papadrakakis M (2005) Inelastic analysis of framed structures using the fiber approach. In: Proceedings of the 5th international congress on computational mechanics (GRACM 05), Limassol, Cyprus, 29 June–1 July 2005, 1:231–238
8. Petrangeli M, Ciampi V (1997) Equilibrium based iterative solutions for the non-linear beam problem. Int J Numer Meth Eng 40:423–437
9. Zeris CA, Mahin S (1988) Analysis of reinforced concrete beam-columns under uniaxial excitation. ASCE J Struct Eng 114:804–820

10. Ciampi V, Carlesimo L (1986) A nonlinear beam element for seismic analysis of structures 8th Eur Conf Earthquake Eng, Lisbon, 6.3:73–80
11. Taylor RLT, Filippou FC, Saritas A, Auricchio F (2003) A mixed finite element method for beam and frame problems. Comp Mechan 31:192–203
12. Coleman J, Spacone E (2001) Localization issues in force-based frame elements. J Struct Eng 127:1257–1265
13. Ceresa P, Petrini L, Pinho R (2007) Flexure-shear fiber beam-column elements for modeling frame structures under seismic loading – state of the art. J Earthquake Eng 11:46–88
14. Vecchio FJ, Collins MP (1986) Modified compression-field theory for reinforced concrete elements subjected to shear. ACI J 83:219–231
15. Bairan GJM, Mari AR (2007) Shear-bending-torsion interaction in structural concrete members: a nonlinear coupled sectional approach. Arch Comput Meth Eng 14:249–278
16. Petrangeli M, Pinto PE, Ciampi V (1999) A fibre element for cyclic bending and shear. I: theory. ASCE J Struct Eng 125:994–1001
17. Saritas A, Filippou FC (2004) Modelling of shear yielding members for seismic energy dissipation. Proceedings of the 13th world conference on earthquake engineering, Vancouver, BC, Canada
18. Marini A, Spacone E (2006) Analysis of reinforced concrete elements including shear effects. ACI Struct J 103:645–655
19. Navarro GJ, Miguel SP, Fernandez PMA, Flippou FC (2007) A 3D numerical model for reinforced and prestressed concrete elements subjected to combined axial, bending, shear and torsion loading. Eng Struct 29:3404–3419
20. De Borst R (1991) The zero-normal-stress condition in plane-stress and shell elastoplasticity. Commun Appl Num Math 7:29–33
21. Dvorkin E, Pantuso D, Repetto E (1995) A formulation for the MITC4 shell element for finite strain elasto-plastic analysis. Comput Meth Appl Mech Eng 125:17–40
22. Klinkel S, Govindjee S (2002) Using finite strain 3D-material models in beam and shell elements. Eng Comput 19:902–921
23. Yamada Y, Yoshimura N, Sakurai T (1968) Plastic stress-strain matrix and its application for the solution of elastic-plastic problems by the finite element method. Int J Mech Sci 10: 343–354
24. Berman JW, Bruneau M (2007) Experimental and analytical investigation of tubular links for eccentrically braced frames. Eng Struct 29:1929–1938
25. Papachristidis A (2010) Numerical simulation of structures under static and dynamic loading with high performance finite elements; PhD Thesis, National Technical University of Athens Athens, Greece
26. Richards P, Uang CM (2005) Effect of flange width-thickness ratio on eccentrically braced frames link cyclic rotation capacity. ASCE J Struct Eng 131:1546–1552
27. Ibarra LF, Medina RA, Krawinkler H (2005) Hysteretic models that incorporate strength and stiffness deterioration. Earthquake Eng Struct Dynam 34:1489–1511
28. European committee for standardisation (2000) Eurocode 2 (EC2) design of concrete structures – Part 1: general rules and rules for buildings, Brussels, Belgium
29. Scott BD, Park R, Priestley MJN (1982) Stress-strain behavior of concrete confined by overlapping hoops at low and high strain rates. ACI J 79(1):13–27

Seismic Simulation and Base Sliding of Concrete Gravity Dams

M. Basili and C. Nuti

Abstract A simplified procedure to estimate possible base sliding of concrete gravity dams induced by an earthquake is proposed on the basis of results obtained by parametric analysis. A simple mechanical model is developed to take into account the most relevant parameters influencing seismic response such as dam-water and dam-foundation interaction. In order to catch base residual displacement, a threshold value for the sliding foundation resistance is fixed. The dam is modelled as an elastic linear single degree of freedom system. The hydrodynamic effects of the water in the reservoir are taken into account with generalized supplementary mass and force as well as by adding supplementary damping. The foundation resistance is modelled with the Mohr-Coulomb criterion including a frictional and a cohesive component and the presence of a passive wedge resistance is also considered. A comprehensive numerical analysis of the response of concrete gravity dams subjected to several natural earthquake records relative to events mainly happened in Italy is carried out to estimate base residual displacement. Different parameters are considered in the analysis such as dam height, foundation rock parameters, water level, seismic intensity. As a result a simplified methodology is developed to evaluate base residual displacement, once known dam geometry, response spectrum of the seismic input, and the soil characteristics. The procedure permits to assess seismic safety of the dam with respect to base sliding, as well as water level reduction necessary to render the dam safe enough.

Keywords Concrete gravity dam · Seismic base sliding

M. Basili (✉)
University of Rome "Sapienza", Via Antonio Gramsci, Rome, Italy
e-mail: michela.basili@uniroma1.it

C. Nuti
University of "Roma Tre", Via Corrado Segre, Rome, Italy
e-mail: c.nuti@uniroma3.it

M. Papadrakakis et al. (eds.), *Computational Methods in Earthquake Engineering*,
Computational Methods in Applied Sciences 21, DOI 10.1007/978-94-007-0053-6_19,
© Springer Science+Business Media B.V. 2011

1 Introduction

Assessment of dams seismic safety represents an important issue since these structures are generally designed according to simple static criteria and low seismic actions. Several aspects are involved in seismic stability of concrete gravity dams. The main directly regard the structure and its possible cracking and deterioration related to mechanical degradation of the materials during strong seismic events, but also important aspects are related to the interaction of the dam with the boundary elements, namely, the impounded water in the reservoir and the foundation rock, which both contribute to reasonably modify the dam dynamic response. At this purpose, there is a wide literature where, generally, each problem is separately deepened by developing models more and more sophisticated (e.g. [2, 10]). However all these aspects must be combined together to bring the evaluation of stability and safety of concrete gravity dams. An effective way to solve the problem is to define simple models where the most relevant aspects which influence seismic response are taken into account (e.g. [8, 9]). Usually papers deal with the evaluation of stresses within the dam considering elastic response. In literature only few exploratory investigations on earthquake induced base sliding of concrete gravity dams are known [3–5, 8].

Possible base plastic movement reduces forces in the upper part of the dam, reducing structural damage, allowing in some cases, to survive to seismic event. At this purpose, this study aims to evaluate possible residual displacements due to base sliding of concrete gravity dams produced by an earthquake developing a simplified mechanical model where the most important aspects are considered (dam-water-foundation interaction). The study originates by the need of estimating seismic safety against base sliding of existing Italian concrete gravity dams. The objective is to define a simplified procedure without requiring non linear dynamical analysis on complex finite element models. At this purpose, a non linear single degree of freedom system with non linearity of the substructure, having fixed a threshold value for the sliding foundation resistance modelled with the Mohr-Coulomb yielding criterion including a frictional and a cohesive component, is subjected to several natural earthquakes and seismic response is carried out. A comprehensive and systematic analysis of all the parameters which influence dam response is carried out. The procedure permits preliminary assessment of seismic safety with respect to base sliding, as well as water level reduction necessary to render the dam safe enough.

2 Mechanical Model

Dam response can be computed by performing the analysis on a generalized single degree of freedom system. If the system is dynamically excited the response of the generalized single degree of freedom system may be approximated as:

$$v(z,t) = \psi(z)y(t) \tag{1}$$

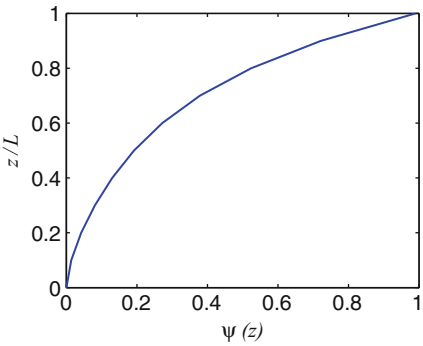


Fig. 1 Fundamental mode shape function chosen for the analysis

once having chosen the shape function $\psi(z)$, the amplitude of motion relative to the base is represented by the generalized coordinate $y(t)$. The assumed shape function has been taken from [9], where the fundamental vibration mode shape $\psi(z)$ for a standard dam cross section has been evaluated, Fig. 1. It is normalized in order to assume the unity at the top of the dam ($\psi(L) = 1$); in this way the $y(t)$ function represents the top displacement of the dam. The equivalent linear model proposed by Fenves and Chopra [7] is taken as starting point for this study. The model allows dam-water-foundation interaction. By including the interaction between dam and water results on the equivalent SDOF system in introducing an added force in the system and modifying the properties of the dam by adding a supplementary mass and damping. By including the interaction between flexible dam and foundation results in modifying the natural frequency and damping ratio of the equivalent SDOF. The dam has mass density $m(z)$ and Young modulus E.

The dynamic equilibrium of the equivalent linear SDOF system on a fixed base excited by horizontal earthquake ground motion represented by the base acceleration a_g, simultaneously considering the dam-water-foundation interaction, is expressed as [8]:

$$\tilde{M}\ddot{y}(t) + 2\tilde{\xi}\tilde{\omega}\tilde{M}\dot{y}(t) + \tilde{\omega}^2\tilde{M}y(t) = -\left(\frac{\tilde{\omega_f}}{\omega}\right)^2 \tilde{L}a_g(t) \tag{2}$$

where:

$\tilde{M} = m^* + \mathrm{Re}(B_1(\omega_r))$ equivalent SDOF mass, sum of two terms, one relative to dam and the other relative to water,
$\tilde{L} = l^* + B_0(\omega_r)$equivalent SDOF participation factor, sum of two terms, one relative to dam and the other relative to water,
ω equivalent SDOF system fundamental frequency without considering interaction with water or foundation rock,
$\tilde{\omega}$ equivalent SDOF system fundamental frequency considering interaction with water and foundation rock,
$\tilde{\omega_f}$ equivalent SDOF system fundamental frequency considering interaction with foundation rock,

$\tilde{\omega}_r$ equivalent SDOF system fundamental frequency considering interaction with water,
$\tilde{\xi}$ equivalent SDOF system damping ratio considering interaction with water and foundation rock.

Generalized dam mass and participation factor are expressed respectively as:

$$m^* = \int_0^L m(z)\psi(z)^2 dz;$$
$$l^* = \int_0^L m(z)\psi(z) dz;$$

whereas the hydrodynamic terms are expressed as complex functions in the frequency domain [7].

In order to catch residual displacement, the equivalent SDOF system proposed by Fenves and Chopra for linear analysis (2) is enriched by modelling the non linearity of the substructure, having fixed a threshold value for the sliding foundation resistance modelled with the Mohr-Coulomb yielding criterion including a frictional and a cohesive component. It is possible to rewrite Eq. (2) by dividing it for the quantity $\tilde{M}$ and defining the quantity:

$$p = \left(\frac{\tilde{\omega_f}}{\omega}\right)^2 \frac{\tilde{L}}{\tilde{M}} \tag{3}$$

as:

$$\ddot{y}(t) + 2\tilde{\xi}\tilde{\omega}\dot{y}(t) + \tilde{\omega^2} y(t) = -p a_g(t) \tag{4}$$

dividing Eq. (4) for p and multiplying it for the quantity:

$$M_{dw} = \left(\frac{\tilde{\omega_f}}{\omega}\right)^2 \tilde{L} \tag{5}$$

defining $D(t) = y(t)/p$, after rearranging we obtain:

$$M_{dw}\ddot{D}(t) + 2\tilde{\xi}\tilde{\omega}M_{dw}\dot{D} + \tilde{\omega^2}M_{dw}D = -M_{dw}a_g(t) \tag{6}$$

The solution of Eq. (6) gives the response of the dam in terms of the relative displacement $D(t)$ of an equivalent SDOF system having the following dynamic characteristics:

M_{dw}: equivalent mass,
$\tilde{\xi}$: equivalent damping ratio,
$\tilde{\omega}$: equivalent natural frequency.

The foundation rock sliding resistance depends on the geotechnical parameters and dam geometry and it is expressed as the sum of a contribute due to cohesion R_{yc} and a contribute due to friction $R_{y\phi}$:

$$R_y = R_{yc} + R_{y\phi} = cA + N\tan\phi \tag{7}$$

where c is the cohesion, ϕ the friction angle, A is the contact area and N is the force normal to the surface evaluated as:

$$N = P_d - U_w \tag{8}$$

where P_d is the dam weight and U_w is the uplift pressure force resultant acting at the dam bottom.

When the base shear force is lower than the threshold value represented by the sliding foundation resistance R_y, the rock behaves as an elastic material. As the base shear force equals the foundation resistance, plastic displacements arise and the energy input is dissipated at price of permanent deformations for the system attained at the end of the dynamic input. In the context of a simplified approach such behavior can be modelled with a mono dimensional elastic-plastic constitutive law. The displacement of the foundation is:

$$D_f = \begin{cases} \frac{V}{k_f} & V < R_y \\ \frac{V}{k_f} + \forall & V = R_y \end{cases} \tag{9}$$

where V is the base shear force and k_f is the elastic stiffness of the foundation rock, and the symbol $\forall$ means whichever value. The value chosen for the elastic stiffness k_f varies with the elastic modulus of the foundation rock E_f; it has been chosen by utilizing the curves reported in [11] which have been estimated for a shallow foundation on a homogeneous semi space. When the base shear force equals the threshold value R_y, plastic displacements are attained. During the earthquake the plastic displacement increases as many times the base shear force reaches the foundation rock resistance. In order to model the possibility of sliding between the dam and foundation rock by means of an elastic plastic element, the elastic stiffness of the equivalent SDOF system $K = \tilde{\omega}^2 M_{dw}$ is rearranged into two terms which work as elements in series. The first term is the elastic stiffness of the foundation rock k_f and the second term is consequently evaluated as:

$$K_d = -\frac{K k_f}{K - k_f} \tag{10}$$

A schematic representation of the equivalent SDOF system is depicted in Fig. 2.

In conclusion, the parameters to be estimated considering dam with water and foundation interaction with the possibility of sliding are summarized: M_{dw}, K_d, $\tilde{\xi}$, k_f, R_y, p.

The approximations inherent to this model are mainly connected to the non linear behavior of the foundation rock considered only with reference to the translational displacement. That means not only to disregard possible rotational displacement, but also to not consider the coupling terms deriving by the simultaneous effect of the translational and rotational displacement.

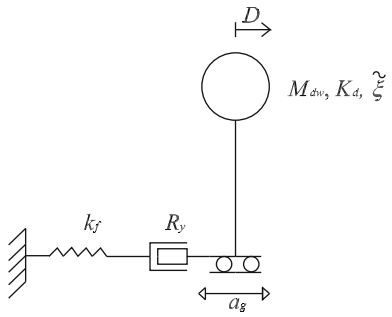


Fig. 2 Equivalent SDOF non linear model

The case of dam embedded in the foundation is also considered. The embedment plays role increasing the sliding foundation resistance for the contribution of a passive wedge resistance.

The relationship between the forces acting on the equivalent SDOF system and the forces acting on the dam follows the now popular procedure utilized in push-over analysis for the reduction of a multi-DOF system into a generalized SDOF system. As a result, dam base shear force is obtained by multiplying SDOF system base shear force by the coefficient p. Therefore, when performing the analysis on the generalized SDOF system, each force term R_i must be inserted by dividing the value of the action by the p coefficient.

In order to estimate system dynamical characteristics, simplified expressions proposed by [9] are used. Dam fundamental period T (or equivalently frequency ω) with the hypothesis of rigid rock foundation and empty reservoir, is valued as a function of the concrete Young modulus E (expressed in kPa) and the dam height L (expressed in meters):

$$T \cong 12\frac{L}{\sqrt{E}} \tag{11}$$

The natural vibration period $\tilde{T_f}$ (or $\tilde{\omega_f}$) of the equivalent SDOF system representing the fundamental mode response of the dam on flexible foundation rock with empty reservoir is estimated as:

$$\tilde{T_f} = R_f T \tag{12}$$

the factor $R_f > 1$ depends on the properties of the dam and the foundation rock.

The natural vibration period $\tilde{T}$ (or $\tilde{\omega}$) of the equivalent SDOF system representing the fundamental mode response of the dam on flexible foundation rock with impounded water is estimated as:

$$\tilde{T} = R_f R_r T \tag{13}$$

the factor $R_r > 1$ depends on the properties of the dam, the depth of the water and the absorptiveness of the reservoir bottom materials.

The damping ratio of the equivalent SDOF system is:

$$\tilde{\xi} = \frac{1}{R_r R_f^3}\xi + \xi_r + \xi_f \tag{14}$$

where ξ is the damping ratio of the dam on rigid foundation and empty reservoir, ξ_r is the added damping due to water interaction and ξ_f is the added damping due to dam foundation rock interaction.

R_r and ξ_r depend on several parameters the more significant are: the dam Young modulus E, the ratio L_w/L of water depth to dam height and the wave reflection coefficient α. Such coefficient represents the ratio of the amplitude of the reflected hydrodynamic pressure wave to the amplitude of a vertically propagating pressure wave incident on the reservoir bottom ($\alpha = 1$ indicates that pressure waves are completely reflected, whereas smaller values indicate increasingly absorptive materials). R_f and ξ_f are two variables respectively defined as period lengthening ratio and added damping ratio due to dam-foundation rock interaction. Such variables depend on several parameters which the most significant are: the moduli ratio E/E_f where E_f is the Young modulus of the foundation and the constant hysteretic damping factor η_f. For the latter parameter, in absence of informations on damping properties of the foundation rock, a value $\eta_f = 0.1$ should be adopted. Finally, the generalized mass $\tilde{M}$ of the equivalent SDOF system can be conveniently computed as:

$$\tilde{M} = R_r^2 m^* \tag{15}$$

whereas the generalized earthquake coefficient $\tilde{L}$ is expressed as:

$$\tilde{L} = l^* + \frac{\gamma_w L_w^2}{2}\left(\frac{L_w}{L}\right)^2 A_p \tag{16}$$

γ_w is the water density, and A_p = the integral of the function $2p(z/L_w)/\gamma L_w$ over the depth of the impounded water for ($L_w/L = 1$). The expression of the function $p(z/L_w)/\gamma L_w$ is given in [9] as a function of the parameter α and the ratio:

$$R_w = \frac{T_1^r}{T_r} \tag{17}$$

where $T_1^r = 4L_w/C$ is the fundamental vibration period of the impounded water (C is the velocity of water waves in the water) and $T_r = R_r T$.

In this study the variation lows of R_r and ξ_r with the parameters (E, L_w/L, α) furnished in tables in [9], have been interpolated and reported in analytical form for the case of interest which will be described in the next sections, having assumed $\alpha = 0.9$ and $E = 241.29 \times 10^5$ kN/m^2. Once having fixed α and E, the two variables R_r and ξ_r depend with non linear expressions on the ratio L_w/L only:

$$R_r = a_1\left(\frac{L_w}{L}\right)^2 + a_2\frac{L_w}{L} + a_3 \tag{18}$$

Table 1 Coefficients for the variation lows of R_r and ξ_r with the ratio L_w/L

a_1	a_2	a_3	b_1	b_2	b_3	b_4	b_5
1.79	–2.05 6	1.59	–1.07	3.05	–3.12	1.37	–0.22

Table 2 Coefficients for the variation laws of R_f and ξ_f with the ratio E/E_w

c_1	c_2	d_1	d_2
1.2255	0.1327	0.0638	0.8838

$$\xi_r = b_1 \left(\frac{L_w}{L}\right)^4 + b_2 \left(\frac{L_w}{L}\right)^3 + b_3 \left(\frac{L_w}{L}\right)^2 + b_4 \frac{L_w}{L} + b_5 \tag{19}$$

where the values for the coefficients a_i and b_j ($i = 1-3$, $j = 1-5$) are reported in Table 1.

Moreover, expressions furnished in tables in [9] for R_f and ξ_f, here are interpolated and reported in analytical form (having assumed $\eta_f = 0.1$) as function of the ratio E/E_f:

$$R_f = c_1 \left(\frac{E}{E_f}\right)^{c_2} \tag{20}$$

$$\xi_f = d_1 \left(\frac{E}{E_f}\right)^{d_2} \tag{21}$$

where the values for the coefficients c_i and d_i ($i = 1-2$) are reported in Table 2.

If the ratio $E_f/E > 4$ the $R_f \cong 1$.

3 Actions Considered

In this section the actions considered to model the base sliding dam response subjected to an earthquake are illustrated. The actions are divided into static and dynamic ones.

3.1 Static Actions

The static forces acting on the dam considered in the analysis are:

P_d: dam weight,
P_w: horizontal hydrostatic force,
U_w: uplift pressures resultant force,
R_p: contribution of a passive wedge resistance, when applicable.

Each force is computed considering the planar problem having assumed dam stripes of one meter, once the dam geometry, the water level upstream and downstream are known.

The horizontal hydrostatic force is computed as:

$$P_w = \frac{1}{2}\gamma_w L_w^2 \tag{22}$$

where γ_w is the water density and L_w is the water level in the reservoir.To compute the uplift pressures resultant force U_w, the parameters to be considered are: the water level in the reservoir (L_w), the position of the drain from the upstream face (X), the drain effectiveness (η), the elevation of the drainage tunnel (Z), the eventual presence of water downstream (L_{w2}). Generally, to take into account the effectiveness of the drainage system it is possible to increase the water level in correspondence of the drainage tunnel by the quantity $\bar{Z}$:

$$\bar{Z} = f(\eta, L_w, Z, L_{w2}) \geq Z \tag{23}$$

Depending on the dam geometry, the resultant force is then calculated by integrating the uplift pressure on the dam basis, Fig. 3.

According with the Italian Code, a constraint on the maximum uplift pressure on the line of the drainage system is imposed. In fact, in this point, the maximum hydrostatic pressure should not be considered lower than:

$$\gamma_w \bar{Z} = \gamma_w[L_{w2} + 0.35(L_w - L_{w2})] \tag{24}$$

In the simplified model such force acts reducing the sliding foundation resistance, Eq. (8).

To consider the contribution of a passive wedge resistance to the sliding resistance of the dam the resultant force obtained on the distribution of the passive resistance stress σ_{hp} is evaluated:

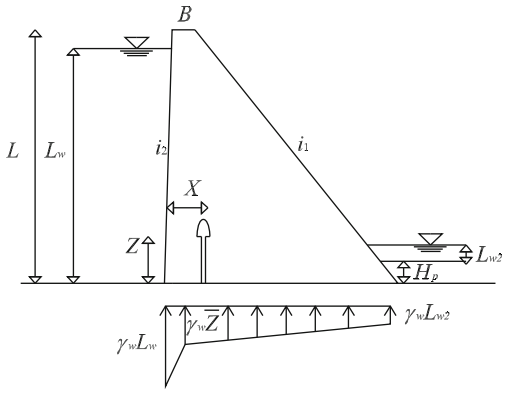


Fig. 3 Section geometry of the dam and uplift pressures on the basis

$$R_p = \int_0^{H_p} \sigma_{hp} dz \tag{25}$$

where H_p is the height of the embedment. The assumed hypothesis to calculate the passive resistance are:

1. The force mobilizes instantaneously without needing residual displacement,
2. The geotechnical parameters refer to the rock of the base foundation, however, to take into account superficial fracture the residual values are utilized,
3. The effect of the interstitial water is not taken into account on the computation of the vertical stress of the embedment.

The passive resistance stress $\boldsymbol{\sigma}_{hp}$ is evaluated as:

$$\boldsymbol{\sigma}_{hp} = 2c\sqrt{K_p} + \boldsymbol{\sigma}_v K_p \tag{26}$$

where c is the cohesion, $\boldsymbol{\sigma}_v$ is the vertical tension induced by the embedment and K_p is:

$$K_p = \frac{1 + sen\phi}{1 - sen\phi} \tag{27}$$

being $\boldsymbol{\phi}$ the friction angle.

Since for the hypothesis (1). the passive resistance mobilizes as the plastic threshold of the foundation rock is reached, it means, that this contribution induces an increase of the resulting sliding foundation resistance. As a result, the threshold value of the resultant sliding resistance $\tilde{R}_y$ is:

$$\tilde{R}_y = R_y + R_p \tag{28}$$

3.2 Dynamic Actions: Earthquake Time History

In order to perform seismic dynamic analysis several time histories taken from real earthquake records have been used. The registrations are taken from the Italian Earthquake strong motion database [12] which refers to seismic events happened in Italy during the period from years 1972 to 1998 and severe events have been taken from the Pacific Earthquake Engineering Research Center, PEER [13], and from the European Strong Motion Database, ESD [6]. To perform the analysis, signals referred to soil type A (rock) have been used.

The data concerning with the acceleration time histories used, are reported in Table 3, where for each event the following data are given: station name, earthquake, date, magnitude, epicentral distance, file name, horizontal peak ground acceleration. In total, 47 natural earthquakes have been used for the analysis.

Table 3 Data from Italian Earthquake strong motion database PEER and ESD database: station name, earthquake, date, magnitude, epicentral distance, file name, horizontal peak ground acceleration, vertical peak ground acceleration

Station	Earthquake	Date	Mw	Ep.D. (km)	Name	HPGA (g)
Assisi-Stallone	Umbria Marche	26/09/1997	6	21	A-AAL018	0.19
Nocera Umbra-Biscontini	Umbria Marche	06/10/1997	5.5	10	E-NCB000	0.26
Nocera Umbra 2	Umbria Marche	03/04/1998	5.1	10	R-NC2000	0.38
Tolmezzo-Diga Ambiesta	Friuli	06/05/1976	6.5	23	A-TMZ000	0.36
Borgo-Cerreto Torre	Umbria Marche	26/09/1997	6	25	A-BCT000	0.07
Tarcento	Friuli	11/09/1976	5.3	8	TRT000	0.21
Borgo-Cerreto Torre	Umbria Marche	14/10/1997	5.6	12	J-BCT000	0.34
Nocera Umbra 2	Umbria Marche	05/04/1998	4.8	10	S-NC2000	0.17
Borgo-Cerreto Torre	Umbria Marche	12/10/1997	5.2	11	I-BCT000	0.17
Assisi-Stallone	Umbria Marche	06/10/1997	5.5	20	E-AAL018	0.10
Borgo-Cerreto Torre	Umbria Marche	26/09/1997	5.7	23	B-BCT000	0.18
San Rocco	Friuli	15/09/1976	6	17	B-SRO000	0.06
Nocera Umbra-Biscontini	Umbria Marche	03/10/1997	5.3	8	C-NCB000	0.19
Tolmezzo-Diga Ambiesta	Friuli	07/05/1976	5.2	27	C-TMZ000	0.12
Nocera Umbra-Biscontini	Umbria Marche	07/10/1997	4.2	10	F-NCB000	0.05
Nocera Umbra-Biscontini	Umbria Marche	07/10/1997	4.5	10	G-NCB000	0.07
Nocera Umbra-Biscontini	Umbria Marche	11/10/1997	5.6	14	H-NCB000	0.09
Cascia	Umbria Marche	14/10/1997	5.6	23	J-CSC000	0.05
San Rocco	Friuli	11/09/1976	5.3	15	SR-ONS	0.03
San Rocco	Friuli	11/09/1976	5.5	17	W-SRO000	0.09
Nocera Umbra 2	Central Italy	05/04/1998	4.8	10	S-NC2090	0.15
Nocera Umbra 2	Central Italy	03/04/1998	5.1	10	R-NC2090	0.31
Nocera Umbra-Biscontini	Central Italy	14/10/1997	5.6	23	J-NCB090	0.05
Assisi-Stallone	Central Italy	26/09/1997	5.7	24	B-AAL108	0.15
Borgo-Cerreto Torre	Central Italy	26/09/1997	6	25	A-BCT090	0.11
Auletta	Campano Lucano	23/11/1980	6.9	25	Auletta-NS	0.06
Torre del Greco	Campano Lucano	23/11/1980	6.9	80	Torre-NS	0.06
Bagnoli-Irpino	Campano Lucano	23/11/1980	6.9	23	Bagnoli-NS	0.13
Villetta Barrea	Lazio Abruzzo	11/05/1984	5.5	6	A-VLB000	0.15
Milazzo	Basso Tirreno	15/04/1978	6	34	MLZ000	0.07
Ponte Corvo	Lazio Abruzzo	07/05/1984	5.9	22	PON-NS	0.06
Lazio Abruzzo	Southern Italy	07/05/1984	5.9	5	ATI-WE	0.12
Lazio Abruzzo	Southern Italy	11/05/1984	4.8	8	D-VLB000	0.15
Gubbio	Central Italy	29/04/1984	5.6	17	I-GBB090	0.07
Sortino	Sicily, Italy	13/12/1990	5.6	29	SRT270	0.11
Sturno	Campano Lucano	23/11/1980	6.9	32	Sturno-NS	0.23
Loma Prieta	California	18/101989	6.9	28.6	LOMAP	0.473
Kocaeli	Turkey	17/08/1999	7.4	5.3	IZMIT	0.152
Kocaeli	Turkey	17/08/1999	7.4	47	GBZ000	0.244
Chi-Chi	Taiwan	20/09/1999	7.6	152.7	TAP051	0.112
N. Palm Springs	California	08/07/1986	6	46.2	ARM360	0.129
Bucarest	Romania	04/03/1977	7.5	4	Bucarest	0.194
Dayhook	Iran	06/09/1978	7.4	11	Dayhook	0.385
Montenegro	Montenegro	15/04/1979	6.9	65	Montenegro	0.256
Kozani	Grecia	13/05/1995	6.5	7	Kozani	0.208
Sakarya	Turkey	17/08/1999	7.6	34	Sakarya	0.361
Ulcinj	Montenegro	15/04/1979	6.9	21	Ulcinj	0.224

4 Illustration of Parametric Analysis: Influence of Dam-Water-Foundation Mechanic Parameters

The model illustrated in the previous sections is here subjected to parametric analysis. As applicative example a typical concrete gravity dam, depicted in Fig. 3, with geometrical characteristics reported in Table 4 is utilized to perform the analysis.

Width to height ratio of concrete gravity dams has a small variation, usually from 0.7 to 0.8, here 0.7 is considered. When not differently specified, dam height is $L = 86.8\,\text{m}$. The Young modulus of concrete is $E = 241.29 \times 10^5\,\text{kN/m}^2$. Instead, maximum water level in the reservoir is $L_w/L = 0.96 \cong 1$. Values where else different, will be specified during the parametric analysis. The foundation is always considered embedded in the rock. The basic value for the foundation Young modulus is $E_f = 526.5 \times 10^5\,\text{kN/m}^2$ (which corresponds to mechanical characteristics of soil type A) which implies $k_f = 205.5 \times 10^5\,\text{kN/m}$ [11]. The foundation rock has unit weight of $25\,\text{kN/m}^3$.

The purpose is to investigate the influence of each parameter on dam response in terms of base sliding by means of the simplified procedure. For each case, dynamic analysis with the selected set of accelerograms is carried out. Three main sensitivity analysis are treated:

– Variation of the foundation parameters: resistance and deformability,
– Variation of the water level in the reservoir,
– Variation of the dam geometry: dam height.

The variation of the foundation parameters is possible by changing the threshold level R_y which, for a given dam geometry and water level, is a function of the coefficients c and ϕ (resistance parameters). Similarly, it is possible to vary the elastic stiffness k_f, which changes in function of the foundation rock elastic Young modulus E_f (deformability parameter).The variation of the water level in the reservoir L_w acts modifying the equivalent mass of the system M_{dw} and consequently the period $\tilde{T}$, but also modifying system damping properties $\tilde{\xi}$. At the same time varying the water level changes the resultant uplift force acting at the dam base due to static pressure, with reduction on foundation sliding resistance. The variation of the dam geometry is considered by varying the dam height L. Height variation modifies both the period $\tilde{T}$ and the system damping properties $\tilde{\xi}$.

In the following, before presenting results of dynamical analysis, the influence of each variable parameter is observed. Attention is focused on the resultant sliding resistance $\tilde{R}_y$ representing a static quantity, and on the limit acceleration a_L, representing a dynamical quantity, here defined as the limit response acceleration, which, when overtaken, produces sliding of the dam:

$$a_L = \frac{\tilde{R}_y - P_w}{M_{dw}} \tag{29}$$

Table 4 Geometrical parameters of the dam considered for the parametric analysis

L (m)	B (m)	i_1	i_2	L_w (m)	L_{w2} (m)	X (m)	Z (m)	H_p (m)
86.8	5	0.7	0	83.8	5	2.8	3.5	5

where $\tilde{R}_y$ is the resultant sliding resistance, P_w is the water pressure static resultant (Eq. (22)), and M_{dw} is the equivalent mass of the SDOF system (Eq. (5)).

4.1 Influence of Resistance Foundation Parameters

The first sensitivity analysis concerns the variation of resistance foundation parameters c and ϕ. The cases examined are reported in Table 5 for the different values of the couples c and ϕ.

Such values are chosen on the basis of typical strength of foundation rock where concrete gravity dams are built, therefore they represent the possible range of variation of R_y.

The period of the equivalent SDOF system is $\tilde{T} = 0.30\,\text{s}$ (Eq. (13)), the mass is $M_{dw} = 1690\,\text{ton}$ (Eq. (5)), the dam stiffness is $K_d = 7.62 \times 10^5\,\text{kN/m}$ (Eq. (10)), the damping ratio is $\tilde{\xi} = 7\%$ (Eq. (18)), $p = 3.57$ (Eq. (3)), whereas the resultant sliding resistance is reported in Table 5 (Eq. (28)), one can see that cases are ordered for decreasing foundation resistance. In all the treated cases the contribution of the passive wedge resistance is just included in the resultant sliding resistance (see Eq. (28)). The value of the passive wedge resistance for the different geotechnical parameters is reported in Table 5.

Total sliding resistance $\tilde{R}_y$ is shown in Fig. 4a, where the cohesive component R_{yc}, the attritive component $R_{y\phi}$ and the passive residence component R_p, are also given. The highest value of the total sliding resistance is obtained for $c = 120\,\text{kPa}$ and $\phi = 35°$, whereas the lowest is reached for $c = 0\,\text{kPa}$ and $\phi = 34°$. The attritive component $R_{y\phi}$ plays the major contribution on the resistance among the three components, above all the combinations of the geotechnical parameters. Instead, the cohesive component (where $c \neq 0$) and the passive wedge resistance are comparable; for cases 1 and 2 the cohesive part is greater than the passive wedge resistance, whereas for case 4 the latter prevails. Obviously, the relative contribution varies if dam height and water level are changed, as shown in the other cases considered. In Fig. 4b, the development of the limit acceleration a_L is reported as a function of the resistance foundation parameters. The hierarchy of decreasing limit acceleration follows the one reported for the resultant sliding resistance. Due to variation of the resistance parameters, the value of the limit acceleration varies in the range $0.2 - 2\,\text{m/s}^2$.

Table 5 Variation of resistance foundation parameters. Values of resultant sliding resistance and passive wedge resistance with the variation of c and ϕ

Case	Resistance coefficient	$\tilde{R}_y$ (kN)	R_p (kN)
1	$c = 120\,\text{kPa}$, $\phi = 35°$	13025	970.37
2	$c = 180\,\text{kPa}$, $\phi = 29°$	12100	1110.1
3	$c = 0\,\text{kPa}$, $\phi = 39°$	11963	385.41
4	$c = 50\,\text{kPa}$, $\phi = 35°$	11456	593.07
5	$c = 0\,\text{kPa}$, $\phi = 34°$	9953.9	310.15

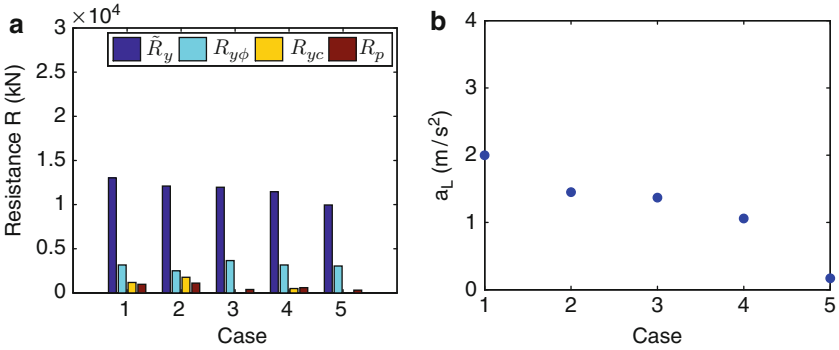


Fig. 4 Variation of (**a**) resistance foundation parameters, different contributions to the resultant sliding resistance. (**b**) Limit acceleration, (cases 1–5 refer to Table 5)

4.2 Influence of Deformability of the Foundation

The second sensitivity analysis concerns variation of the Young modulus E_f which determines the stiffness of the foundation. This latter plays role both in the elastic response and in the non elastic response. In fact, in the elastic response such term modifies the resultant stiffness of the system, and therefore the period $\tilde{T}$, at the same time it affects the yielding displacement, once chosen a predefined threshold level for the sliding resistance R_y.

Three cases are considered:

1. $E_f = 526.5 \times 10^4$ kN/m^2 which corresponds $k_f = 202.5 \times 10^4$ kN/m,
2. $E_f = 526.5 \times 10^5$ kN/m^2 which corresponds $k_f = 202.5 \times 10^5$ kN/m,
3. $E_f = 526.6 \times 10^6$ kN/m^2 which corresponds $k_f = 202.5 \times 10^6$ kN/m.

The parameters of the equivalent SDOF system are reported in Table 6. The first case represents the situation of a system with high value of the yielding displacement and a long period for the equivalent SDOF system, the second case falls within those treated previously and represents a typical foundation rock at the base of concrete gravity dams, finally the third case is representative of a system with low value of yielding displacement, modelling at limit a rigid plastic behavior. The first case represents an upper bound limit for dam period, whereas the third case is the bound limit of a particularly stiff system, with the usual assumption of no interaction with the foundation rock. In fact, interaction between dam and foundation is often disregarded in practice.

For each of the three values of foundation Young modulus the analyses are repeated with the five different resistance parameters c and ϕ couples, which assume the values reported in Table 7.

As E_f decreases, as the resultant sliding resistance increases. This is an effect due to the variability of the coefficient p.

In Figs. 5a–b, the different contributions to the resultant sliding resistance $\tilde{R}_y$ intended as the sum of the cohesive component R_{yc}, the attritive component $R_{y\phi}$

Table 6 Parameters of the SDOF system varying the foundation Young modulus E_f

Case	M_{dw} (ton)	K_d (kN/m)	$\widetilde{T}$ (s)	$\widetilde{\xi}$	p
$E_f = 526.5 \times 10^4$ kN/m^2	916	2.42×10^5	0.41	26	1.94
$E_f = 526.5 \times 10^5$ kN/m^2	1688.9	7.62×10^5	0.3	7	3.57
$E_f = 526.6 \times 10^6$ kN/m^2	2062	11×10^5	0.27	5	4.35

Table 7 Variation of the deformability foundation parameter: values of resultant sliding foundation resistance with the variation of c and ϕ

Deformability parameter	Case	Resistance coefficient	$\widetilde{R}_y$ (kN)
$E_f = 526.6 \times 10^4$ kN/m^2	1	$c = 120$ kPa, $\phi = 35°$	23998
	2	$c = 180$ kPa, $\phi = 29°$	22295
	3	$c = 0$ kPa, $\phi = 39°$	22042
	4	$c = 50$ kPa, $\phi = 35°$	21107
	5	$c = 0$ kPa, $\phi = 34°$	18340
$E_f = 526.6 \times 10^6$ kN/m^2	1	$c = 120$ kPa, $\phi = 35°$	10668
	2	$c = 180$ kPa, $\phi = 29°$	9910.7
	3	$c = 0$ kPa, $\phi = 39°$	9798.4
	4	$c = 50$ kPa, $\phi = 35°$	9382.7
	5	$c = 0$ kPa, $\phi = 34°$	8152.7

and the passive residence component R_p, are reported for the five cases examined. Independently on the variation of the deformability parameter, the attritive part always constitutes the most important component in the computation of the resultant sliding resistance. Moreover, the resistance hierarchy as function of the resistance foundation parameter is independent on the deformability parameter E_f. In Fig. 6, the development of the limit acceleration a_L is reported for the different foundation resistance parameters for the three cases of deformability. It is noticed that the solution without considering dam-foundation interaction ($E_f = 526.6 \times 10^6$ kN/m^2) gives the lowest limit acceleration. That means that, disregarding it, generally leads to conservative results. However, limit acceleration obtained with case of normal foundation flexibility ($E_f = 526.6 \times 10^5$ kN/m^2) is just greater. The situation of a highly flexible foundation instead, leads to values of the limit acceleration generally higher with respect to the previous cases, especially if the resistance foundation parameters are taken as very good.

4.3 Influence of Water Level in the Reservoir

The third sensitivity analysis concerns the variation of water level in the reservoir, in particular, three different levels are considered:

1. Ratio $L_w/L \cong 1$,

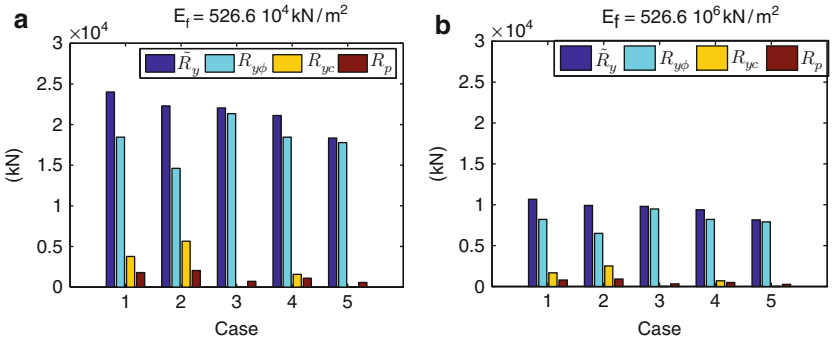


Fig. 5 Variation of the foundation parameters: resistance. Different contributions to the resultant sliding resistance. (**a**) $E_f = 526.6 \times 10^4$ kN/m^2. (**b**) $E_f = 526.6 \times 10^6$ kN/m^2

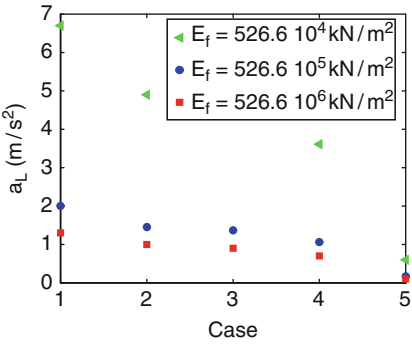


Fig. 6 Variation of limit acceleration with the resistance foundation parameters for the three assumed values of deformability (cases 1–5 refer to Table 5)

Table 8 Parameters of the SDOF system varying the water level in the reservoir

Case	M_{dw} (ton)	K_d (kN/m)	$\widetilde{T}$ (s)	$\widetilde{\xi}$	p
$L_w/L \cong 1$	1688.9.3	7.62×10^5	0.3	7	3.57
$L_w/L = 0.75$	1075.3	7.05×10^5	0.25	6.9	3.31
$L_w/L = 0.5$	793.3	5.56×10^5	0.24	6.8	2.67

2. $L_w/L = 0.75$,
3. Ratio $L_w/L = 0.5$.

The first case ($L_w/L \cong 1$) generally corresponds to the situation of normal flood level, it is part of the examples treated before and, for this reason, it will be not discussed. Parameter values for the SDOF system obtained for the three cases are summarized in Table 8.

Let observe that varying the water level, the mass of the equivalent SDOF system changes too. In particular, it diminishes as the water level lowers. Analyses are

Table 9 Variation of the water level in the reservoir: values of resultant sliding foundation resistance with the variation of c and ϕ

Case	Resistance coefficient	$\tilde{R}_y$ (kN) $L_w/L \cong 1$	$\tilde{R}_y$ (kN) $L_w/L = 0.75$	$\tilde{R}_y$ (kN) $L_w/L = 0.5$
1	$c = 120$ kPa, $\phi = 35°$	13,025	14,496	18,600
2	$c = 180$ kPa, $\phi = 29°$	12,100	13,403	17,108
3	$c = 0$ kPa, $\phi = 39°$	11,963	13,426.1	17,381
4	$c = 50$ kPa, $\phi = 35°$	11,456	12,806	16,509
5	$c = 0$ kPa, $\phi = 34°$	9,953.9	11,171.9	14,463.9

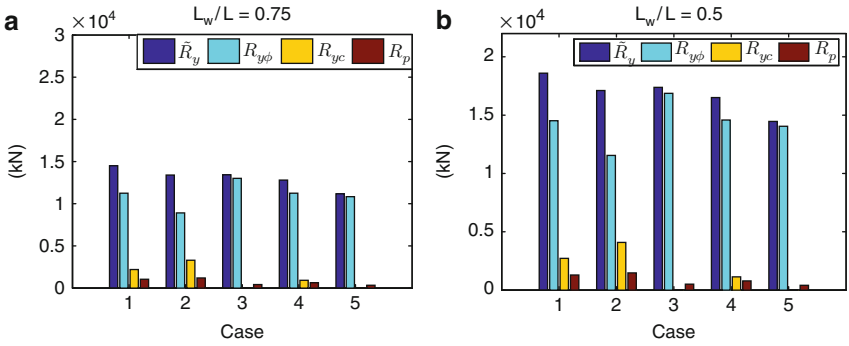


Fig. 7 Variation of the water level in the reservoir different contributions to the resultant sliding resistance varying the geotechnical parameters. (**a**) $L_w/L = 0.75$ (**b**) $L_w/L = 0.50$

repeated for the three water levels, with the five cases of different resistance parameters (c and ϕ previously considered, see Table 5). Values of the resultant sliding resistance are reported in Table 9 whereas the different contributions of the resistance terms are depicted in Fig. 7a,b. By comparing the values of the resultant sliding resistance $\tilde{R}_y$ for the three water levels it is observed that decreasing the water level form $L_w/L \cong 1$ to $L_w/L = 0.75 - 0.5$ the order of decreasing resultant resistance changes. In particular, in the latter two cases, the resistance obtained with $c = 0$ kPa and $\phi = 39°$ exceeds those obtained for $c = 180$ kPa and $\phi = 29°$, whereas the decreasing hierarchy remains unchanged for the other couples. By decreasing the water level the uplift force decreases and this benefits most for the attritive component of the sliding resistance, since the normal force increases. For this reason rocks with higher ϕ gives an higher sliding resistance. Resistance increases more than linearly by decreasing water level. In fact, independently on the different couples of c and ϕ, by changing from $L_w/L \cong 1$ to $L_w/L = 0.75$, the resultant sliding resistance increases in mean more than 10%, and by changing from $L_w/L \cong 1$ to $L_w/L = 0.5$ it increases in mean more than 40%. In Fig. 4a–b the different distributions of the sliding resistance components for case $L_w/L = 0.75$ and $L_w/L = 0.5$ respectively, are represented by varying couples of geotechnical parameters (cases 1–5). The case of full reservoir was depicted in Fig. 4a.

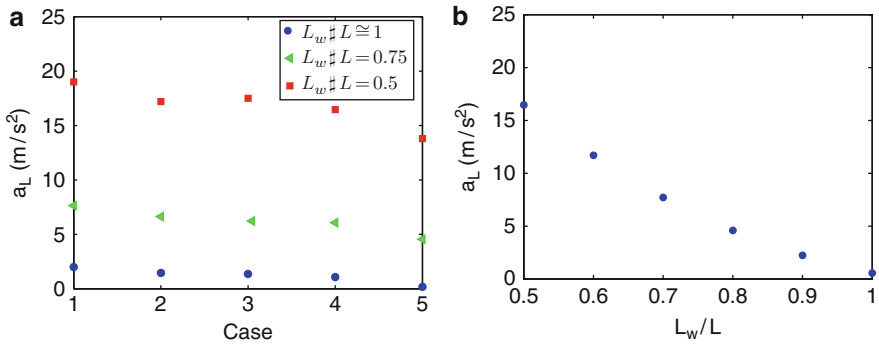


Fig. 8 (**a**) Variation of limit acceleration with the resistance foundation parameters for the three assumed values of Water level (cases 1–5 refer to Table 5). (**b**) Development of limit acceleration versus water level to dam height ratio for case 4

The decrease of L_w reduces uplift pressures, therefore friction component increases due to normal force which multiplies the tangent of ϕ, while R_{yc} and R_p are not affected by variation of water level, base shear resistance increases. The decrease of L_w reduces hydrostatic force and equivalent water mass as well. these three contributions result in a relevant increase of limit acceleration, Fig. 8a. For example, reduction of the water level with respect to normal flood, increases limit acceleration about four times, and impounding only half reservoir (50% reduction), the limit acceleration is in the range 15−20 m/s^2 (1.5−2 g), values which are not generally reached for any natural earthquake. Despite of these effects, the variation of the equivalent fundamental period and damping ratio is not strong. By contrast, the reduction of L_w increase base sliding acceleration but also base sliding force and corresponding shear force in the dam. Therefore, if this is the case, the reduction of water level can favor development of cracks and damage due to seismic response. In Fig. 8b as an example, for a foundation type (here is reported case 4), the development of limit response acceleration versus water level to dam height ratio is reported. The range considered is from full reservoir to half impounded reservoir ($L_w/L = 0.5-1$). The limit acceleration increases more than linearly as water level ratio decreases. Results confirm that the reduction of the water level in the reservoir, even of a small quantity, is a useful and very effective provision to prevent base sliding. The range considered is from full reservoir to half impounded reservoir ($L_w/L = 0.5-1$). The limit acceleration increases more than linearly as water level ratio decreases.

4.4 Influence of Dam Height

The last sensitivity analysis regards the variation of the dam geometry in particular the variation of dam height. The following cases are considered:

1. $L = 50$ m,
2. $L = 70$ m,
3. $L = 86.8$ m,
4. $L = 100$ m.

Case 3 is part treated in the previous examples. The parameters of the equivalent SDOF system are reported in Table 10.

Each analysis is repeated with the five cases of different resistance parameters (c and ϕ), which have values reported in Table 5.

By observing the values of the resultant sliding resistance, Table 11, it appears that for low height ($L = 50$ m) dams the cohesion plays an important role. In fact the resistance hierarchy is made by the decrease of cohesion. Approaching $L = 70$ m until $L = 86.8$ m, the effect of friction becomes more evident, in fact the resistance hierarchy changes, in particular the first case corresponds to high values of cohesion and friction angle. At $L = 100$ m friction has predominance in the resistance hierarchy. In any case of dam height, the combination of the geotechnical parameters which gives lowest sliding resistance corresponds to case 5 ($c = 0$ kPa, $\phi = 34°$). By observing the distribution of the individual resistance components, Figs. 4, 9a–b, and 10a, the frictional component $R_{y\phi}$ always prevails on the cohesive component R_{yc} and on the passive wedge resistance R_p. Such difference increases with dam height. It must be noticed that by varying the dam height L, for each couple of the geotechnical parameters, the passive wedge resistance is kept constant, due to constant depth of the embedment ($H_p = 5$ m). For this reason, such contribute

Table 10 Parameters of the SDOF system varying dam height

Case	M_{dw} (ton)	K_d (kN/m)	$\tilde{T}$ (s)	$\tilde{\xi}$	p
1	553.25	7.62×10^5	0.17	7.3	3.57
2	1084.4	7.62×10^5	0.24	7.3	3.57
3	1688.9	7.62×10^5	0.3	7	3.57
4	2213	7.62×10^5	0.35	7.3	3.57

Table 11 Values of resultant sliding foundation resistance with the variation of c and ϕ for different dam height

Case	Resistance coefficient	$\tilde{R}_y$ (kN) $L = 50$ m	$\tilde{R}_y$ (kN) $L = 70$ m	$\tilde{R}_y$ (kN) $L = 86.8$ m	$\tilde{R}_y$ (kN) $L = 100$ m
1	$c = 120$ kPa, $\phi = 35°$	5,313.8	9,038.9	13,025	16,762
2	$c = 180$ kPa, $\phi = 29°$	5,383.3	8,666.2	12,100	15,281
3	$c = 0$ kPa, $\phi = 39°$	4,045.6	7,808.5	1,1963	15,923
4	$c = 50$ kPa, $\phi = 35°$	4,249	7,699.2	11,456	15,010
5	$c = 0$ kPa, $\phi = 34°$	3,358.9	6,493.2	9,953.9	13,252.9

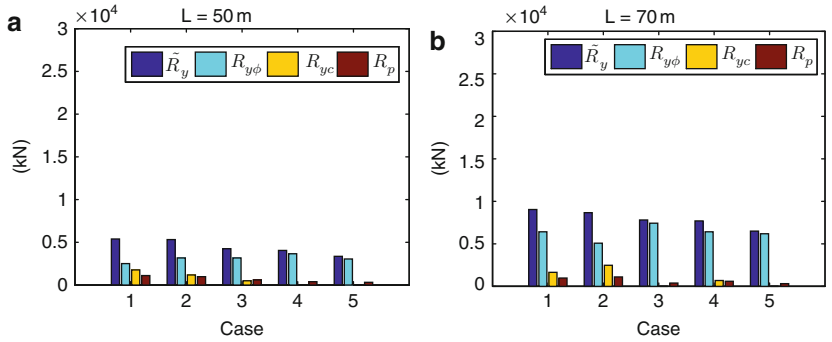


Fig. 9 Variation of the dam geometry. Different contributions to the resultant sliding resistance varying the geotechnical parameters. (**a**) $L = 50$ m. (**b**) $L = 70$ m

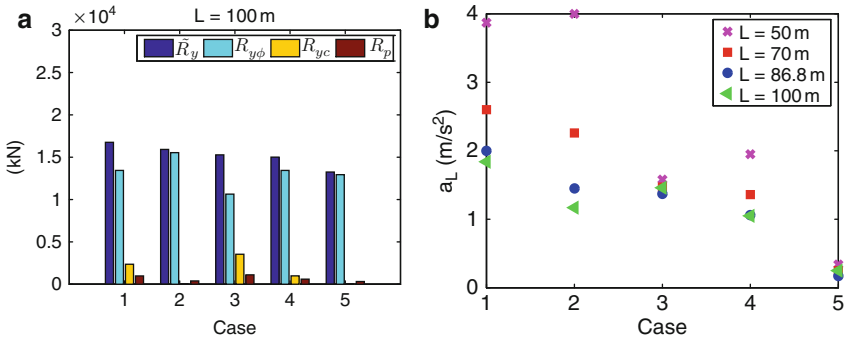


Fig. 10 Variation of the dam geometry. Different contributions to the resultant sliding resistance varying the geotechnical parameters. (**a**) $L = 100$ m. (**b**) Variation of limit acceleration with the resistance foundation parameters for the four assumed values of dam height (cases 1–5 refer to Table 5)

loses importance as the height of the dam increases. In Fig. 10b the development of the limit acceleration for the different values of the geotechnical parameters is reported for dam height $L = 50, 70, 100$ m respectively. Despite of the previous investigations, since the resistance hierarchy (among the five cases examined) varies more than one time with the height, the trend is not regular. It appears that, on equal terms, limit acceleration decreases with increasing dam height. The lowest values are reached for a dam of $L = 100$ m high.

5 Discussion of Results

In this section results of dynamic analysis relative to the parametric analysis are presented. In order to make comparisons graphs are reported using convenient variables.

As input measure, the acceleration ratio β defined as:

$$\beta = \frac{a_L}{a(\tilde{T})} \tag{30}$$

where a_L is the limit response acceleration defined in (29), which, when overtaken, produces sliding of the dam and $a(\tilde{T})$ represents the spectral acceleration evaluated at the period $\tilde{T}$ from the acceleration response spectra of the seismic action with damping ratio $\xi = 5\%$. When β is greater than unity the structural system remains in the elastic field, the sliding foundation resistance is greater than the shear force developed by the seismic action. Whereas, when β is lower than the unity, the system exhibits non linear response and plastic displacement occurs. Looking at each case, the value of a_L is known and for each accelerogram the corresponding β is obtained. Bazzurro and Cornell [1], have shown that β is a good scaling parameter to discuss non linear response.

As output measure the ratio between maximum displacement at the top of the dam and displacement at dam top when maximum sliding resistance in foundation is reached, named ductility factor μ is utilized:

$$\mu = \frac{D_{max}}{D_y} = \frac{y_{max}}{y_y} \tag{31}$$

where D_{max} and D_y are respectively the maximum displacement and the yielding displacement of the equivalent SDOF system, whereas y_{max} and y_y are respectively the maximum displacement and the yielding displacement at the dam top. In particular, at the end of the earthquake, the dam top displacement coincides with the dam base displacement and represents the residual displacement, since the dam body is considered linear elastic. Base residual displacement can be valued then in terms of ductility factor as:

$$y_R = y_{max} - y_y = y_y(\mu - 1) \tag{32}$$

being the yielding displacement y_y valued as:

$$y_y = p \cdot D_y = p \cdot \frac{\tilde{R}_y}{K} \tag{33}$$

In the following results obtained for several earthquakes are reported in graphs $\beta - \mu$. The analysis showed that plastic displacement happens in downstream direction only, therefore the maximum plastic displacement coincides with residual displacement.

5.1 *Influence of Foundation Resistance Parameters*

The first results reported investigate dam seismic response with different sliding resistance values. For each couple of values of resistance parameters c and ϕ, dynamic analysis are repeated using several earthquakes and results are shown in Fig. 11a. Non linear response is kept done until β is in the range $0.5 < \beta < 1$. This is verified for all the five different foundation resistance cases. As the spectral acceleration $a(\tilde{T})$ increases, and consequently β decreases, the response in terms of ductility increases. When $\beta < 0.5$ the non linear behavior becomes more evident and the obtained values of the ductility factor μ are quite high and disperse. In order to catch more in detail the behavior in the part where non linearity is more evident, some results referring to few specific accelerograms with name AAAL018, ATMZ000, LOMAP are reported in Fig. 11b. They have been chosen since their spectral amplitude is maximum around the fundamental period of the equivalent SDOF system ($\tilde{T} = 0.3$ s). In particular they are ordered for increasing spectral amplitude (from AAAL018 to LOMAP). Let focus attention at one accelerogram at time, for example AAA108: for the signal five points are depicted corresponding to the five different geotechnical parameters. Each point corresponds to one case of resistance parameters c and ϕ (1–5 with resistance decreasing from 1 to 5, see Table 5). As the resultant foundation resistance $\tilde{R}_y$ decreases consequently β decreases and μ grows. The dependence of μ versus β has an exponential trend. By changing accelerogram, the curve moves to left and increases slope especially at low β. For ATMZ000 and LOMAP records, points corresponding to foundation parameter indicated with number 5 are not visible in the scale of the graph. Combining different sliding resistance and seismic input, different μ can correspond to the same β value.

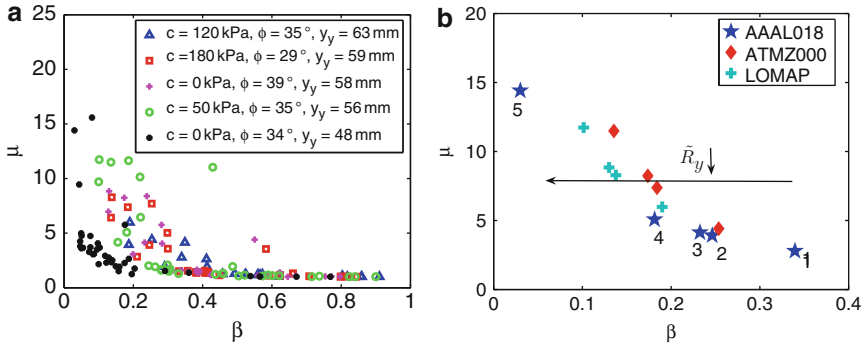


Fig. 11 Dam $L = 86.8$ m, $E_f = 526 \times 10^5$ kN/m^2, $\tilde{T} = 0.3$ s. (**a**) Results of dynamic analysis varying the geotechnical parameters c and ϕ (cases 1–5) (**b**) particular

5.2 *Influence of Deformability Foundation Parameters*

The second parametric analysis outlines the influence of deformability foundation parameter (E_f) on dam seismic response. Results of dynamic analysis with low and high elastic foundation Young modulus are presented in Figs. 12a–b respectively, the basic one ($E_f = 526 \times 10^5$ kN/m^2) has been presented previously (Fig. 11). The effect of changing the foundation elasticity modulus evidently affects the variation of the equivalent fundamental period and the equivalent damping ratio, namely, by increasing it, $\tilde{T}$ and $\tilde{\xi}$ actually decrease. In particular, a very high value of the damping ratio is observed for the lowest Young modulus ($\tilde{\xi} = 26\%$). Also the generalized mass M_{dw} reflects the effect of different E_f. In fact, it decreases by decreasing the foundation elasticity modulus. This implies a lower dynamic action induced on the equivalent SDOF system. In the case of low elastic foundation stiffness, Fig. 12a, since the natural period of the equivalent structure noticeably grows ($\tilde{T} = 0.41$ s), by observing the acceleration response spectra in this range, it is noticed that many signals have a low contribution in terms of spectral acceleration. Only few cases show non linear behavior and essentially they correspond to situations of low values of the sliding resistance (especially case 5, c =0 kPa, $\phi = 34°$). However, the ductility level is maintained at low values also for very low values of the acceleration ratio β. This is a necessary consequence of the reduced seismic action acting together with the high damping ratio. In this situation the damage level is less evident if compared with the previous cases.

Instead, concerning the case of high foundation stiffness ($k_f = 202.5 \times 10^6$ kN/m), Fig. 12b, the number of events for which plastic response is observed grows with respect to the previous case. The effect is related to the shorter period of the structure, which is generally associated to the zone of maximum amplification response for most of the accelerograms, but also for the low dissipative capacity of the equivalent system. This case can be interpreted at limit as disregarding

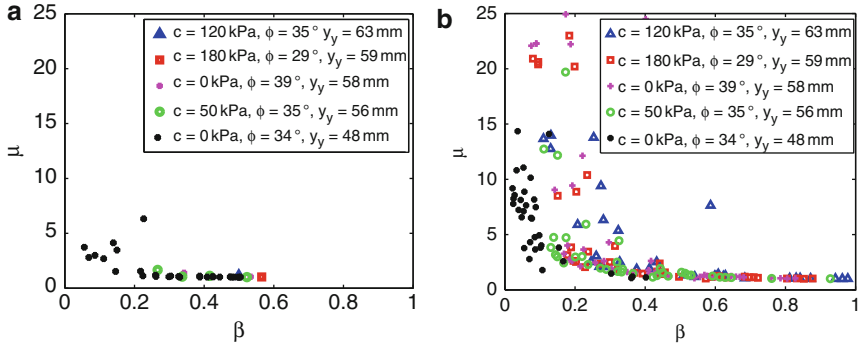


Fig. 12 Results of dynamic analysis varying the geotechnical parameters c and ϕ (cases 1–5). (**a**) Dam $L = 86.8$ m, $E_f = 526 \times 10^4$ kN/m^2, $\tilde{T} = 0.41$ s. (**b**) Dam $L = 86.8$ m, $E_f = 526 \times 10^6$ kN/m^2, $\tilde{T} = 0.27$ s

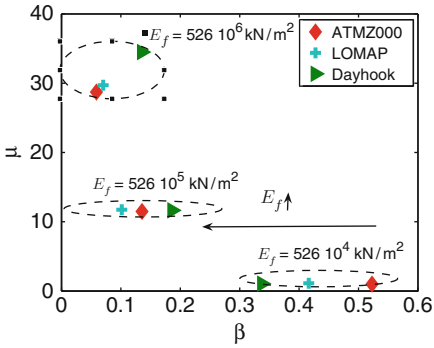


Fig. 13 Dam $L = 86.8$ m, particular of the results of dynamic analysis for three selected accelerograms and different foundation Young modulus with $E_f = 526 \times 10^4$ kN/m^2 – $E_f = 526 \times 10^5$ kN/m^2 – $E_f = 526 \times 10^6$ kN/m^2 (case: $c = 50$ kPa and $\phi = 35°$)

foundation structure interaction; this generally implies lower damping resources for the entire system. However, until $\beta \geq 0.3$, the non linear response is not strongly evident, instead for $\beta < 0.3$ the ductility factor grows rapidly and unexpectedly, approaching intolerable levels for the structure.

In Fig. 13 a detail from Figs. 11, 12a–b, chosen a couple of foundation resistance parameters ($c = 50$ kPa and $\phi = 35°$) and three accelerograms among the most severe, is reported for the three cases varying E_f. Three points correspond to each accelerogram. By increasing the foundation Young modulus, β decreases. This is caused by an increasing spectral acceleration joint with a lower limit acceleration, sice the equivalent mass M_{dw} decreases. The ductility factor generally increases with the higher foundation Young modulus having fixed the sliding foundation resistance. The trend shows an exponential dependence of μ versus β.

5.3 *Influence of Water Level in the Reservoir*

Results obtained by varying the water level in the reservoir, for a constant value of the other variables, for the different couples of geotechnical parameters, are depicted in Fig. 14a for the ratio $L_w/L = 0.75$. Non linear response is observed in few cases only. In fact, the resultant sliding resistance is increased considerably and at the same time the hydrostatic component P_w is low, due to the reduced water level. That implies higher values of the limit acceleration a_L, which correspond to higher values of the acceleration ratio β. For the cases corresponding to high values of the resultant sliding resistance (c and ϕ of cases 1, 2, 3), plastic response is observed for two events only. Such number increases as the foundation resistance decreases (cases 4 and 5 respectively). However, the ductility factor maintains generally low values.

Finally, results concerning the case of half impounded reservoir ($L_w/L = 0.5$) are not reported because, in such case, independently on the foundation resistance type, dam response remains in the elastic region and residual displacements are not attended.

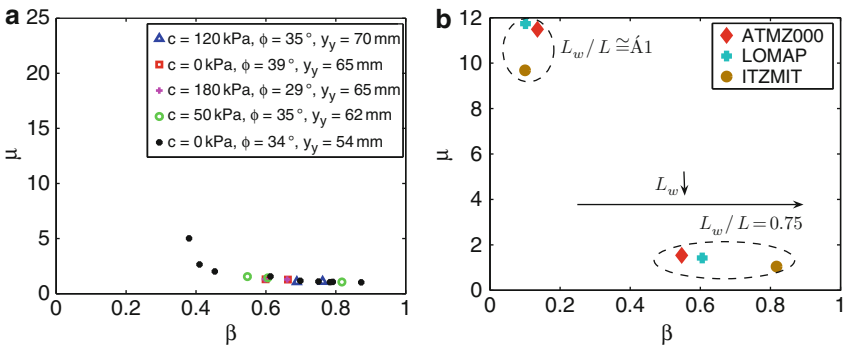


Fig. 14 Dam $L = 86.8$ m, $E_f = 526 \times 10^5$ kN/m^2, $\tilde{T} = 0.25$ s, water level ratio $L_w/L = 0.75$. (**a**) Results of dynamic analysis varying the geotechnical parameters c and ϕ (cases 1–5). (**b**) Particular of the results of dynamic analysis for three selected accelerograms and different water level ratio $L_w/L \cong 1, 0.75$ (case: c =50 kPa and $\phi = 35°$)

In order to catch more in detail the effect of water level reduction, a particular of the results with reference to three accelerograms only and a given foundation resistance ($c = 50$ kPa and $\phi = 35°$) is depicted in Fig. 14b varying the water level L_w. For each accelerogram two points are reported which refer to $L_w/L \cong 1$ and $L_w/L = 0.75$. Once fixed one accelerogram, as the water level diminishes as β increases. In fact, the numerator of the acceleration ratio, namely the limit acceleration, increases. Consequently, the attended values of the ductility factor are lower, as the water level diminishes. The dependence of the ductility factor versus β seems exponential. The reduction of water level strongly increase seismic safety with respect to sliding, when the water level is reduced with respect to normal flood level ($L_w/L \cong 1$) of 25%, the corresponding ductility factor reduces more than 80%.

5.4 *Influence of Dam Height*

The last parametric analysis investigates variation of dam height L on dam seismic response. By varying L the fundamental period changes (Eq. (11)), despite that, once chosen the deformability characteristics of the foundation rock, water level ratio and wave reflection coefficient, the equivalent damping ratio remains constant. Results for $L = 50, 70, 86.8, 100$ m are reported in Figs. 15a–b, 11a, and 16a respectively.

Given dam height L, an exponential trend is able to fit with sufficient accuracy the relation between acceleration ratio β and mean value of μ. Curve fitting has better accuracy for higher dams and $\beta > 0.5$. To catch more in detail the influence of dam height, in Fig. 16b results of dynamic analysis for a given foundation resistance (c = 50 kPa and ϕ = 35°) are depicted for few accelerograms

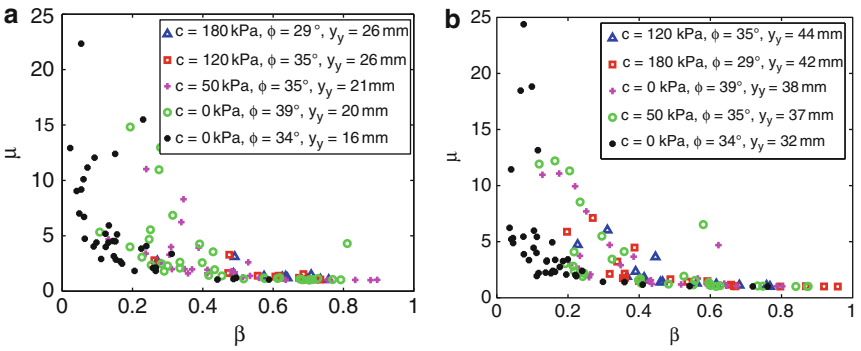


Fig. 15 Results of dynamic analysis varying the geotechnical parameters c and ϕ cases 1–5. (**a**) Dam $L = 50\,\text{m}$, $E_f = 526 \times 10^5\,\text{kN/m}^2$, $\tilde{T} = 0.17\,\text{s}$, $L_w/L \cong 1$. (**b**) Dam $L = 70\,\text{m}$, $E_f = 526 \times 10^5\,\text{kN/m}^2$, $\tilde{T} = 0.24\,\text{s}$, $L_w/L \cong 1$

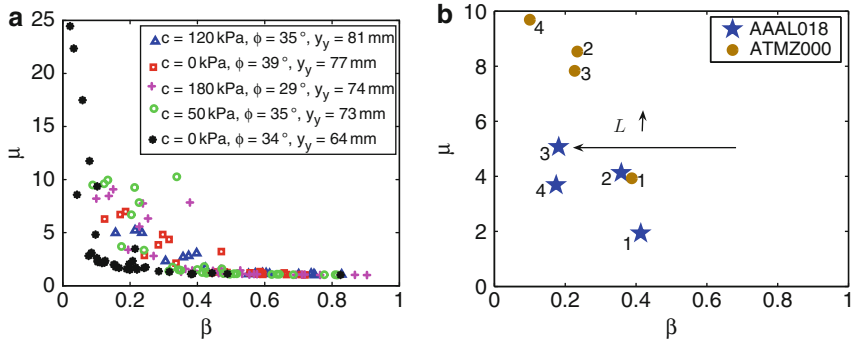


Fig. 16 Results of dynamic analysis varying the geotechnical parameters c and ϕ (cases 1–5). (**a**) Dam $L = 100\,\text{m}$, $E_f = 526 \times 10^5\,\text{kN/m}^2$, $\tilde{T} = 0.35\,\text{s}$, $L_w/L \cong 1$. (**b**) Particular of the results of dynamic analysis for two selected accelerograms and different dam height (1) $L = 50\,\text{m}$, (2) $L = 70\,\text{m}$, (3) $L = 86.8\,\text{m}$, (4) $L = 100\,\text{m}$(for $c = 50\,\text{kPa}$ and $\phi = 35°$)

(AAAL018, ATMZ000) for the four dams. For each input four points indicate seismic response of the four different dams. Generally, by increasing L, β decreases due to decrease of limit acceleration. Instead ductility factor does not always increase when β is decreasing. It grows with spectral acceleration. Since the selected seismic inputs refer to soil type A, generally maximum spectral acceleration is observed for periods around $0.2 \leq \tilde{T} \leq 0.3$. Cases L=50 m with period $\tilde{T} = 0.17\,\text{s}$ and $L = 100\,\text{m}$ with period $\tilde{T} = 0.35\,\text{s}$, correspond to low spectral accelerations for the most part of the selected inputs, as a consequence reached ductility factor is generally lower. Instead, for cases $L = 70$ and 86.8 m ductility factor is greater. It appears that the range $70 < L \leq 90\,\text{m}$ is the most critical for residual displacement expecting particularly high spectral acceleration related to the seismic input. Such considerations appear more clear by looking at Fig. 16b, focusing on one accelerogram, for example AAAL108. The greatest β is observed for $L = 50\,\text{m}$ (point 1),

whereas the lowest for $L = 100\,\text{m}$ (point 4), despite of that, higher μ are observed for $L = 86.8\,\text{m}$ and $L = 70\,\text{m}$ (points 2 and 3 respectively). By changing accelerogram the trend is similar but results appear very different from one accelerogram to one other, because response strongly depends on the shape of the acceleration spectra in relation to dam structural period.

6 Conclusions

In this study the evaluation of residual displacement on concrete gravity dams produced by an earthquake has been carried out. A simplified mechanical model has been utilized for the scope, which takes into account the most relevant aspects influencing response such as dam-water-foundation interaction. A non linear single degree of freedom system with non linearity of the substructure, having fixed a threshold value for the sliding foundation resistance modelled with the Mohr-Coulomb yielding criterion including a frictional and a cohesive component, has been subjected to several natural earthquakes and seismic response is carried out. The effect of the presence of a passive wedge resistance has been included too. A comprehensive and systematic analysis of all the parameters which influence dam response has been carried out. The main results can be summarized in the following. Structural response in terms of base sliding improves as foundation resistance of the flexible rock increases and the number of events for which non linear behavior is observed reduces as the resultant sliding foundation resistance grows. In the examples examined, the attritive component of the sliding force always prevailed on the cohesive part, however both components can vary depending on dam geometry and uplift pressures. The attritive component increases as dam height increases and water level decreases, whereas the cohesive component gains importance as the dam becomes short. Also the effect of the passive wedge resistance plays a positive role on dam response reduction. Concerning foundation deformability, it has been observed that a very low elastic foundation modulus (generally not achievable in real cases) leads to a veri flexible structural system with high damping properties. For this reason, seismic effect is not evident and dam response is mainly limited to the elastic field. Instead, a higher elastic foundation modulus (at limit tending to infinity, which means to disregard dam-foundation interaction), generally leads to an increased structural response. In this sense, the fact of not considering foundation deformability, as it is often done in practice, seems to lead to conservative results in terms of sliding displacement. The effect of varying water level in the reservoir plays an important role both in the static than in the dynamic field. It has been observed that reducing the water level a significant increase of the sliding foundation resistance and a decrease of the equivalent mass is reached, hence, the attended structural response is less serious. As a consequence, also the limit response acceleration increases. It is possible to diminish residual displacement of gravity dams just decreasing the water level in the reservoir, even of a small quantity. Concerning dam height it has been seen that there is a strong dependence of the structural response on the type of seismic input. Dam

fundamental period is directly related to height. Due to the shape of analyzed seismic spectra on soil type A which have their maxima in the range of periods 0.2–0.3 s, the most critical range of height for base sliding is around 70−90 m. Despite of the variable parameter, it seemed that the relation between acceleration ratio β and ductility factor μ is quite regular until β is not too small, say 0.5, and it can be fitted by an exponential trend. Attended μ can be estimated from each parametric analysis when β is in the range $0.5 < \beta < 1$. Up till $\beta \geq 0.5$ the residual displacement request seems compatible with the functionality of the dam since the ductility factor has low values (just more than the unity), instead, as β is lower than 0.5 the non linear behavior becomes evident, the response observed is more disperse varying the foundation rock type and the seismic input, and large ductility factor obtained seems inadmissible with the functionality and safety of the structure. In such cases the proposed simplified procedure based on the equivalent non linear SDOF appears meaningless since inadmissible values for base sliding are obtained, in general more sophisticated analysis using a refined structural model should be used.

References

1. Bazzurro P, Shome N, Cornell CA et al (1998) Earthquakes, records, and nonlinear MDOF responses. Earthquake Spectra 14:469–500
2. Calayir Y, Karaton M (2005) A continuum damage concrete model for earthquake analysis of concrete gravity dam-reservoir systems. Soil Dynam Earthquake Eng 25:857–869
3. Chavez JW, Fenves G (1995) Earthquake response of concrete gravity dams including base sliding. J Struct Eng 121(5):865–875
4. Chopra AK, Zhang L (1991) Earthquake-induced base sliding of concrete gravity dams. J Struct Eng 117(12):3698–3719
5. Danay A, Adeghe LN (1993) Seismic-induced slip of concrete gravity dams. J Struct Eng 119(1):108–129
6. European Strong Motion Database. Available via http://www.isesd.cv.ic.ac.uk/ESD/frameset.htm
7. Fenves G, Chopra AK (1985) Simplified earthquake analysis of concrete gravity dams: separate hydrodynamic and foundation interaction. J Eng Mech 111:715–735
8. Fenves G, Chopra AK (1985) Simplified earthquake analysis of concrete gravity dams: combined hydrodynamic and foundation interaction. J Eng Mech 111:736–756
9. Fenves G, Chopra AK (1987) Simplified earthquake analysis of concrete gravity dams. J Eng Mech 113(8):1688–1708
10. Mao M, Taylor CA (1997) Non linear seismic cracking analysis of medium-height concrete gravity dams. Comput Struct 64:1197–1204
11. Nuti C, Pinto CE (1989) Analisi dell'interazione terreno struttura in condizioni sismiche. In: Mele M (ed) Interazione Terreno Struttura in Prospettiva Sismica, CISM-Collana di Ingegneria Strutturale, 6 (in Italian)
12. Scasserra G, Stewart JP, Kayen RE, Lanzo G (2009) Database for earthquake strong motion studies in Italy. J Earthquake Eng 13(6):852–881
13. Peer Strong Motion Database. Available via http://peer.berkeley.edu/smcat/

Dynamic Interaction of Concrete Dam-Reservoir-Foundation: Analytical and Numerical Solutions

George Papazafeiropoulos, Yiannis Tsompanakis, and Prodromos N. Psarropoulos

Abstract The majority of concrete dams worldwide have behaved relatively well during seismic events. However, there are several cases where global failure or substantial damages have occurred. The need for new dam construction and retrofitting of existing dams necessitates the use of advanced design approaches that can take realistically into account the potential dam-reservoir-foundation interaction. Seismic design of concrete dams is associated with difficulties to estimate the dynamic distress of the dam as well as the response of the dam-reservoir-foundation system and to assess the impact of the various parameters involved. In this chapter, after an extensive literature review on the dynamic interaction of concrete dams with retained water and underlying soil, results from numerical simulations are presented. Initially, analytical closed-form solutions that have been widely used for the calculation of dam distress are outlined. Subsequently, the numerical methods based on the finite element method (FEM) which is unavoidably used for complicated geometries of the reservoir and/or the dam, are reviewed. Emphasis is given on FEM-based procedures and the boundary conditions and interactions involved. Numerical results are presented to illustrate the impact of various key parameters on the distress and response of concrete dams considering dam-foundation interaction phenomena. It is shown that in general the water level and the thickness of the soil layer have a substantial impact on the dynamic characteristics of the dam-reservoir-foundation system in terms of its eigenfrequencies and damping. Moreover, simplified equivalent soil springs are calculated for the assessment of the additional dam dynamic distress due to the presence of the reservoir.

G. Papazafeiropoulos
Department of Applied Mechanics, Technical University of Crete, Greece
e-mail: gpapazafeiropoulos@yahoo.gr

Y. Tsompanakis (✉)
Department of Applied Mechanics, Technical University of Crete, Greece
e-mail: jt@science.tuc.gr

P.N. Psarropoulos
Department of Infrastructure Engineering, Hellenic Air-Force Academy, Greece
e-mail: prod@central.ntua.gr

M. Papadrakakis et al. (eds.), *Computational Methods in Earthquake Engineering*, Computational Methods in Applied Sciences 21, DOI 10.1007/978-94-007-0053-6_20,
© Springer Science+Business Media B.V. 2011

Keywords Concrete dams · Seismic design · Hydrodynamic pressures · Dynamic soil-structure interaction · Analytical solutions · Finite element simulations

1 Introduction

The distress of a concrete dam is affected by several parameters, such as the compressibility of the impounded water, the various dynamic interactions which can be incorporated in the general term "dam-reservoir-foundation interaction", the possible existence of a sedimentary material at the bottom of the reservoir, the effect of surface (sloshing) waves, and the selection of an appropriate upstream boundary condition to represent the infinite extent of the reservoir in the upstream direction. The impact of these factors has been investigated in the past by many researchers analytically, numerically, or even experimentally as it will be briefly discussed in the sequence. The main scope of this chapter is to present the most commonly used analytical and numerical methods for the evaluation of the seismic distress and response of concrete dams and their interaction with the retained water and the foundation soil layer.

The methods used for the analysis of concrete dams under earthquake loading range from the simple pseudo-static method initially proposed by Westergaard [54] to advanced numerical methods that include not only the well-known FEM, BEM and FEM-BEM hybrid numerical approaches, but methods utilizing semi-discrete hyperelements. In between these two extreme categories there exist some other methods, such as the Fenves and Chopra [24] refined pseudo-static method (the so-called "equivalent lateral force method") and the methodology suggested by the EM-1110-2-6053 (2007) US Army Corps of Engineers guidelines [21]. The method proposed by Westergaard assumes that the hydrodynamic effect on a rigid dam is equivalent to the inertial force resulting from a mass distribution added on the dam body. The refined pseudo-static method suggested by Fenves and Chopra takes into account the influence of the dam response on the foundation distress, as the latter is considered flexible. The guidelines of US Army Corps of Engineers recommend that if high tensile stresses develop at the base of the dam then a finite element analysis may have to be conducted to incorporate the variation of the natural period due to cracking at the base. Whenever the aforementioned assumptions are not satisfied, then the engineer has to carry out sophisticated numerical simulations of the whole dam structure and its interaction with the foundation and the retained water.

Concrete dams do not have a considerable structural damping compared to other civil engineering structures. However, there are other sources of damping due to the radiation of waves in the unbounded upstream direction and the absorption of incidental waves at the reservoir bottom, which can lead to substantial decrease in the dynamic response of the dam. Many researchers have studied the impact of each type of interaction on the dynamic distress and response of a concrete dam. Three main approaches have been developed to simulate the resulting fluid-structure interaction: (a) the added mass approach, (b) the Eulerian approach, and (c) the

Lagrangian approach. In several studies, this interaction is taken into account by assuming that the dam behaves in an elasto-plastic way through a FEM-based iterative procedure, as stated by Akköse et al. [2, 3].

Another type of dynamic interaction is the dam-foundation interaction. The foundation on rock, which is usually modeled as being bonded with the dam, has been considered to behave linearly elastically [2, 3, 8], or visco-elastically [5]. Nonlinear base sliding behavior has been examined by Chopra and Zhang [13], where the concept of critical acceleration is used to study the horizontal base displacements of rigid and flexible dams. This type of behavior was also studied by Danay and Adeghe [18], where an empirical formula was developed to estimate the sliding displacement of a concrete gravity dam using statistical methods. In all the aforementioned studies the rocking displacement (rotation) of the dam is considered negligible when it is free to slip horizontally. Nevertheless, the rocking motion can significantly reduce the normal stresses at the base of the dam, which contribute to its sliding resistance. The sliding displacement has proved to decrease in the case of compliant foundation [10]. For this reason, various possibilities of dam-foundation interface de-bonding have been considered [4, 30], whereas energy dispersion in infinite foundation has been studied by Du et al. [20].

As it can be easily observed from the representative literature review, the numerical method most commonly used is the FEM approach, which has been also employed in the present study. The BEM approach has also been widely used in this field, e.g. by Fan and Li [23] and Aznárez et al. [5] to model the far-field reservoir domain and the dam foundation, respectively, whereas in Koh et al. [31] the IBEM (Indirect BEM) was used to simulate the whole reservoir domain. Both the dam foundation and the reservoir were modeled via BEM by Câmara [9]. Two variations of BEM have been efficiently applied, the DRBEM (Dual Reciprocity BEM, by Fahjan et al. [22]) to model the near-field reservoir domain and the SBFEM (Scaled Boundary FEM, by Lin et al. [38]) to represent the whole dam-reservoir-foundation system.

2 Dam–Reservoir Interaction

In order to cope with fluid-structure interaction problems, three approaches have been developed in the past:

(a) The *added mass approach*, initially proposed by Westergaard [54], and later adopted by Ghobarah et al. [27], Tinawi and Guizani [51], Lee and Fenves [36], Du et al. [20], Arabshahi and Lotfi [4]).
(b) The *Eulerian approach*, where the unknown variables are the displacements of the structure and the pressures (or velocity potentials) of the fluid [23, 25, 26, 28, 32, 34, 37, 40, 42, 48, 49, 52, 53].
(c) The *Lagrangian approach*, in which the displacements are the unknown variables for both the fluid and the structure [2, 3, 6–8, 46, 55].

The first of the three aforementioned approaches is implemented through analytical closed-form solutions, while the latter two utilize the finite element method.

2.1 Added Mass Approach

2.1.1 Fundamental Solution

Westergaard [54] calculated the additional hydrodynamic pressures during a seismic event in the case of a rigid dam with a vertical upstream face as follows:

$$p(y) = \frac{8a_0\rho h}{\pi^2} \sum_{n=1,3}^{n} \frac{1}{n^2 c_n} \sin\left(\frac{n\pi y}{2h}\right) \tag{1}$$

in which

$$c_n = \sqrt{1 - \frac{16\rho h^2}{n^2 g K T^2}} \tag{2}$$

where a_0 is the maximum horizontal acceleration of the seismic excitation, ρ is the density of the retained water, h is the depth of the reservoir, g the gravity constant, K is the bulk modulus of water, T is the period of the horizontal acceleration, and y is the distance between the free water surface and the level of the reservoir under consideration (see Fig. 1). Equation 1 has physical meaning as long as c_n is a real number. This is valid if the period of the excitation T is higher that the fundamental eigenperiod of the reservoir layer, T_0, which can be calculated via Eq. 2 by setting $n = 1$ and $c_1 = 0$.

The following formula for the fundamental eigenfrequency is derived:

$$f_0 = \frac{1}{4h}\sqrt{\frac{K}{\rho}} = \frac{V_P}{4h} \tag{3}$$

where V_P is the velocity of sound in the reservoir. Chopra [12] derived an analytical solution of the hydrodynamic pressure on a vertical rigid dam and proved that

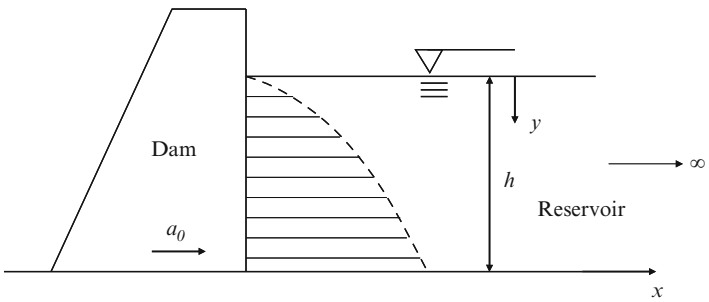


Fig. 1 The dam-reservoir system examined by Westergaard [54]. The dam is rigid with a vertical upstream face

Westergaard's solution is valid only in the cases where the excitation frequency is less than the fundamental frequency f_0 given by Eq. 3.

Whenever the retained water is considered incompressible (i.e., $K \to \infty$), Eq. 2 yields $c_n = 1$. The same result will be obtained if a quasi-static excitation is assumed (i.e., $T \to \infty$). If the excitation is ideally static, the resulting pressures can be considered as inertial forces, since in such case the inertial body forces of the dam and the hydrodynamic thrust are essentially in phase. Therefore, the reservoir pressures are equivalent to an additional height-wise mass distribution added on the dam's body to simulate the hydrodynamic effect. This concept is known as "added mass approach" and is valid when either the retained water is considered as incompressible, or the frequency content of the dynamic loading is relatively low, i.e. the excitation can be considered as quasi-static.

2.1.2 Inclined Upstream Face

Chwang [15] developed an exact solution to calculate the hydrodynamic reservoir pressures which occur behind a dam with inclined upstream face. The fluid in the reservoir is considered as incompressible and inviscid, while the dam is assumed to be rigid. The pressure distribution (vertical to the dam's upstream face) is obtained by the following equation:

$$p(y) = \rho a_0 h \left[\frac{4}{\pi^2} \int_0^{\pi/2} \left(\frac{\frac{y}{h}}{\frac{y}{h} + \tan^2\theta} \right)^{\alpha} \frac{\theta d\theta}{\sin\theta \cos\theta} - \cot\alpha\pi + \frac{\cos\alpha\pi}{h} s(y) \right]$$

$$(0 < y < h) \tag{4}$$

a is equal to θ/π, where θ is the angle between the dam's upstream face and its base, shown in Fig. 2. This should not be confused with variable θ which appears in the

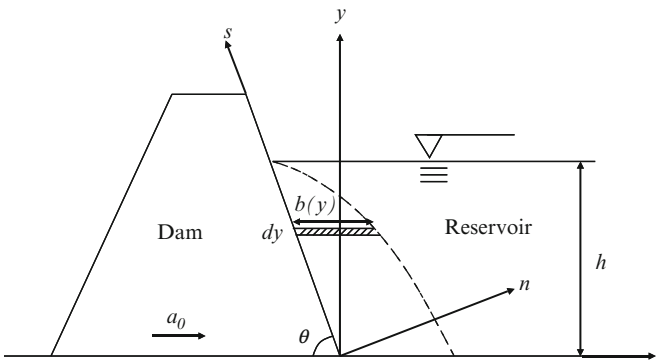


Fig. 2 The dam-reservoir system examined by Chwang [15] and Chwang and Housner [16]. The dam is rigid with inclined upstream face

definite integral of Eq. 4, where it merely serves as an integration variable without any physical meaning. Chwang and Housner [16] investigated the added-mass effect in the case of oblique upstream face of the dam (Fig. 2) using the Von Karman's momentum-balance method. The momentum-balance method is approximate and concludes to the following equation for estimating the hydrodynamic pressures:

$$\ln\left(\frac{A^2-\beta Ay+2y^2}{2h^2}\right) = \begin{cases} \dfrac{2\beta}{(8-\beta^2)^{1/2}}\left[\tan^{-1}\left[\dfrac{\beta}{(8-\beta^2)^{1/2}}\right]-\tan^{-1}\left[\dfrac{2A-\beta y}{y\,(8-\beta^2)^{1/2}}\right]\right] (\beta^2<8) \\ \dfrac{\beta}{(\beta^2-8)^{1/2}}\left[\ln\left[\dfrac{\beta-(\beta^2-8)^{1/2}}{\beta+(\beta^2-8)^{1/2}}\right]-\ln\left[\dfrac{2A-\beta y-(\beta^2-8)^{1/2}\,y}{2A-\beta y+(\beta^2-8)^{1/2}\,y}\right]\right] (\beta^2>8) \end{cases} \tag{5}$$

where

$$\beta = \cot(\theta) \tag{6}$$

θ denotes the angle between the upstream face and the base of the dam. Equation 5 is solved for $A(y)$ and the pressure distribution can be obtained by:

$$p(y) = \frac{A(y)+\beta y}{2} \tag{7}$$

It can be observed that the pressure magnitude increases as the upstream face of the dam gets closer to the vertical of the reservoir surface. In addition, the pressure distribution near the bottom of the reservoir (derived by the theory of Chwang [15]) is smaller than the corresponding distribution which is based on the momentum theory developed by Chwang and Housner [16]. These distributions were verified numerically by Sharan [49], where numerical and analytical results showed a quite satisfactory agreement.

2.1.3 Inclined Upstream Face and Reservoir Bottom

Liu [39] studied the case of the reservoir having the triangular shape shown in Fig. 3, which can be considered as an adequate and accurate simplification of many real dams. The earthquake excitation is assumed to act in an inclined direction, defined by angle of $\gamma\pi$ with respect to the horizontal axis. The imposed acceleration has amplitude equal to a_0 and the inclined bottom of the reservoir is assumed to have slope equal to $\beta\pi$ with respect to the horizontal axis, while $\alpha\pi$ denotes the angle between the upstream face of the dam and its base. Moreover, s represents the distance

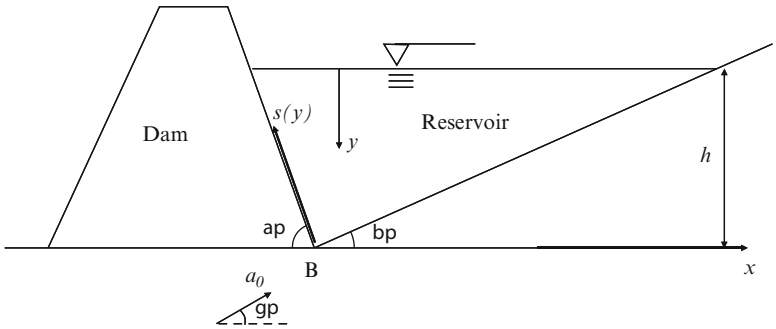


Fig. 3 The dam-reservoir system examined by Liu [39]. The dam is rigid with an inclined upstream face, while the bottom of the reservoir is also inclined

from the origin of axis (point B in Fig. 3) to any point on the upstream dam face. The hydrodynamic pressures are given from the following formula:

$$p(y)=\frac{h\rho a_0}{\sin\alpha\pi\,\sin\beta\pi}\,\frac{1}{\Gamma(\alpha)\Gamma(\beta)\Gamma(1-\alpha-\beta)}$$

$$\times\left\{\frac{4[\sin[(\alpha+\gamma)\pi]\cos\beta\pi+\sin[(\beta-\gamma)\pi]\cos\alpha\pi]}{\sin[(\alpha+\beta)\pi]}\int_0^{\pi/2}\frac{\left(\frac{y}{h}\right)^{\alpha}}{(\tan^2\theta+\frac{y}{h})^{\alpha+\beta}}\,\frac{(\tan\theta)^{2\beta}\theta d\theta}{\sin\theta\cos\theta}\right\}$$

$$-\rho a_0\frac{\sin[(\alpha+\gamma)\pi]\cos[(\alpha+\beta)\pi]+\sin[(\beta-\gamma)\pi]}{\sin[(\alpha+\beta)\pi]}\left[\frac{h}{\sin\alpha\pi}-s(y)\right](0<y<h) \tag{8}$$

in which y is the distance of a point at the upstream face of the dam from the free surface of the reservoir and Γ denotes the Gamma function.

It has to be noticed that all aforementioned solutions ignore the effect of waves on the free surface of the reservoir (sloshing waves). Hence, they are valid for short-duration seismic events. In addition, the solutions of Westergaard [54] and Chwang [15] are special cases of the solution proposed by Liu [39] for $\alpha = 1/2, \beta = \gamma = 0$ and $\beta = \gamma = 0$, respectively.

Results presented by Liu [39] showed that, while the increase of angle $\alpha\pi$ increases the resulting hydrodynamic pressures, conversely, when $\beta\pi$ gets higher values the pressures decrease regardless of the angle $\alpha\pi$. In certain cases, the hydrodynamic pressures may become negative (e.g. for $\alpha\pi = 15°$ and $\beta\pi = 30°$). This is an indication that the total hydrodynamic thrust which results from appropriate integration along the dam's height can receive very small values.

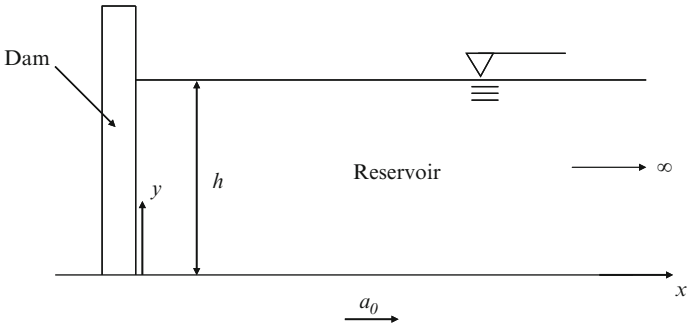


Fig. 4 The dam-reservoir system examined by Lee and Tsai [35]. The dam is flexible with a vertical upstream face

2.1.4 Flexible Cantilever Dam

Lee and Tsai [35] (Fig. 4) investigated the dynamic interaction between the retained water and a flexible dam utilizing modal superposition analysis. They considered the flexible dam as an Euler-Bernoulli beam and calculated the hydrodynamic pressure distributions at the upstream face of the dam by:

$$p(y,t) = \frac{4\rho V_P}{\pi}\sum_{k=1}^{\infty}\frac{(-1)^{(k+1)}}{2k-1}\cos\lambda_k y\int_0^t \ddot{u}_g(\tau)J_0[\lambda_k C(t-\tau)]d\tau + \frac{2\rho V_P}{h}\sum_{k=1}^{\infty}\sum_{n=1}^{\infty}\cos\lambda_k y\int_0^h \phi_n(y)\cos\lambda_k y dy \times\int_0^t \ddot{Y}_n(\tau)J_0[\lambda_k C(t-\tau)]d\tau \quad (9)$$

where V_P is the velocity of sound in the reservoir, $\ddot{u}_g$ is the ground acceleration in the upstream–downstream direction, $\varphi_n(y)$ is the n-th mode shape of the cantilever, J_0 is the Bessel function of the first kind and zero order, $\ddot{Y}_n$ are the generalized time-dependent coordinates and the parameters λ_k are given by:

$$\lambda_k = \frac{(2k-1)\pi}{2h} \quad (10)$$

The added mass W_{ij}, which vibrates together with the structure during the imposed excitation, results from the hydrodynamic effect due to the current deflection of the structure and the current response of the entire system. It is a function of the mode shapes of both the structure and the reservoir, and it is derived by the equation:

$$W_{n,m} = \frac{2\rho V_P}{h}\sum_{k=1}^{\infty} Q_{nk}Q_{mk}E_k \quad (11)$$

where

$$E_k = \frac{1}{2\lambda_k} \int_0^{\lambda_k V_P \Delta t} J_0(\tau) d\tau = \frac{1}{2\lambda_k} \left\{ \frac{\pi\tau}{2} [J_0(\tau) H_{-1}(\tau) + H_0(\tau) J_1(\tau)] \right\} \Big|_{\tau=0}^{\tau=\lambda_k V_P \Delta\tau} \tag{12}$$

$$Q_{nk} = \int_0^h \phi_n(y) \cos \lambda_k y dy \tag{13}$$

and Δt is the time step. The generalized load induced from the hydrodynamic pressure is denoted by $P_n(t)$, that is:

$$P_n(t) = \int_0^h \phi_n(y) P(y,t) dy \tag{14}$$

Equation 14 can be simplified as follows: the hydrodynamic pressure generalized load of (14) is separated into two parts, one which is induced from the hydrodynamic pressure, while the dam structure is rigid, which is given by:

$$P_n^r(t) = \frac{4\rho V_P}{\pi} \sum_{k=1}^{\infty} \frac{(-1)^{k+1}}{2k-1} Q_{nk} \int_0^t \ddot{u}_g(\tau) J_0[\lambda_k V_P (t-\tau)] d\tau \tag{15}$$

and another one which is induced from the hydrodynamic pressure due to the deformation of the structure which is equal to:

$$P_n^f(t) = \frac{2\rho V_P}{h} \sum_{k=1}^{\infty} \sum_{m=1}^{\infty} Q_{nk} Q_{mk} \int_0^t \ddot{Y}_m(\tau) J_0[\lambda_k V_P (t-\tau)] d\tau \tag{16}$$

Equation 16 can be written as:

$$P_n^f(t) = F_n(t) + \sum_{m=1}^{\infty} W_{nm} \ddot{Y}_m(t) \tag{17}$$

in which

$$F_n = \frac{2\rho V_P}{h} \sum_{k=1}^{\infty} Q_{nk} Q_{mk} G_{mk} \tag{18}$$

$$G_{mk} = \frac{1}{2\lambda_k} \sum_{l=1}^{L-1} \ddot{Y}_m(l\Delta t) \int_{\lambda_k V_P \Delta t(L-l-1)}^{\lambda_k V_P \Delta t(L-l+1)} J_0(\tau) d\tau \tag{19}$$

The generalized mass M_n associated with the n-th mode shape $\varphi_n(y)$ is defined as:

$$M_n = \int_0^h \phi_n^2(y) m(y) dy \tag{20}$$

while the generalized force at the dam body resulting from the earthquake excitation is:

$$V_n(t) = \ddot{u}_g(t) \int_0^h m(y) \phi_n(y) dy \tag{21}$$

The modal equation which describes the vibration of the dam in the time domain is the following:

$$M_n \ddot{Y}_n(t) + \sum_{m=1}^{\infty} W_{nm} \ddot{Y}_m(t) + \omega_n^2 M_n Y_n(t) + V_n(t) + P_n^r(t) + F_n(t) = 0 \tag{22}$$

which is used to calculate the generalized coordinates $Y_n(t)$ and the dynamic response of the dam is obtained as:

$$u(y,t) = \sum_{n=1}^{\infty} \phi_n(y) Y_n(t) \tag{23}$$

In certain cases the consideration of flexible dam structures permits the assumption of incompressible retained water. Based on an analysis including the response of a dam at its first mode of vibration, Chopra [14] concluded that if the fundamental frequency of the dam (in the absence of water) is less than half of the fundamental frequency of the reservoir, then the water may be treated as incompressible. This result needs further investigation as it was extracted based on the assumption that surface wave effects are negligible. In any case, the validity of the incompressibility assumption is governed by the relative flexibility of the dam with respect to the reservoir. Certainly, as the dam becomes more flexible, the error associated with the above assumption diminishes.

Küçükarslan et al. [34] conducted finite element transient analyses considering dam–reservoir interaction. The dam was considered flexible, having vertical upstream face. The simulation was performed with linear four-noded rectangular elements. Sommerfeld's boundary condition was implemented for the radiating waves. Numerical results were successfully compared with those of the exact solution of Lee and Tsai [35].

2.1.5 Effect of Reservoir Sediments

Cheng [11] examined the effect of the existence of sediments at the bottom of the reservoir, where the sediment was modelled as a poroelastic material. It was

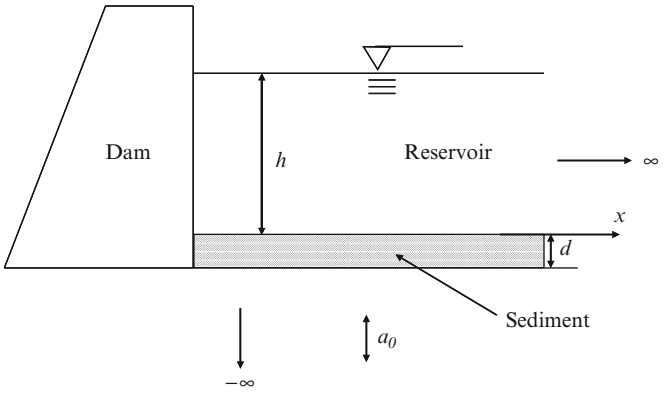


Fig. 5 The dam-reservoir system examined by Cheng [11]. The dam is rigid with a vertical upstream face, while at the bottom of the reservoir there exists a sediment layer

found that for a modest amount of sediment and slight desaturation of pore water, significant changes in the hydrodynamic response curves can be observed. The model examined is shown in Fig. 5.

A vertical harmonic excitation was considered in that study. The pressure distribution along the dam height can be obtained by solving the differential equation of the hydrodynamic pressures in the frequency domain. The hydrodynamic force on the dam is taken when the pressures are integrated appropriately height-wise and is estimated as:

$$F = \rho a_0 h^2 \frac{\sqrt{a_r^2 + a_i^2}(1 - \cos\lambda_r^*)}{\lambda_r^{*2}\sqrt{b_r^2 \sin^2\lambda_r^* + (b_i \sin\lambda_r^* - \cos\lambda_r^*)^2}} \tag{24}$$

where

$$a_r \approx \frac{\rho_{fd} E_{fd} \cos\theta}{\rho_w E_{s1} \sin^2\theta + \rho_{fd} E_{fd} \cos^2\theta} \tag{25}$$

$$a_i \approx -\frac{\sqrt{\rho_w E_{s1}}\sqrt{\rho_{fd} E_{fd}} \sin\theta}{\rho_w E_{s1} \sin^2\theta + \rho_{fd} E_{fd} \cos^2\theta} \tag{26}$$

$$b_r \approx \frac{\sqrt{\rho K}\sqrt{\rho_{fd} E_{fd}}}{\rho_w E_{s1} \sin^2\theta + \rho_{fd} E_{fd} \cos^2\theta} + \sqrt{\frac{n E_s^3 K}{2 E_{s1}^3 E_{aw} g}\omega k} \tag{27}$$

$$b_i \approx \frac{\sqrt{\rho K}(\rho_{fd} E_{fd} - \rho_w E_{s1}) \sin\theta \cos\theta}{\sqrt{\rho_w E_{s1}}(\rho_w E_{s1} \sin^2\theta + \rho_{fd} E_{fd} \cos^2\theta)} + \sqrt{\frac{n E_s^3 K}{2 E_{s1}^3 E_{aw} g}\omega k} \tag{28}$$

$$\lambda_r^* = \frac{\omega h}{V_P} \tag{29}$$

ρ_{fd} is the density of the foundation material, E_{fd} is the elastic modulus of the foundation, E_s is the elastic modulus of the drained sediment, n the effective porosity, k the hydraulic conductivity, E_{aw} the apparent bulk modulus of pore water, ρ_w the mass density of the saturated sediment. In the following three equations S_r is the degree of saturation, P_a the average absolute pore water pressure in the pores, E_{s1} the apparent elasticity modulus for dilatational waves propagating into the sediment, d the sediment thickness, and ω the cyclic harmonic excitation frequency:

$$\frac{1}{E_{aw}} = \frac{1}{K} + \frac{1 - S_r}{P_a} \tag{30}$$

$$E_{s1} = E_s + \frac{E_{aw}}{n} \tag{31}$$

$$\theta = \sqrt{\frac{\rho_w}{E_{s1}}}\omega d \tag{32}$$

2.1.6 Comments on the Added Mass Concept

The *added mass concept* is fundamental in seismic concrete dam design. Although it seems a rather simplified procedure, it is often utilized in cases where the computational cost of simulating the whole dam-reservoir model is unaffordable. Nevertheless, such cases are very common in engineering practice, since dam–foundation interface non-linearities are usually present and need to be included in the analysis [4, 20]. The most characteristic cases are base sliding and uplifting, in which dam-foundation interface elements increase the computational cost. In these studies the hydrodynamic effects of the reservoir were simulated as added masses on the dam. A plastic-damage model for earthquake analysis of concrete dams was developed by Lee and Fenves [36], in which emphasis was given on advanced constitutive models. Moreover, the inclusion of the reservoir domain requires a huge computational effort, thus, the added mass approach was implemented. The effect of monolith interaction on the overall dynamic response of concrete gravity dams was investigated by Ghobarah et al. [27]. In that study the monoliths were represented by beam elements connected by shear links. The effect of hydrodynamic interaction was considered as added mass to the dam structure. Therefore, it is evident that the added-mass approach is vital for the evaluation of complicated dam geometries, for dams comprised by individual monoliths, or in cases in which the dam-foundation interaction is associated with substantial non-linearities, as the computational cost of the solution is greatly reduced.

2.2 Eulerian Finite Element Procedures

2.2.1 Dam-Reservoir Interaction

In the Eulerian-based FEM approaches the variables describing the response of the fluid are the pressures, the velocities, or the velocity potentials. The hydrodynamic pressure distribution in the reservoir is governed by the pressure wave equation. Assuming that water is linearly compressible and neglecting its viscosity, the small-amplitude irrotational motion of water is governed by the two-dimensional wave equation:

$$\nabla^2\phi(x,y,t) = \frac{1}{V_P^2}\ddot{\phi}(x,y,t) \tag{33}$$

the relations between pressure p, the velocity vector $\{v\}$ and the velocity potential φ are as follows:

$$\{v\} = \nabla\phi \tag{34}$$

$$p = -\rho\dot{\phi} \tag{35}$$

The velocity potential distribution within each finite element is represented in terms of nodal parameters $\bar{\phi}$ by:

$$\phi = [N]\{\bar{\phi}\} \tag{36}$$

For the case of an earthquake excitation at the dam-reservoir boundary the boundary condition usually imposed is:

$$\frac{\partial p(x,y,t)}{\partial n} = -\rho a_n(x,y,t) \tag{37}$$

where ρ is the density of water, p is the pressure given by (35) and $a_n(x,y,t)$ is the component of acceleration on the boundary along the direction of the inward normal n. According to finite element method formulation, Eq. 33 results in the following matrix form:

$$[G]\{\ddot{P}\} + [H]\{P\} = \{F\} \tag{38}$$

where the terms of the matrices are given by the following relations:

$$G_{ij} = \sum G_{ij}^e, \quad H_{ij} = \sum H_{ij}^e, \quad F_i = \sum F_i^e \tag{39}$$

$$G_{ij}^e = \frac{1}{V_P^2}\int_{A_e} N_i N_j \, dA \tag{40}$$

$$H_{ij}^{e} = \int_{A_e} \left(\frac{\partial N_i}{\partial x} \frac{\partial N_j}{\partial x} + \frac{\partial N_i}{\partial y} \frac{\partial N_j}{\partial y} \right) dA \tag{41}$$

$$F_{i}^{e} = \int_{s_e} N_i \frac{\partial p}{\partial n} ds \tag{42}$$

in which A_e denotes the element's area and s_e is the prescribed length along the boundary of each finite element.

2.2.2 Impact of Compliant Reservoir Bottom

Usually, an absorbing boundary condition is imposed at the reservoir-bottom interface. It has been observed that the existence of compliant soil (or sediments) on the bottom of the reservoir has significant effect on the seismic distress and response of a concrete gravity dam. The soft soil layers do not behave as totally reflective boundaries like rigid rock, and there exists dynamic interaction between the reservoir and the underlying soil.

As far as the reservoir bottom is concerned, the following boundary condition [34, 37] is considered appropriate:

$$\frac{\partial p}{\partial n} = -\rho a_n - \bar{q} \frac{\partial p}{\partial t} \tag{43}$$

where $\bar{q}$ is a damping coefficient which characterizes the effects of the reservoir bottom materials given by:

$$\bar{q} = \frac{1 - a_b}{c(1 + a_b)} \tag{44}$$

and

$$a_b = \frac{1 - \dfrac{\rho V_P}{\rho^r V^r}}{1 + \dfrac{\rho V_P}{\rho^r V^r}} \tag{45}$$

where c is the velocity of the sound in water, ρ^r and V^r denote the density and primary wave velocity of the material comprising the reservoir bottom, respectively. To incorporate the reservoir bottom effect into the finite element solution, Eq. 38 is rewritten as follows:

$$[G]\{\ddot{P}\} + [C]\{\dot{P}\} + [H]\{P\} = \{F\} \tag{46}$$

in which [C] is the diagonal damping matrix, and its terms contain the damping coefficient $\bar{q}$.

2.2.3 Truncation Boundary Conditions

To simulate infinite upstream direction, the reservoir is usually separated into a small region adjacent to the dam, called *near-field reservoir* and the *far-field reservoir* which extends from the upstream boundary of the near-field reservoir to infinity, or any other physical boundary existent in real conditions. Whenever the far-field reservoir is neglected for computational reasons, the boundary imposed at the upstream direction of the near-field reservoir is called *truncation boundary*. The boundary condition imposed at the truncation boundary while calculating the near-field reservoir is of critical importance, as the computational domain is significantly reduced compared to the initial reservoir configuration.

Various approaches of describing the boundary conditions if the far-field is truncated are available in the literature:

- The Sommerfeld radiation condition for the truncated surface is given by [34]:

$$\frac{\partial p}{\partial n} = -\frac{\dot{p}}{V_P} \tag{47}$$

- The Sharan's boundary condition [49]:

$$\frac{\partial p}{\partial n} = -\frac{\pi}{2h} p - \frac{1}{V_P} \dot{p} \tag{48}$$

- The far-boundary condition [41]:

$$\frac{\partial p}{\partial n} = -\frac{p}{h} \mathrm{Z} \tag{49}$$

  where

$$\mathrm{Z} = -\frac{\sum_{k=1}^{\infty} \frac{(-1)^{k+1}}{2k-1} e^{-f_k x} \cos(\lambda_k y)}{\sum_{k=1}^{\infty} \frac{(-1)^{k+1}}{(2k-1) f_k} e^{-f_k x} \cos(\lambda_k y)} \tag{50}$$

  in which

$$f_k = \sqrt{\lambda_k^2 - \left(\frac{\omega}{V_P}\right)^2} \tag{51}$$

  and λ_k is given by Eq. 10
- The far-boundary condition developed by Higdon [29] which will be presented in a following section that describes the Lagrangian finite element approach

Notice that the above boundary conditions can be imposed for compressible fluids. If the reservoir is assumed incompressible, V_P becomes infinite and the various boundary conditions degenerate into their incompressible counterparts [23, 32].

2.2.4 Free Surface (Sloshing) Waves

The sloshing oscillations are characterised by the presence of gravity surface waves, which behave in a different manner than the acoustic waves. Gravity waves are non-conservative and their velocity depends on their wavelength. It has been shown [50] that for most concrete gravity dams free-surface waves are negligible. However, in cases where the duration of the excitation is long, the surface wave effect has to be taken into account by imposing an appropriate boundary condition at the free surface of the reservoir. The effects of surface waves (or sloshing waves) of the retained water have been neglected repeatedly in the past ([25,26,33,40,48,49,52], etc.). In such cases the pressure along the free surface is assumed to be equal to zero:

$$p = 0 \tag{52}$$

Nevertheless, in some more recent studies sloshing effects are considered by imposing the following boundary condition [28,42] at the free surface:

$$\ddot{p} + g\frac{\partial p}{\partial y} = 0 \tag{53}$$

Moreover, sloshing waves have been studied rigorously for the design of liquid storage tanks and tuned liquid dampers against dynamic loading. In these cases, advanced boundary conditions have been developed to take realistically into account sloshing phenomena.

2.3 Lagrangian Finite Element Procedures

2.3.1 Dam-Reservoir Interaction

In the Lagrangian finite element procedures the equations of motion of the fluid are obtained using energy principles, contrary to the Eulerian approach, where the governing equations are solved in the discretized domain. In the former approach fluid is assumed to be linearly elastic, inviscid and irrotational. For a general three-dimensional fluid, stress–strain relationships can be written in matrix form as follows:

$$\begin{Bmatrix} p \\ p_x \\ p_y \\ p_z \end{Bmatrix} = \begin{bmatrix} C_{11} & 0 & 0 & 0 \\ 0 & C_{22} & 0 & 0 \\ 0 & 0 & C_{33} & 0 \\ 0 & 0 & 0 & C_{44} \end{bmatrix} \begin{Bmatrix} \varepsilon_v \\ w_x \\ w_y \\ w_z \end{Bmatrix} \tag{54}$$

or

$$\{p\} = [C_f]\{\varepsilon\}$$

p is the mean pressure, C_{11} is the bulk modulus of water ($C_{11} = K$), ε_v is the volumetric strain, p_x, p_y, p_z are the rotational pressures C_{22}, C_{33}, C_{44} are constraint parameters and w_x, w_y, w_z are rotations about the x, y, z axes, respectively. As the irrotational condition is generally not verified a priori, it must be imposed. Otherwise the solution may be corrupted by spurious modes and the frequency analysis may result to a number of zero-frequency modes. To impose this condition, the constraint parameters C_{22}, C_{33}, C_{44} are taken approximately ten to 1,000 times greater than C_{11} [46]. Using the finite element approximation the total strain energy of the fluid system may be written as:

$$\Pi_e = \frac{1}{2}\{U_f\}^T[K_f]\{U_f\} \tag{55}$$

where $\{U_f\}$ and $[K_f]$ are the nodal displacement vector and stiffness matrix of the fluid system, respectively. Moreover $[K_f]$ is calculated by summation of the stiffness matrices of the fluid elements:

$$[K_f] = \sum K_f^e \tag{56}$$

in which the stiffness matrix of each element is obtained as:

$$K_f^e = \int_{V_e} [B_f^e]^T [C_f][B_f^e] dV_e \tag{57}$$

where $[B_f^e]$ is the strain-displacement matrix of the element. An important characteristic of fluid systems is the ability to displace without volume changes. This movement is known as sloshing waves in which the displacement is in vertical direction. The increase in potential energy of the system due to the free surface motion can be written as:

$$\Pi_s = \frac{1}{2}\{U_{sf}\}^T[S_f]\{U_{sf}\} \tag{58}$$

where

$$[S_f] = \sum S_f^e$$
$$S_f^e = \rho g \int_{A_e} \{\bar{h}_s\}^T \{\bar{h}_s\} dA_e \tag{59}$$

$\{\bar{h}_s\}$ is a vector consisting of interpolation functions of the free surface fluid element and $\{U_{sf}\}$ is the vertical nodal displacement vector.

Finally, the kinetic energy of the fluid system can be written as:

$$T = \frac{1}{2}\{\dot{U}_f\}^T[M_f]\{\dot{U}_f\} \tag{60}$$

where

$$[M_f] = \sum M_f^e$$
$$M_f^e = \rho \int_{V_e} [\bar{H}]^T [\bar{H}] dV_e \tag{61}$$

$[\bar{H}]$ is a matrix consisting of interpolation functions of the fluid element and $\{\dot{U}_f\}$ is the nodal velocity vector of the fluid. Equations 55, 58 and 60 are combined and using the Lagrange's equation [17]:

$$\frac{\partial}{\partial t}\left(\frac{\partial T}{\partial q_i}\right) - \frac{\partial T}{\partial q_i} + \frac{\partial \Pi_t}{\partial q_i} = Q_i \tag{62}$$

the following set of equations is obtained:

$$[M_f]\{\ddot{U}_f\} + [K_f^*]\{U_f\} = \{R_f\} \tag{63}$$

where $[K_f^*]$, $\{\ddot{U}_f\}$ and $\{R_f\}$ are system stiffness matrix that includes the free surface stiffness, nodal acceleration vector and time-varying nodal force vector for the fluid system, respectively. In addition, q_i and Q_i represent the generalized coordinate and force, respectively.

The total potential energy results from addition of strain energy and the potential energy due to surface waves: $\Pi_t = \Pi_e + \Pi_s$. Along the dam-reservoir boundary continuity of displacements is imposed, i.e. the nodal displacement of the reservoir is equal to the nodal displacement of the dam:

$$\{U_n^-\} = \{U_n^+\} \tag{64}$$

where U_n is the normal component of the interface displacement. Eventually, the coupled matrix differential equations are extracted, which describe the motions of the dam and the retained water.

2.3.2 Truncation Boundary Condition

In the case of a displacement–based formulation, the boundary conditions described for the Eulerian case cannot be utilized to represent infinite reservoir domain in the upstream direction. When the waves present are merely acoustic, the Sommerfeld condition reproduces efficiently the outgoing-waves problem. However, a fluid dynamic problem involving free surface is characterized by the contemporaneous presence of acoustic and gravity (sloshing) waves. The acoustic waves are characterized by propagation velocity independent of the exciting frequency, whereas the sloshing waves are dispersive and their velocity depends on frequency and water

depth. While the acoustic wave velocity is given by Eq. 3, the gravity wave velocity is given by:

$$V_S = \lambda_S f \tag{65}$$

where

$$f = \sqrt{\frac{g}{2\pi\lambda_S}\tanh\left(\frac{2\pi h}{\lambda_S}\right)} \tag{66}$$

in which λ_S is the sloshing wavelength and h the depth of the reservoir. It is evident that the sloshing wave velocity depends on the wavelength, and consequently on the frequency. Therefore, the Sommerfeld boundary condition is inadequate to handle problems which involve acoustic and sloshing wave propagation.

An accurate non-reflecting boundary condition was initially proposed by Higdon [29]. This boundary condition can be used to solve both pressure- and displacement-formulated problems. The Sommerfeld condition can be considered as the first approximation of this more general non-reflecting boundary condition. Assuming that the x-axis is normal to the truncation boundary which is located at $x = A$ and that the interior of the reservoir corresponds to $x > A$, for a generic variable field $\varphi(x, y)$ (displacement, pressure, etc.) Higdon's absorbing boundary of order J is defined as

$$\left[\prod_{j=1}^{J}\left(\frac{\partial}{\partial t} - c_j\frac{\partial}{\partial x}\right)\right]\phi(x, y) = 0 \tag{67}$$

For the imposition of the Higdon boundary condition Eq. 67 is applied to both displacement components u_x and u_y. An exact response is obtained if the set J of parameters c_j contains all possible wave speeds for the examined problem [46].

3 Dam-Foundation Interaction

3.1 Sliding Response

3.1.1 Analytical Solutions

Chopra and Zhang [13] developed an analytical procedure considering hydrodynamic effects to determine the response history of earthquake-induced sliding of a rigid or flexible dam monolith supported without bonding on a horizontal rock surface. Their results indicated that this approximate procedure, which has been widely used in estimating the deformations of embankment dams, cannot provide accurate estimates of the concrete dam sliding displacement, as its precision can only be used to approximate the order of magnitude. In addition, base sliding was shown to be more important than rocking of the dam for the cases

considered. The reasons for this deficiency will be further explained in the sequence. Furthermore, Danay and Adeghe [18] obtained an empirical formula which can give approximate results as far as the sliding displacement is concerned.

3.1.2 Experimental Results

A shaking table study of concrete dam monoliths was performed by Donlon and Hall [19]. The three small-scale concrete gravity dam models examined showed good performance, which is attributed to the favourable crack orientations that can be attributed to sliding failure resistance in each case. Plizzari et al. [47] presented results of centrifuge modeling of concrete gravity dams. Among the types of dam models tested in the centrifuge there was a concrete dam which was cast on a rock foundation, so that failure was expected to occur along the dam-foundation interface. Using water for upstream loading ensured that uplift pressure inside the crack was maintained. Comparison of the experimental data with numerical fracture mechanics-based finite-element solutions showed an excellent consistency of the results.

Mir and Taylor [43] performed a series of shaking table tests to assess the possible failure mechanisms of medium to low height dams which were subjected to simple motions and artificial earthquake excitations. The hydrodynamic pressure was simulated using Westergaard's added mass approach. Although the main failure mechanism was observed to be base cracking, after the full crack development at the interface, a tendency of the models to slide and rock was observed in some cases. The dynamically induced sliding characteristics of a typical low height gravity dam monolith cracked at its base were examined in a series of dynamic slip tests on a concrete gravity dam model, conducted on a shaking table by Mir and Taylor [44]. A comparison of the observed displacements with those calculated via the popular Newmark's sliding block method indicated that the latter gives conservative estimates of seismic induced sliding of gravity dams.

3.1.3 Finite Element Approaches

In any case, to obtain realistic estimates of the base sliding displacement for a dam, it is necessary to include the effects of dam-foundation interaction. Dam-foundation interaction generally reduces the amount of base sliding and the earthquake response of a gravity dam, primarily due to increased energy dissipation. The assumption of rigid foundation can overestimate the base sliding displacement significantly compared to more realistic estimates obtained from including dam-foundation interaction, particularly for tall dams. Chavez and Fenves [10] conducted finite element analyses for a dam monolith. The monolith was modelled using plane stress finite elements with linear elastic material properties, while the base of the dam was assumed rigid. The foundation layer was idealized as a homogeneous, isotropic and viscoelastic half-plane. The main finding of this study was that

the accumulated sliding displacement is influenced by the duration, the amplitude and the characteristics of the free-field ground motion. Sliding is more pronounced when the duration and the amplitude get higher. Moreover, sliding increases when the ground motion has several significant cycles. In addition, sliding displacements are strongly dependent on the value of the coefficient of friction. This dependency decreases for shorter dams and for dams founded on a flexible foundation layer. Finally, water compressibility is also an important factor which has to be considered when determining the base sliding of dams, particularly when a stiff foundation layer is present [10].

3.2 Rocking Response

An important result of Chopra and Zhang [13] was that, even if the ground motion contains spikes of downstream acceleration large enough to initiate tipping, the influence of the resulting rocking of the dam on its sliding motion is negligible. Thus, the rocking motion may be ignored when evaluating the sliding response. This observation is valid, provided that the dam is directly founded on rock. Conversely, it can be unrealistic when the dam is founded on a compliant soil layer. Usually when soft soils are encountered, embankment dams are more preferable than concrete dams. However, in certain situations, the local site conditions may not permit the construction of embankment dams, and the construction of a concrete dam is unavoidable. If a concrete dam is constructed on a soft soil layer, sliding effects are trivial and the rocking response is progressively increased. Inadequate results are available for this issue, thus, further research is needed to cope with the aforementioned cases.

4 Numerical Results

4.1 Examined Model

A series of two-dimensional (plane-strain) dynamic finite element analyses of a typical concrete dam founded on soft soil shown in Fig. 6 have been conducted [45]. Along the soil-rock interface horizontal and vertical fixity conditions are assumed. The height of the dam is equal to H, while the thickness of the soft soil is equal to Y. The width of its base is set equal to $13H/20$ and the width of its crest is equal to $H/5$. The dimensions of the examined model were suitably chosen to simulate approximately a real dam structure, while its numerical simulation does not require excessive computational effort. The dam retains a water reservoir, the depth of which is equal to d.

A sinusoidal steady-state harmonic excitation is imposed along the soft soil-rigid rock interface. The main parameters of the above model examined in this study

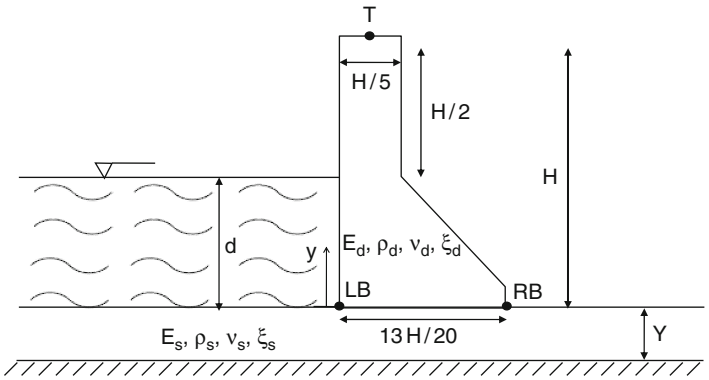


Fig. 6 The examined system: A typical concrete dam founded on a soft soil layer

are: (a) the dimensionless depth of the reservoir, which is equal to the ratio of the reservoir depth d to the dam height H, (b) the dimensionless soil thickness ratio, namely, the ratio of the soil thickness Y to the dam height H, (c) the ratio of the modulus of elasticity of the dam E_d to the modulus of elasticity of the soil E_s, expressed as E_d/E_s, (d) the ratio of the mass density of the dam ρ_d to the mass density of the soil ρ_s, expressed as ρ_d/ρ_s, and (e) the frequency of the imposed harmonic steady-state excitation f. Steady-state analyses with harmonic excitations were performed that covered uniformly a frequency range between 0 and 5 Hz.

The 2-D numerical simulations of the model depicted in Fig. 1 were performed utilizing the finite element software ABAQUS [1], which can perform linear dynamic analyses using standard Rayleigh material damping (which takes into account a mass-proportional component and a stiffness-proportional component). The Rayleigh damping constants were adjusted so that the overall model had critical hysteretic damping ratio equal to $\xi = 5\%$ for the whole frequency range considered. Regarding discretization of the system, the underlying soil layer and the dam were discretized with four-noded bilinear plane strain quadrilateral finite elements having dimensions 0.5×0.5 m. Three-noded triangular elements were used on the downstream oblique face of the dam, while the retained water was modelled using linear acoustic quadrilateral elements of the same dimensions as the soil quadrilaterals.

4.2 Hydrodynamic Pressure Distributions

The dynamic dimensionless water pressure distributions which develop for various values of the ratios Y/H, E_d/E_s and ρ_d/ρ_s, in the case of near-resonance and $d/H = 0.5$ are plotted in Fig. 7. The vertical axes of the graphs in Figs. 7–10 depict the distance from the reservoir bottom y normalized to the depth of the water d, while the horizontal axes represent the dimensionless values of the hydrodynamic pressure p. The pressures are normalized with respect to the acceleration imposed at the

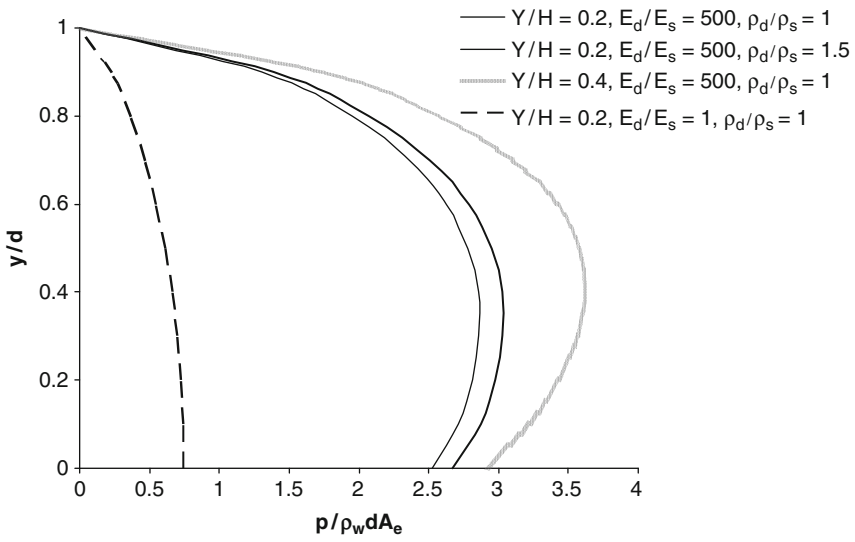


Fig. 7 Normalized dynamic pressure distributions in the case of near-resonance for d/H = 0.5 and for various values of Y/H, E_d/E_s and ρ_d/ρ_s ratios

base of the model (A_e), and not the altered (mainly amplified) acceleration at the soil surface (A_f) which will be used in the sequence. The solid curves refer to the case in which the foundation of the dam is relatively soft ($E_d/E_s = 500$), while the dashed curve corresponds to rigid rock foundation with modulus of elasticity equal to that of concrete ($E_d/E_s = 1$).

By observing Fig. 7 it can be noticed that the normalized pressure distributions in the case of soft soil foundation are substantially higher than those observed for rigid rock, which are almost identical to the values proposed by Westergaard for the distress of rigid dams with fixed base. Thus, it is verified that the results of Westergaard's approach are quite accurate as long as the foundation of the dam is rigid. Another trend observed is that increased pressures develop as the thickness of the soft soil layer increases. Therefore, the presence of rigid rock near the base of the dam seems to be beneficial for its distress. Finally, it is apparent that in the case of $Y/H = 0.2$ and $E_d/E_s = 500$ the curves for the two density ratios ρ_d/ρ_s (1 and 1.5) are almost identical. This reveals that the relative density of the dam and its foundation does not practically affect the distress of the structure. The hydrodynamic distress of the dam is primarily determined by E_d/E_s ratio.

The corresponding diagram for full reservoir ($d/H = 1$) is shown in Fig. 8. It can be noticed that, whereas in the case of $d/H = 0.5$ the dimensionless pressure distributions for $Y/H = 0.4$ are higher than those for $Y/H = 0.2$, the opposite happens when $d/H = 1$. However, the pressure distributions which correspond to rigid rock are always lower than those of the more flexible foundation. While in the two previous dynamic pressure diagrams the normalization was performed with respect to the maximum imposed acceleration at the bedrock (A_e), in the corresponding dynamic pressure diagrams shown in Figs. 9 and 10 the normalization is carried out with

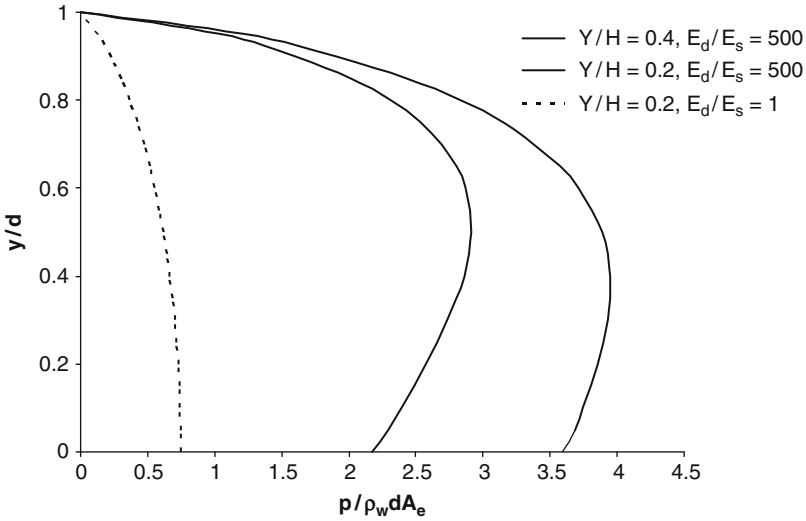


Fig. 8 Normalized dynamic pressure distributions in the case of resonance for $d/H = 1$ and $\rho_d/\rho_s = 1.5$ and for various values of Y/H and E_d/E_s ratios

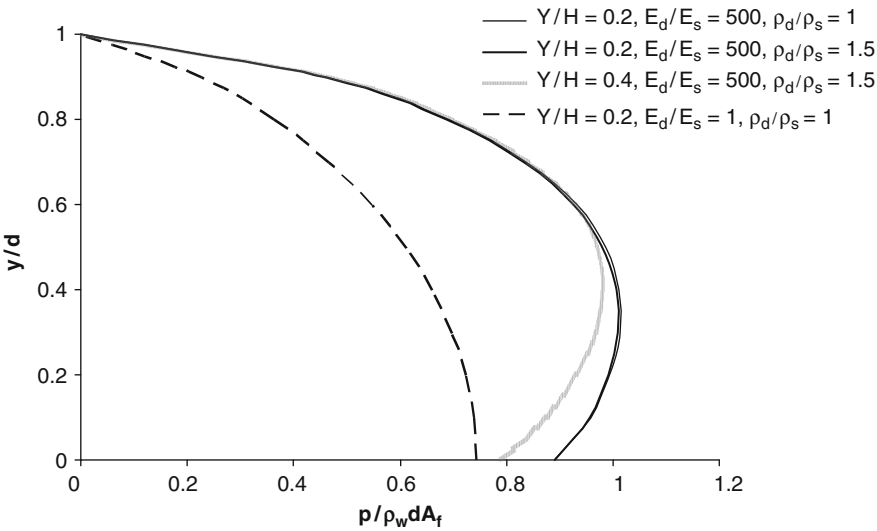


Fig. 9 Normalized dynamic pressure distributions in the case of near-resonance for $d/H = 0.5$ and for various values of Y/H, E_d/E_s and ρ_d/ρ_s ratios

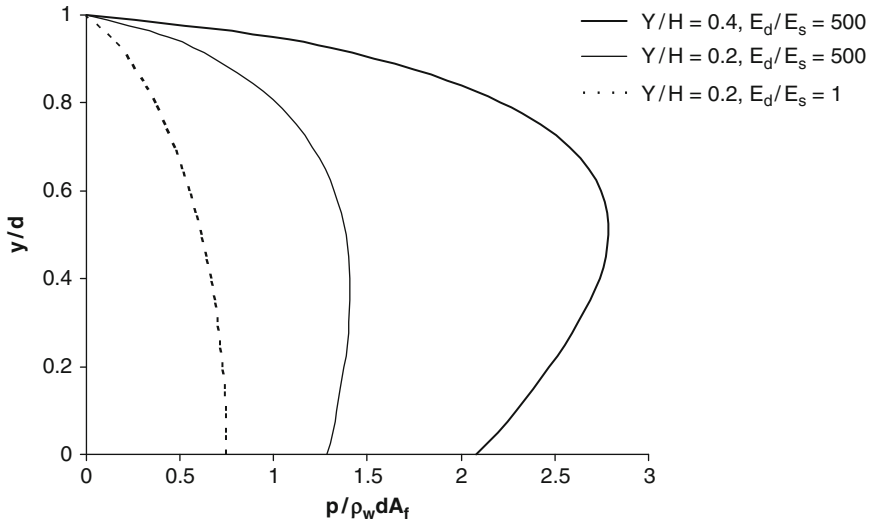


Fig. 10 Normalized dynamic pressure distributions in the case of resonance for $d/H = 1$ and $\rho_d/\rho_s = 1.5$ and for various values of Y/H and E_d/E_s ratios

respect to the maximum acceleration developed along the soil-dam interface (A_f). The normalization with respect to A_f is performed using the dynamic amplification factors, which are discussed in the sequence.

4.3 Hydrodynamic Thrust

If the real and the imaginary part of the above pressure distributions are integrated height-wise with proper calculus methods, derivative quantities are obtained which describe the dynamic distress of the dam (shear force and bending moment at its base). More specifically, Fig. 11 illustrates the variation of the amplitude of the resultant shear force at the dam base versus the frequency of the imposed steady-state excitation, for two values of dimensionless soil thickness, two values of dimensionless relative stiffness, and two values of dimensionless relative density. In all cases, the reservoir is half filled ($d/H = 0.5$). One possible case of resonance is observed both for thick and for thin soft soil layer, while the resultant force imposed on the dam seems to be insensitive to variations in frequency for the case of rigid rock ($E_d/E_s = 1$). Note also the invariance of the curves for the two density ratios ($\rho_d/\rho_s = 1$ and $\rho_d/\rho_s = 1.5$) and for same foundation conditions ($Y/H = 0.2$ and $E_d/E_s = 500$).

The resonant frequencies of the various peaks reveal that as the soil layer becomes thinner the overall dam-foundation-reservoir system becomes stiffer, thus, its fundamental eigenfrequency increases. At certain frequencies the resultant dynamic force can be much higher than that resulting from Westergaard's method,

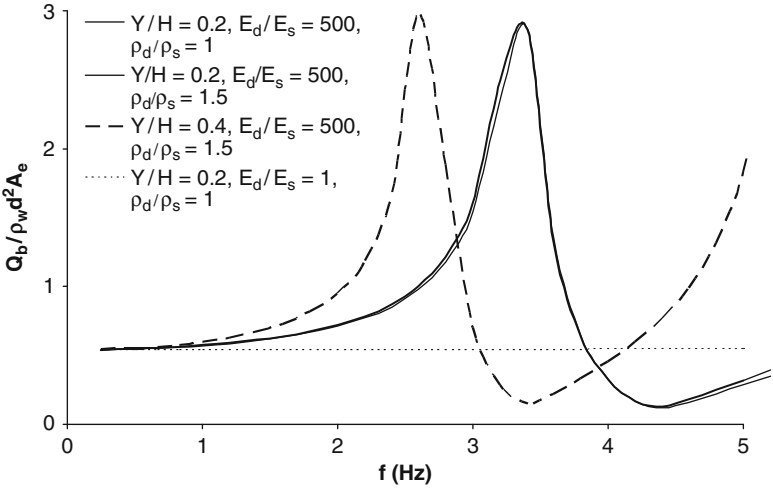


Fig. 11 Normalized dynamic shear force at the dam's base versus the steady-state excitation frequency f, for $d/H = 0.5$ and various values of $Y/H, E_d/E_s$ and ρ_d/ρ_s ratios

represented in Fig. 11 by the dot line which shows the (constant) force for the stiffer foundation case. In Fig. 12 the density and stiffness ratios are set equal to $E_d/E_s = 500$ and $\rho_d/\rho_s = 1.5$ respectively, and the impact of d/H and Y/H on the dynamic normalized base shear force is examined. It is obvious that with decreasing level of reservoir and soil layer thickness, the system becomes stiffer, and that leads to higher resonant frequency. However, it is the more flexible system which develops the highest dimensionless dynamic shear force. It is evident that shear forces are strongly related to frequency. Therefore, extra attention is needed when using simplifying methods in seismic design of dams (as well as any kind of infrastructures in general), since those approaches cannot take into account the frequency content characteristics of the imposed excitations.

To realize the effect of material and/or radiation damping on the resultant shear forces (and bending moments), it is necessary to handle them as complex numbers and calculate their real (in-phase) and imaginary (90° out-of-phase) components. In Fig. 13 the real, the imaginary and the resulting magnitude of the shear force are plotted as functions of frequency in the case of $d/H = 0.5, Y/H = 0.4, E_d/E_s = 500$ and $\rho_s/\rho_d = 1.5$. For frequencies lower than 2 Hz, the magnitude of the shear force is equal to its real part, as its imaginary part is nearly zero. For higher frequencies the out-of-phase component dominates the overall response to a greater extent.

Furthermore, it is evident that there exists a frequency (approximately at 2.7 Hz) in which the out-of-phase part obtains its maximum value (in absolute terms), while at the same frequency the real part becomes zero. This is the resonant frequency of the system, and at this frequency the overall response is dominated by the out-of-phase part, i.e., by the system's damping mechanisms. For frequencies greater than 3.3 Hz, the influence of the first eigenmode is minimized, while the influence of the second eigenmode gradually increases.

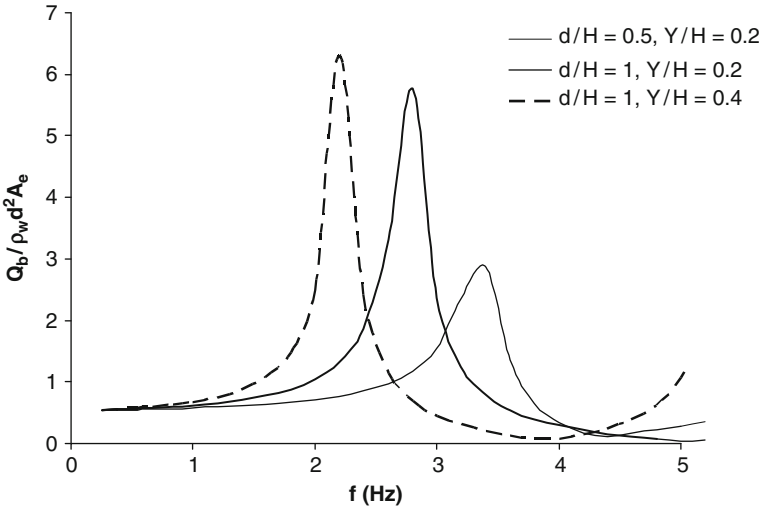


Fig. 12 Normalized dynamic shear force at the dam's base versus the steady-state excitation frequency f, for $E_d/E_s = 500$ and $\rho_d/\rho_s = 1.5$ and various values of d/H and Y/H ratios

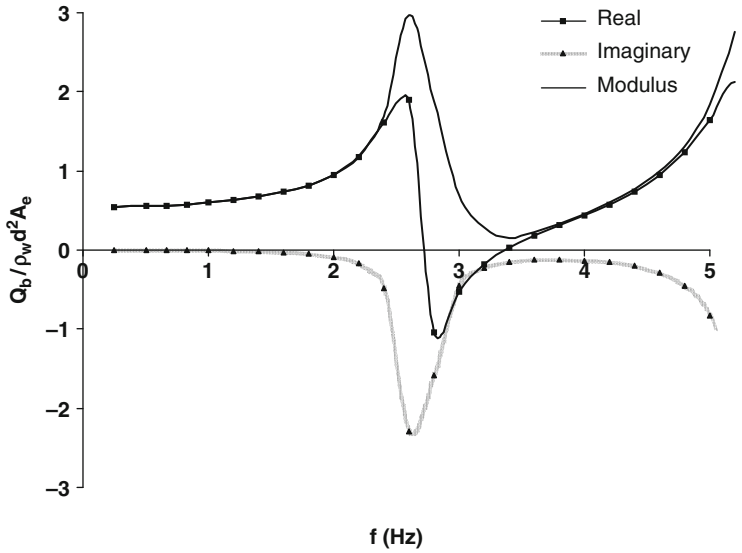


Fig. 13 Normalized dynamic shear force imposed on the dam's base by the retained water versus the steady-state excitation frequency f, for $d/H = 0.5, Y/H = 0.4, E_d/E_s = 500$ and $\rho_s/\rho_d = 1.5$

4.4 Dynamic Amplification Factors

Typically, the response of a concrete dam founded on soft soil is evaluated in terms of its horizontal displacement and rotation considering it as a rigid body. The horizontal displacement of the dam is calculated as the mean value of the dynamic

horizontal displacements of the two ends of its base. In general, the Amplification Factor between two arbitrary points X and Y, *AF(XY)* is defined by:

$$\mathrm{AF(XY)} = \frac{\mathrm{FFT[Y(t)]}}{\mathrm{FFT[X(t)]}} \tag{68}$$

where *FFT[Y(t)]* and *FFT[X(t)]* denote the Fast Fourier Transforms of the corresponding time-histories of points X and Y, respectively. Regarding translational amplification factors, functions $X(t)$ and $Y(t)$ can be displacement, velocity, or acceleration time-histories, provided that in the above equation both are expressed in terms of the same quantity (displacement, velocity, or acceleration). Typically point X lies on the rigid bedrock and point Y at the soil surface. In this study point Y is located at the middle of dam's base to account for the amplification of the motion due to the existence of the soil layer under the dam.

In the sequence, as the amplification factor refers to translational motion (horizontal movement), it is called translational amplification factor (AF_{trans}). Figure 14 depicts the translational amplification factor at the base of the dam in the case of $Y/H = 0.2, E_d/E_s = 500$ and $\rho_d/\rho_s = 1.5$, which is calculated as the mean value of the two amplification factors at the left-base (LB) and right-base (RB) corner points shown in Fig. 6. For the rigid foundation case the amplification factor is equal to unity, since the base of the dam is rigid and the response at the dam-soil interface is identical to the acceleration time-history imposed at the bedrock. As the relative distance between the rigid rock-soil interface and the dam base gets larger, resonant frequencies seem to become smaller and their corresponding peaks larger.

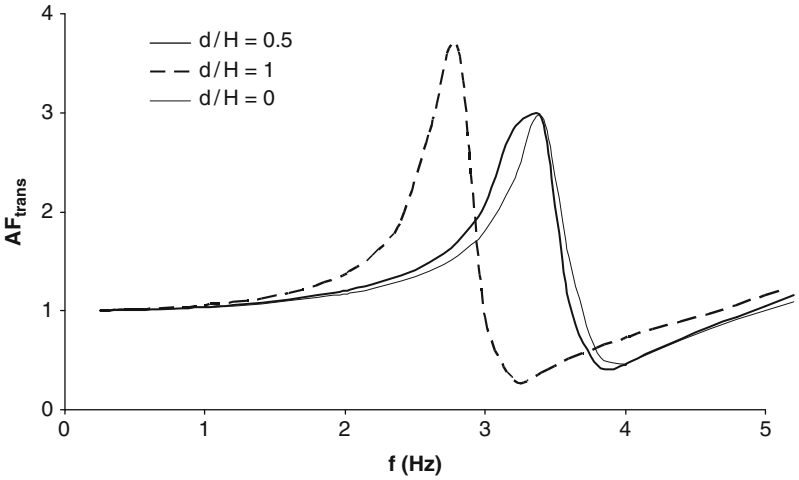


Fig. 14 Translational amplification factor at the dam base versus the steady-state excitation frequency f, for $Y/H = 0.2, E_d/E_s = 500$ and $\rho_d/\rho_s = 1.5$ and various values of water level d/H

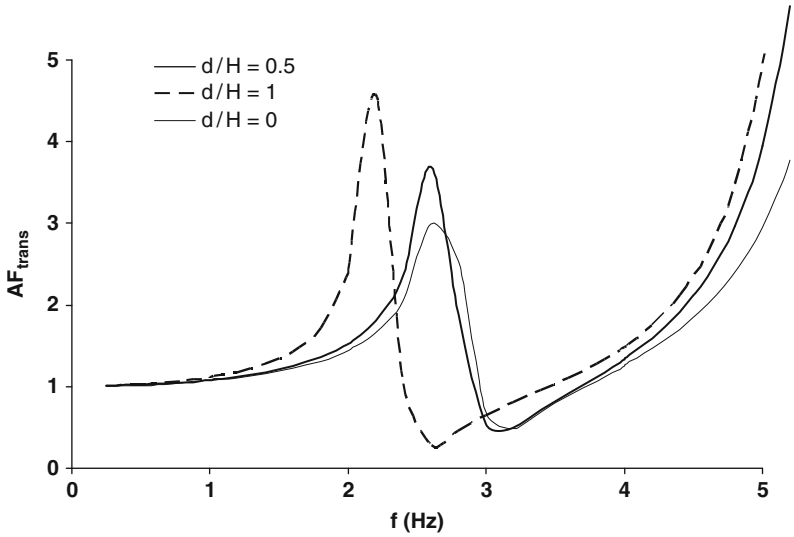


Fig. 15 Translational amplification factor at the dam base versus the steady-state excitation frequency f, for $Y/H = 0.4$, $E_d/E_s = 500$ and $\rho_d/\rho_s = 1.5$ and various values of water level d/H

This phenomenon verifies that the presence of a thick soft soil layer beneath the dam base may have detrimental consequences in its response, especially for earthquakes with low frequency content.

Figure 15 depicts the translational amplification factor at the base of the dam for $Y/H = 0.4, E_d/E_s = 500$ and $\rho_d/\rho_s = 1.5$. In the case of $d/H = 0$, in which the water reservoir is empty, the peak values of amplification are equal. However, they do not appear in the same frequency. Generally, a decrease in the layer thickness renders the whole system stiffer and increases its fundamental eigenfrequency. Therefore, the system with $Y/H = 0.2$, being stiffer than the one with $Y/H = 0.4$, has higher resonant frequencies, as it can be verified by Figs. 14 and 15. In addition, the maximum amplification factors of the stiffer system are lower than those of the softer system. As aforementioned this trend was also observed in the shear force diagrams.

4.5 Quasi-Static Equivalent Soil Spring Concept

In order to reduce the computational cost of the dynamic interaction analyses, the soil layer of the model shown in Fig. 6 is substituted by a translational and a rotational spring. The two springs account for the compliance of the underlying soil in an approximate but computationally efficient and accurate way taking into account the water height in the reservoir. Due to the existence of the water at the upstream

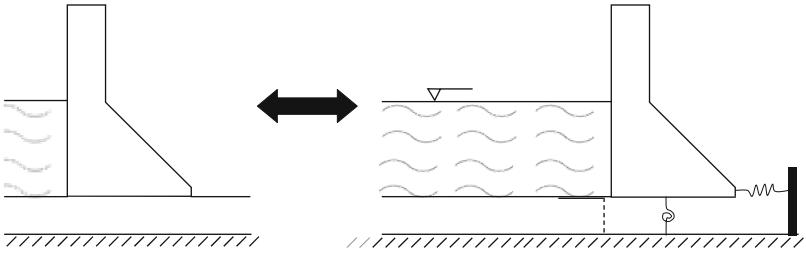


Fig. 16 *Left plot*: the examined concrete dam; *Right plot*: the soil layer is substituted with two equivalent springs (translational and rotational)

direction of the dam it is not realistic to assess the distress and the response of the dam by assuming that they result only due to its own inertial forces. The proposed springs correlate the forces induced to the dam by the retained water with the translational and/or rotational response due to the presence of the reservoir.

Both springs are characterized by their dynamic impedance H_{trans} and H_{rot}, respectively. In general, the dynamic impedance of the foundation of the dam H_j that relates actions F_j with deformations U_j is given by the equation:

$$H_j = \frac{F_j}{U_j} \tag{69}$$

where j = trans (translational) or rot (rotational). Referring to equation (69) it is essential to note that, in general, the dynamic action and the corresponding deformation are out-of-phase. In fact, each of the above quantities is composed by an in-phase (real) part and a 90° out-of-phase (imaginary) part. Thus, using complex notation the above ratio can be expressed as:

$$H_j = \frac{F_j}{U_j} = K_j + iC_j \tag{70}$$

in which K_j is the real part of the impedance H_j, which takes into account stiffness and/or inertia effects and from now on will be called as "stiffness coefficient", and C_j denotes the imaginary component which takes into account damping effects and will be called from now on as "damping coefficient". Figure 16 shows the equivalent spring model as a simplification of the real conditions.

Figure 17 presents the translational stiffness coefficients of the equivalent springs K_{trans} for the cases of half-filled reservoir and full reservoir, respectively, in the case of $E_d/E_s = 500$ and $\rho_d/\rho_s = 1.5$. It is evident that for low frequencies the stiffness coefficients decrease monotonically, and in the higher frequency range they obtain their maxima and minima. The stiffness coefficients in the case of full reservoir are lower than those for half filled and their local maxima and minima are smoother. This fact confirms the aforementioned remark that the higher the water level gets the more flexible the system becomes. As far as the rotational springs are concerned, the

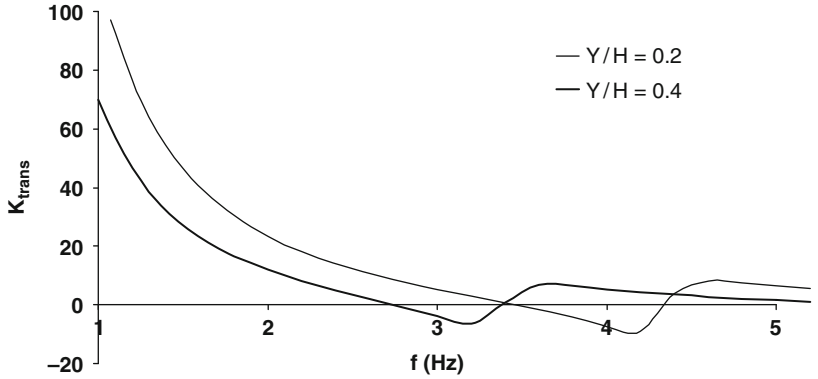


Fig. 17 Translational stiffness coefficients versus the steady-state excitation frequency f, for $d/H = 0.5$, $E_d/E_s = 500$, $\rho_d/\rho_s = 1.5$ and for two cases of foundation layer thickness

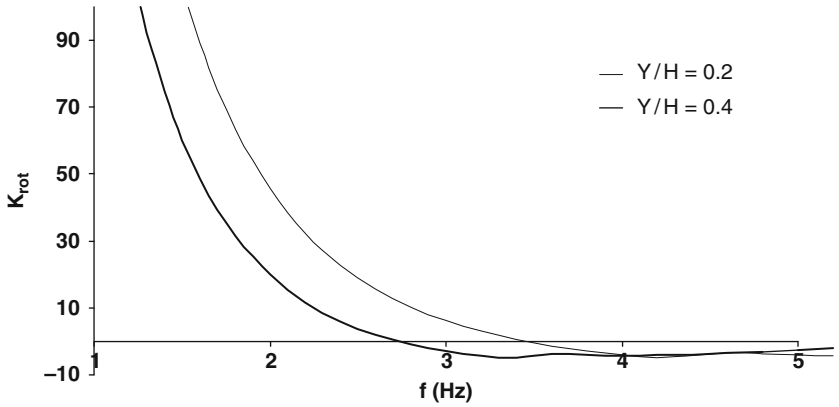


Fig. 18 Rotational stiffness coefficients versus the steady-state excitation frequency f, for $d/H = 0.5$, $E_d/E_s = 500$, $\rho_d/\rho_s = 1.5$ and for two cases of foundation layer thickness

corresponding stiffness coefficients K_{rot} are shown in Fig. 18, where the same trends as in the case of translational stiffness are observed, while the maxima and minima are much more flattened.

5 Conclusions

Following an extensive literature review on the available analytical and numerical methods, the dynamic analysis of a characteristic rigid concrete dam was conducted to assess the impact of dam-reservoir-foundation dynamic interaction on its dynamic response. It was found that the dynamic response of a concrete dam is affected by

many factors, such as the dam-reservoir-foundation geometry and the constitutive properties of the dam and the underlying soil. In some cases, sliding potential of the dam-soil interface may have also an important effect. The conducted numerical simulations included the relative stiffness and relative density of the dam with respect to the foundation, the thickness of the underlying compliant soil layer and the percentage of the reservoir fill. Results showed that indeed dynamic dam-reservoir-foundation interaction is a very complicated problem that involves many parameters. Analytical solutions provide only a qualitative approach of this complex interaction, whereas for a complete and accurate quantitative calculation numerical solutions should be used. Numerical methods possess a large computational potential and can encounter problems of complicated geometry as well as non-linear material behaviour. Based on the literature review and the capabilities of the numerical procedures, it is concluded that the dam-reservoir-foundation dynamic interaction problem has to be analysed on a case-by-case basis so that the various parameters involved are taken realistically into account.

References

1. ABAQUS (2008) User's manual, Version 6.8. Dassault Systèmes Simulia Corporation, Providence RI, USA
2. Akköse M, Adanur S, Bayraktar A, Dumanoğlu AA (2008) Elasto-plastic earthquake response of arch dams including fluid–structure interaction by the Lagrangian approach. Appl Math Model 32:2396–2412
3. Akköse M, Bayraktar A, Dumanoğlu AA (2008) Reservoir water level effects on nonlinear dynamic response of arch dams. J Fluids Struct 24:418–435
4. Arabshahi H, Lotfi V (2008) Earthquake response of concrete gravity dams including dam–foundation interface nonlinearities. Eng Struct 30:3065–3073
5. Aznárez JJ, Maeso O, Domínguez J (2006) BE analysis of bottom sediments in dynamic fluid-structure interaction problems. Eng Anal Boundary Elem 30:124–136
6. Bayraktar A, Hançer E, Akköse M (2005) Influence of base-rock characteristics on the stochastic dynamic response of dam–reservoir–foundation systems. Eng Struct 27:1498–1508
7. Bayraktar A, Hançer E, Dumanoğlu AA (2005) Comparison of stochastic and deterministic dynamic responses of gravity dam–reservoir systems using fluid finite elements. Finite Elem Anal Des 41:1365–1376
8. Bilici Y, Bayraktar A, Soyluk K, Haciefendioğlu K, Ateş Ş, Adanur S (2009) Stochastic dynamic response of dam–reservoir–foundation systems to spatially varying earthquake ground motions. Soil Dyn Earthquake Eng 29:444–458
9. Câmara RJ (2000) A method for coupled arch dam-foundation-reservoir seismic behaviour analysis. Earthquake Eng Struct Dyn 29:441–460
10. Chavez JW, Fenves GL (1995) Earthquake response of concrete gravity dams including base sliding. ASCE J Struct Eng 121(5):865–875
11. Cheng A (1986) Effect of sediment on earthquake induced reservoir hydrodynamic response. J Eng Mech 112:654–664
12. Chopra AK (1967) Hydrodynamic pressures on dams during earthquakes. ASCE J Eng Mech 93:205–223
13. Chopra AK, Zhang L (1991) Earthquake-induced base sliding of concrete gravity dams. ASCE J Struct Eng 117(12):3698–3719
14. Chopra AK (1968) Earthquake behavior of dam–reservoir systems ASCE J Eng Mech 94:1475–1499

15. Chwang AT (1978) Hydrodynamic pressures on sloping dams during earthquakes. Part 2. Exact theory. J Fluid Mech 87(2):343–348
16. Chwang AT, Housner GW (1978) Hydrodynamic pressures on sloping dams during earthquakes. Part 1. Momentum method. J Fluid Mech 87(2):335–341
17. Clough RW, Penzien J (1993) Dynamics of structures, 2nd edn. McGraw-Hill, Singapore
18. Danay A, Adeghe LN (1993) Seismic-induced slip of concrete gravity dams. ASCE J Struct Eng 119(1):108–129
19. Donlon WP, Hall JF (1991) Shaking table study of concrete gravity dam monoliths. Earthquake Eng Struct Dyn 20:769–786
20. Du X, Zhang Y, Zhang B (2007) Nonlinear seismic response analysis of arch dam-foundation systems- part I dam-foundation rock interaction. Bull Earthquake Eng 5:105–119
21. EM-1110-2-6053 (2007) Earthquake design and evaluation of concrete hydraulic structures. US Army Corps of Engineers, Washington, DC
22. Fahjan YM, Börekçi OS, Erdik M (2003) Earthquake-induced hydrodynamic pressures on a 3D rigid dam–reservoir system using DRBEM and a radiation matrix. Int J Numerical Methods Eng 56:1511–1532
23. Fan SC, Li SM (2008) Boundary finite-element method coupling finite-element method for steady-state analyses of dam-reservoir systems. ASCE J Eng Mech 134(2):133–142
24. Fenves GL, Chopra AK (1984) Earthquake analysis of concrete gravity dams including reservoir bottom absorption and dam-water-foundation rock interaction. Earthquake Eng Struct Dyn 12:663–680
25. Ghaemian M, Ghobarah A (1998) Staggered solution schemes for dam-reservoir interaction. J Fluids Struct 12:933–948
26. Ghaemian M, Ghobarah A (1999) Nonlinear seismic response of concrete gravity dams with dam–reservoir interaction. Eng Struct 21:306–315
27. Ghobarah A, El-Nady A, Aziz T (Sept 1994) Simplified dynamic analysis for gravity dams. ASCE J Struct Eng 120(9):2697–2716
28. Gogoi I, Maity D (2007) Influence of sediment layers on dynamic behavior of aged concrete dams. ASCE J Eng Mech 133(4):400–413
29. Higdon RL (1994) Radiation boundary condition for dispersive waves. SIAM J Numerical Anal 31:64–100
30. Javanmardi F, Léger P, Tinawi R (2005) Seismic water pressure in cracked concrete gravity dams: experimental study and theoretical modeling. ASCE J Struct Eng 131(1):139–150
31. Koh HM, Kim JK, Park JH (1998) Fluid-structure interaction analysis of 3-D rectangular tanks by a variationally coupled BEM-FEM and comparison with test results. Earthquake Eng Struct Dyn 27:109–124
32. Küçükarslan S (2003) Dam-reservoir interaction for incompressible-unbounded fluid domains using an exact truncation boundary condition. In: Proceedings of 16th ASCE engineering mechanics conference, University of Washington, Seattle, 16–18 July 2003
33. Küçükarslan S (2005) An exact truncation boundary condition for incompressible–unbounded infinite fluid domains. Appl Math Comput 163:61–69
34. Küçükarslan S, Coşkun SB, Taşkın B (2005) Transient analysis of dam–reservoir interaction including the reservoir bottom effects. J Fluids Struct 20:1073–1084
35. Lee GC, Tsai CS (1991) Time-domain analyses of dam-reservoir system. I: exact solution. ASCE J Eng Mech 117(9):1990–2006
36. Lee J, Fenves GL (1998) A plastic-damage concrete model for earthquake analysis of dams. Earthquake Eng Struct Dyn 27:937–956
37. Li X, Romo MPO, Aviles JL (1996) Finite element analysis of dam-reservoir systems using an exact far-boundary condition. Comput Struct 60(5):751–762
38. Lin G, Du J-G, Hu Z-Q (2007) Dynamic dam-reservoir interaction analysis including effect of reservoir boundary absorption. Sci China Ser E Technol Sci 50(I):1–10
39. Liu PLF (1986) Hydrodynamic pressures on rigid dams during earthquakes. J Fluid Mech 165:131–145
40. Maity D (2005) A novel far-boundary condition for the finite element analysis of infinite reservoir. Appl Math Comput 170:1314–1328

41. Maity D, Bhattacharyya SK (1999) Time-domain analysis of infinite reservoir by finite element method using a novel far-boundary condition. Finite Elem Anal Des 32:85–96
42. Maity D, Bhattacharyya SK (2003) A parametric study on fluid–structure interaction problems. J Sound Vib 263:917–935
43. Mir RA, Taylor CA (1995) An experimental investigation into earthquake induced failure of medium to low height concrete gravity dams. Earthquake Eng Struct Dyn 24:373–393
44. Mir RA, Taylor CA (1996) An investigation into the base sliding response of rigid concrete gravity dams to dynamic loading. Earthquake Eng Struct Dyn 25:79–98
45. Papazafeiropoulos G, Tsompanakis Y, Psarropoulos PN (2009) Analytical and numerical modeling of hydrodynamic distress of rigid and flexible concrete dams. In: Papadrakakis M, Lagaros ND, Fragiadakis M (eds) Proceedings of COMPDYN-2009: 2nd international conference on computational methods in structural dynamics and earthquake engineering, Rhodes, Greece, 22–24 June 2009
46. Parrinello F, Borino G (2007) Lagrangian finite element modelling of dam–fluid interaction: accurate absorbing boundary conditions. Comput Struct 85:932–943
47. Plizzari G, Waggoner F, Saouma VE (1991) Centrifuge modeling and analysis of concrete gravity dams. J Struct Eng 121(10):1471–1479
48. Saini SS, Bettess P, Zienkiewicz OC (1978) Coupled hydrodynamic response of concrete gravity dams using finite and infinite elements. Earthquake Eng Struct Dyn 6:363–374
49. Sharan SK (1985) Finite element analysis of unbounded and incompressible fluid domains. Int J Numerical Methods Eng 21:1659–1669
50. Taylor RE (1981) A review of hydrodynamic load analysis for submerged structures excited by earthquakes. Eng Struct 3:131–139
51. Tinawi R, Guizani L (1994) Formulation of hydrodynamic pressures in cracks due to earthquakes in concrete dams. Earthquake Eng Struct Dyn 23:699–715
52. Tsai CS, Lee GC (1991) Time-domain analyses of dam-reservoir system. II: substructure method. J Eng Mech 117(9):2007–2026
53. Usuki S (1977) The application of a variational finite element method to problems in fluid dynamics. Int J Numerical Methods Eng 11:563–577
54. Westergaard HM (1931) Water pressure on dams during earthquakes. ASCE Trans 98:418–433
55. Wilson EL, Khalvati M (1983) Finite elements for the dynamic analysis of fluid-solid systems. Int J Numerical Methods Eng 19:1657–1668

Numerical Analysis of Externally-Induced Sloshing in Spherical Liquid Containers

Spyros A. Karamanos, Lazaros A. Patkas, and Dimitris Papaprokopiou

Abstract Motivated by the earthquake response of industrial pressure vessels, the present chapter investigates externally-induced sloshing in spherical liquid containers. Assuming ideal and irrotational flow, small-amplitude free-surface elevation, the problem is solved through a variational (Garlerkin) formulation that uses either a numerical finite element formulation or a semi-analytical methodology in terms of harmonic global functions that allows for high-precision computations. Considering modal analysis and an appropriate decomposition of the container-fluid motion, the sloshing frequencies and the corresponding sloshing (or convective) masses are calculated, leading to a simple and efficient method for predicting the dynamic behavior of spherical liquid containers. In both solution methodologies, the accuracy and convergence of the results are examined. The calculated sloshing frequencies and masses are in very good comparison with available semi-analytical or numerical solutions, and previously reported experimental data. It is also shown that consideration of only the first sloshing mass is adequate to represent the dynamic behavior of the spherical liquid container within a good level of accuracy.

Keywords Sloshing · Liquid container dynamics · Earthquake excitation · Finite elements · Hydrodynamic pressure · Harmonic functions

1 Introduction

The calculation of hydrodynamic forces on the wall of vibrating liquid containers constitutes an important issue for safeguarding the structural integrity of industrial tanks and vessels. In particular, liquid sloshing on the free surface may have a significant influence on the response of the container. Mathematically, assuming an ideal

S.A. Karamanos (✉), L.A. Patkas, and D. Papaprokopiou
Department of Mechanical Engineering, University of Thessaly,
Volos 383 34, Greece
e-mail: skara@mie.uth.gr

M. Papadrakakis et al. (eds.), *Computational Methods in Earthquake Engineering*,
Computational Methods in Applied Sciences 21, DOI 10.1007/978-94-007-0053-6_21,
© Springer Science+Business Media B.V. 2011



Fig. 1 Applications of spherical pressure vessels in refineries and in LNG carriers

liquid and irrotational flow, the linear sloshing formulation leads to an eigenvalue problem in terms of the fluid velocity potential, which represents the oscillations of liquid free surface inside a non-moving container. In the presence of external excitation, the above problem becomes transient and its solution provides the hydrodynamic pressures and force on the container's wall [1, 2].

Earthquake-induced sloshing has been recognized as an important issue for the structural safety of liquid storage tanks or vessels. Housner [3] presented a solution for the hydrodynamic effects in non-deformable upright-cylindrical and rectangular containers, splitting the solution in two parts, namely the impulsive part and the convective part. This work has been extended [4–6] to account for shell deformation effects on the response of upright cylinders. In subsequent works, uplifting of unanchored tanks and soil-structure interaction effects were examined [7–10]. Rammerstorfer et al. [11] presented a thorough overview of liquid storage tanks under seismic loading, with an extensive literature review, including fluid-structure and soil-structure interaction effects.

In the above studies, vertical-cylindrical tanks were mainly investigated. On the other hand, relatively few publications have been reported on liquid sloshing in other geometries, such as horizontal cylinders or spheres, which have significant industrial applications in refineries, power plants and LNG tankers, as shown in Fig. 1. It is interesting to note that the API 650 seismic provisions for liquid storage tanks [12] refer exclusively to vertical cylinders, whereas the recent European rules [13], and the New Zealand recommendations [14] refer to industrial pressure vessels of horizontal cylindrical and spheres) in a very approximate manner.

Solutions for linearized liquid sloshing in non-deformable spherical liquid containers has been investigated through semi-analytical or special-purpose numerical solution methodologies of the eigenvalue problem leading to the calculation of sloshing frequencies [15–17]. To the authors' knowledge, the only works reported on externally-induced sloshing (transient problem) in spherical vessels are the early paper by Budiansky [18], which employed an integral equation approach, and the recent paper by Papaspyrou et al. [19], which is based on the mathematical model introduced in [17] for the eigenvalue problem, but it is restricted to the half-full spherical container.

The present chapter examines linear liquid sloshing in spherical non-deformable containers subjected to horizontal external excitation, based on modal analysis. The

study is motivated by the earthquake design and analysis of industrial pressure vessels of spherical shape. Those vessels are thick-walled to resist high levels of internal pressure, required for the liquefied gas, and, therefore, they remain practically undeformed. Two solution methodologies are adopted and presented in the present chapter:

1. The first solution methodology is a general-purpose finite element formulation that could be used in vessels of axi-symmetric shape; the spherical vessel is a special case of such vessels. Using appropriate trigonometric functions for the sloshing potential in the third direction, sloshing frequencies and modes, representing fluid motion within the motionless container, are calculated solving a two-dimensional eigenvalue problem, through a finite element discretization that employs constant-strain triangular elements, and a static condensation technique that increases computational efficiency. Subsequently, the transient problem of externally-induced sloshing is solved through a modal analysis, and an efficient methodology for the calculation of sloshing (or convective) masses is developed, which can be used for the seismic design and analysis of industrial vessels.
2. The second methodology is based on a semi-analytical special-purpose variational formulation, where the velocity potential is expressed through series of non-orthogonal spatial functions. In this methodology the boundary-value problem reduces to a system of ordinary linear differential equations, where sloshing frequencies, modes and masses are computed with either direct integration or modal analysis; the latter approach leads to the calculation of sloshing frequencies and masses.

The results are presented in the form of sloshing frequencies and masses in spherical vessels with respect to the liquid height within the spherical container. The accuracy and the convergence of the solution methodologies are also examined. Finally, the results are compared with available experimental data and other semi-analytical and numerical results reported elsewhere. The calculated sloshing frequencies and masses could be used for the simple and efficient seismic analysis of industrial vessels.

2 General Formulation

Assuming ideal fluid conditions, the liquid motion in a undeformed (rigid) container, under horizontal excitation displacement X in the x direction (Fig. 2) is a function of time t and is described by the flow potential $\Phi(x, y, z, t)$, so that the liquid velocity is the gradient of Φ ($\mathbf{u} = \nabla\Phi$), which satisfies the Laplace equation,

$$\nabla^2\Phi = \frac{\partial^2\Phi}{\partial x^2} + \frac{\partial^2\Phi}{\partial y^2} + \frac{\partial^2\Phi}{\partial z^2} = 0 \quad \text{in}\,\Omega \tag{1}$$

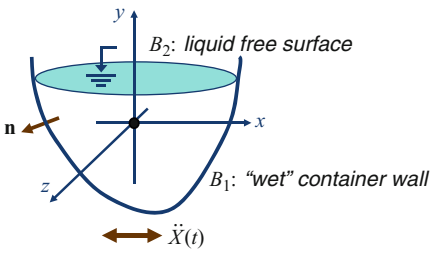


Fig. 2 Schematic representation of a liquid container under horizontal external excitation

subjected to the following boundary conditions at the wet surface of the vessel wall and the free surface

$$\frac{\partial \Phi}{\partial n} = \dot{X}\ (\mathbf{e}_x \cdot \mathbf{n}) \quad \text{on } \mathrm{B}_1 \tag{2}$$

$$\frac{\partial^2 \Phi}{\partial t^2} + g\frac{\partial \Phi}{\partial y} = 0 \quad \text{on } \mathrm{B}_2 \tag{3}$$

where $\dot{X} = dX/dt$, and $\mathbf{e}_x$ is the unit vector in the x direction and $\mathbf{n}$ is the outward normal unit vector at any point of the lateral (wet) surface B_1. The unknown potential Φ can be decomposed additively in two parts, the sloshing motion potential Φ_S, and the uniform motion potential Φ_U:

$$\Phi_U = \dot{X}(t)\ x \tag{4}$$

One may readily show that Φ_U satisfies Laplace equation (1) and the non-homogeneous boundary condition (2). Therefore, the sloshing potential Φ_S should satisfy

$$\nabla^2 \Phi_S = 0 \,\text{in}\, \Omega \tag{5}$$

and the following boundary conditions

$$\frac{\partial \Phi_S}{\partial n} = 0 \,\text{on}\, \mathrm{B}_1 \tag{6}$$

$$\frac{\partial^2 \Phi_S}{\partial t^2} + g\frac{\partial \Phi_S}{\partial y} = -\frac{\partial^2 \Phi_U}{\partial t^2} \text{on}\, \mathrm{B}_2 \tag{7}$$

Considering an admissible function $\varphi^*(x, y, z)$ and using Green's theorem, the variational form (weak statement) of problem (5)–(7) is expressed as follows:

$$\int_\Omega (\nabla \Phi_S)\left(\nabla \varphi^*\right) d\Omega + \frac{1}{g}\int_{B_2} \frac{\partial^2 \Phi_S}{\partial t^2}\varphi^* dB_2 = -\frac{1}{g}\int_{B_2} \frac{\partial^2 \Phi_U}{\partial t^2}\varphi^* dB_2 \tag{8}$$

In the absence of external excitation $X(t) = 0$, then $\Phi_U = 0$, the boundary condition (7) becomes homogeneous, and solutions of the problem (5)–(7) are sought in the form

$$\Phi_S = \phi_S(x, y, z)\ e^{i\omega t} \tag{9}$$

leading to the following eigenvalue problem

$$\nabla^2 \phi_S = 0 \text{ in } \Omega \tag{10}$$

$$\frac{\partial \phi_S}{\partial n} = 0 \text{ on } B_1 \tag{11}$$

$$\frac{\partial \phi_S}{\partial y} - \frac{\omega^2}{g}\phi_S = 0 \text{ on } B_2 \tag{12}$$

The solution provides the so-called sloshing (eigen) frequencies ω_n and the corresponding sloshing modes $\Psi_n(x, y, z)$ $(n = 1, 2, 3, \ldots)$, which satisfy the orthogonality conditions

$$\int_{\Omega} (\nabla \Psi_m) \cdot (\nabla \Psi_n)\, d\Omega = \int_{B_2} \Psi_m \Psi_n \, dB_2 = 0, \quad m \neq n \tag{13}$$

Upon calculation of ω_n and $\Psi_n(x, y, z)$, the solution of the transient problem (5)–(7) can be expressed in terms of Ψ_n as follows:

$$\Phi_S(x, y, z, t) = \sum_{n=1,2,3,\ldots}^{\infty} \dot{Y}_n(t) \Psi_n (x, y, z) \tag{14}$$

where the dot denotes derivative with respect to time, and functions $Y_n(t)$ are generalized coordinates. The admissible function $\varphi^*(x, y, z)$ in Eq. 8 is also expressed in the same manner

$$\varphi^*(x, y, z) = \sum_{n=1,2,3,\ldots}^{\infty} b_n \Psi_n (x, y, z) \tag{15}$$

where b_n are arbitrary constants. Inserting (14) and (15) into the variational equation (8), and using the orthogonality of $\Psi_n(x, y, z)$, one readily obtains a series of uncoupled linear ordinary differential equations in terms of $Y_n(t)$:

$$\bar{M}_n \ddot{Y}_n + \omega_n^2 \bar{M}_n Y_n = -\bar{P}_n \ddot{X}, \quad n = 1, 2, 3, \ldots \tag{16}$$

where

$$\bar{M}_n = \frac{1}{g} \int_{B_2} \Psi_n^2 \, dB_2, \quad n = 1, 2, 3, \ldots, \tag{17}$$

$$\bar{P}_n = \frac{1}{g} \int_{B_2} \Psi_n x \, dB_2, \quad n = 1, 2, 3, \ldots \tag{18}$$

The hydrodynamic pressures $p(x, y, z, t)$ are calculated directly from the fluid potential Φ through the Bernoulli equation ($p = -\rho\dot{\Phi}$) and the total hydrodynamic force at the container wall is obtained through an appropriate integration of those pressures on the wet surface of the container in the direction of the earthquake excitation:

$$F = -\rho \int_{B_1} \left(\frac{\partial \Phi_U}{\partial t} + \frac{\partial \Phi_S}{\partial t} \right) (\mathbf{e}_x \cdot \mathbf{n})\, dB_1 \tag{19}$$

Equation 19 indicates that the total horizontal force F can be expressed as a summation of the uniform motion force F_U:

$$F_U = -\rho \int_{B_1} \frac{\partial \Phi_U}{\partial t} (\mathbf{e}_x \cdot \mathbf{n})\, dB_1 = -\mathsf{M}_L \ddot{X} \tag{20}$$

where M_L is the total liquid mass, and the force F_S associated with sloshing:

$$F_S = -\rho \int_{B_1} \frac{\partial \Phi_S}{\partial t} (\mathbf{e}_x \cdot \mathbf{n})\, dB_1 = -\sum_n \bar{F}_n \ddot{Y}_n \tag{21}$$

where

$$\bar{F}_n = \rho \int_{B_1} \Psi_n (\mathbf{e}_x \cdot \mathbf{n})\, dB_1 \tag{22}$$

Therefore, the total hydrodymanic force on the container's wall is

$$F = -\sum_{n=1,2,3,\ldots}^{\infty} \bar{F}_{nc}\, \ddot{Y}_n - \mathsf{M}_L \ddot{X} \tag{23}$$

Using the following change of variables

$$a_n = \left(\frac{\bar{M}_n}{\bar{P}_n} \right) Y_n, \quad n = 1, 2, 3, \ldots \tag{24}$$

and

$$u_n = a_n + X, \quad n = 1, 2, 3, \ldots \tag{25}$$

the liquid motion equations (16) become

$$\ddot{a}_n + \omega_n^2 a_n = -\ddot{X}(t), \quad n = 1, 2, 3, \ldots \tag{26}$$

or equivalently,

$$\ddot{u}_n + \omega_n^2 (u_n - X) = 0, \quad n = 1, 2, 3, \ldots \tag{27}$$

Equation 26 express the liquid motion with respect to the container and Eq. 27 express the total liquid motion (including the motion of the container). In those equations, dissipation effects can be easily considered, introducing a damping term, so that Eq. 26 becomes

$$\ddot{a}_n \; + \; 2\xi_n\omega_n a_n + \omega_n^2 a_n \; = \; - \; \ddot{X}(t), \; n = 1, 2, 3, \ldots \tag{28}$$

where ξ_n is the damping ratio of mode n. Equivalently, Eq. 28 in the presence of damping can be written

$$\ddot{u}_n \; + 2\xi_n\omega_n \left(\dot{u}_n - \dot{X}\right) + \; \omega_n^2 \left(u_n - X\right) \; = \; 0, \; n = 1, 2, 3, \ldots \tag{29}$$

Furthermore, the hydrodynamic force in Eq. 23 becomes

$$F \; = \; - \sum_{n=1,2,3,\ldots}^{\infty} \mathsf{M}_{nC} \; \ddot{a}_n - \mathsf{M}_L \ddot{X} \tag{30}$$

or equivalently,

$$F \; = \; - \sum_{n=1,2,3,\ldots}^{\infty} \mathsf{M}_{nC} \; \ddot{u}_n - \mathsf{M}_I \ddot{X} \tag{31}$$

where

$$\mathsf{M}_{nC} = \frac{\bar{P}_n \bar{F}_n}{\bar{M}_n}, \; n = 1, 2, 3, \ldots \tag{32}$$

and

$$\mathsf{M}_I = \mathsf{M}_L - \sum_{n=1,2,3,\ldots}^{\infty} \mathsf{M}_{nC} \tag{33}$$

Note that the force F_S associated with sloshing can be written as follows

$$F_S \; = \; - \sum_{n=1,2,3,\ldots}^{\infty} \mathsf{M}_{nC} \; \ddot{a}_n \tag{34}$$

Equation 33 implies that the total mass M_L can be considered as the sum of the convective (or sloshing) masses M_{nC} ($n = 1, 2, 3, \ldots$) associated with free-surface elevation (convective motion), and the impulsive mass M_I, which follows the container motion $X(t)$.

In the above analysis, the key step towards calculation of the dynamic response of the container, is the solution of eigenvalue problem (10)–(12) for the sloshing frequencies ω_n and mode shapes $\Psi_n(x, y, z)$. In non-deformable rectangular and vertical-cylindrical liquid storage tanks, analytical expressions exist for ω_n and

$\Psi_n(x, y, z)$ (e.g. [1, 2]), and the above methodology becomes trivial. On the other hand, such analytical expressions do not generally exist for vessels of different geometry (e.g. spherical liquid containers), and should be computed numerically. In the following, the above general formulation is applied for the analysis of liquid vessels of spherical shape

3 Finite Element Analysis of Sloshing in Spherical Vessels

In this section, a finite element formulation and solution methodology is presented for the sloshing analysis in non-deformable spherical liquid containers, subjected to horizontal external excitation. It is important to note that the methodology can be also employed for the sloshing analysis of axisymmetric liquid containers of arbitrary meridional shape shown in Fig. 3; spherical containers can be considered as a special case of such axisymmetric containers (Fig. 4).

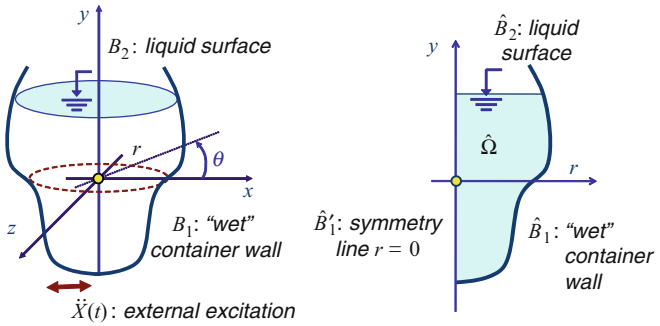


Fig. 3 Axisymmetric liquid container with arbitrary meridian shape

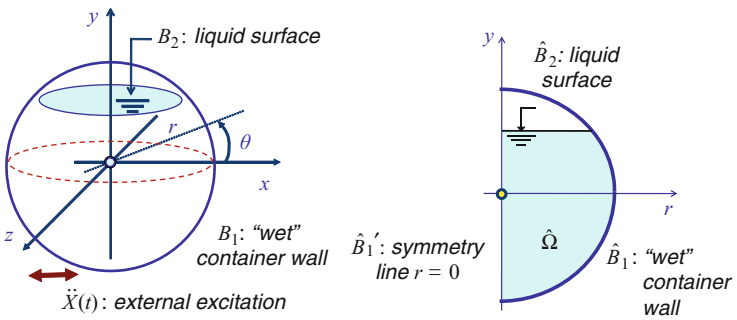


Fig. 4 Spherical liquid container

3.1 Finite Element Discretization and Solution

In axisymmetric vessels, a Cartesian system *x, y, z* is considered. Furthermore, the cylindrical coordinates r, y, θ are also considered, which are related to the Cartesian coordinates *x, y, z* as follows:

$$x = r\cos\theta \tag{35}$$

$$z = r\sin\theta \tag{36}$$

Horizontal external excitation is assumed in the x axis (Fig. 3), and the flow potential can be written as a sum of the uniform motion potential

$$\Phi_U = \dot{X}(t)\, r\, \cos\theta \tag{37}$$

and the potential associated with sloshing Φ_S, which should satisfy the Laplace equation (5) in the three-dimensional fluid domain, the kinematic boundary condition (6) at the wet surface $\hat{\mathrm{B}}_1$, whereas the boundary condition (7) on the free-surface becomes

$$\frac{\partial^2\Phi_S}{\partial t^2} + g\frac{\partial\Phi_S}{\partial y} = -\dddot{X}\ r\ \cos\theta \tag{38}$$

Therefore, taking into account the requirement of periodicity in terms of θ coordinate, and the form of the excitation term on the right-hand side of (38), the solution of ϕ_S in the eigenvalue problem (10)–(12) is sought in the following form

$$\phi_S(r, y, \theta) = \varphi(r, y)\cos\theta \tag{39}$$

Substitution into the Laplace equation (10), results in the following equation in the two-dimensional domain $\hat{\Omega}$ (Fig. 3)

$$\nabla^2\varphi + \frac{1}{r}\left(\frac{\partial\varphi}{\partial r}\right) - \frac{1}{r^2}\varphi = 0 \tag{40}$$

where in Eq. 40,

$$\nabla^2\varphi = \frac{\partial^2\varphi}{\partial r^2} + \frac{\partial^2\varphi}{\partial y^2} \tag{41}$$

Furthermore, φ should satisfy the following boundary conditions

$$\frac{\partial\varphi}{\partial n} = 0, \quad \text{on}\,\hat{\mathrm{B}}_1, \tag{42}$$

$$-\omega^2\varphi + g\frac{\partial\varphi}{\partial y} = 0, \quad \text{on}\,\hat{\mathrm{B}}_2. \tag{43}$$

$$\varphi = 0, \quad \text{at} \quad r = 0 \tag{44}$$

The weak form of the boundary-value problem (42)–(44) is obtained considering an admissible function $\varphi^* = \varphi^*(r, y)$ as follows

$$\int_{\hat{\Omega}} (\nabla\varphi)\cdot\left(\nabla\varphi^*\right) d\hat{\Omega} - \int_{\hat{\Omega}} \frac{1}{r}\left(\frac{\partial\varphi}{\partial r}\right)\varphi^* d\hat{\Omega} + \int_{\hat{\Omega}} \frac{1}{r^2}\varphi\,\varphi^* d\hat{\Omega} + \frac{1}{g}\int_{\hat{B}_2}\left(\frac{\partial^2\varphi}{\partial t^2}\right)\varphi^* d\hat{B}_2 = 0 \tag{45}$$

Subsequently, assuming the following discretization for φ

$$\varphi = [\mathbf{N}]\, q \tag{46}$$

$$\nabla\varphi = [\mathbf{B}]\, q \tag{47}$$

and a similar discretization of φ^* as follows

$$\varphi^* = [\mathbf{N}]\, q^* \tag{48}$$

$$\nabla\varphi^* = [\mathbf{B}]\, q^* \tag{49}$$

where $\mathbf{q}^*$ is an arbitrary vector, then a system of homogeneous equations is obtained,

$$\left([\mathbf{K}] - \omega^2\,[\mathbf{M}]\right)\mathbf{q} = 0 \tag{50}$$

where matrices $[\mathbf{M}]$ and $[\mathbf{K}]$ are defined as follows

$$[\mathbf{M}] = \frac{1}{g}\int_{\hat{B}_2} [\mathbf{N}]^{\mathrm{T}}[\mathbf{N}] d\hat{B}_2 \tag{51}$$

$$[\mathbf{K}] = \int_{\hat{\Omega}} [\mathbf{B}]^T\,[\mathbf{B}] d\hat{\Omega} - \int_{\hat{\Omega}} \frac{1}{r}[\mathbf{N}]^{\mathrm{T}}\frac{\partial[\mathbf{N}]}{\partial r}\mathrm{d}\hat{\Omega} + \int_{\hat{\Omega}} \frac{1}{r^2}[\mathbf{N}]^{\mathrm{T}}[\mathbf{N}]\mathrm{d}\hat{\Omega} \tag{52}$$

The solution of the discretized eigenvalue problem (50) provides the sloshing frequencies ω_n and the eigenvectors $\mathbf{u}_n$, so that the corresponding eigenfunctions of the initial eigenvalue problem (10)–(12) are written as follows:

$$\Psi_n\,(r, y, \theta) = [\mathbf{N}]\,\mathbf{u}_n \cos\theta, \quad n = 1, 2, 3, \ldots \tag{53}$$

Inserting (53) into Eqs. 17, 18, and considering $x = r\cos\theta$, one obtains

$$\bar{M}_n = \frac{\pi}{g}\mathbf{u}_n^T\left(\int_{\hat{B}_2} r\,[\mathbf{N}]^T\,[\mathbf{N}]\;d\hat{B}_2\right)\mathbf{u}_n, \quad n = 1, 2, 3, \ldots \tag{54}$$

$$\bar{P}_n = \frac{\pi}{g}\mathbf{u}_n^T \left(\int_{\hat{B}_2} r^2 \, [\mathbf{N}]^T \; d\hat{B}_2 \right) \mathbf{u}_n, \quad n = 1, 2, 3, \ldots \tag{55}$$

Furthermore, from Eq. 22

$$\bar{F}_n = \rho\pi \; u_n^T \int_{\hat{B}_1} r \; [\mathbf{N}]^{\mathrm{T}} \hat{\mathbf{n}} d\hat{B}_1, \quad n = 1, 2, 3, \ldots \tag{56}$$

Upon computation of the above integrals, the sloshing masses M_{nC} are readily computed from Eq. 32, and the impulsive mass M_I from Eq. 33.

3.2 Numerical Implementation

The above modal-analysis methodology is implemented in a finite element programming environment and is used to compute sloshing frequencies and masses in spherical liquid containers. Triangular constant-strain elements with linear shape functions are employed to discretize the two-dimensional liquid domain $\hat{\Omega}$. Typical finite element meshes are shown in Fig. 5 for the half-full container.

It is important to notice that matrix [**M**] in the discretized eigenvalue problem (50) is computed through an appropriate integral on boundary $\hat{B}_2$, which is on the liquid free-surface. Therefore, the only non-zero elements of matrix [**M**] are the ones corresponding to nodes located on boundary $\hat{B}_2$. Separating the nodes on $\hat{B}_2$ from the rest of the nodes, the discretized eigenvalue problem can be written as follows,

$$\left[\begin{Bmatrix} [\mathbf{K}_{aa}] & [\mathbf{K}_{ab}] \\ [\mathbf{K}_{ba}] & [\mathbf{K}_{bb}] \end{Bmatrix} - \omega^2 \begin{Bmatrix} [\mathbf{M}_{aa}] & [\mathbf{0}] \\ [\mathbf{0}] & [\mathbf{0}] \end{Bmatrix} \right] \begin{pmatrix} \mathbf{u}_a \\ \mathbf{u}_b \end{pmatrix} = \mathbf{0} \tag{57}$$

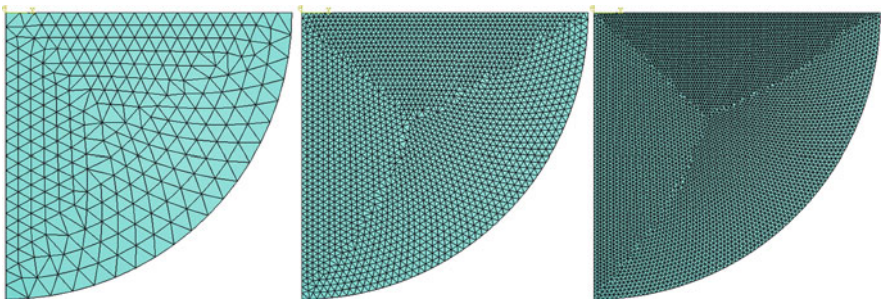


Fig. 5 Finite element meshes used in the finite element analysis with 20, 60 and 100 elements on the free surface boundary $\hat{B}_2(h = 1)$

where $\mathbf{u}_a$ corresponds to the nodes on $\hat{B}_2$, and $\mathbf{u}_b$ refers to remaining nodes, not located on $\hat{B}_2$. Matrix $[\mathbf{M}]$ is singular, and the number of non-infinite eigenvalues of (57) is equal to the number of nodes on boundary $\hat{B}_2$, whereas the rest of the eigenvalues have an infinite value. This causes numerical problems in the solution of the eigenvalue problem. Typical static condensation is employed to eliminate nodes $\mathbf{u}_b$ from the above problem. In such a case, the equations of the eigenvalue problem (57) can be replaced by the following set of equations:

$$\mathbf{u}_b = -\left[\mathbf{K}_{bb}\right]^{-1}\left[\mathbf{K}_{ba}\right]\mathbf{u}_a \tag{58}$$

$$\left(\left[\mathbf{K}'\right] - \omega^2\left[\mathbf{M}_{aa}\right]\right)\mathbf{u}_a = \mathbf{0} \tag{59}$$

where $[\mathbf{M}_{aa}]$ and $\left[\mathbf{K}'\right]$ are square symmetric matrices, and

$$\left[\mathbf{K}'\right] = \left[\mathbf{K}_{aa}\right] - \left[\mathbf{K}_{ab}\right]\left[\mathbf{K}_{bb}\right]^{-1}\left[\mathbf{K}_{ba}\right] \tag{60}$$

In all finite element meshes employed, the number of nodes on the free surface NF is significantly smaller than the total number of nodes N. Therefore, instead of solving the $N \times N$ eigenvalue problem (57), the condensed $NF \times NF$ eigenvalue problem (59) is solved, reducing significantly the computational cost and improving the numerical accuracy. Upon calculation of eigenfrequencies and eigenvectors $\mathbf{u}_a$ of problem (59), the eigenvectors $\mathbf{u} = [\mathbf{u}_a\ \mathbf{u}_b]^T$ of the complete problem (57) are calculated through Eq. 58.

3.3 Numerical Results

Using the above solution methodology, sloshing frequencies ω_n and masses M_{nC} are computed for a spherical vessel. Some representative results are presented in this paragraph, whereas for more numerical results the reader is referred to the paper by Karamanos et al. [20]. In Fig. 6, the sloshing frequencies are depicted in terms of the liquid depth ($h = H/R$) in a normalized form $\left(\lambda_n = \omega_n^2 R/g\right)$. The computed frequencies compare very well with test data [22]. The convergence of the numerical solution is shown in Table 1 in terms of the number of elements NFE in the free surface of the liquid ($NFE = NF - 1$), for the case of half-full spherical container. For the case of nearly-full containers ($h \to 2$), all sloshing frequencies approach an infinite value $\left(\lim_{h\to 2}\lambda_n = \infty\right)$. On the other hand, the sloshing frequencies corresponding to the nearly-empty container ($h \to 0$) are very consistent with the limit values reported in [18] $\left(\lim_{h\to 0}\lambda_n = 2n^2 - 1\right)$.

Figure 7 depicts the sloshing masses M_{nC} for spherical liquid containers filled up to an arbitrary depth ($0 < h < 2$), subjected to transverse excitation, normalized by the total liquid mass in the container M_L. The numerical results show that the

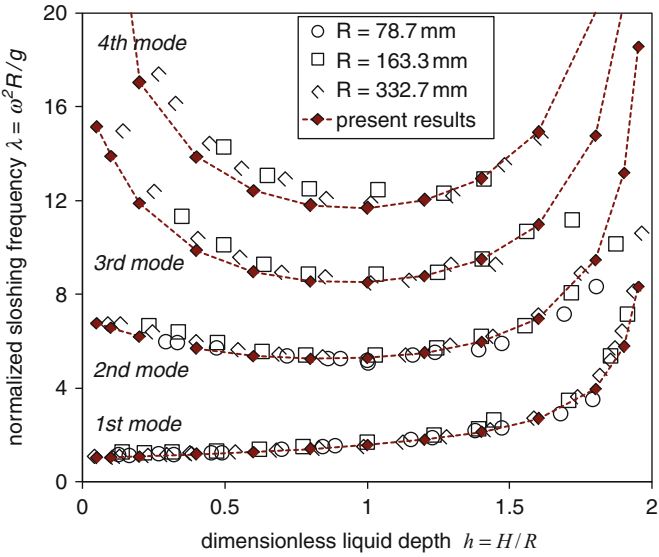


Fig. 6 Variation of sloshing frequencies corresponding to the first four sloshing modes with respect to the liquid height parameter h, computed from the finite element methodology; comparison with the experimental results from [22]

Table 1 Convergence of the first three sloshing frequencies with respect to the number of finite elements on the free surface ($NFE = NF - 1$) on the liquid surface $\hat{B}_2$ for $h = 1.4$ and $h = 1$, computed from the finite element solution methodology

Number of elements on free surface	λ_1	λ_2	λ_3	λ_4
20	1.5622	5.3413	8.7801	12.408
40	1.5610	5.2934	8.5761	11.867
60	1.5605	5.2834	8.5360	11.764
80	1.5604	5.2801	8.5226	11.729
100	1.5603	5.2785	8.5161	11.713
Ref. [16]	1.5602	5.2756	8.5044	11.684
Refs. [17, 18]	1.5602	5.2756	8.5044	11.684

first sloshing (convective) mass M_{1C} is a substantial part of the total liquid mass M_L, whereas the sloshing masses corresponding to higher modes are significantly smaller. In the case of nearly-full containers ($h \to 2$) the behavior becomes "impulsive", in the sense that the impulsive mass is approximately equal to the total liquid mass ($\mathsf{M}_I \to \mathsf{M}_L$). In such a case, sloshing effects are inconsequential. On the other hand, when the liquid height is very small ($h \to 0$), the behavior becomes "convective" in the sense that the impulsive mass is practically equal to zero $\mathsf{M}_I \to 0$. Furthermore, in the limit ($h \to 0$), the entire liquid mass is practically equal to the first sloshing mass ($\mathsf{M}_{1C} \to \mathsf{M}_L$), whereas sloshing masses corresponding to higher modes vanish [$\mathsf{M}_{nC} \to 0,\ n \geq 2$].

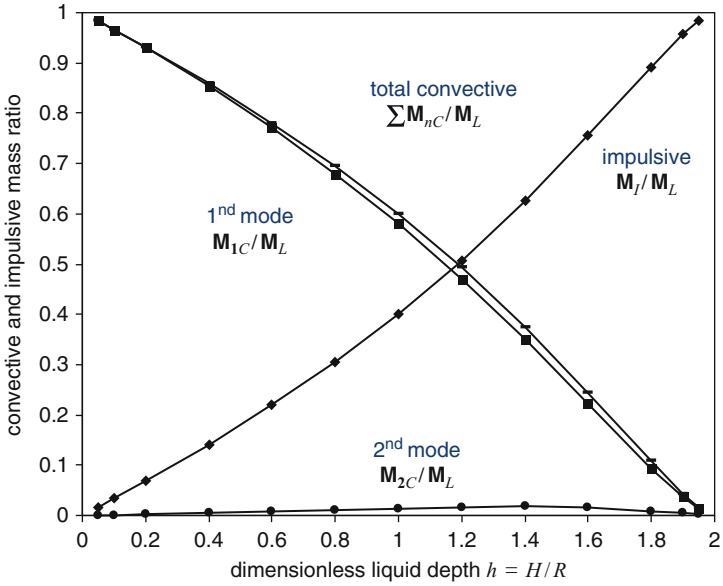


Fig. 7 Variation of sloshing masses corresponding to the first two sloshing modes and impulsive mass with respect to the liquid height parameter h, computed from the finite element methodology

4 Semi-analytical Solutions of Sloshing in Spherical Vessels

In this section, non-deformable spherical vessels are analyzed under horizontal excitation, using a special-purpose variational semi-analytical approach. First, in paragraph 4.1, the special case of hemi-spherical vessel is examined ($h = 1$), in terms of its sloshing frequencies and masses. Subsequently, in paragraph 4.2, a semi-analytical formulation and solution is presented for spherical vessels with arbitrary liquid height. The results are compared with the finite element results of the previous section, as well as with other semi-analytical results from previous publications.

The liquid with density ρ is contained inside a non-deformable spherical vessel ($h = 1$) of internal radius R. The origin of the Cartesian axes *x, y, z* coincides with the sphere centroid. In this section, spherical coordinates are considered, r, φ, θ, which are related to Cartesian coordinates *x, y, z* as follows (Fig. 8):

$$x = r \sin\varphi \cos\theta \tag{61}$$

$$y = r \cos\varphi \tag{62}$$

$$z = r \sin\varphi \sin\theta \tag{63}$$

The above convention is followed throughout Sect. 4. The spherical vessel is subjected to an arbitrary horizontal excitation along the Cartesian x axis with displacement $X(t)$.

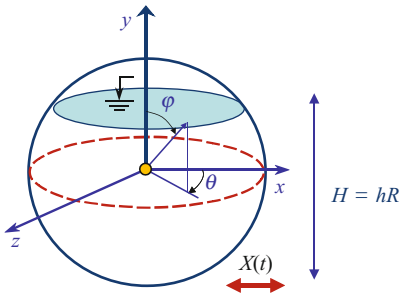


Fig. 8 Geometry of spherical vessel and spherical coordinates

4.1 Variational Solution for Half-Full Spherical Vessels

Galerkin's discretization is considered for the variational form of the problem expressed by Eq. 8:

$$\Phi_S = \sum_{n=1}^{\tilde{N}} s_n(t) N_n(r,\varphi,\theta) = [\mathrm{N}]\,\dot{\mathbf{s}} \tag{64}$$

$$\varphi^* = \sum_{n=1}^{\tilde{N}} s_n^* N_n(r,\varphi,\theta) = [\mathrm{N}]\,\mathbf{s}^* \tag{65}$$

where $N_n(r,\varphi,\theta)$ are known spatial functions, [**N**] is a row-matrix containing functions $N_n(r,\varphi,\theta)$, $\dot{\mathbf{s}}$ is a column vector with the unknown functions $\dot{s}_n(t)$ to be determined, the dot denotes time derivative, $\mathbf{s}^*$ is an arbitrary vector and $\tilde{N}$ is the truncation size. Differentiation of the above equations gives

$$\nabla\Phi_S = [\mathrm{B}]\,\dot{\mathbf{s}} \tag{66}$$

$$\nabla\varphi^* = [\mathrm{B}]\,\mathbf{s}^* \tag{67}$$

Substituting Eqs. 64–67 into the variational equation (8), one results in the following system of second-order linear ordinary differential equations:

$$[\mathbf{M}]\ddot{\mathbf{s}} + [\mathbf{K}]\mathbf{s} = -\mathbf{f}\,\ddot{X} \tag{68}$$

where

$$[\mathbf{M}] = \frac{1}{g}\int_{\mathrm{B}_2} [\mathbf{N}]^T [\mathbf{N}] dB_2 \tag{69}$$

$$[\mathbf{K}] = \int_{\Omega} [\mathbf{B}]^T [\mathbf{B}]\, d\Omega \tag{70}$$

$$\mathbf{f} = \frac{1}{g}\int_{B_2} x\, [\mathbf{N}]^{\mathrm{T}} dB_2 \tag{71}$$

The system of equations (68) can be integrated directly to provide the unknown functions $s_n(t)$ and their derivatives, so that the sloshing potential is determined. However, such an approach is computationally non-efficient and, alternatively, a modal analysis can be followed, as described in the following, based on the solution of the corresponding eigenvalue problem.

More specifically, the sloshing frequencies and the corresponding eigen-vectors are computed from the solution of the corresponding free-vibration eigenvalue problem

$$\left([\mathbf{K}] - \omega_n^2 [\mathbf{M}]\right) \mathbf{v}_n = 0 \quad n = 1, 2, 3, \ldots, \tilde{N} \tag{72}$$

where ω_n is the sloshing frequency of the nth mode, and $\mathbf{v}_n$ is the corresponding eigenvector. It is important to notice that the eigenvalue problem (72) constitutes the discretized form of the initial eigenvalue problem (10)–(12), presented in Sect. 2. Furthermore, it is straightforward to show that the eigen-functions (sloshing modes) $\Psi_n(r, \varphi, \theta)$ of problem (10)–(12) can be expressed in terms of the eigen-vectors of problem (72) as follows:

$$\Psi_n(r, \varphi, \theta) = [\mathbf{N}]\, \mathbf{v}_n \tag{73}$$

In our case, spherical harmonics are employed as base functions to express the sloshing potential:

$$N_n(r, \varphi, \theta) = r^n\, {P_n}^1(\mu) \cos\theta, \quad n = 1, 2, \ldots, \tilde{N} \tag{74}$$

where $\mu = \cos\varphi$ and ${P_n}^1(\mu)$ is the associated Legendre polynomial. The elements of the $3 \times \tilde{N}$ matrix $[\mathbf{B}]$ are

$$B_{1n} = \frac{\partial N_n}{\partial r} = n\, r^{n-1}\, {P_n}^1(\mu)\, \cos\theta, \quad n = 1, 2, \ldots, \tilde{N} \tag{75}$$

$$B_{2n} = \frac{1}{r}\frac{\partial N_n}{\partial \varphi} = -\, r^{n-1} \frac{\partial\, {P_n}^1(\mu)}{\partial \varphi} \cos\theta, \quad n = 1, 2, \ldots, \tilde{N} \tag{76}$$

$$B_{3n} = \frac{1}{r \sin\varphi} \cdot \frac{\partial N_n}{\partial \theta} = -r^{n-1}\, {P_n}^1(\mu)\, \frac{1}{\sin\varphi} \sin\theta, \quad n = 1, 2, \ldots, \tilde{N} \tag{77}$$

Substituting (74)–(77) into Eqs. 69–71, one obtains the symmetric matrices $[\mathbf{M}]$ and $[\mathbf{K}]$ and vector $\mathbf{f}$ with elements:

$$M_{mn} = \frac{\pi R^{m+n+2}}{g\,(m+n+2)}\, {P_m}^1(0)\, {P_n}^1(0), \quad m, n = 1, 2, \ldots, \tilde{N} \tag{78}$$

$$K_{mn} = \frac{\pi R^{m+n+1}}{m+n+1}\, (a_{mn} + b_{mn} + c_{mn}), \quad m, n = 1, 2, \ldots, \tilde{N} \tag{79}$$

where

$$a_{mn} = m\,n \int_0^1 {P_m}^1(\mu)\,{P_n}^1(\mu) d\mu, \quad m,n = 1,2,\ldots,\tilde{N} \tag{80}$$

$$b_{mn} = \int_0^1 \frac{{P_m}^1(\mu)\cdot {P_n}^1(\mu)}{1-\mu^2} d\mu, \quad m,n = 1,2,\ldots,\tilde{N} \tag{81}$$

$$c_{mn} = \int_0^1 \frac{\partial {P_m}^1(\mu)}{\partial \mu}\cdot\frac{\partial {P_n}^1(\mu)}{\partial \mu}\left(1-\mu^2\right) d\mu, \quad m,n = 1,2,\ldots,\tilde{N} \tag{82}$$

and

$$f_m = -\frac{\pi R^{m+3}}{g\,(m+3)} {P_m}^1(0), \quad m = 1,2,\ldots,\tilde{N} \tag{83}$$

An important observation regarding matrix [**M**] and vector **f** is that

$$M_{mn} = 0 \quad \text{if} \quad m = 2,4,6,\ldots \quad \text{or} \quad n = 2,4,6,\ldots \tag{84}$$

$$f_m = 0 \quad \text{if} \quad m = 2,4,6,\ldots \tag{85}$$

Therefore, separating odd and even equations, the homogeneous ODE system of the eigen-value problem (72) can also be written as follows,

$$\left[-\omega_k^2 \begin{Bmatrix} [\mathbf{M}_{aa}] & [\mathbf{0}] \\ [\mathbf{0}] & [\mathbf{0}] \end{Bmatrix} + \begin{Bmatrix} [\mathbf{K}_{aa}] & [\mathbf{K}_{ab}] \\ [\mathbf{K}_{ba}] & [\mathbf{K}_{bb}] \end{Bmatrix}\right] \begin{pmatrix} \mathbf{v}_{a,n} \\ \mathbf{v}_{b,n} \end{pmatrix} = \begin{pmatrix} \mathbf{0} \\ \mathbf{0} \end{pmatrix} \tag{86}$$

where

$$\mathbf{v}_{a,n} = \begin{bmatrix} v_1 & v_3 & v_5 & \ldots \end{bmatrix}^T \tag{87}$$

$$\mathbf{v}_{b,n} = \begin{bmatrix} v_2 & v_4 & v_6 & \ldots \end{bmatrix}^T \tag{88}$$

Using typical static condensation, Equations (86) can be replaced by the following set of equations:

$$\mathbf{v}_{b,n} = -\left[\mathbf{K}_{bb}\right]^{-1}\left[\mathbf{K}_{ba}\right]\mathbf{v}_{a,n} \tag{89}$$

$$\left(\left[\mathbf{K}'\right] - \omega_n^2[\mathbf{M}_{aa}]\right)\mathbf{v}_{a,n} = 0 \tag{90}$$

where $[\mathbf{M}_{aa}]$ and $\left[\mathbf{K}'\right]$ are square symmetric matrices with dimension $\tilde{N}/2$, and

$$\left[\mathbf{K}'\right] = [\mathbf{K}_{aa}] - [\mathbf{K}_{ab}]\left[\mathbf{K}_{bb}\right]^{-1}\left[\mathbf{K}_{ba}\right] \tag{91}$$

Therefore, instead of solving the eigen-value problem (72) or (86), one can solve the reduced eigen-value problem expressed by equations (90), eliminating the zero-mass equations, thus increasing the computational efficiency and the accuracy of the results.

Upon calculation of sloshing frequencies and the corresponding eigen-vectors, sloshing masses and hydrodynamic forces are calculated, using the procedure described by Eqs. 19–34, where the sloshing mode functions $\Psi_n(r, \varphi, \theta)$ are given by Eq. 73. One can easily show that $\bar{M}_n$, $\bar{P}_n$ and $\bar{F}_n$ can be written as follows:

$$\bar{M}_n = \mathbf{v}_n^T [\mathbf{M}] \mathbf{v}_n, \quad n = 1, 2, 3, \ldots NM \tag{92}$$

$$\bar{P}_n = \mathbf{v}_n^T \mathbf{f}, \quad n = 1, 2, 3, \ldots NM \tag{93}$$

$$\bar{F}_n = \rho \, \Psi_n^T \, \boldsymbol{\beta}, \quad n = 1, 2, 3, \ldots NM \tag{94}$$

where NM is the number of modes considered in the modal analysis

$$\boldsymbol{\beta} = \int_{B_1} [\mathbf{N}]^T (\mathbf{n} \cdot \mathbf{e}_x) dB_1 \tag{95}$$

Considering the harmonic shape functions of Eq. 74 and taking into account that $\mathbf{n} \cdot \mathbf{e}_x = \sin\varphi \cos\theta$, the following expression for the elements of $\boldsymbol{\beta}$ is obtained:

$$\beta_m = \pi R^{m+2} \int_0^1 {P_m}^1 (\mu) \sqrt{1 - \mu^2} d\mu \tag{96}$$

In Table 2, the convergence of the variational methodology for the first three sloshing frequencies of the half-full spherical vessel is shown. Excellent comparison

Table 2 Convergence of the first three sloshing frequencies with respect to the order of truncation computed from the present semi-analytical variational methodology for a half-full spherical container ($h = 1$)

	$\lambda_1 = \omega_1^2 R/g$		$\lambda_2 = \omega_2^2 R/g$		$\lambda_3 = \omega_3^2 R/g$	
$\tilde{N}$	Refs. [17, 18]	Present method	Refs. [17, 18]	Present method	Refs. [17, 18]	Present method
2	1.3333	1.7292				
4	1.5810	1.5618	2.9741	13.9530		
6	1.5550	1.5602		5.8041		98.334
8	1.5582	1.5602	4.3928	5.3063		13.633
10	1.5590	1.5602		5.2764		9.1101
12	1.5595	1.5602	5.1566	5.2756		8.5725
14	1.5597	1.5602	5.2919	5.2756	6.7591	8.5094
16	1.5599	1.5602	5.2720	5.2756		8.5047
18	1.5599	1.5602	5.2742	5.2756	7.9737	8.5045
20	1.5600	1.5602	5.2744	5.2756		8.5045
22	1.5600	1.5602	5.2747	5.2756	8.4691	8.5045
24	1.5600	1.5602	5.2748	5.2756	8.5071	8.5045
26	1.5600	1.5602	5.2749	5.2756	8.5028	8.5045
28	1.5600	1.5602	5.2750	5.2756	8.5035	8.5045
30	1.5601	1.5602	5.2751	5.2756	8.5036	8.5045
40	1.5601	1.5602	5.2753	5.2756	8.5040	8.5045

is obtained in terms of the converged values with the corresponding sloshing frequencies from recent publications [16, 17], which follow a different semi-analytical solution methodology. It is interesting to note that relatively few terms are required for convergence, and that the convergence rate of the present solution methodology is significantly superior than the one reported in [16] and [17].

The sloshing mass ratios of the half-full sphere over the entire liquid mass M_L are tabulated in Table 3, indicating that sloshing masses corresponding to higher modes ($NM \geq 4$) are negligible. Furthermore, it can be concluded that for the half-full spherical vessel, approximately 60% of the total mass is impulsive and 40% of the total mass is impulsive. In Fig. 9, the sloshing force obtained from the above analysis, for a half-full spherical container is compared with the test data of Stofan and Armstead [23]. The container is subjected to sinusoidal external excitation, $X(t) = X_{\max} \sin \omega t$, where ω is the excitation frequency, the ratio of the displacement amplitude of the sinusoidal excitation $X_{\max}$ over the sphere diameter D is equal to 6.7×10^{-3}, and the force amplitude is normalized by $F_N = 4\rho g\, R^2 X_{\max}$. The present results are in good agreement with the test data. Differences between

Table 3 Converged values of sloshing masses for the first four sloshing modes and impulsive mass computed from the present semi-analytical variational methodology for a half-full spherical container ($h = 1$), computed from the semi-analytical variational methodology

$\frac{\mathsf{M}_{1C}}{\mathsf{M}_L}$	$\frac{\mathsf{M}_{2C}}{\mathsf{M}_L}$	$\frac{\mathsf{M}_{3C}}{\mathsf{M}_L}$	$\frac{\mathsf{M}_{4C}}{\mathsf{M}_L}$	$\sum \frac{\mathsf{M}_{nC}}{\mathsf{M}_L}$	$\frac{\mathsf{M}_I}{\mathsf{M}_L}$
0.5797	0.0146	0.0037	0.0015	0.6059	0.3941

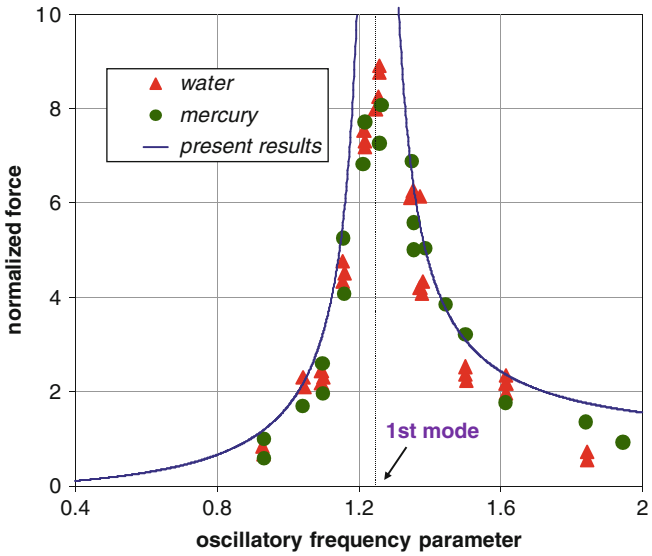


Fig. 9 Comparison between experimental results in water and mercury, and present results, for half-full spherical vessels under sinusoidal excitation, computed from the semi-analytical variational methodology (Test data reported by Stofan and Armstead [23])

the present results and the test data exist at values of ω very close to the first sloshing frequency ω_1 (resonance), due to nonlinear effects, which are not considered in the present study. For more results from this solution methodology, the reader is referred to the paper by Patkas and Karamanos [21].

4.2 Variational Solution for Spherical Vessels with Arbitrary Liquid Height

A non-deformable spherical container of internal radius equal to R is considered (Fig. 8), and the liquid surface inside the container is at an arbitrary position ($0 < h < 2$). The origin of the Cartesian axes *x, y, z* coincides with the sphere centroid, and the spherical coordinates r, φ, θ are related to the Cartesian coordinates *x, y, z* as expressed by Eqs. 61–63. The vessel is subjected to an arbitrary horizontal excitation along the x axis with displacement $X(t)$.

Sloshing frequencies and hydrodynamic forces are computed expressing the unknown function in a series of the spherical harmonic functions of Eq. 74 through a variational formulation, which is based on Eq. 8. More specifically, Eq. 8 for the purposes of the present analysis is integrated by parts to provide

$$\int_B \frac{\partial \Phi_S}{\partial n}\,\varphi^*\,dB - \int_\Omega \left(\nabla^2 \Phi_S\right)\varphi^*\,d\Omega + \frac{1}{g}\int_{B_2} \frac{\partial^2 \Phi_S}{\partial t^2}\,\varphi^*\,dB_2 = -\frac{\dddot{X}}{g}\int_{B_2} x\,\varphi^*\,dB_2 \tag{97}$$

If harmonic functions are used to express the sloshing potential Φ_S, then $\nabla^2 \Phi_S = 0$ and the above equation becomes

$$\int_{B_1} \frac{\partial \Phi_S}{\partial n}\,\varphi^*\,dB_1 + \int_{B_2} \frac{\partial \Phi_S}{\partial n}\,\varphi^*\,dB_2 + \frac{1}{g}\int_{B_2} \frac{\partial^2 \Phi_S}{\partial t^2}\,\varphi^*\,dB_2 = -\frac{\dddot{X}}{g}\int_{B_2} x\,\varphi^*\,dB_2 \tag{98}$$

Therefore, the volume integral in the left-hand side of Eq. 97 is transformed to a boundary integral, which is easier to calculate. Thus, matrix [**K**] is computed as follows

$$[\mathbf{K}] = \int_{B_1} [\mathbf{N}]^T \frac{\partial [\mathbf{N}]}{\partial n}\,dB_1 + \int_{B_2} [\mathbf{N}]^T \frac{\partial [\mathbf{N}]}{\partial n}\,dB_2 \tag{99}$$

Note that a similar variational formulation was used by Moissev and Petrov [15] for the eigenvalue sloshing problem in spherical containers.

Substitution of the spherical harmonic functions $N_n(r, \theta, \Psi)$ of Eq. 74 into Eqs. 69, 99 and 71 provides the elements of [**M**], [**K**] and **f** respectively. To compute the integrals of the shape functions on B_1 and B_2, the two cases $h > 1$ and $h < 1$

are considered separately. If $h > 1$, the y axis is chosen upward (as shown in Fig. 7), so that at the free surface B_2, the following equations are valid

$$r = \frac{h-1}{\cos\varphi} R \tag{100}$$

$$\frac{\partial N_n}{\partial n} = \cos\varphi \left(\frac{\partial N_n}{\partial r} - \frac{\sin\varphi}{H-R} \cdot \frac{\partial N_n}{\partial \varphi} \right) \tag{101}$$

and

$$\int_{B_2} \ldots dB_2 = 2\pi (H-R)^2 \int_0^{\varphi_0} \ldots \frac{\sin\varphi}{\cos^3\varphi} d\varphi \tag{102}$$

whereas at "wet" surface of the spherical container B_1, $r = R$, and

$$\int_{B_1} \ldots dB_1 = 2\pi R^2 \int_{\varphi_0}^{\pi} \ldots \sin\varphi \, d\varphi \tag{103}$$

where φ_0 is given by the following equation:

$$\varphi_0 = \arccos(h-1) \tag{104}$$

If $h < 1$, the y axis is chosen downward (opposite to the one shown in Fig. 7), so that at the free surface B_2 the following equations are valid,

$$r = \frac{1-h}{\cos\varphi} R \tag{105}$$

$$\frac{\partial N_n}{\partial n} = \cos\varphi \left(\frac{\partial N_n}{\partial r} - \frac{\sin\varphi}{R-H} \cdot \frac{\partial N_n}{\partial \varphi} \right) \tag{106}$$

and

$$\int_{B_2} \ldots dB_2 = 2\pi (H-R)^2 \int_{\varphi_0}^{\pi} \ldots \frac{\sin\varphi}{\cos^3\varphi} d\varphi \tag{107}$$

whereas at "wet" surface of the spherical container B_1, $r = R$, and

$$\int_{B_1} \ldots dB_1 = 2\pi R^2 \int_{\varphi_0}^{\pi} \ldots \sin\varphi \, d\varphi \tag{108}$$

where φ_0 is given by the following expression

$$\varphi_0 = \arccos(1-h) \tag{109}$$

Inserting harmonic functions $N_n(r,\varphi,\theta)$ and conducting the appropriate integrations, the elements of [**M**], [**K**] and **f** are given by the following expressions:

$$M_{mn} = \begin{cases} \frac{(H-R)^{n+m+2}}{g} \int_\alpha^\beta \frac{P_n{}^1(\mu)\, P_m{}^1(\mu)}{\mu^{n+m+3}}\, d\mu, & h > 1 \\ & m,n = 1,2,\ldots \tilde{N} \\ \frac{(R-H)^{n+m+2}}{g} \int_\alpha^\beta \frac{P_n{}^1(\mu)\, P_m{}^1(\mu)}{\mu^{n+m+3}}\, d\mu, & h < 1 \end{cases} \quad (110)$$

$$K_{mn} = \begin{cases} (m+1)\,(H-R)^{n+m+1} \int_\alpha^\beta \frac{P_n{}^1(\mu)\, P_{m-1}{}^1(\mu)}{\mu^{n+m+3}}\, d\mu + \\ \quad + mR^{n+m+1} \int_{-1}^\gamma P_n{}^1(\mu)\, P_m{}^1(\mu)\, d\mu, \quad h > 1 \\ & m,n = 1,2,\ldots \tilde{N} \\ -(m+1)\,(R-H)^{n+m+1} \int_\alpha^\beta \frac{P_n{}^1(\mu)\, P_{m-1}{}^1(\mu)}{\mu^{n+m+3}}\, d\mu + \\ \quad + mR^{n+m+1} \int_\gamma^1 P_n{}^1(\mu)\, P_m{}^1(\mu)\, d\mu, \quad h < 1 \end{cases} \quad (111)$$

$$f_m = \begin{cases} \frac{(H-R)^{m+3}}{g} \int_\alpha^\beta \frac{P_m{}^1(\mu)\sqrt{1-\mu^2}}{\mu^{m+4}}\, d\mu, & h > 1 \\ & m = 1,2,\ldots \tilde{N} \\ \frac{(R-H)^{m+3}}{g} \int_\alpha^\beta \frac{P_m{}^1(\mu)\sqrt{1-\mu^2}}{\mu^{m+4}}\, d\mu, & h < 1 \end{cases} \quad (112)$$

where

$$\begin{aligned} \alpha = \gamma &= \tfrac{H-R}{R}, \quad \beta = 1, \quad h > 1 \\ \alpha = \gamma &= \tfrac{R-H}{R}, \quad \beta = 1, \quad h < 1 \end{aligned} \quad (113)$$

Using matrices [**M**] and [**K**], the sloshing frequencies of a spherical container with arbitrary liquid height can be computed, from the corresponding eigenvalue problem

$$\left([\mathbf{K}] - \omega_n^2 [\mathbf{M}]\right) \mathbf{v}_n = 0, \quad n = 1,2,3,\ldots \tilde{N} \quad (114)$$

Table 4 shows the values of normalized sloshing frequencies $\left(\lambda_n = \omega_n^2 R/g\right)$ with respect to the liquid height parameter h. The sloshing frequencies are in very good agreement with the finite element results depicted in Fig. 6, and compare very well with the numerical results of McIver [16], as well as the experimental values of McCarty and Stephens [22], also shown in Fig. 6. It is interesting to note that the present numerical results indicate that convergence is more rapid for relatively shallow containers (small values of h), as shown in Table 4. Sloshing frequencies approach an infinite value for $h \to 2$, whereas for small values of h the numerical values of $\lambda_n = \omega_n^2 R/g$ are consistent with the analytical values obtained by Budiansky [18] ($\lambda_n = 2n^2 - 1, \quad n = 1,2,3,\ldots$).

Table 4 Normalized values of sloshing frequencies $\left(\lambda_n = \omega_n^2 R/g\right)$ for the first four modes computed from the semi-analytical variational methodology; comparison with the semi-analytical results of McIver [16]

	Present methodology				McIver [16]			
H	λ_1	λ_2	λ_3	λ_4	λ_1	λ_2	λ_3	λ_4
0.05	1.0170	6.7726	15.1315	30.020				
0.1	1.0347	6.5638	13.8911	26.757				
0.2	1.0723	6.2008	11.8764	17.032	1.0723	6.2008	11.8821	17.359
0.4	1.1583	5.6742	9.8543	13.866	1.1583	5.6742	9.8551	13.869
0.6	1.2625	5.3683	8.9418	12.421	1.2625	5.3683	8.9418	12.423
0.8	1.3924	5.2406	8.5509	11.800	1.3924	5.2406	8.5509	11.800
1.0	1.5602	5.2756	8.5045	11.684	1.5602	5.2756	8.5044	11.684
1.2	1.7882	5.4930	8.7793	12.021	1.7882	5.4930	8.7793	12.021
1.4	2.1232	5.9729	9.4763	12.938	2.1232	5.9728	9.4762	12.938
1.6	2.6864	6.9574	10.9566	14.918	2.6864	6.9571	10.9557	14.916
1.8	3.9595	9.4551	14.7598	20.033	3.9593	9.4535	14.7548	20.022
1.9	5.7615	13.1776	20.4520	27.702				
1.95	8.3121	18.5527	28.6891	38.816				

Furthermore, the elements of $\boldsymbol{\beta}$ are the following:

$$\beta_n = \begin{cases} \pi R^{n+2} \int_{-1}^{\gamma} P_m{}^1(\mu)\, \sqrt{1-\mu^2}\, d\mu, & h > 1 \\ \\ \pi R^{n+2} \int_{\gamma}^{1} P_m{}^1(\mu)\, \sqrt{1-\mu^2}\, d\mu, & h < 1 \end{cases} \qquad n = 1, 2, \ldots \tilde{N} \tag{115}$$

and are used to calculate the sloshing masses and the hydrodynamic forces, whereas the total liquid mass M_L is given by the following expression in terms of the liquid height:

$$\mathsf{M}_L = \rho \frac{4}{3} \pi R^3 \left[1 - \frac{1}{4} (2-h)^2\, (1+h) \right] \tag{116}$$

Table 5 shows the variation of the first four sloshing masses M_{nC} and the impulsive mass M_I with respect to the liquid height. The numerical results show that the first sloshing mass M_{1C} constitutes a substantial part of the total liquid mass M_L, whereas the sloshing masses M_{nC} corresponding to higher modes are significantly smaller $(n \geq 2)$. The sloshing and impulsive masses are in excellent agreement with the finite element results,plotted in Fig. 7. The behavior is quasi-impulsive for $h \to 2$ whereas for small values of h (i.e. for $h \to 0$), the total liquid mass is practically equal to the first sloshing mass. It can be shown [18], that the first sloshing mode for the nearly empty container $(h \to 0)$, coincides with the first term of the series solution $\left(N_1 = r\, P_1^1(\mu) \cos\theta\right)$.

Table 5 Ratios of sloshing masses for the first four sloshing modes M_{nC} and impulsive mass M_I over the total liquid mass M_L for spherical container with respect to the liquid height ($h = 1$), computed from the semi-analytical variational methodology

H	$\frac{\mathsf{M}_{1C}}{\mathsf{M}_L}$	$\frac{\mathsf{M}_{2C}}{\mathsf{M}_L}$	$\frac{\mathsf{M}_{3C}}{\mathsf{M}_L}$	$\frac{\mathsf{M}_{4C}}{\mathsf{M}_L}$	$\sum \frac{\mathsf{M}_{nC}}{\mathsf{M}_L}$	$\frac{\mathsf{M}_I}{\mathsf{M}_L}$
0.05	0.98315	0.000102	0.0000005	0.0000000	0.98326	0.01674
0.1	0.96594	0.000387	0.0000064	0.0000003	0.96634	0.03366
0.2	0.93038	0.001374	0.0000667	0.0000104	0.93184	0.06816
0.4	0.85437	0.004341	0.0005155	0.0001406	0.85947	0.14053
0.6	0.77117	0.007850	0.0013969	0.0004640	0.78136	0.21864
0.8	0.67990	0.011396	0.0025337	0.0009401	0.69619	0.30381
1.0	0.57969	0.014576	0.0037169	0.0014976	0.60594	0.39406
1.2	0.46981	0.016874	0.0047195	0.0020190	0.49844	0.50156
1.4	0.35009	0.017526	0.0052523	0.0023532	0.38440	0.61560
1.6	0.22222	0.015419	0.0048997	0.0022806	0.26162	0.73838
1.8	0.09363	0.009185	0.0031036	0.0014989	0.12608	0.87392
1.9	0.03655	0.004387	0.0015438	0.0007635	0.05586	0.94414
1.95	0.01364	0.001851	0.0006696	0.0003361	0.01810	0.98190

5 Conclusions

Two solution methodologies have been developed for externally-induced sloshing in spherical liquid containers, subjected to horizontal excitation. The first methodology results in an eigenvalue problem, which is solved using either standard finite elements for the sloshing frequencies and modes. The second methodology is semi-analytical, and it is based on a Galerkin discretization in terms of harmonic functions that allows for high-precision calculation of sloshing frequencies and masses with very good convergence. In both methodologies, the application of a static condensation technique results in a significant reduction of the size of the eigenvalue problem, increasing significantly both computational efficiency and accuracy of the methodology. The calculation of sloshing frequencies and masses leads to a simple and efficient methodology for predicting the dynamic response of spherical vessels. Furthermore, the results indicate that seismic force calculations based on the first sloshing mass only are adequate to represent sloshing behavior accurately. The results are in very good agreement with results from analytical or numerical solutions reported elsewhere, as well as with available experimental data.

References

1. Abramson HN (1966) The dynamic behavior of liquids in moving containers. Southwest Research Institute, NASA SP-106, Washington, DC
2. Ibrahim RA, Pilipchuk VN, Ikeda T (2001) Recent advances in liquid sloshing dynamics. Appl Mech Rev ASME 54(2):133–177
3. Housner GW (1957) Dynamic pressures on accelerated fluid containers. Bull Seismol Soc Am 47:15–35

4. Veletsos AS (1974) Seismic effects in flexible liquid storage tanks. In: Proceedings of the fifth world conference on earthquake engineering, vol 1. Rome, Italy, pp 630–639
5. Haroun MA, Housner GW (1981) Earthquake response of deformable liquid storage tanks. J Appl Mech ASME 48:411–417
6. Haroun MA (1983) Vibration studies and tests of liquid storage tanks. Earth Eng Struct Dyn 11:179–206
7. Natsiavas S (1988) An analytical model for unanchored fluid-filled tanks under base excitation. J Appl Mech ASME 55:648–653
8. Veletsos AS, Tang Y (1990) Soil-structure interaction effects for laterally excited liquid storage tanks. Earth Eng Struct Dyn 19:473–496
9. Malhotra PK (1995) Base uplifting analysis of flexibly supported liquid-storage tanks. Earth Eng Struct Dyn 24(12):1591–1607
10. Fisher FD (1979) Dynamic fluid effects in liquid-filled flexible cylindrical tanks. Earth Eng Struct Dyn 7:587–601
11. Rammerstorfer FG, Fisher FD, Scharf K (1990) Storage tanks under earthquake loading. Appl Mech Rev ASME 43(11):261–283
12. American Petroleum Institute (2000) Seismic Design of Storage Tanks, Appendix E, Welded steel tanks for oil storage, API Standard 650, Washington, DC
13. Comité Européen de Normalization (2006) Part 4: Silos, tanks and pipelines, Eurocode 8, part 4, Annex A, Design of structures for earthquake resistance, CEN ENV-1998, Brussels
14. Priestley MJN, Davidson BJ, Honey GD, Hopkins DC, Martin RJ, Ramsey G, Vessey JV, Wood JH (1986) Seismic design of storage tanks, Recommendations of a Study Group of the New Zealand National Society for Earthquake Engineering
15. Moiseev NN, Petrov AA (1966) The calculation of free oscillations of a liquid in a motionless container. Adv Appl Mech 9:91–154
16. McIver P (1989) Sloshing frequencies for cylindrical and spherical containers filled to an arbitrary depth. J Fluid Mech 201:243–257
17. Evans DV, Linton CM (1993) Sloshing Frequencies. Quart J Mech Appl Math 46:71–87
18. Budiansky B (1960) Sloshing of liquids in circular canals and spherical tanks. J Aero/Space Sci 27(3):161–173
19. Papaspyrou S, Valougeorgis D, Karamanos SA (2003) Refined solutions of externally induced sloshing in half-full spherical containers. J Eng Mech 129(12):1369–1379
20. Karamanos SA, Papaprokopiou D, Platyrrachos MA (2009) Finite element analysis of externally-induced sloshing in horizontal-cylindrical and axisymmetric industrial vessels. J Press Vess Technol ASME 131(5): 051301
21. Patkas LA, Karamanos SA (2007) Variational solutions of liquid sloshing in horizontal-cylindrical and spherical containers. J Eng Mech ASCE 133(6):641–655
22. McCarty JL, Stephens D (1960) Investigation of the natural frequencies of fluids in spherical and cylindrical tanks. Report NASA TN D-252, Washington, DC
23. Stofan AJ, Armstead AL (1962) Analytical and experimental investigation of forces and frequencies resulting from liquid sloshing in a spherical tank. Technical Note, NASA TN D-1281, Washington, DC

A Bilevel Optimization Model for Large Scale Highway Infrastructure Maintenance Inspection and Scheduling Following a Seismic Event

Manoj K. Jha, Konstantinos Kepaptsoglou, Matthew Karlaftis, and Gautham Anand Kumar Karri

Abstract Major highway infrastructure elements, in need of post-earthquake maintenance for improved highway life-cycle, motorist's guidance, and safety, include bridges, pavements, interchanges, and tunnels. In addition, there are numerous, minor infrastructure elements vital to motorist's guidance and safety, such as overhead and roadside appurtenances, including signs, guardrails, and luminaries. The maintenance and upkeep of all infrastructure components is crucial for mobility, driver safety and guidance, and overall efficient functioning of a highway system. Successive research efforts have been made in developing optimal Maintenance Repair and Rehabilitation (MR&R) strategies for major infrastructure components, such as pavements and bridges. However, there has been limited studies reported on Maintenance Inspection and Scheduling (MI&S) of minor infrastructure elements, such as signs, guardrails, and luminaries, particularly after the occurrence of seismic events. Typically, a field inspection of such elements is carried out at fixed time intervals to determine their condition, which is used to develop optimal MR&R plan over a given planning horizon, which is not. In this paper we introduce a bilevel model for developing an optimal MI&S plan for large-scale highway infrastructure elements, following a seismic event. At the lower level a set of optimal inspection routes is obtained, which is used at the upper level to obtain optimal maintenance schedule over a given planning horizon. Separate algorithms are developed for solving the lower and upper level optimization models, including a genetic algorithm for solving the lower level model and a customized heuristic for solving the upper level model. A numerical example using a real highway network from Maryland is presented. Finally, directions for future work are discussed.

M.K. Jha and G.A.K. Karri
Department of Civil Engineering, Morgan State University, 1700 E. Cold Spring Lane, Baltimore, MD 21251, USA
e-mail: manoj.jha@morgan.edu; kgautham.anand@gmail.com

K. Kepaptsoglou and M. Karlaftis (✉)
School of Civil Engineering, National Technical University of Athens, 5 Iroon Polytechniou Str, Zografou Campus, 15773, Athens, Greece
e-mail: kkepap@transport.ntua.gr; mgk@transport.ntua.gr

M. Papadrakakis et al. (eds.), *Computational Methods in Earthquake Engineering*, Computational Methods in Applied Sciences 21, DOI 10.1007/978-94-007-0053-6_22,
© Springer Science+Business Media B.V. 2011

1 Introduction

Highways are major lifelines and therefore have a primary role in human activities. Furthermore, they consist of various infrastructure elements, highly prone to earthquakes; as a result, a seismic event can drastically affect and degrade highway operations, and disrupt highway connectivity between areas. In that context, reactions such as post-event inspection, repair and maintenance are required for restoring operations of highways after seismic events [12]. Past work on post-event actions has mainly focused on bridges, which are probably the most sensitive parts of the highway with respect seismic events (for example, see [11, 12]). Alternatively, when it comes to developing an effective post-earthquake maintenance plan for roadside features, such as signs, guardrails, and luminaries it is not the cost of individual features that is of great concern, rather it is their quantity which often makes it difficult to develop an optimal maintenance plan. For example, along any highway section, especially in urban areas one can find numerous roadside signs, guardrails, and luminaries. One missing or damaged sign or guardrail may lead to confusion and endanger the motoring public that may eventually lead to disastrous consequences, including liability concerns. Due to the capital intensive nature of highway elements, such as pavements and bridges most of the research in the last decade have been focused in developing optimal maintenance repair and rehabilitation (MR&R) policies for those elements, both in the normal and post earthquake level.

This work is an extension of previous work [7, 9] in developing a maintenance management model for roadside features, with particular application to post-earthquake conditions. We introduce a bilevel optimization approach in which a set of optimal inspection routes are obtained at the lower level along which optimal MR&R policies are obtained at the upper level. In our previous work, we developed a model for obtaining an optimal maintenance plan of three roadside features namely, signs, guardrails, and luminaries. The optimization model formulation was based on the analysis of pavement maintenance by the pioneering work of Golabi et al. [3]. One of the limitations of our previous work (not applicable in the case of post-event approach) was that we treated the MR&R trigger at routine (fixed) intervals. This assumption allows the MR&R modeling computationally convenient as it treats the sequential decision-making over a given planning horizon to exhibit Markovian property. Many researchers, while acknowledging this limitation, have still assumed Markovian property for obtaining optimal MR&R for similar applications, such as pavement and bridge maintenance. The sequential nature of decision making also allowed the application of dynamic programming in solving the optimization model even though it has been acknowledged that dynamic programming becomes computationally inefficient as the size of a problem increases.

The rest of the paper provides a brief synopsis of prior modeling efforts and the new probabilistic bilevel formulation and possible solution approach with a genetic algorithm and a customized heuristic. A numerical example is then presented followed by conclusions, recommendations, and directions for future work.

2 Methodology

In developing optimal MR&R strategy for individual roadside features we extended Golabi's analysis for pavement and bridge maintenance modeling [3, 4]. The deterministic approach is first presented which sets the stage for developing the probabilistic approach.

2.1 Routine Maintenance (Deterministic Approach)

The formulation for routine maintenance [7] assumes maintenance inspection and implementation of maintenance actions (also referred to as "policies" in the literature) at predetermined discrete time intervals (typically, every year).

Let k $= 1, 2, \ldots\ldots, K$ be the total number of roadside features within the analysis highway section. Let $j = 1, 2, \ldots\ldots, J$ represent possible maintenance actions (policies) to be undertaken, $i = 1, 2, \ldots I$ possible condition states of the appurtenances, and $t = 1, 2, \ldots\ldots, T$ possible time periods for the analysis. Then the objective function for the routine maintenance case can be expressed as:

$$Min \sum_{t=1}^{T} \sum_{k=1}^{K} \sum_{i=1}^{I} \sum_{j=1}^{J} \alpha^t w_{kij}^t \, c(k, i, j) \tag{1}$$

where, α^t is the discount factor at time t, w_{kij}^t is the probability that feature k will be in condition state i if action j is applied in time t; and $c(k, i, j)$ is the maintenance cost of feature k for applying action j resulting in its condition state i. The constraints are given as:

$$w_{kij}^t \geq 0 \quad \forall k, i, j, t \tag{2}$$

$$\sum_i \sum_j w_{kij}^t = 1 \quad \forall k, t \tag{3}$$

$$\sum_j w_{kij}^1 = q_{ki}^1 \quad \forall k, i \tag{4}$$

$$\sum_j w_{k(i+1)j}^t = \sum_i \sum_j w_{kij}^{t-1} \, p_{ki(i+1)}(j) \quad \forall k, (i+1) \tag{5}$$

$$\sum_k \sum_i \sum_j \alpha^t c(k, i, j) \leq B^t \quad \forall t \tag{6}$$

Equation (2) ensures that condition probability is always non-negative. Equation (3) ensures that total condition probability is 1. Equation (4) implies that condition state at the beginning of the analysis (year 1) is known and Eq. (5) specifies the likelihood that condition state will move from i to $(i + 1)$ in year t if action j is applied in

the previous year $(t-1)$. Equation (6) implies that the total maintenance cost in a given year cannot exceed available budget for that year. B^t is the available budget in year t.

2.2 Reactive Maintenance (Probabilistic Approach)

Due to random incidents, such as earthquakes, inclement weather and accidents the roadside features may deteriorate earlier than their expected life-span, which leads to reactive maintenance. The conditions in this case are identified from a random inspection rather than inspections at fixed-time (discrete) intervals. In addition, a minor fix may be satisfactory in lieu of full replacement of the damaged roadside features depending on the level of deterioration.

We assume that while earthquakes are unpredictable and damage caused by such incidents is also unpredictable, the required inspection of roadside features will depend on the probability of an earthquake. The deterministic formulation is modified as follows to reflect the probabilistic case [9]:

$$Min \sum_{t=1}^{T} \sum_{k=1}^{K} \sum_{i=1}^{I} \sum_{j=1}^{J} \alpha^t w_{kij}^t \; c(k,i,j) \left[1 + \min\left\{\gamma(P_{ki}^t), 1\right\}\right] \tag{7}$$

where,

$$\begin{cases} \gamma(P_{ki}^t) = 1 \; if \; P_{ki}^t \geq C \\ 0 \quad otherwise \end{cases} \tag{8}$$

In Eq. (8) P_{ki}^t is the probability of an earthquake affecting feature k which is in condition i at time t. If this probability is greater than a threshold value, say C (on a scale of 0–1) then appropriate maintenance action should be undertaken to improve the feature's condition to bring it up to an acceptable level subject to the budget constraint. The acceptable level of service (or, quality) C of deteriorated features can be adjusted by user feedback and experience in practical situations. The other constraints under this case are same as Eqs. (2)–(6).

Please note that in the above formulation the definition of t has been revised. $T = 1, \ldots, T$ are random time intervals (instead of fixed time intervals) at which earthquake probabilities affecting the feature condition are estimated. This can be estimated by analyzing historical trends specific to a geographic region and traffic conditions. In the above formulation we have still not addressed two key issues: (1) the assumption that MR&R actions are undertaken at fixed intervals only and (2) the possibility of a minor (intermediate) repair scenario, in addition to the "do nothing" alternative. These issues will be addressed in our future work.

2.3 The Bilevel Optimization Approach

Bilevel Programming concept [20], is fairly new, and is being applied increasingly on various transportation problems. In a bilevel optimization problem two separate levels of the objective function are defined, namely the lower level and the upper level. The optimal lower level decision variables are first obtained which are fed to the variables in the upper level since upper level objective is expressed a function of some of the lower level variables. Upon the upper level optimization the final optimal solution and corresponding decision variables are obtained. The entire process works as a loop, i.e., the process is repeated until no significant improvement is noted in the objective functions at both levels. As an example, a typical formulation of the bi-level programming problem used for the Dynamic Network Design Problem [10, 21] is described as follows:

Upper Level Problem

$$\begin{aligned} &\underset{\mathbf{u}}{Minimize}\ \ F\ (\mathbf{u},\ \mathbf{v}(\mathbf{u})) \\ &subject\ to\ G\ (\mathbf{u},\ \mathbf{v}(\mathbf{u})) \leq 0 \end{aligned} \tag{9a}$$

Lower Level Problem

$$\begin{aligned} &\underset{\mathbf{x}}{Minimize}\ \ f\ (\mathbf{u},\ \mathbf{v}) \\ &subject\ to\ \mathbf{g}\ (\mathbf{u},\ \mathbf{v}) \leq 0 \end{aligned} \tag{9b}$$

In the above formulation, F and $\mathbf{u}$ are the objective function and decision vector of upper-level decision makers (system designer) respectively, while G is the constraint set of the upper-level decision vector. f and $\mathbf{v}$ are the objective function and decision vector of lower-level decision makers (users traveling in the network) respectively, while $\mathbf{g}$ is the set of constraints of the lower-level decision vector. It is noted here that $\mathbf{v}(\mathbf{u})$ is implicitly defined by the lower-level problem (i.e., the upper-level objective function F cannot be computed until $\mathbf{v}(\mathbf{u})$ is determined in the lower-level problem).

Le et al. [13] formulated a bilevel model for the terminal location for a logistics problem. They designed the lower level model as per the behavior of the individual vehicle using the terminal minimizing its own cost, and the upper level as the behavior of the planner for minimizing the total cost of the logistics system and the optimal size and location of the terminals. A Genetic Algorithm (GA) was used to obtain the optimal solution. Huang and Liu [6] proposed a bilevel approach for a logistics distribution network with balancing requirements. It promises to give a flexible network. The upper level is to minimize the total cost and the lower level is designed to obtain the balanced workload for the network. A GA is used to solve the problem. A bilevel programming model is designed for toll optimization on a multicommodity transportation network [2]. The upper level objective is set to maximize the revenue and the lower level is to minimize the total travel cost, i.e., to obtain the shortest path in the network. The model is applied on two examples. Murray-Tuite and Mahmassani [19] developed a bilevel formulation to determine the vulnerable links in a transportation network. At the lower level, the traffic assignment is done optimally and the vehicles are assigned accordingly. At the upper level, the

disruption is minimized in the network based on a vulnerability index. The classical Traveling Salesman Problem (TSP) is also solved by bilevel programming [17]. The toll optimization problem is reduced to a TSP problem and is solved by relaxing the bounds. Hejazi et al. [5] and Yin [22] proposed a GA based solution tool for bilevel programming models. Mathur and Puri [18] studied the bilevel programming model for a bottleneck of a non convex problem. They studied the nature of the problem and proposed a formulation and solution methodology.

2.4 Bilevel Formulation for Maintenance Inspection and Scheduling

In this paper, the bilevel programming model is designed as a two-stage optimization problem, where the optimal values of one set of variables obtained at the lower level are used to determine another set of variables at the upper level. In the maintenance inspection and scheduling problem (see, [1, 8]) the optimal inspection routes need to be obtained first. The field obtained conditions of the highway features at random time intervals along the optimal inspection routes are then used in the second stage (upper level) to obtain optimal maintenance schedule over a given planning horizon. In the proposed bilevel formulation we obtain the optimal inspection routes in the lower level and obtain optimal MR&R plan along those routes in the upper level.

2.5 Overview of the Lower Level

Before maintenance repair and rehabilitation (MR&R) can be performed an inspection of roadside features is necessary. From the inspection a maintenance schedule can be developed subject to budgetary constraints. In order to inspect a city's highway network it is necessary to develop optimal inspection routes subject to many constraints, such as work shift duration and overtime limitations. The problem formulation can be modified from the benchmark Capacitated Arc Routing Problem (CARP) where the arc capacity can be defined as the allowable work shift duration. For example a crew can begin inspecting an arc at 8:00 a.m. in the morning and may not be able to inspect the desired number of arcs in a given 8 hour day. Moreover, there may be arcs which may have to be traversed without inspection in order to get back to the maintenance office at the end of the day. This problem may also resemble the classical vehicle and crew scheduling problem. The problem can thus be summarized as follows: Find optimal travel and inspection routes for a maintenance crew subject to the work shift constraint. Figures 1 and 2 provide an example of the Baltimore Country (Maryland, USA) highway network and a sample optimal set of inspection routes. The formulation to this model has been provided in [1, 8]; therefore, has been skipped here for brevity.

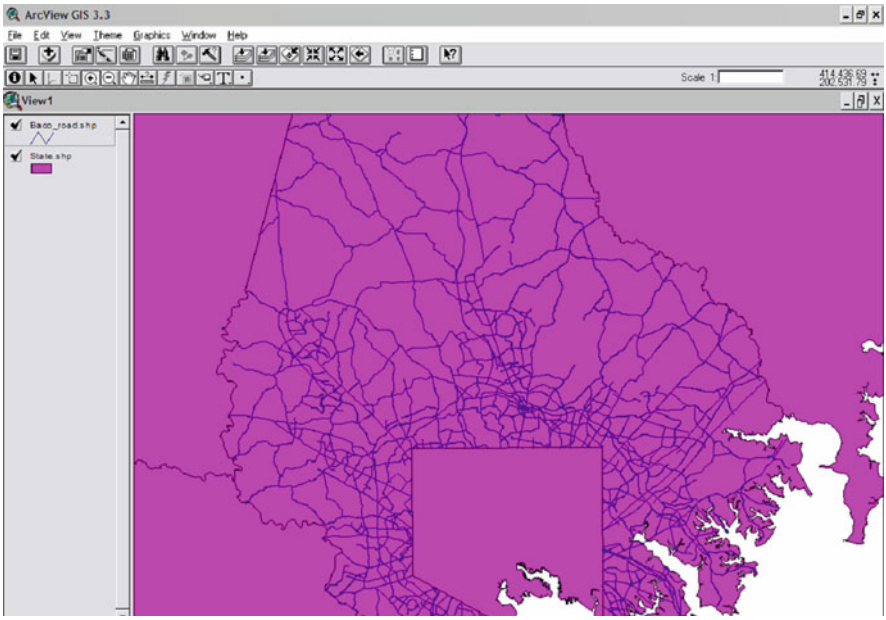


Fig. 1 Baltimore county (Maryland, USA) highway network

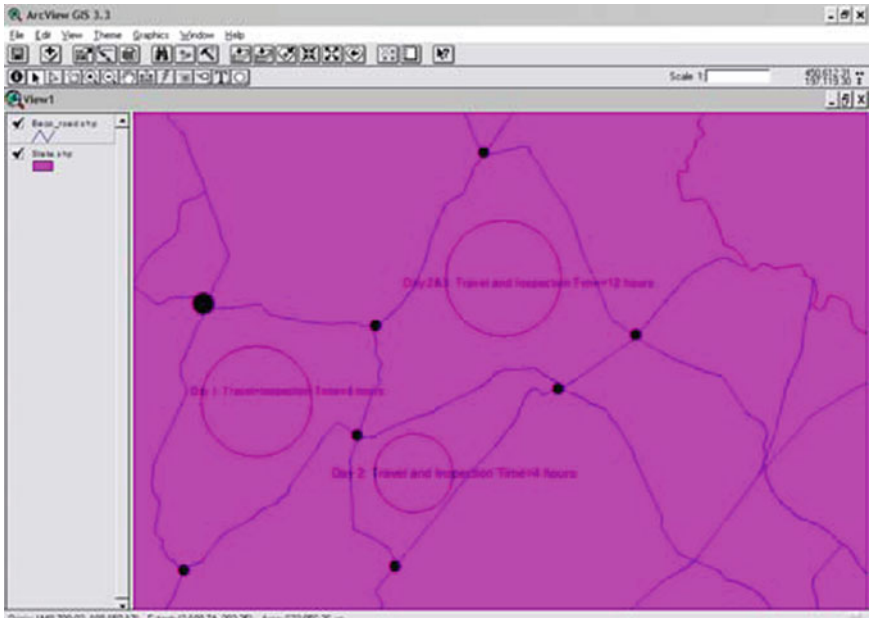


Fig. 2 Sample optimal inspection routes over a 3-day period

2.6 Overview of the Upper Level

In the upper level we employ the probabilistic reactive maintenance formulation presented in the preceding section (Eqs. (7) and (8)), to obtain the optimal MR&R schedule for the inspected highway features along the optimal routes.

3 Solution Algorithms

In order to solve the lower level model a genetic algorithm based approach was presented in our previous works (see, [8]). Alternatively, it can also be solved using a Floyd Algorithm which can provide the shortest path across nodes whether or not a directed path is provided. The algorithm can be modified in future works to account for additional constraints, such as the requirement of returning to the maintenance office at the end of the work day and avoiding invalid tours (i.e., tours consisting of non existing arcs between nodes).

The upper level problem is a classical (MR&R) optimization problem, which has been solved by Dynamic Programming for a single highway feature, i.e., pavement deterioration [14]). For multiple highway features (such as signs, guardrails, and luminaries) a (GA) based heuristic was proposed [7, 9] due to the computational infeasibility of Dynamic Programming. The new probabilistic formulation can also be solved by a GA described in Jha and Abdullah [9].

4 A Numerical Example

The numerical example consists of a road network consisting of 21 nodes and 33 arcs (links) as shown in Fig. 3. The inspection and travel times of the arcs are shown in Table 1.

4.1 Lower Level Optimization

Given a graph G which has nodes (n_i) and links (l_{i-j}), shortest distance and path between any two nodes can be obtained using the Floyd's Algorithm. Let there be n nodes in a graph. Let d_{i-j} be the distance from i to j if the link l_{i-j} exists else it value is infinite. Then pseudo code for the algorithm is given as:

For $k = 1$ *to* n
  For $i = 1$ *to* n
    For $j = 1$ *to* n
      $d_{i-j} = min(d_{i-j},\ d_{i-k} + d_{k-j})$
    End
  End
End

$$\forall \quad i, j, k \ = \ 1, 2, 3..n \ \in G$$

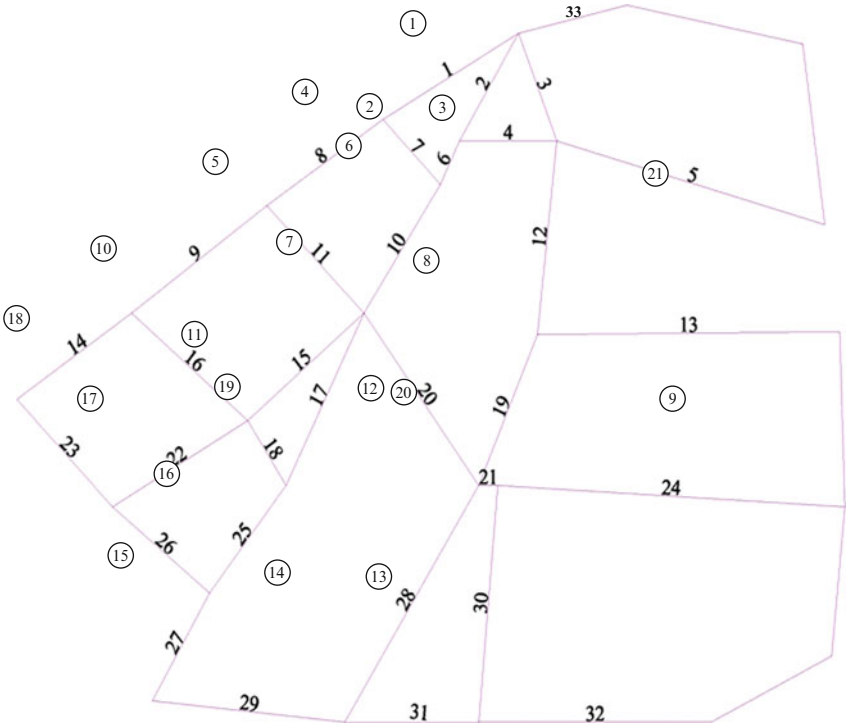
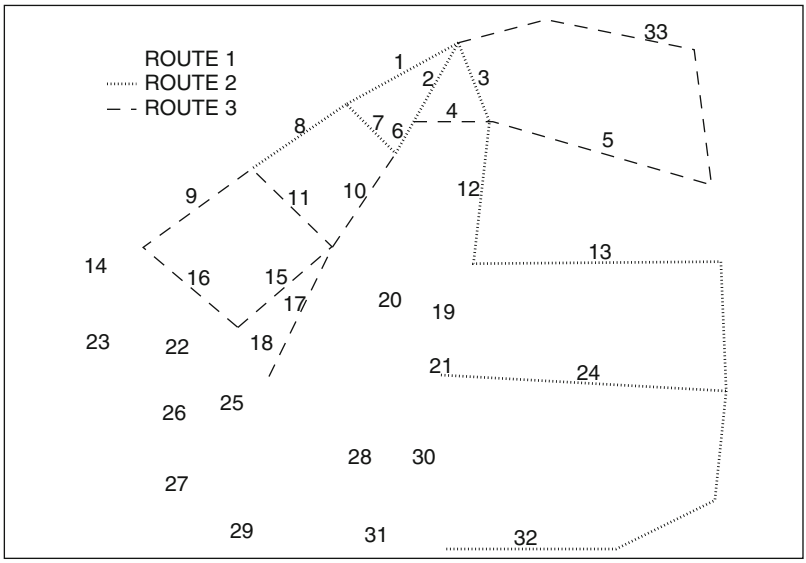


Fig. 3 Example highway network

Table 1 Travel and inspection times for the example network

ARC	Travel time (min)	Inspection time (min)	ARC	Travel time (min)	Inspection time (min)
1	10	22	18	4	20
2	7	12	19	9	15
3	6	12	20	12	31
4	6	11	21	1	10
5	12	21	22	10	37
6	3	10	23	8	21
7	5	13	24	22	51
8	9	16	25	8	18
9	10	18	26	8	14
10	9	15	27	7	25
11	9	17	28	16	53
12	11	21	29	12	19
13	29	56	30	13	16
14	9	14	31	8	17
15	9	14	32	31	68
16	9	18	33	34	76
17	11	25			



Optimal Routes:
Route 1 : 25, 18, 22, 14, 23, 26, 27, 29, 31, 28, 20, 19, 21, 30 (TT+IT = 472 min)
Route 2 : 32, 24, 13, 12, 6, 7, 8, 1, 2, 3 (TT+IT = 457 min)
Route 3 : 33, 5, 4, 11, 10, 17, 15, 16, 9 ((TT+IT = 356 min))

Fig. 4 Optimal results for the lower level optimization

The above algorithm is employed to obtain the optimal inspection routes for the network shown in Fig 3. The optimal results are shown in Fig 4.

4.2 Upper Level Optimization

A total of 450 guardrails, 700 signs, and 367 luminaries are found along the example highway network. Their average annual conditions under normal circumstances (1 = excellent; 0 = poor) over a 10 year planning horizon is shown in Table 2.

In order to consider the reactive approach 15 random inspections over the 10 year period are performed at varying time intervals to account for the feature deterioration due to accidents and inclement weather. The optimal results (Tables 3 and 4) are obtained using a genetic algorithm. The results for the deterministic case (based on routine annual inspections at discrete time intervals) are shown in Table 3. The results indicate that the guardrails need to be replaced in the sixth year, signs in the eight year, and luminaries in the fifth and tenth years over the 10 year time horizon.

The results for the probabilistic case (based on 15 random inspections at varying time intervals depending on the likelihood of accidents and inclement weather) are shown in Table 4. It can be seen that the results are quite different in this case. Please note that in this example only two policies (do nothing or complete

Table 2 Condition states of roadside features along the example highway network

Element/period	1	2	3	4	5	6	7	8	9	10
GR	1	1	1	0.7	0.7	0.7	0.3	0.3	0.3	0.3
S	1	1	1	1	1	0.7	0.7	0.7	0.3	0.3
L	1	1	1	1	1	0.3	0.3	0.3	0.3	0.3

Table 3 Optimal decision variables for the deterministic case

	λ_k									
Infrastructure element	1	2	3	4	5	6	7	8	9	10
GR	0	0	0	0	0	1	0	0	0	0
S	0	0	0	0	0	0	0	1	0	0
L	0	0	0	0	1	0	0	0	0	1

Table 4 Optimal decision variables for the probabilistic case

	λ_k														
Infrastructure element	1	2	3	4	5	6	7	8	9	10	11	12	13	14	15
GR	0	1	0	0	0	0	1	0	1	0	1	0	0	0	1
S	0	0	0	0	1	0	1	0	0	0	1	0	0	1	1
L	0	0	1	0	0	0	1	0	0	0	0	0	0	0	1

replacement) are considered. Additional policies can be considered in future works, which will require the encoding of decision variables in the genetic algorithm using real numbers.

5 Conclusions and Future Work

In this paper we developed a probabilistic bilevel optimization model for obtaining optimal inspection routes and MR&R policies over a planning horizon for roadside features, following an earthquake. The bilevel optimization approach seems to be efficient and superior to the two stage approach presented in our previous works. Several extensions of this research need to be worked in the future. The most significant ones include: (1) using a sophisticated deterioration function in performing optimization and considering a budget constraint. A simple parabolic deterioration function has been introduced in one of our recent works [15, 16]; (2) applying the optimization model to relatively complex highway networks with possibility of several intermediate maintenance actions; (3) extending the GAs to handle additional maintenance actions by encoding the decision variables to real numbers; (4) incorporating errors associated with uncertainty in maintenance inspection; and (5) empirical examination of the probabilistic factor in the upper level formulation.

Acknowledgements This work was jointly carried out at the Center for Advanced Transportation and Infrastructure Engineering Research, Morgan State University and the National Technical University of Greece, Athens. The authors wish to acknowledge Dr. Jawad Abdullah for his assistance with some of the work.

References

1. Abdullah J (2007) Models for the effective maintenance of roadside features. Doctoral dissertation, Morgan State University, Baltimore, MD
2. Brotcorne L, Labbe M, Marcotte P, Savard G (2001) A bilevel model for toll optimization on a multicommodity transportation network. Transport Sci 35(4):345–358
3. Golabi K, Kulkarni RB, Way GB (1982) A statewide pavement management system. Interfaces 12(6):5–21
4. Greenfield D (1996) An OR bridge to the future. ORMS Online Edition 23(6)
5. Hejazi SR, Memariani A, Jahanshahloo G, Sepehri MM (2002) Linear bilevel programming solution by genetic algorithm. Com Oper Res 29(13):1913–1925
6. Huang B, Liu N (2004) Bilevel programming approach to optimizing a logistic distribution network with balancing requirements. Trans Res Record 1894:188–197
7. Jha MK, Abdullah J (2006a) A Markovian approach for optimizing highway life-cycle with genetic algorithms by considering maintenance of roadside appurtenances. J Frankl Inst 343:404–419
8. Jha MK, Kepaptsoglou K, Karlaftis M, Abdullah J (2006) A genetic algorithms-based decision support system for transportation infrastructure management in urban areas. In: Taniguchi E, Thompson R (eds) Recent advances in city logistics: proceedings of the 4th international conference on city logistics. Elsevier, New York
9. Jha MK, Abdullah J (2006b) A probabilistic approach to Maintenance Repair And Rehabilitation (MR&R) of roadside features. In: Proceedings of the 14th Pan-American conference on traffic and transportation engineering (PANAM XIV), Las Palmas de Gran Canaria, Spain
10. Kang M (2008) An alignment optimization model for a simple highway Network, Doctoral dissertation, University of Maryland, College park, MD
11. Karlaftis M, Kepaptsoglou K, Lambropoulos S (2007) Fund allocation for transportation network recovery following natural disasters. J Urban Plan Dev ASCE 133(1):1–8
12. Kepaptsoglou K, Karlaftis M, Bitsikas T, Panetsos P, Lambropoulos S (2006) A methodology and decision support system for scheduling inspections in a bridge network following a natural disaster. IABMAS 2006 proceedings. Balkema Publishers, Porto, Portugal
13. Le Y, Miao L, Wang H, Wang C (2006) A bilevel programming model and a solution method for public logistics terminal planning. In: Proceedings of the 85th transportation research board conference, Washington, DC
14. Madanat S (1991) Optimizing sequential decisions under measurement and forecasting uncertainty: application to infrastructure inspection, maintenance and rehabilitation. D.Sc. dissertation, Massachusetts Institute of Technology, Boston, MA
15. Maji A, Jha MK (2007a) Modeling highway infrastructure maintenance schedule with budget constraint. Trans Res Record 1991:19–26
16. Maji A, Jha MK (2007b) Maintenance schedule of highway infrastructure elements using a genetic algorithm. In: Proceedings of the international conference on civil engineering in the new millennium: opportunities and challenges (CENeM-2007), Bengal Engineering and Science University, Shibpur, Howrah, India
17. Marcotte P, Savard G, Semet F (2004) A bilevel programming approach to the travelling salesman problem. Oper Res Lett 32(3):240–248
18. Mathur K, Puri MC (2005). A bilevel bottleneck programming problem. Eur J Oper Res 85:337–344
19. Murray-Tuite PM, Mahmassani HS (2004). Methodology for determining vulnerable links in a transportation network. Trans Res Record 1882:88–96
20. Samanta S, Jha MK (2006). A bilevel model for station locations optimization along a rail transit line. In: Allan J et al. (eds) Computers in railways X (COMPRAIL 2006). WIT Press, Southampton, UK
21. Yang H, Yagar S (1994). Traffic assignment and traffic control in general freeway-arterial corridor systems, Transport Res B Meth 28:463–486
22. Yin Y (2000). Genetic-algorithms based approach for bilevel programming models. J Transp Eng ASCE 126(2):115–120

Lifetime Seismic Reliability Analysis of Corroded Reinforced Concrete Bridge Piers

Dan M. Frangopol and Mitsuyoshi Akiyama

Abstract For structures located in aggressive environments and earthquake regions, it is important to consider the effect of material corrosion on seismic performance. This chapter presents a seismic analysis methodology for corroded reinforced concrete (RC) bridges. It is shown that the analytical results are in good agreement with the experimental results regardless of the amount of steel corrosion. The proposed method is applied to lifetime seismic reliability analysis of corroded RC bridge piers, and the relationship between steel corrosion and seismic reliability is presented. After the occurrence of crack corrosion, seismic reliability of the pier is significantly reduced. If corrosion cracks in the bridge pier are detected by visual inspection, additional detailed inspections need to be performed.

Keywords Seismic reliability analysis · Reinforced concrete bridge piers · Failure probability · Salt attack · Life-cycle assessment

1 Introduction

For the lifetime assessment of existing structures in marine environment and earthquake regions, the effects of corrosion due to chloride attacks on the seismic performance need to be taken into consideration. In this chapter a methodology is presented to include the effects of material corrosion on the deterioration of seismic performance of RC bridge piers.

D.M. Frangopol
Department of Civil and Environment Engineering,
ATLSS Engineering Research Center, Lehigh University,
117 ATLSS Drive, Bethlehem, PA 18015-4729, USA
e-mail: dan.frangopol@lehigh.edu

M. Akiyama (✉)
Department of Civil and Environment Engineering, Tohoku University,
6-6-06 Aramaki-Aza-Aoba, Aoba-ku, Sendai 980-8579, Japan
e-mail: akiyama@civil.tohoku.ac.jp

M. Papadrakakis et al. (eds.), *Computational Methods in Earthquake Engineering*,
Computational Methods in Applied Sciences 21, DOI 10.1007/978-94-007-0053-6_23,
© Springer Science+Business Media B.V. 2011

Recently, there have been experimental studies on RC columns with chloride-induced corrosion of steel reinforcement subjected to cyclic loading [1–4]. The analytical methods to evaluate the relationship between load and displacement of RC columns can be examined by using experimental data. These methods need to consider (a) the reduction of steel bar volumes, (b) cracking of concrete cover due to the expansion of corrosion products, (c) bond degradation between concrete and steel, and (d) non-uniformity of corrosion along the steel bars in RC columns. Therefore, it is difficult to establish an accurate modeling of corroded RC bridge piers. Also, spatial corrosion distributions are usually approximated by averaged uniformity along the steel bars using the weight loss $C = (w - w_2)/w \times 100$, where w is the weight of intact reinforcing bar and w_2 is the remaining weight after removing the corrosion product. Due to modeling error and simplification of spatial corrosion distribution, the demand and capacity of RC bridge piers cannot be predicted with certainty.

To include the uncertainty and its effects into the lifetime seismic performance assessment, methods of probability and statistics are required. The reliability models to evaluate the failure probabilities for flexure, shear and/or spalling limit states for corroded RC bridge slab are reported in Frangopol et al. [5], and Stewart and Rosowsky [6]. However, studies on the seismic reliability of RC bridge piers subjected to corrosion are scarce. For RC bridge piers in earthquake prone regions subjected to airborne chlorides, it is important in their lifetime assessment to investigate the relationship between the deterioration of seismic reliability and corrosion amounts of steel bars under uncertainty.

This chapter presents a seismic analysis method of RC bridges with steel corrosion subjected to cyclic loading. This method is used in seismic reliability analysis of existing corroded RC bridge piers. The relationship between steel corrosion and seismic reliability is also presented. Based on this relationship and the inspection of steel corrosion at the site, seismic reliability at the time of inspection could be computed and an optimal seismic rehabilitation method to minimize the seismic risk within remaining lifetime could be selected.

2 Basic Equation to Obtain the Seismic Risk

When only seismic hazard and one limit state are considered, the expected risk is given by;

$$R = C(S) \int_{\alpha} \left[-\frac{dH(\alpha)}{d\alpha} \right] P[S|\Gamma = \alpha] \, d\alpha \tag{1}$$

where $C(S)$ is the consequences associated with limit state S, $P[S|\Gamma = \alpha]$ is the conditional probability that the limit state S is reached given that ground motion intensity Γ (such as peak ground acceleration or velocity) is equal to α (fragility curve), and $H(\alpha)$ is the probability that the ground motion intensity α is exceeded at least once during a time interval T (hazard curve).

In seismic risk estimation, a fragility curve describes the probability that the actual structural damage D, exceeds a damage threshold of structural capacity C when the structure is subjected to a specified ground motion intensity α. This conditional probability is expressed as:

$$P(S|\Gamma = \alpha) = P\left[D \geq C \,|\, \Gamma = \alpha\right] \tag{2}$$

where C = the structural capacity (e.g. inter-story drift ratio at a collapse threshold), and D = the structural demand.

In computing of the conditional probability $P[S|\Gamma = \alpha]$ of structures subjected to aggressive environment (e.g. marine environment), the effect of corrosion on this probability has to be taken into consideration.

3 Lifetime Seismic Analysis Method for Corroded Reinforced Concrete Bridge Piers

When seismic fragility curves are created, it is important to take into consideration the effect of material corrosion on seismic performance. However, it is impossible to evaluate the seismic capacity and demand of corroded structures by using a very simple model such as design equations in seismic codes. Therefore, when the seismic risk or reliability for structures constructed in severe environment is estimated, it is necessary to use the seismic analysis model which can be applied to the corroded structures. In this study, RC bridge piers subjected to salt attack are analyzed.

Recently, there have been experimental studies on RC columns with chloride-induced corrosion of steel reinforcement subjected to cyclic loading [1–4]. Based on these studies, the analytical methods to evaluate the relationship between load and displacement of RC columns can be examined.

Figure 1 shows the seismic analysis model for corroded RC bridge piers. Structural capacity is defined as the horizontal displacement of the top of the bridge pier at the occurrence of buckling of longitudinal bars. Since, as shown in Fig. 1b, the longitudinal bars in RC columns are prevented from bucking by the cover and the ties, bucking does not occur at Euler's critical stress. Naito et al. [7] proposed the buckling model of longitudinal bars and ductility evaluation method of RC columns taking the preservation of the cover and the ties into consideration. In this chapter, the effect of steel corrosion on the deformation at the occurrence of buckling of longitudinal bars is considered based on the buckling model proposed by Naito et al [7]. The preservation forces of ties and cover concrete, q_c and Q_w as shown in Fig. 1b, could be obtained based on the amount of steel corrosion due to chloride attack as:

$$Q_w = a_{wle}\sigma_{wy} \tag{3}$$

$$q_c = 0.03 \cdot \beta_1 \beta_2' d_{se} D_r' \sigma_c^{2/3} \tag{4}$$

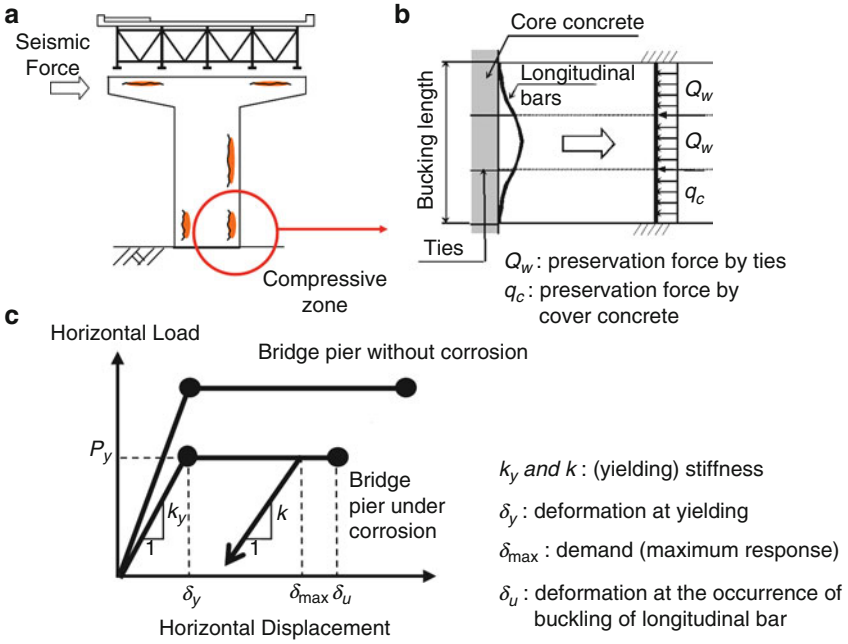


Fig. 1 Seismic analysis model for corroded RC bridge piers to obtain the structural capacity C and demand D in Eq. 2 [(**a**) RC bridge piers with steel corrosion; (**b**) buckling model of a rebar in the plastic hinge of RC columns; and (**c**) lateral load and displacement relation of corroded pier]

$$a_{wle} = \begin{cases} N_w a'_w / N_L & \text{if } N_L < 5 \\ N_w a'_w / (0.2N_L + 4) & \text{if } N_L \geq 5 \end{cases} \tag{5}$$

$$\beta_1 = 1 - 0.75(\varepsilon_{\max}/\varepsilon_c) \quad \text{if } \beta_1 \geq 0.25 \tag{6}$$

$$\beta'_2 = \begin{cases} 1.0 \text{ (without corrosion crack)} \\ \exp(-0.074C_w) \text{ (with corrosion crack)} \end{cases} \tag{7}$$

where a_{wle} is the effective cross-sectional area of ties given for each tie; σ_{wy} is the yield strength of ties; β_1 is the coefficient linking the compression strain and the decreased tensile strength associated with the damage resulting from the compression due to flexural moment; β_2 is the coefficient associated with the damage of cover concrete resulting from steel expansion due to corrosion; d_{se} is the distance from center of cross section of the bar to the edge of the cover; D'_r is cross-sectional area of bars after corrosion; σ_c and ε_c are the concrete compressive strength and strain at the compressive strength, respectively; $\varepsilon_{\max}$ is strain at the compressive longitudinal bars; N_w is the number of ties confining the longitudinal bars perpendicular to loading direction; N_L is the number of longitudinal bars perpendicular to loading direction, and C_w is averaged weight loss of longitudinal bars.

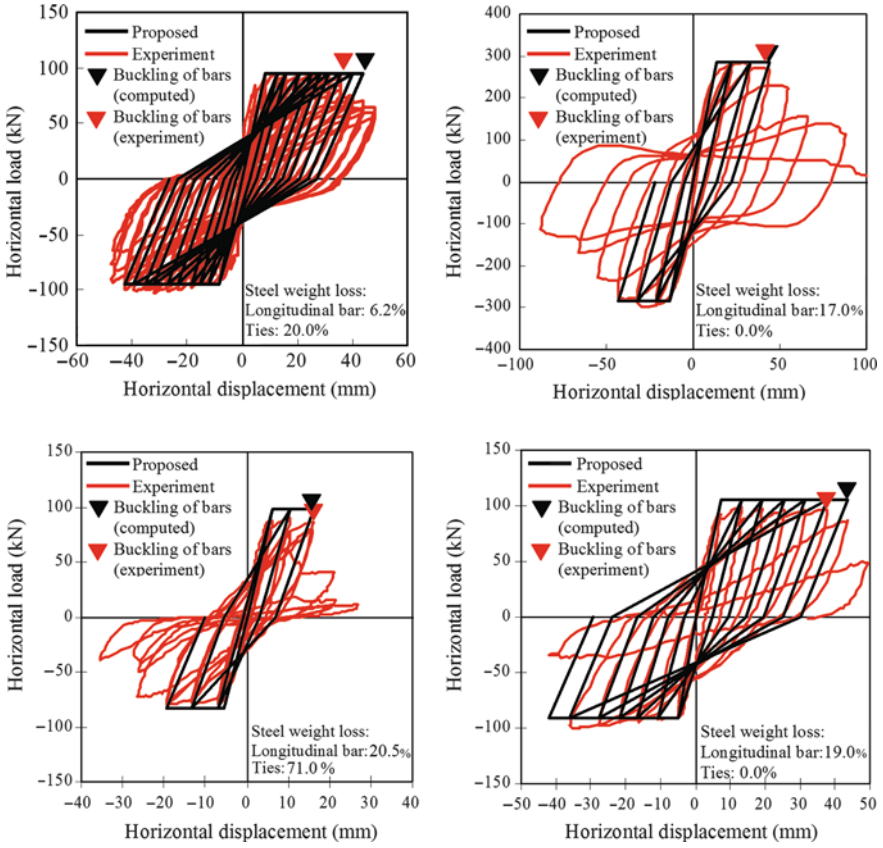


Fig. 2 Comparison of the relationship between horizontal load and displacement of corroded columns (experimental results are reported in [2–4]) [(**a**) Specimen B [5]; (**b**) Specimen #5 [4]; (**c**) Specimen N5 [6]; and (**d**) Specimen ES1 [6]]

Also, the effects of corrosion on flexural strength and stiffness of column are taken into consideration as shown in Fig. 1c. Steel cross-sectional area reduced by corrosion is used in the conventional method to obtain the flexural strength and stiffness.

Figure 2 shows the comparison of computed results with test results of the relationships between horizontal load and displacement of corroded RC columns subjected to cyclic loading. These test results were reported in [2–4]. The specimens with large steel corrosion of ties (see Fig. 2c) exhibit brittle behavior after the occurrence of buckling of longitudinal bars. However, since the load and displacement relations before the buckling occurrence exhibit ductile behavior, these can be modeled by the proposed seismic analysis method regardless of the amount of steel weight loss.

The statistical parameters of model uncertainty can be obtained by comparing the computed results with experimental ones as shown in Fig. 3. Figures 3a–c show the

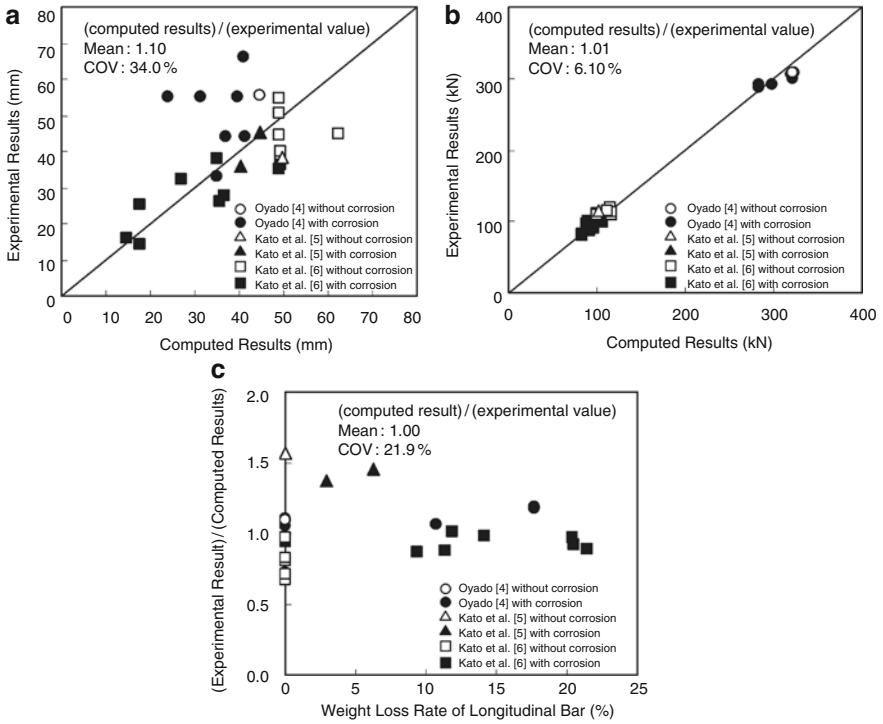


Fig. 3 Comparison of computed and experimental results [(**a**) comparison of occurrence of buckling; (**b**) comparison of flexural strength; and (**c**) comparison of stiffness]

comparison between the computed results and experimental results of deformation at the occurrence of buckling of bars, flexural strength and stiffness, respectively. The total number of specimens is 27 [2–4]. The deformation at the occurrence of buckling of longitudinal bars can be obtained by substituting q_c and Q_w reduced by steel corrosion into Naito's model. The accuracy for corroded columns is almost the same as that for non-corroded columns. In the seismic reliability analysis, the statistical parameters in Fig. 3a–c are used as model uncertainty.

4 Seismic Reliability Analysis of Corroded Reinforced Concrete Bridge Piers

Based on hazard curve and fragility curve, as shown in Eqs. 1 and 2, the failure probability can be obtained as;

$$P_f = \int_0^\infty \left[-\frac{H(\alpha)}{d\alpha} \right] P\left(C \leq D | \Gamma = \alpha\right) d\alpha \tag{8}$$

where $H(\alpha)$ is hazard function of ground motion intensity α (i.e., probability that intensity at site will equal or exceed α). The maximum velocity at the bed rock is assumed as ground motion intensity α.

Using the equation of the failure probability proposed in [8, 9], Eq. 8 can be simplified and expressed as;

$$P_f = H(\alpha^{\hat{C}}) \exp\left[\frac{1}{2}\frac{k^2}{b^2}\left(\beta_{D|\alpha}^2 + \beta_C^2\right)\right] \tag{9}$$

$$H(\alpha) = k_0 \alpha^{-k} \tag{10}$$

$$\hat{D} = a \cdot \alpha^b \tag{11}$$

where k and k_0 are coefficients for linear regression of hazard $H(\alpha)$ on ground motion intensity in proximity of the region of interest of the limit state (i.e., region that contributes most to the failure probability) in logarithmic space; $\alpha^{\hat{C}}$ is ground motion intensity corresponding to median displacement capacity $\hat{C}$; $\beta_{D|\alpha}$ is dispersion measure for displacement demand D at given level α (standard deviation of natural logarithm); β_C is dispersion measure for displacement capacity C, and a and b are regression coefficients for linear regression of median displacement demand $\hat{D}$ on intensity α at the region of interest.

The displacement capacity C (i.e., the displacement level at which the performance level will be exceeded), is assumed to have a median value $\hat{C}$ and to be lognormally distributed with dispersion β_C. $\hat{C}$ and β_C are obtained based on Monte Carlo Simulation taking the statistics shown in Fig. 3 and material variability of concrete and reinforcing bars into consideration.

To obtain the parameters *a, b* and $\beta_{D|\alpha}$, the simulated earthquake motions at bedrock are made by using the method of Sawada et al. [10]. These earthquake motions satisfy the properties of maximum acceleration, maximum velocity, and maximum displacement of previously observed earthquake motions. Earthquake motions at bedrock are made by stationary waves with a spectrum form and uniform random phases; stationary waves are multiplied by an envelope function. The earthquake motions at bedrock are then adjusted to ensure each maximum velocity in a time domain. Equation 11 is created by dynamic increment analysis using many simulated motions, and parameters *a, b* and $\beta_{D|\alpha}$ are estimated. Each pier is modeled as one degree system with the horizontal load and displacement relation as shown in Fig. 1c. When dynamic increment analyses are performed, the model uncertainties involved in the evaluation of flexural strength and stiffness as shown in Figs. 3b and c, and material variability of concrete and reinforcing bars are also considered by Monte Carlo Simulation. Figure 4 shows an example of the relationship between the median displacement demand $\hat{D}$ and maximum velocity of corroded bridge piers.

The hazard curve used in the present example as shown in Fig. 5 refers to the city of Sendai in Japan [11]. The ten bridge piers analyzed are designed according to Japan Specifications for Highway Bridges [12]. Natural period of these bridge piers ranges from 0.39 to 0.89 s. Table 1 shows the structural details of piers.

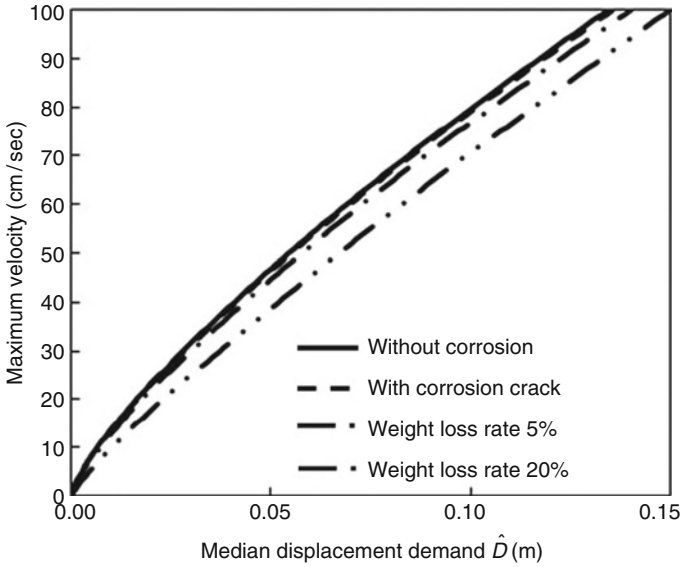


Fig. 4 An example of the relationship between median displacement demand and maximum velocity

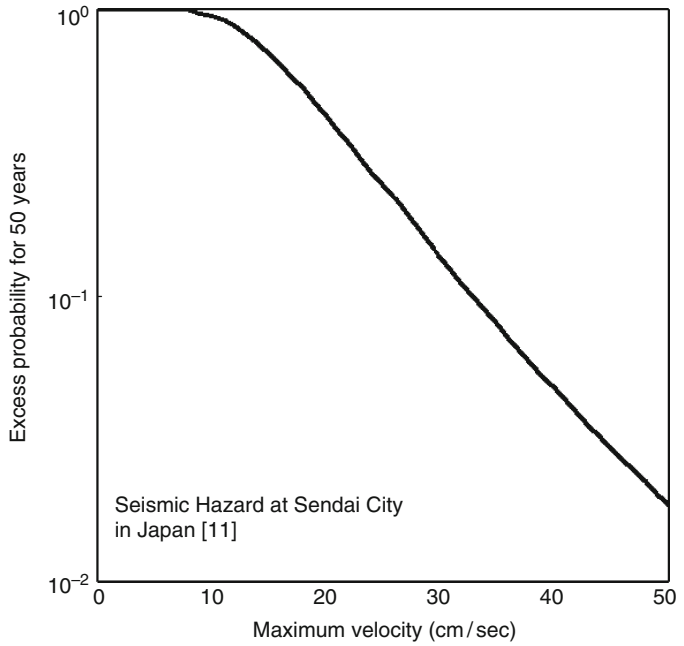


Fig. 5 Seismic hazard curve at Sendai City in Japan [11]

Table 1 Structural details of RC piers analyzed

Pier No.	Section dimensions (cm)	Pier height (cm)	Longitudinal reinforcement ratio (%)	Area ratio of ties (%)	Natural Period (s)
1	500 × 125	550	2.31	1.03	0.39
2	460 × 120	600	3.36	1.03	0.43
3	500 × 220	1, 000	1.31	0.53	0.48
4	470 × 230	1, 200	1.62	0.53	0.57
5	600 × 300	1, 500	1.02	0.53	0.63
6	550 × 290	1, 600	1.31	0.53	0.66
7	620 × 250	1, 500	1.75	0.76	0.68
8	600 × 350	2, 000	1.19	0.53	0.76
9	780 × 420	2, 500	1.23	0.53	0.85
10	610 × 400	2, 500	1.45	0.76	0.89

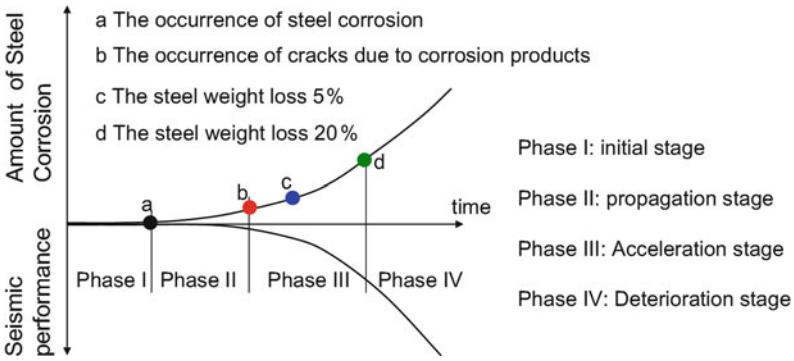


Fig. 6 Relationship between amount of steel corrosion and seismic performance (Adapted from [13])

Figure 6 shows the relationships between time and corrosion amounts, and time and seismic performance. According to JSCE standard specification for concrete structures [13], four stages are considered herein: initial stage, propagation stage, acceleration stage, and deterioration stage. Steel corrosion and cracking due to corrosion products initiate at the boundary between initial stage and propagation stage, and propagation stage and acceleration stage, respectively. The speed of steel corrosion in propagation stage is higher than that in acceleration stage, and seismic performance may be rapidly diminished in the deterioration stage. The corrosion amounts as the weight loss at the boundary between propagation stage and acceleration stage is set as 20% [14]. This study focuses also on the weight loss 5% in the acceleration stage. Kodama et al. [15] show that based on the observation of existing marine RC structures, the structure has very severe cracking due to steel corrosion after more than 5% weight loss. The steel corrosion amount at the occurrence of corrosion crack is evaluated based on the modified Qi and Seki's method [16].

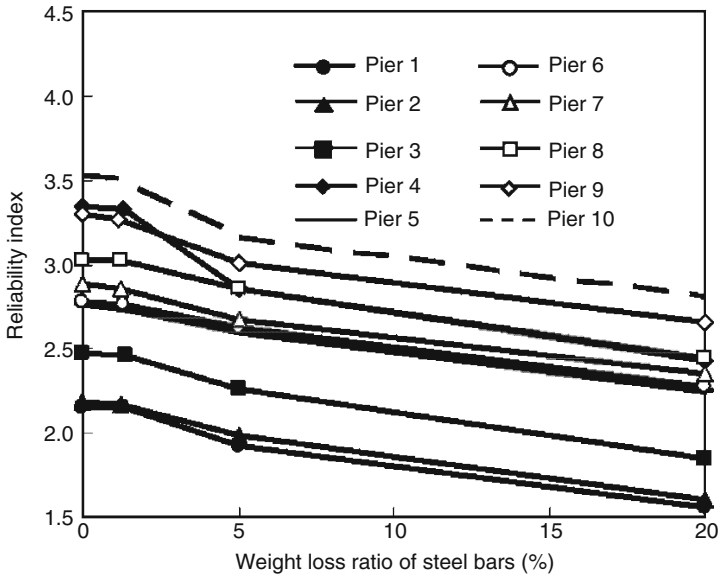


Fig. 7 Relationship between weight loss ratio of steel bars and reliability index

It is assumed that each pier as shown in Table 1 has four states; no corrosion, the weight loss corresponding to the occurrence of corrosion crack, weight loss 5%, and weight loss 20%. Figure 7 shows the relationship between the weight loss ratio and reliability index $\beta = -\Phi^{-1}(Pf)$, where Φ is the cumulative distribution function of the standard normal distribution. As shown in Fig. 7, after the occurrence of steel corrosion, the seismic reliability of bridge pier is decreasing with steel corrosion. This means that if corrosion crack is detected by visual inspection, seismic reliability of bridge piers is not the same as that for intact ones and additional detailed inspections need to be performed.

5 Conclusions

In lifetime seismic reliability of corroded RC structures, it is important to take into consideration the effect of material corrosion on seismic performance. This chapter presents the seismic analysis method of corroded RC bridges piers. It is shown that within the occurrence of buckling of longitudinal bars, the analytical results are in good agreement with the experimental results regardless of the amount of steel corrosion. The proposed method is applied to seismic reliability analysis of corroded RC bridge piers, and the relationships between steel corrosion and seismic reliability are presented.

Life-cycle safety management of RC bridges located in marine environment and seismic regions should be based on the recognition of the effect of corrosion on bridge reliability. Much future effort is needed to establish such a life-cycle methodology to consistently deal with insufficient data and knowledge associated with long-term performance and total cost of structures located in aggressive environments and seismic regions.

References

1. Yamamoto T, Kobayashi K (2006) Report of research project on structural performance of deteriorated concrete structures by JSCE 331 – review of experimental study. In: Proceedings of the International Workshop on life cycle management of coastal concrete structures, Nagaoka, Japan
2. Oyado M (2007) Mechanical properties of corroded reinforced concrete structures. Ph.D. thesis, Graduate School of Systems and Information Engineering, Tsukuba University, Japan (in Japanese)
3. Kato E, Iwanami M, Ito H, Yokota H (2005) Influence of rebar corrosion on structural performance of RC column subjected to cyclic loading. Proc JCI 27(2):1489–1494 (in Japanese)
4. Kato E, Iwanami M, Yokota H, Nakamura K, Ito H (2004) Influence of rebar corrosion on structural performance of RC beams subject to reversed cyclic loading. Technical Note of the Port and Airport Research Institute, 1079 (in Japanese)
5. Frangopol DM, Lin KY, Estes AC (1997) Reliability of reinforced concrete girders under corrosion attack. J Struct Eng ASCE 123(3):286–297
6. Stewart MG, Rosowsky DV (2003) Structural safety and serviceability of concrete bridges subjected to corrosion. J Infrastruct Syst ASCE 4(4):146–155
7. Naito H, Akiyama M, Suzuki M (2002) Ductility design of concrete encased steel piers. In: Proceedings of the 1st FIB congress, Osaka, Japan
8. Cornell CA, Jalayer F, Hamburger R, Foutch D (2002) Probability basis for 2000 SAC Federal Emergency Management Agency steel moment frame guidelines. J Struct Eng ASCE 128(4):526–533
9. Yun S, Hamburger R, Cornell C, Foutch D (2002) Seismic performance evaluation for steel moment frames. J Struct Eng ASCE 128(4):534–545
10. Sawada T, Hirao K, Tsujihara O, Mikami, A (2001) A simulation method of earthquake ground motions on engineering bedrock based on attenuation of peak values. J Struct Mech Earth Eng JSCE 682:311–322 (in Japanese)
11. National Research Institute for Earth Science and Disaster Prevention, J-SHIS (Japan Seismic Hazard Information Station), http://www.j-shis.bosai.go.jp/
12. Japan Road Association (2002) Specifications for highway bridges. Part V: seismic design. Maruzen, Japan
13. JSCE (2005) Standard specifications for concrete structures “maintenance”. JSCE Guidelines for concrete No.4. Maruzen, Japan
14. Amino T, Habuchi T, Morikawa A, Iwanami M, Yokota H (2006) Comparison between actual situations of superstructures of jetty damaged by chloride induced corrosion and deterioration prediction considering the variations in deterioration factors. In: Proceedings of the international workshop on life cycle management of coastal concrete structures, Nagaoka, Japan
15. Kodama S, Tanabe T, Yokota H, Hamada H, Iwanami M, Hibi T (2001) Development of maintenance management system for existing open-piled piers. Technical Note of the Port and Harbor Research Institute, Ministry of Land, Infrastructure and Transport, 1001 (in Japanese)
16. Qi L, Seki H (2001) Analytical study on crack generation situation and crack width due to reinforcing steel corrosion, J Mater Concrete Struct Pavements 669:161–171 (in Japanese)

Advances in Life Cycle Cost Analysis of Structures

Chara Ch. Mitropoulou, Nikos D. Lagaros, and Manolis Papadrakakis

Abstract Life cycle cost assessment (LCCA) of structural systems refers to an evaluation procedure in which all costs arising from owing, operating, maintaining and ultimately disposing are considered. LCCA is considered as a very significant assessment tool in the field of the seismic behaviour of structures. In this chapter two test cases are examined where the application of LCCA plays significant role for the extraction of important conclusions. In the first case LCCA is implemented for the assessment of the European seismic design codes and in particular EC2 and EC8 with respect to the recommended behaviour factor q. The assessment is performed on a multi-storey RC building which was optimally designed. In the second test case, 3D RC buildings are assessed with reference to life cycle cost calculated based on multicomponent incremental dynamic analysis and the significance of considering randomness on both record and incident angle is demonstrated.

Keywords Performance-based design · Prescriptive design procedures · Behaviour factor · Life-cycle cost analysis · RC buildings · Structural optimization · Pushover analysis

1 Introduction

For years, construction industry was focused primary on two concerns related to the design and construction processes of the structures. The first, of utmost importance to architects, was the architectural design of a structure that would satisfy aesthetic and functionality goals. The second concern, the primary focus of structural engineers and constructors, was the structural design and construction of a sound structure satisfying the provisions of the design codes for the estimated

Ch.Ch. Mitropoulou (✉), N.D. Lagaros, and M. Papadrakakis
Institute of Structural Analysis and Seismic Research, National Technical University Athens, Zografou Campus, Athens 157 80, Greece
e-mail: chmitrop@central.ntua.gr; nlagaros@central.ntua.gr; mpapadra@central.ntua.gr

M. Papadrakakis et al. (eds.), *Computational Methods in Earthquake Engineering*, Computational Methods in Applied Sciences 21, DOI 10.1007/978-94-007-0053-6_24,
© Springer Science+Business Media B.V. 2011

construction cost. Even though, these are significant concerns, they are not the only that should be addressed when planning for the future. A third one that is receiving more attention recently is the operation cost of the structure over its life. The combination of economic theory and computer technology allows for a more advanced approach to the design and construction of structures than ever before. Instead of merely looking at the structure in terms of cost to design and build, investors can broaden their perspective to include operations, maintenance, repair, replacement, and disposal costs. The sum of initial and future costs associated with the construction and operation of a structure over a period of time determines its life cycle cost.

In the most of the existing seismic design codes the future cost of a structure over a period of life is not taken into consideration. The balance between the construction cost and the safety of the structure is one of the main scopes of the existing design codes. The prescriptive (or limit-state) concept of the most existing building design codes, where the structure is considered safe and no collapse will occur if a number of checks, is expressed mainly in terms of forces, are satisfied. A typical limit state based design can be viewed as one (ultimate strength) or two (serviceability and ultimate strength) limit state approach. According to a prescriptive design code, the strength of the structure is assessed in one limit state while a serviceability limit state is usually checked in order to ensure that the structure will not deflect or vibrate excessively during its functioning. The structures are allowed to absorb energy through inelastic deformation by designing them with reduced loading which is specified by the behaviour factor [1, 2] "q" also known as reduction factor [3] "R". It is generally accepted that the capacity of a structure to resist seismic actions in the nonlinear range through energy dissipation permits their design for smaller seismic loads than those required for linear elastic response. Smaller seismic loads can be translated in smaller structural elements and in lower construction cost without taking into account the potential damage cost during the life of a structure. For that reason the application of the reduction factor q, which expresses the behaviour mechanisms of a structure under seismic loadings during its lifetime, is strongly connected with the initial and the life cycle cost of a structure. The main objective of the first part of the current study is to examine the validity of the behaviour factor q in designing safe and economic RC structures using Eurocodes 2 and 8 [4, 5].

Assuming that it is critical, the LCCA to be taken into consideration in the seismic design of the structures, the exact calculation of life cycle cost (LCC) is also important by examining the factors that may influence its value. The calculation of LCC includes the calculation of the limit states dependent costs. Limit state dependent cost, as considered in this study, represents monetary-equivalent losses in present values due to seismic events that are expected to occur during the design life of a new structure or the remaining life of an existing or a retrofitted structure. The limit state dependent cost consists of the damage cost, loss of contents, rental loss and income loss. The cost of the human fatality, that is associated with the limit-state dependent cost, is also accounted for in the present study. The value of the cost components of LCC can vary according to the structural behaviour of the structure under an earthquake hazard. The main objective of the second part of the

current study is to examine the influence of the incident angle of attack of the two horizontal components of the records on the seismic response of multi-storey RC buildings and furthermore the value of LCC which is correlated to the structural behaviour of the structure.

2 Literature Survey-LCC

In construction industry decision making for structural systems situated in seismically active regions, requires consideration of the damage and other losses costs resulting from earthquakes occurring during the lifespan of the structure. Thus, the life cycle cost assessment (LCCA) procedure can become an essential component of the design process in order to control the initial and the future cost of building ownership. A considerable amount of work has been done in estimating losses due to earthquakes. In particular in the work by Beck et al. [6] a measure, to be incorporated into the seismic risk assessment framework for economic decision-making of commercial buildings, was introduced denoted as the probable frequent loss which is defined as the mean loss resulting from shaking with 10% exceedance probability in 5 years. Liu et al. [7] presented a two-objective optimization procedure for designing steel moment resisting frame buildings within a performance-based seismic design framework, where initial material and lifetime seismic damage costs are treated as two separate objectives. In the work by Sanchez-Silva and Rackwitz [8] it is underlined that structures should be optimal with respect to economic investment, benefits derived from their existence, expected consequences in case of failure, and the degree of protection to human life and limb. Takahashi et al. [9] presented a decision methodology for the management of seismic risk where the decision criterion aims at minimizing the expected life-cycle cost, including the initial cost of the design and the expected cost of damage due to future earthquakes. Frangopol and Liu [10] reviewed the recent development of life-cycle maintenance and management planning for deteriorating civil infrastructure with emphasis on bridges. Kappos and Dimitrakopoulos [11] implemented decision making tools, namely cost-benefit and life-cycle cost analyses, in order to examine the feasibility of strengthening the reinforced concrete buildings. A probabilistic framework to estimate long-term earthquake-induced economical loss for woodframe structures was proposed and demonstrated in the work by Pei and Van De Lindt [12].

3 Life Cycle Cost Analysis

The total cost C_{TOT} of a structure, may refer either to the design-life period of a new structure or to the remaining life period of an existing or retrofitted structure. This cost can be expressed as a function of time and the design vector as follows [13]

$$C_{TOT}(t, \boldsymbol{s}) = C_{IN}(\boldsymbol{s}) + C_{LS}(t, \boldsymbol{s}) \tag{1}$$

where C_{IN} is the initial cost of a new or retrofitted structure, C_{LS} is the present value of the limit state cost; s is the design vector corresponding to the design loads, resistance and material properties, while t is the time period. The term "initial cost" of a new structure refers to the cost just after construction. The initial cost is related to the material and the labour cost for the construction of the building which includes concrete, steel reinforcement, labour cost for placement as well as the non-structural component cost. The term "limit state cost" refers to the potential damage cost from earthquakes that may occur during the life of the structure. It accounts for the cost of the repairs after an earthquake, the cost of loss of contents, the cost of injury recovery or human fatality and other direct or indirect economic losses related to loss of contents, rental and income. The quantification of the losses in economical terms depends on several socio-economic parameters. It should be mentioned that in the calculation formula of C_{LS} a regularization factor is used that transforms the costs in present values. The most difficult cost to quantify is the cost corresponding to the loss of a human life. There are a number of approaches for its estimation, ranging from purely economic reasoning to more sensitive that consider the loss of a human being irreplaceable. Therefore, the estimation of the cost of exceedance of the collapse prevention damage state will vary considerably according to which approach is adopted.

Damage may be quantified by using several damage indices (DIs) whose values can be related to particular structural damage states. The idea of describing the state of damage of the structure by a specific number, on a defined scale in the form of a damage index, is attractive because of its simplicity. So far a significant number of researchers has studied various damage indices for reinforced concrete or steel structures, a detailed survey can be found in the work by Ghobarah et al. [25]. Damage, in the context of life cycle cost analysis (LCCA), means not only structural damage but also non-structural damage. The latter including the case of architectural damage, mechanical, electrical and plumbing damage and also the damage of furniture, equipment and other contents. The maximum interstory drift (θ) has been considered as the response parameter which best characterises the structural damage, which has been associated with all types of losses. It is generally accepted that interstorey drift can be used as one limit state criterion to determine the expected damage. The relation between the drift ratio limits with the limit state, employed in this study (Table 1), is based on the work of Ghobarah [14] for ductile RC moment resisting frames. On the other hand, the intensity measure which has been associated with the loss of contents like furniture and equipment is the maximum response floor acceleration. The relation of the limit state with the values of the floor acceleration used in this work (Table 1) are based on the work of Elenas and Meskouris [15].

The limit state cost (C_{LS}), for the ith limit state, can thus be expressed as follows

$$C_{LS}^{i,\theta} = C_{dam}^{i} + C_{con}^{i,\theta} + C_{ren}^{i} + C_{inc}^{i} + C_{inj}^{i} + C_{fat}^{i} \tag{2a}$$

$$C_{LS}^{i,acc} = C_{con}^{i,acc} \tag{2b}$$

where C_{dam}^{i} is the damage repair cost, $C_{con}^{i,\theta}$ is the loss of contents cost due to structural damage that is quantified by the maximum interstorey drift, C_{ren}^{i} is the loss of

Table 1 Limit state drift ratio limits for bare Moment Resisting Frames and contents DI

Limit state	Interstorey drift (%) [14]	Contents DI (g) [15]
(I) – None	$\theta \leq 0.1$	$\ddot{u}_{floor} \leq 0.05$
(II) – Slight	$0.1 < \theta \leq 0.2$	$0.05 < \ddot{u}_{floor} \leq 0.10$
(III) – Light	$0.2 < \theta \leq 0.4$	$0.10 < \ddot{u}_{floor} \leq 0.20$
(IV) – Moderate	$0.4 < \theta \leq 1.0$	$0.20 < \ddot{u}_{floor} \leq 0.80$
(V) – Heavy	$1.0 < \theta \leq 1.8$	$0.80 < \ddot{u}_{floor} \leq 0.98$
(VI) – Major	$1.8 < \theta \leq 3.0$	$0.98 < \ddot{u}_{floor} \leq 1.25$
(VII) – Collapsed	$\theta > 3.0$	$\ddot{u}_{floor} > 1.25$

Table 2 Limit state costs – calculation formula [18–20]

Cost category	Calculation formula	Basic cost
Damage/repair (C_{dam})	Replacement cost × floor area × mean damage index	1,500 €/m^2
Loss of contents (C_{con})	Unit contents cost × floor area × mean damage index	500 €/m^2
Rental (C_{ren})	Rental rate × gross leasable area × loss of function	10 €/month/m^2
Income (C_{inc})	Rental rate × gross leasable area × down time	2,000 €/year/m^2
Minor injury ($C_{inj,m}$)	Minor injury cost per person × floor area × occupancy rate* × expected minor injury rate	2,000 €/person
Serious injury ($C_{inj,s}$)	Serious injury cost per person × floor area × occupancy rate* × expected serious injury rate	2×10^4 €/person
Human fatality (C_{fat})	Human fatality cost per person × floor area × occupancy rate* × expected death rate	2.8×10^6 €/person

∗ Occupancy rate 2 persons/100 m^2.

rental cost, C_{inc}^{i} is the income loss cost, C_{inj}^{i} is the cost of injuries and C_{fat}^{i} is the cost of human fatality. These cost components are related to the damage of the structural system. $C_{con}^{i,acc}$ is the loss of contents cost due to floor acceleration [16]. Details about the calculation formula for each limit state cost along with the values of the basic cost for each category can be found in Table 2 [17]. The values of the mean damage index, loss of function, down time, expected minor injury rate, expected serious injury rate and expected death rate used in this study are based on [18–20]. Table 3 provides the ATC-13 [18] and FEMA-227 [19] limit state dependent damage consequence severities.

Based on a Poisson process model of earthquake occurrences and an assumption that damaged buildings are immediately retrofitted to their original intact conditions after each major damage-inducing seismic attack, Wen and Kang [13] proposed the following formula for the limit state cost function considering N limit states

$$C_{LS} = C_{LS}^{\theta} + C_{LS}^{acc} \tag{3a}$$

Table 3 Limit state parameters for cost evaluation

	FEMA-227 [19]				ATC-13 [18]	
Limit state	Mean damage index (%)	Expected minor injury rate	Expected serious injury rate	Expected death rate	Loss of function (%)	Down time (%)
(I) – None	0	0	0	0	0	0
(II) – Slight	0.5	3.0E-05	4.0E-06	1.0E-06	0.9	0.9
(III) – Light	5	3.0E-04	4.0E-05	1.0E-05	3.33	3.33
(IV) – Moderate	20	3.0E-03	4.0E-04	1.0E-04	12.4	12.4
(V) – Heavy	45	3.0E-02	4.0E-03	1.0E-03	34.8	34.8
(VI) – Major	80	3.0E-01	4.0E-02	1.0E-02	65.4	65.4
(VII) – Collapsed	100	4.0E-01	4.0E-01	2.0E-01	100	100

$$C_{LS}^{\theta}(t,s) = \frac{\nu}{\lambda}\left(1 - e^{-\lambda t}\right)\sum_{i=1}^{N} C_{LS}^{i,\theta} \cdot P_i^{\theta} \tag{3b}$$

$$C_{LS}^{acc}(t,s) = \frac{\nu}{\lambda}\left(1 - e^{-\lambda t}\right)\sum_{i=1}^{N} C_{LS}^{i,acc} \cdot P_i^{acc} \tag{3c}$$

where

$$P_i^{DI} = P(DI > DI_i) - P(DI > DI_{i+1}) \tag{4}$$

and

$$P(DI > DI_i) = (-1/t) \cdot \ln[1 - \bar{P}_i(DI - DI_i)] \tag{5}$$

P_{i} is the probability of the ith limit state being violated given the earthquake occurrence and C_{LS}^{i} is the corresponding limit state cost; $P(DI - DI_i)$ is the exceedance probability given occurrence; DI_i, DI_{i+1} are the damage indices (maximum interstorey drift or maximum floor acceleration) defining the lower and upper bounds of the ith limit state; $\overline{P}_i(DI - DI_i)$ is the annual exceedance probability of the maximum damage index DI_{i}; ν is the annual occurrence rate of significant earthquakes modelled by a Poisson process and t is the service life of a new structure or the remaining life of a retrofitted structure. Thus, for the calculation of the limit state cost of Eq. (3b) the maximum interstorey drift DI is considered, while for the case of Eq. (3b) the maximum floor acceleration is used. The first component of Eqs. (3b) or (3c), with the exponential term, is used in order to express C_{LS} in present value, where λ is the annual monetary discount rate. In this work the annual monetary discount rate λ is taken to be constant, since considering a continuous discount rate is accurate enough for all practical purposes according to Rackwitz [21, 22]. Various approaches yield values of the discount rate λ in the range of 3–6% [18], in this study it was taken equal to 5%.

Each limit state is defined by drift ratio limits or floor acceleration, as listed in Table 1. When one of the *DIs* is exceeded the corresponding limit state is assumed to be reached. The annual exceedance probability $\overline{P}_i(DI > DI_i)$ is obtained from a relationship of the form

$$\overline{P}_i(DI > DI_i) = \gamma(DI_i)^{-k} \tag{6}$$

The above expression is obtained by best fit of known $\overline{P}_i - DI_i$ pairs for each of the two *DIs*. These pairs correspond to the 2%, 10% and 50% in 50 years earthquakes that have known probabilities of exceedance $\overline{P}_i$. In this work the maximum value of DI_i (interstorey drift or floor acceleration) corresponding to the three hazard levels considered, are obtained through a number of non-linear dynamic analyses. The selection of the proper external loading for design and/or assessment purposes is not an easy task due to the uncertainties involved in the seismic loading. For this reason a rigorous treatment of the seismic loading is to assume that the structure is subjected to a set of records that are more likely to occur in the region where the structure is located. In our case as a series of twenty artificial accelerograms per hazard level is implemented.

According to Poisson's law the annual probability of exceedance of an earthquake with a probability of exceedance p in t years is given by the formula

$$\overline{P} = (-1/t) \cdot \ln(1 - p) \tag{7}$$

This means that the 2/50 earthquake has a probability of exceedance equal to $\overline{P}_{2\%} = -\ln(1 - 0.02)/50 = 4.04 \times 10^{-4} (4.04 \times 10^{-2}\%)$.

4 Multicomponent Incremental Dynamic Analysis

The main objective of an IDA study is to define a curve through a relation between the seismic intensity level and the corresponding maximum response of the structural system. The intensity level and the structural response are described through an intensity measure (IM) and an engineering demand parameter (EDP), respectively. The IDA [23] study is implemented through the following steps: (i) define the nonlinear FE model required for performing nonlinear dynamic analyses; (ii) select a suit of natural records; (iii) select a proper intensity measure and an engineering demand parameter; (iv) employ an appropriate algorithm for selecting the record scaling factor in order to obtain the IDA curve performing the least required nonlinear dynamic analyses and (v) employ a summarization technique for exploiting the multiple records results.

Selecting IM and EDP is one of the most important steps of the IDA study. In the work by Giovenale et al. [24] the significance of selecting an efficient IM is discussed while an originally adopted IM is compared with a new one. The IM should be a monotonically scalable ground motion intensity measure like the peak ground acceleration (PGA), peak ground velocity (PGV), the $\xi = 5\%$ damped spectral acceleration at the structure's first-mode period ($\mathrm{SA}(\mathrm{T}_1, 5\%)$) and many others. In the current work the $\mathrm{SA}(\mathrm{T}_1, 5\%)$ is selected, since it is the most commonly used intensity measure in practice today for the analysis of buildings. On the other hand, the damage may be quantified by using any of the EDPs whose values can be related to particular structural damage states. A number of available response-based EDPs were discussed and critically evaluated in the past for their applicability in seismic damage evaluation [25]. In the work by Ghobarah et al. [25]

the EDPs are classified into four categories: engineering demand parameters based on maximum deformation, engineering demand parameters based on cumulative damage, engineering demand parameters accounting for maximum deformation and cumulative damage, global engineering demand parameters. In the current work the maximum interstorey drift θ_{max} is chosen, belonging to the EDPs which are based on the maximum deformation. The reason for selecting θ_{max} is because there is an established relation between interstorey drift values and performance-oriented descriptions such as immediate occupancy, life safety and collapse prevention [26]. Furthermore, there is a defined relation between drift ratio and damage-state [14] that is required for LCCA.

According to the MIDA framework a set of natural records, each one represented by its longitudinal and transverse components, are applied to the structure in order to account for the randomness on the seismic excitation. The difference of the MIDA framework from the original one component version of the IDA, proposed by Vamvatsikos and Cornell [23], stems from the fact that for each record a number of MIDA representative curves can be defined depending on the incident angle selected, while in most cases of the one component version of IDA only one IDA representative curve is obtained. MIDA is based on the idea of considering variable incident angle for each record, taking into account randomness both on the seismic excitation and the incident angle. In MIDA the relation of IM-EDP is defined similarly to the one component version of the IDA, i.e. both horizontal components of each record are scaled to a number of intensity levels to encompass the full range of structural behaviour from elastic to yielding that continues to spread, finally leading to global instability. In order to preserve the relative scale of the two components of the records, the component of the record having the highest $SA(T_1, 5\%)$ is scaled first, while a scaling factor that preserves their relative ratio is assigned to the second component.

MIDA is implemented over a set of record-incident angle pairs. According to MIDA a sample of N pairs of record-incident angle is generated by means of LHS [27], MIDA is conducted for each pair and a representative curve is developed. Afterwards all these representative MIDA curves are used in order to define the 16%, 50% and 84% median curves. LHS is a strategy for generating random sample points ensuring that every part of the random space is represented. Latin hypercube samples are generated by dividing each random variable into N non-overlapping segments of equal probability. Thus, if M random variables are considered the random variable space is partitioned into N^M cells. For each random variable, a single value is randomly selected from each segment, producing a set of N values. The values of each random variable are randomly matched with each other to create N samples. In the current implementation both record and incident angle are considered as uniformly distributed random variables over a set of M_{rec} records and in the range 0 to 180 degrees, respectively. In order to implement the proposed procedure the number of simulations N_{sim} (pairs of record-incident angle) should be a whole multiplier of the number of records M_{rec}. The number of incident angles combined with each record $\mathrm{m} = 1, 2, \ldots, M_{rec}$ is equal to $\mathrm{n_{angle}} = M_{rec}/N_{sim}$, hence for each record $\mathrm{n_{angle}}$ angles uniformly distributed in the range of 0–180 degrees are generated in order to define the N_{sim} pairs.

5 Numerical Results

In this chapter two test cases have been considered.

5.1 Three and Six Storey Symmetrical Test Example

A multi-storey 3D RC building, shown in Fig. 1, has been considered in order to study the application of the MIDA framework in LCCA. The test example corresponds to an RC building having symmetrical plan view. Two test cases with three and six storeys have been examined for this test example. The cross-section of the beams and the columns along with the longitudinal and transverse reinforcement for all test cases are given in Table 4. Concrete of class C20/25 (nominal cylindrical strength of 20 MPa) and steel of class S500 (nominal yield stress of 500 MPa) are assumed. The slab thickness for all test cases is equal to 15 cm and is considered to contribute to the moment of inertia of the beams with an effective flange width. In addition to the self weight of the beams and the slab, a distributed dead load of $2\,\mathrm{kN/m^2}$ due to floor finishing and partitions and imposed live load with nominal value of $1.5\,\mathrm{kN/m^2}$, are considered. A centreline model was formed, for both test examples, using the OpenSEES [28] simulation platform. The members

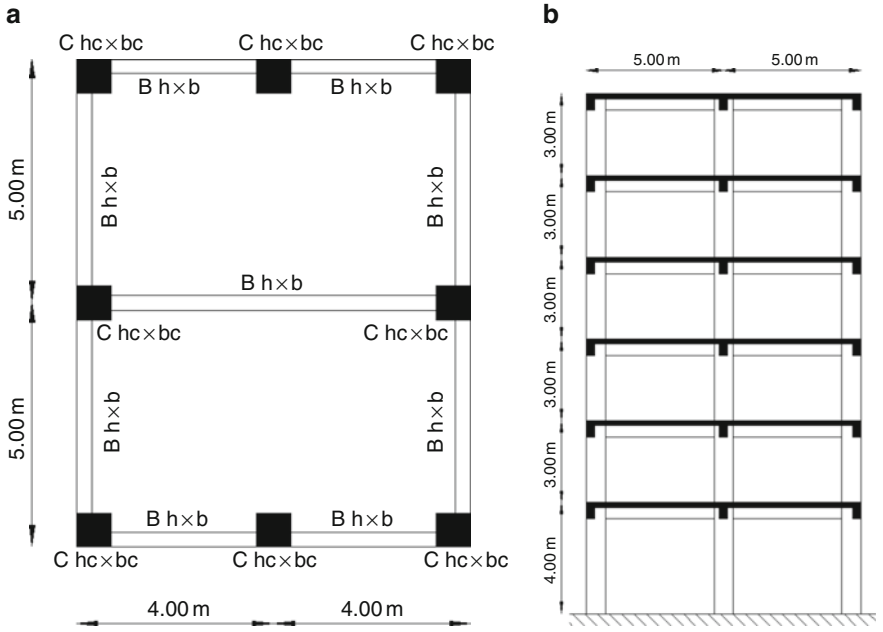


Fig. 1 Symmetric test example: (**a**) plan view and (**b**) side view for the six storey case

Table 4 The two designs

		Columns	Beams
Symmetric	Three storey	0.40 × 0.40, LR: 6Ø28, TR: (4)Ø10/20 cm	0.25 × 0.55, LR: 6Ø24 TR: (4)Ø8/20 cm
	Six storey	0.50 × 0.50, LR: 8Ø32, TR: (4)Ø10/15 cm	0.25× 0.55, LR: 6Ø28, TR: (4)Ø8/20 cm

LR longitudinal reinforcement, *TR* transverse reinforcement

are modelled using the force-based fibre beam-column element, while in order to account for the shear failure a nonlinear shear force-shear distortion (V-γ) law is adopted based on the work of Marini and Spacone [29].

In the parametric study performed the following abbreviations are used: *IDA(no_recs)* stands for the implementation of the two components of *no_recs* records along the structural axes; while *MIDA(no_recs,no_angles)* stands for the implementation of the two components of *no_recs* records along *no_angles* randomly selected orthogonal systems varying by the incident angle. Before proceeding to the parametric study a significant part of the life-cycle cost analysis is explained. As it is shown in Eq. (1) initial and limit-state costs are the two components of the life-cycle cost. The limit-state cost calculation procedure requires the assessment of the structural capacity in at least three hazard levels of increased intensity.

In this work five pairs of annual probability of exceedance ($\overline{P}_i$) and maximum interstorey drift (θ_i) corresponding to five hazard levels are implemented for obtaining a better fit curve. The numerical investigation is composed by two parts. In the first part the influence of the two variants (*IDA*, *MIDA*) was examined with reference to the maximum interstorey drift corresponding to the 50/50, 10/50, 5/50, 3/50 and 2/50 hazard levels defined in accordance to the hazard curves of the city of San Diego, California (Latitude (N) 32.7°, Longitude (W) −117.2°). In both variants *no_recs* records (*no_recs* = 10, 20, 40 or 60) are employed, which are applied along the structural axes or alongside a randomly selected orthogonal system. The records were randomly selected from the three lists given in [30]. The records composing the three lists have been selected from the PEER strong-motion database [31] according to the following features: (i) Events occurred in specific area (longitude −124° to −115°, latitude 32° to 41°). (ii) Moment magnitude (M) is equal to or greater than 5. (iii) Epicentral distance (R) is smaller than 150 km. To make sure that the randomly selected list of*no_recs* records (when *no_recs* = 10, 20 or 40) of both *IDA(no_recs)* and *MIDA(no_recs,no_angles)* implementations is not dominated by a few events, it was decided to discard records from the same earthquake and to keep only one. This was performed by means of LHS selecting only one, two or more records from the same earthquake depending on the value of *no_recs*; since the records belong to 12 earthquakes.

The implementation of *IDA(no_recs)* was examined first where the two components of *no_recs* records are applied along the structural axes while four variants are examined using different number of records (10, 20, 40 and 60

records). In the second group of implementations IDA(60) is compared with the *MIDA(no_recs,no_angles)* where the two components of *no_recs* records are applied along *no_angles* randomly selected orthogonal systems varying on the incident angle. The differences between IDA(60) and MIDA(60,1) stand for the incident angle used for each record in each implementation. In IDA(60) the two components of each record are applied along the structural axes while in MIDA(60,1) the incident angle is randomly chosen between 0 and 180 degrees for each record. Although in the three storey symmetric test case the 50% median values obtained for IDA(60) and MIDA(60,1) almost coincide, the corresponding 16% and 84% medians vary significantly. Same results are obtained for the six storey symmetric test case. Thus, it can be concluded that taking into account the incident angle as a random parameter in the MIDA framework is crucial; although the records of the three lists have different recording angle the randomness on the incidence of attack of the earthquake hazard cannot be taken into account in a robust way.

In the last group of implementations it was also examined the influence of applying 20 randomly selected records along the structural axes IDA(20) or along 3, 5 or 15 randomly chosen incident angles. It can be seen that applying the two components of the records along the structural axes either underestimates or overestimates the drift median values compared to the three MIDA implementations. Furthermore, all MIDA implementations provide very good estimates of the 50% median drift values compared to MIDA(20,15) which is considered as the "correct" one. Thus, implementing few (five) randomly chosen incident angles are enough for taking into account the randomness on the incidence of attack of the earthquake in a robust way.

In the last part of this study it was examined the influence of the variability of the median drift values on the calculation of the limit state cost. In this part the following abbreviations are used: $C_{LS}(50)$, $C_{LS}(16)$ and $C_{LS}(84)$ corresponding to the limit state cost calculated based on the 50%, 16% and 84% drift median values, respectively. The results of the life-cycle cost analysis for the test cases examined are shown in Fig. 2. In the three storey symmetric test case the performance of the four IDA implementations are almost identical with respect to $C_{LS}(50)$, while they vary up to 100% with reference to $C_{LS}(16)$. In the six storey symmetric test case, though, the four IDA implementations vary from 6% to 45% with reference to $C_{LS}(50)$; the percentage variations of IDA are estimated with reference to IDA(60). Comparing the four implementations that require 60 non-linear dynamic analyses per hazard level, i.e. IDA(60), MIDA(60,1), MIDA(10,6) and MIDA(20,3) implementations, it can be seen that for both test cases $C_{LS}(50)$ varies up to 40% while the variation increases to 95% for the $C_{LS}(16)$; the percentage variations are also estimated with reference to MIDA(60,1). On the other hand, the variation of $C_{LS}(50)$ cost estimated with reference to the MIDA(20,15) implementation is limited to 1% for MIDA(20,5), while the variation obtained for MIDA(10,6) and MIDA(20,5) implementations is up to 30%.

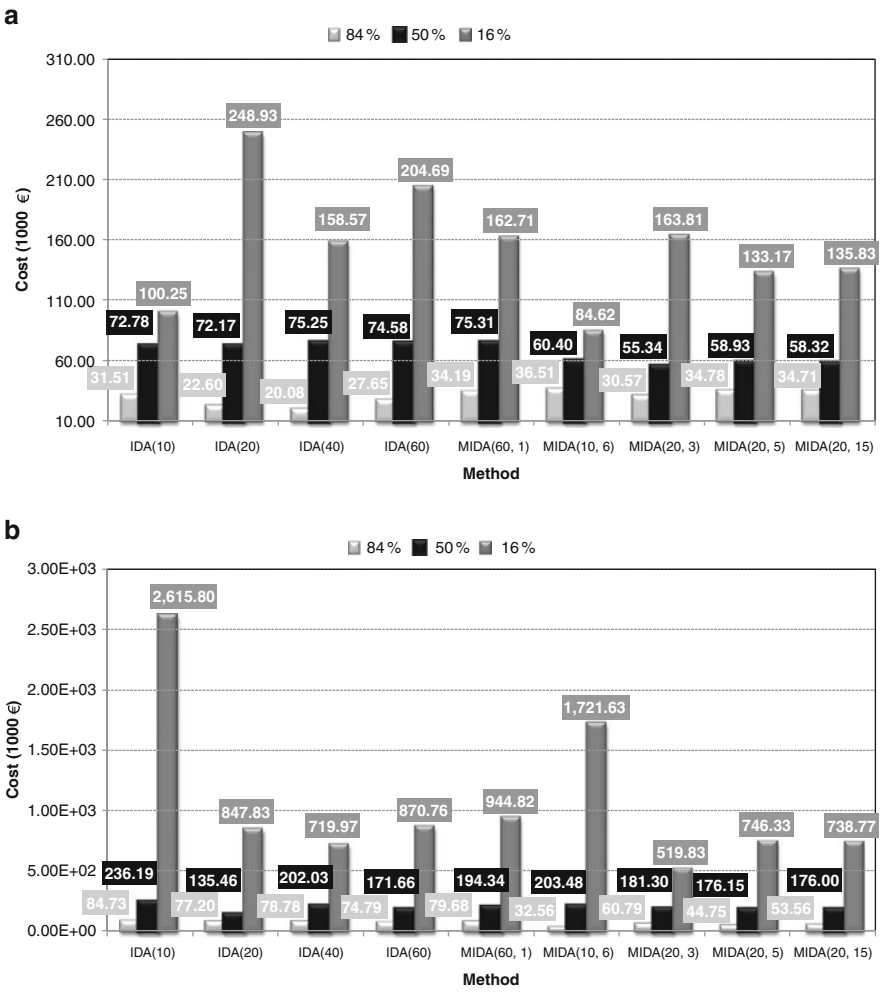


Fig. 2 Symmetric test example – life cycle cost analysis results: (**a**) three-storey and (**b**) six-storey cases

5.2 Five Storey Non-symmetrical Test Example

The plan and front views of the five storey non-symmetrical test example are shown in Fig. 3. The structural elements (beams and columns) are separated into 10 groups, 8 for the columns and 2 for the beams, resulting into 50 design variables.

The optimum designs achieved for different values of the q factor are presented in Table 5. It can be seen that the initial construction cost of design $D_{q=1}$ is increased by the marginal quantity of 7% compared to $D_{q=2}$, while it is 10% and 12% more expensive compared to $D_{q=3}$ and $D_{q=4}$, respectively. It can therefore be said that

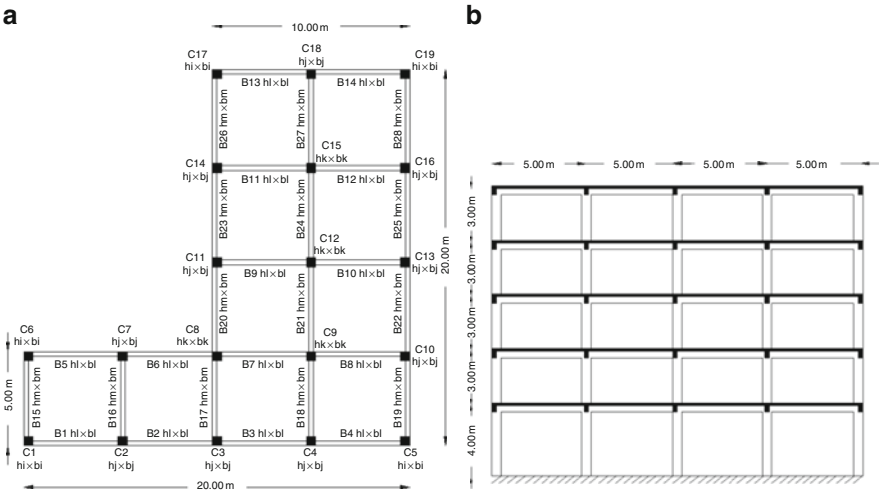


Fig. 3 Five storey test example – (**a**) plan view, (**b**) front view

the initial cost of RC structures, designed on the basis of their elastic response for the design earthquake, is not excessive taking into consideration the additional costs of a building structure which are practically the same for all designs $q = 1$ to 4. When the four designs are compared with respect to the cost of the RC skeletal members, design $D_{q=1}$ is increased by 40% compared to $D_{q=2}$ and by 67% and 92% compared to $D_{q=3}$ and $D_{q=4}$, respectively. Table 3 provides the ATC-13 [18] and FEMA-227 [19] limit state dependent parameters required for the calculation of the following costs: damage repair, loss of contents, loss of rental, income loss, cost of injuries and that of human fatality.

In the first step three $(\overline{P}_i - \theta_i)$ and three $(\overline{P}_i - \ddot{u}_{floor,i})$ pairs are defined corresponding to the three hazard levels

$$\begin{aligned} \overline{P}_{50\%} &= 1.39\% & \theta_{50\%} &= 0.14\% & \ddot{u}_{floor,50\%} &= 0.36\,\mathrm{g} \\ \overline{P}_{10\%} &= 2.10 \times 10^{-1}\% & \theta_{10\%} &= 0.42\% & \ddot{u}_{floor,10\%} &= 0.96\,\mathrm{g} \\ \overline{P}_{2\%} &= 4.04 \times 10^{-2}\% & \theta_{2\%} &= 1.24\% & \ddot{u}_{floor,2\%} &= 2.18\,\mathrm{g} \end{aligned} \tag{8}$$

The *abscissa* values for both $(\overline{P}_i - \theta_i)$ and $(\overline{P}_i - \ddot{u}_{floor,i})$ pairs, corresponding to the median values of the maximum interstorey drifts and maximum floor accelerations for the three hazard levels in question, are obtained through 20 non-linear time history analyses performed for each hazard level 50/50, 10/50 and 2/50. The median values of the four designs are shown in Fig. 3a and b. The *ordinate* values, corresponding to the annual probabilities of exceedance, are calculated using Eq. (7). Subsequently, exponential functions for the two *DIs*, as the one described in Eq. (6), is fitted to the pairs of Eq. (8). Once the two functions of the best fitted curve are defined the annual probabilities of exceedance $\overline{P}_i$ for each of the seven limit states

Table 5 Five storey test example – Optimum designs obtained for different values of behaviour factor q

		Optimum designs			
		q = 1	q = 2	q = 3	q = 4
Columns	h1 × b1	0.80 × 0.80, LR: 34Ø32, TR: (4)Ø10/10 cm	0.60 × 0.60, LR:8Ø24+ 12Ø28, TR: (4)Ø10/20 cm	0.55 × 0.55, LR:8Ø20+12Ø24, TR: (2)Ø10/20 cm	0.55 × 0.55, LR:8Ø24+ 4Ø28, TR: (2)Ø10/20 cm
	h2 × b2	0.85 × 0.85, LR: 34Ø32, TR: (4)Ø10/10 cm	0.60 × 0.60, LR:8Ø24+ 12Ø28, TR: (4)Ø10/20 cm	0.55 × 0.55, LR:8Ø22+ 12Ø26, TR: (2)Ø10/20 cm	0.55 × 0.55, LR:8Ø24+ 4Ø28, TR: (2)Ø10/20 cm
	h3 × b3	0.80 × 0.80, LR: 28Ø32, TR: (4)Ø10/10 cm	0.60 × 0.60, LR:8Ø24+ 12Ø28, TR: (4)Ø10/20 cm	0.50 × 0.50, LR:4Ø22+ 12Ø26, TR: (2)Ø10/20 cm	0.50 × 0.50, LR:4Ø26+ 4Ø32, TR: (2)Ø10/20 cm
	h4 × b4	0.70 × 0.70, LR:8Ø22+ 12Ø26, TR: (4)Ø10/10 cm	0.55 × 0.55, LR:8Ø24+ 12Ø28, TR: (4)Ø10/20 cm	0.55 × 0.55, LR:8Ø18+ 4Ø22, TR: (2)Ø10/20 cm	0.55 × 0.55, LR:8Ø18+ 4Ø22, TR: (2)Ø10/20 cm
	h5 × b5	0.70 × 0.70,LR: 26Ø32, TR: (4)Ø10/10 cm	0.55 × 0.55, LR:4Ø28+ 8Ø24, TR: (4)Ø10/20 cm	0.55 × 0.55, LR:8Ø24+ 4Ø28, TR: (2)Ø10/20 cm	0.55 × 0.55, LR:8Ø20+ 4Ø24, TR: (2)Ø10/20 cm
	h6 × b6	0.70 × 0.70, LR: 24Ø32, TR: (4)Ø10/10 cm	0.50 × 0.55, LR:12Ø28+ 8Ø24, TR: (4)Ø10/20 cm	0.45 × 0.45, LR:4Ø24 + 4Ø28, TR: (2)Ø10/20 cm	0.45 × 0.45, LR:4Ø26 + 4Ø32, TR: (2)Ø10/20 cm
	h7 × b7	0.65 × 0.65, LR:15Ø18 + 16Ø20, TR: (4)Ø10/10 cm	0.35 × 0.60, LR:8Ø18 + 8Ø20, TR: (2)Ø10/20 cm	0.35 × 0.55, LR:7Ø16 + 5Ø20, TR: (2)Ø10/20 cm	0.50 × 0.30, LR:5Ø18 + 6Ø16, TR: (2)Ø10/20 cm
	h8 × b8	0.60 × 0.65, LR:24Ø20+ 20Ø18, TR:(7)Ø10/10 cm	0.40 × 0.60, LR: 18Ø18, TR: (2)Ø10/20 cm	0.35 × 0.55, LR:8Ø18+ 5Ø20, TR: (2)Ø10/20 cm	0.55 × 0.30, LR:8Ø18, TR: (2)Ø10/20 cm
Beams	h9 × b9	0.45 × 0.55,LR: 15Ø20, TR: (2)Ø10/10 cm	0.30 × 0.50, LR: 9Ø18, TR: (2)Ø10/20 cm	0.30 × 0.55, LR:3Ø20+ 4Ø14, TR: (2)Ø10/20 cm	0.25 × 0.45, LR:4Ø16 + 4Ø14, TR: (2)Ø10/20 cm
	h10 × b10	0.50 × 0.55, LR: 24Ø18, TR: (2)Ø8/15 cm	0.30 × 0.55, LR: 10Ø18, TR: (2)Ø8/15 cm	0.30 × 0.55, LR:6Ø20, TR: (2)Ø8/15 cm	0.25 × 0.45, LR:4Ø16, TR: (2)Ø8/15 cm
$C_{IN,RCFrame}$ (1,000 €)		1.85E + 02	1.32E + 02	1.11E + 02	9.62E + 01
C_{IN} (1,000 €)		8.10E + 02	7.57E + 02	7.36E + 02	7.21E + 02

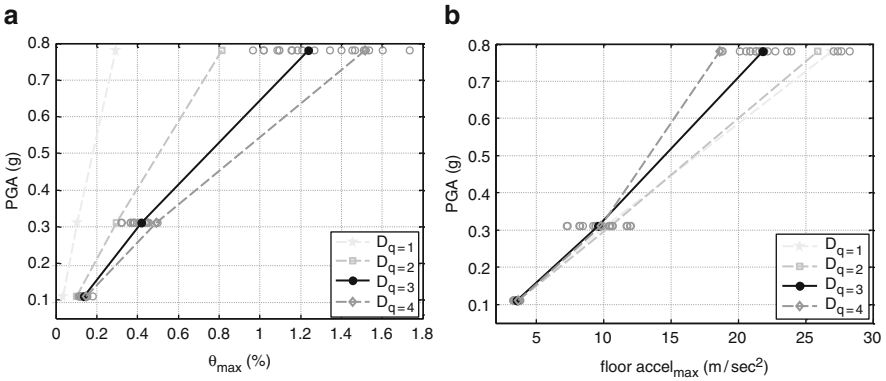


Fig. 4 Five storey test example – 50% median values of the maximum (**a**) interstorey drift values and (**b**) floor accelerations for the four designs

of Table 1 are calculated. Substituting $\overline{P}_i$ into Eq. (5) the exceedance probabilities of the limit state given occurrence are computed and the probabilities P_i are then evaluated from Eq. (4). This procedure is performed for each one of the DIs, i.e. interstorey drifts and floor accelerations. The limit state cost of Eq. (3a) is calculated adding the two components of Eqs. (3b) and (3c).

Figure 4 depicts the optimum designs obtained with reference to the behaviour factor, along with the initial construction, limit state and total life-cycle costs. It can be observed from this figure that although design $D_{q=1}$ is worst, compared to the other three designs with reference to C_{IN}, with respect to C_{TOT} the design $D_{q=4}$ is the most expensive. Comparing design $D_{q=3}$, obtained for the behaviour factor suggested by the Eurocodes for RC buildings, with reference to C_{TOT}, it can be seen that it is 50% and 20% more expensive compared to $D_{q=1}$ and $D_{q=2}$, respectively; while it is 10% less expensive compared to $D_{q=4}$.

The contribution of the initial and limit state cost components to the total life-cycle cost are shown in Fig. 5. C_{IN} represents the 75% of the total life-cycle cost for design $D_{q=1}$ while for designs $D_{q=2}$, $D_{q=3}$ and $D_{q=4}$ represents the 59%, 50% and 45%, respectively. Although the initial cost is the dominant contributor for all optimum design; for design $D_{q=1}$ the second dominant contributor is the cost of contents due to floor acceleration while for designs $D_{q=2}$, $D_{q=3}$ and $D_{q=4}$ damage and income costs are almost equivalent representing the second dominant contributors. It is worth mentioning, that the contribution of the cost of contents due to floor acceleration on the limit-state cost is only 20% for design $D_{q=4}$ while it is almost 85% for design $D_{q=1}$. This is due to the fact that the latter design is much stiffer and thus increased floor accelerations inflict significant damages on the contents. It has also to be noticed that although the four designs differ significantly, injury and fatality costs represent only a small quantity of the total cost: 0.015% for design $D_{q=1}$, while for designs $D_{q=2}$, $D_{q=3}$ and $D_{q=4}$ represents the 0.25%, 1.0% and 2.3% of the total cost, respectively (Fig. 6).

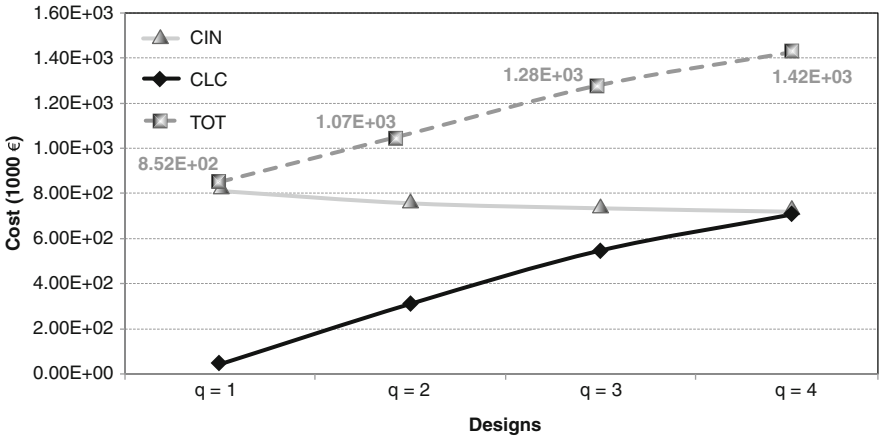


Fig. 5 Five storey test example – Initial (CIN), expected (CLC) and total expected (TOT) life-cycle costs for different values of the behaviour factor q ($t = 50$ years, $\lambda = 5\%$)

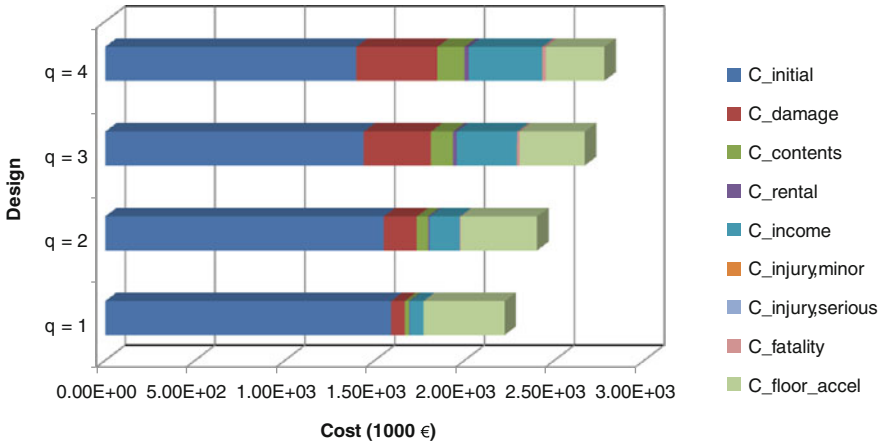


Fig. 6 Five storey test example – Contribution of the initial cost and limit state cost components to the total expected life-cycle cost for different values of the behaviour factor q

6 Conclusions

In this chapter incremental dynamic analysis is incorporated into the life cycle cost analysis procedure in order to assess two reinforced concrete buildings. In this work the way the incremental dynamic analysis is implemented in 3D structures is examined. Furthermore, an investigation was performed on the effect of the behaviour factor q in the final design of reinforced concrete buildings under earthquake loading

in terms of safety and economy. The main findings of this study can be summarized in the following:

- Based on the first part of the study, the first conclusion is that the significant variation on both drift median values and the values of the limit state costs estimated based on these values with reference to the number of records used in IDA implementation is an indication that selecting 10–20 records for assessing the structural capacity by means of IDA is not always correct for 3D structural systems.
- Also the implementation of both IDA and MIDA shows that, although in IDA(60) implementation a relatively large suit of records is used having different recording angles the randomness on the incidence of attack of the earthquake hazard cannot be taken into account in a robust way. MIDA(60,1) implementation represents a more suitable way to take into account randomness on both record and incident angle.
- Finally, comparing both drift values and the corresponding limit state costs for MIDA(20,3), MIDA(20,5) and MIDA(20,15) implementations it can be seen that few (five) randomly chosen incident angles are enough for taking into account the randomness on the incidence of attack of the earthquake in a robust way.
- Based on the second part of the study we can conclude that the initial cost of reinforced concrete structures designed based on elastic response $D_{q=1}$ is not excessive since it varies, for the two representative test cases considered, from 3% to 15% compared to the initial cost of the designs $D_{q=2}$ to $D_{q=4}$, respectively. In fact, the designs $D_{q=1}$ are only by 10% more expensive compared to the cost of the designs obtained for the value of the behaviour factor suggested by the Eurocode ($q = 3$). In the case, though, that the four designs are compared with reference to the cost of the RC skeletal members alone, design $D_{q=1}$ is 95% more expensive compared to $D_q (q = 2, 3, 4)$.
- Also the examination of cost components of LCC reveals that the contribution of the cost of contents due to floor acceleration on the limit-state cost was in the range 20% to 29% for design $D_{q=4}$ while it was found in the range 76% to 85% for design $D_{q=1}$. This is due to the fact that the latter design is much stiffer compared to the other ones and thus increased floor accelerations inflict significant damages on the contents.

Acknowledgments The first author acknowledges the financial support of the John Argyris Foundation.

References

1. Fajfar P (1998) Towards nonlinear methods for the future seismic codes. In: Booth E (ed) Seismic design practice into the next century. Balkema, Rotterdam
2. Mazzolani FM, Piluso V (1996) The theory and design of seismic resistant steel frames. E & FN Spon, London

3. ATC-19 (1995) Structural response modification factors. Applied Technology Council. Redwood City, CA
4. PrEN 1992–1–1:2002 (2002) Eurocode 2: design of concrete structures – Part 1: general rules and rules for buildings. Commission of the European Communities, European Committee for Standardization, December 2002
5. EN 1998–1:2003 (2003) Eurocode 8: design of structures for earthquake resistance. Part 1: general rules, seismic actions and rules for buildings. Commission of the European Communities, European Committee for Standardization, October 2003
6. Beck JL, Porter KA, Shaikhutdinov RV (2004) Simplified estimation of seismic life-cycle costs. In: Frangopol DM, Bruhwiler E, Faber MH, Adey B (eds) Life-cycle performance of deteriorating structures: assessment, design, and management. Reston, VA: ASCE/SEI, pp 229–236
7. Liu M, Burns SA, Wen YK (2003) Optimal seismic design of steel frame buildings based on life cycle cost considerations. Earthquake Eng Struct Dyn 32:1313–1332
8. Sanchez-Silva M, Rackwitz R (2004) Socioeconomic implications of life quality index in design of optimum structures to withstand earthquakes. J Struct Eng 130(9):969–977
9. Takahashi Y, Der Kiureghian A, Ang AH-S (2004) Life-cycle cost analysis based on a renewal model of earthquake occurrences. Earthquake Eng Struct Dyn 33:859–880
10. Frangopol DM, Liu M (2007) Maintenance and management of civil infrastructure based on condition, safety, optimization, and life-cycle cost. Struct Infr Eng 3(1):29–41
11. Kappos AJ, Dimitrakopoulos EG (2008) Feasibility of pre-earthquake strengthening of buildings based on cost-benefit and life-cycle cost analysis, with the aid of fragility curves. Nat Hazards 45(1):33–54
12. Pei S, Van De Lindt JW (2009) Methodology for earthquake-induced loss estimation: an application to woodframe buildings. Struct Saf 31(1):31–42
13. Wen YK, Kang YJ (2001) Minimum building life-cycle cost design criteria. I: methodology. J Struct Eng 127(3):330–337
14. Ghobarah A (2004) On drift limits associated with different damage levels. In: Fajfar P, Krawinkler H (eds) International workshop on performance-based seismic design. Bled, Slovenia, June 28–July 1
15. Elenas A, Meskouris K (2001) Correlation study between seismic acceleration parameters and damage indices of structures. Eng Struct 23:698–704
16. Wen YK, Kang YJ (2001) Minimum building life-cycle cost design criteria. II: applications. J Struct Eng 127(3):338–346
17. Ellingwood BR, Wen Y-K (2005) Risk-benefit-based design decisions for low-probability/high consequence earthquake events in mid-America. Prog Struct Eng Mater 7(2):56–70
18. ATC-13 (1985) Earthquake damage evaluation data for California. Applied Technology Council, Redwood City, CA
19. FEMA 227 (1992) A benefit–cost model for the seismic rehabilitation of buildings. Federal Emergency Management Agency, Building Seismic Safety Council, Washington, DC
20. Kang Y-J, Wen YK (2000) Minimum life-cycle cost structural design against natural hazards, Structural Research Series No. 629. Department of Civil and Environmental Engineering, University of Illinois at Urbana-Champaign, Urbana, IL
21. Rackwitz R (2006) The effect of discounting, different mortality reduction schemes and predictive cohort life tables on risk acceptability criteria. Reliab Eng Syst Safe 91(7):469–484
22. Rackwitz R, Lentz A, Faber M (2005) Socio-economically sustainable civil engineering infrastructures by optimization. Struct Saf 27(3):187–229
23. Vamvatsikos D, Cornell CA (2002) Incremental dynamic analysis. Earthquake Eng Struct Dyn 31(3):491–514
24. Giovenale P, Cornell CA, Esteva L (2004) Comparing the adequacy of alternative ground motion intensity measures for the estimation of structural responses. Earthquake Eng Struct Dyn 33(11):951–979
25. Ghobarah A, Abou-Elfath H, Biddah A (1999) Response-based damage assessment of structures. Earthquake Eng Struct Dyn 28(1):79–104

26. FEMA 273 (1997) NEHRP Guidelines for seismic rehabilitation of buildings. Federal Emergency Management Agency, Washington, DC
27. Olsson A, Sandberg G, Dahlblom O (2003) On latin hypercube sampling for structural reliability analysis. Struct Saf 25(1):47–68
28. McKenna F, Fenves GL (2001) The OpenSees command language manual – Version 1.2. Pacific Earthquake Engineering Research Centre, University of California, Berkeley
29. Marini A, Spacone E (2006) Analysis of reinforced concrete elements including shear effects. ACI Struct J 103(8):645–655
30. Lagaros ND (2010) The impact of the earthquake incident angle on the seismic loss estimation. Eng Struct 32:1577–1589
31. Pacific Earthquake Engineering Research (PEER): NGA Database (2005) http://peer.berkeley.edu/smcat/search.html. Accessed Dec 2008

Use of Analytical Tools for Calibration of Parameters in P25 Preliminary Assessment Method

İhsan E. Bal, F. Gülten Gülay, and Semih S. Tezcan

Abstract There exist several vulnerability assessment procedures including code-based detailed analysis methods as well as preliminary assessment techniques which are based on inspection and experience to identify the safety levels of buildings. Various parameters affect the seismic behaviour of buildings, such as dimensions and lay-out of structural members, existence of structural irregularities, presence of soft story or/and weak story, short columns and pounding effects, construction and the workmanship quality, soil conditions, etc. The objective of this study is to examine the effect of four essential structural parameters on the seismic behaviour of existing RC structures by using the most updated analytical tools. The effect of the concrete quality, corrosion effects, short columns and vertical irregularities have been examined. Parametric studies have been carried out on case study real buildings extracted from the Turkish building stock, one of which was totally collapsed in Kocaeli Earthquake of 1999. A control building has been considered for each sample structure with ideal parameters (i.e. without vertical irregularity or good quality of concrete, etc.). Nonlinear static push-over and cyclic analyses have been performed on 2D and 3D models. Base shear versus top displacement curves are obtained for each building in two orthogonal directions. Comparisons have been made in terms of shear strength, energy dissipation capability and ductility. The mean values of the drop in the performance are computed and factors are suggested to be utilized in preliminary assessment techniques, such as the recently proposed P25 method which is shortly summarized in this Chapter.

İ.E. Bal (✉)
EUCENTRE, Pavia, Italy
e-mail: ihsan.bal@eucentre.it

F.G. Gülay
Faculty of Civil Engineering, Istanbul Technical University, Istanbul, Turkey
e-mail: gulayg@itu.edu.tr

S.S. Tezcan
Department of Civil Engineering, Boğaziçi University, Istanbul, Turkey
e-mail: tezokan@superonline.com

M. Papadrakakis et al. (eds.), *Computational Methods in Earthquake Engineering*,
Computational Methods in Applied Sciences 21, DOI 10.1007/978-94-007-0053-6_25,
© Springer Science+Business Media B.V. 2011

Keywords Analytical tools · Calibration of parameters · P25 method · Preliminary assessment

1 Introduction

The majority of the existing buildings in developing and even developed countries located in the earthquake prone areas do not have sufficient seismic safety that is required by the current earthquake resistant design codes. For preventing loss of lives after future earthquakes, the collapse vulnerable buildings should be evaluated and necessary measures should be taken if existing seismic safety is not sufficient. Most earthquake loss assessment studies present that a high percentage (around 5–7%) of the existing buildings will experience medium or heavy damage in Istanbul, for example, where the building inventory is quite large and a serious seismic activity is expected in the near future [1, 13].

Following the devastating Kocaeli and Düzce earthquakes of August and November 1999, Turkish Government was faced with an enormous financial burden as a result of its statutory obligation to cover the full costs of rebuilding. In order to offset such catastrophic burdens in the future, probable to occur during the expected Istanbul earthquake, researchers and the local authorities were in search of wise and feasible solutions in order to decrease life loss during a future shaking. A key element for successful implementation of such a "campaign" of decreasing the life losses in near future is the prioritization of the buildings so that the collapse vulnerable structures can be identified to be retrofitted or demolished before the expected earthquake. Until recently, the only way of doing so was assumed to follow a code-based assessment procedure, what is categorized as "detailed assessment" in this study, to assess every single building in the earthquake vulnerable part of the city to identify the "unsafe" ones. Unfortunately, such an approach is not feasible in terms of financial sources available as the first reason; and it would possibly take some decades to be completed, as the second.

To minimize the probable losses, many researchers have been working on some simplified preliminary methods to identify the collapse vulnerable buildings by using certain parameters, developed by engineering experience obtained from past earthquakes. Most of these methods are of simplistic nature and of walk-down survey type. Such very simple methods that are based on observing the buildings without entering into them are called as "rapid assessment" methods in this study. On the contrary, methods that are based on combining the observation (i.e. qualitative score) with some simple calculations and require an engineering team to spend some considerable time inside the building are called "preliminary assessment" methods in this work. Preliminary assessment techniques do not usually require heavy analytical work since they are based on some basic factors adversely influencing the earthquake behaviour of RC buildings, such as presence of soft story or/and weak story, short columns, pounding possibility, etc.

Starting from 1970s, some rapid assessment methods are suggested to screen the existing structures in earthquake prone regions [3]. A rapid screening method was first codified in ATC 21 and ATC 21-1 to be applied prior to detailed assessment, in 1988 [7]. New versions were also issued by FEMA later in 2002 [8]. Several researchers have then worked on alternative methods to define the collapse risk of existing buildings by using certain parameters that affect the response of RC buildings. After 1992 Erzincan earthquake, Hassan and Sözen suggested the "Capacity Index Method" [9]. "Japanese Seismic Index Method" is another preliminary assessment technique that was originally developed for Japan [10] and then modified and applied to the buildings in Turkey [11]. P25 Preliminary Assessment Method is a recently developed preliminary assessment method, first suggested by [12], then developed and calibrated with real damaged buildings, through an intensive research project funded by TUBITAK (The Scientific and Technological Research Council of Turkey) [15, 17, 18, 24].

Preliminary assessment methods, including P25 Method, build on structural parameters of the examined building considered for the assessment. Parameters affecting the seismic structural behaviour of buildings, however, are actually numerous. The height of the structure, dimensions and lay-out of structural members, reinforcement detailing, the existence of various structural irregularities, the presence of soft story or/and weak story, short columns and heavy overhangs, pounding effects, construction and the workmanship quality, soil conditions are some of them. Seven different scores are calculated based on different possible collapse modes (i.e. collapse due to soft storey or short columns, etc.) and factors between 0.65 and 1 are used to multiply the base scores to represent the final score. The main purpose of this presented study is to put a light on these factors and to calibrate them with analytical results. It should be noted that, all previous preliminary assessment methods, without exception, are based on such single scalar factors that are using engineering judgment, which is a vague definition. The short column factor in most of the methods, for example, has been used as a single value such as 0.50 if short columns exist and 1.00 if they do not. P25 Preliminary Assessment Method; however, categorizes each parameter and represents them with more engineering way. Additionally, the parameters and the factors presented in the method are calibrated analytically as well as with the real case study structures even though the presented numerical calibration can be considered as simplistic and the number of case studies is certainly not enough.

This study focuses on some of the parameters included in the method effecting the earthquake behavior of the buildings, namely the effect of concrete quality, the loss of cross-section of steel reinforcement due to corrosion, some common vertical irregularities and short column formation. The objective is to investigate the effect of the change in these parameters on the lateral load capacity, energy dissipation capability and the overall ductility of the existing RC buildings. This piece of information will then be utilized in the aforementioned P25 Method. Static monotonic and cyclic non-linear analyses of the case study buildings have been performed to reach the aim. The case study structures were designed according to the old seismic code of Turkey, one of them was totally collapsed in Kocaeli Earthquake of 1999.

The buildings are selected from the Turkish buildings stock but they can also represent the majority of the existing under-designed or non-engineered RC buildings in the European-Mediterranean region.

2 Description of the Case Study Buildings

2.1 Case Study Building B1

B1 is a five-story building with a total height of 15 m. It does not exhibit any building irregularity and the plan is symmetrical in both directions with 4 × 4 m spans (see Fig. 1). The dimensions of the columns at the perimeter axes are 30 × 30 cm with 8Ø14, the dimensions of the interior columns, C2, are 40 × 40 cm with 10Ø14 longitudinal reinforcements. The characteristic tensile strength of the steel is 220 MPa (round bars). The beam dimensions are 25 × 50 cm. The combined loads are taken as 8.0 kN/m at the exterior beams and 10.0 kN/m at the interior beams while it is constant as 3.1 kN/m at the roof beams. The other details of the building can be found in [25]. The typical storey plan and elevation are shown in Fig. 1.

2.2 Case Study Building B2

The second case study structure, B2, is a real residential building located in Kadıköy, Asian part of Istanbul [18]. It is a small five-storey building with the plan dimensions of 15.6 × 4.5 m. The dimensions of C1 columns are 20 × 50 cm with 8Ø14 reinforcement and the cross-sectional dimensions of C2 columns are 20 × 60 cm with 10Ø14

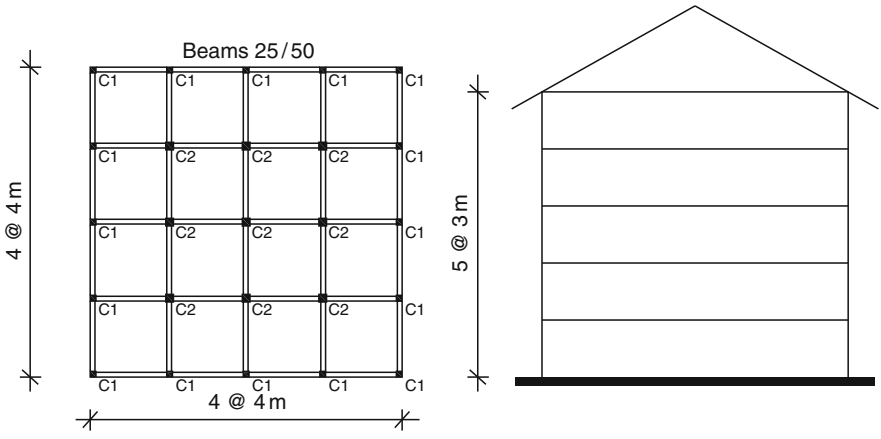


Fig. 1 Story plan (*left*) and the elevation (*right*) of the case-study building B1

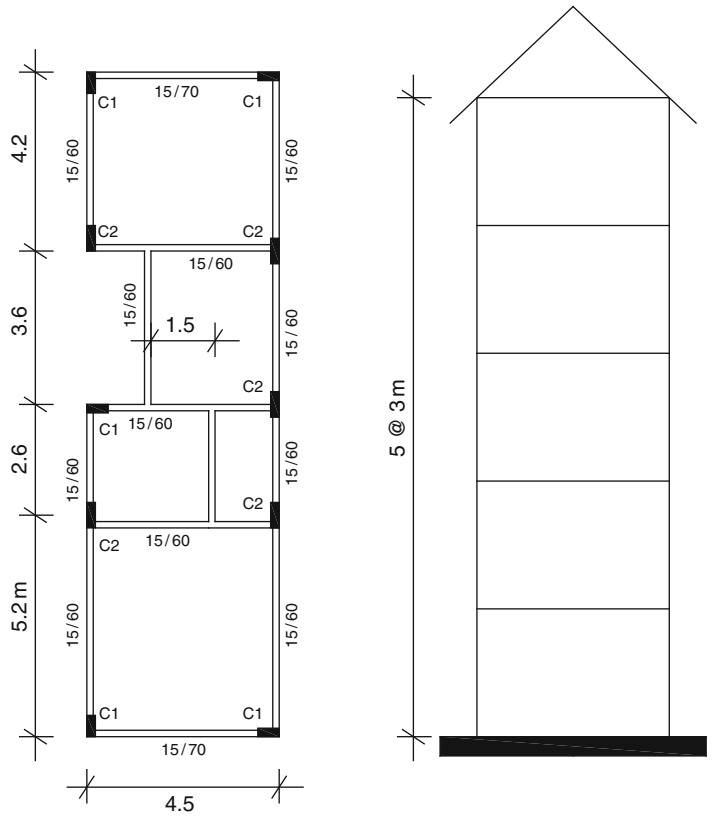


Fig. 2 Story plan (*left*) and the elevation (*right*) of the case-study building B2

Table 1 Beam reinforcement details for B2 building

	Middle sections		Support sections	
Dimensions (cm)	Bottom	Top	Bottom	Top
15 × 70	3Ø12	2Ø12	2Ø12	3Ø12
15 × 60	3Ø12	2Ø12	2Ø12	3Ø12

reinforcement. The beam dimensions are either 15 × 70 cm or 15 × 60 cm, as shown in Fig. 2. The characteristic steel tensile strength is 220 MPa, as defined by the code, and the average concrete compressive strength is 16 MPa. The reinforcement details of the two types of beams are shown in Table 1.

2.3 Case Study Building B3

The last case Study Building, B3, is a real building with seven floors. It was an RC structure that collapsed during the 1999 Kocaeli Earthquake. The slab system

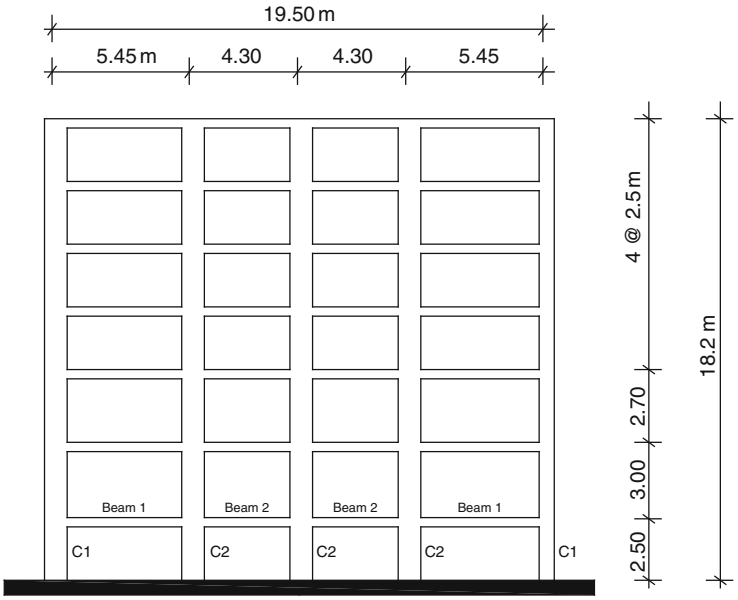


Fig. 3 A representative frame from the case study building B3

Table 2 Beam reinforcement details for B3 building

			Middle Sections		Support Sections	
Floor	Beam	Dimensions (cm)	Bottom	Top	Bottom	Top
Ground and first	B1	37 × 60	5Ø16	3Ø16	3Ø16	5Ø16
Second to seventh	B1	37 × 60	4Ø16	2Ø16	2Ø16	4Ø16
Ground and first	B2	37 × 60	5Ø12	3Ø12	3Ø12	5Ø12
Second to seventh	B2	37 × 60	4Ø12	2Ø12	2Ø12	4Ø12

Table 3 Column reinforcement details for B3 building

Floor	Column	Reinforcement
Ground and First	C1	20Ø16
Second and Third	C1	14Ø16
Fourth to Seventh	C1	6Ø16
Ground and First	C2	24Ø16
Second and Third	C2	20Ø16
Fourth to Seventh	C2	10Ø16

was designed with embedded shallow beams of 30 cm height. The elevation of an internal main frame of the building is shown in Fig. 3. The reinforcement details of the columns and the beams are shown in Tables 2 and 3.

3 Effects of Concrete Quality and Rebar Corrosion on the Seismic Response of RC Buildings

3.1 Concrete Quality

Developments in the concrete production technology, increasing awareness and improving official supervision systems help better concrete material to be used in RC construction. In recent decades in which there was a construction boom in many European-Mediterranean countries however, bad quality of concrete was used without proper control and curing. One case study, Turkish building stock, has been investigated in this study to give an idea to the reader about the statistical distribution of concrete quality in a large scale RC building stock.

The concrete quality of existing structures has been an essential question to be answered and it has been previously investigated by many researchers (see Table 4) in Turkey. Although the 1998 earthquake code, which requires the lowest concrete strength to be 20 MPa, was published and assigned in the beginning of 1998, the rigorous control of the concrete assembling process was only initiated following the introduction of the new set of construction supervising laws (No 585 and No 4708) after the year 2000. Extensive use of ready mix concrete started after 2000 whilst before that, even if ready mix concrete was used, the quality was poor and uncontrolled. It is noted by [16] that almost half of the samples which were taken from the ready mix concrete process did not satisfy the requirements of the related standards. If the largest data pool for Turkish building stock in Table 4 [14] is considered, it can be seen that the average concrete compressive strength of the building stock has been found about 17 MPa with a standard deviation of approximately 8 MPa. The gamma distribution, between values of 2 and 40 MPa, is suggested for the concrete compressive strength by the authors [14]. It was observed by them that an average of 16.5% of the existing building stock exhibits a level of concrete strength which is less than or equal to 8MPa. More interestingly, 3.3% of the existing buildings (which would result in around 21,000 buildings within the province and surrounding districts of Istanbul) are found to exhibit a level of compressive strength that is less than or equal to 4 MPa.

Table 4 Previous studies about the concrete quality of existing buildings in Turkey

# of buildings	Reference	Region	Mean Strength (MPa)	St. Dev.
102	N/A[a]	Adana	8.9	2.9
511	[2]	Istanbul and around	16.5	8.3
60	[23]	Kocaeli, Adapazarı and Istanbul	19.0	9.0
50	[20]	Erzincan	8.8	2.8
287	N/A[b]	Istanbul (Kadıköy)	13.0	N/A
1178	[14]	Istanbul and around	16.7	8.3

[a] Personal communication with the local authority in Adana
[b] Personal communication with the laboratory of the Municipality of Kadıköy

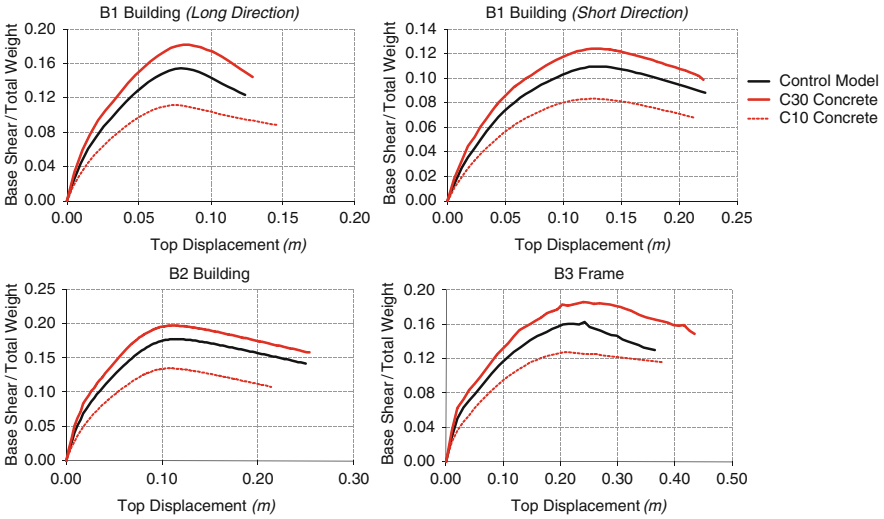


Fig. 4 DAP analysis results for the case study buildings for three different concrete qualities

In this work, case study buildings have been analyzed several times with different concrete qualities assigned, in order to observe the effect of the concrete quality on the lateral load response. Varying concrete qualities, as C10, C20, and C30 MPa have been applied. C20 concrete quality is used as the control model. Nonlinear Displacement-Based Adaptive Pushover (DAP) has been used for analysis [21]. Analyses have been stopped when any of the members has reached the limit state 3 strains ($\varepsilon_c = 0.0075$ and $\varepsilon_s = 0.035$) defined by [13].

As observed in Fig. 4, concrete quality is a parameter that is clearly proportional to the building overall strength; however, the overall ductility is not necessarily in correlation with it. Diagrams showing the difference in the base shear strength, energy dissipation capability and ductility has been given in Sect. 3.3. Discussion on how to implement such observations in the P25 Method has also been provided in Sect. 3.3.

3.2 Rebar Corrosion

Corrosion of reinforcing bars is a common issue even the modern structures suffer from. Steel is a material that can corrode in time and it gains volume as a result. This is the reason corrosion manifests itself as vertical cracks in the concrete cover in most of the cases. This causes loss of anchorage between the reinforcement and the concrete material. Additionally, loss of section of rebars is inevitable. This leads to significant decrease in the flexural and shear capacity of the member.

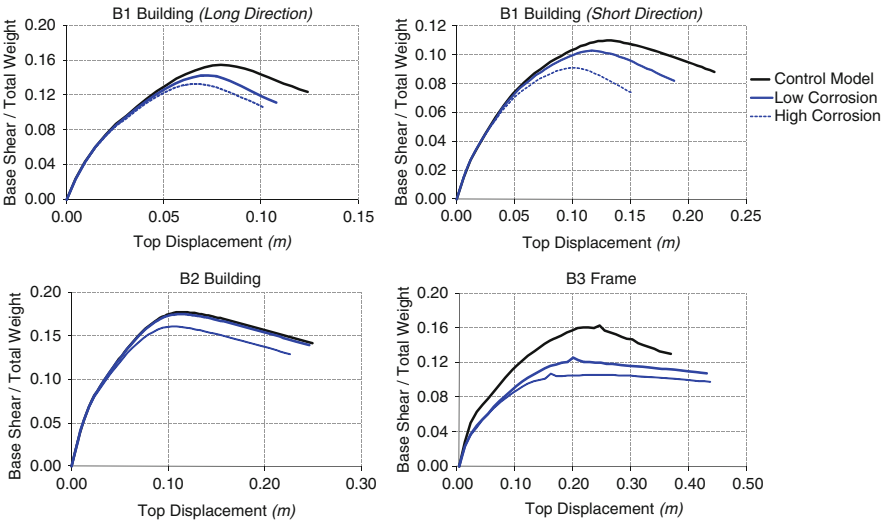


Fig. 5 DAP analysis results for the case study buildings for different corrosion levels

In this study low and high corrosion levels are considered for the case study buildings. The reinforcement is decreased 20% at the lowest 15% height of the existing columns at the ground floor and that is defined as low corrosion. Following, the reinforcement is decreased 30% up to the mid-height of the total existing columns at the ground floor and that is defined as the high corrosion case. The control building is assumed without any corrosion called as the control model. Due to its difficulty in numerical modelling, the loss of anchorage between concrete and steel has been neglected; nevertheless, adaptation of existing empirical bar-slip model could be a solution for this problem. This issue is left outside of the scope of this Chapter.

The results of the analyses show that the corrosion, in addition to the loss of strength, causes loss of ductility, and thus decrease in the energy dissipation capacity. The increase in ductility in B3 building (see Fig. 5) can be attributed to the fact that this frame has strong columns and flexible and weak beams; therefore, loss of rebars in columns allows the columns to reach the given strain limit states later than that of the control model thus leading larger displacement capacities. Discussions on the results and their conversions into useful parameters in the P25 Method have been provided in Sect. 3.3.

3.3 Quantitative Results

Capacity Decrease Factors (CDF) obtained from the analyses for high and low corrosion levels and C10 and C30 concrete qualities are tabulated as compared with the well-designed building with C20 concrete and no corrosion (control model),

Table 5 The capacity decrease factors (CDF) from the analytical solutions

		CDF from analyses											
		B1/long dir.			B1/short dir.			B2 building			B3 frame		
Parameter	CDF used in P25	Max. shear based	Energy based	Ductility based	Max. shear based	Energy based	Ductility based	Max. shear based	Energy based	Ductility based	Max. shear based	Energy based	Ductility based
High Corr.	0.80	0.92	0.79	0.91	0.94	0.78	0.68	0.99	0.97	0.91	0.77	0.94	1.19
Low Corr.	0.90	0.86	0.71	0.93	0.83	0.55	0.82	0.91	0.82	0.99	0.66	0.86	1.17
C10	0.77	0.72	0.88	1.31	0.76	0.73	0.93	0.76	0.64	0.86	0.79	0.85	1.04
C30	1.19	1.18	1.24	1.04	1.13	1.14	0.91	1.11	1.14	1.02	1.14	1.42	1.19

in terms of maximum base shear ratio, energy dissipation capability ratio and for the ductility ratio for three case study buildings (see Fig. 7; Table 5). A CDF is calculated by the capacity (load bearing capacity, energy dissipation capacity or ductility capacity) of the case evaluated divided by the capacity of the control model. The mean values of each different material defects are proposed as CDF values to be utilized for the P25 Method. The CDF factor is simply calculated as the ratio of the maximum base shear strength (or the maximum energy dissipation capacity calculated as the area below the curve or ductility) over the corresponding value obtained from the control model. Additionally, for the CDF factor for the concrete quality, the results obtained from analysis are then compared to that of a simple expression where the compressive strength of the concrete is the main parameter. Equation 1 below is based on the modulus of elasticity of the concrete of the building to that of the control model which has 20 MPa concrete quality. Modulus of elasticity is in general given as a constant multiplied by the square-root of the concrete compressive strength as calculated in most of the up-to-date design codes. Based on this information, the suggested equation is given as:

$$CDF_{concrete} = \sqrt{\frac{f_c}{20}} \tag{1}$$

where f_c is the average compressive strength of the structure in MPa. Comparative results between the suggested equation and the analytical findings can be seen in Fig. 6. A good agreement, with 2.5% average error, is obtained from the proposed expression.

Existence of corrosion in the reinforcements, the second parameter investigated in this study, causes about 16% decrease in the lateral load bearing capacity and 20% decrease in the energy dissipation capability. The calculated Capacity Decrease Factors *(CDF)* for corrosion at the lateral load capacity of three different structures are around 10–20%. It should be noted that the effect of corrosion is examined here only as a function of the decrease in the reinforcement bar diameters and the loss of the cover concrete. In fact, there would be additional effects of the corrosion,

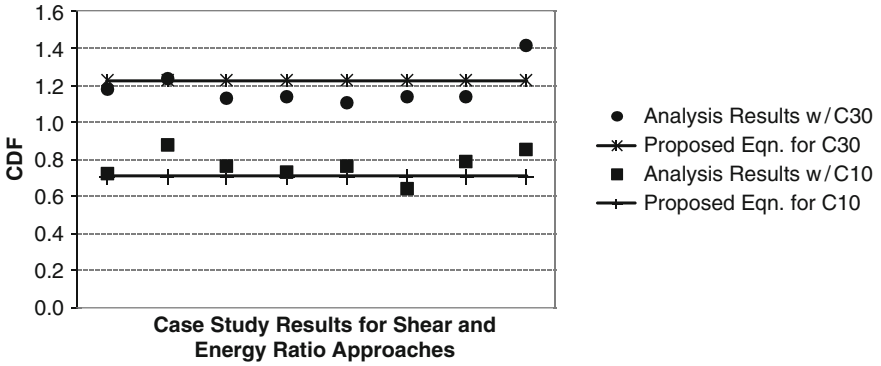


Fig. 6 Comparison between analytically defined CDF values and the results of the proposed equation (see Eq. 1)

namely the loss of adhesion between concrete and steel, and also deterioration of the concrete material. These issues may cause slip between concrete and steel, leading thus, for instance, to pinching effects where the loss of energy dissipation capability would be more than what is presented here.

The presented study provides a quantitative way to account for the effect of the examined parameters on the overall vulnerability of the existing RC structures which have similar deficiencies with the existing Turkish RC structures. The effect of the concrete quality change is presented as a function of a simple expression while the effect of the corrosion is provided in a tabulated form. The percentage deviations from the base model are also shown in Fig. 7.

The anomaly in Fig. 7a that exhibits itself as the increase in ductility despite the low concrete quality may be explained with the fact that the beams in the shorter direction of B1 building are the deepest in the building and decrease in concrete quality changes the failure mechanism of these governing sections from concrete failure to steel failure.

4 Quantification of the Effects of the Short Columns on the Seismic Response of RC Buildings

Columns commonly have values of shear span ratio above about 2.5, thus the mechanisms of force transfer by flexure or by shear may be considered as practically independent. If the shear span ratio is less than about 2.5, these two mechanisms of force transfer tend to merge into one, as the shear span itself becomes a two dimensional element. The most important issue related to shortening the column is the decrease in the shear span ratio leading thus a coupling between flexural and shear deformations and a premature shear failure of the column, unless the design of the column takes into account the increasing shear demand.

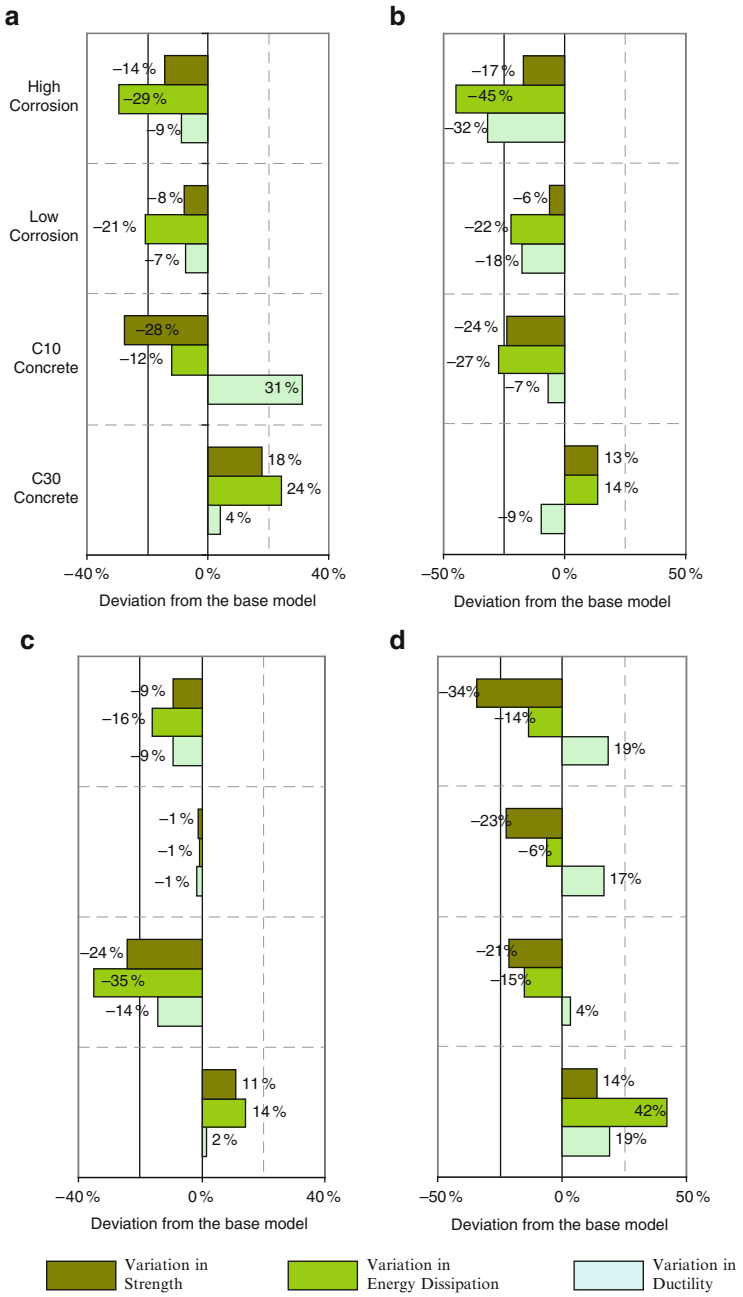


Fig. 7 The percentage deviations from the base model: (**a**) B1 building long direction, (**b**) B1 building short direction, (**c**) B2 building, and (**d**) B3 frame

Short column irregularity is a shear failure problem and it has long been recognized that shear strength of reinforced concrete columns is reduced with increasing ductility (see [19] for a comprehensive summary). The strength degradation is even more pronounced with cyclic loads. This is the reason that cyclic pushover analysis has been applied to the case study buildings with short columns to obtain a clearer insight to the effect of the short columns on the earthquake response.

Nine cases consisting three different free column lengths and three different number of short columns (i.e. "rare", "some" and "many") have been examined and the results are given in Tables 6 and 7. Restrained lengths of the short columns are supported laterally in the mathematical model. Ruaumoko2D software [5] has been used for the analyses. SINA degrading stiffness model has been used to represent the stiffness degradation of the short columns due to shear forces accumulated by cyclic loading (see Fig. 8). Analyses have been stopped when the drop in the strength has exceeded 20%.

In Fig. 8, α and β are bi-linear factors for positive and negative cracking to yield, respectively. $F_{cr}(i)$ is the cracking moment or force at "i", F_{cc} is the crack closing moment or force at "i". The "i" refers to different actions on the member. More details of the model can be found in the relative reference for the software [5]. Increasing cyclic displacement has been applied to the building following a first mode (inversed triangle) displacement pattern (see Fig. 9). Analyses have been stopped in the step where any of the members has reached the limit states described above.

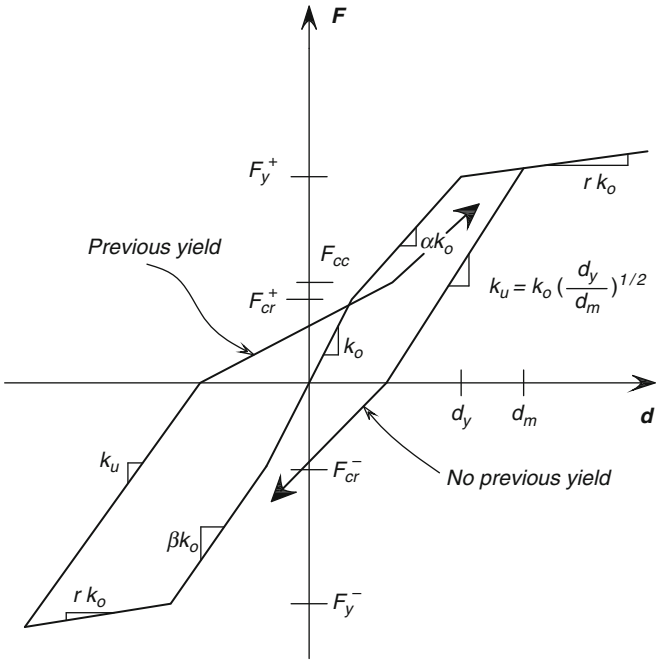


Fig. 8 SINA degrading stiffness hysteretic model (Modified from [5])

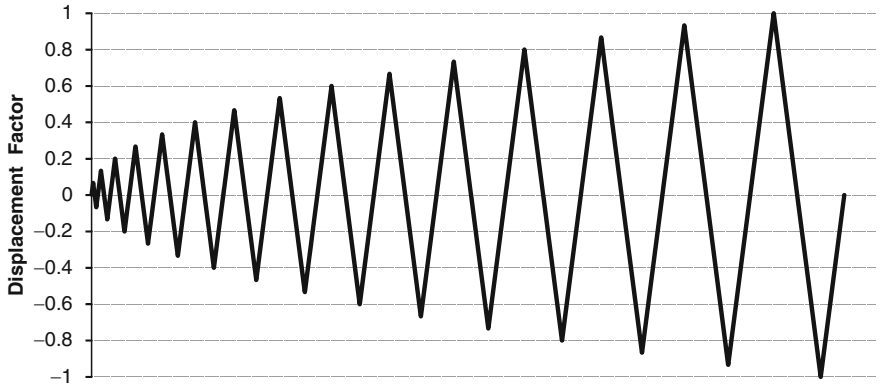


Fig. 9 Displacement history used for the short column analyses

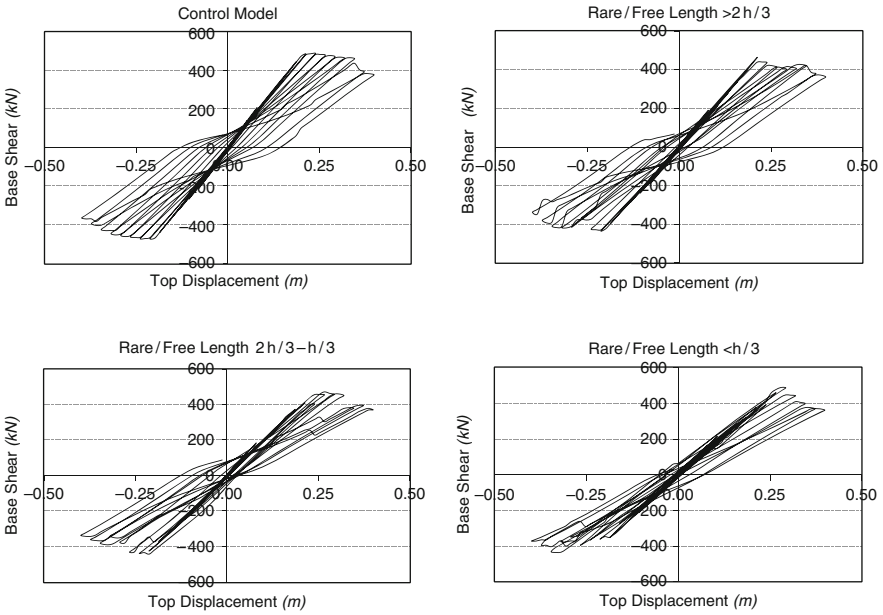


Fig. 10 Cyclic pushover plots for B1 when short columns "Rarely" exist in the building

Due to limitations in space, base shear versus top displacement plots of only one building (B1 in long direction) have been presented here between Figs. 10–12. The most pronounced outcome of these figures is the decrease in the lateral stiffness and strength along with significantly decreased energy dissipation capacity.

Among all investigated cases, the worst strength and ductility degradation is observed in the case where the column free length is around half of the critical storey height and short columns consist of more than 30% of the columns of that storey.

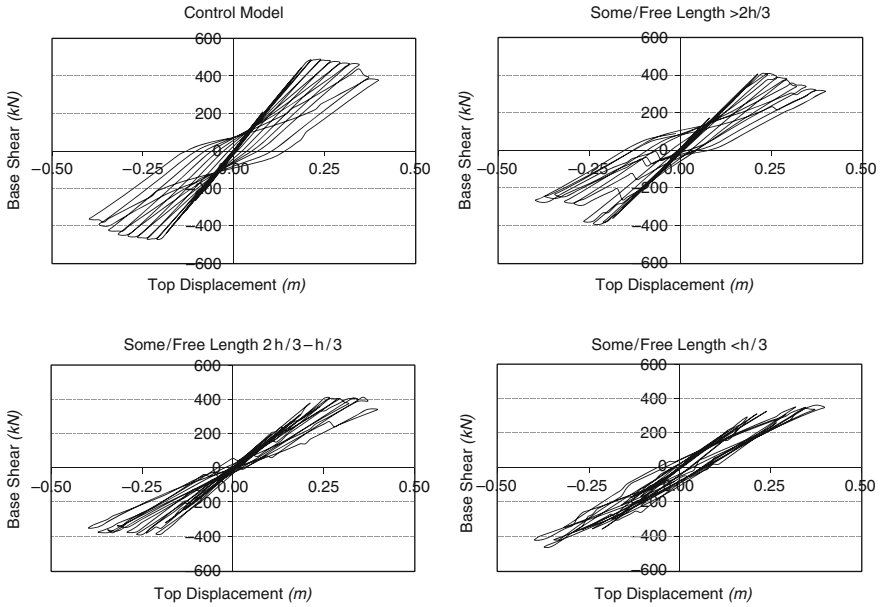


Fig. 11 Cyclic pushover plots for B1 when "Some" short columns exist in the building

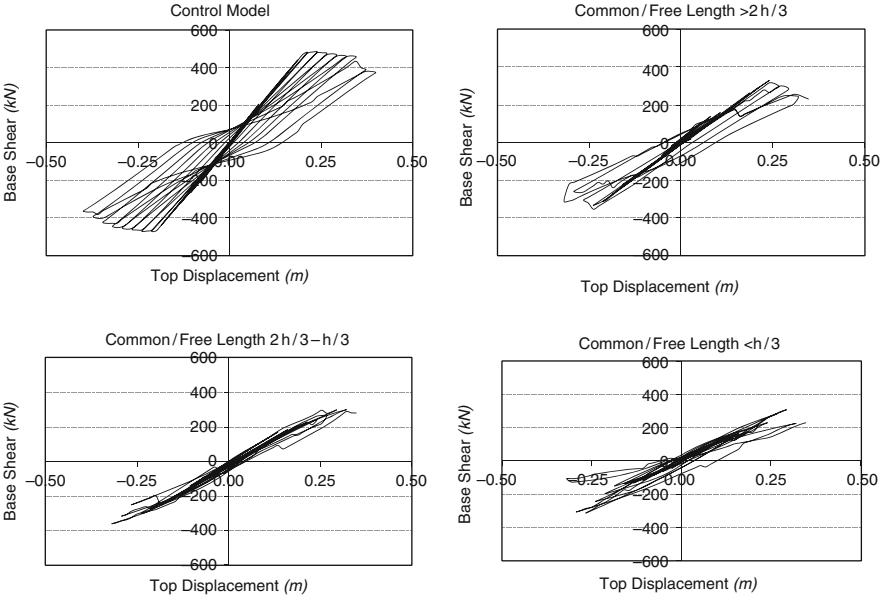


Fig. 12 Cyclic pushover plots for B1 when "Many" short columns exist in the building

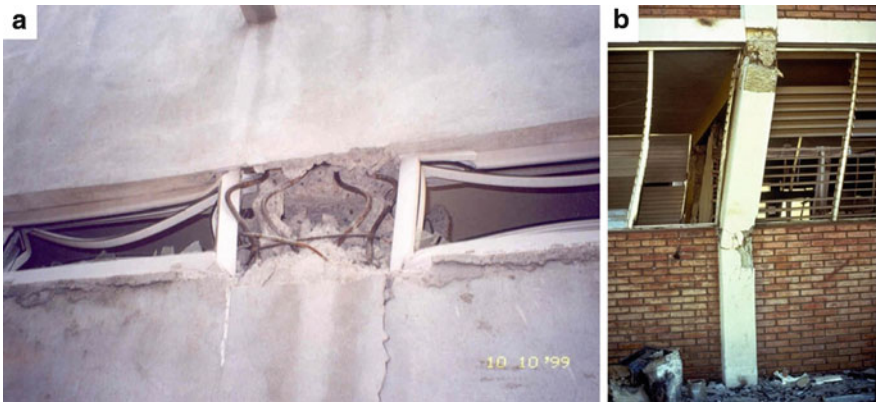


Fig. 13 Short column failures (**a**) from Kocaeli Earthquake of 1999 and (**b**) from Nicaragua Earthquake of 1972

Short columns which are restrained up until their mid-height (see Fig. 13b) and have the free length as half of the storey height exhibit the most unfavourable behaviour. The reason behind this is the development of the failure mechanism of the structure. In cases where the short columns are too short (less than 1/3 of the storey height) the stiffness of that critical storey increases drastically and the development of ductility is shifted to upper floor starting at the very beginning of the cycles. It is often forgotten that the earthquake forces are distributed as function of stiffness, thus, a floor with short columns is not necessarily the critical floor in which the most of the plastic deformations are expected. This aspect is well captured in the analyses thanks to the DAP methodology that has been used.

It is observed in recent earthquakes that the short columns around the band-windows (the free length of the column is less than 30% of the storey height in such cases) fail in shear but they do not cause a storey-mechanism or total collapse (see Fig. 13a). On the other hand, brittle failure of some of the storey columns at their mid-height can easily cause a shear-sway mechanism and decrease the overall energy dissipation capacity of the building (see Fig. 13b). Mid-height restrained short columns are mainly observed around the windows of the residential floors whilst the very short columns are found in commercial basement or ground floors. The short band windows, if they are placed at the basement floor, may be formed as holes on the earth-retaining walls which makes the stiffness difference between the rest of the frame and the short column segment even higher than the case of short column formed with infill walls.

Due to the brittle failure of the short columns, the important parameter that has to be accounted for is the energy dissipation rather than the strength of the building. It has been observed during the analyses that, even if the drop in the strength due to the existence of short columns is not significant the energy dissipation capability may drop quite significantly. For a given building and a given number of short columns, the drop in strength may be around 10% while the drop

Table 6 Energy based CDFs in existence of short columns

	B1 building			B2 building			B3 building		
Number of short columns	>2 h/3 (%)	2 h/3 − h/3 (%)	<h/3 (%)	>2 h/3 (%)	2 h/3 − h/3 (%)	<h/3 (%)	>2 h/3 (%)	2 h/3 − h/3 (%)	<h/3 (%)
Rare (<%5)	14	31	40	42	69	48	–	–	–
Some (%5–30)	24	52	51	51	80	58	77	84	86
Many (>%30)	50	78	68	45	89	53	77	93	88

Table 7 Suggested CDFs to be used in P25 Method (averaged from Table 6)

	Proposed CDF	
Number of short columns	>2h/3	≤2 h/3
Rare (<%5)	70	50
Some (%5–30)	50	30
Many (>%30)	45	20

in energy dissipation capability can easily reach up to 90%. This is the reason why the quantification of the existence of short columns has been done only in terms of the drop in the energy dissipation capability as shown in Table 6. Note that the B3 frame could not be run with the case where the short columns are rare (i.e. less than 5%) since even a single short column in that frame would result the number of short columns to be more than 5% in a floor.

The results of the analyses have been tabulated so that some simplistic CDFs can be used for the P25 Method. Suggested factors are given in Table 7. In Table 7, two different column free heights, >2 h/3 and ≤2 h/3, are considered for the sake of simplicity to facilitate the field application of the method. Experience during the pilot field applications of the method [18] showed that identification of the short column existence is much easier if column free heights are categorized in two groups instead of three, as done in the earlier versions of P25 Method.

5 Quantification of the Effect of Vertical Irregularities on the Seismic Response

There are several types of vertical irregularities existing in the RC building stock. The type of vertical irregularity investigated here is the columns of the upper floors supported by cantilever beams (see Fig. 14). In order to investigate the effect of such vertical irregularities, 1.5 m long cantilever beams, attached to columns, have been created in the case study buildings. Corbels have been represented with two or three frame elements and they are connected from the end of the cantilever to the column



Fig. 14 Vertical irregularity failure from Kocaeli Earthquake of 1999 (From [6])

(see Figs. 15 and 16). A nonlinear shear spring has been inserted in the point where the bottom of the corbel meets the column. Shear springs fail when the shear on the column reaches the shear strength. Shear strength of columns has been calculated by using the empirical formulae by [4].

It was observed that the type of irregularity studied in this chapter caused 10–35% decrease in the lateral strength and in the energy dissipation capacity. Two types of such irregularity have been considered: corbels along the full height of the ground floor columns and corbels from the mid-height of the columns. Corbels have been defined only at one side of the B1 building. In B2 building, corbels have been defined once at single side and then at both sides of the building. In cases where the corbels are full length of the columns, the situation is assumed as "Low" level of vertical irregularity. The rest of the investigated cases have been assumed as "High" level of vertical irregularity. Displacement-Based Adaptive Pushover (DAP) has been applied on the case study structures in positive and negative directions. Seismostruct software [22] has been used and displacement-based distributed-plasticity elements have been employed to model the structures.

The change in shear capacity, energy dissipation capability and the overall ductility have been defined in the form of CDF again. The calculated CDFs for the vertical irregularities exercised on the case study buildings have been given in Fig. 18.

As can be observed in Figs. 17 and 18, the vertical irregularities cause significant decrease in base shear capacity, energy dissipation capability and ductility. In the case when there are high vertical irregularities in the building, up to 45% decrease



Fig. 15 Considered vertical irregularities: (*left*) corbel along the full height of the column, and (*right*) corbel along half length of the column

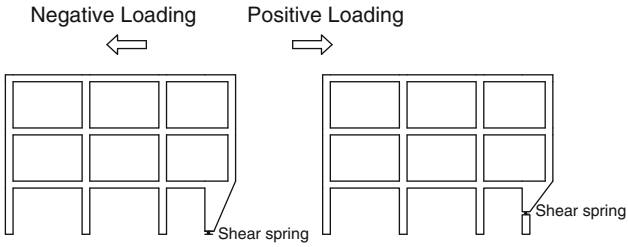


Fig. 16 Loading directions, position of the shear springs and combination of vertical irregularities used in modeling: corbels are along the full length of the ground floor columns (*left*), and corbels are from the mid-height of the ground floor columns (*right*).

in energy dissipation capability seems possible. Similarly, heavy vertical irregularity (i.e. existence of columns standing on the cantilevers in both façades of the building) the decrease in ductility is observed around 41% in the worst case. Base shear capacity, the indicator that seems to be affected the least, is observed to decrease around 10–15% when heavy vertical irregularities exist on the case study buildings. Such decreases in ductility and energy dissipation capacity are mainly attributed to

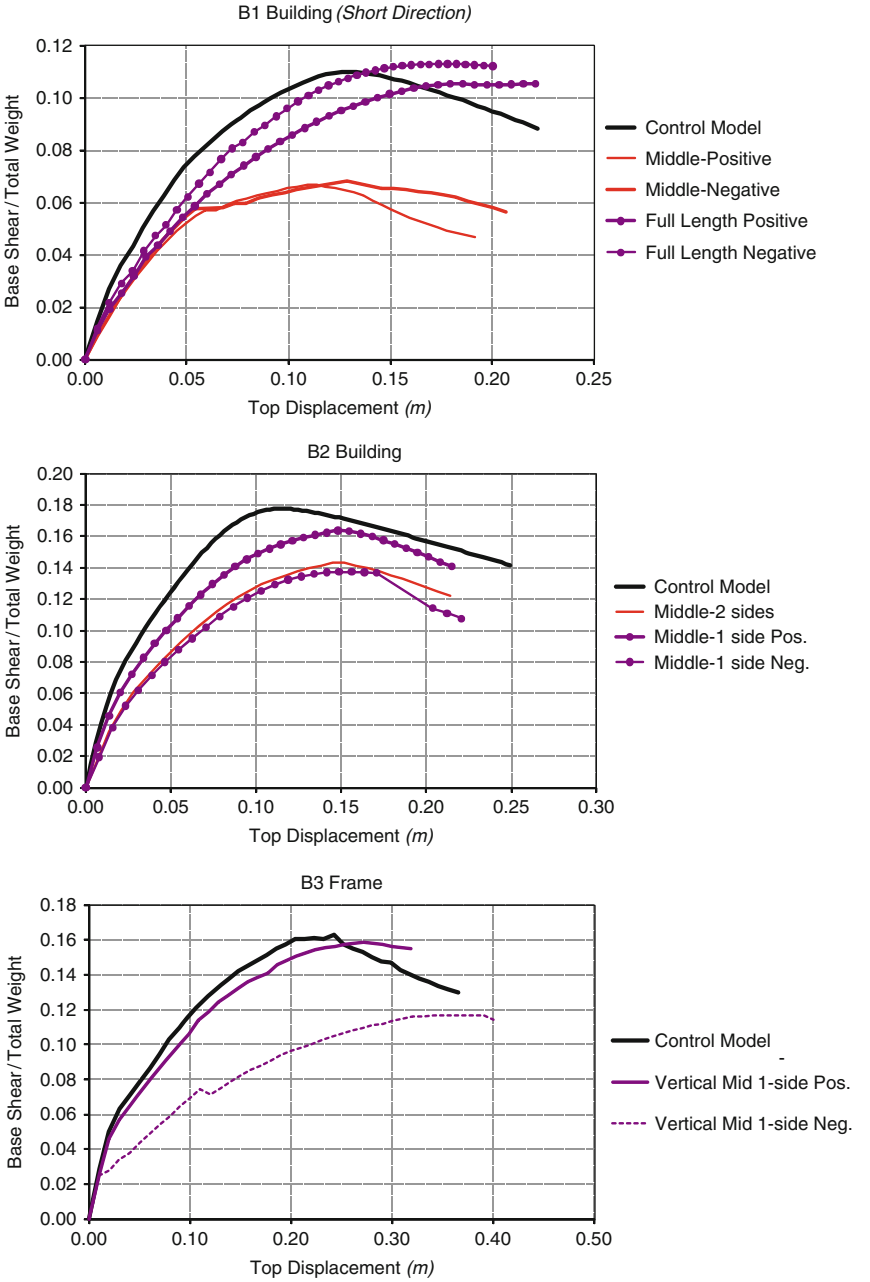


Fig. 17 DAP results for the three case studies for varying combinations of the vertical irregularities

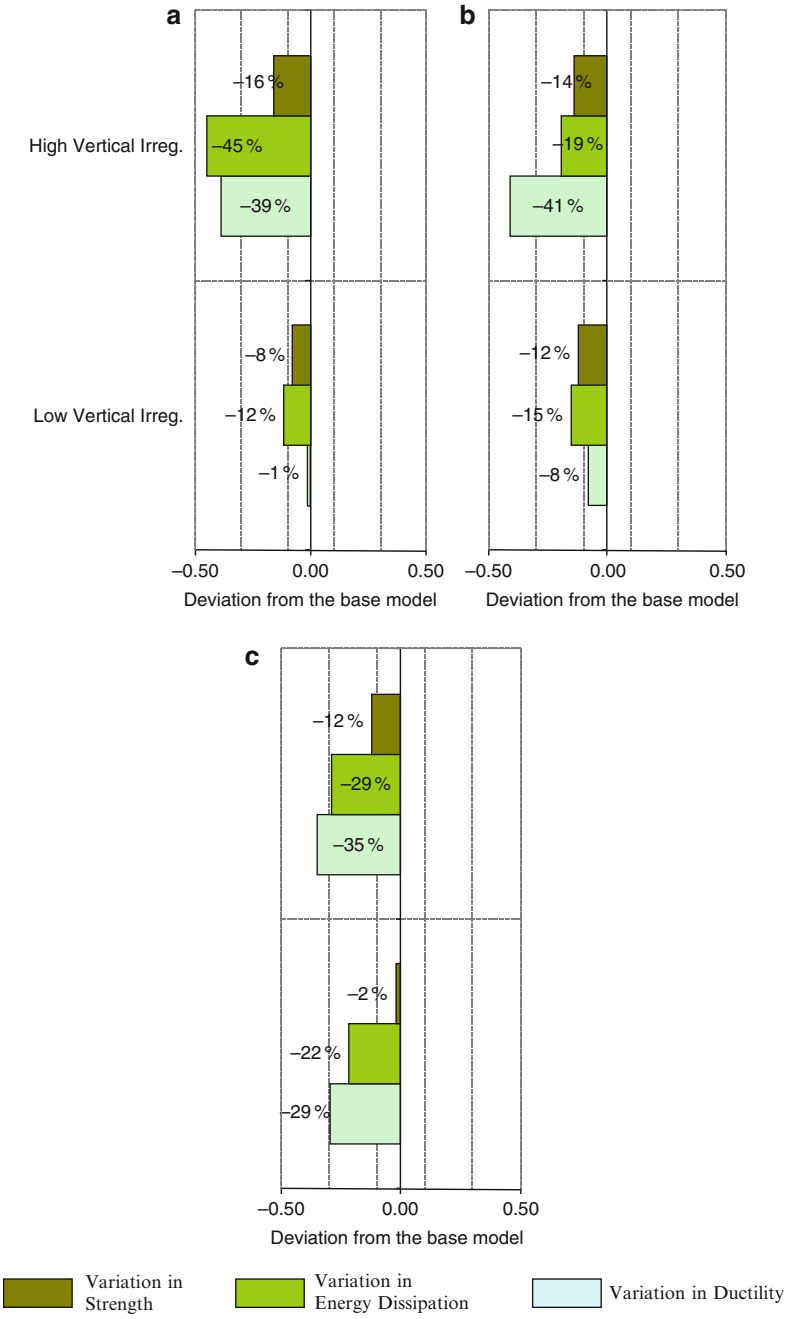


Fig. 18 The percentage deviations from the base model: (**a**) B1 building short direction, (**b**) B2 building, and (**c**) B3 frame

premature shear failure of the façade columns due to the increased shear demand on these members. Pushover plots in Fig. 17 also exhibit such a brittle behavior that manifests itself with sudden drops in the stiffness.

Suggested CDFs to be used in P25 Method are 0.65–0.70 when the vertical discontinuity is intense (i.e. the columns in both façades of the structure are supported on corbels). The CDF value when the discontinuity is at medium level is proposed as 0.90 reflecting the cases in which only some columns (corner columns in most of the cases) supported by corbels.

6 Conclusions

In this study the focus is on the quantification of some important structural parameters in terms of their effects on the seismic response of existing ordinary residential buildings. The aim for such an endeavor was to come up with some average and rather simplistic factors (called as CDFs in this chapter) that are expected to represent a given structural deficiency with a single scalar value.

The effects of the material quality, in terms of concrete quality and loss of diameter of the rebars have been investigated. It was found that concrete quality is a parameter that is clearly proportional to the building overall strength; however, the overall ductility is not necessarily in correlation with it. The effects of concrete quality on the overall building response has been quantified into single scalar values and the same values tried to be reached by a proposed simple formula that is based on the square-root of the strength of the concrete material. The proposed formula seemed in good agreement with the CDFs found in the analyses.

Analyses results show that the corrosion, additionally to the loss of strength, causes loss of ductility, and thus the energy dissipation capacity. The effects of loss of concrete cover and loss of rebar section have been included but the adverse effects of loss of anchorage between steel rebars and concrete material has been neglected due to difficulties in modelling and lack of empirical and experimental data.

Existence of short column in RC buildings has also been examined. The drop in energy dissipation capacity fluctuates between 30% and 70%, depending on the relative height of the short column and the number of short columns.

Vertical irregularities that are created by perimeter columns supported on corbels that are connected to the ground floor columns have been investigated as well. The CDF value suggested is around 0.65 or 0.70 in cases when such columns are frequent in the building (i.e. the perimeter columns in two façades of a building are supported on corbels). The CDF value is around 0.90 when the number of such columns is small (i.e. only the corner columns are sitting on corbels).

The method of quantification used herein is rather simplistic and the number of case studies is certainly not enough. However, all previous preliminary assessment methods, without exception, are based on such single scalar factors that are defined by engineering judgment. Therefore, this study should be evaluated by considering

it as a trial research work to overcome the previous use of parameters that are mostly based on engineering judgment or based only on engineering judgment that are meaningful but still vague.

Finally, the factors proposed to be used in P25 Method, or in any other similar assessment method, have been obtained by averaging the analyses results for three different buildings. In future studies, this number should certainly be increased and some sort of uncertainty should be associated with the average values so that the final outcome of the P25 Method is in probabilistic fashion.

References

1. BU-ARC (2002) Earthquake risk assessment for Istanbul metropolitan area. Project Report, Boğaziçi University and American Red Cross, Boğaziçi University Publications, Istanbul, Turkey
2. Akçay B, Önen YH, Öztekin E (2001) Definition of the concrete characteristics on structures in Istanbul (in Turkish). 16th Turkish Technical Congress and Seminar of Civil Engineering, 1–3 November, Ankara, Turkey
3. Bresler B (1997) Evaluation of earthquake safety of existing buildings: developing methodologies for evaluating the earthquake safety of existing buildings, Earthquake Engineering and Research Center, University of California, UCB/EERC77/06, 1977
4. Biskinis DE, Roupakias GK, Fardis MN (2004) Degradation of shear strength of reinforced concrete members with inelastic cyclic displacements. ACI Struct J 76(101):773–783
5. Carr AJ (2008) Ruaumoko2D – a program for inelastic time-history analysis. Department of Civil Engineering, University of Canterbury, New Zealand
6. Celep Z, Kumbasar N (2004) Introduction to the earthquake engineering and earthquake resistant design, 3rd edn. Beta Dagitim, Istanbul (in Turkish)
7. FEMA 154 (1988) Rapid visual screening of buildings for potential seismic hazards: a handbook Applied Technology Council, Federal Emergency Management Agency, Washington, DC
8. FEMA 154 (2002) Rapid visual screening of buildings for potential seismic hazards: a handbook, 2nd edn. Applied Technology Council, Federal Emergency Management Agency, Washington, DC
9. Hassan AF, Sözen MA (1997) Seismic vulnerability assessment of low-rise buildings in regions with infrequent earthquakes ACI Struct J 94(1):31–39
10. Ohkubo M (1990) The method for evaluating seismic performance of existing reinforced concrete buildings. Seminar in Structural Engineering, Department of AMES, University of California, San Diego, CA
11. Boduroğlu H, Özdemir P, İlki A, Şirin S, Demir C, Baysan F (2004) Towards a modified rapid screening method for existing medium rise RC buildings in Turkey. 13th World Conference on Earthquake Engineering, Vancouver, Canada, paper 1452, 2004
12. Bal IE (2005) Rapid assessment techniques for collapse vulnerability of reinforced concrete buildings (in Turkish). MSc thesis, Istanbul Technical University, Civil Engineering Department
13. Bal IE, Crowley H, Pinho R (2008a) Displacement-based earthquake loss assessment for an earthquake scenario in Istanbul. J Earthquake Eng 12(S2):12–22
14. Bal IE, Crowley H, Pinho R, Gülay G (2008b) Detailed assessment of structural characteristics of Turkish RC building stock for loss assessment models. Soil Dyn Earthquake Eng 28(10–11): 914–932
15. Bal IE, Gülay FG, Tezcan SS (2008c) A new approach for the preliminary seismic assessment of RC buildings: P25 Scoring Method. 14th WCEE, Beijing, China, paper 09-01-121, October, 2008

16. Öztekin E, Suvakçı A (1994) Concrete classification in Istanbul for buildings which ready mix concrete is used (in Turkish). Proceedings of the 3rd National Concrete Congress of Concrete, Istanbul, Turkey
17. Gülay FG, Bal IE, Gökçe T (2008a) Correlation between detailed and preliminary assessment techniques in the light of real damage states. J Earthquake Eng 12(S2):129–139
18. Gülay FG, Bal İE, Tezcan SS (2008b) Calibration of the P25 Scoring Method developed for the seismic safety of reinforced concrete buildings and its application on a pilot region (in Turkish). Final Report, Research Project No 106M278, TUBITAK (Turkish Scientific and Technical Research Council)
19. Miranda AP, Calvi GM, Pinho R, Priestley MJN (2005) Displacement-based assessment of RC columns with limited shear resistance, technical report. IUSS Press, Pavia, Italy
20. Akyüz S, Uyan M (1993) On the concrete quality of the buildings damaged during 1992 Erzincan earthquake 2nd National Earthquake Engineering Conference, 10–23 March, Istanbul, Turkey
21. Antoniou S, and Pinho R (2004) Development and verification of a displacement-based adaptive pushover procedure J Earthquake Eng 8:5
22. SeismoStruct Software (2010) Seismosoft, Version 5.0.3. [available at www.seismosoft.com]
23. Özturan T (2000) Structural material problems in Istanbul, 2nd Istanbul and Earthquake Symposium, May 27, Istanbul, Turkey
24. Tezcan SS, Bal IE, Gülay FG (2009) Risk management and a rapid scoring technique for collapse vulnerability of R/C buildings. In: Ilki A, Karadogan F, Pala S, Yuksel E (eds) Chapter 13, Seismic risk assessment and retrofitting with special emphasis on existing low rise structures. Springer, Dordrecht
25. Başaran V (2006) Comparison of the results obtained by pushover analysis and seismic index method for existing buildings (in Turkish). MSc thesis, Graduate School of Natural and Applied Sciences, Afyon Kocatepe University

Index

A
Aleatory, 285, 286
Analytical solutions, 364, 378, 473–474, 486, 568
Analytical tools, 559–581

B
Bearings, 50, 51, 57, 100, 101, 106, 107, 109–115, 121, 308, 321, 325, 568
Behaviour/Behavior factor, 62, 112, 202, 206, 212, 213, 218, 540, 552–555
Bilinear, 3, 22, 25, 26, 32–35, 38, 48, 69, 83, 85, 87, 90, 93, 126, 180, 190, 202, 208, 214, 408, 422, 476
Boundary element method, 246, 378, 379, 398
Bridges, 41–63, 99–122, 305, 422, 516, 517, 527–537, 541
Brittle behavior, 531, 580

C
Calibration of parameters, 559–581
Collapse assessment, 1–17
Collapse capacity spectra, 22, 34–39
Collapse tests, 5–6, 8
Concentrically braced frames, 178, 179, 184, 186, 189
Concrete
  dams, 455–486
  gravity dam, 427–454, 457, 466, 468, 470, 474
Constitutive law, 110, 151, 156–160, 204, 205, 249, 405, 411, 414, 424, 431
Cumulative damage effects, 9

D
Deformed shape, 125, 138, 140, 143, 180
Deterioration, 2–4, 6–13, 15, 17, 22, 293, 422, 428, 518, 522, 525, 527, 528, 535, 569
Discrete element methods (DEM), 246, 248, 250–252, 255, 256, 260, 266, 267
Discrete elements, 222, 223, 228, 232, 234, 251, 252, 255, 267
Drift, 9, 14–17, 23, 26, 27, 29, 50, 59, 124, 130, 131, 140, 142–144, 168, 169, 193–196, 202, 203, 207, 209, 211, 213–215, 218, 288, 292, 296, 301, 306, 307, 542–544, 546, 549, 555
Ductility, 22, 48, 62, 69, 83–84, 92, 93, 100, 101, 107, 108, 113, 125, 184, 190, 191, 193, 202–204, 206, 208, 218, 303, 447, 448, 450–452, 454, 529, 561, 566–569, 571, 572, 576, 577, 580
Dynamic instability, 23–24, 29, 39, 292, 293, 296, 303
Dynamic soil-structure interaction, 48–49, 105, 490

E
Earthquake engineering, 6, 8, 321
Earthquake excitation, 22, 37, 120, 243, 256, 258, 281, 460, 467, 474, 494
Earthquake response, 245, 246, 258, 266, 474, 571
Elastic and inelastic response, 129
Elastodynamics, 357–374
Epistemic, 285–287, 297, 303
Equivalent plastic strain, 179–184, 195
Eurocode 8 (EC8), 41–63, 103, 104, 125, 178, 290–292
Extended incremental dynamic analysis, 285–303

M. Papadrakakis et al. (eds.), *Computational Methods in Earthquake Engineering*, Computational Methods in Applied Sciences 21, DOI 10.1007/978-94-007-0053-6,
© Springer Science+Business Media B.V. 2011

F
Failure probability, 313, 315, 316, 326, 533
Fibre beam-column element, 402, 408, 414, 548
Finite element models, 8, 42, 48–49, 51, 59, 61, 102–107, 178, 189–190, 428
Finite elements, 47, 48, 59, 126, 139, 142–144, 147, 156–171, 202–205, 247, 251, 267, 335–337, 354, 357–374, 391, 402, 414, 419, 421, 456, 457, 464, 467–476, 491, 496–502, 510–512
Force-based element, 402, 404–405, 409, 415, 417, 424

G
Ground motion selection process, 42
Ground motion, 8–9, 12, 28–32, 34, 42, 44, 45, 47, 54, 59, 60, 62, 63, 67–94, 100, 124, 125, 127–128, 201, 209, 239, 242–245, 247, 266, 269, 270, 281–282, 286, 287, 290–293, 295–303, 306–309, 311, 312, 322, 326, 429, 475, 528–529, 533, 545

H
Harmonic functions, 366, 508, 510, 512
Hydrodynamic pressure, 433, 458–463, 465, 476–479, 490, 494

I
Interstory/Interstorey drift, 29–31, 50, 59, 124–125, 129–133, 138–140, 143, 144, 209, 210, 215, 218, 322, 529, 542–546, 548, 551, 553
Irregular buildings, 52–57, 59–60, 62

L
Large mass method, 358, 362–363, 365, 367–370
Large spring method, 358–359, 362, 363, 365, 367–370, 374
Latin hypercube sampling (LHS), 286, 288, 546, 548
Life-cycle cost assessment, 541
Life-cycle cost analysis, 539–555
Liquid container dynamics, 489–512
Local buckling, 180, 182, 190, 191, 193, 197, 198, 417

M
Masonry, 48, 221–234, 266, 267
Masonry structures, 221, 268
Moderate large displacements, 381, 386, 398
Mode shape, 25, 124–130, 134, 136, 139, 141–144, 202, 231–233, 292, 429, 462, 464, 495
Moment-shear interaction, 411
Monuments, 221, 222, 238–241, 246, 247, 266–268, 271, 273
Multidrum columns and colonnades, 245, 248, 256, 261

N
Natural-mode method, 402–404, 424
Nonlinear, 4, 25, 48, 67–84, 86, 88, 93, 94, 110, 111, 115, 117–119, 126, 160, 161, 163–165, 180, 202, 205, 218, 232, 244, 249, 251, 286, 306, 307, 327, 328, 358, 374, 377–398, 405, 421, 457, 508, 540, 545, 548, 566, 576
Non-linear analysis, 52–59, 80, 81, 180, 202–203, 233, 394–396, 398, 561
Nonlinear dynamic analysis, 43, 45–50, 52, 63, 377–398, 545
Nonlinear finite element analysis, 171
Non-linear static (pushover) analysis, 23, 106–107, 121, 206–209
Non-linear time-history analysis, 114, 551

O
Objective damage index, 202–204, 209, 217
Overstrength, 107, 113, 167, 202, 203, 208, 218

P
P-delta, 21–27, 31–34, 36, 37, 39
Penalty method, 357–374
Performance-based design, 67, 202
Performance-based earthquake engineering, 19
P25 method, 561, 566, 568, 575, 580
Preliminary assessment, 428, 559–581
Pushover analysis, 23–27, 32, 99–122, 202, 206, 211, 218, 232, 303, 432, 571

R
R/C building, 45–50, 58, 541, 547, 553, 560–561, 565–575, 580
Recorded accelerograms, 43
Rectangular hollow section, 178, 396, 418
Reinforced concrete, 2, 45, 46, 49, 100, 125, 148, 202, 206, 218, 286, 288, 303, 422, 542, 555, 571
Reinforced concrete bridge piers, 527–537
Reinforced concrete buildings, 45, 125, 541, 554
Response scatter, 60, 61
Restoration, 266, 271, 280, 282
Retrofit, 125, 131, 138, 143, 305, 540–544, 560
Rigid blocks, 222–223, 230–233, 241, 242, 244–246, 250, 252, 253, 258, 260, 268–269
Robust analysis, 346–351
Robust performance, 337, 339–340, 346–348
Robust synthesis, 345, 351–353
Rocking, 239, 241–245, 247, 258–261, 266, 276–279, 281, 282, 457, 473, 475
Rotation, 3, 7, 8, 11–13, 15, 17, 25, 26, 107, 108, 111, 114, 115, 117–119, 124, 125, 129–144, 158, 178, 180, 185–187, 193, 194, 197, 198, 225, 231, 242, 244, 248–252, 254–256, 267, 289, 290, 292–295, 301, 303, 334–336, 380, 381, 384, 402, 417, 421, 431, 457, 471, 481, 484, 485

S
Salt attack, 529
Seismic assessment, 42, 100, 107, 108, 123, 125, 410
Seismic base sliding, 427–454
Seismic design, 101, 178, 179, 184, 201, 202, 208, 213, 480, 491, 540
Seismic reliability analysis, 527–537
Seismic safety, 202, 213–218, 428, 451, 560
Shaking table, 245, 247, 474
Shear center, 380
Shear deformation coefficients, 379, 383, 384, 390, 391, 393, 394
Short-term static and dynamic loading, 165
Site response, 48, 49, 68, 69, 71–82, 84–94
Sliding, 114, 221, 233, 239, 241–243, 247, 250, 252, 258, 260, 261, 266, 267, 276–278, 281, 282, 427–454, 457, 466, 473–475, 486
Sloshing, 456, 461, 470, 472, 489–512
Smart beam, 354
Special concentrically braced frames, 178
Steel structures, 410, 424, 542
Stochastic load, 332
Structural concrete, 148–150, 165–171
Structural optimization, 539

T
Time-dependent boundary conditions, 357–374
Timoshenko beam, 377–399, 405, 412, 417, 421, 422
Torsion, 49, 50, 53, 99–122, 125, 135, 137, 139–141, 143, 144, 334, 401–424
Torsional effects, 207, 413, 421
Transient dynamics, 42, 63
Twin bridge, 50–52, 57–59, 61

U
Uncertainty, 42, 63, 69, 79, 82–93, 274, 286, 287, 293, 299–301, 303, 310, 313, 322, 328, 331–355, 525, 528, 532, 581

V
Variability, 42, 43, 59, 69, 79–82, 84, 86, 125, 139, 144, 228, 251, 285, 286, 293, 299, 306, 313, 440, 533, 549

Y
Yield mechanism, 178–179, 184–185, 187, 193, 195, 199